

**Copper(II) and Zinc(II) complexes of aroyl
hydrazones as potential Antitubercular agents**

Abeda Jamadar

PhD

University of York

Department of Chemistry

September 2012

Abstract

There is a continuing need to make new antitubercular drugs due to development of resistance towards present drugs. To do this, series of pyruvate hydrazones (PVAHs) and their respective Cu(II) complexes and Zn(II) complexes were synthesized and fully characterised. Variable temperature NMR studies of PVAHs indicate the presence of *E* and *Z* isomers in the solution. Determination of the obtained single crystal X-ray structures reveals that Cu(II) ion binds to PVAH ligand in 1:1 ratio resulting in square pyramidal geometry in most of the Cu(II) complexes, whereas Zn(II) ion binds to two PVAH ligands in 1:2 ratio giving rise to octahedral geometry. The electrochemical studies of Cu(II) complexes of PVAH performed using cyclic voltammogram indicate the presence of quasi-reversible behaviour assigned to a $\text{Cu}^{2+}/\text{Cu}^{1+}$ peak potential. This indicates structural reorganisation of Cu(II) square pyramidal geometry towards Cu(I) tetrahedral geometry. The tetrahedral geometry of a synthesized Cu(I) complex of PVAHs was confirmed by X-ray crystal structure.

The stability studies of selected PVAH ligands and their metal complex indicate that the investigated compounds were stable in extreme basic conditions, but they were unstable in extreme acidic conditions due hydrolysis of azomethine bond. However, stability of these compounds in physiological conditions, i.e. in PBS buffer, reveals that ligand hydrolyses slowly over a period of time, whereas the Cu(II) complex remains quite stable over a monitored period of 120 hours. Interestingly, dihydrazide analogue of PVAH was fairly stable in PBS buffer. EPR studies of investigated Cu(II) complexes in DMSO indicate that PVAHs remains strongly coordinated to Cu(II) centre.

The evaluation of the antimycobacterial activity showed that the anionic PVAHs and Zn(II) complexes are essentially inactive. Some of the corresponding neutral Cu(II) complexes, however, exhibit promising antimycobacterial activities if tested under high iron (8 μg Fe per mL) conditions. As observed for the related antimycobacterial agent isoniazid, the activity of the complexes decreases if the *M. tuberculosis* cells are grown under low iron (0.02 μg Fe per mL) conditions. The Cu(II) complexes may thus have a similar mode of action and may require an iron-containing heme-dependent peroxidase for activation.

A series hydrophobic cinnamaldehyde hydrazones (CAHs) and their Cu(II) complexes were also synthesized and tested for their antitubercular activity under similar conditions to that of PVAH series. But they failed to show any inhibitory activity due to their poor cellular uptake owing to their limited solubility in aqueous buffer.

Title page	i
Abstract	ii
Table of Contents	iii
List of Figures	ix
List of Schemes	xviii
List of Tables	xix
Acknowledgements	xxi
Declaration	xxii

Table of Contents

1. Chapter 1: Introduction	1
1.1. Overview	1
1.2. A brief introduction to tuberculosis	1
1.3. Mechanism of action of few antitubercular drugs	3
1.3.1. Isoniazid	3
1.3.1.1. Pharmacokinetics of INH metabolism in the human body	6
1.3.2. Pyrazinamide	8
1.3.3. Ethambutol	8
1.3.4. Rifampin	9
1.3.5. Flurorquinolone	9
1.4. Drawback of present antitubercular drugs	10
1.5. Cause for resistant strain of bacteria	11
1.5.1. The lipophilic cell wall of mycobacteria	11
1.5.2. Mutation in the katG gene	12
1.5.3. Acetylation of the hydrazinic chain (-NH-NH ₂)	13
1.6. Persistent/ latent bacteria	14
1.6.1. Role of glyoxylate shunt pathway in persistent bacteria	14
1.6.1.1. ICL inhibitors	15
1.7. Hydrazones and metal complexes as antitubercular agents	21
1.7.1. Hydrazones as antitubercular agents	22
1.7.2. Metal complexes as antitubercular agents	26
1.8. Project Aims	34

2. Chapter 2: Synthesis and Characterisation	35
2.1. Introduction	35
2.2. Synthesis of pyruvate hydrazones (PVAHs)	37
2.3. Synthesis of Cu(II) complexes of pyruvate PVAHs	40
2.3.1. ESI-MS of Cu(II) complexes of PVAHs	41
2.4. Synthesis of Zn(II) complexes of PVAHs	44
2.5. Nuclear magnetic resonance (NMR) studies	45
2.5.1. ¹ H NMR spectroscopic analysis of NaHL9	45
2.5.2. <i>E/Z</i> isomerisation of pyruvate hydrazone ligands	46
2.5.3. Trends in the ¹ H NMR data	49
2.5.4. ¹³ C NMR spectra of PVAHs	54
2.5.5. NMR analysis of the Zn(II) complexes of PVAHs	57
2.6. Infrared spectroscopic (IR) studies	60
2.7. Synthesis of Cu(I) complexes	65
2.7.1. ¹ H NMR analysis of the Cu(I) complexes	67
2.7.2. ³¹ P NMR analysis of [L9Cu ₂ (PPh ₃) ₅]PF ₆	68
2.7.3. Infrared analysis of the Cu(I) complexes	71
2.8. Synthesis of a di-hydrazide analogue of PVAH	72
2.8.1. Attempted reduction of a PVAH	72
2.8.2. Synthesis and characterisation of NaH ₃ D1	74
2.9. Synthesis of cinnamaldehyde hydrazones (CAHs)	80
2.10. NMR analysis of CAHs	81
2.10. Synthesis of Cu(II) complexes of CAHs	84
2.11. Infrared analysis of CAHs and their Cu(II) complexes	85
2.12. Reduction of azomethine (C=N) bond	86
2.13. Summary of chapter-2	87
3. Chapter 3: Structural investigation in the solid by single crystal X-ray crystallography	88
3.1. Introduction	88
3.1.1. Geometries of copper and zinc present in the biological system	89
3.2. Structural aspects of pyruvate hydrazone ligands	91
3.2.1. NaHL9.2H ₂ O	91
3.2.2. NaHL11.2H ₂ O	92
3.2.3. Packing diagram of NaHL9.2H ₂ O and NaHL9.2H ₂ O	94
3.2.4. Interaction of NaHL9.2H ₂ O and NaHL9.2H ₂ O with sodium	94

3.2.5.	H ₂ L20.H ₂ O	95
3.2.6.	Comparison of PVAHs with the literature data	96
3.3.	Structural aspects of cinnamaldehyde hydrazone ligands	99
3.4.	Significance of hydrogen bonding in medicinal chemistry	104
3.5.	Structural investigation of Cu(II) complexes of PVAHs	105
3.5.1.	Monomeric square pyramidal Cu(II) complexes	105
3.5.1.1.	[Cu(II)(L9)(H ₂ O) ₂]	105
3.5.1.2.	[Cu(II)(L11)(H ₂ O) ₂].H ₂ O	107
3.5.1.3.	Comparing [Cu(II)(L9)(H ₂ O) ₂] and [Cu(II)(L11)(H ₂ O) ₂].H ₂ O	108
3.5.1.4.	Comparing [Cu(II)(L8)(MeOH) ₂], [Cu(II)(L13)(H ₂ O)(MeOH)], [Cu(II)(L17)(H ₂ O) ₂] and [Cu(II)(L18)(MeOH) ₂]	111
3.5.2.	The dimeric Cu(II) square pyramidal complex	118
3.5.3.	Cu(II) octahedral complex of HL15	120
3.6.	Structural investigation of Cu(I) complexes of PVAHs	125
3.6.1.	Structural aspects of [Cu(I) ₂ HL9(PPh ₃) ₅]PF ₆ and [Cu(I) ₂ HL8(PPh ₃) ₅]PF ₆	125
3.6.2.	Structural aspects of [Cu(I) ₂ HL9(PPh ₃) ₄]PF ₆ .2Et ₂ O.2H ₂ O	126
3.6.3.	Comparison of [Cu(I) ₂ HL9(PPh ₃) ₅]PF ₆ [Cu(I) ₂ HL9(PPh ₃) ₄]PF ₆ .2Et ₂ O.2H ₂ O and [Cu(I) ₂ HL8(PPh ₃) ₅]PF ₆	128
3.7.	Structural diversity observed in copper complexes of pyruvate hydrazones	132
3.8.	Structural investigation of Zinc(II) complexes of PVAHs	135
3.8.1.	Structural aspects <i>mer</i> - [Zn(II)(HL7) ₂].H ₂ O.DMSO, <i>mer</i> - [Zn(II)(HL8) ₂].H ₂ O and <i>mer</i> - [Zn(II)(HL9) ₂].H ₂ O.CH ₃ OH	135
3.8.2.	Comparison of <i>mer</i> - [Zn(II)(HL7) ₂].H ₂ O.DMSO, <i>mer</i> - [Zn(II)(HL8) ₂].H ₂ O and <i>mer</i> - [Zn(II)(HL9) ₂].H ₂ O.CH ₃ OH	138
3.8.3.	Structural aspects of <i>mer</i> - [Zn(II)(HL13) ₂]	140
3.9.	Summary of chapter-3	142
4.	Chapter 4: Electrochemistry and EPR studies	144
4.1.	Introduction	144
4.2.	Redox properties of pyruvate hydrazones and their copper complexes	148
4.2.1.	Electrochemical investigation of PVAHs	149
4.2.2.	Electrochemical investigation of copper complexes PVAHs	150
4.2.2.1.	Electrochemical investigation of Cu(II) complexes of PVAHs	151

4.2.2.2.	Electrochemical investigation of Cu(I) complexes of PVAHs	159
4.2.2.3.	Comparing electrode potentials of Cu(II) complexes of PVAHs	168
4.3.	Electron Paramagnetic (EPR) studies	171
4.3.1.	EPR spectra of CuSO ₄ and [Cu(II)L14(H ₂ O) ₂]	171
4.3.2.	Comparison of EPR spectra of investigated Cu(II) complexes of PVAHs	172
4.4.	Summary of chapter-4	176
5.	Chapter 5: Stability studies and Antitubercular activity	177
5.1.	Introduction	177
5.2.	Stability studies of PVAHs and CAHs and their metal complexes at different pH	178
5.2.1.	Stability studies of NaHL20 and its Cu(II) and Zn(II) complexes	179
5.2.1.1.	Stability studies of NaHL20 at different pH	181
5.2.1.2.	Stability studies of [Cu(II)L20(H ₂ O) ₂] at different pH	186
5.2.1.3.	Stability studies of <i>mer</i> -[Zn(II)(HL20) ₂] at different pH	188
5.2.2.	Stability studies of NaHL9	189
5.3.	Stability studies of CAHs at different pH	192
5.3.1.	Stability of HCA1	192
5.3.2.	Stability studies of HCA5	194
5.3.3.	Stability of Cu(II) complexes of CAHs	197
5.4.	Stability studies in PBS buffer	200
5.4.1.	Stability studies of PVAHs in PBS buffer	200
5.4.2.	Stability of Cu(II) complexes of PVAHs in PBS buffer	203
5.4.3.	Stability studies of <i>mer</i> -[Zn(HL11) ₂] in PBS buffer	205
5.4.4.	Stability studies of the di-hydrazide analogue NaH ₃ D1	206
5.4.5.	Stability studies of CAHs in PBS buffer	207
5.5.	Comparing CLogP values of PVAHs and CAHs	209
5.6.	Antitubercular activity	210
5.6.1.	Antitubercular activity of PVAHs and their metal complexes	210
5.6.2.	Structure activity relationship (SAR) of active compounds (Cu(II) complexes) of the PVAHs series	220
5.6.3.	Antitubercular studies involving the CAH series	220
5.7.	Summary of chapter-5	223

6. Conclusions and Future Work	225
6.1. Overall conclusions	225
6.2. Future Work	229
7. Experimental	231
7.1. Materials	231
7.2. Instrumentation	231
7.3. X-ray crystallography	232
7.4. Stability studies using UV/vis spectroscopy	233
7.5. Electrochemistry	235
7.6. General synthetic procedure and characterisation detail of PVAHs	236
7.7. Synthetic procedure and characterisation detail of the dihydrazide analogue; NaH ₃ D1	250
7.8. General synthetic procedure and characterisation detail of Cu(II) complexes of PVAHs	251
7.9. Synthesis and characterisation detail of Cu(I) complexes of HL8 ⁻ and HL9 ⁻	262
7.10. General synthetic procedure and characterisation detail of Zn(II) complexes of PVAHs	265
7.11. General synthetic procedure and characterisation detail of CAHs	279
7.12. General synthetic procedure and characterisation detail of Cu(II) complexes of CAHs	289
7.13. Single crystal X-ray data	297
7.14. Antitubercular assay	317
Abbreviations	319
References	322
Appendices 1-23	CD
Appendix 1: VT NMR of NaHL13	
Appendix 2: ESI-MS spectra of selected Cu(II) complexes of PVAHs	
Appendix 3: X-ray crystallography data for NaHL9.2H ₂ O	
Appendix 4: X-ray crystallography data for NaHL11.2H ₂ O	

- Appendix 5:** X-ray crystallography data for $\text{H}_2\text{L20}\cdot\text{H}_2\text{O}$
- Appendix 6:** X-ray crystallography data for $[\text{Cu}(\text{L7})(\text{H}_2\text{O})(\text{MeOH})]$
- Appendix 7:** X-ray crystallography data for $[\text{Cu}(\text{L8})(\text{MeOH})_2]$
- Appendix 8:** X-ray crystallography data for $[\text{Cu}(\text{L9})(\text{H}_2\text{O})_2]$
- Appendix 9:** X-ray crystallography data for $[\text{Cu}(\text{HL9})_2\text{Cl}_2]$
- Appendix 10:** X-ray crystallography data for $[\text{Cu}(\text{L11})(\text{H}_2\text{O})_2]\cdot\text{H}_2\text{O}$
- Appendix 11:** X-ray crystallography data for $[\text{Cu}(\text{L13})(\text{H}_2\text{O})(\text{MeOH})]$
- Appendix 12:** X-ray crystallography data for
 $[\text{Cu}(\text{HL15})_2\text{Cu}(\text{HL15})(\text{L15})\text{Na}_23\text{H}_2\text{O}\cdot\text{CH}_3\text{OH}$
- Appendix 13:** X-ray crystallography data for $[\text{Cu}(\text{L17})_2(\text{H}_2\text{O})_2]$
- Appendix 14:** X-ray crystallography data for $[\text{L8Cu}_2(\text{PPh}_3)_5]\text{PF}_6$
- Appendix 15:** X-ray crystallography data for $[\text{L9Cu}_2(\text{PPh}_3)_5]\text{PF}_6$
- Appendix 16:** X-ray crystallography data for $[\text{L9Cu}_2(\text{PPh}_3)_4]\text{PF}_6\cdot 2\text{Et}_2\text{O}\cdot 2\text{H}_2\text{O}$
- Appendix 17:** X-ray crystallography data for *mer*- $[\text{Zn}(\text{HL7})_2]\cdot\text{H}_2\text{O}\cdot\text{DMSO}$
- Appendix 18:** X-ray crystallography data for *mer*- $[\text{Zn}(\text{HL8})_2]\cdot\text{H}_2\text{O}$
- Appendix 19:** X-ray crystallography data for *mer*- $[\text{Zn}(\text{HL9})_2]\cdot\text{H}_2\text{O}\cdot\text{CH}_3\text{OH}$
- Appendix 20:** X-ray crystallography data for *mer*- $[\text{Zn}(\text{HL13})_2]$
- Appendix 21:** X-ray crystallography data for HCA2
- Appendix 22:** X-ray crystallography data for HCA5
- Appendix 23:** PBS plots

List of figures

Figure 1.1: Map indicating TB affected areas	1
Figure 1.2: Schematic representation of the mycobacterial cell wall	2
Figure 1.3: Structure of fatty acid pathway inhibitors a) isoniazid, b) pyrazinamide, c) ethionamide and d) thiacetazone	3
Figure 1.4: Formation of active species of INH via step a) INH radical and step b) INH anion	4
Figure 1.5: Crystal structure of active site of InhA with bound INA-NADH adduct	4
Figure 1.6: Molecular representation of active site of InhA with bound INA-NADH adduct	5
Figure 1.7: Proposed metabolic pathway and metabolites of INH in the human body	6
Figure 1.8: Schiff base of conjugate of INH and vitamin B ₆	7
Figure 1.9: Arabinogalactam and peptidoglycan biosynthesis inhibitors a) Ethambutol b) Cycloserin c) amoxicillin	9
Figure 1.10: Rifampin	9
Figure 1.11: Fluoroquinolone antibiotics a) ciprofloxacin and b) levofloxacin	10
Figure 1.12: Amphipathic derivatives of INH	11
Figure 1.13: Synthetic analogue of the BH-NADH adduct	12
Figure 1.14: Acetylation of INH by NAT enzymes	13
Figure 1.15: Isocitrate lyase pathway	15
Figure 1.16: Isocitrate lyase inhibitors	16
Figure 1.17: Active site of the of the ICL C191S mutant with glyoxylate (GA) and 3-nitropropionate bound	17
Figure 1.18: Schematic diagram of the interactions of ICL with glyoxylate and succinate	17
Figure 1.19: Active site of ICL (pyruvyl moiety (purple) attached to the thiolate of Cys ¹⁹¹)	18
Figure 1.20: Sesterterpene sulphate	19
Figure 1.21: Hyrtiosin	19
Figure 1.22: (3-Bromo-4,5-dihydroxyphenyl)-(2,3-dibromo-4,5-dihydroxy-phenyl)-methanone	20
Figure 1.23: Biological applications of hydrazones	21
Figure 1.24: a) Thiosemicarbazones b) Semicarbazones c) Dithiocarbazates Hydrazide/hydrazones.	22
Figure 1.25: Isoniazid derivatives a) hydrazone b) Cyanoborane adduct of hydrazone	23
Figure 1.26: Cpf conjugate of fluoro-substituted hydrazone	24
Figure 1.27: Phthalazinyl hydrazone	25

Figure 1.28: Structures of pyruvic acid hydrazones (L1-L4) (left) investigated by docking studies involving ICL, L4 binding in the ICL active site	26
Figure 1.29: Iron complex of INH	28
Figure 1.30: Scheme illustrating the mode of action of self-activating antitubercular metallodrugs of INH	28
Figure 1.31: Schematic representation of the function of Mtb. FurA	30
Figure 1.32: Crystal structure of Δ I-SM co-crystallised with Zn^{2+}	31
Figure 1.33: Structure of <i>cis</i> -platin	32
Figure 1.34: Metal complex of fluorinated INH-hydrazones	33
Figure 1.35: Copper complex of carboxyamidrazone	33
Figure 1.36: Palladium complex of ciprofloxacin	34
Figure 2.1: Hydrazone	35
Figure 2.2: Positive high resolution ESI-MS spectrum of $[Cu(II)L9(H_2O)_2]$	41
Figure 2.3: Measured (top) and simulated (middle, bottom) positive ion high-resolution ESI-MS spectrum of $[Cu(II)L9(H_2O)_2]$	43
Figure 2.4: 1H NMR spectrum of NaHL11 recorded in d_6 -DMSO	45
Figure 2.5: 1H NMR spectrum (7.20 – 7.90 ppm) of a solution of NaHL9 in d_6 -DMSO showing major and minor peaks in the aromatic region	46
Figure 2.6: Stacked NMR spectra of NaHL9 in d_6 -DMSO recorded at the indicated temperatures	47
Figure 2.7: a) <i>Z</i> - amide form and b) <i>Z</i> - imine form and c) <i>E</i> isomers of PVAHs	48
Figure 2.8: Structure of investigated hydrazone/s for <i>Z</i> \rightarrow <i>E</i> isomerisation process	49
Figure 2.9: Plot of the 1H NMR chemical shifts of the N-H proton of the <i>Z</i> isomer of thirteen indicated PVAHs in d_6 -DMSO vs σ	54
Figure 2.10: ^{13}C NMR spectrum of NaHL9 in d_6 -DMSO	55
Figure 2.11: Plot of the ^{13}C NMR chemical shift of the C=N carbon of indicated thirteen PVAHs in d_6 -DMSO versus σ	56
Figure 2.12: 1H NMR spectrum of <i>mer</i> - $[Zn(HL9)_2]$ in d_6 DMSO shown in the range from 2.0 to 13.0 ppm	58
Figure 2.13: Stacked NMR spectra of NaHL9 in d_6 DMSO (top) and <i>mer</i> - $[Zn(HL9)_2]$ (bottom) in the region 7- 16.5 ppm	59
Figure 2.14: Overlaid IR spectra of NaHL9 (magenta), sodium pyruvate (red) and 4-methyl benzoic acid hydrazide (blue) in the region 1500-1750 cm^{-1} (bottom) and their corresponding structures (top)	61

Figure 2.15: Overlaid IR spectra of NaHL9 (blue), [Cu(II)L9(H ₂ O) ₂] (green) and <i>mer</i> -[ZnH(L9) ₂] (red) shown in the region 1000 – 1700 cm ⁻¹	63
Figure 2.16: Overlaid IR spectra of ligand NaHL9 (blue), [Cu(II)L9(H ₂ O) ₂] (green) and <i>mer</i> -[Zn(HL9) ₂] (red) in the region 1550 – 1670 cm ⁻¹	64
Figure 2.17: ¹ H NMR spectrum of [Cu(I) ₂ HL9(PPh ₃) ₅]PF ₆ in <i>d</i> ₄ -MeOH in the range 1.5-8.0 ppm	67
Figure 2.18: a) ¹ H NMR spectrum of [Cu(I) ₂ HL9(PPh ₃) ₅]PF ₆ in <i>d</i> ₄ -MeOH in the range 7.1 – 7.8 ppm (left) b) Structure of [Cu(I) ₂ HL9(PPh ₃) ₅]PF ₆ (right)	68
Figure 2.19: Stacked ³¹ P { ¹ H}S NMR spectra of a) [Cu(I) ₂ HL9(PPh ₃) ₅]PF ₆ at 298 K b) [Cu(I) ₂ HL9(PPh ₃) ₅]PF ₆ at 200 K c) free PPh ₃ at 298 K in <i>d</i> ₄ -MeOH	69
Figure 2.20: Stacked ³¹ P { ¹ H} NMR spectra of a) [Cu(I) ₂ HL9(PPh ₃) ₅]PF ₆ b) [Cu(I) ₂ HL9(PPh ₃) ₅]PF ₆ with added four equivalents PPh ₃ c) [Cu(I) ₂ HL9(PPh ₃) ₅]PF ₆ with added seven equivalents of PPh ₃ d) free PPh ₃ in <i>d</i> ₄ -MeOH	70
Figure 2.21: ¹ H NMR spectrum of NaH ₃ D1 in the region 1-18 ppm in <i>d</i> ₆ -DMSO	75
Figure 2.22: ¹ H NMR spectrum of NaH ₃ D1 in the region 2.20 – 2.40 ppm (right) and 7.20 – 7.80 ppm (left) in <i>d</i> ₆ -DMSO	76
Figure 2.23: a) Structure of NaH ₃ D1 showing <i>Z</i> isomer (left) and b) <i>E</i> isomer (right) with respect to azomethine bond (C=N) indicated in red	77
Figure 2.24: ¹ H NMR spectrum of NaH ₃ D1 in the region 3.60-5.80 ppm in <i>d</i> ₆ -DMSO	77
Figure 2.25: ¹ H- ¹ H COSY spectrum of NaH ₃ D1 in the selected region in <i>d</i> ₆ -DMSO	78
Figure 2.26: ¹ H NMR spectrum of NaH ₃ D1 in the region 9.70 – 10.20 ppm (left) and 16.30 – 16.40 ppm (right) of selected region in <i>d</i> ₆ -DMSO	79
Figure 2.27: ¹ H NMR spectrum of HCA3 in <i>d</i> ₆ -DMSO	82
Figure 2.28: Hammett plot of the ¹ H NMR chemical shifts of the amide (N-H) proton of ten indicated CAHs in <i>d</i> ₆ DMSO vs σ	83
Figure 2.29: Hammett plot of the ¹ H NMR chemical shifts of the azomethine proton (HC=N) proton of ten indicated CAHs in <i>d</i> ₆ DMSO vs σ	83
Figure 2.30: Overlaid IR spectra of ligand, HCA3 (blue) and its Cu(II) complex [Cu(II)(CA3) ₂] (magenta) in the region 1100 – 1700 cm ⁻¹	85
Figure 3.1: Structure of 2-pyridineformamide 3-piperidyl thiosemicarbazone (H Ampip)	88
Figure 3.2: Structure of a) [Cu(H Ampip)Cl ₂], b) [Zn(H Ampip)Br ₂], c) [Fe(Ampip) ₂]	89

Figure 3.3: Schematic representation of superoxide dismutase	90
Figure 3.4: ORTEP plot of the molecular structure of NaHL9.2H ₂ O	91
Figure 3.5: ORTEP plot of the molecular structure of NaHL11.2H ₂ O	92
Figure 3.6: a) Crystal structure packing. b) planes showing separation between two crystallographically equivalent ligands NaHL9.2H ₂ O	93
Figure 3.7: a) Crystal structure packing. b) planes showing separation between two crystallographically equivalent ligands NaHL11.2H ₂ O	93
Figure 3.8: Schematic representation of the Na ⁺ octahedral complex	94
Figure 3.9: ORTEP plot of the molecular structure of H ₂ L20.H ₂ O	95
Figure 3.10: Crystal packing diagram showing intermolecular hydrogen bonding interactions	96
Figure 3.11: General structure of pyruvate hydrazones with atom numbering scheme	97
Figure 3.12: ORTEP plot of the molecular structure of HCA2 and HCA5	99
Figure 3.13: Asymmetric unit cell of a) HCA2 and b) HCA5 showing the two planes passing through the aromatic rings	100
Figure 3.14: a) Crystal structure packing diagram showing interactions for CA4Cl b) Intramolecular hydrogen bonding interactions c) C-H--- π interactions for HCA2	101
Figure 3.15: a) Crystal structure packing diagram showing interactions for CA4NO ₂ b) Intramolecular hydrogen bonding interactions c) C-H--- π interactions for HCA5	102
Figure 3.16: General structure of CAH with atom numbering scheme	103
Figure 3.17: ORTEP plot of the molecular structure [Cu(II)(L9)(H ₂ O) ₂]	105
Figure 3.18: Addison's model to calculate τ values	106
Figure 3.19: ORTEP plot of the molecular structure [Cu(II)(L11)(H ₂ O) ₂].H ₂ O	107
Figure 3.20: Schematic representation of square pyramidal Cu(II) complexes, showing the atom numbering scheme used in this chapter	109
Figure 3.21: Planes passing through the copper complexes of two crystallographically independent molecules a) [Cu(II)(L9)(H ₂ O) ₂], b) [Cu(II)(L11)(H ₂ O) ₂].H ₂ O	111
Figure 3.22: ORTEP plot of the molecular structure [Cu(II)(L8)(MeOH) ₂]	112
Figure 3.23: Crystal packing of [Cu(II)(L8)(MeOH) ₂] showing hydrogen bonds with the symmetry generated molecules	112
Figure 3.24: ORTEP plot of the molecular structure [Cu(II)(L18)(MeOH) ₂]	113

Figure 3.25: ORTEP plot of the molecular structure [Cu(II)(L17)(H ₂ O) ₂]	114
Figure 3.26: ORTEP plot of the molecular structure [Cu(II)(L13)(MeOH)(H ₂ O)]	114
Figure 3.27: Crystal packing of [Cu(II)(L17)(H ₂ O) ₂] showing C-H--- π and intramolecular hydrogen bonding interactions	115
Figure 3.28: Crystal packing of [Cu(II)(L13)(H ₂ O)(MeOH)] showing C-H--- π and intramolecular hydrogen bonding interactions	115
Figure 3.29: a) ORTEP plot and b) crystal packing diagram of [Cu ₂ (HL9) ₂ Cl ₂]	118
Figure 3.30: ORTEP plot of the molecular structure [Cu(HL15) ₂]Na[Cu(HL15)(L15)]3H ₂ O.CH ₃ OH	121
Figure 3.31: Mercury plot of [Cu(HL15) ₂]Na[Cu(HL15)(L15)].3H ₂ O.CH ₃ OH showing the coordination around the sodium cation and intermolecular hydrogen bonding	122
Figure 3.32: Numbering scheme for [Cu(HL15) ₂] showing immediate bonds surrounding the Cu(II) centre, R= Ar-3-F, Feng Liu's copper complex R= Ar-2-OH	123
Figure 3.33: ORTEP plot of the molecular structure [Cu ₂ (I)HL9(PPh ₃) ₅]PF ₆	125
Figure 3.34: ORTEP plot of the molecular structure [Cu ₂ (I)HL8(PPh ₃) ₅]PF ₆	126
Figure 3.35: ORTEP plot of the molecular structure [Cu ₂ (I)HL9(PPh ₃) ₄]PF ₆ .2Et ₂ O.2H ₂ O	127
Figure 3.36: General structure of the Cu(I) complex showing the atom numbering scheme, R = 4-Me for [Cu ₂ (I)HL9(PPh ₃) ₅]PF ₆ , R= 4NO ₂ for [Cu ₂ (I)HL8(PPh ₃) ₅]PF ₆	128
Figure 3.37: Mercury plot of [Cu ₂ (I)HL9(PPh ₃) ₄]PF ₆ .2Et ₂ O.2H ₂ O illustrating the strongly asymmetric didentate carboxylate coordination to Cu(1) and intramolecular hydrogen bonding	129
Figure 3.38: Fujisawa three-coordinate Cu(I) complex	130
Figure 3.39: Schematic representation of different coordination modes of PVAH hydrazones	132
Figure 3.40: General structure showing numbering scheme for copper complex of PVAHs	134
Figure 3.41: a) ORTEP plot (50% probability ellipsoids) of the molecular structure of <i>mer</i> -[Zn(II)(HL7) ₂].H ₂ O.DMSO b) planes showing the meridional arrangement of the ligands around the Zn(II) centre.	136
Figure 3.42: ORTEP plot of the molecular structure of <i>mer</i> -[Zn(II)(HL8) ₂].H ₂ O	136
Figure 3.43: ORTEP plot of the molecular structure of <i>mer</i> -[Zn(II)(HL9) ₂].H ₂ O.CH ₃ OH	137

Figure 3.44: Mercury plot of <i>mer</i> -[Zn(II)(HL7) ₂]·H ₂ O.DMSO showing π interactions	138
Figure 3.45: Numbering scheme for zinc complexes showing immediate bonds around the Zn(II) centre, <i>mer</i> -[Zn(II)(HL7) ₂]·H ₂ O.DMSO, <i>mer</i> -[Zn(II)(HL8) ₂]·H ₂ O, <i>mer</i> -[Zn(II)(HL9) ₂]·H ₂ O.CH ₃ OH	139
Figure 3.46: ORTEP plot of the molecular structure of <i>mer</i> -[Zn(II)(HL13) ₂]	141
Figure 4.1: a) Normal Cu-S (cysteine) bonding interactions b) Cu-S (cysteine) bonding interaction in plastocyanin	145
Figure 4.2: Bis(1-methyl-4,5-diphenylimidazol-2-yl) ketone	146
Figure 4.3: X-band EPR spectrum of plastocyanin and D _{4h} CuCl ₄ ²⁻	147
Figure 4.4: CV of NaHL3 in DMSO over the potential range from +1.0 to -1.0 in the forward sweep at the scan rate of 100 mV s ⁻¹	149
Figure 4.5: CV of scan rate dependence for CuCl ₂ in DMSO over the potential range 7 from +1.0 to -0.5 in the forward sweep at the scan rate of 100, 200, 300, 400 mV s ⁻¹	150
Figure 4.6: CV of [Cu(II)L9(H ₂ O) ₂] in DMSO over the potential range from +1.0 to -1.0 in the forward sweep at the scan rate of 10 mV s ⁻¹	151
Figure 4.7: CV for [Cu(II)L9(H ₂ O) ₂] recorded at different scan rates in DMSO over the potential range from +1.0 to -0.5 V in the forward sweep at scan rates of 10 - 300 mV s ⁻¹	152
Figure 4.8: Scan rate dependence for [Cu(II)L9(H ₂ O) ₂] in DMSO over the potential range from +1.0 to -0.5 V in the forward sweep at the scan rate of 10 - 300 mV s ⁻¹	153
Figure 4.9: CV of NaHL8 in DMSO over the potential range from +1.0 to -1.0 in the forward sweep at the scan rate of 10 mV s ⁻¹	155
Figure 4.10: CV of [Cu(II)L8(H ₂ O) ₂] in DMSO over the potential range from +1.0 to -1.0 V in the forward sweep at the scan rate of 10 mV s ⁻¹	156
Figure 4.11: CV of scan rate dependence for [Cu(II)L9(H ₂ O) ₂] in DMSO over the potential range from +1.0 to -1.0 V in the forward sweep at the scan rate of 10- mV s ⁻¹	157
Figure 4.12: CV of scan rate dependence for [Cu(II)L8(H ₂ O) ₂] in DMSO over the potential range from +1.0 to -0.5 V in the forward sweep at the scan rate of 10 - 300 mV s ⁻¹	158
Figure 4.13: Structural reorganisation from Cu(II) → Cu(I) complex of PVAHs	159
Figure 4.14: CV of PPh ₃ in DMSO over the potential range from +0.5 to -0.5 V in the forward sweep at the scan rate of 30 mV s ⁻¹	160
Figure 4.15: CV of [HL9Cu ₂ (I)(PPh ₃) ₅]PF ₆ in DMSO over the potential range	161

	from -1.0 to +1.0 V in the forward sweep at the scan rate of 10 mV s ⁻¹	
Figure 4.16:	Ouali's Cu(I) complex	162
Figure 4.17:	CV of scan rate dependence for [Cu(I) ₂ HL9(PPh ₃) ₅]PF ₆ in DMSO over the potential range from +1.0 to -1.0 in the forward sweep at the scan rate of 10- 300 mV s ⁻¹	162
Figure 4.18:	Comparison of the CVs of [Cu(II)L9(H ₂ O) ₂] and [Cu(I) ₂ HL9(PPh ₃) ₅]PF ₆ in DMSO over the potential range from +1.0 V to -1.0 V at the scan rate of 10 mV s ⁻¹	163
Figure 4.19:	Overlaid CV of Cu(II)L8(H ₂ O) ₂ and [Cu(I) ₂ HL8(PPh ₃) ₅]PF ₆ in DMSO over the potential range from +1.0 V to -1.0 V at the scan rate of 10 mV s ⁻¹	164
Figure 4.20:	Overlaid CVs of [Cu ₂ (I)HL8(PPh ₃) ₅]PF ₆ , [Cu(II)L8(H ₂ O) ₂] and NaHL8 in DMSO over the potential range from -0.2 V to -1.0 V at the scan rate of 10 mV s ⁻¹	166
Figure 4.21:	Overlaid CV of [Cu(I) ₂ HL8(PPh ₃) ₅]PF ₆ , [Cu(I) ₂ HL9(PPh ₃) ₅]PF ₆ and TPP in the DMSO over the potential range from +1.0 V to -0.6 V at the scan rate of 50 mV s ⁻¹	168
Figure 4.22:	Structure of 2-aminopyridine-2-aminobiphenyl (N ₃ O-mpy)	170
Figure 4.23:	X-band EPR spectrum of a frozen solution of CuSO ₄ in DMSO	171
Figure 4.24:	X-band EPR spectrum of a frozen solution of [Cu(II)L14(H ₂ O) ₂] in DMSO	172
Figure 4.25:	Overlaid X-band EPR spectra of [Cu(II)L8(H ₂ O) ₂], [Cu(II)L13(H ₂ O) ₂], [Cu(II)L16(H ₂ O) ₂], [Cu(II)L14(H ₂ O) ₂]	173
Figure 4.26:	Overlaid X-band EPR spectra of CuSO ₄ , [Cu(II)L13(H ₂ O) ₂] and [Cu(II)L13(H ₂ O) ₂] at pH < 1.5 (black)	174
Figure 5.1:	Structures of a) the starting hydrazide b) the hydrazone NaHL21 c) the Cu(II) complex and d) the Zn(II) complex of NaHL20	179
Figure 5.2:	Electronic absorption spectra recorded for hydrazide (black spectrum), NaHL20 and its Cu(II) and Zn(II) complex in HEPES buffer at pH 7.4 and a concentration of 0.05 mM	180
Figure 5.3:	Electronic absorption spectra recorded for NaHL20 during acid titration using 0.01 M HCl in the pH range 1.4-4.4	181
Figure 5.4:	Titration curve obtained for NaHL20 at 300 nm during acid titration in the pH range 1.4-4.4	182
Figure 5.5:	Electronic absorption spectra recorded for NaHL20 during base titration using 0.01 NaOH in the pH range 4.3-11.6	183
Figure 5.6:	Titration curve obtained for NaHL20 at 310 nm during	183

base titration using 0.01 NaOH in the pH range 4.3-11.6	
Figure 5.7: Electronic absorption spectra recorded for [Cu(II)L20(H ₂ O) ₂] during acid using 0.01 HCl titration in the pH range 5.7 –2.4	186
Figure 5.8: Electronic absorption spectra recorded for [Cu(II)L20(H ₂ O) ₂] during titration with using 0.01 M NaOH base in the pH range 5.9 –12.2	187
Figure 5.9: Titration curve obtained for [Cu(II)L20(H ₂ O) ₂] at 346 nm in the pH range 1 2.4-12.3	187
Figure 5.10: Electronic absorption spectra recorded for [Zn(II)(HL20) ₂] in the pH range 1.4-11.9	188
Figure 5.11: Electronic absorption spectra recorded for NaHL9 during acid titration using 0.01 M HCl in the pH range 3.5-5.6	189
Figure 5.12: Electronic absorption spectra recorded for NaHL9 during base titration using 0.01 M NaOH in the pH range 5.8-11.6	190
Figure 5.13: Titration curve obtained for NaHL9 at 270 nm in the pH range 3.5-11.6	191
Figure 5.14: Electronic absorption spectra recorded for HCA1 in the pH range of 1-12	192
Figure 5.15: Titration curve obtained for HCA1 at 360 nm in the pH range 1.5-12.0	193
Figure 5.16: Electronic absorption spectra recorded for HCA5 during acid titration using 0.01 M HCl in the pH range of 7.1-1.7	194
Figure 5.17: Electronic absorption spectra recorded for HCA5 during base titration using 0.01 M NaOH in the pH range of 7.1-12.31	196
Figure 5.18: Titration curve obtained for HCA5 at 310 nm in the pH range 2.1 – 12.3	196
Figure 5.19: Electronic absorption spectra recorded for [Cu(CA1) ₂] during acid titration using 0.01 M HCl in the pH range of 7.9-2.4	198
Figure 5.20: Electronic absorption spectra recorded for [Cu(CA1) ₂] during base titration using 0.01 M NaOH in the pH range of 8.7-14.0	198
Figure 5.21: Titration curve obtained for [Cu(CA1) ₂] at 382 nm in the pH range 2.4-11.8	199
Figure 5.22: Electronic absorption spectra recorded for NaHL11 in PBS buffer - Day 1-6	201
Figure 5.23: Exponential decay obtained for NaHL11 at 270 nm over the period of 6 days in terms of hours with a t _{1/2} of 38 hours	201
Figure 5.24: Electronic absorption spectra recorded for NaHL14 in PBS buffer (0 – 120 hrs)	202
Figure 5.25: Exponential decay obtained for NaHL14 at 270 nm over the	202

	period of 6 days in terms of hours with a $t_{1/2}$ of 54 hours	
Figure 5.26:	Electronic absorption spectra recorded for $[\text{Cu}(\text{II})\text{L20}(\text{H}_2\text{O})_2]$ in PBS buffer - Day 1-6	203
Figure 5.27:	Electronic absorption spectra recorded for $[\text{Cu}(\text{II})\text{L14}(\text{H}_2\text{O})_2]$ in PBS buffer (0-49 hours)	204
Figure 5.28:	Electronic absorption spectra recorded for <i>mer</i> - $[\text{Zn}(\text{HL11})_2]$ in PBS buffer - Day 1-6	205
Figure 5.29:	Exponential decay of the absorption of <i>mer</i> - $[\text{Zn}(\text{HL11})_2]$ at 270 nm over the period of 6 days(117 hours) with a $t_{1/2}$ of 32 hours	205
Figure 5.30:	Electronic absorption spectra recorded for $\text{NaH}_3\text{D1}$ in PBS buffer (0 - 98 hr)	206
Figure 5.31:	Electronic absorption spectra recorded for HCA1 in PBS buffer solution over a period of 50 hours then acidified to pH 1.5 with HCl	208
Figure 5.32:	Suggested mechanism of action of Cu(II) complexes of PVAHs	214
Figure 5.33:	a) Formation of active pharmacophore, isonicotinic acyl radical from isonicotinic acid hydrazide (INH) b) formation of INH-NAD adduct	216
Figure 5.34:	Graphical representation of MICs of listed compounds in table 5.5 in μM concentration	219

List of schemes:

Scheme 1.1: Conversion of isocitrate to glyoxylate and succinate	14
Scheme 2.1: Hydrazone formation	36
Scheme 2.2: General synthetic scheme for the preparation of PVAHs	37
Scheme 2.3: General mechanism for the formation of PVAHs	38
Scheme 2.4: Synthesis of Cu(II) complexes of PVAHs	40
Scheme 2.5: Reduction of Cu(II) to Cu(I) complex with an addition of proton	42
Scheme 2.6: Synthesis of Zn(II) complexes of PVAHs	44
Scheme 2.7: Resonance forms of PVAHs	62
Scheme 2.8: Synthesis of Cu(I) complexes - $[\text{Cu(I)}_2\text{LR}(\text{PPh}_3)_5]\text{PF}_6$	66
Scheme 2.9: Suggested mechanism for the hydrolysis of hydrazones and oximes	72
Scheme 2.10: Attempted reduction of the azomethine (C=N) bond of NaHL9	73
a) NaBH_4 , refluxing under water for 24 hr, MeOH or H_2 , Pd/C (10%), 24 hr, MeOH	
Scheme 2.11: General synthetic scheme for $\text{NaH}_3\text{D1}$ a) NaHCO_3 , reflux in methanol for 4 hours	73
Scheme 2.12: Proposed mechanism for the formation of the di-hydrazide analogue; $\text{NaH}_3\text{D1}$	74
Scheme 2.13: Synthesis of cinnamaldehyde hydrazones and their Cu(II) complexes i) EtOH, 4h heated under reflux	80
Scheme 2.14: Synthesis of Cu(II) complexes of CAHs i) copper acetate dehydrate, MeOH, 2h	84
Scheme 2.15: Reduction of C=C bond i) H_2 , Pd/C (10%), 18 hours	86
Scheme 4.1: Synthesis of Cu(II) complex of PVAHs	149
Scheme 4.2: Synthesis of Cu(I) complex of PVAHs	159
Scheme 5.1: Mechanism for hydrolysis of PVAHs	185
Scheme 5.2: Reduction of HCA1 at olefin bond resulting in HCA1R	195
Scheme 5.3: Decomplexation of CAH from a Cu(II) complex	199

List of tables:

Table 2.1: Library of PVAHs with their compound codes and yields	39
Table 2.2: ¹ H NMR chemical shifts (in ppm) for the indicated PVAH protons, recorded in <i>d</i> ₆ -DMSO (NaHL1-NaHL20)	50
Table 2.3: ¹ H substituents-induced chemical shifts of N-H of the Z isomer for ligands NaHL1 - NaHL20	51
Table 2.4: Selected vibrational frequencies for NaHL9, [Cu(II)L9(H ₂ O) ₂] and [Zn(HL9) ₂]	64
Table 2.5: Compound code of CAHs along with their respective substituent and yield	81
Table 3.1: Comparison of selected bond lengths (Å) and bond angles (°) for the octahedral Na ⁺ environment in NaHL9.2H ₂ O and NaHL11.2H ₂ O	94
Table 3.2: Selected bond lengths (Å) for NaHL9.2H ₂ O, NaHL21.2H ₂ O, H ₂ L21.H ₂ O and two examples from the literature	97
Table 3.3: Selected bond angles (°) of NaHL9.2H ₂ O, NaHL11.2H ₂ O, H ₂ L21.H ₂ O and two examples from the literature	98
Table 3.4: Selected bond lengths (Å) and bond angles (°) for HCA2 and HCA5	103
Table 3.5: Selected bond lengths (Å) of [Cu(II)(L9)(H ₂ O) ₂] and [Cu(II)(L11)(H ₂ O) ₂]	109
Table 3.6: Selected bond angles (°) and τ values for complexes 1 and 2 of [Cu(II)(L9)(H ₂ O) ₂] and [Cu(II)(L11)(H ₂ O) ₂].H ₂ O	110
Table 3.7: Selected bond lengths (Å) for [Cu(II)(L8)(MeOH) ₂], [Cu(II)(L13)(H ₂ O)(MeOH)], [Cu(II)(L17)(H ₂ O) ₂] and [Cu(II)(L18)(MeOH) ₂]	116
Table 3.8: Selected bond angles (°) for [Cu(II)(L8)(MeOH) ₂], [Cu(II)(L13)(H ₂ O)(MeOH)], [Cu(II)(L17)(H ₂ O) ₂] and [Cu(II)(L18)(MeOH) ₂]	117
Table 3.9: Selected bond lengths (Å) and bond angles (°) of [Cu ₂ (HL9) ₂ Cl ₂]	119
Table 3.10: Selected bond lengths (Å) and bond angles (°) of neutral [Cu(HL15) ₂] and anionic Na[Cu(HL15)(L15)] in comparison with an example described in the literature	123
Table 3.11: Selected bond lengths (Å) [Cu ₂ (I)HL9(PPh ₃) ₅]PF ₆ , [Cu ₂ (I)HL9(PPh ₃) ₄]PF ₆ .2Et ₂ O.2H ₂ O, [Cu ₂ (I)HL8(PPh ₃) ₅]PF ₆	128
Table 3.12: Selected bond angles (°) for [Cu ₂ (I)HL9(PPh ₃) ₅]PF ₆ , [Cu ₂ (I)HL9(PPh ₃) ₄]PF ₆ .2Et ₂ O.2H ₂ O and [Cu ₂ (I)HL8(PPh ₃) ₅]PF ₆	131
Table 3.13: Selected bond lengths (Å) and bond angles (°) of NaHL9, [Cu(II)(L9)(H ₂ O) ₂], Cu(II)(HL9) ₂ Cl ₂ , Cu(II)(HL15) ₂ , [Cu ₂ (I)HL9(PPh ₃) ₅]PF ₆	134
Table 3.14: Selected bond lengths (Å) and bond angles (°) of	139

selected Zn(II) complexes of PVAHs

Table 3.15: Selected bond lengths (Å) and bond angles (°) of <i>mer</i> -[Zn(II)(HL13) ₂]	141
Table 4.1: ΔE values of [Cu(II)L9(H ₂ O) ₂] and ferrocene at different scan rate	154
Table 4.2: Electrode peak potentials [Cu(I) ₂ HL9(PPh ₃) ₅]PF ₆ and [Cu(II)L9(H ₂ O) ₂] reported versus SCE	163
Table 4.3: Electrode peak potentials [Cu(I) ₂ HL8(PPh ₃) ₅]PF ₆ and Cu(II)L8(H ₂ O) ₂ reported versus SCE	164
Table 4.4: ΔE values for [Cu(I) ₂ HL9(PPh ₃) ₅]PF ₆ and [Cu(I) ₂ HL8(PPh ₃) ₅]PF ₆ reported versus SCE	165
Table 4.5: Redox peak potentials of NO ₂ reported versus SCE	166
Table 4.6: E _{pa} and E _{pc} values for copper complexes at a scan rate of 100 mV s ⁻¹ reported versus SCE	169
Table 4.7: EPR data for selected for selected Cu(II) complexes of PVAHs	175
Table 5.1: Selected compounds with their structure and CLogP values	209
Table 5.2: MIC values of selected hydrazides along with INH under different conditions	211
Table 5.3: MIC values of selected PVAHs under different conditions	212
Table 5.4: MIC values of selected Cu(II) complexes of PVAHs obtained under the indicated conditions	213
Table 5.5: MIC values of selected hydrazides, PVAHs and their respective Cu(II) complexes in pM concentration under high iron conditions	218

Acknowledgments

Firstly I would like to thank my supervisor Dr. Anne-K. Duhme-Klair for giving me an opportunity to work in her group, for guidance and help throughout the PhD. I would like to thank my IPM, Prof. Robin Perutz for his ideas during the TAP meetings. I would also like to thank the Medical Research Council and Holbeck Charitable Trust for the Dorothy Hodgkin Post-graduate award funding.

My extended thanks to a number of people at the chemistry department in York. Trevor Dransfeild and Karl Heaton for the mass spec service, Heather Fish for the variable temperature NMR, Adrian Whitwood, Rob Thatcher and Sam Hart for crystallography. Special thanks to Adrian Whitwood for being very patient and helpful while teaching the skills of single crystal X-ray crystallography. Phil Helliwell and Graeme McAllister for elemental analysis and Steve Hau and Mike at stores. Naser Jasim's help for ^{13}P NMR and Iman for general assistance.

Many thanks to project students Chris McDonald and Peter Morris who have contributed towards this project. A huge thanks to Dr. Manjula Sritharan and her research group, especially Kiranmayi for all the antitubercular studies.

I feel really happy to have met such great friends at York, who have greatly contributed towards my time at York. A special thanks to Maria who has been my close companion and for her help related to chemistry and non-chemistry issues. I would like to extend my thanks to my current and past group members Cath, Chris C, Dan, Emma, Stephen and Shima. Thanks to all my friends including Luisa, Christine, Aimee, Andy, Rob T, Rob M, Natalie, Shalini and all the Chechik, Perutz and SLUGGS group members.

The list of acknowledgments would not be complete without mentioning my mentor Prof. Subhash Padhye who I met during my M.Sc at University of Pune, India. I express my deep sense of gratitude towards him as he has greatly contributed towards my journey of research. I would like to thank him for his guidance and support during my tough times. My sincere thanks to his wife Ms. Kalpana Padhye for her support and his current research groups members Prasad and Alok.

Lastly, I would like to thank my parents and all my family members who have helped me to achieve my dreams.

Declaration:

The following work was carried out by or with the assistance of other researchers:

- The synthesis and related studies on CAHs were carried out by MChem project student Chris McDonald
- The synthesis and related studies on NaHL12, NaHL13, [CuL12(H₂O)₂] and [CuL13(H₂O)₂] were carried out by BSc project student Peter Morris
- X-ray crystallography was carried out with the help of Dr. Adrian Whitwood, Dr. Robert Thatcher and Dr. Sam Hart
- Variable temperature (VT) ¹H NMR spectroscopic investigations were carried out by Heather Fish and VT ³¹P NMR spectra were recorded by Dr. Naser Jasim
- ESI-MS was carried out by Dr. Trevor Dransfield and Dr. Karl Heaton.
- Elemental analysis were performed by Dr. Phil Helliwell and Dr. Graeme McAllister
- EPR spectra were recorded in Dr. Victor Chechik's laboratory by Mr. Kazim Naqvi
- Antitubercular activity studies were carried out by our collaborator Dr. Manjula Sritharan and her research group at the University of Hyderabad, India.

All other work was performed by the author.

Chapter-1
Introduction

1.0 Introduction

1.1 Overview

Tuberculosis (TB) is a globally significant disease that has led to billions of deaths worldwide. Although the current methods of treating TB are effective, the persistence of bacilli and the widespread emergence of resistance against current antibiotics is a significant cause of concern. The broad goal of this bio-inorganic project was to design an array of novel metal-based antitubercular agents using simple yet potent organic ligands, such as hydrazones.

1.2 A brief introduction to tuberculosis

Tuberculosis is one of the most serious infectious airborne diseases, affecting one third of the world's population. Statistics from 2009 indicate that around 9.2 million people develop TB every year, while 2 million people succumb to the disease (WHO, 2009). As indicated in figure 1.1, TB has severely affected Asian and African countries¹ and if the spread of the disease is not contained, it could pose a worldwide threat with an estimated 1 billion people affected by 2020.²

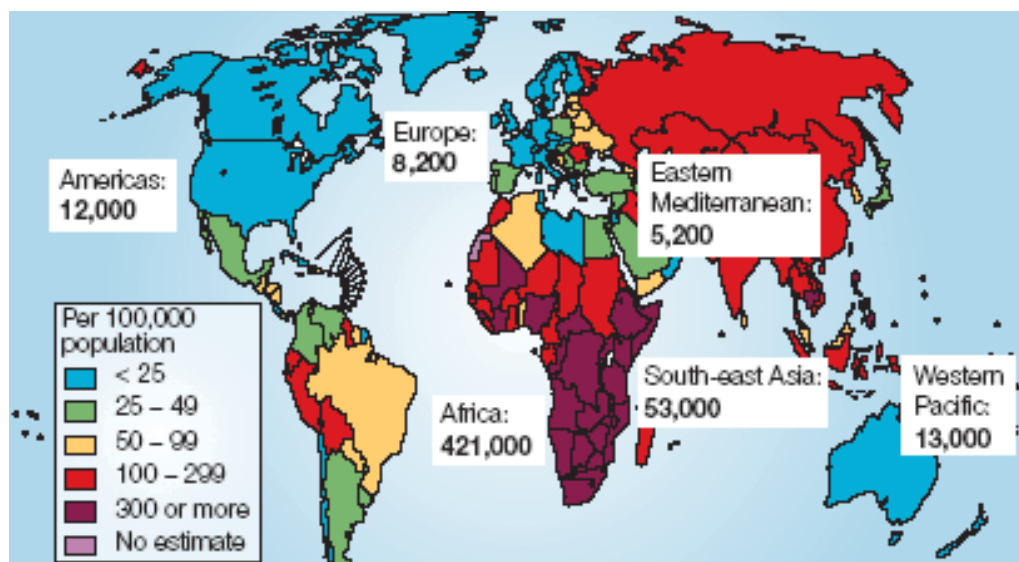


Figure 1.1: Map indicating TB affected areas.¹

TB generally affects the respiratory system but may also spread to other parts of body such as the brain, spleen, bones and gastrointestinal tract. The symptoms of TB are a persistent dry cough for more than 3 weeks and in later stages coughing up of blood, loss of appetite, anaemia and diarrhoea. If not treated

in time TB can eventually lead to death in certain cases.³ TB is caused by a bacterial species known as *Mycobacterium tuberculosis* (Mtb), which is generally characterised as an aerobic, slow growing and non-motile species. The majority of mycobacterial species replicate freely in the natural ecosystem, but only a small number of them are able to successfully inhabit the intracellular environment of mononuclear phagocytes in higher vertebrates. These species include *Mycobacterium leprae*, *Mycobacterium lepraemurium*, *Mycobacterium avium* subsp. *Paratuberculosis*, and the members of the *Mycobacterium tuberculosis* complex.⁴

The cell wall of Mtb consists of a lipid bilayer made up of peptidoglycans and complex lipids such as mycolic acid, as shown in figure 1.2. The extraordinary structure of the cell wall allows the bacteria to lie dormant in latent infections for many years.⁵

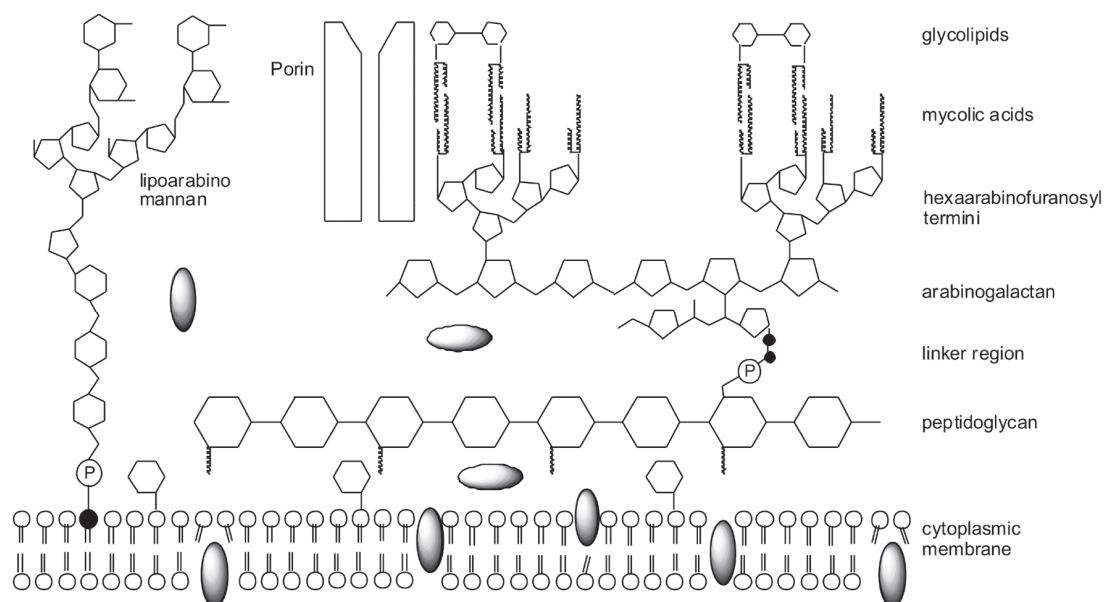


Figure 1.2: Schematic representation of the mycobacterial cell wall⁵

Due to the lipophilic nature of the cell wall, hydrophilic molecules cannot cross the cell wall efficiently, which is a major concern as this can lead to drug resistance.⁶ Directly Observed Therapy-Short course (DOTS) therapy is used to treat TB, which is a combination of widely used first line drugs such as isoniazid, rifampin, ethambutol and pyrazinamide prescribed for 2 months, followed by isoniazid and pyrazinamide for the next 4-5 months.⁷ The mechanism of these four widely used drugs is discussed in detail in the following section.

1.3 Mechanism of action of few antitubercular drugs

The complex lipid bilayer of the cell wall, arising from the extensive long chain fatty acid framework, acts as a barrier against chemical damage. Most of the antitubercular drugs, which include isoniazid⁸, pyrazinamide⁹, ethionamide¹⁰ and thiacetazone¹¹ (figure 1.3) act on the fatty acid biosynthesis mechanisms. The suggested mode of action for these antibiotics involves the inhibition of enzymes, such as InhA, FabH, MabA, Kas B involved in the fatty acid synthesis pathways.¹²⁻¹⁴

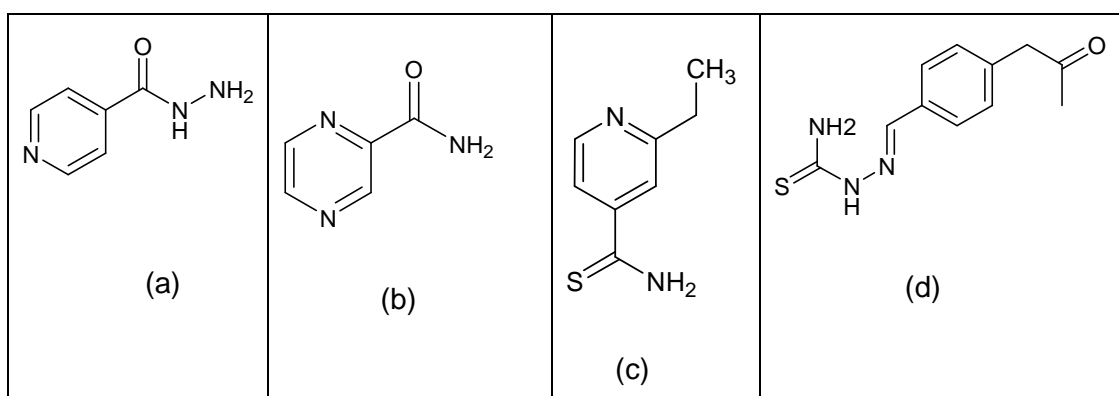


Figure 1.3: Structure of fatty acid pathway inhibitors a) isoniazid, b) pyrazinamide, c) ethionamide and d) thiacetazone

1.3.1 Isoniazid

Isonicotinic acid hydrazide, commonly called isoniazid (INH), discovered in 1952, was a major breakthrough in antitubercular drug design as it is a highly active and inexpensive that does not possess serious side effects. Since its discovery, isoniazid is the most commonly used drug worldwide for treating TB infections. This frontline anti-TB drug has a remarkably low minimum inhibitory concentration (MIC) of 0.1-0.7 μ M in the human body and is very specific to Mtb.¹⁵ This has encouraged several researchers to investigate the mechanism of action of INH.

INH inhibits mycolic acid biosynthesis,⁸ however, it has been proposed that the molecule itself does not possess any inhibitory action¹⁵ but instead acts as a pro-drug, which was thoroughly investigated by Rozwarski *et al.*¹⁶ Once inside the bacterial cell, INH is converted into its activated form, the INH radical or anion with the help of Mtb catalase-peroxidase (KatG), as indicated in figure 1.4.

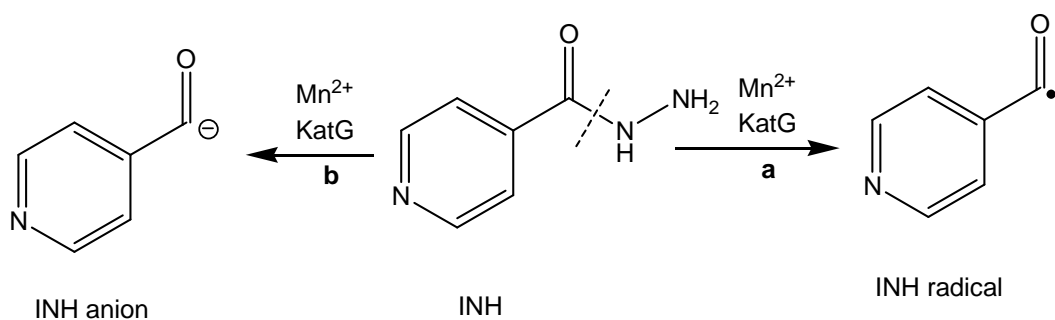


Figure 1.4: Formation of active species of INH via step a) INH radical and step b) INH anion¹⁶

The resulting active species of INH form a covalent bond with nicotinamide adenine dinucleotide (NADH) to produce an isonicotinic acyl (INA)-NADH adduct, which then inhibits the InhA enzyme.¹⁵⁻¹⁷ InhA is an enoyl-acyl carrier protein (ACP) reductase that is known to catalyse the NADH dependent reduction of an alkene bond within a fatty acid chain. The resulting products of the InhA catalysis are used by Mtb to generate mycolic acids, which are long chain fatty acids, and are considered to be essential components of the bacterial cell wall. The INA-NADH adduct occupies the active site of the InhA enzyme, as indicated by crystal structure analysis (figure 1.5) and binds to the neighbouring amino acid side chains.¹⁶

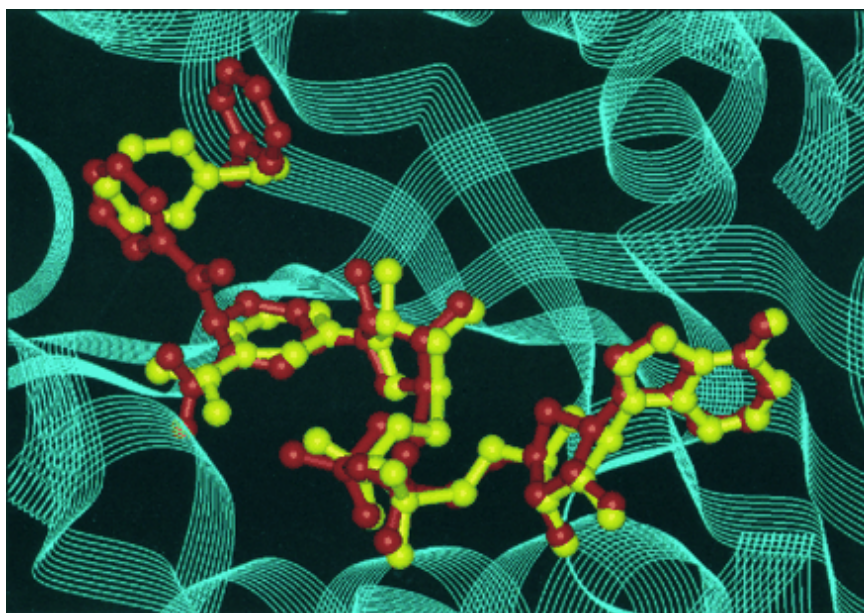


Figure 1.5: Crystal structure of active site of InhA with bound INA-NADH adduct¹⁶

The molecular representation of the active site of InhA with the bound INH-NADH adduct is illustrated in figure 1.6. The INA moiety of the INA-NADH adduct is shown in red, whereas the NADH is shown in blue and the amino acid side chains are shown in green. Numbers indicated in black are in Å units and represents the atomic spacing between the selected atoms. The conformational difference between the active site of the native enzyme and that of bound INA-NADH adduct is the orientation of Phe¹⁴⁹ amino acid side chain. In the native form of the enzyme, the side chain of Phe¹⁴⁹ lies directly above the nicotinamide ring. In the bound INA-NADH adduct, however, the side chain of Phe¹⁴⁹ is rotated away from the nicotinamide ring, thus allowing space for INA group, as indicated in figure 1.6.¹⁶ Upon blocking the active site of InhA the enzyme fails to produce the fatty acid chains, which form the integral part of the cell wall. This may eventually lead to bacterial cell death. Ser⁹⁴ indicated in magenta (figure 1.6), is responsible for INH resistance which is converted into Ala in resistant strains.

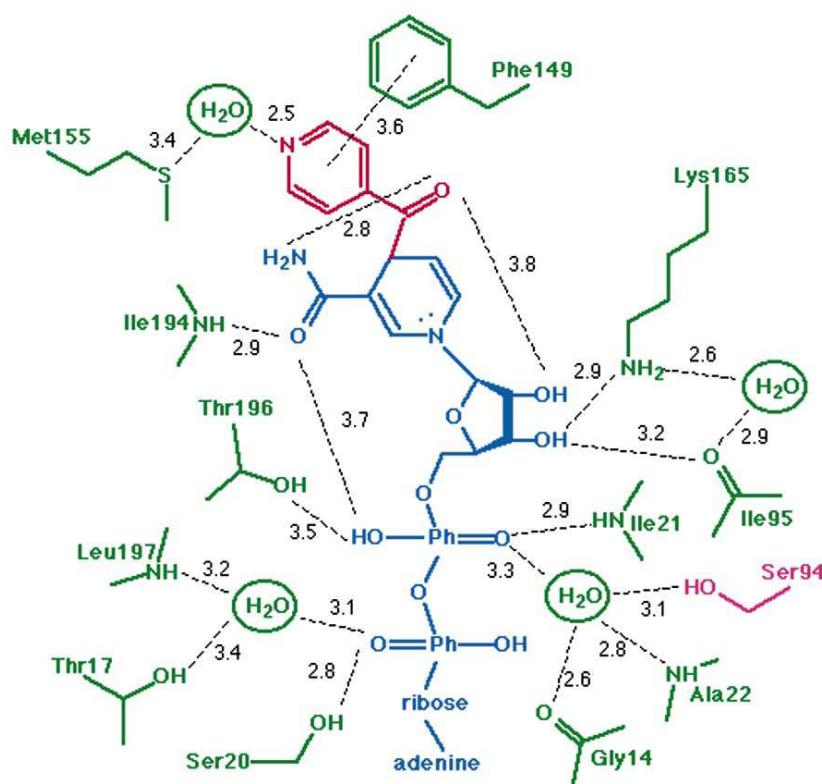


Figure 1.6: Molecular representation of active site of InhA with bound INA-NADH adduct¹⁶

1.3.1.1 Pharmacokinetics of INH metabolism in the human body

A detailed investigation of the pharmacokinetics of INH in the human body was performed by Ellard and Gammon.¹⁸ The analysis of blood and urine samples suggests that INH is eventually metabolised into a series of metabolites by the human body, as indicated in figure 1.7. Some of these metabolites may inactivate INH and hence prove an obstacle in the mechanism of its action on Mtb. Depending on the rate at which these metabolites are produced, they can be classified as slow and fast inactivators of INH. Hence, the therapeutic dose and length of the treatment may vary in different individuals.

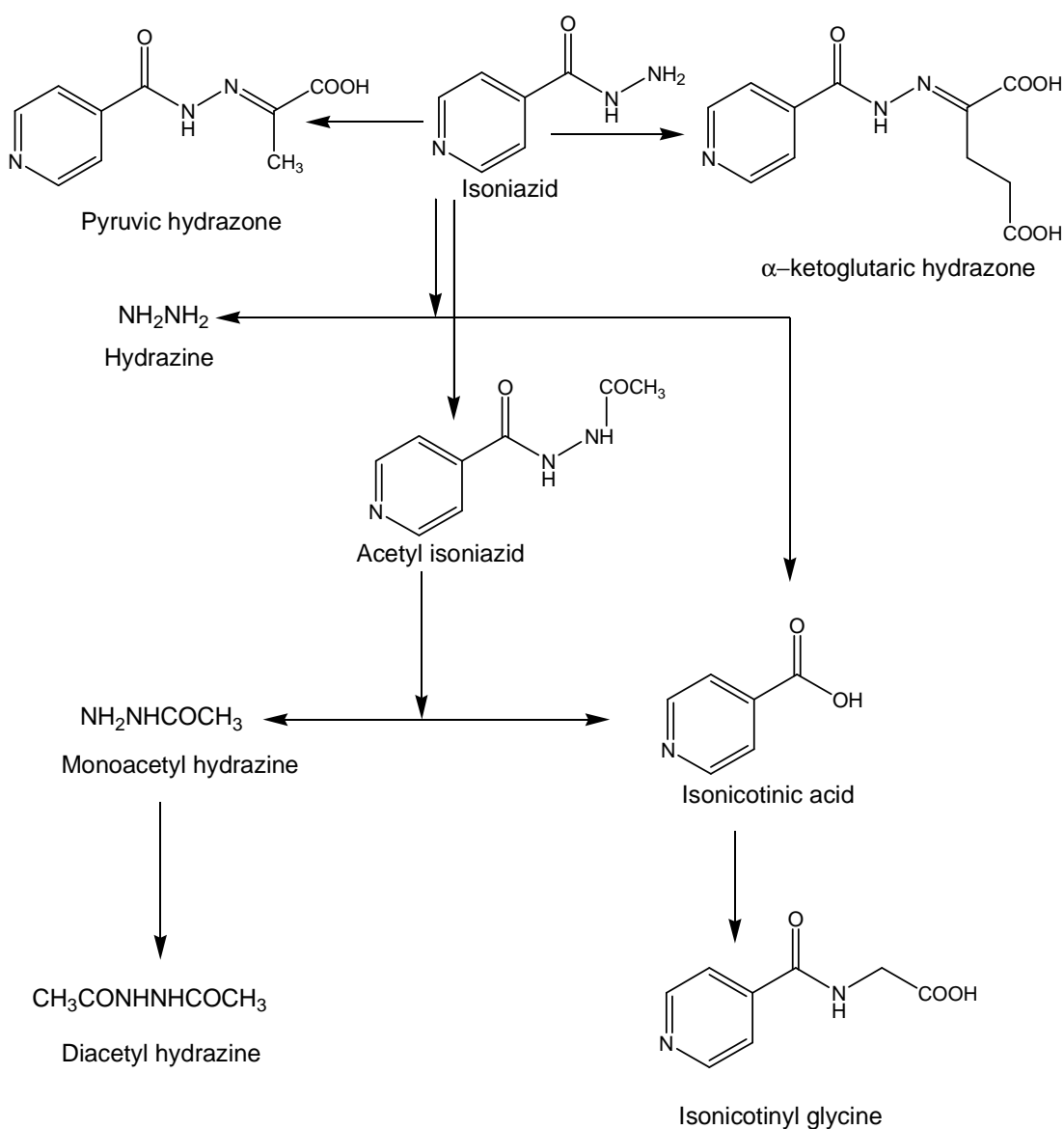


Figure 1.7: Proposed metabolic pathway and metabolites of INH in the human body¹⁸

Ellard and Gammon proposed that INH can be converted directly into its acid form in human body as indicated in the figure 1.7. Although it was also hypothesized that isonicotinic acid can be formed via the intermediate acetyl isoniazid. This intermediate product is caused by the enzymes known as acetylators present in the human body. The acetylators which can be classified as fast and slow acetylators determine the rate of formation of acetyl isoniazid. The calculated values indicate that fast acetylators acetylate the INH three to four times faster than the slow acetylators. Furthermore, it was observed that in slow acetylators, the rate of formation of isonicotinic acid and isonicotinyl glycine was increased when compared to that of fast acetylators. Isonicotinyl glycine, another metabolite of INH, is a result of conjugation of amino acid glycine with isonicotinic acid.¹⁸

Subsequently, hydrazine and its other analogues, which include mono-acetyl and di-acetyl hydrazine, are also produced as by-products of these metabolites. An enzyme that catalyses the hydrolysis of acetyl isoniazid to give isonicotinic acid and mono-acetyl hydrazine that undergoes further acetylation resulting in the formation of di-acetyl hydrazine, which is excreted from the body as evident from the urine samples of INH administered individuals. The amount of di-acetyl hydrazine excreted also depends on the rate of the acetylation process, which can be accredited to the fast and slow forms of these enzymes.

INH is also known to form Schiff base conjugates with pyruvic acid and α -ketoglutaric acid in the body to give the respective hydrazones, as shown in figure 1.7. This could prove to be a drawback as it could conjugate with carbonyl-containing compounds that might be essential for normal metabolic processes. For example, INH is known to combine with vitamin B₆ (figure 1.8) resulting in patients suffering from the effects of B₆ deficiency.¹⁹ Hence, TB patients who are being INH are given additional supplements of vitamin B₆.

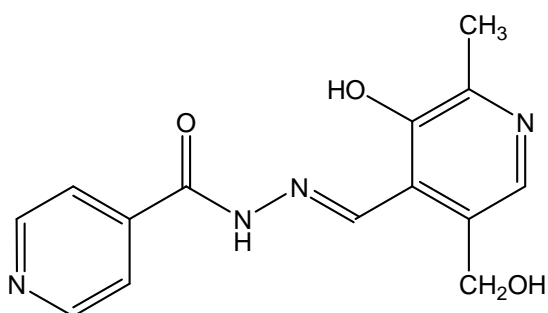


Figure 1.8: Schiff base of conjugate of INH and vitamin B₆

1.3.2 Pyrazinamide

Pyrazinamide (PZA), which is one of the drugs used in DOTS therapy, has shortened the original treatment regime of TB from the original 9-12 months to the current 6 months course. The mechanism of action of PZA is not completely understood despite it being a structural analog of INH and also acting as a prodrug. It is found to inhibit fatty acid synthase-I, thereby disrupting the cell wall biosynthesis.⁹ In its active form, pyrazinoic acid (POA) is formed by the bacterial pyrazinamidase (PZase) enzyme in a lower pH cellular environment.²⁰⁻²¹

Interestingly, PZA is known to kill mycobacteria which lie in a semi-dormant state, residing in the acidic environment. However, other antitubercular drugs fail to eradicate these bacteria, which is one of the main reasons so as to why PZA helps in shortening the TB therapy. PZA is only active against mycobacteria in a low acidic environment, whereas other bacteria are insensitive to PZA. It was found that even though POA is produced in acidic environments, it fails to accumulate in certain strains of mycobacteria due to highly active POA efflux mechanisms. Those bacteria which were deficient in this efflux pump are highly susceptible to PZA, whereas those for example *M. smegmatis* are natural resistant of PZA due to extremely active POA efflux.²⁰ Studies by Bamaga *et al.* have illustrated that mutations in the *pncA* gene encoding PZase have led to the development of PZA resistant bacteria.²²

1.3.3 Ethambutol

Ethambutol inhibits Mtb by targeting the arabinogalactam and peptidoglycan biosynthesis pathway of the bacterium.²³ Other drugs that inhibit this pathway include cycloserin²⁴ and amoxicillin²⁵ (figure 1.9). Ethambutol is known to inhibit arabinofuranosyl transferase(s) of arabinogalactam. Moreover, Häusler *et al.* have shown that even small changes in the parent pharmacophore decreased the antitubercular activity exhibited by ethambutol.²⁶

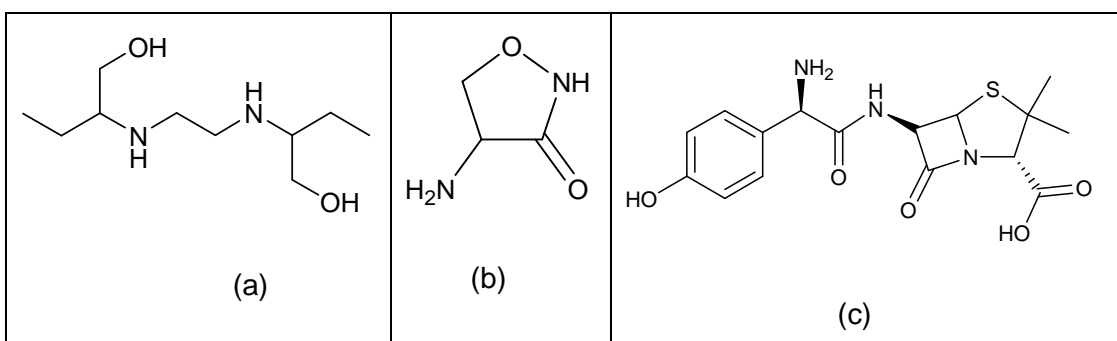


Figure 1.9 : Arabinogalactam and peptidoglycan biosynthesis inhibitors a) Ethambutol b) Cycloserin c) amoxicillin

1.3.4 Rifampin

Rifampin as depicted in figure 1.10, binds to the β -subunit of the DNA-dependent polymerase thereby inhibiting bacterial RNA synthesis.²⁷⁻²⁹

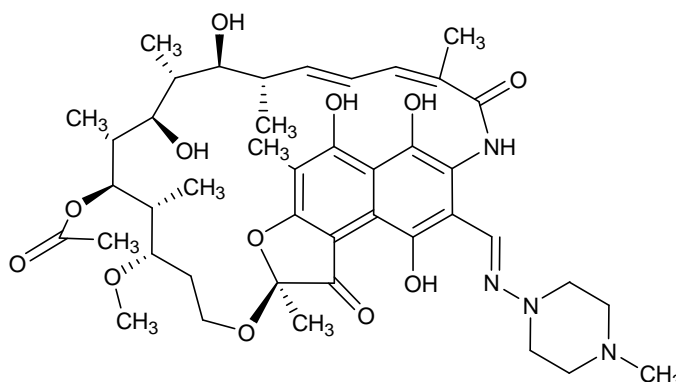


Figure 1.10: Rifampin

1.3.4 Fluoroquinolone

Fluoroquinolones, as depicted in figure 1.11, are the second line of antitubercular agents used in targeting resistant strains of mycobacteria. These compounds target the bacterial DNA gyrase enzymes, viz. topoisomerase II (topoII) and DNA topoisomerase IV (topoIV) in Gram-negative and Gram-positive bacteria. Fluoroquinolones block the ligation step of the cell cycle, producing single and double stranded breaks, which consequently leads to cell death.³⁰⁻³¹

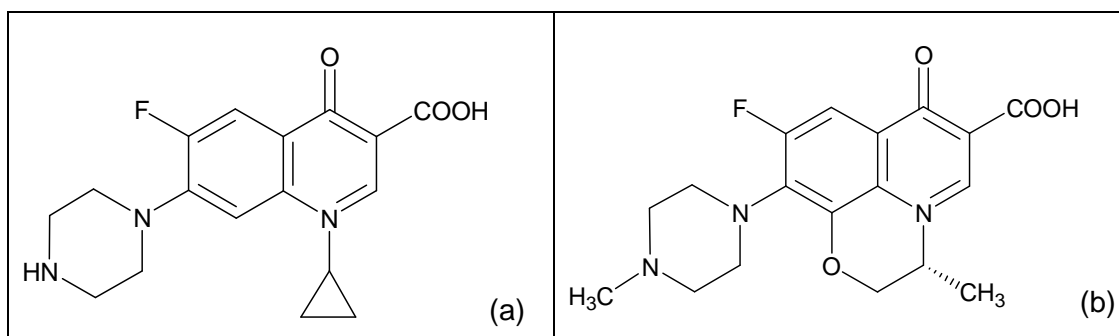


Figure 1.11: Fluoroquinolone antibiotics a) ciprofloxacin and b) levofloxacin

1.4 Drawback of present antitubercular drugs

The length of the DOTS therapy (6-12 months) has resulted in patient non-compliance and eventually led to the emergence of multidrug resistant TB (MDR-TB) in some patients.³² The major drawback of the drugs presently used to treat TB infections is that they only typically target the actively growing bacteria, while there is a notable absence of drugs which can target latent infections.³³ These latent infections could lead to the reactivation of the disease in patients with compromised immune systems. This is most notably seen in HIV patients, with TB being a major cause of death in AIDS patients⁷. Drug related adverse side effects can cause significant morbidity, arising from serious conditions such as drug-induced hepatitis and severe gastrointestinal distress. Most common side effects of TB drugs include fever and rashes.³⁴

As a consequence, there is an urgent need for the development of new antitubercular compounds to overcome these drawbacks. The new antitubercular agent must be effective against resistant and persistent strains of the bacteria, whilst keeping the side effects to a minimum. In order to design more efficient antitubercular drugs, it will be useful to understand the mechanism involved in resistance and persistence.

1.5 Cause for the resistant state of mycobacteria

The increasing number of resistance cases is a major concern amongst the health organisation throughout the world. A survey done by the WHO in 2008 has found that around half a million people develop MDR-TB worldwide. In addition, 10,000 new cases of extensive drug resistant TB (XDR-TB) emerged in 2008. XDR is a term used when a bacterial species is resistant against most, or all, antibiotics capable of treating such infections.³⁵

1.5.1 The lipophilic cell wall of mycobacteria

One of the limitations for certain types of antimicrobial agents is the ability to cross the lipid membrane of the bacterial cell, failing to do so may result in the resistance of a drug. Rastogi *et al.* succeeded in overcoming this mycobacterial resistance by synthesizing an amphipathic derivative of the drug isoniazid, as indicated in figure 1.12.³⁶ These amphipathic analogs of INH exhibited promising activity against mycobacteria which were 100 % resistant to INH.

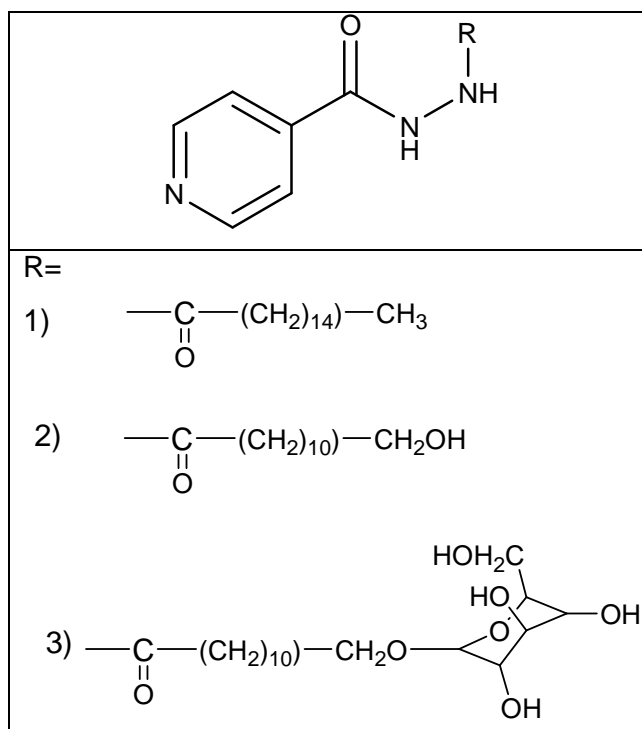


Figure 1.12: Amphipathic derivatives of INH³⁶

It was proposed that the lipophilic part of the molecule acts as a carrier of the INH drug, which allows it to cross the lipid membrane of the bacterial cell wall. Once inside the cell, the INH part of the molecule is responsible for the inhibitory

action against mycobacteria. INH is a very hydrophilic and polar molecule, which prevents effective absorption by the cell but it is a very potent drug. Hence attempts could be made to modify the drug to overcome the resistance problem caused by its inability to cross the lipid barrier effectively.

1.5.2 Mutation in the *katG* gene

Resistance can also develop through mutations in the *katG* gene, which is responsible for converting INH into its active form. Bernadou *et al.*,³⁷⁻³⁹ have made synthetic analogs of truncated INH-NADH (minus the ADP moiety), where the the isonicotinic ring was substituted with a benzoyl ring (BH-NADH). These analogs can directly bind to the active site of InhA, inhibiting the enzyme, hence bypassing the KatG dependent step. However, these truncated adducts lead to very poor activity against InhA, due to the lack of an ADP moiety. To overcome this problem, they synthesised a bisubstrate analogue of BH-NADH adduct. A representative example from the series is shown in figure 1.13.

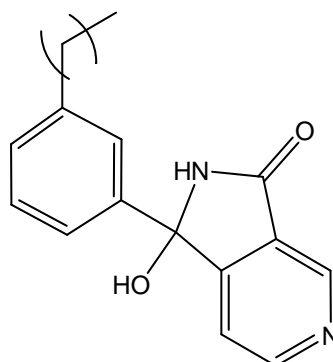


Figure 1.13: Synthetic analogue of the BH-NADH adduct³⁹

This analogue is more likely to accurately mimic the bonding profile of the InhA substrate and would be recognised by the active site of InhA. This will provide more affinity and selectivity towards the catalytic site of InhA. Interestingly, some of these derivatives not only inhibit the InhA enzyme, but also exert promising MIC values against active strains bacteria of Mtb. However, the possibility that an additional hydrophobic moiety might be responsible for the increased uptake of the benzoyl hydrazone across the lipid cell membrane cannot be discounted. Moreover, the compound depicted in figure 1.13 did not inhibit InhA but exhibited potential antimycobacterial activity. This suggests that some of the synthesized BH-NADH

derivatives may not inhibit InhA actively and act against Mtb through a different mechanism of action.

While the compounds above may have future potential as antitubercular drugs, they could also prove active against the KatG mutant resistant strains. These studies also suggest that hydrazides other than INH can also act as potential inhibitors of InhA and thus could be a useful strategy in antitubercular drug design.

Moreover, impairment of KatG may also result from a lack of redox active species in the environment, leading to INH resistance.⁴⁰ KatG appears to utilize superoxide anions to activate INH, as the INH turnover by the purified enzyme is completely abolished in the presence of a catalytic quantity of superoxide dismutase (SOD).⁴¹

1.5.3 Acetylation of the hydrazinic chain (-NH-NH₂)

INH can undergo acetylation in the body through the action of *N*-acetyltransferase (NAT) enzymes. NAT enzymes have been able to acetylate various substrates including INH- and sulfonamide-based antibacterial drugs. Acetylation of the amine functionality of INH, as indicated in figure 1.14, may result in poor antimycobacterial activity. Different forms of NAT enzymes are not only present in the human body but also in Mtb. The effective therapeutic doses of INH have to be taken into account, depending on the effect of fast and slow acetylators.^{18,42}

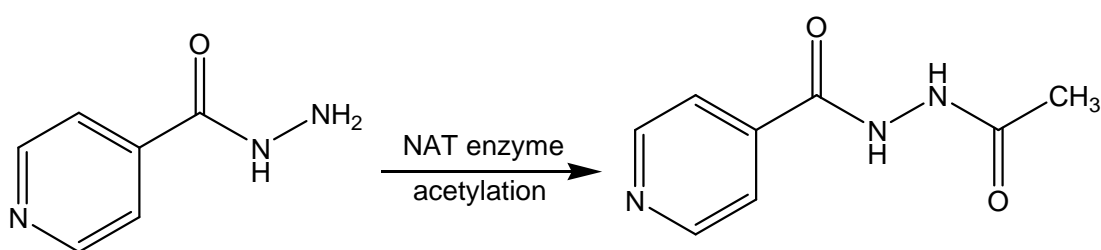


Figure 1.14: Acetylation of INH by NAT enzymes¹⁸

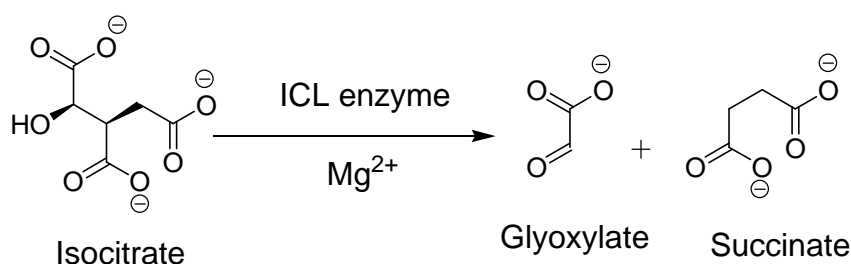
In order to avoid the acetylation of potent hydrazine drugs, an effective strategy would be to block the amine group with an appropriate moiety, possibly a biologically active pharmacophore, which could enhance the activity. For example, as previously discussed, INH can be conjugated to hydrophobic molecules that would allow passive diffusion through the lipid cell wall of the mycobacteria.

1.6 Persistent/ latent bacteria

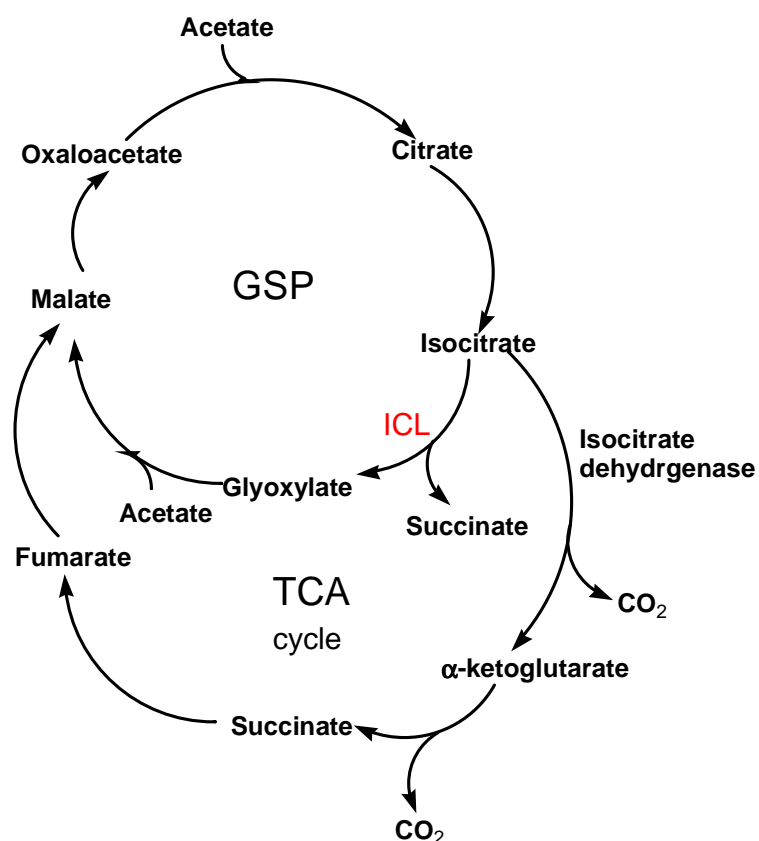
One of the major drawback of drugs presently used to treat Mtb is the failure to target the persistent/latent bacteria present in the host organism, hence TB cannot be completely eradicated. Various research groups are working in this field in order to understand the mechanisms responsible for the persistent state of bacteria. One of the well known processes is the glyoxylate shunt pathway (GSP).⁴³⁻⁴⁶

1.6.1 Role of the glyoxylate shunt pathway in persistent bacteria

The glyoxylate shunt pathway (GSP) has been determined to be important for bacterial survival in the activated macrophage and for persistent infections of Mtb in the host organism. The majority of the microorganisms growing on fatty acids for their carbon source utilise the glyoxylate bypass for the biosynthesis of cellular material. In Mtb, isocitrate lyase activity is increased when the bacilli are in an environment of low oxygen tension or in a transition from an actively replicating to a non-replicating state. The GSP bypasses the loss of two carbon dioxide molecules from the tricarboxylic acid (TCA) cycle, thereby permitting the net incorporation of carbon into cellular structure, as illustrated in figure 1.15. The vital enzymes of the GSP are isocitrate lyase (ICL) and malate synthase. ICL converts isocitrate into succinate and glyoxylate as indicated in scheme 1.1, whereas malate synthase condenses glyoxylate with acetyl coenzyme A (acetyl-CoA) to give malate and coenzyme A (CoA) respectively.⁴³⁻⁴⁶



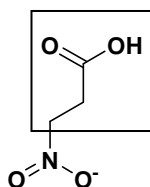
Scheme 1.1: Conversion of isocitrate to glyoxylate and succinate³⁶

Figure 1.15: Isocitrate lyase pathway⁴⁶

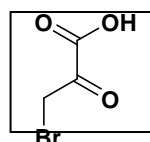
The GSP has been found in most prokaryotes, lower eukaryotes and plants, but there is no evidence thus far of this pathway being present higher vertebrates, hence its inhibition will not interfere with the human metabolic pathways, thus allowing specific targeting of the bacterial survival pathways.⁴⁷

1.6.1.1 ICL inhibitors

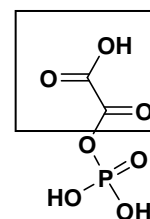
A number of ICL inhibitors (figure 1.16) have been investigated to date, including 3-nitropropionate, 3-bromopyruvate, phosphoenolpyruvate, 3-phosphoglycerate and itaconate.⁴⁸⁻⁵² Since the most common structural motif observed in the known ICL inhibitors is the pyruvate moiety, as highlighted in figure 1.16, incorporation of this moiety may provide an effective route for targeting the ICL enzyme, thereby inhibiting persistent bacteria.



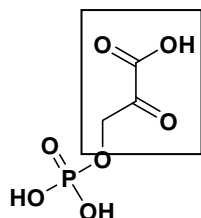
a) 3-nitropropionic acid



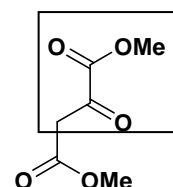
b) 3-bromopyruvic acid



c) phosphoenolpyruvic acid



d) phosphoglyceric acid



e) itaconate

Figure 1.16: Isocitrate lyase inhibitors (a-e)

Sacchettini *et al.*⁵³ investigated the mode of inhibition of 3-bromopyruvate and 3-nitropropionate. It was established that both inhibitors showed activity against bacteria grown on acetates but have no effect on bacteria grown on glucose. In order to gain further insight into the mechanism of action, the inhibitors were co-crystallised with the ICL enzyme and orthorhombic shaped crystals were obtained. The binding of glyoxylate was examined at the active site of ICL which is located at the C-terminal ends of the β -strands, as shown in figure 1.17. It was determined that the carboxylate group or the nitro group of 3-nitropropionate hydrogen bonds with the side chains of residues Asn³¹³, Glu²⁸⁵, Arg²²⁸, His¹⁹³, Ser³¹⁷, Thr³⁴⁷ and Gly¹⁹² of the protein, as shown in figure 1.18. The glyoxylate binds by coordination to the active site Mg²⁺ (indicated as yellow sphere, figure 1.18) and forms hydrogen bonds with amino acid residues such as Ser⁹¹⁰, Gly⁹², Trp⁹³ and Arg²²⁸ of the protein.

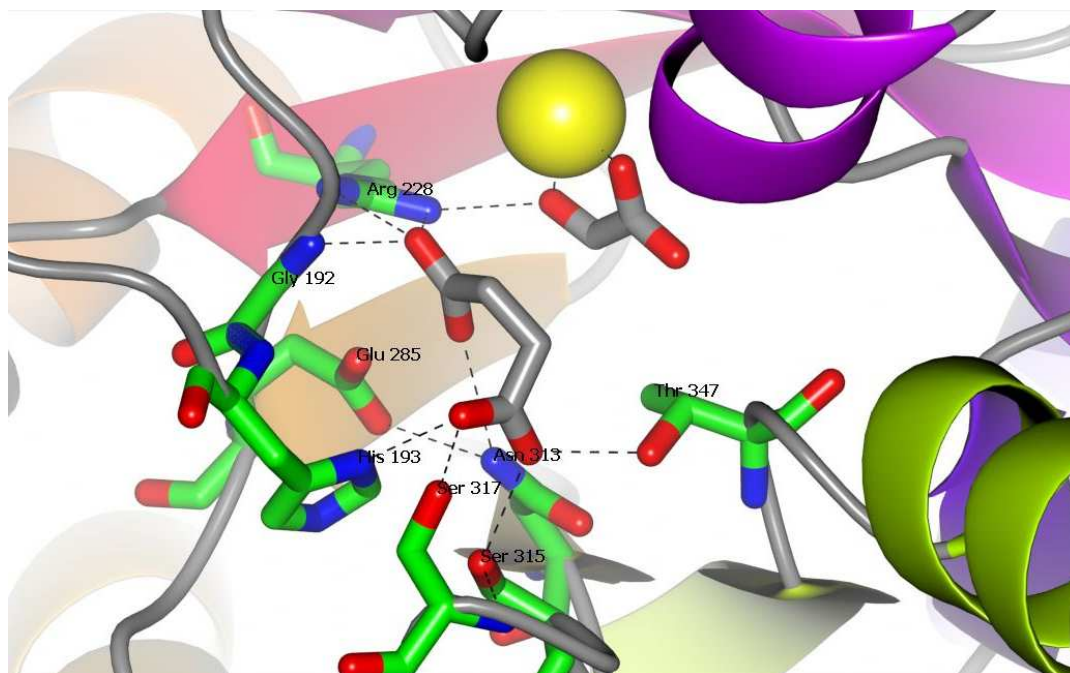


Figure 1.17: Active site of the of the ICL C191S mutant with glyoxylate (GA) and 3-nitropropionate bound.⁵³ Generated using CCP4mg software (PDB code 1F8I)

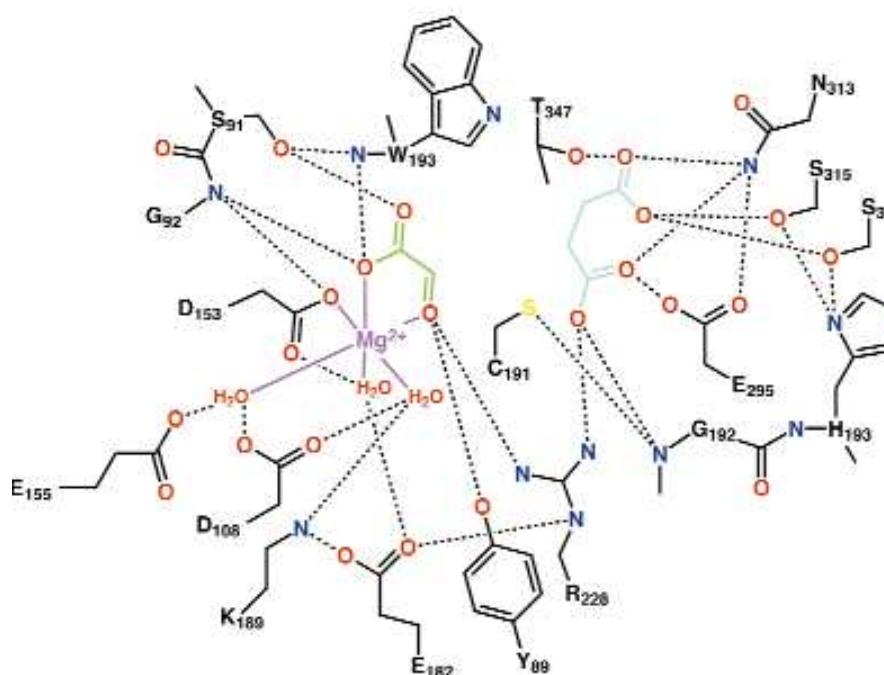


Figure 1.18: Schematic diagram of the interactions of ICL with glyoxylate and succinate⁵³

Moreover, similar co-crystallisation studies with 3-bromopyruvate reveal that it acts as an inhibitor of ICL by forming a covalent adduct with nucleophile Cys¹⁹¹ in the active site, achieved by dehalogenation of the inhibitor. As can be seen in figure

1.19 the pyruvyl moiety forms hydrogen bonds with the side chains of His¹⁹³, Asn³¹³, Ser³¹⁵, Ser³¹⁷, Thr³⁴⁷ and to a solvent molecule (water).

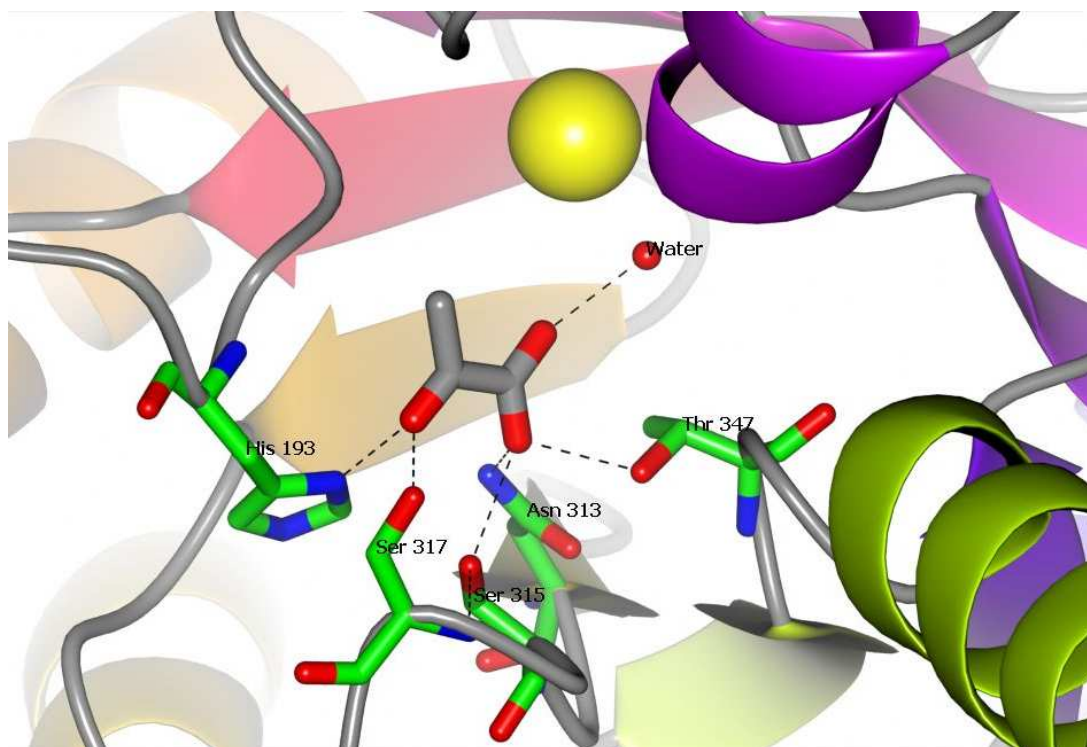
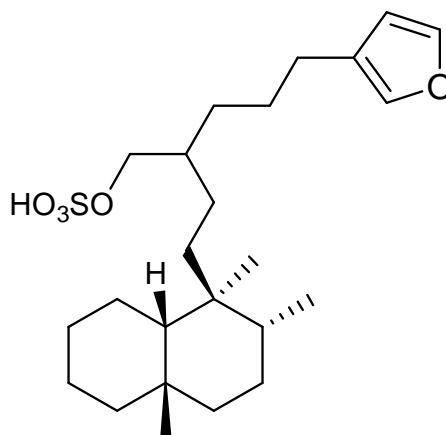


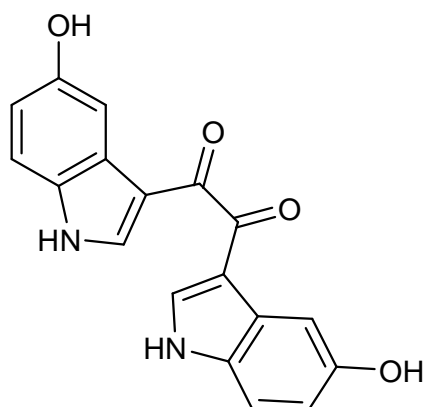
Figure 1.19: Active site of ICL (pyruvyl moiety (purple) attached to the thiolate of Cys¹⁹¹).⁵³ Generated using CCP4mg software (PDB code 1F8M)

Kumar and Bhakuni⁵⁴ investigated the role of metal salts in the ICL enzyme mechanism. Mg²⁺ is vital for the activity of the enzyme, exhibiting almost 100% activity whereas Mn²⁺ yielded around 45% activity. Cd²⁺ and Zn²⁺ inhibited the enzyme, as these metal ions led to the unfolding of the catalytic domain. However, Mg²⁺ and Mn²⁺ did not significantly affect the structure of the enzyme, as such the zinc and cadmium complexes could be explored for any effect the ions could have on the inhibitory action of ICL.

ICL inhibitors containing non-pyruvyl moieties have also been explored. Shin *et al.* and his group isolated seven sesterterpene sulfates from the tropical sponge *Dysidea sp.* and evaluated their inhibitory activity against ICL from *Candida albicans*. Amongst them, the compound as shown in figure 1.20 was found to be most active having an IC₅₀ value of 16.9 μM.⁵⁵

Figure 1.20: Sesterterpene sulfate⁵⁵

5-hydroxy type alkaloids from the tropical marine sponge *Hyrtios sp.* were also investigated. The inhibitory properties of these compounds were investigated using ICL enzyme obtained from *Candida albicans*. The compound as shown in figure 1.21, was the most active of this type of compounds, having an IC_{50} of 89.0 μM .⁵⁶

Figure 1.21: Hyrtiosin B⁵⁶

Synthetically-derived inhibitors have also been investigated in inhibition studies of ICL. Shin *et al.* synthesized a new series of bromophenol derivatives, where the compound as shown in figure 1.22 exhibited the most potent inhibitory activity against ICL from *Candida albicans*.⁵⁷

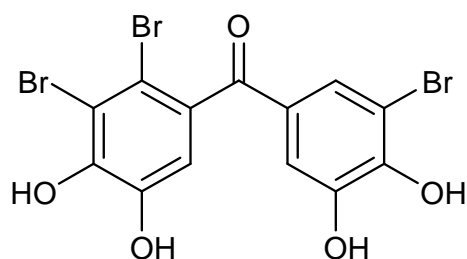


Figure 1.22: (3-Bromo-4,5-dihydroxyphenyl)-(2,3-dibromo-4,5-dihydroxy-phenyl)-methanone⁵⁷

From these literature studies, it can be concluded that ICL is an attractive target to eradicate persistent bacterial strains. Pyruvate-containing molecules have shown to inhibit the ICL enzyme, however, non-pyruvate containing ICL inhibitors have also been explored.

Furthermore, recent studies by Shi *et al.*⁵⁸ show that PZA is known to inhibit ribosomal protein S1 (RpsA), an important protein involved in *trans*-translation process. This process is essential in non-replicating or latent bacteria; therefore PZA may be useful in eradicating persistent mycobacteria.

1.7 Hydrazones and metal complexes as antitubercular agents

Hydrazones and their metal complexes represent an important class of compounds, as they are not only good antitubercular agents⁵⁹⁻⁶⁰ but also have other biological applications, as indicated in figure 1.23. These include anticonvulsant⁶¹⁻⁶², analgesic⁶², anti-inflammatory⁶³⁻⁶⁴, anticancer⁶⁵⁻⁶⁶, antiviral⁶⁷⁻⁶⁸ antimalarial⁶⁹, antigout⁷⁰, antidiabetic⁷¹, antifungal⁷² antiplatelet⁷³ and vasodilator⁷⁴ applications.

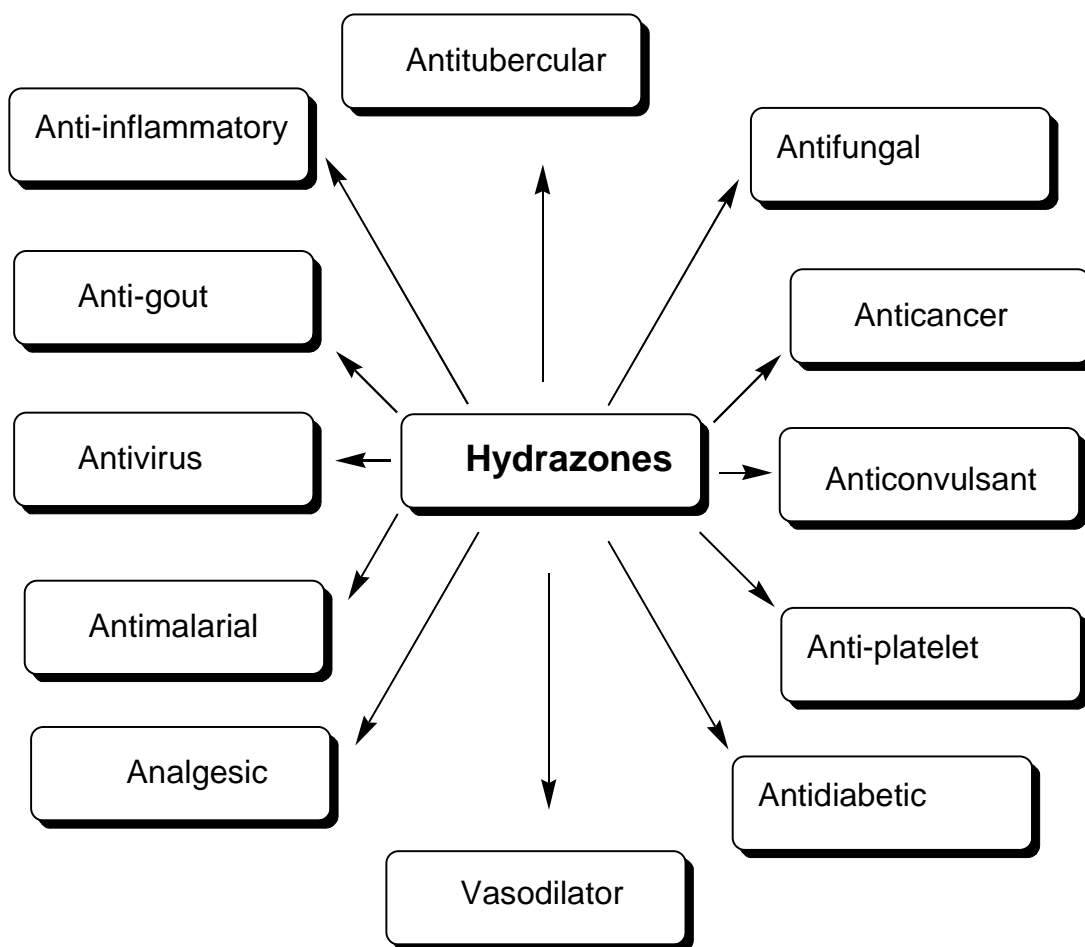


Figure 1.23: Biological applications of hydrazones

Owing to their various pharmacological applications, there has been a growing interest in hydrazones. Various reviews are available in the literature, which have covered various aspects of these compounds, including biological and non-biological applications.⁷⁵⁻⁷⁷

1.7.1 Hydrazones as antitubercular agents

Pavan *et al.* synthesised 20 different substituted thiosemicarbazones (figure 1.24), semicarbazones, dithiocarbazates and hydrazide/hydrazones that were then evaluated against Mtb. One interesting result arising from the study is that the compounds bearing more hydrophobic moieties (R groups) were shown to be more active than those containing hydrophilic groups. This could be attributed to the more facile diffusion of the hydrophobic molecules across the lipid-rich bilayer⁷⁸.

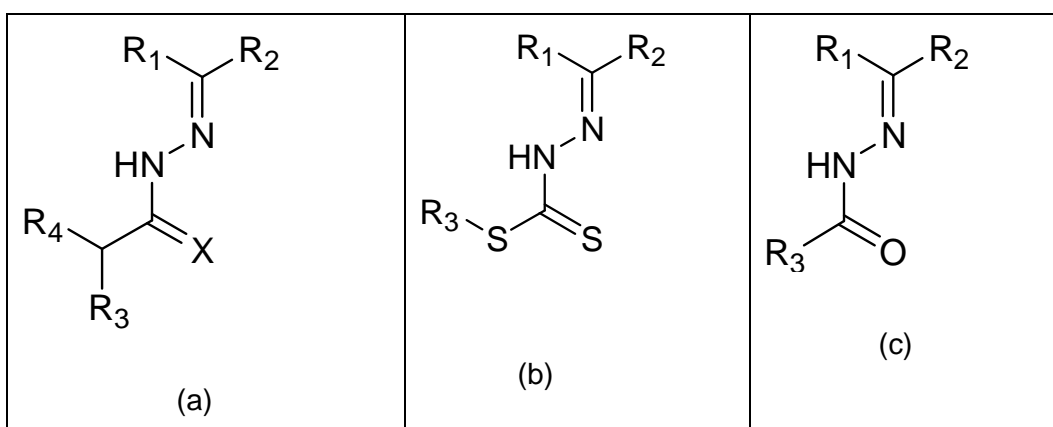


Figure 1.24: a) Thiosemicarbazones (X=S) b) Dithiocarbazates c) Semicarbazones

One other possible mechanism by which these type of ligands may act as antitubercular agents is due to the presence of N, O, S donor binding sites. It is well established that sequestering intracellular iron can cause bacteria to starve, as iron is essential for mycobacterial survival.⁷⁹ Whilst donor atoms such as N, S, O have the ability to coordinate to metal ions in various combinations (such as NNO, ONO, ONS, NNS), the organic framework forms stable 5- or 6-membered chelate rings. Once iron is coordinated to the ligand, it is no longer available for use by the bacteria, thus leading to iron starvation.

A similar observation was made by Vigorita *et al.*,⁸⁰⁻⁸¹ through their investigation of isoniazid related hydrazones, hydrazides and cyanoboranes as shown in figure 1.25.

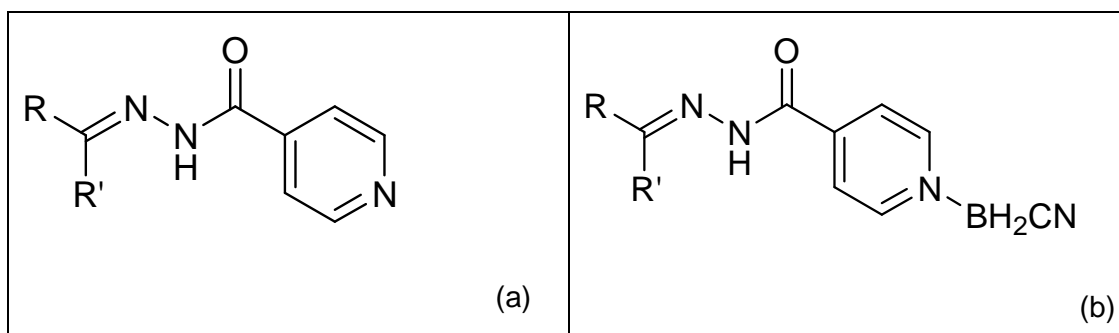
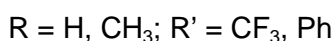


Figure 1.25: Isoniazid derivatives a) hydrazone b) Cyanoborane adduct of hydrazone



Amongst these hydrazones, the ones bearing fluoro- and trifluoro-substituents on the benzene ring were proven to be most active. The cyanoborane adducts, however proved to be more active than the corresponding hydrazones. They displayed EC_{99} (EC_{99} is the lowest concentration effecting 99% reduction in colony forming units) of 1.14 and 0.116 $\mu\text{g ml}^{-1}$, respectively, against *Mtb* Erdman growing within mouse bone marrow macrophages, which is between 10-100 times more when compared with the same strain in culture medium, ($\text{MIC} = 12.5 \mu\text{g ml}^{-1}$). The increase in the activity was attributed to the increase in lipophilicity. It was also observed that the cyanoborane-containing phenyl group was more potent than the trifluoromethyl-group. Interestingly, the tested compounds were found to be active against ethambutol and rifampin resistant strains of *Mtb*.

Further to this, Vavříková *et al.*⁸² synthesized, fluoro- and *tri*-fluoromethyl-substituted hydrazones derived from second-line antitubercular drugs including *para*-amino salicylic acid (PAS), norfloxacin (Nrf) and ciprofloxacin (Cpf). These compounds exhibit greater activity on MDR-TB strains (resistant to at least INH and RIF), when compared to their parent compounds - PAS, Nrf and Cpf, however, did not show any improved activity over normal *Mtb*. These compounds were further tested for cellular cytotoxicity against human cell lines using the MTT assay. Interestingly, these compounds were relatively non-toxic to human hepatocellular carcinoma cells HepG2, PBMC (Peripheral Blood Mononuclear Cells) and human SH-SY5Y neuroblastoma cells within the MIC range of their antitubercular activity. Most of the tested compounds exhibited similar MIC values against MDR-TB cells, however, one of the *para*-substituted fluorohydrazone analogues of Cpf (4FH-Cpf) as indicated in figure 1.26, displayed the highest selectivity index (SI) of 1268.58 as compared to Cpf (110.37). Values of selectivity index (SI) indicate rate between

IC_{50} (mmol L^{-1}) of HepG2 cytotoxicity and MIC ($\mu\text{g mL}^{-1}$). Higher values indicate a greater level of selectivity, which means they possess a higher level of toxicity towards mycobacteria while being less toxic to human cells.

As 4FH-Cpf (figure 1.26), is highly selective towards TB cells, it was chosen for stability studies in rat plasma and in aqueous buffer at varying pH. The HPLC results obtained indicate that 4FH-Cpf undergoes decomposition at a faster rate in acidic buffer solutions. The half life was found to be 2.9 and 11.8 hours in pH 3 and 5 buffer solutions, respectively. The compound is relatively stable at pH 7.4, as no significant decomposition was observed when monitored over 48 hours. Similar results were obtained when the stability of 4FH-Cpf was investigated in rat plasma. Even after 96 hours, the compound appears to be stable, suggesting no enzymatic degradation of the compound in rat plasma. The rate of degradation was very slow and is similar to the decomposition rate when studied in pH 7.4 buffer.⁸²

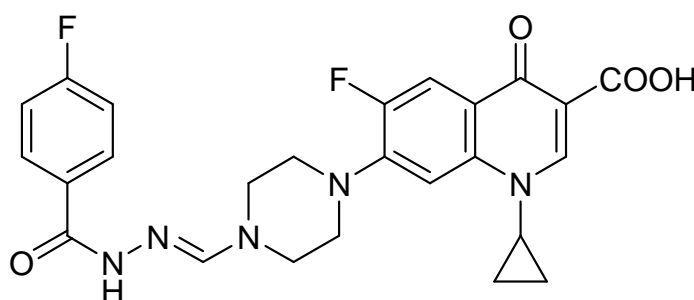


Figure 1.26: Cpf conjugate of fluoro-substituted hydrazone (4FH-Cpf)⁸²

Hence, the above studies by Vavříková and Vigorita suggests that fluoro- and trifluoromethyl-substituted compounds could be useful in the design of novel antitubercular agents.

Interestingly, hydrazones have also been proven to inhibit ICL enzyme. Sriram *et al.*⁸³ synthesized a combinatorial library of novel pthalazinyll hydrazones (figure 1.27) for use as ICL enzyme inhibitors. The compounds were evaluated *in vitro* and *in vivo* against 8 mycobacterial strains and Mtb ICL. The compound shown in figure 1.27 a) inhibited all 8 species of mycobacteria with MICs (minimum inhibitory concentrations) ranging from <0.09 - $12.25 \mu\text{M}$. A structure activity relationship (SAR) analysis reveals that electron withdrawing groups, such as nitro- and halo-substituents, improved activity whereas electron donating groups, such as methoxy-, methyl-, hydroxyl- and dimethylamino- substituents reduced activity. The compounds that displayed high activity were further screened against Mtb cells that

had been grown for six weeks under carbon-deprived conditions. The compounds exhibited %-inhibition values in the range of 45.1-61.6% at 10 μ M concentration and the inhibitor as shown in the figure 1.27 b displayed the highest inhibition of 61.6%.

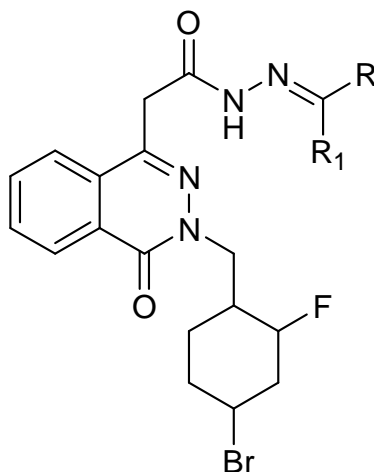


Figure 1.27: Phthalazinyl hydrazone⁸³ a) R-H, R₁-4- NO₂Ph

b) R-H, R₁-3- NO₂Ph

Recently, docking studies reported by Padhye's *et al.*⁸⁴ illustrated that the hydrazones derived from pyruvic acid can bind to the active site of ICL. The hydrazones form hydrogen bonds with surrounding amino acid side chains and the binding energy lies between -7.51 and -8.89 kcal mol⁻¹, where as the parent pyruvic acid shows a binding energy of -8.36 kcal mol⁻¹. Ligand L4, as indicated in figure 1.28, exhibited highest binding energy of -8.89 kcal mol⁻¹, where the amide proton forms a hydrogen bond with the oxygen atom of amino acid Gly²⁸⁷. Moreover, it is also observed with other ligands that the oxygen atom of carboxylate and/or carbonyl functional groups also participates in hydrogen bonding with amino acids such as His, Ser, Asn, which are in close vicinity of the active site.

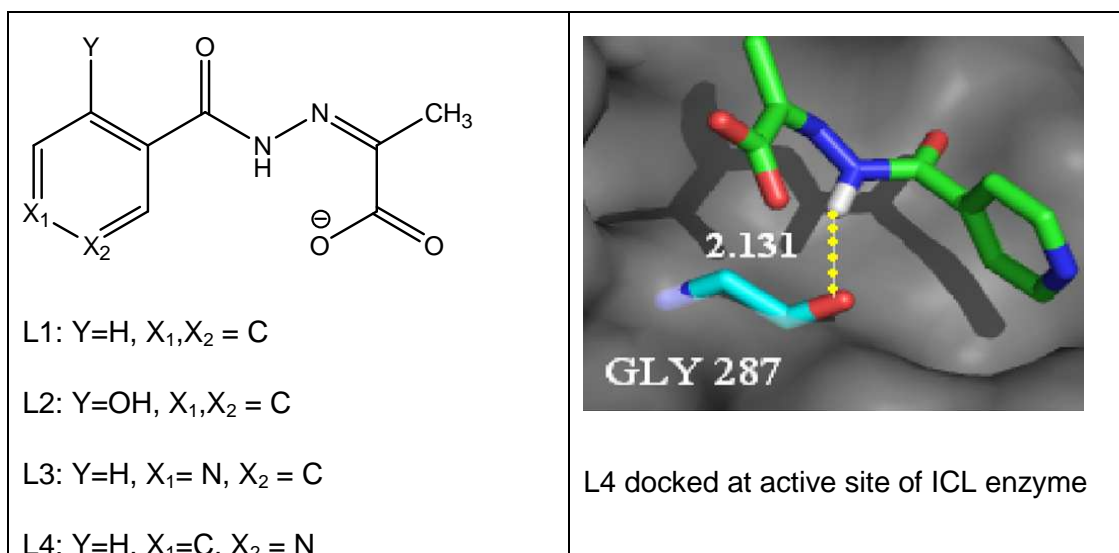


Figure 1.28: Structures of pyruvic acid hydrazones (L1-L4) (left) investigated by docking studies involving ICL, L4 binding in the ICL active site⁸⁴

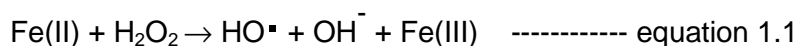
Interestingly, these ligands and their respective Cu(II) complexes are also known to inhibit actively growing Mtb H37RV.

The literature studies performed on hydrazones conclude that this class of compounds can be considered as useful for the discovery of novel antitubercular agents. Moreover, a number of the mentioned hydrazones are also able to inhibit the ICL and can thus serve a dual purpose of eradicating actively growing and persistent bacteria.

1.7.2 Metal complexes as antitubercular agents

Metal complexes can offer certain advantages over organic ligands as they have been reported to possess excellent antimycobacterial activity and are also effective against resistant strains.⁸⁵⁻⁸⁷ Reactive oxygen radicals initiate the transcription of the *katG* gene resulting in the activation of INH drug, therefore, in order to overcome the problem of resistance, redox active species can be introduced along with INH. For example, redox active metal cations, such as Cu(II) or Fe(II) can be considered, as they can cause oxidative stress within the bacterial cell. Oxidative stress caused by metal ions may also be helpful, as it may exert damaging effects on bacterial cells, eventually leading to their death. This could happen due to the Fenton reaction occurring in the cells. Redox active metal ions, such as Fe(II), can react with endogenous hydrogen peroxide to give rise to hydroxyl radicals, as shown in equation 1.1. The resultant reactive oxygen species

can be lethal to the cell by damaging its DNA.⁸⁸ To confirm this theory, Imlay *et al.*⁸⁹ investigated the action of hydrogen peroxide on *Escherichia coli* (*E. coli*). They found that micromolar concentrations of hydrogen peroxide inactivate the isopropylmalate isomerase (IPMI) enzyme, which belongs to the class of iron-sulfur cluster proteins. Inhibition of IPMI prevents the biosynthesis of the amino acid leucine.



Cu(II), which can also undergo redox reactions, is also believed to generate hydroxyl radicals through similar Fenton-like reactions, thus eventually causing toxicity to cells. However, further work carried out by Imlay *et al.*⁹⁰⁻⁹¹ illustrates that copper(II) does not cause DNA damage. It was suggested that intracellular glutathione may chelate free copper, hence it is unavailable to undergo redox reactions producing free radicals. Therefore, in order to investigate the mechanism underlying the Cu toxicity, Cu(I) was incubated with iron-cluster enzyme and it was found that copper displaces iron from the enzyme and binds to sulphur-containing ligands, subsequently leading to enzyme inhibition.

Several researchers are working on metal-based antitubercular compounds, a selection of which is discussed in this section. In order to support the theory of activation of INH by metal ions, Basso *et al.*⁹²⁻⁹⁴ coordinated INH to redox active metal ions, including Fe(II) ($[\text{Fe(III)(CN)}_5(\text{NH}_3)]^{2-}$) and Fe(III) ($[\text{Fe(II)(CN)}_5(\text{NH}_3)]^{3-}$). The study suggests that the Fe ions bind to INH through the heterocyclic nitrogen atom as indicated in figure 1.29. It was proposed that the electron transfer involving the Fe-INH complex takes place via an inner sphere mechanism, resulting in an oxidised species of INH (INH^{ox}), ($[\text{Fe(III)(CN)}_5(\text{INH}^{\text{ox}})]^{2-}$). INH^{ox} is the product of the oxidation process involving isonicotinic acid or isonicotinamide, as indicated in figure 1.30. These oxidative products or activated INH can give rise to the INH radical, which is known to bind the active site of Inh A, leading to inhibition of the enzyme as discussed previously on page 4 and 5.

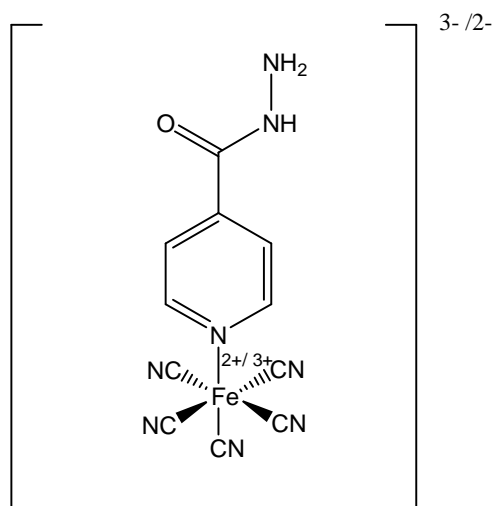


Figure 1.29: Iron complex of INH, $([\text{Fe}(\text{III/II})(\text{CN})_5(\text{INH}^{\text{ox}})]^{2-/3-})^{92-93}$

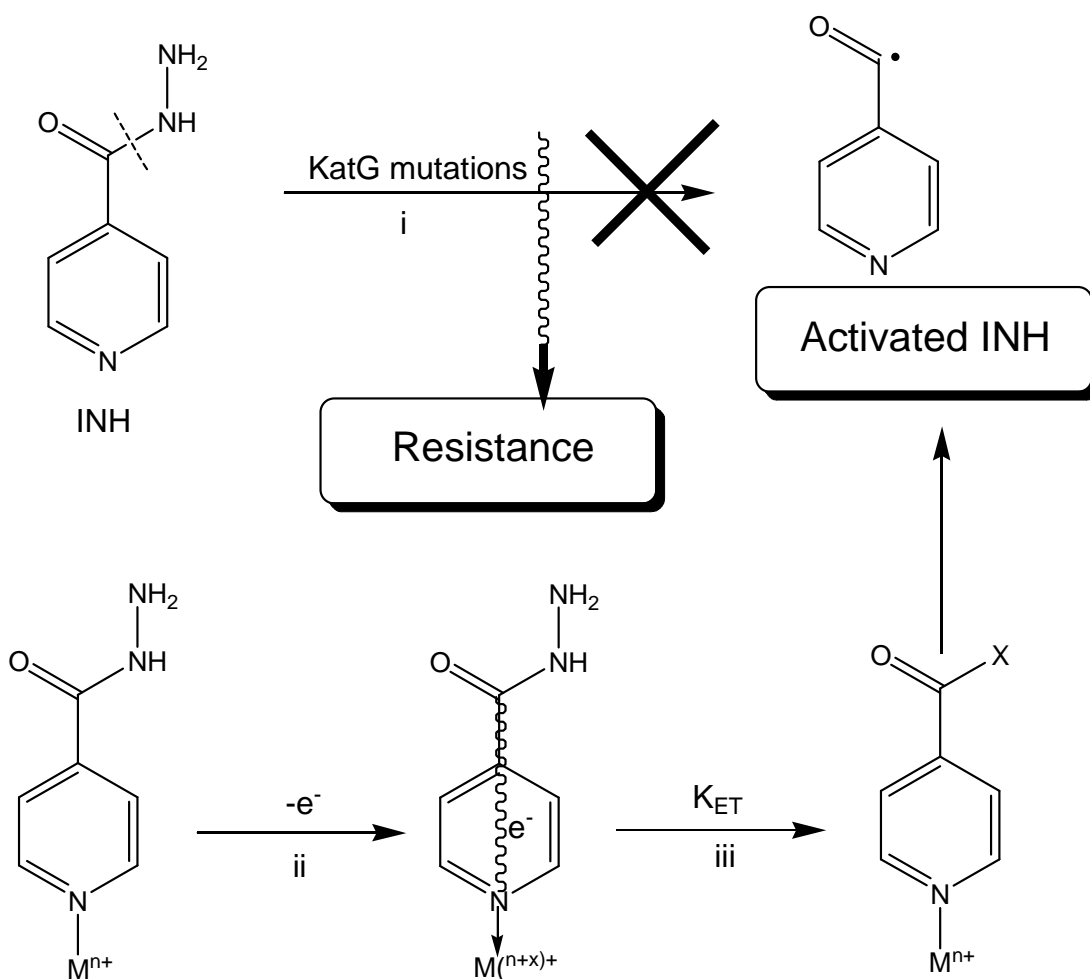


Figure 1.30: Scheme illustrating the mode of action of self-activating antitubercular metallodrugs of INH, ($\text{X}=\text{OH}, \text{NH}_2$) i) Failed activation of INH by mycobacteria due to KatG mutations, ii) Intramolecular electron transfer within the metal complex iii) electron transfer kinetics (K_{ET})⁹²

The synthesised iron complex of INH proved to be active against INH-resistant and INH-sensitive strains of bacteria. It was hypothesized that KatG is not required for INH activation if there is a redox active metal present in close vicinity of the drug. The electron transfer mechanism associated with Fe-INH complex can bypass the KatG activation step by self activating the INH drug. This strategy can be useful in designing novel antitubercular drugs, which can overcome drug resistance caused by KatG mutations. Inhibition of Inh A proved to be unsuccessful with $[\text{Fe(III)(CN)}_6]$. This proves that INH is an essential pharmacophore required to inhibit the InhA enzyme.

Furthermore, other redox active metal ions, such as ruthenium(II) was also coordinated to INH in order to support their theory. However, $[\text{Ru(II)(CN)}_5(\text{INH})]^{3-}$ and $[\text{Ru(II)(NH}_3)_5(\text{INH})]^{2+}$ failed to show any inhibitory action against Inh A. The reason was attributed to the difference in their electrochemical potential. The oxidation potential of $[\text{Fe(II)(CN)}_5(\text{INH})]^{3-}$ was found to be 305 mV vs. SCE, whereas $\text{Ru(II)(CN)}_5(\text{INH})^{3-}$ exhibits a significantly low $E_{1/2}$ value of 112 mV and $[\text{Ru(II)(NH}_3)_5(\text{INH})]^{2+}$ has an extremely high oxidation potential (~750 mV). Hence, this suggests that intramolecular electron transfer reactions, which are associated with electrochemical behaviour of metal complexes, may play a vital role in the design of antitubercular metallodrugs.

Similar studies carried out by Bodiguel *et al.*,⁹⁵ suggest that addition of Mn^{2+} ions to a mixture of INH and KatG, increase the rate of formation of the active species isonicotinic acid as indicated by HPLC results. However, in order to achieve noticeable results a ratio of Mn^{2+} : KatG enzyme of 20:1 had to be used. It was hypothesized that both the process of INH oxidation by enzymatic peroxidation and Mn^{2+} auto-oxidation may occur simultaneously.

Likewise in human beings there are number of metal ion transport proteins present in bacteria in order to transport metal ions like Fe, Cu and Zn across the cell membrane. Depending upon the organism these types of proteins are either involved in uptake or efflux of certain metal ions. For example, ferric uptake regulator (Fur) imports the extracellular essential metal ions such as Fe inside the mycobacteria. Free Cu ion, which is toxic to certain bacterial species is exported out of the cells using copper transporting ATPases.⁹⁶ It has been proposed that the Fur A protein which is a member of ferric uptake regulator family is co-expressed along

with KatG.⁹⁷⁻⁹⁸ The furA gene encoding Fur A protein is located upstream of the katG gene as indicated in figure 1.31.

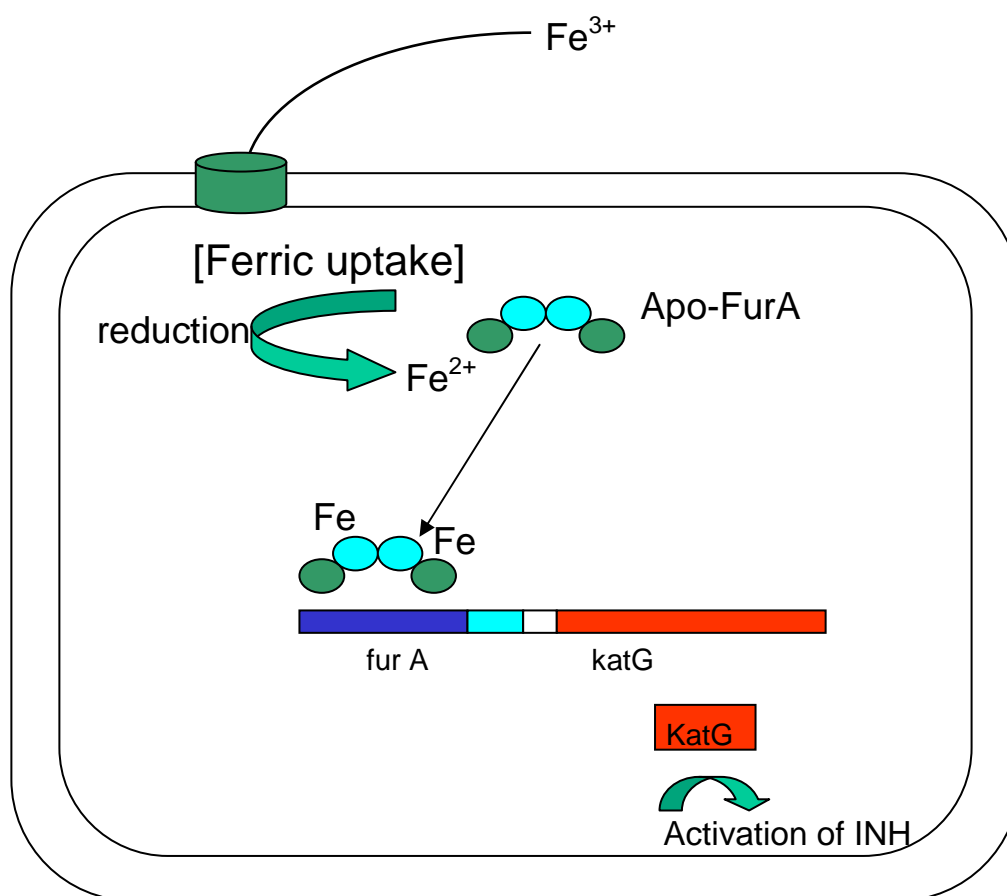


Figure 1.31: Schematic representation of the function of Mtb. FurA⁹⁸

Once inside the bacterial cell, Fe(III) gets reduced to Fe(II) by proteins belonging to iron reductase family. The reduced Fe is associated with the activation of fur A gene which inturn co-transcribes katG gene. The increased levels of KatG helps in boosting the activation of INH drug, hence helps in increasing its antitubercular activity.

As FurA plays a vital role in controlling the activity of KatG, it has attracted considerable attention in the development of novel antitubercular drug design, which could potentially enhance KatG levels thus enhancing INH potency.

Extensive work is being carried out by Yangzhong Liu *et al.*⁹⁹⁻¹⁰¹ on metal-based inhibitors of the RecA intein enzyme, which is responsible for protein splicing in Mtb. The investigation of the inhibitory effect of some of the first row transition metal ions on RecA intein suggests that Cu^{2+} and Zn^{2+} have high affinity towards the enzyme, whereas Co^{2+} , Ni^{2+} , Mn^{2+} and Cd^{2+} show weak inhibition and Mg^{2+} and Ca^{2+} ions fail to exert any inhibitory activity against recA.

One of the mutants of the RecA enzyme of Mtb ($\Delta\text{I-SM}$) was isolated and co-crystallised with Zn^{2+} . The crystal structure in which zinc is binding to the active site of $\Delta\text{I-SM}$ is depicted in figure 1.32. Zinc (indicated in blue spheres) coordinates to four amino acid residues in a tetrahedral manner. The amino acids involved in the coordination are His³⁴⁹, His⁴²⁹, Asn⁴⁴⁰ and Glu⁴²⁴. These studies also suggest that the binding of zinc to $\Delta\text{I-SM}$, results in conformational changes leading to the dimerisation of the protein. Additional NMR spectroscopic studies were carried out in order to confirm these results. Interestingly, the addition of the strong chelating agent EDTA reverses the inhibition of the enzyme by Zn^{2+} , indicating that the binding affinity of zinc is stronger for EDTA than the protein active site.

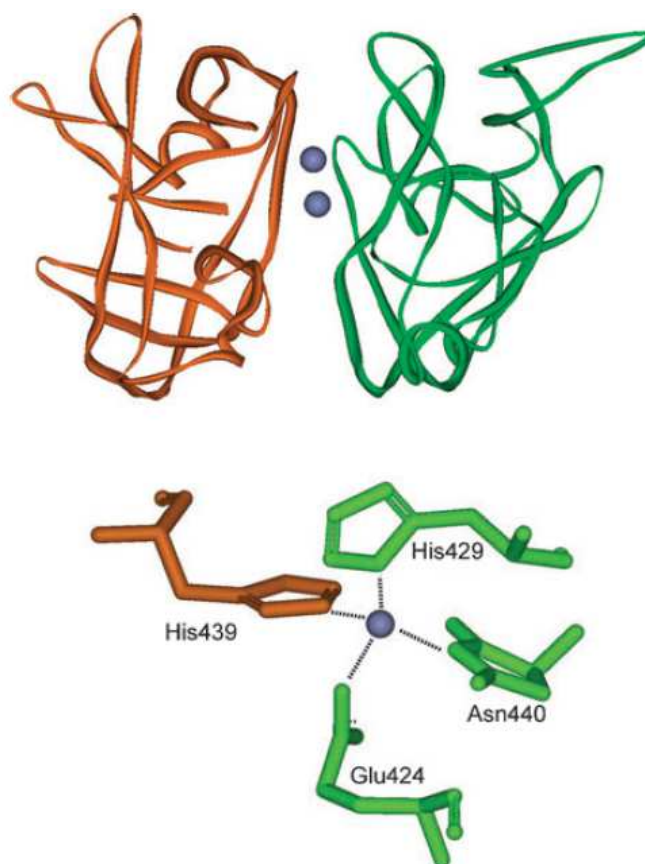


Figure 1.32: Crystal structure of $\Delta\text{I-SM}$ co-crystallised with Zn^{2+} (blue sphere)⁹⁹

Continuing this work, they also examined the interaction of Cu(II) and Cu(I) with Δ I-SM. Although the crystal structure with copper bound to the enzyme could not be obtained, UV/Vis, atomic absorption spectroscopy (AAS), NMR spectroscopy and extended X-ray fine structure (EXFAS) techniques were used to investigate the mechanism. The studies revealed that Cu(II) gets reduced to Cu(I) and in turn oxidises the thiol group of intein. Moreover, the copper binds to intein in a 1:1 ratio and it coordinates to cysteine and histidine side chains. The binding site of the two copper ions Cu(I) and Cu(II) varies as Cu(I) prefers tetrahedral coordination and Cu(II) prefers square planar geometry. Interestingly, it was observed that Cu(II) coordinates to the sulfur donor of cysteine, whereas this was not observed with Cu(I). This observation violates the HSAB principle, which suggests that Cu(I) favours sulfur coordination.

Surprisingly, Liu *et al.* also found that the inhibition of RecA intein can be achieved using the well known anticancer drug *cis*-platin (figure 1.33). A range of platinum(II) compounds were tested and it was found that *cis*-platin exhibits the lowest IC₅₀ of 2.5 μ M, whereas the *trans*-isomer has a significantly high IC₅₀ > 200 μ M. This is also true for anticancer activity, where *trans*-isomer is inactive against cancer cells.

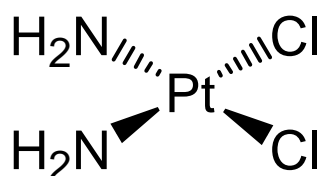


Figure 1.33: Structure of *cis*-platin

Vigorita *et al.*⁸⁷ also studied the *in vitro* antimycobacterial activity of Co²⁺ and Cu²⁺ complexes of fluorinated INH-hydrazones, as can be seen in figure 1.34. It was observed that all metal complexes exhibit excellent activity and two of the lead compounds displayed EC₉₉ values lower than that of the parent drug INH, whilst all of the tested metal chelates significantly inhibited the growth of single-drug-resistant Mtb strain.

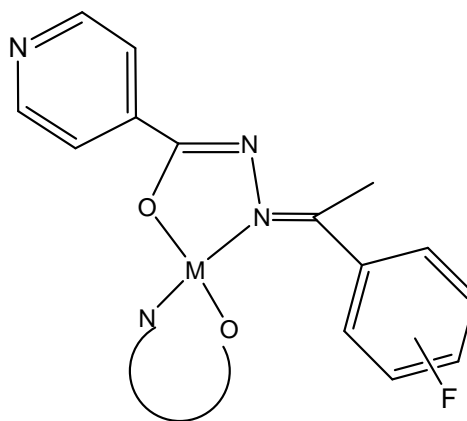


Figure 1.34: Metal complex of fluorinated INH-hydrazones (M= Co²⁺, Cu²⁺)⁸⁷

Schiff bases and their copper complexes as antibacterial agents have also been explored by Padhye *et al.*⁸⁵ Copper complexes of carboxamidrazone, as shown in figure 1.35, exhibited a 32 to 64-fold activity enhancement when compared to their respective ligands and displayed MICs in the range 2-4 μ M. As the metal conjugates are more lipophilic than their organic counter parts, it allows complexes to easily permeate through the mycobacterial cell wall. In addition, the intracellular reduction of Cu(II) to Cu(I), leads to the generation of reactive oxygen species which can be deleterious to bacterial cells.¹⁰²⁻¹⁰⁴

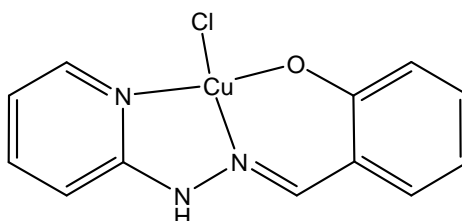


Figure 1.35: Copper complex of carboxamidrazone⁸⁵

Other first row transition metal complexes have also been investigated for their antitubercular activity, including vanadium, iron, cobalt, nickel and zinc complexes.^{86,105-110}

Additionally, metal complexes of second and third row transition metals, such as Pd, Pt, Ru, Ag, Au have been investigated.¹¹¹⁻¹¹⁴ Palladium(II) and platinum(II) complexes of various fluoroquinolones (ciprofloxacin, levofloxacin, ofloxacin, sparfloxacin, and gatifloxacin) have been synthesised by Fonts *et al.* Based on the results obtained, it was proposed that Pd binds to the ligands through the planar β -diketo system of the fluoroquinolone, as shown in figure 1.36.

The complexes display MIC values in the range of 0.31-1.25 $\mu\text{g/ml}$ against Mtb strain H37Rv.¹¹⁵

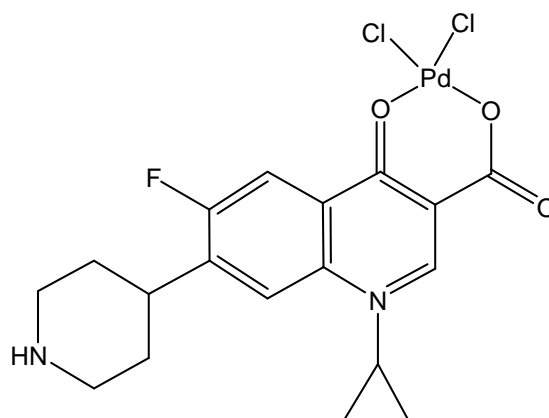


Figure 1.36: Palladium complex of ciprofloxacin¹¹⁵

1.8 Project Aims

In order to address the problem of persistence and resistance in Mtb, there is a need for the development of new novel antitubercular drugs. This can be achieved by either designing new chemical entities or modifying the existing TB drugs in order to overcome their inherent drawbacks.

The aim of the project was to synthesise analogs of the currently available antitubercular drug isoniazid and the Cu(II) and Zn(II) complexes of the analogues obtained. In addition, the stability of the synthesised compounds was to be investigated, under near physiological conditions and in different pH environments. Furthermore, the redox behaviour of the Cu(II) complexes was to be studied using cyclic voltammetry. In order to investigate structural aspects of the compounds, especially the metal complexes, single crystal X-ray diffraction studies were carried out. The results obtained informed the structure activity relationship (SAR) analysis of the compounds with respect to their antitubercular activity.

Chapter-2
Synthesis and Characterisation

2.0 Synthesis and Characterisation

2.1 Introduction:

Schiff base ligands have been extensively studied for their role in biological fields, as well as in coordination chemistry. Apart from their important role in studying the coordination chemistry of metal complexes,¹¹⁶⁻¹²⁰ Schiff base ligands have also played a major role in the development of bioinorganic chemistry for the past few years,¹²¹⁻¹²⁴. In addition to the growing interest in using Schiff base ligands for mimicking metalloenzymes, their metal complexes have also been investigated for their activity against various biological disorders including cancer,¹²⁵⁻¹²⁶ tuberculosis,^{82,127-129} inflammation¹³⁰⁻¹³¹ and diabetes¹³²⁻¹³³.

Hydrazones (figure 2.1) are widely studied due to their chelating ability. Depending on the metal ion, hydrazones can exhibit bidentate,¹³⁴ tridentate¹³⁵ tetradentate¹³⁶ or multidentate¹³⁷⁻¹³⁸ coordination modes depending on the geometric arrangement of the neutral and anionic donor atoms present. Hydrazones (figure 2.1) contain two nucleophilic nitrogen atoms; with the amino nitrogen being the more nucleophilic than the azomethine nitrogen. The C=N double bond, generally called azomethine bond, is conjugated with the lone pair of electrons on the terminal nitrogen atom⁷⁷. The physical and chemical properties of hydrazones depend on these structural fragments. The carbon atom of the hydrazone group has both electrophilic and nucleophilic character which makes it useful in organic synthesis, especially in the synthesis of heterocyclic compounds¹³⁹

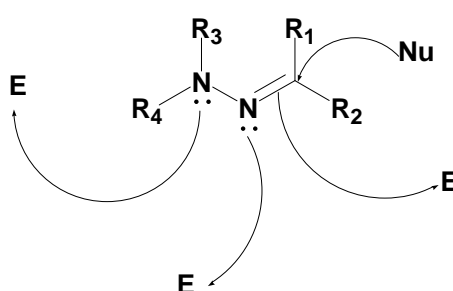
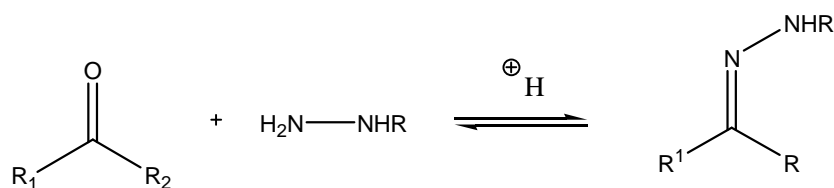


Figure 2.1: Hydrazone, E = electrophile, Nu = nucleophile⁷⁷

The synthesis of hydrazones involves condensation of hydrazine or a hydrazide with an aldehyde or ketone, resulting in the elimination of a water molecule, as shown in scheme 2.1. These types of reactions are classified as reversible acid-catalysed reactions and proceed best at around pH 4.5.¹⁴⁰



Scheme 2.1: Hydrazone formation¹⁴⁰, hydrazine (R - H), hydrazone (R - O=C-R)

It is well established that hydrazones can form *E/Z* isomers¹⁴¹ and/or keto-enol tautomers¹⁴² in solution. This allows hydrazones to be present as the different isomers (*E* or *Z*) as well as neutral, monoanionic, dianionic species depending on pH, medium, reaction conditions and the coordinating metal.¹⁴³⁻¹⁴⁵ Derivatives of hydrazones such as thiosemicarbazone, dithiocarbamate and acyl hydrazones can provide both hard and soft donor atoms, such as oxygen (O), nitrogen (N) and sulphur (S). Various combinations of these donor atoms such as ONO,¹⁴⁶ ONS,¹⁴⁷ NNS¹⁴⁸ have been studied, especially with transition metal ions. Moreover, changing the donor atoms can help to tune the redox property of the metal ion.¹⁴⁹

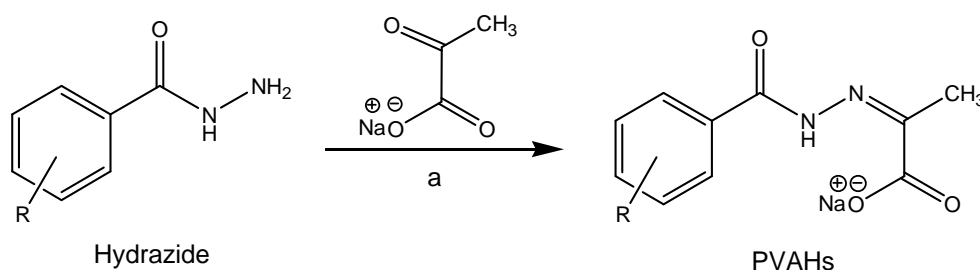
Chapter-2 is divided in two sections; section A describes synthesis and characterisation of pyruvate hydrazones (PVAHs) and their respective metal complexes. Section B deals with synthesis and characterisation of cinnamaldehyde hydrazones (CAHs) and their respective Cu(II) complexes

Section A:

In section A, synthesis and characterisation of twenty pyruvate hydrazones (PVAHs) and their Cu(II) and Zn(II) complexes along with Cu(I) complexes of selected ligands is discussed. In addition, synthesis and characterisation of a dihydrazone analogue of a pyruvate hydrazone is also described.

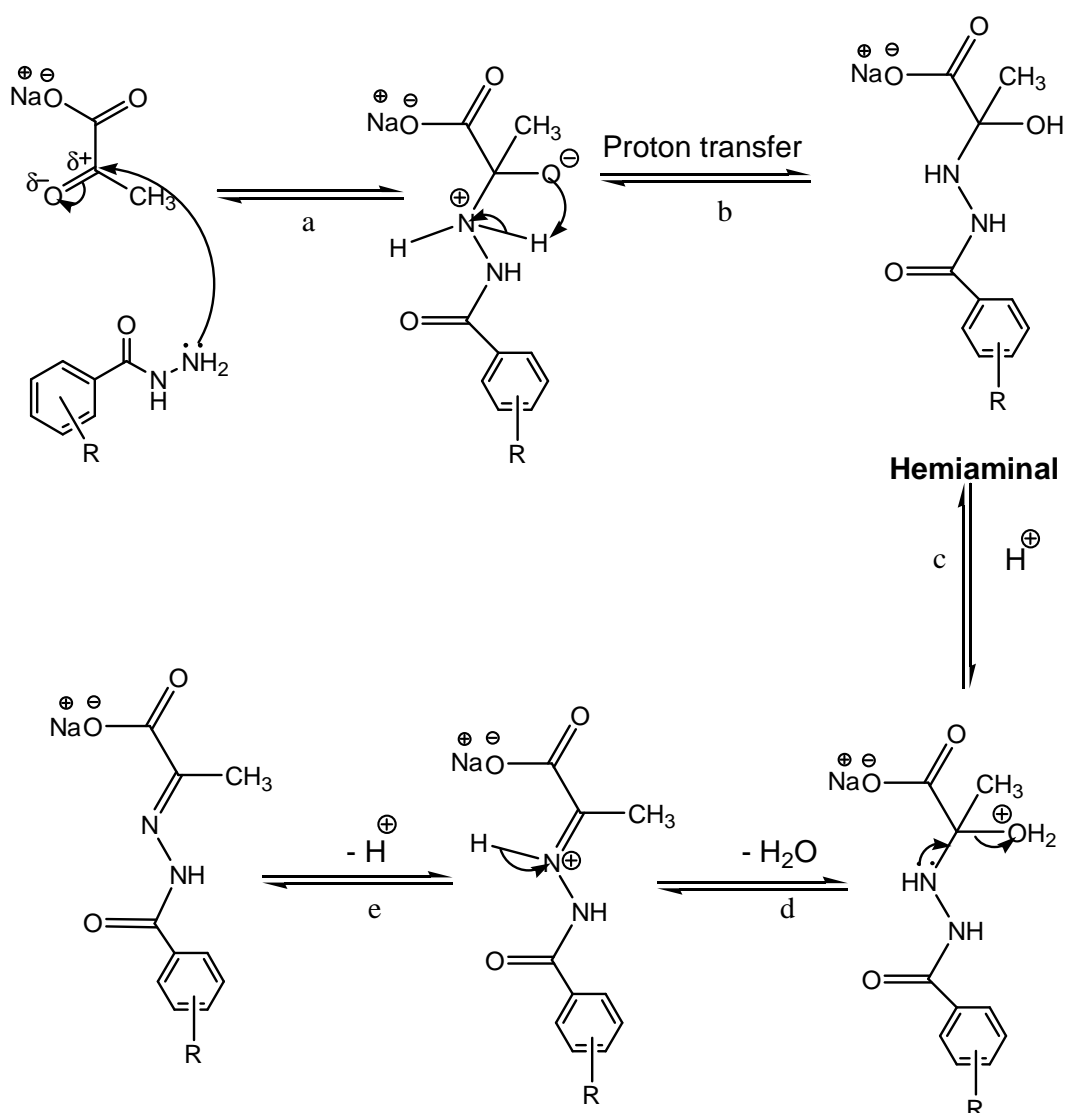
2.2 Synthesis of pyruvate hydrazones (PVAHs)

The synthesis of a Schiff base through the reaction of sodium pyruvate with a hydrazide is a one step condensation reaction, as given in scheme 2.2. PVAH (pyruvate hydrazone) ligands NaHL1-NaHL20, were synthesized according to a reported procedure.¹³⁵ Commercially available hydrazides were used in the syntheses, except for NaHL20. The starting hydrazide for NaHL20, pyrazinoyl hydrazide, was synthesized by condensing methyl pyrazine 2-carboxylate and hydrazine hydrate using standard literature procedures.¹⁵⁰ The details of the preparation of pyrazinoyl hydrazide and PVAHs can be found in the experimental section (chapter -7).



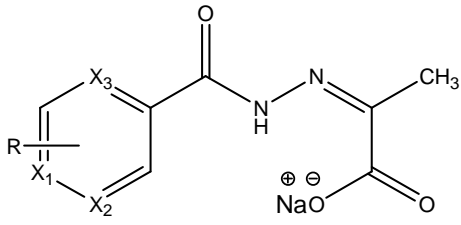
Scheme 2.2: General synthetic scheme for the preparation of PVAHs a) MeOH:H₂O (7:3), reflux, 2 hours, water

The detailed mechanism for the formation of Schiff bases and hydrazones is given in Scheme 2.3. The carbonyl group and the amine group of two biologically active pharmacophores, sodium pyruvate and the respective hydrazide are combined and the azomethine bond is formed via the loss of a water molecule. The reaction begins with the nucleophilic attack of the lone pair on the amine nitrogen onto the electrophilic carbon centre which gives rise to a hemiaminal intermediate. The intermediate then reacts with a proton and the subsequent loss of a water molecule yields the PVAH. These reactions are known to proceed best around pH 4 – 5, as strongly acidic conditions favour the formation of the protonated amine, which cannot behave as a nucleophile (step a). Strong basic conditions do not favour the protonation of the hemiaminal intermediate (step c), hence it cannot act as a good leaving group (step d).¹⁴⁰

Scheme 2.3: General mechanism for the formation of PVAHs¹⁴⁰

A range of hydrazides bearing different R-groups; such as electron-withdrawing, electron-donating, hydrophilic, hydrophobic and heterocyclic groups containing nitrogen have been used to synthesize a series of structurally related PVAHs. Lists of R groups along with their compound codes are provided in table 2.1. The rationale behind using the different substituents or the same substituent at different positions on the aromatic group is that it allows for an analysis of structure activity relationships (SARs) with regards to antitubercular activity. Schiff base compounds have always been a popular choice amongst medicinal chemists, as it is generally a one step reaction with high yields and also the starting materials are mostly inexpensive. Once the biologically active lead compounds are known they can be further modified to improve their efficacy.

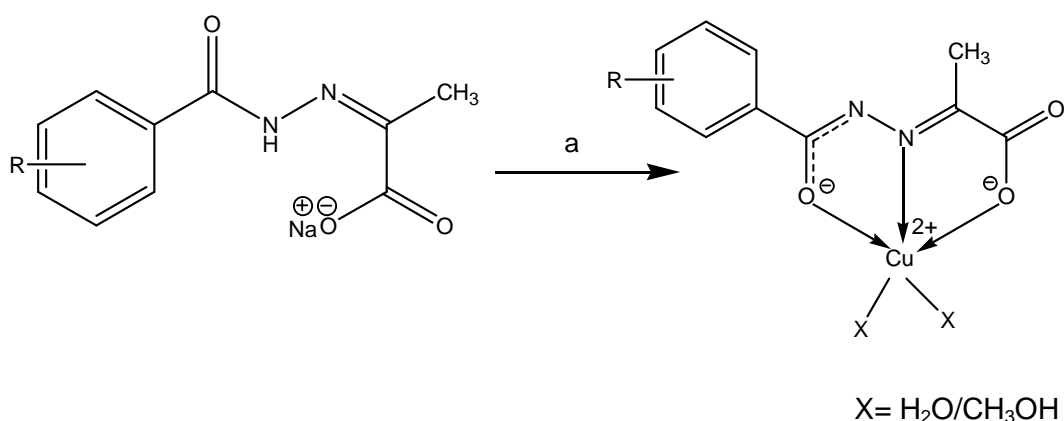
Table 2.1: Library of PVAHs with their compound codes and yields

			
		R (X = C)	Yield
1	NaHL1	H	82 %
2	NaHL2	<i>o</i> -OH	89 %
3	NaHL3	<i>m</i> -OH	87 %
4	NaHL4	<i>p</i> -OH	83 %
5	NaHL5	<i>o</i> -Cl	83 %
6	NaHL6	<i>p</i> -Cl	90 %
7	NaHL7	<i>m</i> -CH ₃ , <i>p</i> -NO ₂	82 %
8	NaHL8	<i>p</i> -NO ₂	95 %
9	NaHL9	<i>p</i> -CH ₃	86 %
10	NaHL10	<i>m</i> -Br	86 %
11	NaHL11	<i>p</i> -Br	96 %
12	NaHL12	<i>m</i> -OCH ₃	81 %
13	NaHL13	<i>p</i> -OCH ₃	83 %
14	NaHL14	<i>p</i> -CF ₃	89 %
15	NaHL15	<i>m</i> -F	80 %
16	NaHL16	<i>p</i> -(CH ₃) ₃ C	96 %
17	NaHL17	<i>o</i> -OH, <i>p</i> -OCH ₃	92 %
Heterocyclic compounds (R = H)			
18	NaHL18	X ₁ = N, X ₂ , X ₃ = C	89 %
19	NaHL19	X ₂ = N, X ₁ , X ₃ = C	82 %
20	NaHL20	X ₁ = C, X ₂ , X ₃ = N	80 %

2.3 Synthesis of Cu(II) complexes of PVAHs

The syntheses of the Cu(II) complexes of the PVAHs were performed in a 1:1 metal-to-ligand ratio. The details of the synthetic procedures used can be found in the experimental section. The X-ray crystal structures (discussed in chapter 4) and elemental analysis data, which can be found in experimental section, indicate that most of the copper complexes are isolated as 1:1 complexes. Initially, the reaction was tried in methanol, according to a procedure reported in the literature that gave crystalline solids upon slow evaporation,¹⁵¹ but this resulted in overall low yields. The low yields isolated are likely due to the high solubility of the Cu(II)-PVAH complexes in methanol. In order to improve the overall yield, the reactions were attempted in water as reported by Turta et al¹⁵². The combination of the aqueous solutions of the reactants gave rise to green precipitates, which were isolated by filtration and washed with water in order to remove any salt impurities. A selection of reactions with different ligands was repeated in water and it was found that the yield increased 2-fold in most of the complexes. ESI-MS confirmed the formation of 1:1 complex and purity was confirmed using elemental analysis.

The ligands behave as tridentate, dianionic ligands and bind to the Cu-centre as shown in Scheme 2.4. The remaining coordination sites on the Cu-centre can be occupied by anions or neutral solvent molecules, such as H₂O or methanol. The negatively charged oxygen donors balance the charge of the positively charged Cu(II) centre, whereas the nitrogen atom donates its lone pair of electrons, allowing the formation of an overall neutral complex.



Scheme 2.4: Synthesis of Cu(II) complexes of PVAHs a) CuCl₂·2H₂O

As reported earlier, pyruvate hydrazones can either form square planar,¹⁵² square pyramidal⁸⁴ or octahedral complexes.¹⁵³ In octahedral complexes, two ligands bind to a single copper centre. Both the octahedral and square pyramidal forms have been observed in the crystal structures of some of the Cu(II) complexes of pyruvate hydrazones but most complexes exist as square pyramidal complexes. One exception is the crystal structure of the octahedral Cu(II) complex of ligand NaHL7, although the elemental analysis supports the formation of a square pyramidal complex. More on the structural aspects of the copper complexes is discussed in chapter-3.

2.3.1 ESI-MS of Cu(II) complexes

According to elemental analysis data and single crystal X-ray structures, the expected molecular ion peak in the ESI-MS positive mode for copper complexes, should either correspond to the $[[\text{Cu(II)LX(H}_2\text{O)}_2]+\text{H}]^+$ or $[[\text{Cu(II)LX(H}_2\text{O)}_2]+\text{Na}]^+$ ions. For example, the sodiated molecular ion peak for $[\text{Cu(II)L9(H}_2\text{O)}_2]$ is expected at m/z 340.0096 for $[\text{M}+\text{Na}]^+$. However, this was not found, instead the mass spectrum of $[\text{Cu(II)L9(H}_2\text{O)}_2]$ exhibits a molecular ion peak one mass unit higher than expected. The ESI-mass spectrum of $[\text{Cu(II)L9(H}_2\text{O)}_2]$ was recorded in acetonitrile and is shown in figure 2.2. The positive ion peak observed at m/z 341.0434 can be assigned to $[\text{M}+\text{H}+\text{Na}]^+$. The additional large peak at m/z 363.0249 corresponds to $[\text{M}+2\text{Na}]^+$, whereas the peak at 323.0349 corresponds to $[\text{M}-\text{H}_2\text{O}+\text{H}+\text{Na}]^+$.

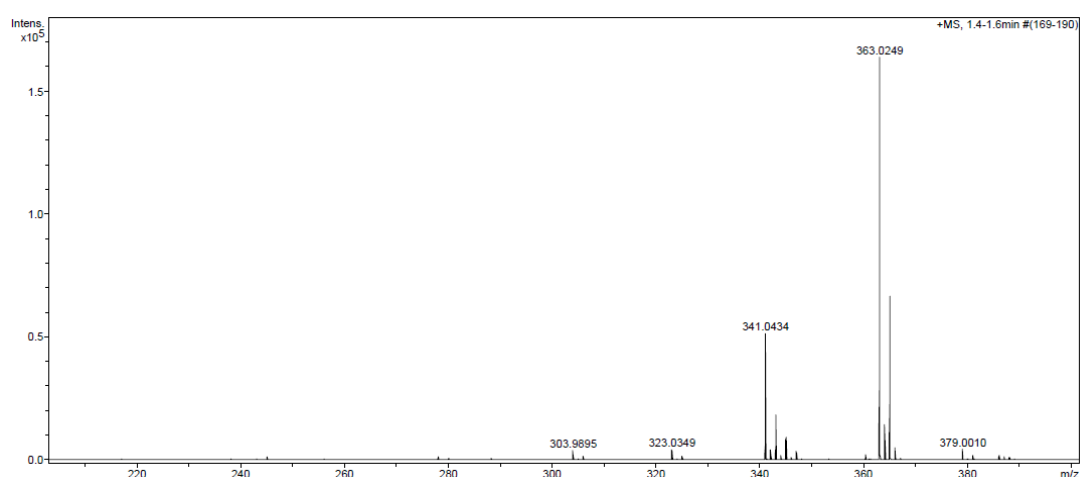
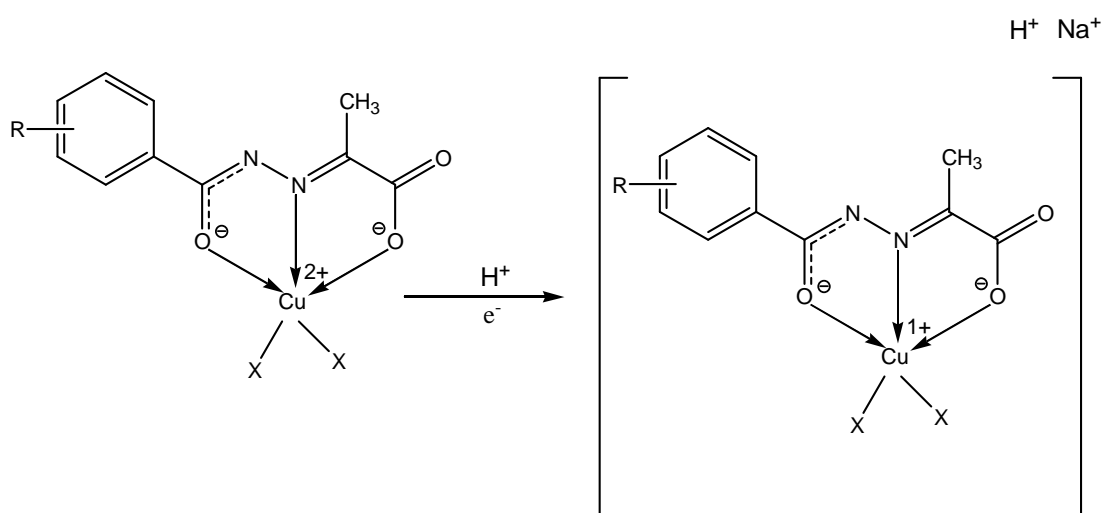


Figure 2.2: Positive high resolution ESI-mass spectrum of $[\text{Cu(II)L9(H}_2\text{O)}_2]$

Since the higher molecular ion peak has only one positive charge, it could be due to addition of one hydrogen atom or one proton, which is likely to be associated with the reduction of Cu(II) to Cu(I). The reduction of Cu(II), in the positive ion mode in the gas phase has been reported in the literature, where the reduction can be due to the transfer of an electron from a solvent molecule to Cu(II) centre in the gas phase.¹⁵⁴⁻¹⁵⁵ The reduction of a Cu(II) complex in presence of solvent molecule, especially a coordinated or non-coordinated water molecule, can be explained with the help of theory proposed by Frański. The water molecule undergoes an electrochemical oxidation, most likely at the ESI source, subsequently giving rise to electrons and protons as given in equation 2.1. These resulting electrons can reduce Cu(II) to Cu(I) as indicated in equation 2.2. Additionally, Frański observed that addition of water increased the formation of Cu(I) species over Cu(II) species.¹⁵⁴



Oxidation of a water molecule in the gas phase can result in an addition of a proton as indicated in Scheme 2.5. This would then result in reduction of Cu(II) to Cu(I) and with an addition of Na ion it would give rise to $[\text{M}+\text{H}+\text{Na}]^+$ molecular ion peak.



Scheme 2.5: Reduction of Cu(II) to Cu(I) complex with an addition of H^+ and Na^+ ESI-mass spectrometer

The molecular ion peak at 323.0349, corresponding to $[M-H_2O+H+Na]^+$, could be due to the loss of a weakly bound water molecule from the coordination sphere of Cu(II) complex. Longer distances of the apically bound water molecules, as expected according to the Jahn-Teller distortion, have been observed in the crystal structure of Cu(II) complexes of PVAHs (chapter - 3). Hence, the bond strength of the apical water molecule is weak as compared to those of the equatorial bonds which results in fragmentation of $[Cu(II)L9(H_2O)_2]$ in the gas phase arising from the loss of a water molecule. Similar behaviour is observed in other Cu(II) complexes of PVAHs and the details can be found in the experimental section. However, $[Cu(II)L7(H_2O)_2]$ does not seem to undergo this reduction in the ESI mode.

The simulations for the corresponding peaks are given in figure 2.3. There is a relatively large difference observed between the calculated (341.0169) and experimental (341.0434) values. As the Cu(II) complex does not ionise very well in the ESI-MS, it gives only a low intensity peak and is thus difficult to measure accurate values at high resolution.

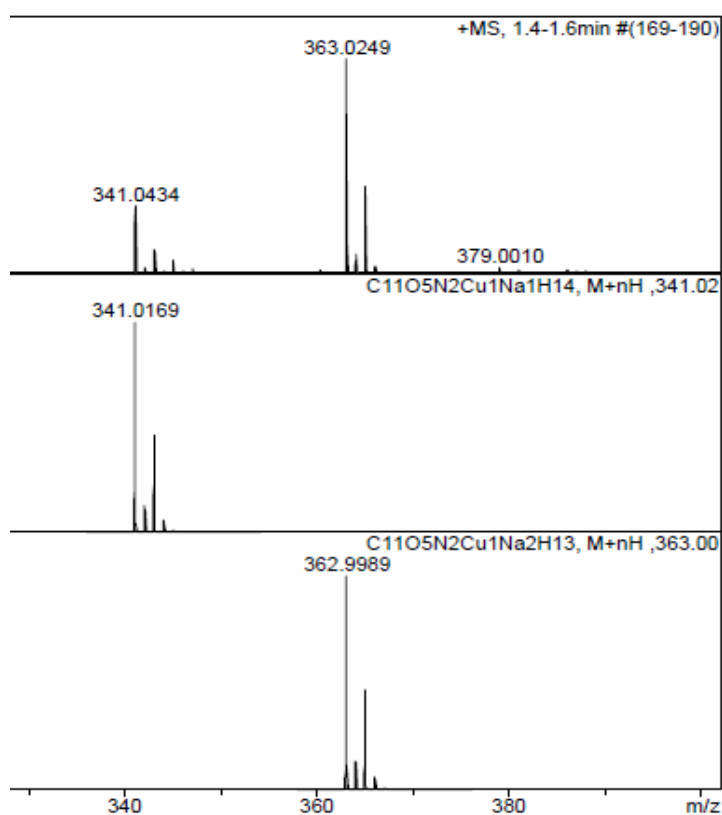
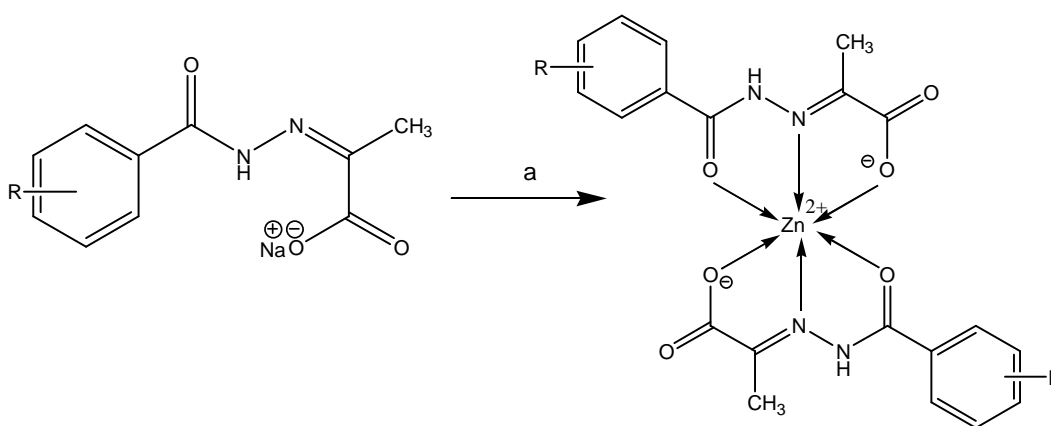


Figure 2.3: Measured (top) and simulated (middle, bottom) positive ion high resolution ESI-MS spectrum of $[\text{Cu}(\text{II})\text{L9}(\text{H}_2\text{O})_2]$

However, the observed and simulated isotopic pattern of the investigated copper complexes of PVAHs matches reasonably well as displayed in the ESI-MS spectrum $[\text{Cu}(\text{II})\text{L9}(\text{H}_2\text{O})_2]$ displayed in figure 2.3. The ESI-MS spectra of $[\text{Cu}(\text{II})\text{L7}(\text{H}_2\text{O})_2]$, $[\text{Cu}(\text{II})\text{L8}(\text{H}_2\text{O})_2]$, $[\text{Cu}(\text{II})\text{L9}(\text{H}_2\text{O})_2]$, $[\text{Cu}(\text{II})\text{L14}(\text{H}_2\text{O})_2]$, $[\text{Cu}(\text{II})\text{L15}(\text{H}_2\text{O})_2]$, $[\text{Cu}(\text{II})\text{L16}(\text{H}_2\text{O})_2]$, $[\text{Cu}(\text{II})\text{L20}(\text{H}_2\text{O})_2]$ can be found in Appendix 1.

2.4 Synthesis of Zn(II) complexes of PVAHs

Unlike Cu(II), Zn(II) forms 1:2 metal : ligand complexes with PVAHs, as shown in scheme 2.6. The composition of the complexes was confirmed by X-ray crystallography, elemental analysis and ESI-mass spectrometry. Most of the mixtures of PVAHs and ZnSO_4 in aqueous solution yielded white precipitates. Good quality crystals suitable for X-ray diffraction were obtained from the NMR samples of $[\text{Zn}(\text{HL7})_2]$, $[\text{Zn}(\text{HL8})_2]$, $[\text{Zn}(\text{HL9})_2]$, and $[\text{Zn}(\text{HL13})_2]$ in d_6 -DMSO. The details of the synthetic and characterisation procedures can be found in experimental section, whereas the crystal structures can be found in chapter-3. The NMR-spectra of the zinc complexes are discussed in the following section.



Scheme 2.6: Synthesis of Zn(II) complexes of PVAHs a) $\text{ZnSO}_4 \cdot 7\text{H}_2\text{O}$

2.5 Nuclear magnetic resonance (NMR) studies:

All the NMR studies described in this chapter were done in d_6 -DMSO. A detailed analysis of a representative example of the ligand NaHL9 by ^1H and ^{13}C NMR spectroscopy is discussed in this chapter. Full characterisation data of ligands NaHL1 - NaHL20 is given in chapter-7.

2.5.1 ^1H NMR spectroscopic analysis of NaHL9

The ^1H NMR spectrum of NaHL9 along with the structure and its atom numbering scheme is illustrated in figure 2.4. The spectrum shows two sets of signals suggesting two different types of species present in the solution. These major and the corresponding minor peaks observed in the spectra can be attributed to the isomers of NaHL9 present in the solution.

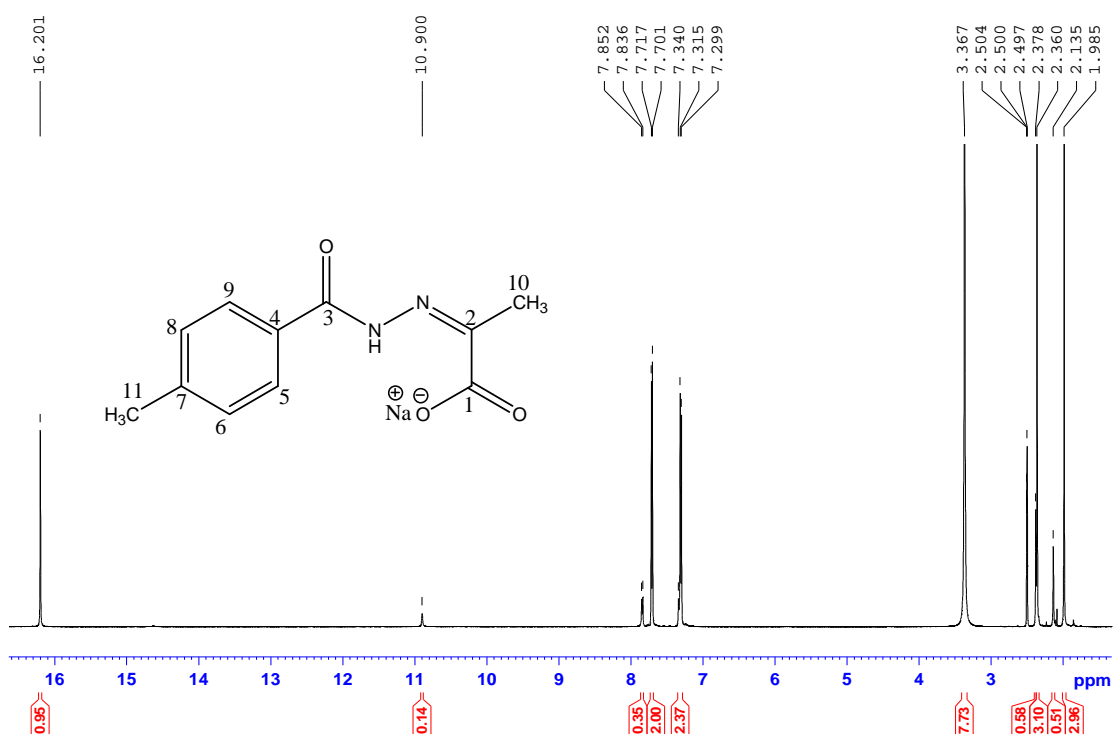


Figure 2.4: ^1H NMR spectrum of NaHL11 recorded in d_6 -DMSO

Before investigating the structure of two isomers, assigning of the peaks will be done. Two sharp singlets of relative integration three are observed at 1.98 and 2.36 ppm and can be assigned to the two CH_3 groups. The peak at 2.36 can be attributed to the aromatic CH_3 group as it is more deshielded than the methyl group C10. These assignments were further confirmed by a 2D COSY experiment. The

NH peak is observed 10.90 ppm and is deshielded if compared to the parent hydrazide (9.69 ppm) owing to the conjugation with the C=N bond. The equivalent peak for the major isomer appears at 16.2 ppm. The aromatic protons of the major isomer give rise to two doublets at 7.30 ppm and 7.70 ppm with a coupling constant of $J_{\text{H-H}} = 8.0$ Hz which is consistent with the *para*-substituted aromatic protons. The aromatic protons corresponding to the minor isomer appear at 7.34 ppm and 7.84 ppm and the coupling constant ($J_{\text{H-H}} = 8.0$ Hz) is the same as that of the major isomer. However, the $J_{\text{H-H}}$ for the resonance at 7.34 ppm cannot be calculated accurately as the resonances of two isomers merge.

2.5.2 *E/Z* isomerisation of pyruvate hydrazone ligands:

It is well established that hydrazones exhibit keto/enol tautomerism and/or *E/Z* isomerism in solution and that the ratio of the isomers depends upon the nature the compounds and the solvent used.^{141,156-157} The NMR spectra of PVAHs exhibited additional minor peaks in addition to the expected major peaks, suggesting two types of species present in the d_6 -DMSO solution. A representative example of NaHL9 showing its ^1H NMR spectrum in the aromatic region 7.20 – 7.90 ppm is illustrated in figure 2.5.

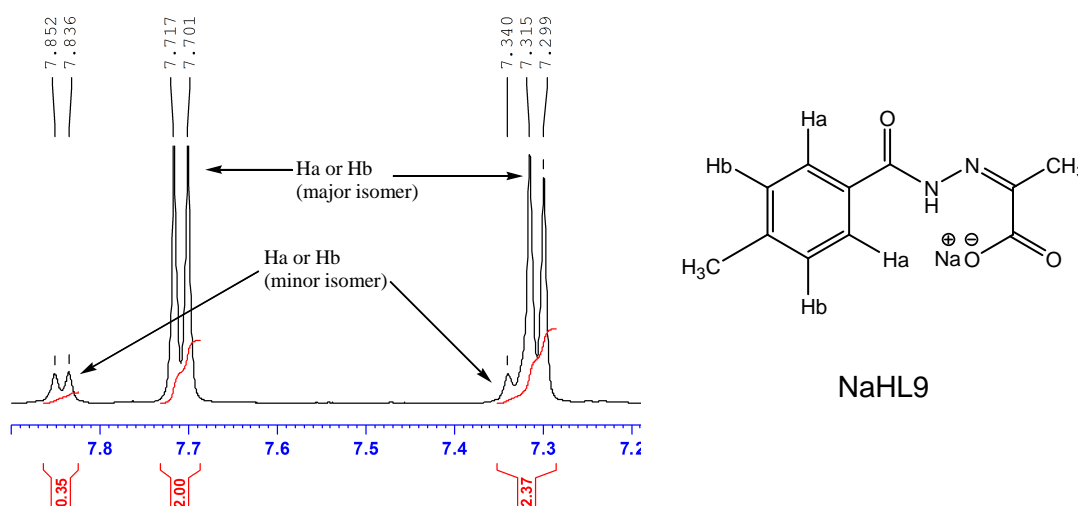


Figure 2.5: ^1H NMR spectrum (7.20 – 7.90 ppm) of a solution of NaHL9 in d_6 -DMSO showing major and minor peaks in the aromatic region

In order to gain further insight, variable temperature (VT) ^1H NMR studies were performed on NaHL9 and NaHL13. The stacked NMR spectra of NaHL9 recorded at different temperatures are shown in figure 2.6. In the aromatic region

between 7.20 and 7.90 ppm, it is observed that the relative integration of the minor peak decreases with an increase in the temperature, whereas the integrals of the isomeric equivalents increase. Likewise, the resonances of the protons of both methyl-groups display a similar behaviour.

The rate of isomerisation is slow at room temperature, due to high activation barrier of the rotation around the azomethine double bond and much slower than the NMR timescale. This gives rise to two distinct NMR resonances for the protons as indicated protons in figure 2.6. The major and minor peak can be assigned to *E* and *Z* isomers.¹⁴¹

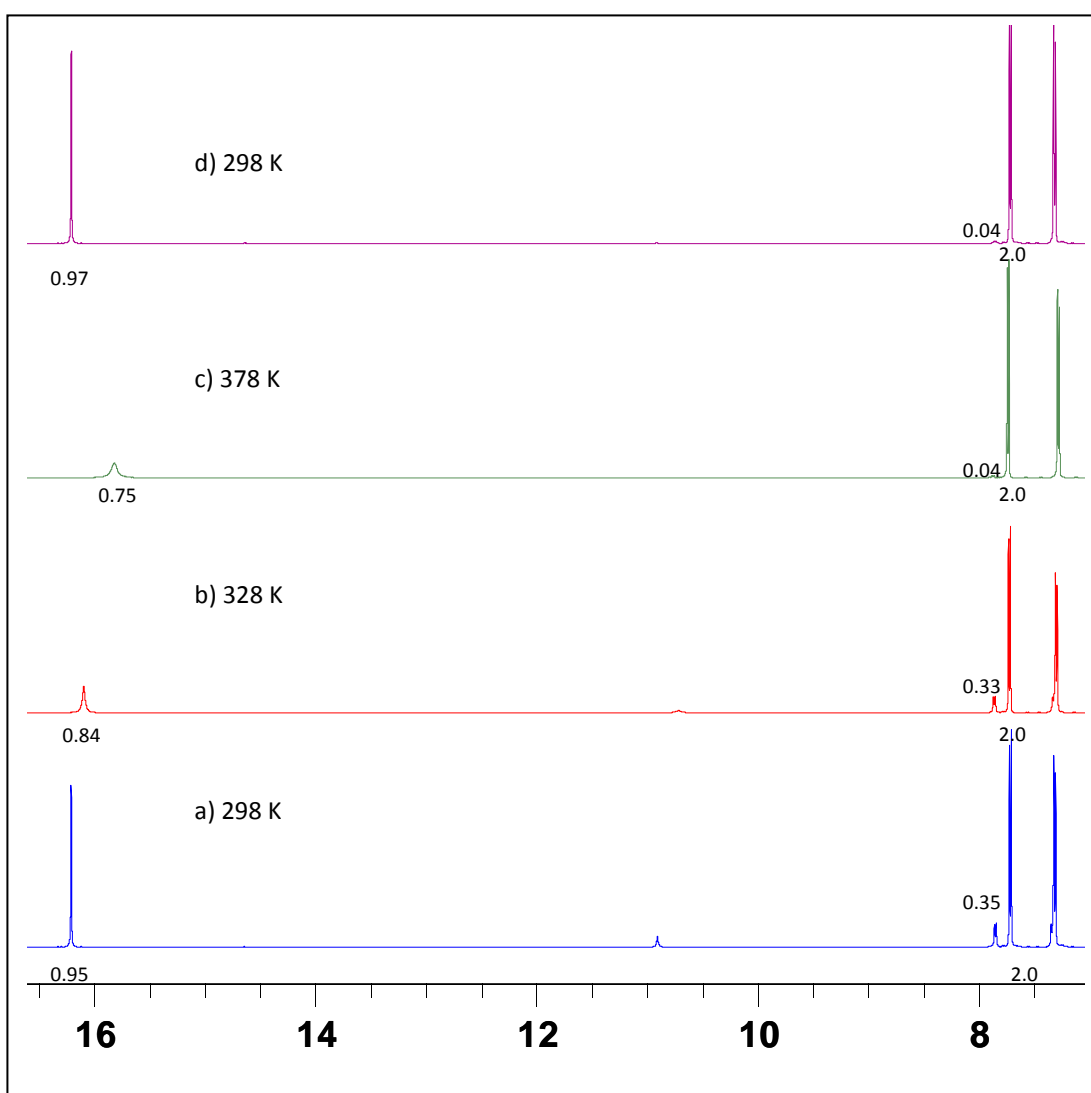


Figure 2.6: Stacked NMR spectra of NaHL9 in d_6 -DMSO recorded at the indicated temperatures

The rate of isomerisation can be increased by heating the solution of isomers to a higher temperature. Heating to high temperatures overcomes the activation energy required to convert the *E* form present in the solution to the *Z* form. As the *Z* form is more stable than the *E* form, the ligand remains in the *Z* form even after cooling the solution back to 298 K (figure 2.6 d). Similar VT results were obtained for ligand NaHL13 and can be found in the Appendix 2.

The structures of the *Z* and *E* isomers of pyruvate hydrazones are illustrated in figures 2.7 a/b and 2.7 c, respectively. The reason for the prevalence of the *Z* isomer in solution could be attributed to the strong intramolecular hydrogen bond N-H---O, as depicted in figure 2.7 a, which makes it a more stable species than the *E* isomer. The resonances at 16.2 and 10.9 ppm can be assigned to the N-H proton of *Z* and *E* isomer, respectively. Owing to the fact that the strong hydrogen bond deshields the amide proton, the (N-H) in the *Z* isomer resonates at higher frequency as compared to the *E* isomer.¹⁵⁶⁻¹⁵⁷ Extreme downfield shift of the proton at 16.2 ppm can also be attributed to the O-H signal of the imine tautomer as indicated in figure 2.7 b.

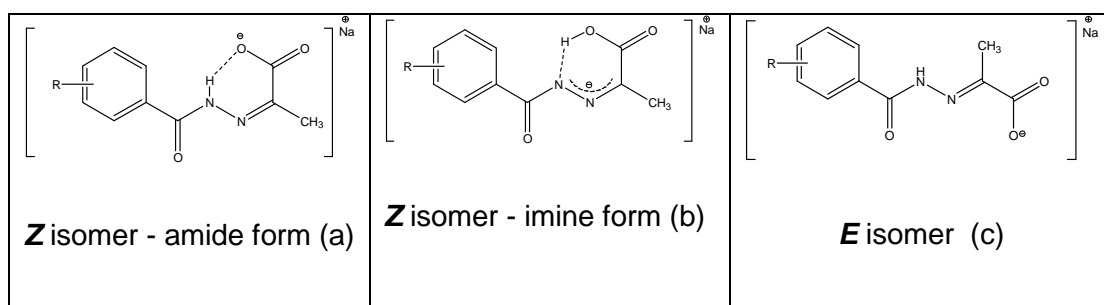


Figure 2.7: a) *Z*-amide form and b) *Z*-imine form and c) *E* isomers of PVAHs

Extensive studies done by Landge *et al.*¹⁵⁸ on hydrazones as depicted in figure 2.8, suggests that the *Z* → *E* isomerisation process takes places through rotation (around C=N bond) pathway rather than inversion pathway via the formation of polar transition state. Moreover, the energy of activation (E_a) and energy of enthalpy (ΔH^\ddagger) lies in the range 6.7 – 11.2 kcal mol⁻¹ and 6.1 – 10.6 kcal mol⁻¹ respectively, depending on the substituent attached to aromatic ring and NMR solvents (d_8 -toluene, CD₃CN) used for the study. These values can be related to breaking of O---H bond and/or rotation around C=N bond. Furthermore, the negative entropy ($\Delta S^\ddagger = -38.0$ to -56.6 cal mol⁻¹ K⁻¹) values, suggests the formation of a

polarised transition state in $Z \rightarrow E$ isomerisation process leading to a rotation pathway. Inversion pathway for $Z \rightarrow E$ isomerisation involves non-polarised transition pathway.

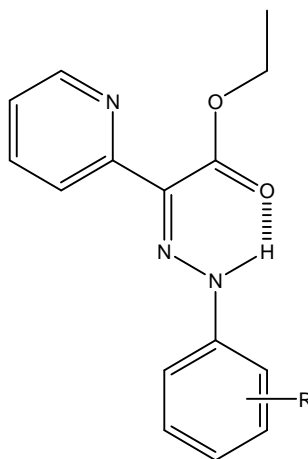


Figure 2.8: Structure of investigated hydrazone/s (Z isomer shown in figure) for $Z \rightarrow E$ isomerisation process¹⁵⁸

2.5.3 Trends in the ^1H NMR data

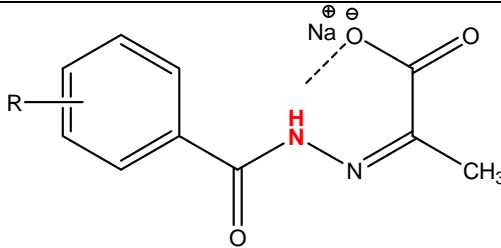
Different substituents on the aromatic ring can influence the electronic properties of Schiff base ligands. The ^1H NMR chemical shifts for the major Z isomers in ligands NaHL1-NaHL20 are listed in table 2.2. Generally, the aromatic protons in PVAHs are more deshielded where there is an electron withdrawing group (EWG) as compared to ligands with electron donating groups (EDG). The same effect is observed for the amide (N-H) proton; however, the aromatic substituents had no or little effect on the resonances of the CH_3 protons. The amide proton resonance for PVAHs exhibits a large range of chemical shifts between 15.48 and 16.77 ppm, which can be correlated with the properties of the different substituents on the aromatic ring. The trend observed in ^1H NMR resonance of the amide protons is discussed in detail below.

Table 2.2: ^1H NMR chemical shifts (in ppm) for the indicated PVAH protons, recorded in d_6 -DMSO (NaHL1-NaHL20)

		R (X = C)	Ar-H	CH ₃	N-H	Ar-R (CH ₃ / OCH ₃)
	Sodium pyruvate		-	2.07	-	-
1	NaHL1	H	7.52, 7.82	2.01	16.17	-
2	NaHL2	<i>o</i> -OH	6.87, 7.18, 7.38, 7.69	2.05	16.02	-
3	NaHL3	<i>m</i> -OH	6.97, 7.26	2.02	15.92	-
4	NaHL4	<i>p</i> -OH	6.88, 7.68	2.01	15.75	-
5	NaHL5	<i>o</i> -Cl	7.31-7.57	2.04	15.48	-
6	NaHL6	<i>p</i> -Cl	7.58, 7.81	2.01	16.48	-
7	NaHL7	<i>m</i> -CH ₃ , <i>p</i> -NO ₂	7.78, 7.87, 8.10	2.00	16.61	2.56
8	NaHL8	<i>p</i> -NO ₂	8.02, 8.34	2.02	16.69	-
9	NaHL9	<i>p</i> -CH ₃	7.70, 7.30	1.98	16.12	2.35
10	NaHL10	<i>m</i> -Br	7.48, 7.78, 7.92	2.01	16.46	-
11	NaHL11	<i>p</i> -Br	7.73	2.01	16.36	-
12	NaHL12	<i>m</i> -OCH ₃	7.13, 7.39	2.00	16.21	3.80
13	NaHL13	<i>p</i> -OCH ₃	7.03, 7.77	1.99	16.09	3.80
14	NaHL14	<i>p</i> -CF ₃	7.89, 7.99	2.01	16.60	-
15	NaHL15	<i>m</i> -F	7.51	2.01	16.41	-
16	NaHL16	<i>p</i> -(CH ₃) ₃ C	7.51, 7.73	1.97	16.17	1.30
17	NaHL17	<i>o</i> -OH, <i>p</i> -OCH ₃	6.47, 6.88, 7.62	2.05	15.81	3.76
Heterocyclic compounds			(R = H)			
18	NaHL18	X ₁ = N, X ₂ , X ₃ = C	7.69, 8.75	2.03	16.46	-
19	NaHL19	X ₂ = N, X ₁ , X ₃ = C	7.55, 8.14, 8.74, 8.97	2.02	16.46	-
20	NaHL20	X ₁ = C, X ₂ , X ₃ = N	8.73, 8.86, 9.22	2.02	16.77	-

The data for the substituent-induced chemical shift (SCS) is given as a proton shift for N-H relative to those of the unsubstituted ligand L1. Positive and negative Δ SCS values indicate shielding and deshielding, respectively and the data is provided in table 2.3.

Table 2.3: ^1H substituents-induced chemical shifts of N-H (indicated in red) of the Z isomer for ligands NaHL1 - NaHL20

					
	R	H-N SCS) (Δ		R	H-N SCS) (Δ
NaHL1	H	0 (16.17 ppm)	NaHL12	<i>m</i> -OCH ₃	+0.04
NaHL5	<i>o</i> -Cl	-0.69	NaHL11	<i>p</i> -Br	+0.19
NaHL4	<i>p</i> -OH	-0.42	NaHL15	<i>m</i> -F	+0.24
NaHL17	<i>o</i> -OH, <i>p</i> - OCH ₃	-0.36	NaHL10, NaHL18, NaHL19	<i>m</i> -Br/ one heterocyclic N	+0.29
NaHL3	<i>m</i> -OH	-0.25	NaHL6	<i>p</i> -Cl	+0.31
NaHL2	<i>o</i> -OH	-0.15	NaHL14	<i>p</i> -CF ₃	+0.43
NaHL13	<i>p</i> -OCH ₃	-0.08	NaHL7	<i>m</i> -CH ₃ , <i>p</i> -NO ₂	+0.44
NaHL9	<i>p</i> -CH ₃	-0.05	NaHL8	<i>p</i> -NO ₂	+0.52
NaHL16	<i>p</i> - (CH ₃) ₃ C	0.00	NaHL20	Two heterocyclic N	+0.66

In the proton NMR experiment, the NaHL1 N-H proton resonates at 16.17 ppm and is used for comparison with other substituted PVAHs. PVAHs containing electron donating hydroxyl substituent viz NaHL2, NaHL3, NaHL4 and NaHL17 give negative Δ SCS values as compared to NaHL1. This may be due to their shielding properties which in turn makes the amide proton electron rich. The hydroxyl group also known as strongly activating group gives rise to more negative values as compared to weakly activating groups, such as H (NaHL1), CH₃ (NaHL9) and *tert*-butyl (NaHL16). In addition, a negative value is also observed for NaHL13,

possessing an electron donating *p*-OCH₃ group. *m*-OCH₃, however, exhibits a slightly positive value.

On the other hand, PVAHs possessing weakly deactivating groups, such as the halogens F (NaHL15), Cl (NaHL6) and Br (NaHL11) exhibit positive values. This indicates that a halogen group renders the amide proton electron deficient resulting in a deshielding of the N-H resonance. *p*-Cl (NaHL6) is the most deshielding as compared to *p*-Br (NaHL11), *m*-F (NaHL15) and *m*-Br (NaHL10).

Moreover, within the series with the same substituent (hydroxyl, methoxy, and bromo), the N-H resonances in *meta*-substituted PVAHs are more deshielded as compared to the *para* substituted ones. Owing to the fact that the resonance effect of certain substituents is much more dominant in *para* position compared with *meta* position. Interestingly, N-H proton of *o*-Cl (15.48 ppm) substituted PVAH is far less deshielded than *p*-Cl (16.48 ppm) as can be seen from the table 2.2. This could be attributed to the intramolecular hydrogen bonding between the partially negative *o*-Cl⁻ ion and the N-H proton.

A strong electron withdrawing group or strongly deactivating group, such as NO₂, has a very large deshielding effect which is reflected in its Δ SCS value of +0.52 ppm in NaHL8. In comparison, electron donating groups, such as hydroxyl, methoxy and methyl groups have negative values. This is in good agreement with literature reports that describe the effect of electron withdrawing and electron donating groups on azomethine protons (N-H) within a series of *para*-substituted aroylhydrazone ligands¹⁵⁹. However, in the di-substituted NaHL7 ligand, the electron donating CH₃ group in *meta*-position in addition to the *para*-substituted NO₂ group lowers the Δ SCS positive value observed for the mono-substituted *p*-NO₂ group in NaHL8. This shows the less electron deficient nature of N-H proton in NaHL7 over NaHL8.

PVAHs containing a heterocyclic nitrogen atom show positive Δ SCS values indicating their strong electron withdrawing nature which results in an electron poor amide proton. The deshielding effect increases with the number of heterocyclic nitrogen atoms. For example, NaHL20 with two heterocyclic nitrogen atoms has the highest Δ SCS value of +0.66 ppm as compared to NaHL18 and NaHL19 possessing, one heterocyclic nitrogen atom. NaHL18 (N at 4th position) and NaHL19 (N at 3rd position) both exhibit a value of + 0.29 ppm, which implies that the position

of the heterocyclic nitrogen within the aromatic ring is less important with regards to the deshielding effect on the amide proton.

Hammett plots were used in order to further investigate the trend observed for the chemical shift of the amide proton of PVAHs with respect to the substituent parameter or commonly called Hammett parameter. The influence of different *para*- and *meta*-aromatic substituents on the chemical shift of the N-H proton resonance can be correlated with the Hammett constant (σ). Hammett reported the quantitative relationship between the rate of a reaction and the substituents present in systems containing substituted benzene rings in 1937¹⁶⁰. Since then 'Hammett values' are used as a practical method of measuring electron withdrawing/donating effects of substituents¹⁶¹⁻¹⁶³. The Hammett parameter (σ) is obtained by comparing the hydrolysis of benzoic acid with the hydrolysis of the appropriate *meta*- or *para*-substituted benzoic acid. *Ortho*-substituted compounds are avoided, because the steric effects of such substituents prevents an accurate analysis of the reaction rates. The sign of the σ parameter indicates the electronic nature of the substituent, with a positive value for electron withdrawing substituents and negative value for electron donating substituents.

For compounds NaHL1-NaHL20, a reasonable correlation of the chemical shifts of the N-H protons with the respective Hammett parameter is observed, as can be seen from figure 2.9. PVAHs containing heterocyclic nitrogen(s) or *ortho* and di-substituted aromatic rings are not included in the correlation, hence thirteen ligands were used for Hammett plot. The chemical shifts for the N-H resonances of the *Z*-isomer NaHL1-NaHL20 are listed in table 2.1.

Electron withdrawing groups (EWGs) cause a downfield shift, indicating increased deshielding of the amide proton, which is also involved in strong intramolecular hydrogen bonding with the carboxylate group. Most of the values lie quite close to the linear fit and are consistent with trend expected for the obtained experimental values. However, the values for *para*- and *meta*- hydroxyl-substituted PVAHs do not correlate as well to the proposed line of best fit, which may be due to intermolecular hydrogen bonding effects.

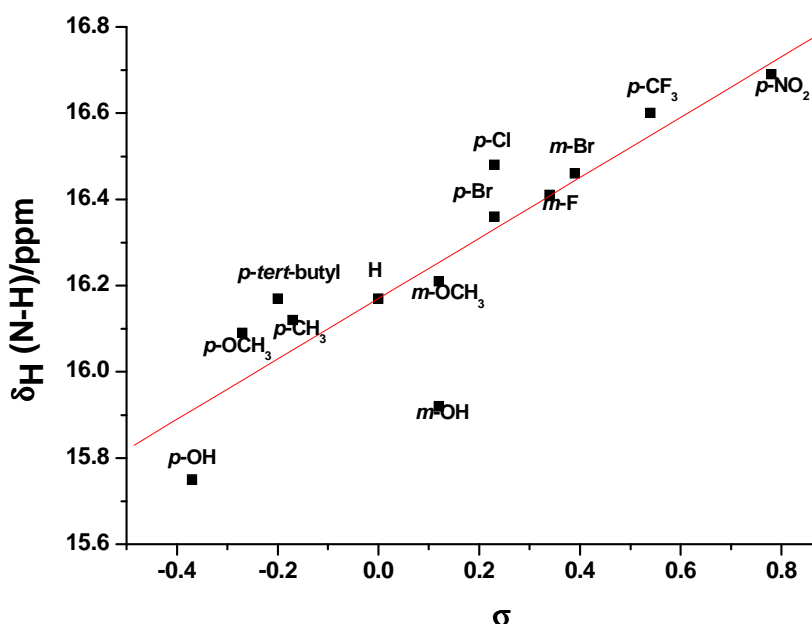


Figure 2.9: Plot of the ^1H NMR chemical shifts of the N-H proton of the Z isomer of thirteen indicated PVAHs in d_6 -DMSO vs σ ($R^2 = 0.77$).

A similar trend is observed in the Hammett plot, where strong electron withdrawing groups, for instance NO_2 , have a significant deshielding effect which is reflected in the chemical shift of the amide proton, whereas electron donating groups, such as CH_3 and $(\text{CH}_3)_3$ are shielding.

2.5.4 ^{13}C NMR spectra of PVAHs

The ^{13}C NMR spectrum of NaHL9 along with its structure and the atom numbering scheme is shown in figure 2.10. In the ^{13}C NMR spectrum of sodium pyruvate the resonance observed at 205.4 ppm can be attributed to the carbonyl (Cii) carbon of the *keto*-group. Upon conjugation as in NaHL9, the resonance is shifted to 150.5 ppm (figure 2.10) and can be assigned to the azomethine carbon (C-2). The carbon atom is less electron-deficient in the azomethine than in the keto group, which can be attributed to the difference in the electronegativities of nitrogen and oxygen, respectively. A similar effect is observed for the resonance of the Ci carbon, where the azomethine bond formation causes a upfield shift of the carboxylate carbon ($\text{Ci} \rightarrow \text{C1}$).

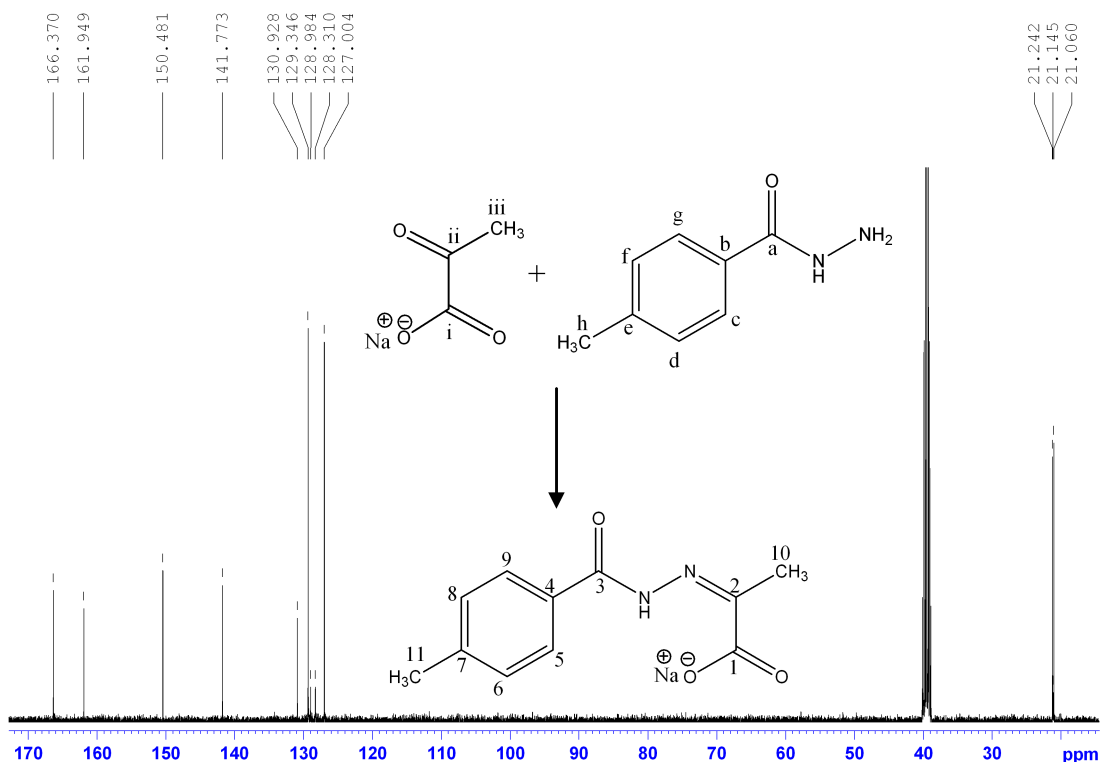


Figure 2.10: ^{13}C NMR spectrum of NaHL9 in d_6 -DMSO

The resonance observed at 166.3 ppm can be assigned to the carboxylate (C1) carbon, whereas the peak at 161.9 ppm is due to the carbonyl carbon (C3). The peaks observed at 127.0 and 129.3 ppm can be assigned to the aromatic carbons (5, 9/ 6, 8), whereas the peaks at 130.9 and 141.7 ppm can be assigned to either C7 or C4. The resonance at 141.7 ppm is likely to be due to the C4 carbon as it is close to the electronegative carbonyl group. The peaks at 21.06 and 21.02 ppm can be assigned to the protons of the CH_3 (C10) or Ar-CH_3 (C11) groups. The quaternary carbon atoms were detected using a ^{13}C -DEPT experiment.

The resonances at 13.9, 21.1, 128.3 and 128.9 ppm for the minor *E* isomer, disappeared when heated to higher temperatures, as observed in the ^1H NMR spectra. When compared with the parent hydrazide, 4-methyl-benzoic acid hydrazide, and sodium pyruvate, the carbons which are in the close vicinity of the azomethine bond (C1,2,3,10) show a considerable upfield shift, whereas the carbons which belong to the hydrazide (C4,5,6,7,8,9,11) show only little downfield shift in the spectrum of NaHL9, except for C3.

Additionally, in the ^{13}C NMR spectrum, the resonances due to the methyl carbon (C10) of the major *Z* isomer and minor *E* isomer are observed at 21.0 and

13.9 ppm respectively. Turner et al observed ^{13}C NMR chemical shifts for the CH_3 group of methyl pyruvate hydrazones at 13.0 and 20.1 ppm for the *Z* and *E* isomers, respectively.¹⁵⁷ Hence, from the NMR studies, it can be confirmed that the observed major and minor resonances observed for NaHL9 correspond to its *Z* and *E* isomer, respectively.

Previously, correlations between the ^{13}C NMR chemical shifts of azomethine ($\text{C}=\text{N}$) carbons and Hammett parameters for Schiff bases have been studied in order to compare the electronic environment of imines and hydrazones.¹⁶⁴ As indicated in figure 2.11, a linear correlation is observed in ^{13}C NMR chemical shifts of the azomethine carbon against the Hammett parameter. It is observed that EWGs cause a downfield shift, whereas electron donating groups (EDGs) cause an upfield shift when compared with the ligand NaHL1, in which there are no substituents on the aromatic ring.

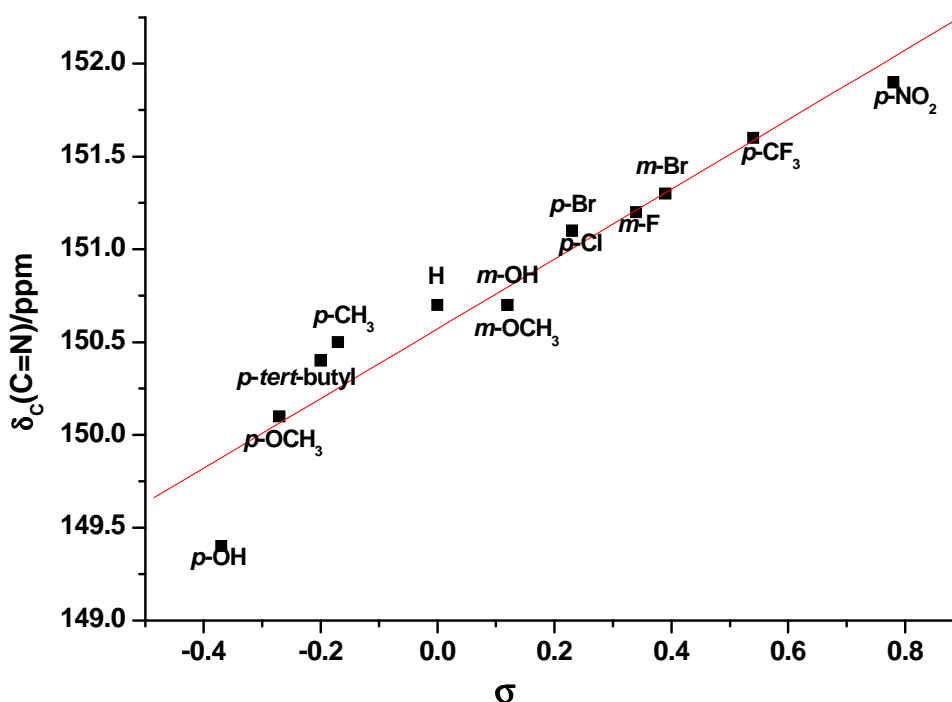


Figure 2.11: Plot of the ^{13}C NMR chemical shift of the $\text{C}=\text{N}$ carbon of indicated thirteen PVAHs in d_6 -DMSO versus σ ($R^2 = 0.92$)

EWGs increase the π -electron density on azomethine carbon which in turn makes it electron deficient causing a downfield shift of carbon resonance. Hence, the PVAHs containing strong EWGs such as *p*-NO₂, *p*-CF₃ cause the carbon resonance of azomethine bond to shift downfield. Whereas, PVAH possessing

EDGs such as *p*-CH₃, *p*-(CH₃)₃ have an inverse effect on the carbon shift, indicating their electron rich nature of the azomethine carbon which is in consistent with the literature.^{163,165}

2.5.5 NMR analysis of the Zn(II) complexes of PVAHs:

As Zn(II) has d¹⁰ configuration and is diamagnetic, the Zn(II) complexes of PVAHs give rise to well-resolved proton NMR spectra with chemical shifts in the same frequency range as those of the free ligands. The NMR experiments were performed in the same solvent as used for the ligands (*d*₆-DMSO) in order to be able to compare the results directly. The composition of the 1:2 (LX:Zn) zinc complexes is evident from the elemental analysis data and X-ray crystal structure. However, it cannot be derived conclusively from the NMR spectrum of [Zn(HL9)₂] whether the species in solution is a 1:1 or 1:2 complex because the environment of the two coordinated PVAH ligands around the Zn(II) centre may be equivalent on the NMR timescale resulting in equivalent protons for both ligands.

As representative example of the ¹H NMR spectra obtained, the spectrum of [Zn(HL9)₂] is shown in figure 2.12. The resonance observed at 2.38 ppm is due to both Ar-CH₃ and CH₃. The two doublets which are typical of a *para*-substituted aromatic ring appear at 7.35 and 7.90 ppm. In comparison to free ligands, there is a very slight downfield shift observed for the resonances of the aromatic protons and Ar-CH₃ whereas the CH₃ proton resonance exhibits a downfield shift of 0.25 ppm. As a result of the coordination of the azomethine nitrogen to Zn(II), the adjacent amide proton observed at 12.69 in [Zn(HL9)₂] shifts considerably downfield by 1.79 ppm as compared to that of free ligand (10.90 ppm, *E* isomer).

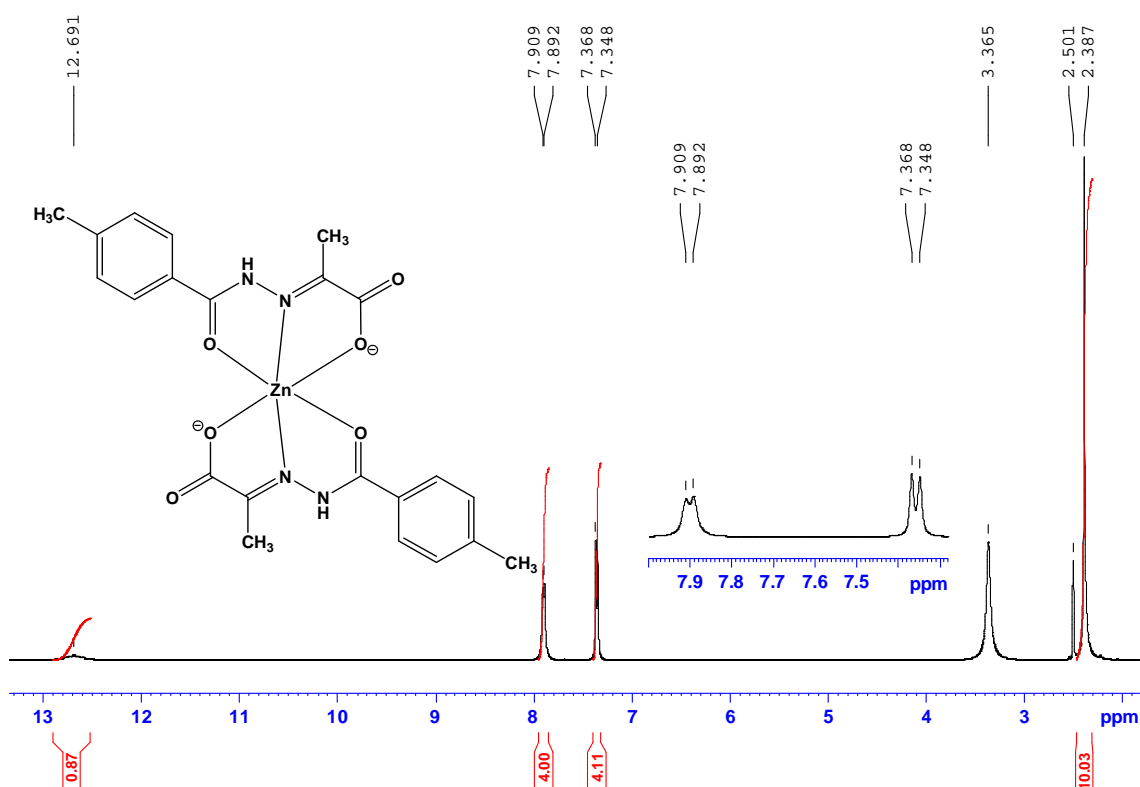


Figure 2.12: ^1H NMR spectrum of $\text{mer}[\text{Zn}(\text{HL9})_2]$ in d_6 DMSO shown in the range from 2.0 to 13.0 ppm

Some line broadening is observed in the spectra of the ^1H NMR spectra of zinc complexes when compared to those of the free ligands. This line broadening in turn gives rise to inaccurate coupling constant values as similar to observed by Bell et al for zinc complexes of hydrazone ligand.¹⁶⁶ It is evident that the two sets of signals observed in the case of the ligands are due to the presence of *E/Z* isomers, where the *Z* isomer is present as the major form. In the case of $[\text{Zn}(\text{HL9})_2]$ the ligand exists in only one form, the *E* form which allows for tridentate metal coordination.

The stacked NMR spectra of NaHL9 and $[\text{Zn}(\text{HL9})_2]$ shown in figure 2.13 indicate the presence of one form as the minor peaks observed in the aromatic region of the ligand are absent. In order to bind to $\text{Zn}(\text{II})$ in a tridentate manner NaHL9 adopts *E* configuration, as observed in the X-ray crystal structure of $[\text{Zn}(\text{HL9})_2]$. The resonance at 16.02 ppm assigned to the hydrogen bonded amide proton in the *Z*-conformer of the sodium salt of the HL9^- is absent in the $\text{Zn}(\text{II})$ -complex; no resonance is observed in the region 14-18 ppm. There is, however, a significant peak at 12.69 ppm which can be attributed to the non-hydrogen-bonded

N-H proton. In case of NaHL9, the N-H proton of the *E*-isomer resonates at 10.90 ppm.

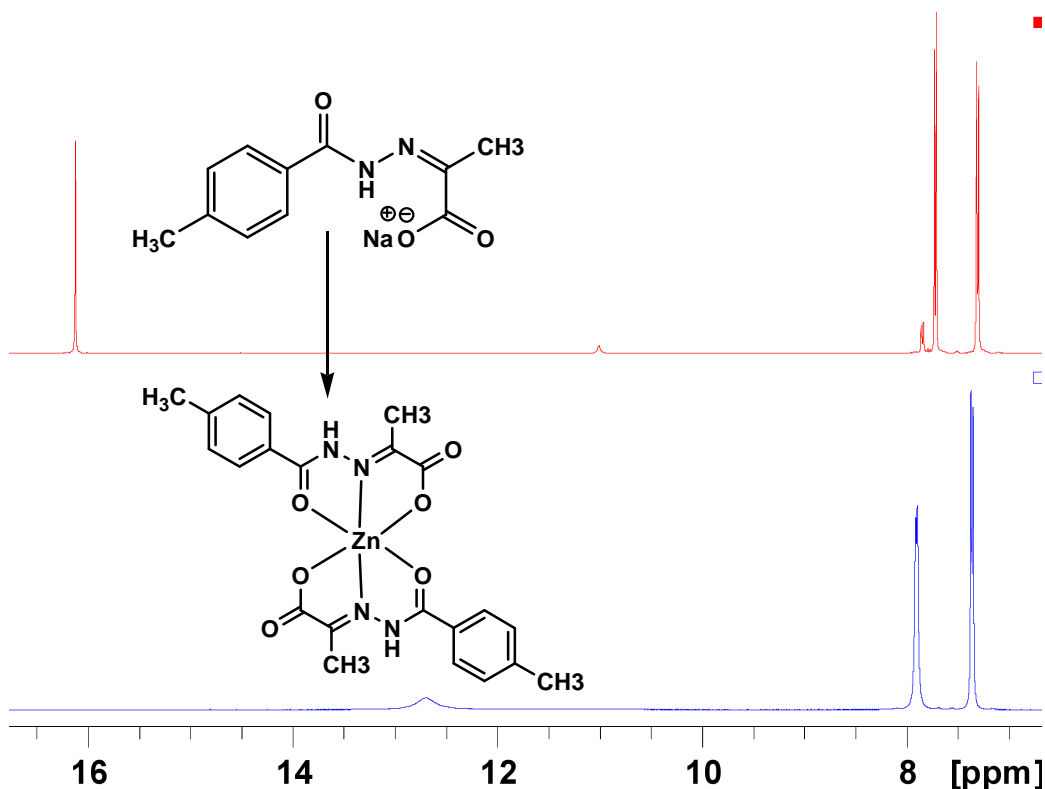


Figure 2.13: Stacked NMR spectra of NaHL9 in d_6 DMSO (top) and mer -[Zn(HL9)₂] (bottom) in the region 7- 16.5 ppm

The quaternary carbons were not observed in the ^{13}C NMR spectrum of the Zn(II) complexes of PVAHs even after an increased number of scans and longer relaxation delay time (10 sec). Hence, only the secondary and tertiary carbons were used for analysis. The signals appearing at 13.5 ppm and 21.2 ppm can be assigned to the CH_3 and Ar-CH_3 carbons, respectively, whereas the aromatic carbons resonate at 128.8 ppm and 129.2 ppm. The fact that the CH_3 carbon resonates at 13.5 ppm suggests that the ligand adopts *E* conformation in order to bind to Zn(II).¹⁵⁷ For the ligand NaHL9, the resonance of the CH_3 carbon of the *E*-isomer appears at 13.9 ppm, whereas it is observed at 21.06 for the *Z*-isomer.

2.6 Infrared spectroscopic (IR) study of PVAHs and their Cu(II) and Zn(II) complexes:

The solid state analyses of PVAHs and their metal complexes were performed using infrared (IR) spectroscopy. IR spectra were recorded from 4000 to 400 cm^{-1} using KBr discs. As representative example NaHL9 and its respective Cu(II) and Zn(II) complexes are discussed in detail here. For comparison, the IR spectra of the starting materials 4-methyl benzoic acid hydrate and sodium pyruvate are also discussed. The IR data for the rest of the investigated PVAHs and their metal complexes can be found in experimental section (chapter-7).

An overlay of the IR spectra of sodium pyruvate, 4-methyl benzoic acid hydrazide and NaHL9 along with their structures is illustrated in figure 2.14. The strong (s) band at 1708 cm^{-1} (figure 2.14, red IR spectrum) in the IR spectrum of sodium pyruvate can be assigned to the ketone (C=O) stretch vibration. This band is absent in the IR spectrum of NaHL9 indicating successful formation of the azomethine (C=N) bond, the stretch vibration of which appears as medium (m) intensity band at 1610 cm^{-1} . A strong band due to the asymmetrical stretch vibration (ν_{sym}) and a weaker band due to the symmetrical stretch vibration (ν_{asym}) of the carboxylate group of sodium pyruvate is observed at 1634 cm^{-1} and 1405 cm^{-1} , respectively¹⁶⁷.

The strong band observed at 1660 cm^{-1} in 4-methyl benzoic acid hydrazide (figure 2.14, blue IR spectrum) can be assigned to the carbonyl stretching frequency which shifts towards lower wavenumber 1649 cm^{-1} in NaHL9 (figure 2.14, magenta IR spectra). The shift towards a lower wavenumber can be accounted for by the resonance forms of the conjugated system, which increase the single bond character of the carbonyl group, as indicated in scheme 2.6.¹⁶⁸ However, there is no significant difference in the carboxylate stretching frequencies of sodium pyruvate and the conjugated hydrazone.

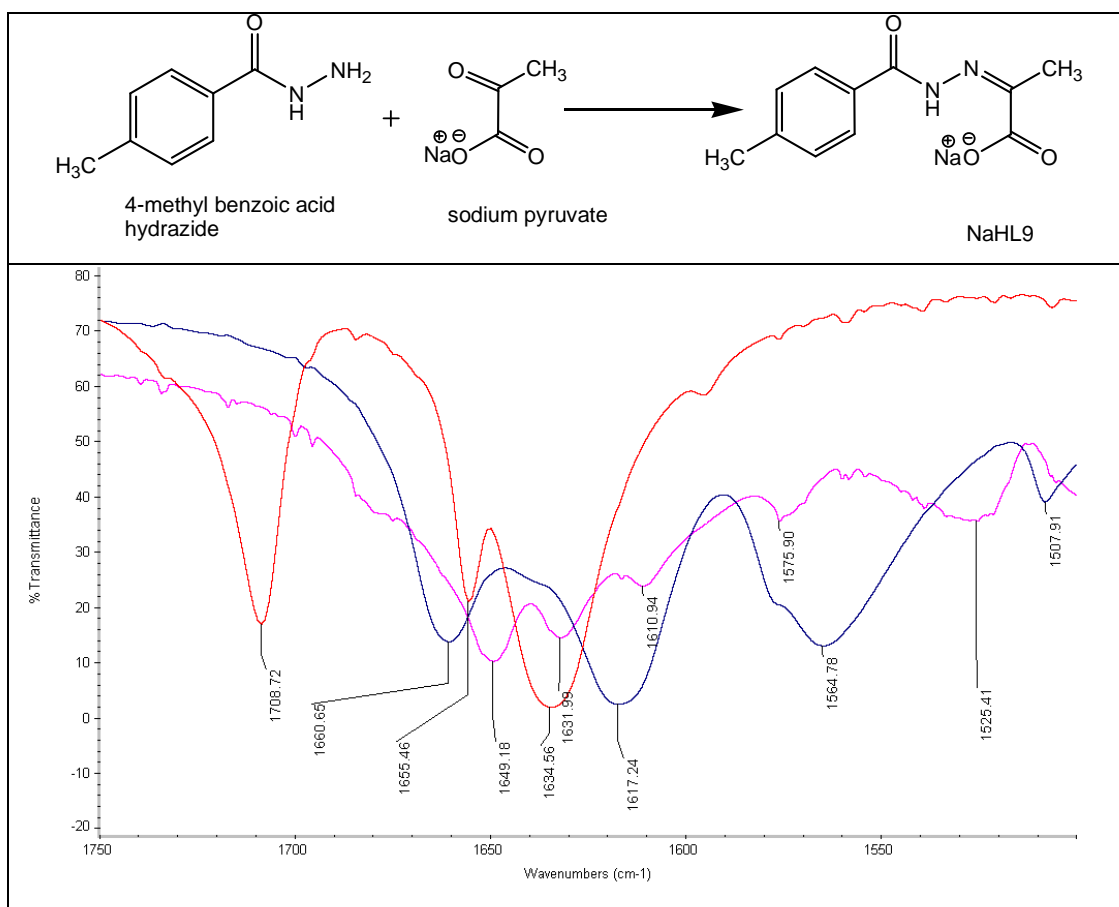
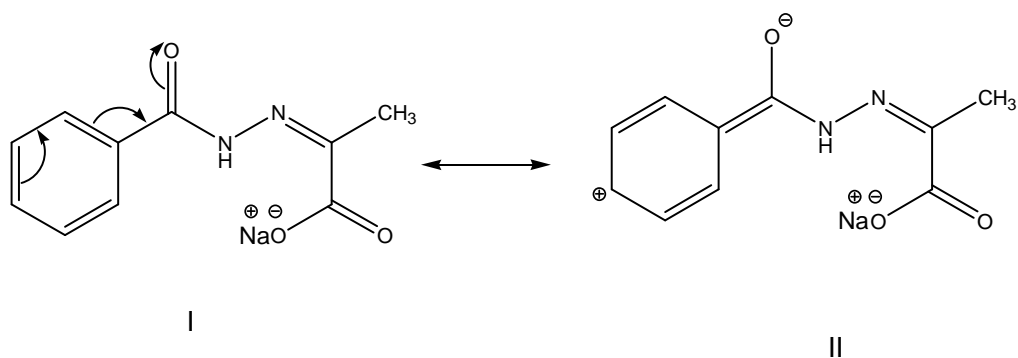


Figure 2.14: Overlaid IR spectra of NaHL9 (magenta), sodium pyruvate (red) and 4-methyl benzoic acid hydrazide (blue) in the region 1500-1750 cm⁻¹ (bottom) and their corresponding structures (top)

Electron withdrawing groups on the aromatic ring cause the $\nu(\text{C}=\text{O})$ to shift towards higher frequencies, whereas electron donating groups have the opposite effect.¹⁶⁸ This trend can be explained with the help of resonance forms. Electron donating groups in *para*-position of the aromatic ring stabilise the positive charge on the aromatic ring which in turn favours the formation of resonance form II (scheme 2.7).¹⁶⁹ Whilst the change in the azomethine stretching frequency of PVAHs is in the range 1580 - 1612 cm⁻¹, the variation in the stretching frequency of the carbonyl group ranges from 1640 – 1690 cm⁻¹. The values are consistent with literature values reported for aroyl-type hydrazones.¹⁷⁰



Scheme 2.7: Resonance forms of PVAHs

The coordination of PVAHs to metal centres is also reflected in their IR stretching frequencies. The overlaid IR spectra of NaHL9 and its Cu(II) and Zn(II) complexes in the region $1000 - 1700 \text{ cm}^{-1}$ and $1550 - 1670 \text{ cm}^{-1}$ are shown in figures 2.15 and 2.16, respectively. The carboxylate asymmetrical stretching frequency of NaHL9 appears at 1632 cm^{-1} . The band merges either with the carbonyl band in $[\text{Cu(II)L9}(\text{H}_2\text{O})_2]$ or the azomethine (C=N) band in $[\text{Zn}(\text{HL9})_2]$, indicating the involvement of the carboxylate group in complexation. However, in other Cu(II) complexes of PVAHs, for example $[\text{Cu(II)L8}(\text{H}_2\text{O})_2]$, all three bands merge together resulting in a strong broad band at 1639 cm^{-1} .

In addition, the copper complexes lack the medium intensity broad band at 3284 cm^{-1} , assigned to the NH vibration and the band at 1649 cm^{-1} due to the C=O stretch vibration, an observation that is consistent with the deprotonation of the -NH group and subsequent coordination of the oxygen of the amide carbonyl to the metal ion via enolization.¹⁷¹ The C=O and C=N stretching frequencies are summarised in table 2.4.

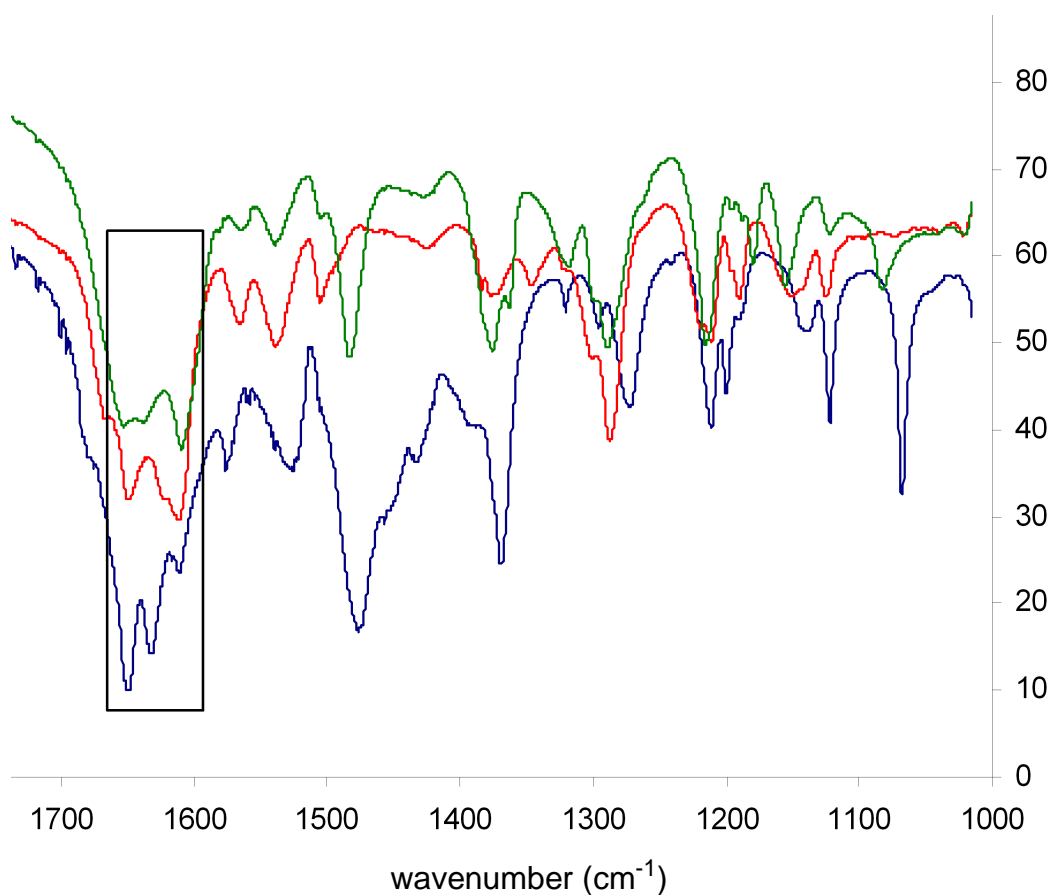


Figure 2.15: Overlaid IR spectra of NaHL9 (blue), [Cu(II)L9(H₂O)₂] (green) and [ZnH(L9)₂] (red) shown in the region 1000 – 1700 cm⁻¹

Moreover, the broad (br) bands of medium intensity located at around 3400 cm⁻¹ in the case of the copper complexes can be attributed to the presence of coordinated water molecules¹⁷². In case of the sodium salts of the ligands, this can be due to the hydrogen bonding of water to the sodium cation as observed in the crystal structures of PVAHs. The elemental analysis and single crystal X-ray structure of ligand confirms the presence of water molecules in the pyruvate hydrazones.

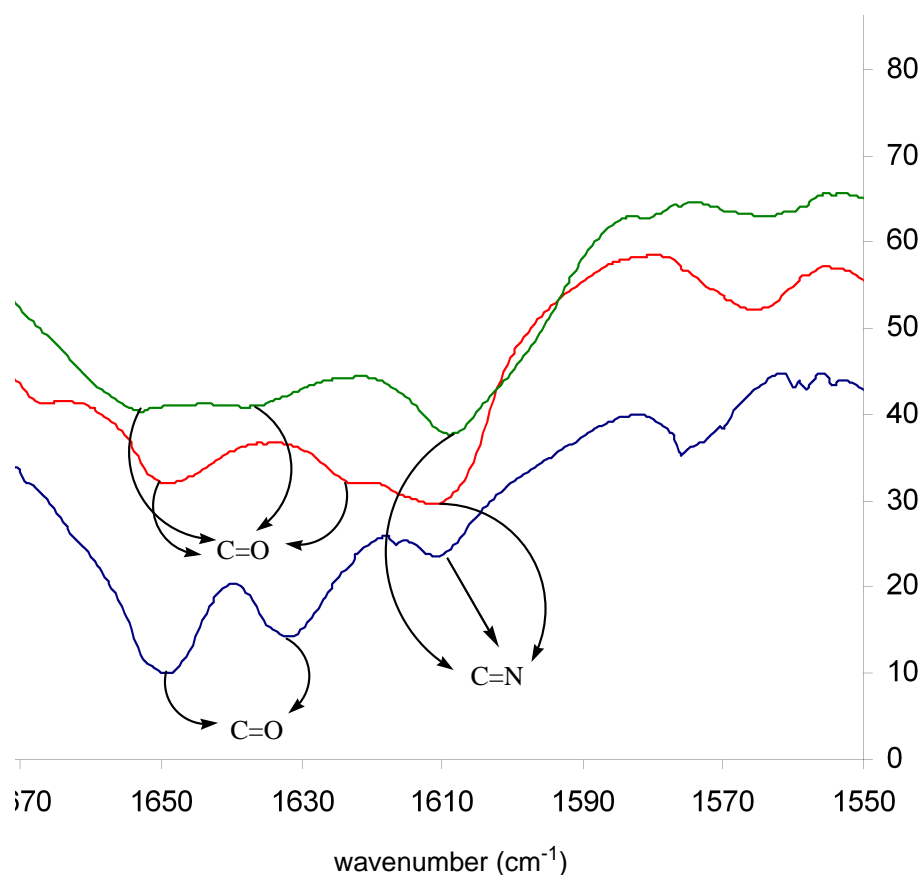


Figure 2.16: Overlaid IR spectra of ligand NaHL9 (blue), [Cu(II)L9(H₂O)₂] (green) and [Zn(HL9)₂] (red) in the region 1550 – 1670 cm⁻¹

Table 2.4: Selected vibrational frequencies for NaHL9, [Cu(II)L9(H₂O)₂] and [Zn(HL9)₂]

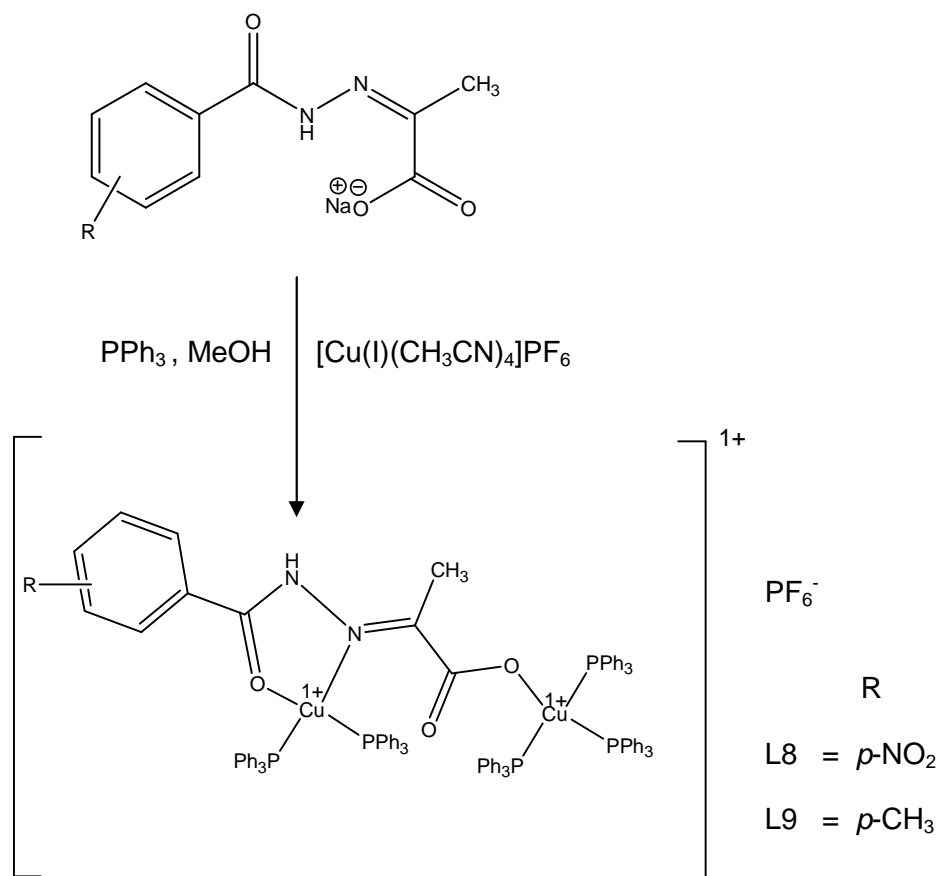
Compound	(v) C=O ¹ (cm ⁻¹) (carbonyl)	(v) O-C=O ² (cm ⁻¹) (carboxylate)	(v) C=N (cm ⁻¹) (azomethine)
NaHL9 (blue spectrum)	1649	1632	1610
[Cu(II)L9(H ₂ O) ₂] (green spectrum)	1653	1637	1609
[Zn(HL9) ₂] (red spectrum)	1649	1623	1611

Hence, the IR studies indicate the successful formation of PVAHs and its coordination to Cu(II) and Zn(II) centres is reflected in their stretching frequencies.

2.7 Synthesis of Cu(I) complexes

In order to gain further insights into structural aspects of the Cu(I) centre, the Cu(I) complexes of NaHL8 and NaHL9 were synthesised. The synthesis was carried out using the Cu(I) precursor $[\text{Cu(I)}(\text{CH}_3\text{CN})_4]\text{PF}_6$, which was synthesised using a literature procedure¹⁷³. The reaction was carried out under a nitrogen atmosphere using Schlenk techniques with dry solvents. Initially, the reaction mixture consisting of the precursor and the hydrazone ligand were stirred in methanol and then the product was precipitated using an excess of diethyl ether. The yellow solid that was formed was isolated by filtration and dried under vacuum. The NMR spectrum of the product confirmed the formation of a diamagnetic Cu(I) complex. However, the Cu(I) complex could not be crystallised as it was unstable when left in solution for a long time. Upon air exposure, the yellow colour of the Cu(I) complex turned green indicating the oxygen sensitivity of complex.

To stabilise the soft Cu(I) centre it was necessary to introduce soft donor atoms, such as P or S. After stirring the reaction mixture consisting of $[\text{Cu(I)}(\text{CH}_3\text{CN})_4]\text{PF}_6$ (2 mmol) and hydrazone (1 mmol) ligand for 10 minutes, triphenylphosphine (PPh_3) (5 mmol) was therefore added to the reaction mixture, yielding a clear solution. The product was precipitated using an excess of diethyl ether, which also helped in removing unreacted PPh_3 due to its high solubility in diethyl ether. The PPh_3 ligand not only provides the soft donor phosphorus atom, but also additional steric bulk that helps to stabilise the 4-coordinate tetrahedral environment around the Cu(I) centre. Interestingly, Samuelson et al illustrated that the stability of Cu(I) complexes when coordinated to a mixture of soft and hard donor atoms is greater than when binding to only soft donor atoms.¹⁷⁴⁻¹⁷⁵ The general scheme for the synthesis of the Cu(I) complexes is given in scheme 2.8. Details of the synthetic procedure can be found in chapter-7.



Scheme 2.8: Synthesis of Cu(I) complexes - $[\text{HLRCu(I)}_2(\text{PPh}_3)_5]\text{PF}_6$

Single crystals for X-ray analysis were obtained from MeOH and diethyl ether. The X-ray crystal structure revealed the presence of two Cu(I) centres, within the Cu(I) complexes of NaHL8 and NaHL9, as indicated in final product shown in scheme 2.8. The Cu(I) crystals obtained from MeOH ($[\text{Cu(I)}_2\text{HL8}(\text{PPh}_3)_5]\text{PF}_6$, $[\text{Cu(I)}_2\text{HL9}(\text{PPh}_3)_5]\text{PF}_6$) indicate that NaHL8 and NaHL9, act as bidentate ligands, coordinating through oxygen and nitrogen atoms instead of ONO, due to the rigidity of the planar ligands. The bidentate coordination mode of PVAHs allow the Cu(I) centre to adopt the preferred tetrahedral geometry which is predicted for a Cu(I) complex. The remaining two tetrahedral coordination sites are occupied by two PPh₃ groups, in a similar way to the structure observed in the case of a recently published Cu(I) hydrazone complex.¹⁷⁶ As expected for Cu(I) complexes, NaHL8/NaHL9 and two PPh₃ groups forms a tetrahedral coordination sphere around one the Cu(I) centre. The second Cu(I) centre also exhibits tetrahedral geometry, where the oxygen atom of the carboxylate group of NaHL8/ NaHL9 binds to the copper centre. The remaining three tetrahedral coordination sites are occupied by PPh₃ groups. The overall positive charge on the overall complex is balanced by a hexafluorophosphate anion.

Interestingly, crystals obtained from diethyl ether for the Cu(I) complex of NaHL9, $[\text{Cu}(\text{I})_2\text{HL9}(\text{PPh}_3)_4]\text{PF}_6$, show coordination of two PPh_3 groups, instead of three around the second Cu(I) centre. This allows the copper centre to adopt a 3-coordinate geometry. On the other hand, tetrahedral coordination site of the other Cu(I) centre remains the same. The crystal structures are discussed in detail in chapter-3.

2.7.1 ^1H NMR analysis of the Cu(I) complexes

Figure 2.17 shows the proton NMR spectrum of $[\text{Cu}(\text{I})_2\text{HL9}(\text{PPh}_3)_5]\text{PF}_6$ and its chemical structure is provided in figure 2.18 b (right). Two singlets of relative integration three are observed at 1.89 and 2.43 ppm and correspond to the two CH_3 groups. The resonance at 2.42 ppm is attributed to the Ar- CH_3 group as it is more deshielded than the methyl group which is next to the azomethine bond. The aromatic protons give rise to two doublets at 7.35 and 7.72 ppm as indicated in figure 2.18 a (left). These assignments were made by comparison with the ligand NaHL9. There is no significant shift in these resonances of the Cu(I) complexes as compared to the free ligand. Multiplets in the aromatic region 7.22 - 7.30 ppm and 7.38 – 7.45 ppm can be assigned to the five PPh_3 groups on the two different Cu(I) centres.

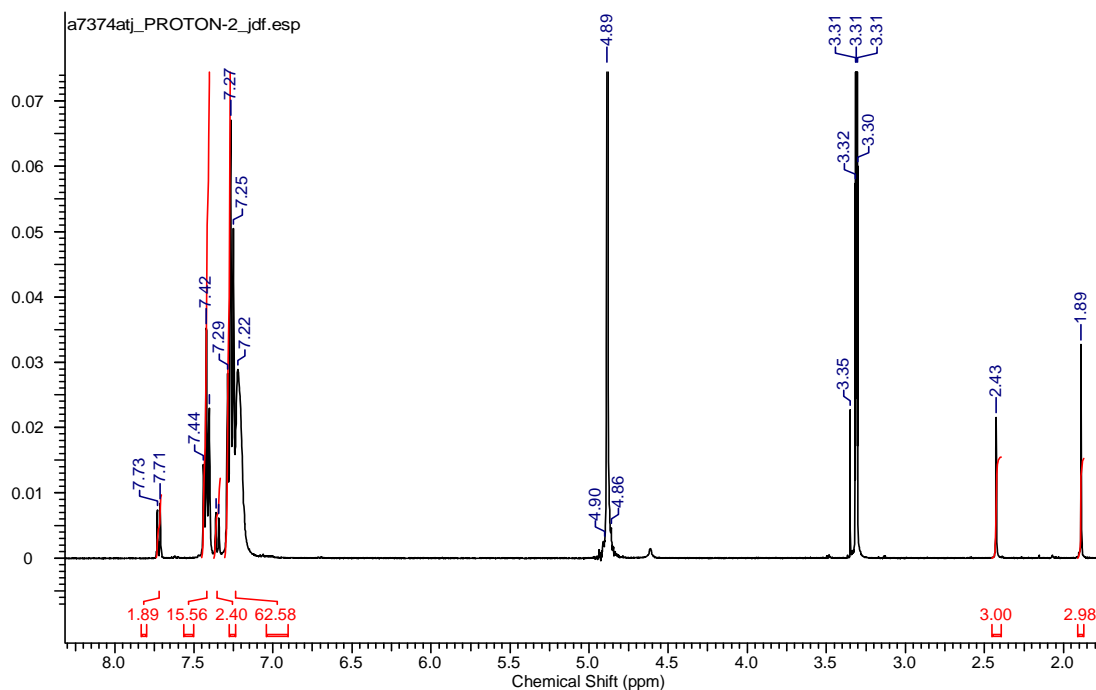


Figure 2.17: ^1H NMR spectrum of $[\text{Cu}(\text{I})_2\text{HL9}(\text{PPh}_3)_5]\text{PF}_6$ in d_4 -MeOH in the range 1.5 – 8.0 ppm.

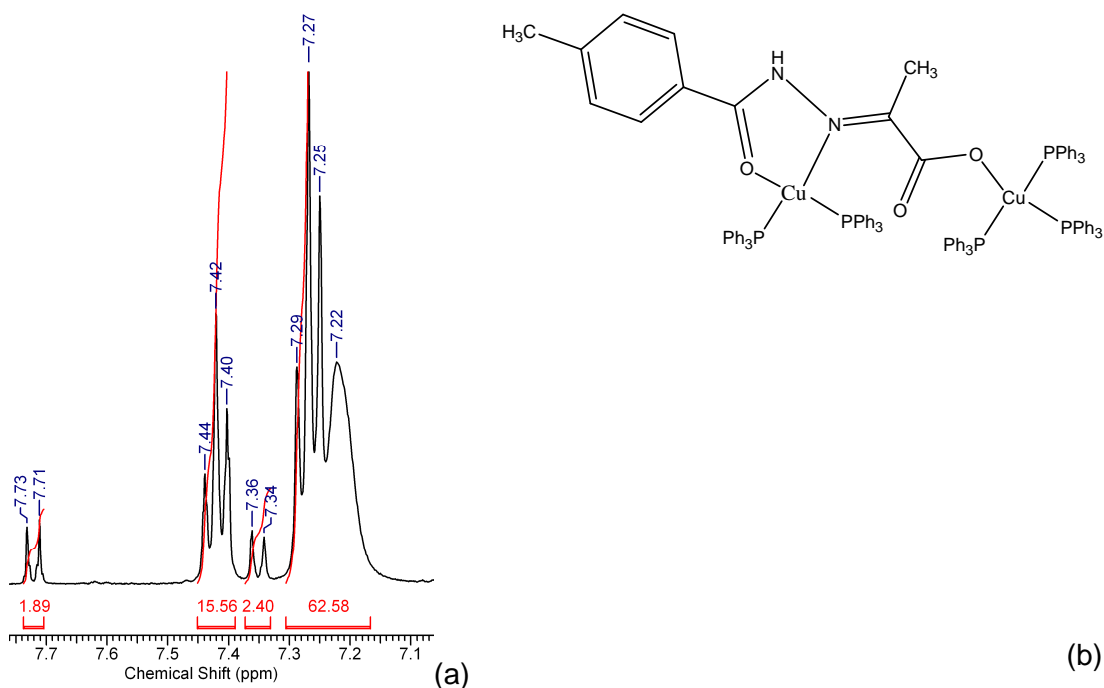


Figure 2.18: a) ^1H NMR spectrum of $[\text{Cu}(\text{I})_2\text{HL9}(\text{PPh}_3)_5]\text{PF}_6$ in $d_4\text{-MeOH}$ in the range 7.1 – 7.8 ppm (left) b) Structure of $[\text{Cu}(\text{I})_2\text{HL9}(\text{PPh}_3)_5]\text{PF}_6$ (right).

The peaks appearing at 3.30 ppm ($d_4\text{-MeOH}$), 3.35 ppm (MeOH) 4.89 ppm (water), are due to the solvent peaks. The presence of the solvent molecule, MeOH, in the compound is also evidenced from the elemental analysis data and the single crystal X-ray structure.

2.7.2 ^{31}P $\{^1\text{H}\}$ NMR analysis of $[\text{Cu}(\text{I})_2\text{HL9}(\text{PPh}_3)_5]\text{PF}_6$

In order to gain more insight into the behaviour of the investigated Cu(I) complexes in solution, detailed ^{31}P $\{^1\text{H}\}$ NMR experiments were carried out on $[\text{Cu}(\text{I})_2\text{HL9}(\text{PPh}_3)_5]\text{PF}_6$. All the ^{31}P spectra referred to in this chapter are proton-decoupled. The ^{31}P NMR spectrum of PPh_3 recorded in $d_4\text{-MeOD}$ exhibits a sharp singlet at -5.0 ppm, whereas the spectrum of the $[\text{Cu}(\text{I})_2\text{HL9}(\text{PPh}_3)_5]\text{PF}_6$ complex displays a broad resonance at 0 ppm at room temperature, as indicated in figure 2.18 a. The ^{31}P chemical shift of PPh_3 in $[\text{Cu}(\text{I})_2\text{HL9}(\text{PPh}_3)_5]\text{PF}_6$ appears downfield compared to free PPh_3 (figure 2.19 c), which is likely due to the decrease in shielding caused by metal centre and is generally known to occur in σ -donor ligands like phosphine.¹⁷⁷ When the solution is cooled down to 200 K, the broad

peak resolves into two peaks as indicated in figure 2.19 b.¹⁷⁸ The two peaks can be attributed to the PPh₃ ligands bound to the two different Cu(I) centres in the dimeric complex.

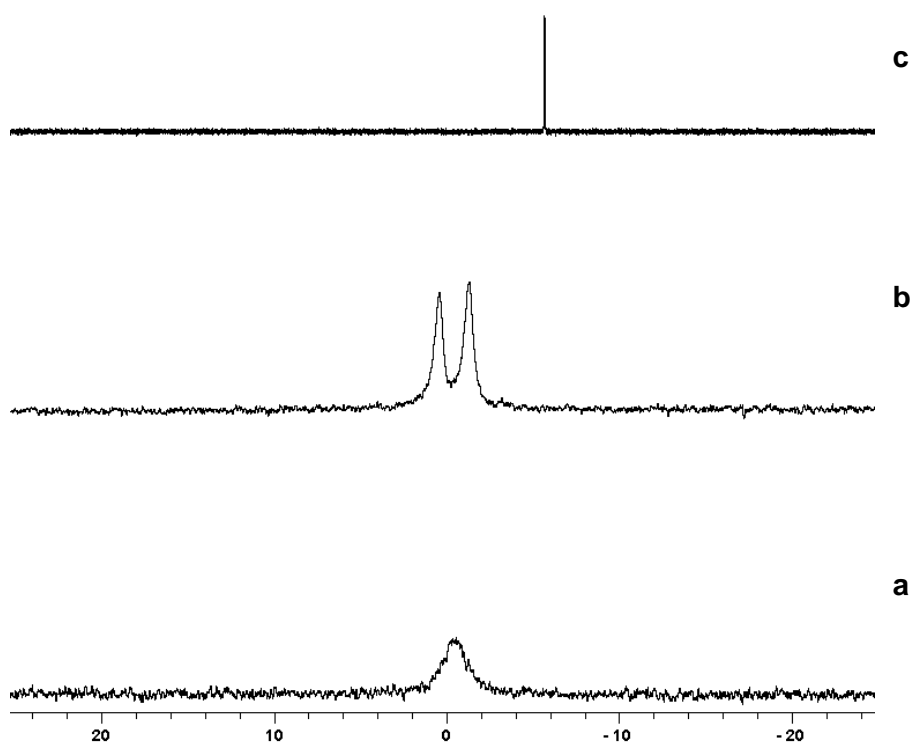


Figure 2.19: Stacked ³¹P {¹H} NMR spectra of a) [Cu(I)₂HL9(PPh₃)₅]PF₆ at 298 K b) [Cu(I)₂HL9(PPh₃)₅]PF₆ at 200 K c) free PPh₃ at 298 K in *d*₄-MeOH

The broad nature of the resonance indicates the fluxional nature of the complex in solution, which is likely due to ligand exchange processes.^{177,179} In order to gain more insight into possible ligand exchange processes, free PPh₃ was added to the solution of the Cu(I) complex. In the resulting spectrum, the resonance broadens further with increasing amounts of free PPh₃, as indicated in figure 2.20 a-c. This observation confirms that ligand exchange processes are occurring. Moreover, even with seven equivalents of PPh₃ added (figure 2.20 c) there is no separate resonance observed that corresponds to free PPh₃ (figure 2.20 d) indicating the fast exchange of the ligands on the NMR timescale.

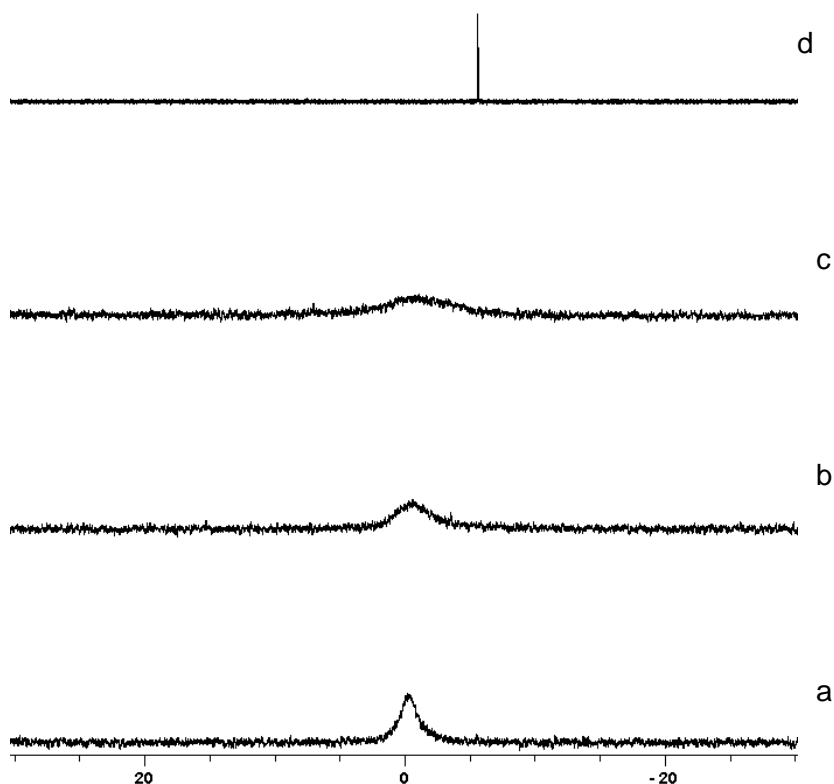


Figure 2.20: Stacked $^{31}\text{P} \{^1\text{H}\}$ NMR spectra of a) $[\text{Cu}(\text{I})_2\text{HL9}(\text{PPh}_3)_5]\text{PF}_6$ b) $[\text{Cu}(\text{I})_2\text{HL9}(\text{PPh}_3)_5]\text{PF}_6$ with added four equivalents PPh_3 c) $[\text{Cu}(\text{I})_2\text{HL9}(\text{PPh}_3)_5]\text{PF}_6$ with added seven equivalents of PPh_3 d) free PPh_3 in d_4 -MeOH

Hence, from above $^{31}\text{P} \{^1\text{H}\}$ NMR experiments it can be concluded that, there is a ligand exchange process occurring either at the Cu(I) centres which is evident from the broad ^{31}P NMR peak of PPh_3 .

The ^{13}C NMR spectra showed no quaternary peaks and the primary and secondary peaks were not very distinctive even in spectra with higher scan rates, as observed for the Zn(II) complexes of PVAHs. Hence the carbon NMR spectra were not used in the analysis.

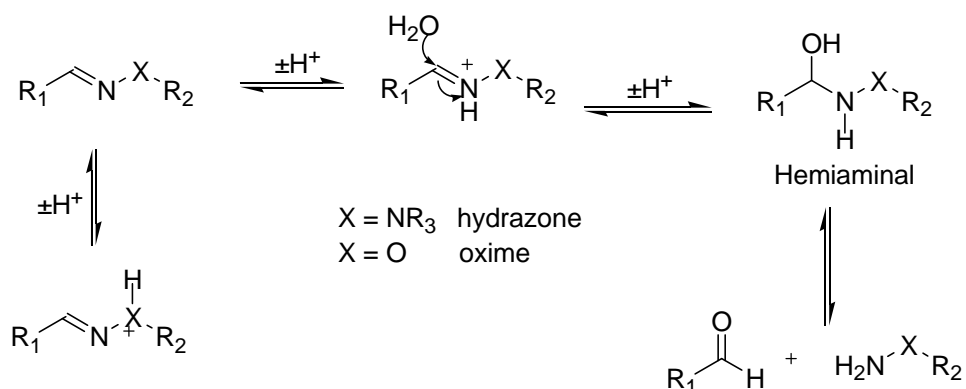
2.7.3 Infrared analysis of the Cu(I) complexes

In order to gain further insight into the solid state structure of the Cu(I) complexes, IR spectra were recorded using KBr discs. The stretching frequencies of the carbonyl and azomethine groups in the Cu(I) complexes tend to merge giving rise to a single broad band, indicating their involvement in complexation. $[\text{Cu}(\text{I})_2\text{HL8}(\text{PPh}_3)_5]\text{PF}_6$ bearing the EWG nitro-group exhibits a band at 1632 cm^{-1} , whereas the corresponding band for $[\text{Cu}(\text{I})_2\text{HL9}(\text{PPh}_3)_5]\text{PF}_6$ with the EDG methyl-group appears at a lower wavenumber of 1617 cm^{-1} . Similar behaviour for EWG/EDG groups is observed and discussed in the previous section for PVAHs. In addition, the C=C ring stretching vibrations at 1475 cm^{-1} observed in free PPh_3 indicate a shift towards higher frequency in both the Cu(I) complexes.

Hence the IR analysis of investigated Cu(I) complexes of PVAHs confirms the coordination of the ligand to the Cu(I) centre.

2.8 Synthesis of a di-hydrazide analogue of PVA

As discussed earlier, the Schiff base condensation reaction is a reversible process and the products obtained can undergo hydrolysis. The stability of these types of compounds under different conditions have been explored in the past by several researchers.¹⁸⁰⁻¹⁸¹ It is evident that the azomethine bond undergoes rapid hydrolysis under extreme acidic and basic conditions, and hydrolysis at a reduced rate at neutral pH. Kalia and Raines have proposed the detailed mechanism for its hydrolysis under acidic conditions as shown in scheme 2.9. The azomethine bond hydrolyses, when it comes in contact with water, as the resultant protonated species is highly susceptible to attack due to the enhanced electrophilicity of the carbon atom.¹⁸² The base hydrolysis may result from the attack of OH⁻ on electrophilic azomethine carbon followed by generation of negative charge on nitrogen. The nucleophilic nitrogen then deprotonates a water molecule resulting into the cleavage of C=N bond via hemiaminal intermediate.



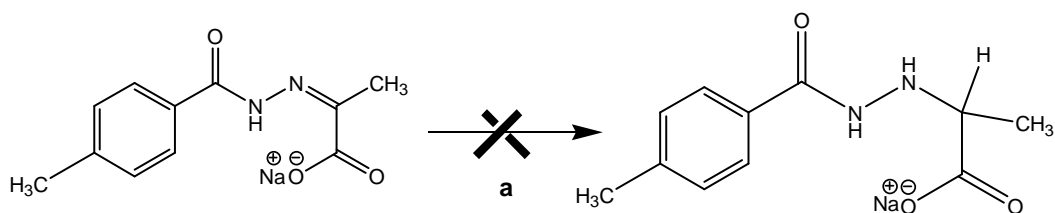
Scheme 2.9: Suggested mechanism for the acid hydrolysis of hydrazones and oximes¹⁸²

Hence, in order to increase the stability of PVAHs, reduction of the C=N bond to form a secondary amine was attempted in order to gain more stability. The resultant C-N bond would then be less susceptible to nucleophilic attack by H₂O.

2.8.1 Attempted reduction of a PVAH

Initially, the reduction was attempted using sodium borohydride (NaBH₄) with NaHL9 according to literature procedures.¹⁸³ Subsequently, a palladium catalyst was used under an atmosphere of hydrogen.¹⁸⁴ Both reactions failed to give the reduced product indicated in scheme 2.10. The reactions were monitored using TLC and the identity of the isolated product was confirmed by ESI-MS. The molecular ion

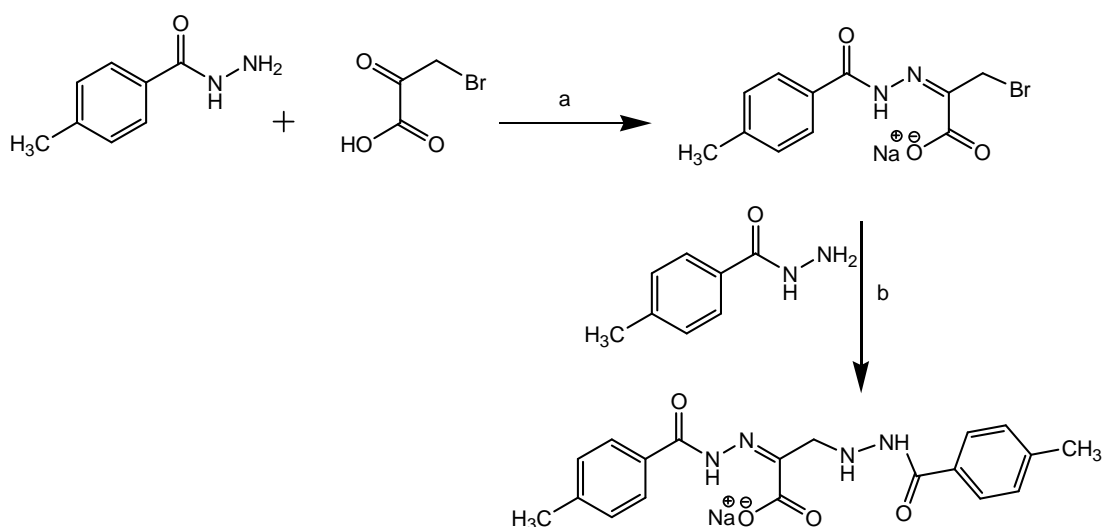
peak remained unchanged from the starting compound NaHL9. The expected product would result in an increased mass due to the addition of two hydrogens across the C=N bond.



Scheme 2.10: Attempted reduction of the azomethine (C=N) bond of NaHL9 a) NaBH_4 , refluxing under water for 24 hr, MeOH or H_2 , Pd/C (10%), 24 hr, MeOH

NaBH_4 is a mild reducing agent, however, the reducing power of NaBH_4 can be improved by adding reagents such as NiCl_2 , TiCl_3 , TiCl_4 , CoCl_2 , I_2 , ZrCl_4 .¹⁸⁵⁻¹⁸⁶

As previously described in chapter-1, 3-bromopyruvate is known to inhibit *M. tuberculosis* ICL, an enzyme found to be implicated in the persistent state of the bacteria. This was illustrated with the help of co-crystallisation studies, which revealed that 3-bromopyruvate forms a covalent adduct with the active site of ICL achieved by dehalogenation of the inhibitor.⁵³ In an attempt to target the ICL, the Schiff base condensation of 3-bromopyruvate with a hydrazide was performed. However, the resultant product (step a) of the reaction was found to have undergone an alkylation reaction (step b) to form the di-hydrazide analogue $\text{NaH}_3\text{D1}$, as shown in scheme 2.11.

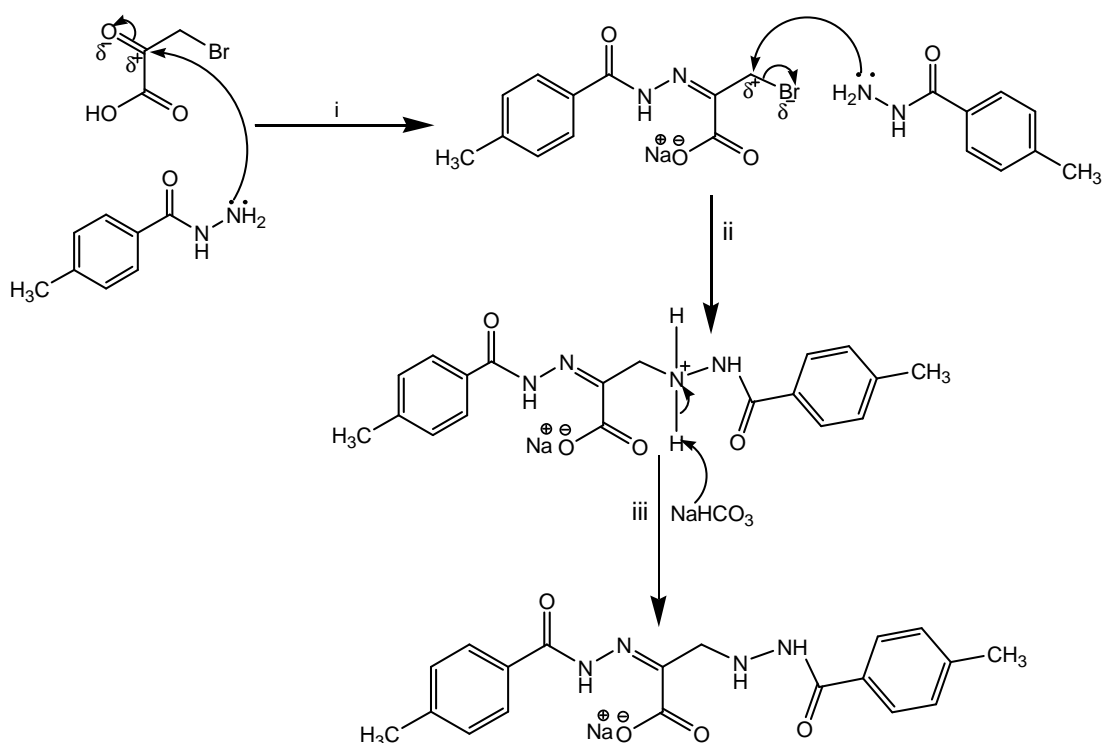


Scheme 2.11: General synthetic scheme for $\text{NaH}_3\text{D1}$ a) NaHCO_3 , reflux in methanol for 4 hours

The di-hydrazide analogue possesses a C-N single bond on one side of the molecule which may provide the hydrolytic stability of the molecule. This type of ligand may thus help to overcome the issues of both hydrophilicity and hydrolysis. Hence, further attempts to reduce the azomethine bond of PVAHs to make them hydrolytically stable were discontinued.

2.8.2 Synthesis and characterisation of NaH₃D1

The proposed mechanism for the formation of NaH₃D1 is given in scheme 2.12. In the first step (i), single molecule of hydrazide attacks the carbonyl carbon to give the bromopyruvate hydrazone, this Schiff base mechanism is similar to discussed in detail for PVAHs in previous section (page 38). This is followed by attack of second molecule (ii) of hydrazide at the adjacent carbon of bromine to undergo alkylation. The intermediate formed undergoes deprotonation of amine proton giving rise to final product (iii). Attack of two molecules of hydrazides on 3-bromopyruvate could also be simultaneous giving rise to the final product or it could be other way round, where alkylation first takes places followed by hydrazone formation.



Scheme 2.12: Proposed mechanism for the formation of the di-hydrazide analogue; NaH₃D1

Successful formation of the dianalogue NaH₃D1 is evident from ESI-MS and is further confirmed by NMR analysis. The positive and negative mass spectrum of NaH₃D1 shows a peak at *m/z* 369.1543 corresponding to [M-Na+2H]⁺, and 367.1409 corresponding to [M-Na]⁻ respectively. NaH₃D1 also exhibits isomers in solution, most likely due to *E/Z* isomerisation, as observed for PVAH (NaHL9). This is evident from the ¹H NMR spectrum recorded in *d*₆-DMSO and the two isomers are roughly in the ratio 3:2, as calculated from the integration values. Figure 2.21 displays the full ¹H NMR spectrum in the region 2.0 to 17.0 ppm.

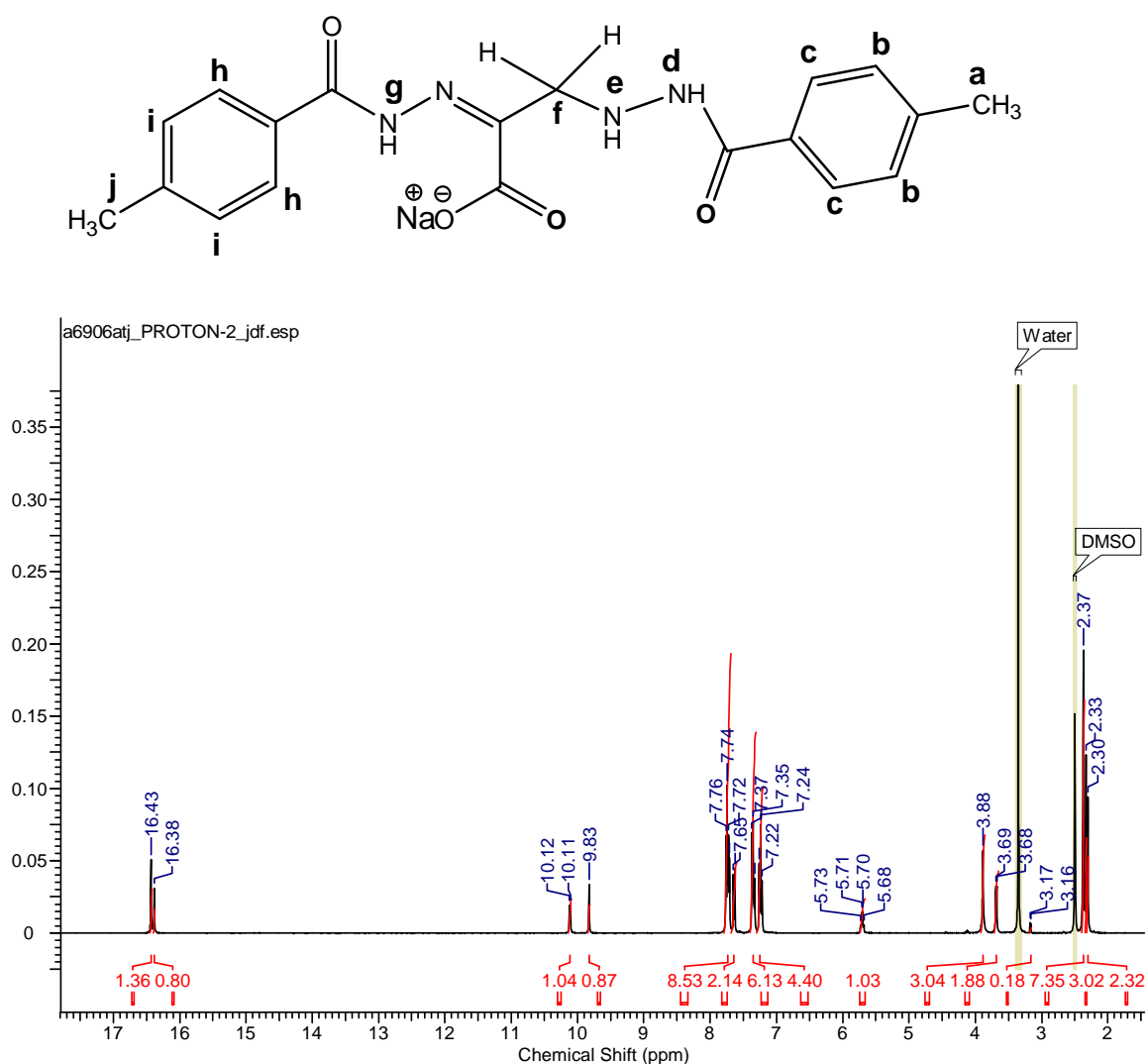


Figure 2.21: ¹H NMR spectrum of NaH₃D1 in the region 1-18 ppm in *d*₆-DMSO

Figure 2.22, shows three singlets in the region 2.30 – 2.40 ppm (right spectrum) due to the two Ar-CH₃ groups labelled **a** and **j** in the two isomers. There are actually 4 singlets, the peak at 2.37 ppm is a result two peaks merging, giving

rise to a broad singlet. The protons of two aromatic rings resonate in the region 7.2 – 7.8 ppm (figure 2.22, left).

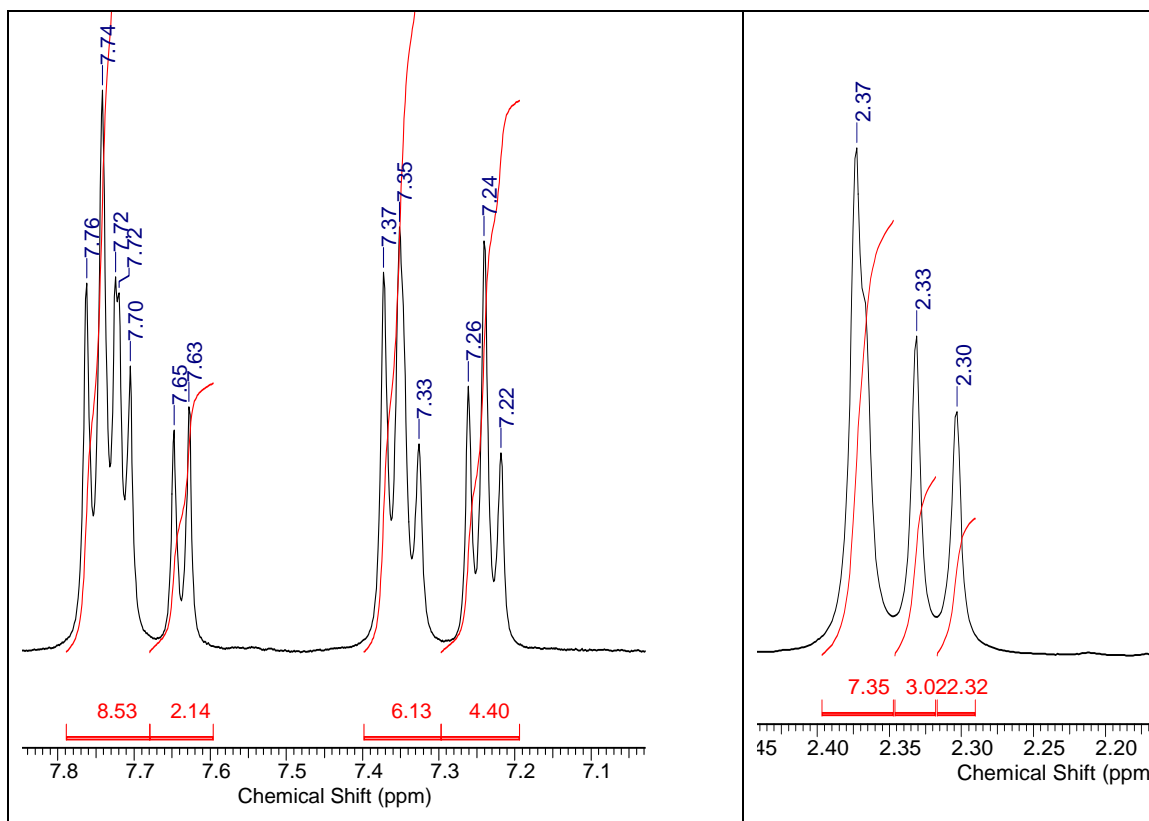


Figure 2.22: ^1H NMR spectrum of $\text{NaH}_3\text{D1}$ in the region 2.20 – 2.40 ppm (right) and 7.20 – 7.80 ppm (left) in d_6 -DMSO

The proton resonances of the methyl and aromatic protons do not provide conclusive information on the isomerisation of $\text{NaH}_3\text{D1}$, however the NMR resonances of the NH and CH_2 protons can help to gain more insight. For instance, the carboxylate oxygen atom can hydrogen bond with the amide proton, as shown in figure 2.23 a (*Z* isomer, left), whereas in the other isomer the same oxygen atom can form a hydrogen bond with the amine proton, as shown in figure 2.23 b (*E* isomer, right). In the *Z* isomer, the NH proton of the amine group labelled as \mathbf{e}_1 resonates at 5.70 ppm with a relative integration of one showing an apparent quartet (ideally should be *dt*) arising from coupling to adjacent the CH_2 protons (\mathbf{f}_1) and the amide proton (\mathbf{d}_1) as indicated in figure 2.24. The ^1H - ^1H COSY spectrum of $\text{NaH}_3\text{D1}$ displayed in figure 2.25 confirms the coupling of the amine proton to the CH_2 and amide protons. The doublet at 3.68 is due to the CH_2 protons and the amide proton also appears as doublet at 10.11 ppm with coupling constants of 6.8 Hz and 6.4 Hz, respectively, in line with the proton splitting pattern of the amine proton.

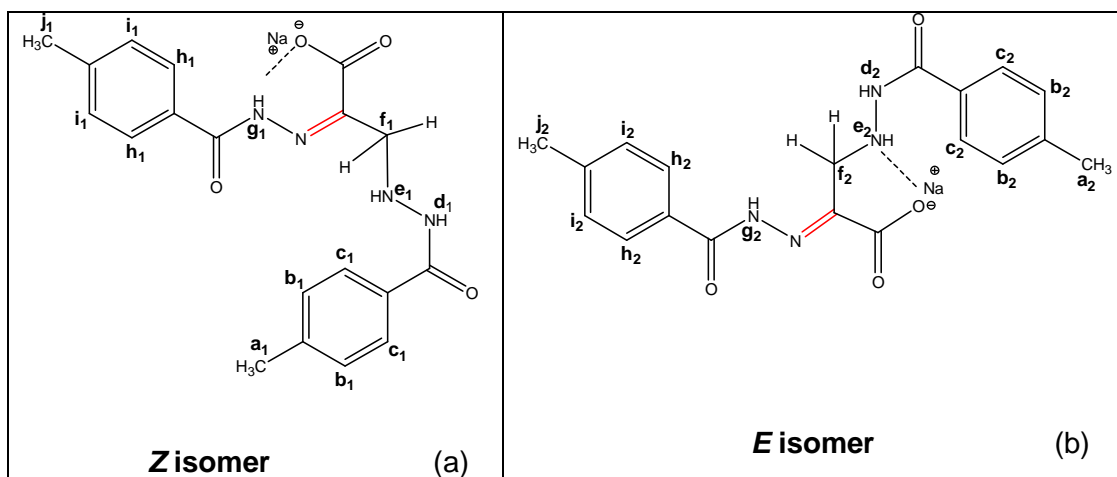


Figure 2.23: a) Structure of NaH₃D1 showing Z isomer (left) and E isomer (right) with respect to azomethine bond (C=N) indicated in red

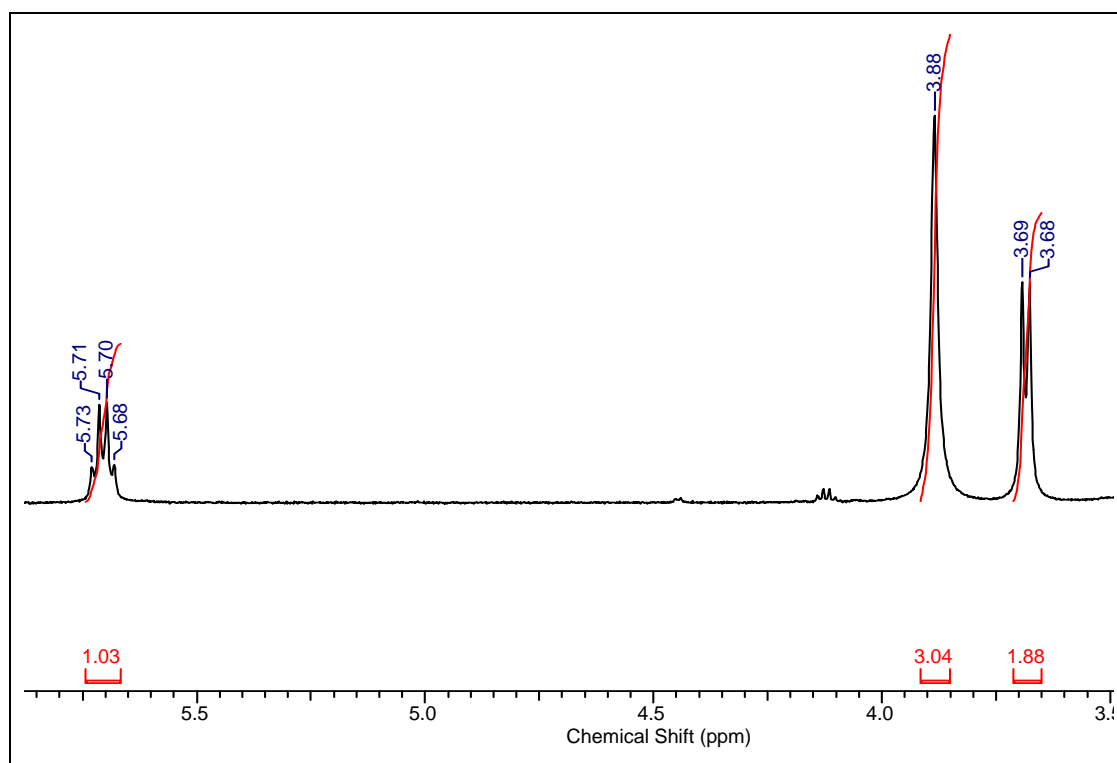


Figure 2.24: ¹H NMR spectrum of NaH₃D1 in the region 3.60 – 5.80 ppm in d₆-DMSO

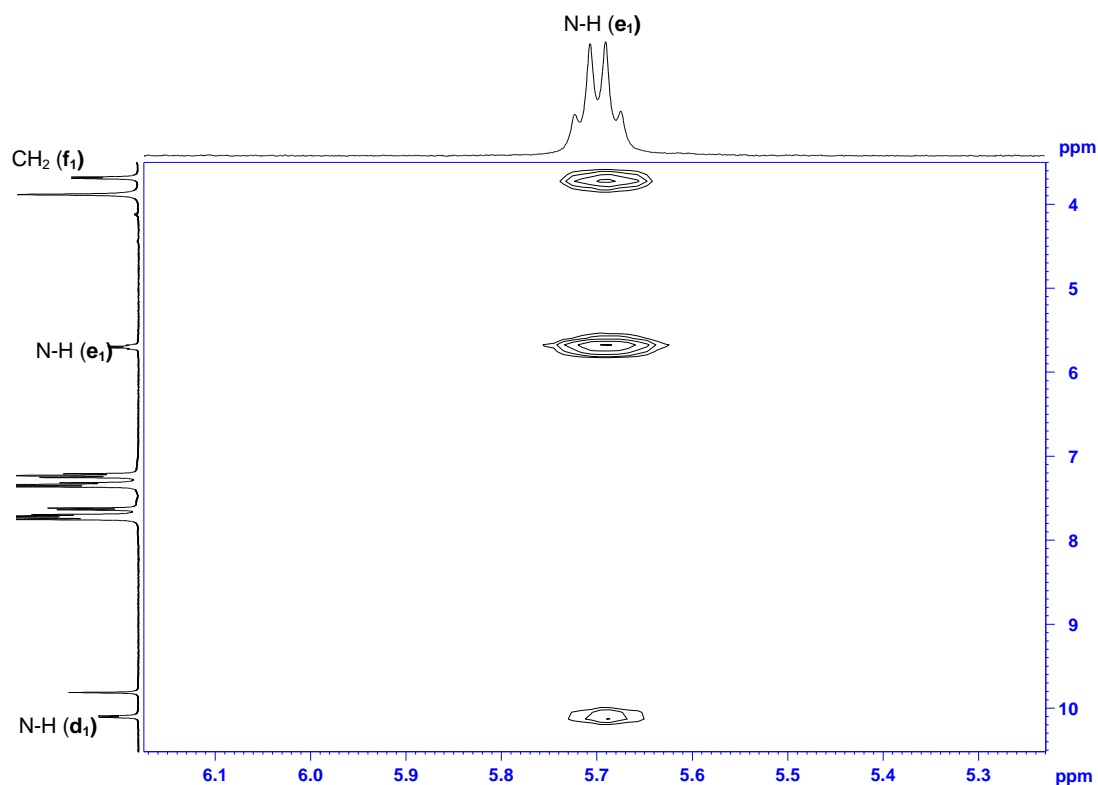


Figure 2.25: ^1H - ^1H COSY spectrum of $\text{NaH}_3\text{D1}$ in the selected region in d_6 -DMSO showing coupling of N-H (\mathbf{e}_1) with CH_2 (\mathbf{f}_1) and N-H (\mathbf{d}_1)

However, in the *E* form, when the amine proton (\mathbf{e}_2) forms a hydrogen bond with the oxygen atom, it shifts considerably downfield to either 16.38/ 16.43 ppm and appears as a singlet (figure 2.26, right). Whereas the CH_2 (\mathbf{f}_2) and amide proton (\mathbf{d}_2) also appears as a singlet at 3.88 (figure 2.24) and 16.38/ 16.43 ppm (figure 2.26, right) respectively. Due to rapid exchange of the amine proton (\mathbf{e}_2) with the carboxylate oxygen atom, the spin-spin coupling constant with adjacent methyl and amide proton is difficult to observe. The other amide proton (\mathbf{g}_2) appears as singlet at 9.83 ppm, while in *Z* form (\mathbf{g}_1) it exhibits significant downfield shift at 16.38/ 16.43 ppm as indicated in figure 2.26.

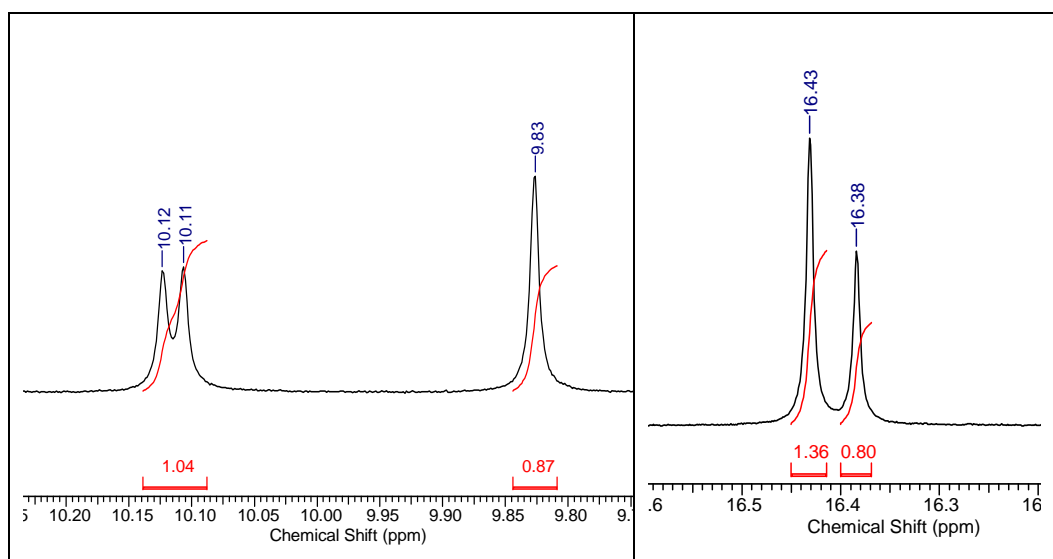


Figure 2.26: ^1H NMR spectrum of $\text{NaH}_3\text{D1}$ in the region 9.70 – 10.20 ppm (left) and 16.30 – 16.40 ppm (right) of selected region in d_6 -DMSO

Hence, it can be concluded from this section that, the attempted reduction of azomethine bond of NaHL9 was unsuccessful. The formation of a di-hydrazide analogue of PVAH, $\text{NaH}_3\text{D1}$, was achieved using 3-bromopyruvate and 4-methyl benzoyl hydrazide in an attempt to make bromopyruvate hydrazones. Due to the C-N single bond character of $\text{NaH}_3\text{D1}$, it can overcome some of the issues of hydrolysis, thus further attempts to reduce azomethine bond were discontinued. As for the NMR spectrum of NaHL9 , the ^1H NMR spectrum of $\text{NaH}_3\text{D1}$ also indicates the presence of *E/Z* isomers in d_6 -DMSO solution. Full characterisation data can be found in the experimental section. In order to explore the stability of $\text{NaH}_3\text{D1}$ towards hydrolysis, its absorption spectrum was monitored under physiological conditions; these studies can be found in chapter-5.

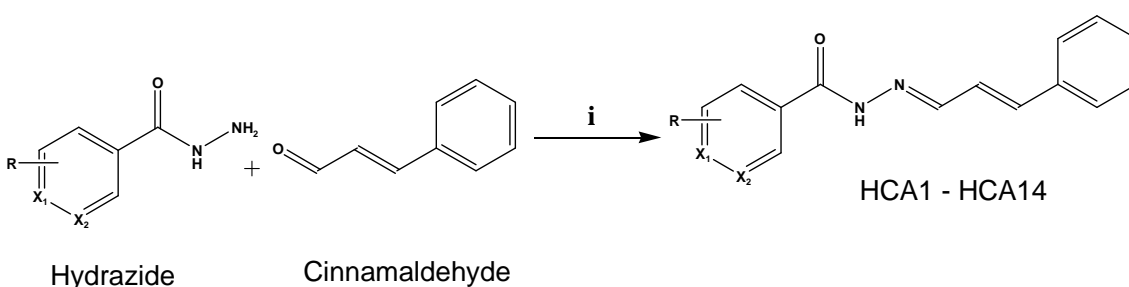
Section B:

Section B mainly focuses on synthesis and characterization of fourteen cinnamaldehyde hydrazone ligands and their respective Cu(II) complexes. Single crystal X-ray structures, stability studies and biological studies will be discussed in subsequent chapters.

Cinnamaldehyde and their derivatives have been extensively studied for their antitubercular properties.¹⁸⁷⁻¹⁹⁰ It has been proven that cinnamaldehyde is known to inhibit the bacterial cell division protein FtsZ.¹⁹¹ Several studies have proven that lipophilic molecules are advantageous over hydrophilic molecules as they can effectively diffuse through the mycobacterial cell wall.¹⁸⁹ In order to explore a lipophilic library of antitubercular compounds, a series of compounds was synthesized by Schiff base condensation of cinnamaldehyde and a selection of substituted hydrazides. In addition to the free ligands, their Cu(II) complexes were also synthesised.

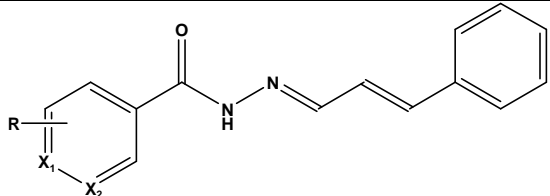
2.9 Synthesis of cinnamaldehyde hydrazones (CAHs)

The synthesis of the cinnamaldehyde hydrazones HCA1-HCA14 was carried out according to literature procedures.¹³⁵ The detailed synthetic procedure can be found in the experimental section and the general synthetic scheme is given in scheme 2.13. CAHs were obtained in good yields and are indicated in table 2.5, along with their compounds codes and substituents.



Scheme 2.13: Synthesis of cinnamaldehyde hydrazones i) EtOH, 4h heated under reflux

Table 2.5: Compound codes of CAHs along with their respective substituents and yields



Compound	R (X=C)	Yield
HCA1	H	70%
HCA2	<i>p</i> -Cl	77%
HCA3	<i>p</i> -CH ₃	79%
HCA4	<i>p</i> -OCH ₃	71%
HCA5	<i>p</i> -NO ₂	84%
HCA6	<i>p</i> -CF ₃	83%
HCA7	<i>p</i> -(CH ₃) ₃ C	79%
HCA8	<i>p</i> -OH	72%
HCA9	<i>m</i> -F	79%
HCA10	<i>m</i> -OH	80%
HCA11	<i>o</i> -OH	71%
HCA12	<i>m</i> -CH ₃ , <i>p</i> -NO ₂	81%
Heterocyclic Compounds	(R=H)	
HCA13	X ₁ =N, X ₂ =C	73%
HCA14	X ₁ =C, X ₂ =C	69%

The formation of the ligands was confirmed using HR-ESI MS, ¹H and ¹³C NMR spectroscopy and the purity of a few hydrazones was confirmed using elemental analysis. The details of the full characterisation can be found in chapter-7.

2.10 NMR analysis of CAHs

¹H NMR spectra of CAHs were recorded in *d*₆-DMSO. As a representative example, the ¹H NMR spectrum of HCA3 is given in figure 2.27. The proton resonance observed at 2.37 ppm can be attributed to the protons of the aromatic methyl substituent. The most deshielded signal observed at 11.67 ppm can be assigned to a N-H proton. As indicated in the inset of figure 2.27, the signals observed in the region 7.0 – 8.3 ppm are part of either the aromatic or the conjugated system (except N-H), where the most downfield proton signal can be attributed to the azomethine proton (H9)

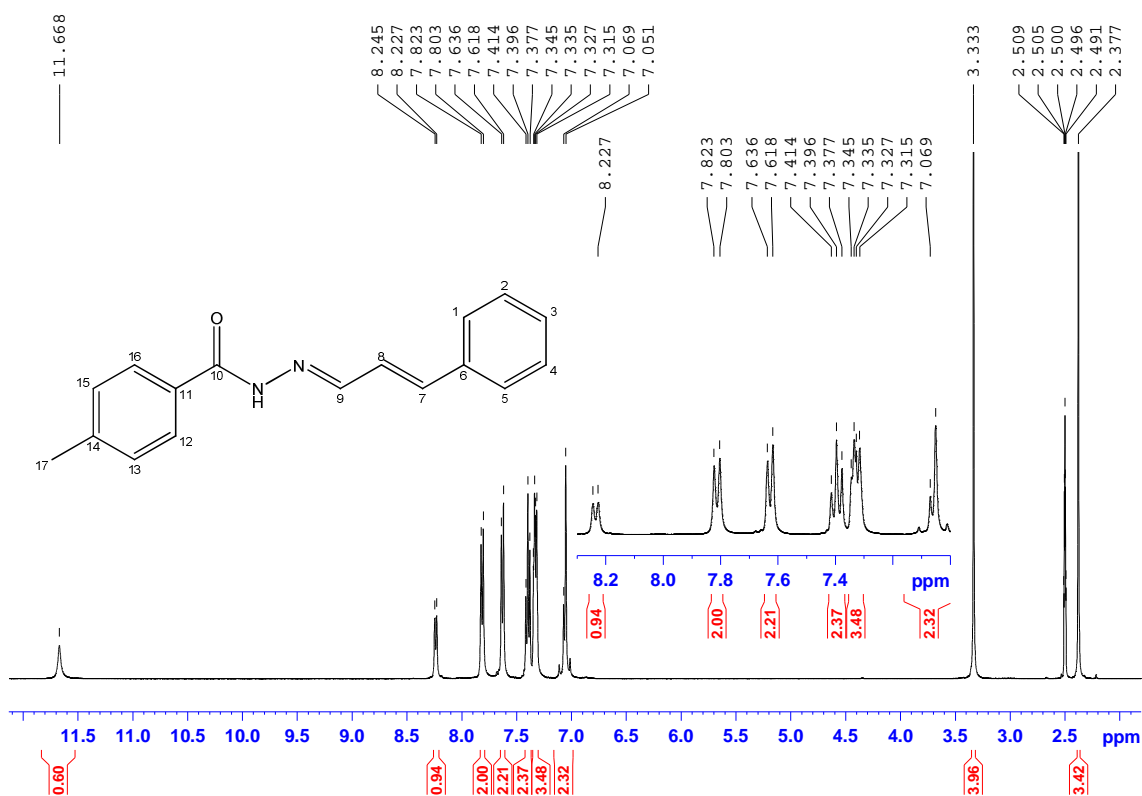


Figure 2.27: ¹H NMR spectrum of HCA3 in *d*₆-DMSO

The ¹³C NMR spectrum of HCA4Me exhibits a downfield signal at 162.7 ppm which can be assigned to the carbonyl carbon (C10), whereas the azomethine carbon (C9) is observed at 149.3 ppm. Other carbon signals fall in the range 125.0 – 142.0 ppm, except the aromatic methyl (C17) which appears at 21.5 ppm. The quaternary carbons C6/11/14 were assigned with the help of a DEPT 135⁰ scan which was also performed on all CAHs along with ¹³C NMR.

Unlike PVAHs, only a few CAHs, HCA13, HCA14 and HCA5, exhibit distinct major and minor peaks in the NMR spectra, which could possibly due to *E/Z* isomers.

Hammett plots for the amide proton (N-H) and the azomethine proton (HC=N) vs substituent parameter (σ) are indicated in figure 2.28 and 2.29, respectively. For compounds HCA1-HCA14, a reasonable correlation is observed between the amide proton and σ , as can be seen from figure 2.28. CAHs containing heterocyclic nitrogen, *ortho* and *di*-substituted are not included in the correlation.

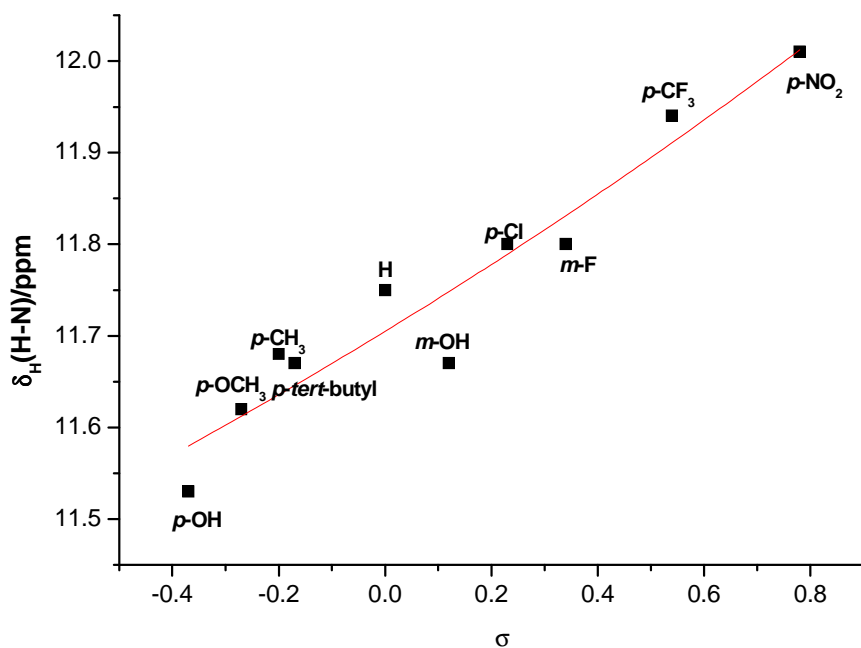


Figure 2.28: Hammett plot of the ^1H NMR chemical shifts of the amide (N-H) proton of ten indicated CAHs in d_6 DMSO vs σ ($R^2 = 0.90$).

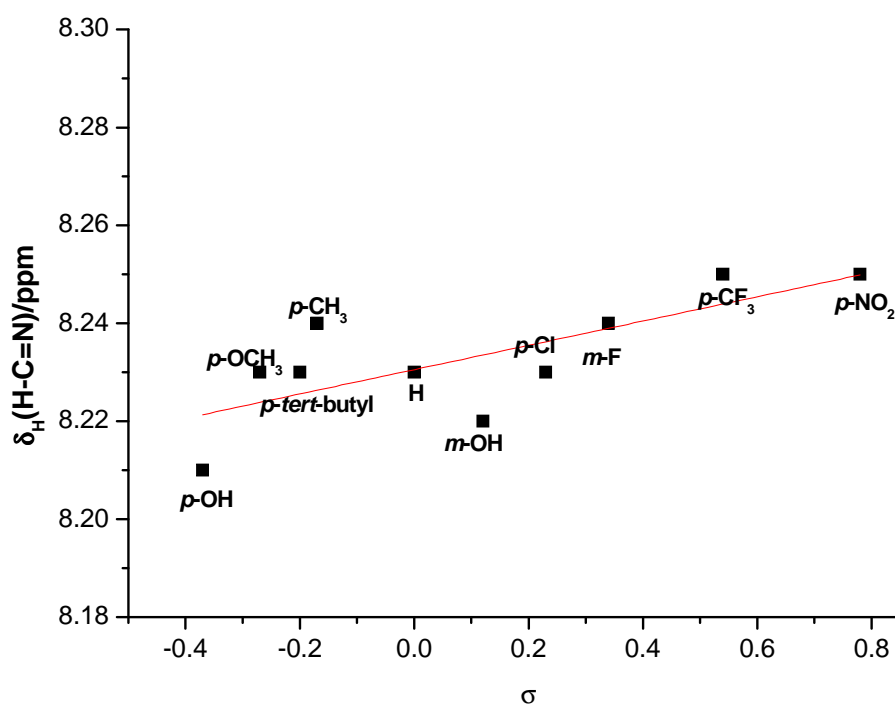


Figure 2.29: Hammett plot of the ^1H NMR chemical shifts of the azomethine proton (HC=N) proton of ten indicated CAHs in d_6 DMSO vs σ ($R^2 = 0.55$).

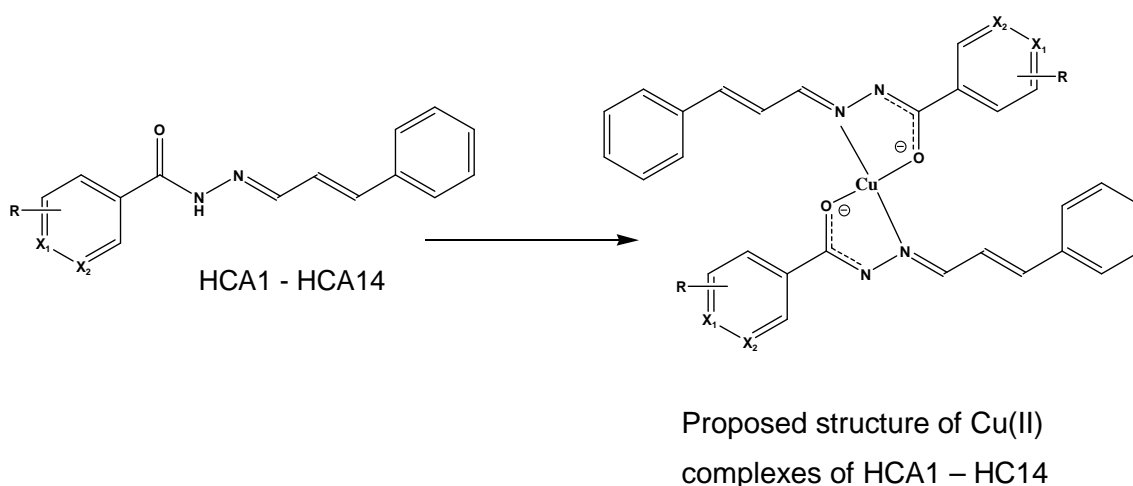
It is observed that EWGs cause a downfield shift of the amide proton, whereas EDG groups cause an upfield shift when compared with the ligand HCA1,

where there are no substituents on the aromatic ring. A similar Hammett plot is obtained from the ^1H NMR chemical shifts for the N-H proton for the PVAHs ligands in d_6 DMSO versus σ .

However, the azomethine proton shows very little or no shift, as can be seen from figure 2.29. This signifies that the EWG/EDG do not have a significant effect on the azomethine proton. The reason for this might be the larger distance from the R group. Similarly observed for PVAHs, where there is no considerable shift observed for methyl protons.

2.11 Synthesis of Cu(II) complexes of CAHs

Cu(II) complexes of CAHs were synthesized using copper(II) acetate and the respective CAH in a 1:2 (M:L) ratio, as indicated in scheme 2.14.



Scheme 2.14: Synthesis of Cu(II) complexes of CAHs i) copper acetate dehydrate, MeOH, 2h

The binding of CAHs to the Cu(II) centre in a 2:1 ratio was confirmed using ESI MS and elemental analysis data. Unfortunately, single crystal X-ray structures of the copper complexes could not be obtained. Owing to the fact that CAHs have two donor atoms, N and O, it is most likely to prefer bidentate mode of binding. Hence, a square planar geometry as expected for four coordinate Cu(II) complexes.¹⁹² This will allow it to maintain an overall neutral charge by binding to two anionic oxygen atoms from two ligands, as indicated in scheme 2.14. Cu(II) complexes of cinnamaldehyde hydrazones are not reported elsewhere. The Ni(II) complex of cinnamaldehyde salicylhydrazone shows a bidentate mode of binding.

The nickel complex achieves octahedral geometry by coordinating to two cinnamaldehyde hydrazones in the equatorial plane, whilst the apical sites are occupied by two solvent molecules.¹⁹³

Interestingly, the positive ESI-MS spectra of Cu(II) complexes of CAHs exhibit peaks at $[M+2H]^+$, suggesting the reduction of Cu(II) to Cu(I), as observed for the Cu(II)-complexes of PVAHs. Details of the characterisation of the Cu(II) complexes of CAHs can be found in chapter-7.

2.11 Infrared (IR) analysis of CAHs and their Cu(II) complexes

In order to gain more insight into the solid state structures of CAHs and their respective Cu(II) complexes, IR spectra were recorded using KBr disc.

A representative example of overlaid IR spectra in the region $1400 - 1700 \text{ cm}^{-1}$ is displayed in figure 2.30. The intense band at 1636 cm^{-1} in HCA3 (blue spectrum) can be assigned to the carbonyl (C=O) bond and the band at 1623 cm^{-1} can be attributed to the azomethine (C=N) bond.

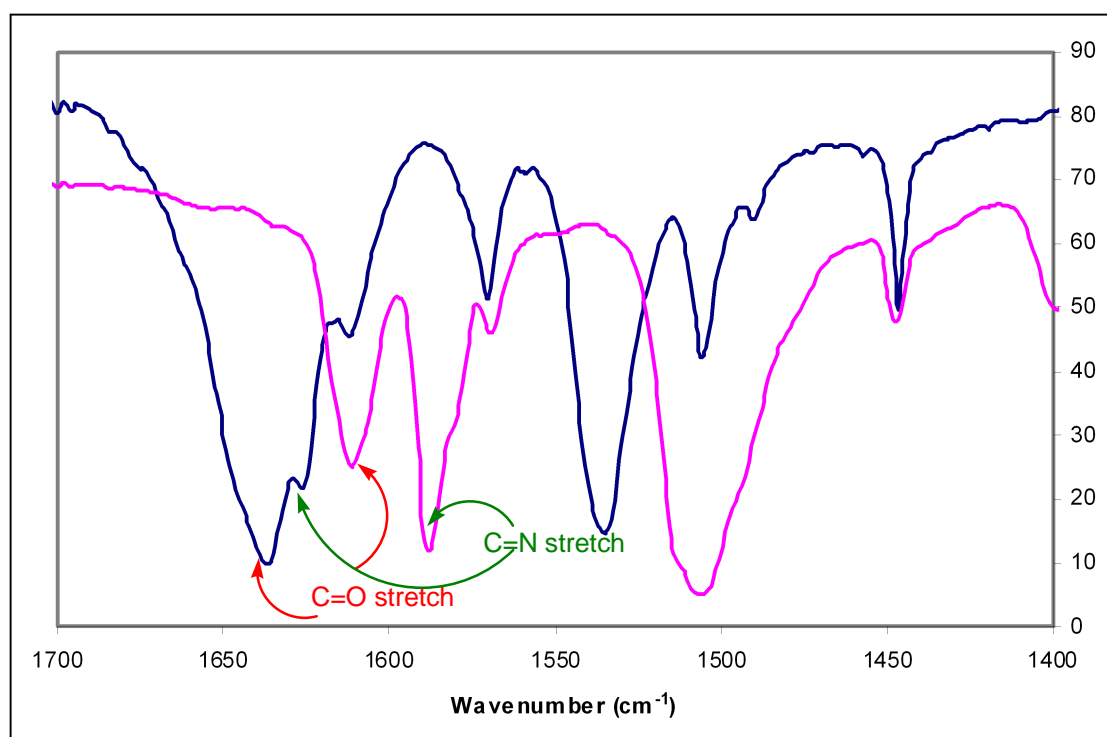


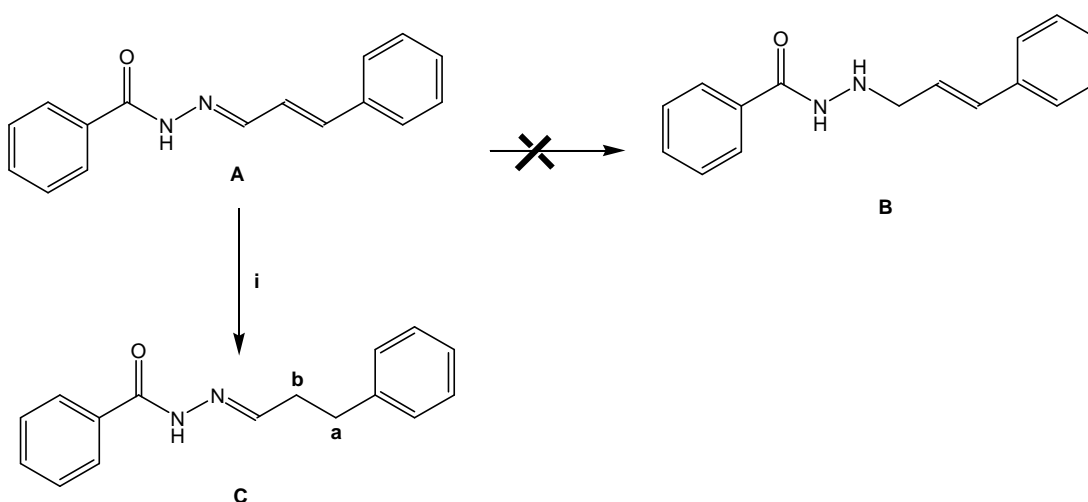
Figure 2.30: Overlaid IR spectra of ligand, HCA3 (blue) and its Cu(II) complex $[\text{Cu(II)(CA3)}_2]$ (magenta) in the region $1100 - 1700 \text{ cm}^{-1}$

The carbonyl and the azomethine stretching frequencies shifts to lower frequencies. 1611 cm^{-1} and 1587 cm^{-1} respectively, in $[\text{Cu}(\text{II})(\text{CA3})_2]$ indicating the coordination of donor atoms O and N. This is similar to what is observed in PVAH compounds. The lowering of the frequency can be attributed to a lengthening of the bond which is due to the shift of the double bond nature of the carbonyl towards single bond character indicating enolisation of C=O bond.¹⁷¹

As expected, CAHs bearing electron withdrawing groups on the aromatic ring have higher frequencies for the $\nu(\text{C}=\text{O})$ band, while those containing electron donating groups have decreased frequencies. The coordination of Cu(II) to HCA3 is also evidenced from the fact that the N-H stretching frequency observed around 3200 cm^{-1} in CAH ligands disappears in copper complexes. Although the crystal structures of Cu(II) complexes of CAHs are not available, similar examples of metal complexes indicate the formation of monoanionic ligands through the loss of amide proton (N-H).

2.12 Reduction of azomethine (C=N) bond

Attempts at reducing the azomethine (C=N) bond of HCA1 failed, as observed for PVAHs. The reduction was first attempted using the reducing agent NaBH_4 but the reaction failed, hence a palladium catalyst under an atmosphere of hydrogen was used. The reduction was confirmed using TLC and ESI-MS (consistent with addition of two hydrogen atoms). However, instead of the azomethine bond getting reduced (product B, scheme 2.15), the olefin bond was reduced to give product C, RHCA1 as indicated in scheme 2.15.



Scheme 2.15: Reduction of C=C bond i) H_2 , Pd/C (10%), 18 hours

The reduction of the C=C bond was confirmed through ^1H , ^{13}C , DEPT and 2D NMR experiments. The proton resonances of the reduced olefin bond labeled as **b** and **a**, appear at 2.59 ppm and 2.83 ppm, respectively, each with a relative integration of two. Their corresponding carbon atom peaks appear at 32.5 ppm and 34.3 ppm, respectively. The stability of the reduced compound, RHCA1 is studied for comparison with HCA1, which will be further discussed in chapter-6

2.13 Summary of Chapter – 2

A series of sodium pyruvate hydrazones with aromatic substituents, ranging from electron withdrawing to electron donating groups were synthesised and characterised by ^1H NMR spectroscopy, ^{13}C NMR spectroscopy, high resolution ESI mass spectrometry, infrared spectroscopy, elemental analysis and melting point analysis. Variable temperature ^1H NMR studies indicate that PVAHs exist as a mixture of *E* and *Z* isomers in solution, with the *Z* form predominating owing to the strong hydrogen bond formed between amide N-H and carboxylate oxygen atom

Furthermore, the Cu(II) and Zn(II) complexes of the PVAHs and Cu(I) complexes of NaHL8 and NaHL9 were synthesised and characterised using the above mentioned techniques, except for the NMR characterisation of the Cu(II) complexes due to their paramagnetic nature. Elemental analysis indicates the formation of 1:1 and 1:2, M:L complexes for Cu(II) and Zn(II) which is further confirmed by the single crystal X-ray structures. The ^1H NMR spectra of the Cu(I) complexes indicate their diamagnetic nature, whereas ^{31}P NMR spectra indicate ligand exchange processes in solution.

Attempts to reduce the azomethine bond using sodium borohydride and palladium catalysts were unsuccessful. The synthesis of a di-hydrazide analogue of pyruvate with 4-methyl benzoyl hydrazide was achieved using bromopyruvate and the product was fully characterised using the above mentioned techniques.

Fourteen cinnamaldehyde hydrazones (HCA1-HCA2) and their respective Cu(II) complexes were synthesised and characterised. Studies indicate a Cu(II):L ratio of 1:2 with possible bidentate mode of binding allowing for a square planar geometry. Reduction of the azomethine bond of HCA1 was unsuccessful, instead the olefinic bond was reduced, as indicated by ESI-MS and NMR analysis.

Chapter-3

Structural investigation in the solid by single crystal X-ray crystallography

3.0 Structural investigation in the solid state by single crystal X-ray crystallography

3.1 Introduction

As discussed in chapter - 2, hydrazones can exist in different forms in solution for example neutral, anionic and dianionic, which allows them to bind to different metal ions, resulting in various geometries around the metal centre.¹⁹⁴⁻¹⁹⁵ Due to their versatile nature, they have been considered as important ligands in the field of coordination chemistry.¹⁹⁶ The geometry adopted by a metal complex of a hydrazone depends on the type of metal and its oxidation state. For example, various geometries of Cu(II) complexes of hydrazones ranging from 6-coordinate octahedral, 5-coordinate square pyramidal and trigonal bipyramidal and 4-coordinate square planar geometry have been reported in the literature,^{134,143,197-198} depending on the ligand donor system. It is well known that, Jahn-Teller distortion is observed for Cu(II) d^9 systems, resulting in distorted octahedral and 5-coordinate geometries.¹⁹⁹ Whereas the ligand mostly binds to Cu(I), d^{10} , in a tetrahedral manner,¹⁷⁶ Zn(II) d^{10} complexes are known to exist in trigonal pyramidal, square pyramidal and octahedral geometry.²⁰⁰⁻²⁰² Apart from mononuclear metal complexes, di-, tri- and polynuclear metal complexes of Schiff bases have also been reported as hydrazone/s are also present as a part of a polydentate ligand system.^{196,200,203-205}

Ketcham *et al.*, investigated the binding of 2-pyridineformamide 3-piperidyl thiosemicarbazone (HAmpip) (Figure 3.1) to first row transition metal ions, such as Cu(II), Fe(III) and Zn(II). The crystal structures of the metal complexes reveal that HAmpip acts as a tridentate ligand and binds through the thione sulphur, imine nitrogen and pyridyl nitrogen atoms. The compound depicted in figure 3.1 is a good example, as it shows how the same ligand can be part of different geometries when coordinated to different metal ions.

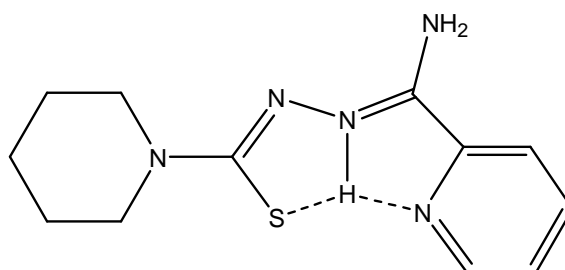


Figure 3.1: Structure of 2-pyridineformamide 3-piperidyl thiosemicarbazone (HAmpip)²⁰⁶

The Cu(II) and Zn(II) complexes, as shown in figure 3.2 a and 3.2 b respectively, exhibit square pyramidal geometry but the Zn(II) complex shows considerable distortion towards trigonal geometry. However, in the case of the Fe(III) complex, as indicated in figure 3.2 c, an octahedral geometry is obtained through coordination to two ligands²⁰⁶.

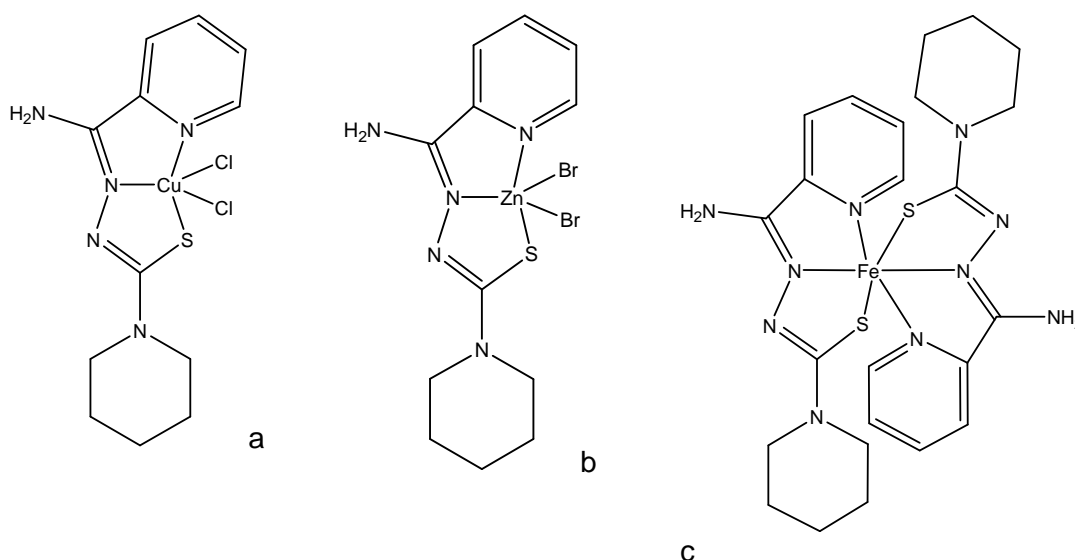


Figure 3.2: Structure of a) [Cu(HAmpip)Cl₂], b) [Zn(HAmpip)Br₂], c) [Fe(Ampip)₂]²⁰⁶

Since, Cu(II) and Zn(II) ion binds to HAmpip with 1:1 and Fe(III) in 1:2 stoichiometry, this coordination behaviour can be used as a useful tool in bioinorganic drug design. This, then would allow the metal ion, to facilitate the transport of two biologically active pharmacophores across the cell membrane.

3.1.1 Geometries of copper and zinc centres present in biological systems

The biological function of several metalloenzymes is closely related to the geometric and electronic properties of the metal sites, influenced by the coordination environment of the enzyme.²⁰⁷ Various coordination geometries of copper and zinc metalloenzymes are present in biological systems. Most of the copper-containing metalloenzymes have a 4-coordinate geometry around the copper centre, for e.g. type I blue copper proteins such as azurin, plastocyanin possess distorted tetrahedral geometry²⁰⁸ and type II copper proteins such as superoxide dismutase have a square planar geometry.²⁰⁹ These Cu centres are surrounded by N, O and S donor atoms

provided by amino acid side chains, such as histidine (N), cysteine (S), methionine (S), aspartate (O) and glutamate (O). The donor atoms from these amino acids are also known to form Zn(II) tetrahedral sites in proteins, such as superoxide dismutase, carbonic anhydrase, β -lactamase, metallothionein and zinc fingers. Superoxide dismutase (CuZnSOD), shown in figure 3.3, possesses two metal centres; the Cu(II) ion is coordinated to histidine molecules via nitrogen atoms whereas Zn(II) binds to three histidine residues and one aspartate residue. Cu(II) adopts square planar geometry with tetrahedral distortion, whereas Zn(II) has a distorted tetrahedron geometry.

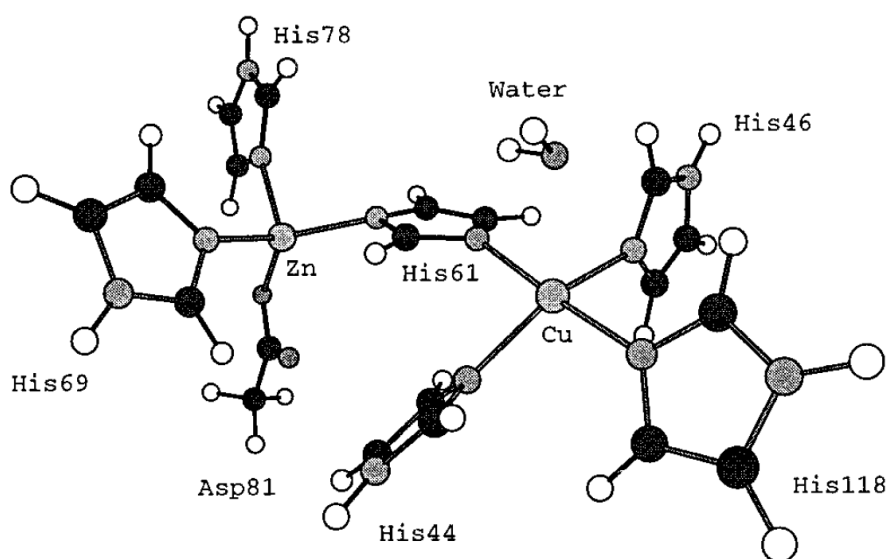


Figure 3.3: Schematic representation of superoxide dismutase²⁰⁹

3.2 Structural aspects of pyruvate hydrazone ligands

As discussed in Chapter-2, the investigated pyruvate hydrazone ligands (PVAHs) are present in the general molecular formula of NaHL_x, predominantly existing in the *Z* form in solution. In order to establish the molecular structure of the ligand in the solid state, crystals of selected ligands were isolated from concentrated solutions of the ligands in ethanol. Crystal data and their refinement data of single crystal X-ray structures described in this chapter can be found in chapter-7 and all other related crystallographic data can be found in Appendices 3-22. Detailed discussions of the crystal structures of ligands NaHL9, NaHL11 and H₂L20 will be given in the following section.

3.2.1 NaHL9.2H₂O

NaHL9.2H₂O crystallises in a rhombohedral R-3 space group and the corresponding ORTEP plot is shown in figure 3.4. Unless otherwise mentioned, ORTEP plots of the crystal structures described in this chapter have 50 % ellipsoid probability. The ligand is essentially planar with *Z* (*syn*) conformation with respect to the imine C=N bond. This is revealed by the torsional angle (C(1)-C(2)-N(1)-N(2)) of 2.06(2)°. ²¹⁰ The molecule is nearly planar with the exception of the Na⁺-counterion, which lies in a different plane with a interplanar angle of 48.09°. Since the hydrazones possess hydrogen bond acceptors as well as donors, the ligand has the opportunity to form hydrogen bonds in the crystal lattice.

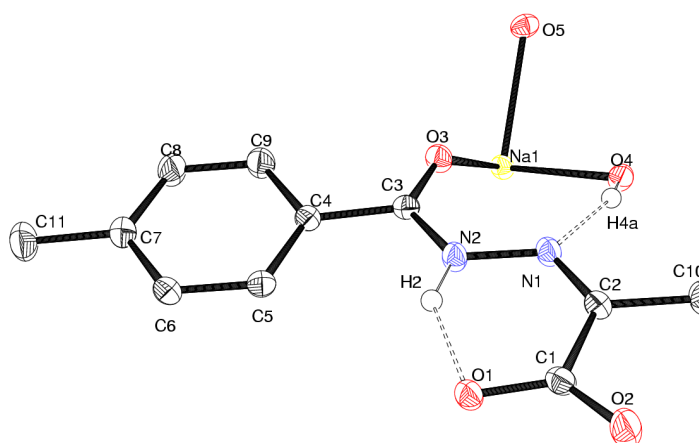


Figure 3.4: ORTEP plot (50% probability ellipsoids) of the molecular structure of NaHL9.2H₂O

Intramolecular hydrogen bonds observed involve N(2)-H bonding to the O(1) of the carboxylate group with a distance of 2.5772(14) Å and an angle of 141.7(16)°. Also, O(1) is ionically bonded to Na⁺ with a distance of 2.3427(15) Å. Moreover, N(1) forms a hydrogen bond with one of the water molecules (O(5)) bonded to sodium. It is also interesting to note that the carbonyl (C(3)-O(3)) oxygen atom is ionically bonded to Na with a distance of 2.3482(10). The C=O bond length is 1.234(2) Å which strongly suggests that ligand exist predominantly in the keto form in the solid state.

3.2.2 NaHL11.2H₂O

NaHL11.2H₂O crystallises in trigonal R-3 space group, as indicated in the figure 3.5. Ligand NaHL11.2H₂O show similar characteristics to that of NaHL9.2H₂O. As expected, the ligand NaHL11 is nearly planar except for the Na⁺ ion and exhibits Z-conformation with respect to the imine (C(2)-N(1)) bond with a torsional angle (C(1)-C(2)-N(1)-N(2)) of 2.58(3).

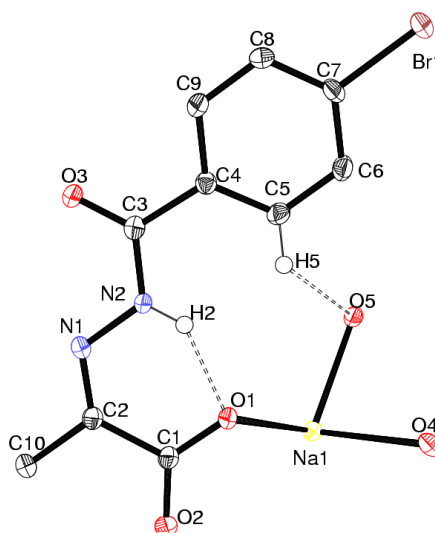


Figure 3.5: ORTEP plot (50% probability ellipsoids) of the molecular structure of NaHL11.2H₂O

3.2.3 Packing diagram of NaHL9.2H₂O and NaHL11.2H₂O

The packing diagram showing the Na⁺ coordination environment and the separation between two planes for NaHL9.2H₂O and NaHL11.2H₂O are shown in Figures 3.6 a, 3.6 b, 3.7 a and 3.7 b, respectively. Mercury software version 2.4 is used in this chapter, to show the packing diagrams and the planes passing through the atoms.

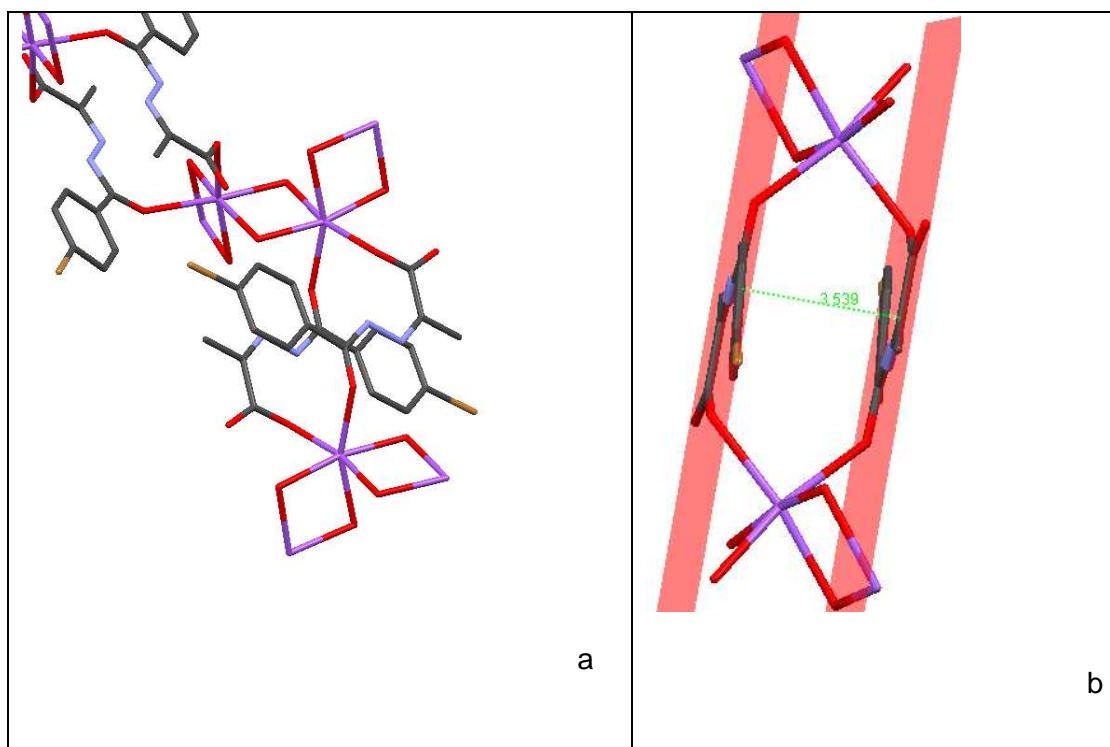


Figure 3.6: a) Crystal structure packing. b) planes showing separation between two crystallographically equivalent ligands NaHL9.2H₂O. Colours of the atom: purple - Na, grey - C, brown - Br, blue - N, red - O

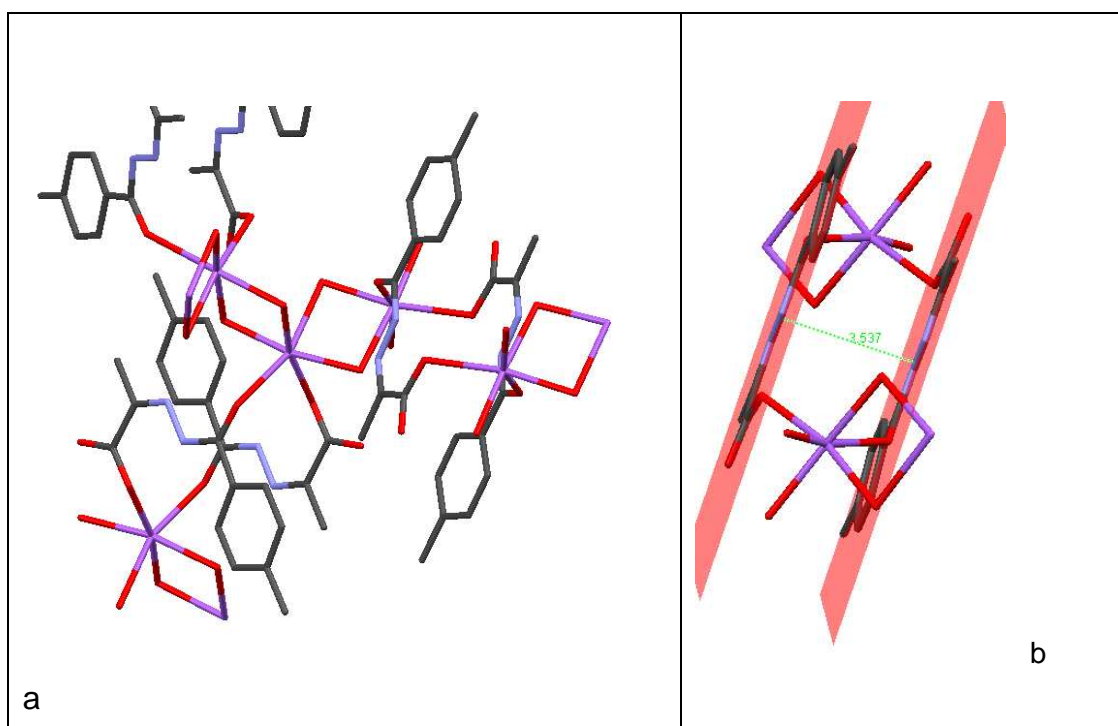


Figure 3.7: a) Crystal structure packing. b) planes showing separation between two crystallographically equivalent ligands NaHL11.2H₂O. Colours of the atom: purple - Na, grey - C, blue - N, red - O

3.2.4 Interaction of NaHL9.2H₂O and NaHL11. 2H₂O with sodium

In the solid state structures of both, NaHL9.2H₂O and NaHL11.2H₂O, the sodium counter ion interacts with the hydrazinic carbonyl oxygen O(3) and the carboxylate donor atom O(1) of an adjacent ligand. The two adjacent ligands are crystallographically equivalent and lie in different planes separated by 3.539 and 3.537 Å for NaHL9.2H₂O and NaHL11.2H₂O, respectively. The Na centre completes its octahedral coordination sphere by binding to four water molecules, with the oxygen atoms bridging between two sodium cations. Three water molecules and carbonyl oxygen lie in one plane, whereas the carboxylate and water molecule occupy the apical positions. General schematic representation showing the Na⁺ coordination sphere is depicted in figure 3.8. The bond lengths and bond angles of NaHL9.2H₂O and NaHL11.2H₂O involving the Na atom are given in table 3.1.

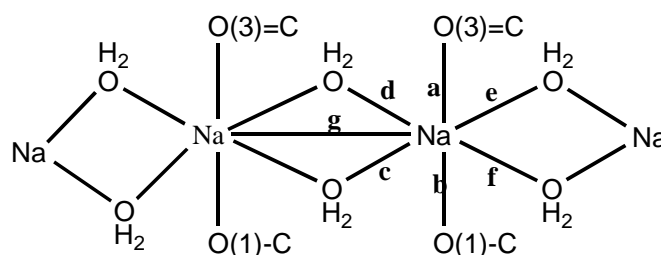


Figure 3.8: Schematic representation of the Na⁺ octahedral complex

Table 3.1: Comparison of selected bond lengths (Å) and bond angles (°) for the octahedral Na⁺ environment in NaHL9.02H₂O and NaHL11.2H₂O

Bonds	NaHL9	NaHL11
a	2.3482(10)	2.3427(15)
b	2.4222(11)	2.4214(15)
c	2.3162(11)	2.3207(16)
d	2.3952(11)	2.3915(17)
e	2.4232(11)	2.4193(17)
f	2.3459(11)	2.3516(16)
g	3.3864(6)	3.3896(8)
d-Na-c	90.86(4)	90.68(5)
e-Na-f	89.40(4)	89.33(6)
a-Na-b	88.03(3)	87.94(6)
a-Na-f	160.98(4)	159.81(6)

As seen from table 3.1, both structures exhibit similar bond lengths and bond angles and are in good agreement with literature values²¹¹. The Na-O bond distances fall in the range 2.31 - 2.43 Å and two of the neighbouring sodium ions (Na---Na) distance measures 3.38 Å. The bond angles, especially α -Na-f, indicate a slight distortion from a perfect octahedral geometry. Furthermore, one of the water molecules participates in hydrogen bonding with N(1), with an O(4)-H(4A)---N(1) bond distance of 3.1579(16) Å and bond angle of 162(2)°.

3.2.5 H₂L20.H₂O

H₂L20.H₂O (figure 3.9) crystallises in the triclinic space group P-1. The ligand crystallised out of a methanolic solution of the corresponding zinc complex, suggesting that the ligand is labile. H₂L20.H₂O adopts *E* (*anti*) conformation with respect to the imine bond similar to the reported crystal structures of pyruvic acid hydrazones.²¹²⁻²¹³ This is further confirmed by the torsional angle (C(6)-C(7)-N(4)-N(3)) of 179.65(11)° which is typical for the *E* isomer of hydrazones.¹⁴⁵ The dissimilarity of geometric isomers, *E* and *Z* present in the ligands may be due to the presence of sodium ion in the crystal lattice and intramolecular hydrogen bonding, which stabilises the *Z* conformation in sodium pyruvate hydrazone.

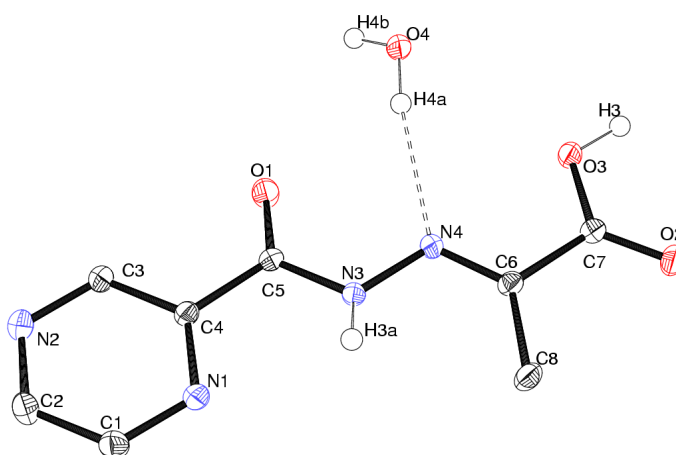


Figure 3.9: ORTEP plot (50% probability ellipsoids) of the molecular structure of H₂L20.H₂O

Moreover, H₂L20.H₂O is essentially planar with the mean plane of deviation of 1.73° as compared to the sodium salts of the deprotonated ligands (5.84 and 7.25°). This can be attributed to the Na⁺ cation, which results in the distortion of the molecule.

Due to the presence of a water molecule in the crystal lattice, the hydrogen bonding interactions differ from those observed for NaHL9.2H₂O and NaHL11.2H₂O.

Although, no intramolecular hydrogen bonding interactions were observed, the nitrogen atom of the imine forms an intermolecular hydrogen bond with water with a bond distance (N(4)- H(4a)-O4) of 3.1579(16) Å. The intermolecular H-bond distance is slightly longer than the intramolecular H-bond distance observed for NaHL9.2H₂O and NaHL11.2H₂O with 2.5772(14) and 2.933(3) Å, respectively. On a similar note, the same water molecule is involved in hydrogen bonding with pyridyl nitrogen N(1), carboxylate oxygen O(3) and carbonyl oxygen O(1) with bond distances of 2.8656(17), 3.082(2) and 2.9683(16) Å, respectively. These hydrogen bonds are absent in NaHL9.2H₂O and NaHL11.2H₂O as the respective oxygen atoms are ionically bonded to Na⁺ as described earlier. The crystal packing of H₂L20.H₂O illustrating hydrogen bonds is shown in figure 3.10.

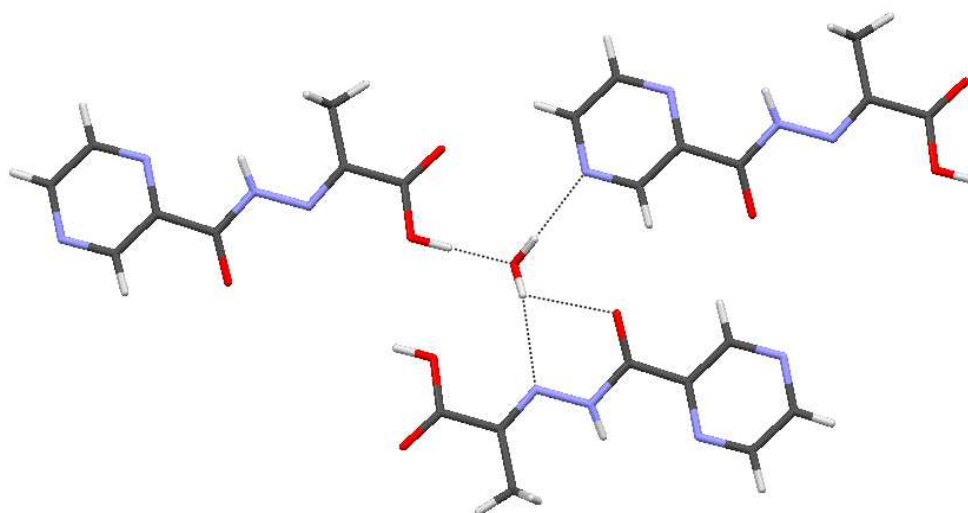


Figure 3.10: Crystal packing diagram of H₂L20.H₂O showing intermolecular hydrogen bonding interactions (indicated with dotted lines). Colours of the atom: grey - C, blue - N, red - O, white - H.

3.2.6 Comparing PVAHs with the literature data

The selected bond lengths and bond angles of NaHL9.2H₂O, NaHL11.2H₂O and H₂L20.H₂O and their comparison with literature data are given in table 3.2. A general schematic representation of PVAH with atom numbering scheme is given in figure 3.11. To our best knowledge, crystal structures of sodiated pyruvate hydrazones do not exist in the literature, hence the ligands are compared to the pyruvic acid

hydrazones. In order to make a direct comparison of equivalent bonds, the numbering system in the schematic representation is not in accordance with the ORTEP plots. The ORTEP plot indicates that the oxygen atom of the hydrazinic carbonyl (C(3)-O(3)) in sodiated ligands (NaHL9.2H₂O and NaHL11.2H₂O) are ionically bonded to the Na⁺ cation. This makes the carbonyl bond length slightly longer than the corresponding bond in H₂L20 and similar bonds reported in the literature. This might be due to the involvement of lone pairs on oxygen in interactions with the sodium cation. Similarly, the bond lengths observed for C(1)-O(2) of the carboxylate moiety for sodiated ligands were slightly longer than the non-sodiated counterpart.

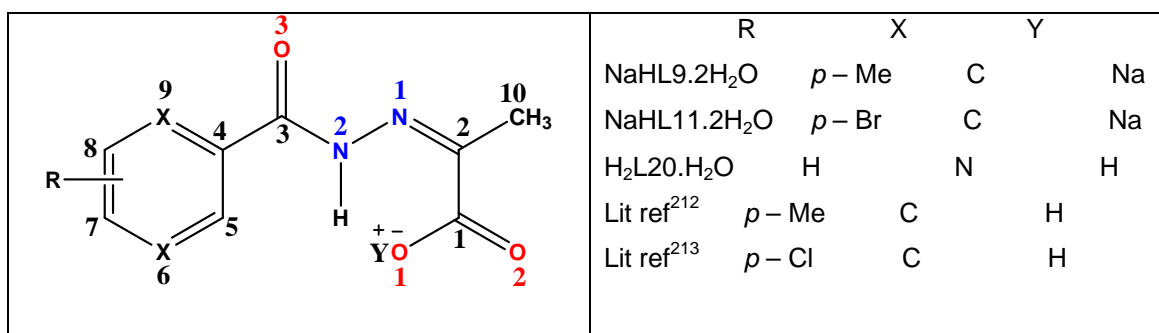


Figure 3.11: General structure of pyruvate hydrazones with atom numbering scheme

Table 3.2: Selected bond lengths (Å) for NaHL9.2H₂O, NaHL20.2H₂O, H₂L20.H₂O and two examples from the literature

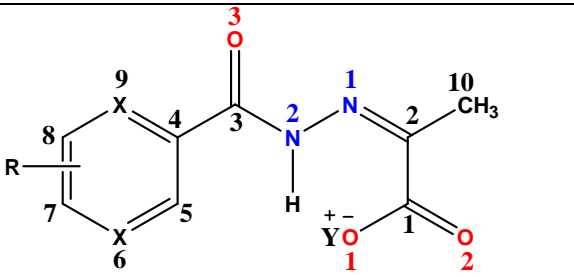
Bonds	NaHL9.2H ₂ O	NaHL11.2H ₂ O	H ₂ L20.H ₂ O	Lit ref ²¹²	Lit ref ²¹³
C(1)-O(2)	1.2380 (16)	1.234(2)	1.2151 (17)	1.213 (3)	1.219 (2)
C(1)-O(1)	1.2743 (16)	1.278(2)	1.3163 (17)	1.312 (3)	1.3161 (19)
C(2)-N(1)	1.2897 (17)	1.290(3)	1.2831(18)	1.277 (3)	1.281 (2)
C(3)-O(3)	1.2330 (15)	1.234(2)	1.2209 (17)	1.222 (2)	1.220 (2)
C(3)-N(2)	1.3522 (16)	1.348(3)	1.3616(18)	1.369 (3)	1.379 (2)
N(1)-N(2)	1.3835 (15)	1.383(2)	1.3745 (16)	1.377 (2)	1.360 (2)
N(2)-H	0.916(18)	0.827()	0.83(3)	0.87 (2)	0.878 (9)
O(1)-H	-	-	0.93(2)	0.83 (2)	0.829 (10)
O-Na	2.4223(11)	2.3427(15)	-	-	-

In contrast to H₂L20.H₂O and compounds listed from references, the bond distances for C(1)-O(1) observed for NaHL9.2H₂O and NaHL11.2H₂O were significantly shorter than for the other ligands. Comparing with typical bond lengths of C-O (1.42 Å) and C=O (1.23 Å), this indicates that the electron density is delocalised in case of

the carboxylate group (O(1)-C(1)-O(2)) in order to make it resonance stabilised. The fact that in NaHL9 and NaHL11 the C(1)-O(1) bond is slightly longer than the C(1)-O(2) bond reflects the interaction of O(1) with the sodium counter ion. The imine bond remains unaffected and is very similar in the protonated and deprotonated ligands. This is seen from the (C(2)-N(1)) bond length, which has a double bond character, typical of Schiff base ligands.²¹⁰

Selected bond angles are given in table 3.3. Owing to the fact that oxygen donor atoms of NaHL9.2H₂O and NaHL11.2H₂O, which include O(3) and O(1), are associated with Na⁺, the N(2)-C(3)-O(3) bond angles were slightly larger than in H₂L20 and literature ligands. Likewise, the N(1)-C(2)-C(1) bond angle observed for sodiated ligands were 126.4 ° and for non-sodiated ligands it ranges from 114.0 – 116.0 °.

Table 3.3: Selected bond angles (°) of NaHL9, NaHL11, H₂L20 and two examples from the literature

	R		X	Y
	NaHL9.2H ₂ O	<i>p</i> -Me	C	Na
NaHL11.2H ₂ O	<i>p</i> -Br	C	Na	
H ₂ L20.H ₂ O	H	N	H	
Lit ref ²¹²	<i>p</i> -Me	C	H	
Lit ref ²¹³	<i>p</i> -Cl	C	H	

Bonds	NaHL9.2H ₂ O	NaHL11.2H ₂ O	H ₂ L20.H ₂ O	Lit ref ²¹²	Lit ref ²¹³
N2-C3-O3	123.37(12)	123.39(17)	121.55(13)	121.82 (19)	121.63 (16)
N2-C3-C4	115.55(11)	115.79(16)	115.10(12)	117.06 (17)	116.93 (13)
C3-N2-N1	119.46(11)	119.59(16)	117.71(12)	116.00 (17)	116.41 (12)
N1-C2-C1	126.45(11)	126.48(16)	115.74(12)	113.55(17)	114.38(13)
C2-C1-O1	118.72(11)	118.46(16)	113.30(12)	118.40(18)	121.04(14)
C(1)-C(2)- N(1)-N(2) (torsional angle)	2.06(2)	2.58(3)	179.65(11)	176.43(17)	177.31(11)

The other bond angles are more or less similar and the small differences can be attributed to crystal packing effects and hydrogen bonding. It is also noted that the R group on the aromatic ring does not have a significant effect on the bond lengths or bond angles of the PVAHs.

3.3 Structural aspects of cinnamaldehyde hydrazone ligands

The crystals of cinnamaldehyde hydrazone ligands (CAHs), which will be discussed further in this section were obtained from ethanolic solutions of the ligands. HCA2 and HCA5 crystallise in the triclinic space group P-1 and the monoclinic space group P21/c, respectively. The ORTEP plots for the corresponding crystal structures are displayed in figures 4.12 a and 4.12 b. The crystal structures indicate that both ligands are protonated at N1, indicating the presence of predominantly the keto form in the solid state, as observed for pyruvate hydrazone ligands.

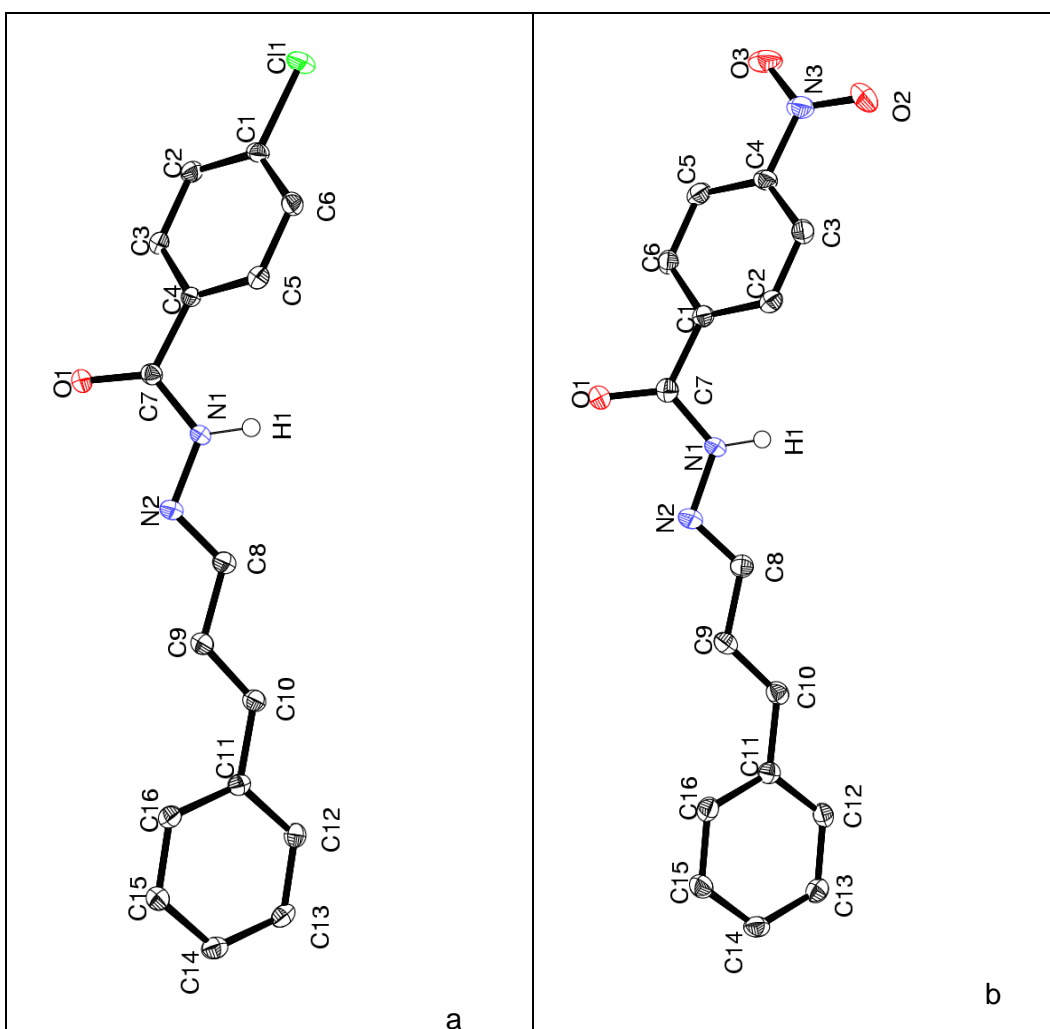


Figure 3.12: ORTEP plot (50% probability ellipsoids) of the molecular structure of a) HCA2 and b) HCA5

The ligands adopt *Z* conformation with respect to imine (C(8)-N(2)) bond, with the two aromatic rings lying in two different planes, which allows them to remain in the lower energy conformation by experiencing less steric hindrance. The torsional angle

(C(9)-C(8)-N(2)-N(1)) of 177.16(12) and 177.09(14) for HCA2 and HCA5 further confirms the Z form. Unlike PVAHs, CAHs crystal structures, are non-planar with a interplanar angle of 57.64 (HCA2) and 53.83 (HCA5), as can be seen from figure 3.13 a and 4.13 b respectively. The interplanar angle is measured by passing the planes through the two aromatic rings. The small difference in the interplanar angle of HCA2 and HCA5 may be attributed to their packing effect of the crystal in the unit cell.

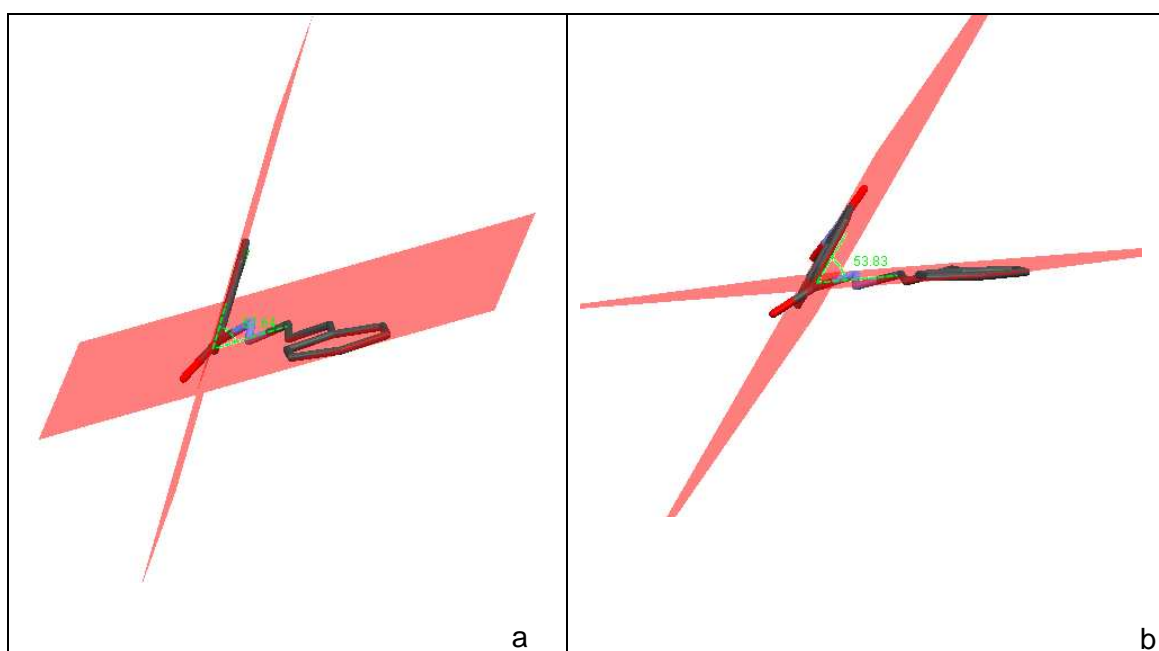


Figure 3.13: Asymmetric unit cell of a) HCA2 and b) HCA5 showing the two planes passing through the aromatic rings

Although, no intramolecular hydrogen bonding was observed for HCA2 and HCA5, the ligands exhibit some interesting intermolecular hydrogen bonding and π -interactions, as displayed in figures 3.14 a and 3.15 a, respectively. The imine proton on N(2)-H forms intermolecular hydrogen bonds with symmetry generated carbonyl O(1) oxygen lone pairs which is indicated in figures 3.14 b and 3.15 b. In addition, C-H \cdots π interactions are also observed, which allow the molecule to pack in a bilayer array. The proton on the aromatic ring interacts with the π electron density of another phenyl ring of adjacent symmetry generated molecule and vice versa. The C-H \cdots π interactions for HCA4Me and HCA5 are illustrated in figures 3.14 c and 3.15 c, respectively. The C-H \cdots π interactions for both the ligands range from 2.7 to 2.9 Å²¹⁴. These C-H \cdots π interactions are not observed in the solid state structures of PVAHs, which could be due to presence of only one aromatic ring.

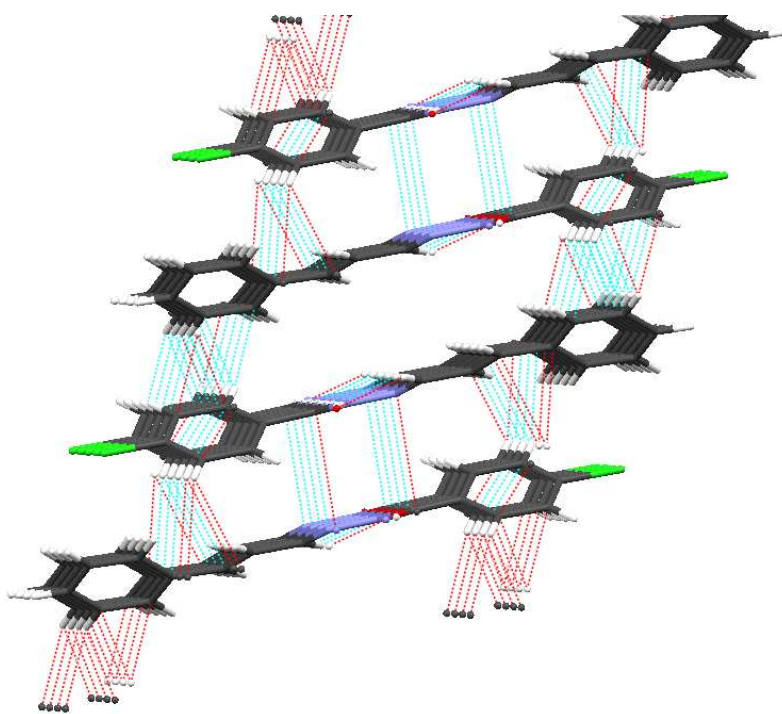


Figure 3.14 a: Crystal structure packing diagram showing interactions for CA4Cl (indicated with dotted lines). Colours of the atom: grey - C, blue - N, red - O, white - H, green-Cl

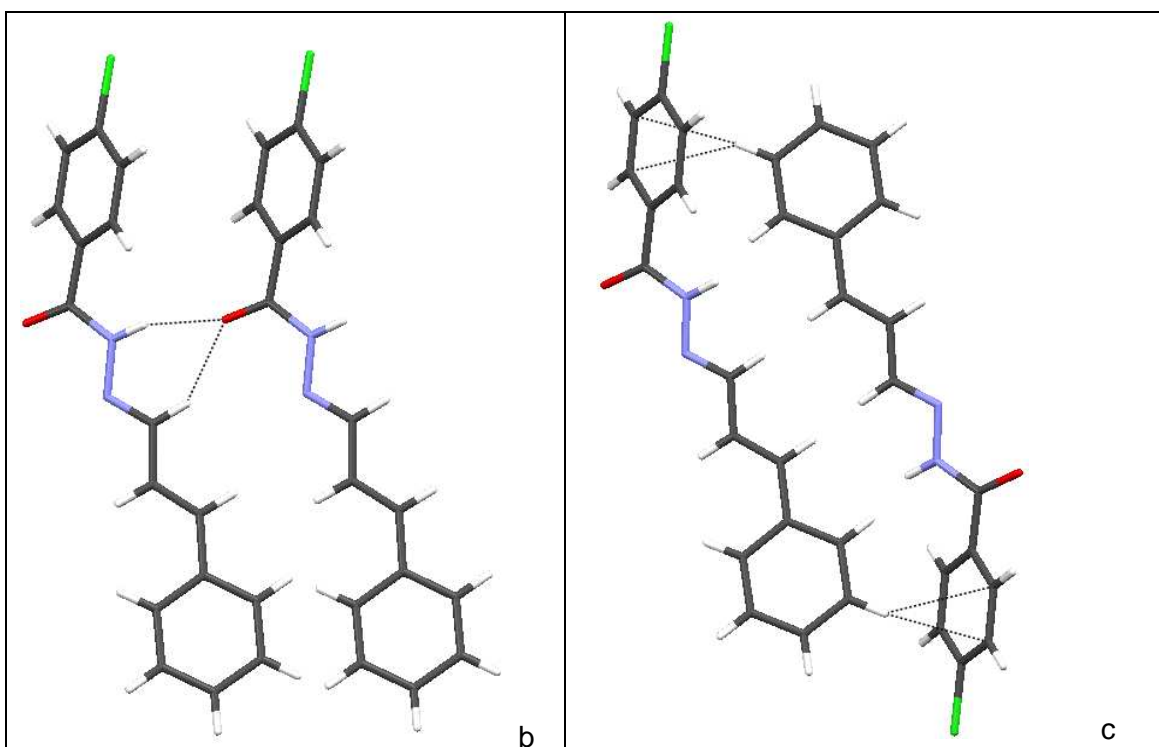


Figure 3.14: b) Intramolecular hydrogen bonding interactions c) C-H... π interactions for HCA2 (indicated with dotted lines). Colours of the atom: grey - C, blue - N, red - O, white - H, green-Cl

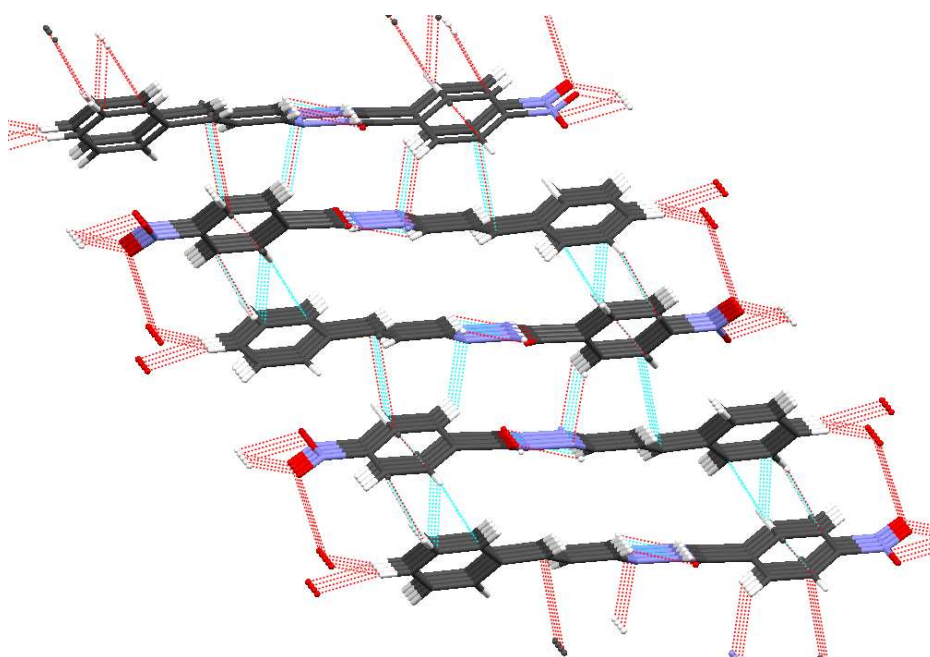


Figure 3.15: a) Crystal structure packing diagram showing interactions for CA4NO2 (indicated with dotted lines). Colours of the atom: grey - C, blue - N, red - O, white - H

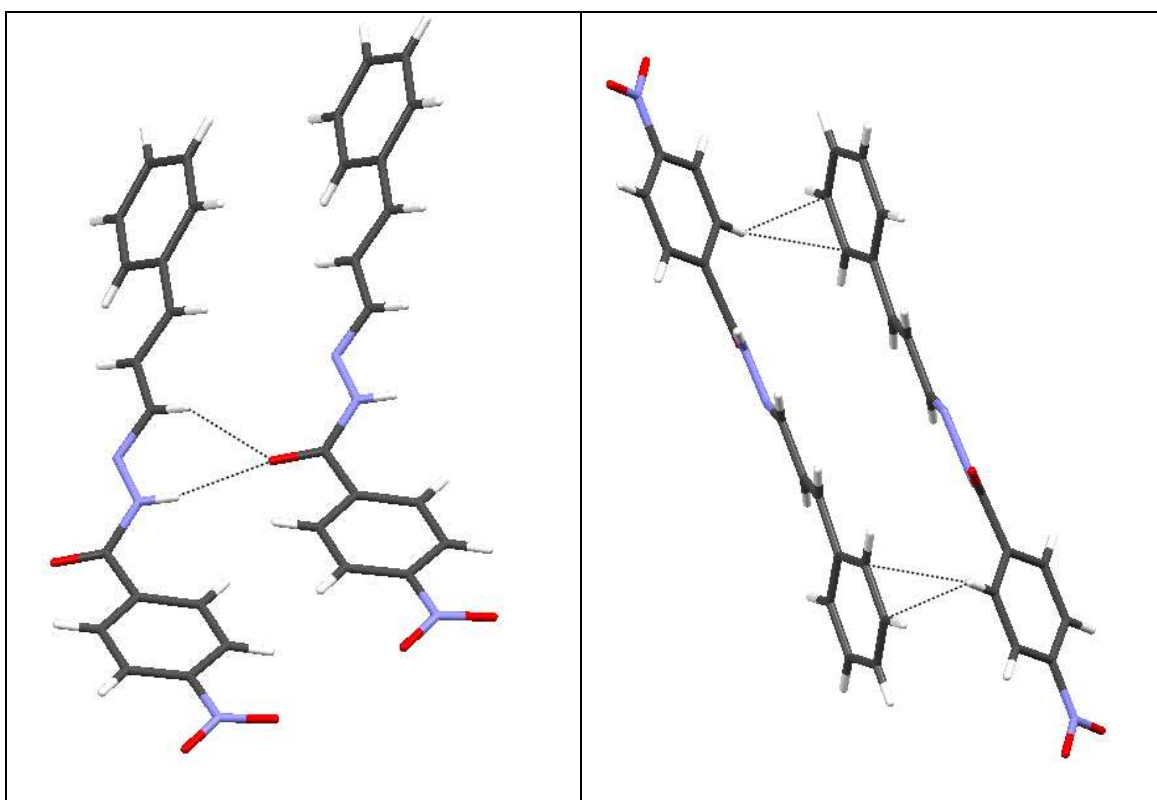
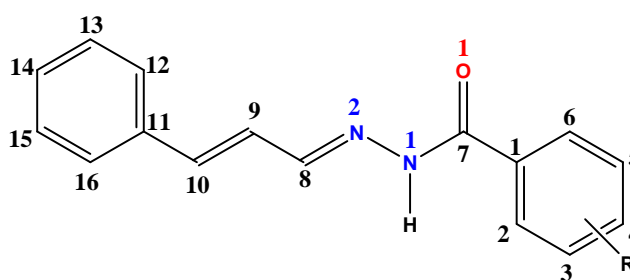


Figure 3.15: b) Intramolecular hydrogen bonding interactions c) C-H... π interactions for HCA5 (indicated with dotted lines). Colours of the atom: grey - C, blue - N, red - O, white – H.

Additionally, weak π - π interactions are also observed for the ligands leading to the formation of π stacks of the molecules. In HCA5, the molecules are also interlinked amongst themselves via C-H---O_{nitro} interactions between aromatic proton on the para-position of C(14) carbon with two oxygen atoms of nitro group on two different molecules. Whereas in CA4Cl, chlorine does not take part in any kind of interactions, but delocalised π -electrons on C(10) – C(11) C-H--- π interactions with one of the proton on aromatic ring. Selected bond lengths and bond angles for HCA2 and HCA5 can be found in table 3.4.



R = *p*-Cl (HCA2), R = *p*-NO₂ (HCA5)

Figure 3.16: General structure of CAH with atom numbering scheme

Table 3.4: Selected bond lengths (Å) and bond angles (°) for HCA2 and HCA5

Bonds	HCA2	HCA5
C(4)-C(7)	1.4974(19)	1.499(2)
C(7)-O(1)	1.2259(18)	1.228(2)
C(9)-C(8)	1.442(2)	1.436(2)
C(7)-N(1)	1.3548(19)	1.353(2)
C(8)-N(2)	1.288(2)	1.286(2)
N(1)-N(2)	1.3838(17)	1.382(2)
N(2)-H	0.88(2)	0.86(2)
O(1)-C(7)-N(1)	123.97(13)	124.07(16)
C(7)-N(1)-N(2)	119.96(12)	120.67(15)
N(2)-C(8)-C(9)	119.50(14)	120.63(16)
C(9)-C(10)-C(11)	126.97(16)	126.25(14)
C(1)-C(2)-N(1)-N(2) (torsional angle)	177.16(12)	177.09(14)

As expected, both ligands show similar bond lengths and bond angles for equivalent bonds suggesting that the R group on the aromatic ring has little or no

influence on the bond distances, as observed for PVAHs. The keto form of ligand is present in the solid state which is confirmed by the presence of the double bond character of the carbonyl C(7)-O(1) moiety, with bond lengths of 1.2259(18) and 1.228(2) Å for HCA2 and HCA5, respectively. The imine, C(8)-N(2) bond lengths observed for ligands HCA2 (1.288(2)) and HCA5 (1.286(2)) is indicative of a double bond and is characteristic of aroyl hydrazones.²¹⁵ Similar lengths for equivalent bonds were observed for both the series of compounds.

3.4 Significance of hydrogen bonding in medicinal chemistry

From the X-ray crystal structures, it is evident that PVAHs and CAHs participate in intra and/or intermolecular hydrogen bonding. Hydrogen bonding interactions play a crucial role in medicinal chemistry, as they can affect drug uptake, distribution, metabolism and excretion (ADME). The importance of the hydrogen bond acceptor and donor properties of a drug is reflected by the Lipinski's rule of five.²¹⁶ One of the rules states that there should be a considerable number of hydrogen bond donor and acceptor atoms, but no more than five H-bond donors (including OHs, NHs and SHs) and no more than ten H-bond acceptors. This is because a large number of hydrogen bond donor atoms can affect the drug permeability through cell membrane.

The LogP value gives an indirect measure of hydrogen bond donor/acceptor properties of a molecule, and it should be below five, in line with the Lipinski's rule of five. A LogP value greater than five could lead to poor drug absorption and can be calculated theoretically and determined experimentally. The ClogP for PVAHs and CAHs were calculated theoretically using OSIRIS Property Explorer.²¹⁷ The ClogP values lie between -1.03 to 2.74 and 2.58 to 5.18 for PVAHs and CAHs respectively depending on the R group attached to the aromatic group, whereas for the well known antitubercular drug isoniazid the calculated value is -0.78. It is evident from the crystal structures that the PVAHs form a greater number of hydrogen-bonding interactions than the CAHs investigated. Hence, the ClogP values are larger for the CAH series as compared to the PVAH series, which implies that CA hydrazones have a more lipophilic character. However, greater ClogP values of active pharmacophores can be useful in antitubercular drug design, since increased lipophilicity would facilitate the passage of the molecule through the lipid bilayer of the waxy mycobacterial cell wall.^{189,218}

Hydrogen bonding interactions are not only vital for the drug delivery mechanism, but also known to determine interactions with the active site of enzymes,

thereby affecting the activities of certain enzymes. For example, the pyruvate moiety which is a resultant of dehalogenation of 3-bromopyruvate is known to form hydrogen bonds with amino acids of the active site of isocitrate lyase (ICL) thus blocking the enzymatic activity. ICL is found in *Mycobacterium tuberculosis* and allows the bacteria to remain in the latent state.⁵³ Furthermore, it has been shown that hydrogen bonding with the active site of catalase peroxidase helps to stabilise the active pharmacophore of isoniazid²¹⁹.

3.5 Structural investigation of Cu(II) complexes of PVAHs

3.5.1 Monomeric square pyramidal Cu(II) complexes

3.5.1.1 [Cu(II)(L9)(H₂O)₂]

Most of the Cu(II) complexes of PVAHs described in this chapter were obtained from slow evaporation of methanolic solutions. [Cu(II)(L9)(H₂O)₂] crystallizes in the triclinic space group P-1 and the ORTEP plot is shown in figure 3.17. Interestingly, the crystal structure of [Cu(II)(L9)(H₂O)₂] possesses two crystallographically independent molecules in the same unit cell.

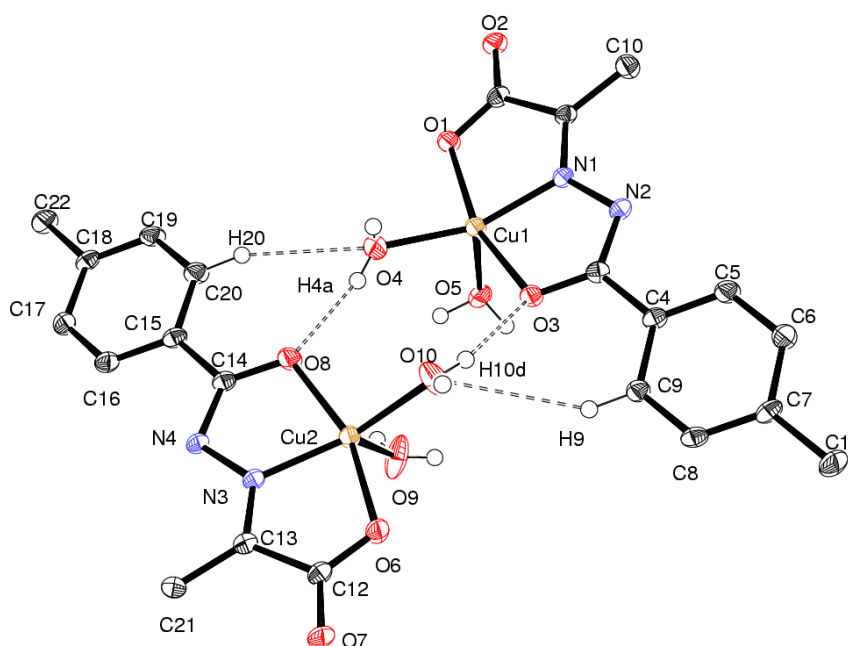


Figure 3.17: ORTEP plot (50% probability ellipsoids) of the molecular structure of [Cu(II)(L9)(H₂O)₂]. Hydrogen atoms apart from water molecules, H9 and H20 are omitted for clarity

The Cu(II) centre is penta-coordinated with three coordination sites occupied by the tridentate ligand L9, which forms two stable 5-membered chelate rings. The other two sites of coordination are occupied by neutral aqua ligands. While the equatorial positions of the Cu(II) centre are occupied by the hydrazinic carbonyl oxygen (O3), the imine nitrogen (N2) atom, one carboxyl oxygen (O3), and one water oxygen (O4), the apical position is taken by oxygen atom (O5) of another water molecule, which is typical of Cu(II) tridentate hydrazone complexes.¹³⁵ Loss of the N(2)-H proton imparts a negative charge on the O(3) atom resulting in a dianionic ligand, which helps stabilise the two positive charges on the Cu(II) centre. The ligand, L9²⁻ remains nearly planar when coordinated to the Cu(II) centre.

It is known that 5-coordinate metal complexes exhibit an extensive range of geometries ranging from regular trigonal bipyramidal to square pyramidal, with most of displaying structures that are intermediate between the two ideal geometries. Hence, the angular structural parameter τ , which was first defined by Addison et al. can be applied to describe these kind of geometries. τ is calculated according to equation, $\tau = (\beta - \alpha)/60$ and angles are as indicated in figure 3.18. For a perfect square pyramidal geometry $\tau = 0$ and for a trigonal bipyramidal geometry $\tau = 1$.²²⁰

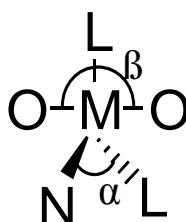


Figure 3.18: Addison's model to calculate τ values²²⁰

The two crystallographically independent complexes present in the unit cell of [Cu(II)(L9)(H₂O)₂] exhibit different τ values. For complex 1, the basal angles N(4)–Cu–O(1) and N(1)–Cu–Cl(1) are 157.41° and 166.42°, respectively, giving a τ value of 0.04, whereas for complex 2, this value is 0.2. Hence, the geometry around the Cu(II) centres of both the complexes of [Cu(II)(L9)(H₂O)₂] can be best described as slightly distorted square pyramidal. Other examples of two crystallographically independent Cu(II) complexes within the same unit cell exhibiting different τ values are known to exist in the literature.¹⁸⁴

As discussed in section 3.2, the corresponding ligand NaHL9 adopts *Z* conformation with a torsional angle of $2.06(2)^\circ$ involving the imine bond (C(1)-C(2)-N(1)-N(2)). However, in order to bind to the Cu(II) centre in a tridentate manner, the ligand changes conformation from *Z* to *E*, which is indicated from the torsional angles of $177.69(19)$ and $177.85(19)^\circ$ ¹⁴⁵ for the two complexes, respectively. It can be noted that the torsional angles are similar to that of the protonated ligand H₂L20. Moreover, the two chelating rings consisting of O(1)-C(1)-C(2)-N(1)-Cu and N(1)-N(2)-C(3)-O(3)-Cu are nearly coplanar with a interplanar angle of 3.48 and 3.77° for the two complex, respectively.

3.5.1.2 [Cu(II)(L11)(H₂O)₂].H₂O

Similar characteristic features were observed for [Cu(II)(L11)(H₂O)₂].H₂O as can be seen from the ORTEP plot (figure 3.19). The complex also crystallises in the triclinic space group P-1.

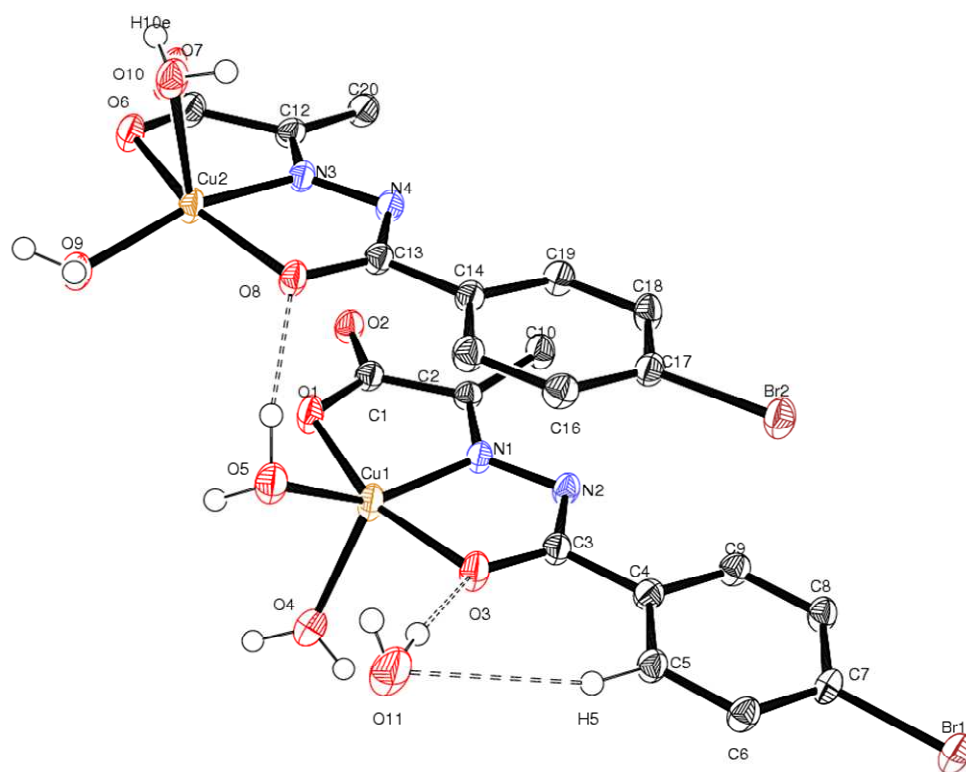


Figure 3.19: ORTEP plot (50% probability ellipsoids) of the molecular structure of [Cu(II)(L11)(H₂O)₂].H₂O. Hydrogen atoms apart from water molecules and H5 are omitted for clarity

3.5.1.3 Comparing [Cu(II)(L9)(H₂O)₂] and [Cu(II)(L11)(H₂O)₂].H₂O

Although no intramolecular hydrogen bonding was observed for [Cu(II)(L9)(H₂O)₂] and [Cu(II)(L11)(H₂O)₂].H₂O, the coordinated aqua ligands were involved in intermolecular hydrogen bonding. In [Cu(II)(L11)(H₂O)₂].H₂O the water molecule in the equatorial position in complex 1, forms a hydrogen bond with carbonyl oxygen (O(5)-H---O(8)) with a bond distance of 2.805(3) Å. The apical water molecule is involved in hydrogen bonding with O(2) of the carboxylate group of the symmetry generated molecule.

Whilst the free ligand NaHL11 adopts a *Z* conformation with a torsional angle of 2.58(3)°, the coordinated ligand has an *E* conformation which is revealed from the torsional angles of 179.3(2) and 179.6(2)¹⁴⁵ for the two complexes, respectively. In addition, the two chelating rings in the corresponding complexes, consisting of O(1)-C(1)-C(2)-N(1)-N(2)-C(3)-O(3)-Cu are nearly planar with a interplanar angle of 4.51 and 2.61°. Selected bond lengths and bond angles for complex 1 and 2 of [Cu(II)(L9)(H₂O)₂] and [Cu(II)(L11)(H₂O)₂].H₂O are tabulated in table 3.5. The general schematic representation of Cu(II) square pyramidal complexes with atom numbering scheme displayed in figure 3.20. will be used throughout this chapter to represent square pyramidal Cu(II) complexes. In order to directly compare the bond lengths and bond angles of different copper complexes, the numbering system may not match with the atom numbers in the ORTEP plots.

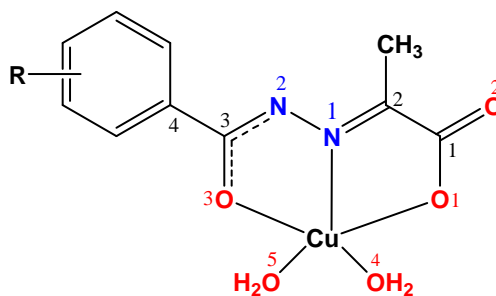


Figure 3.20: Schematic representation of square pyramidal Cu(II) complexes, showing the atom numbering scheme used in this chapter.

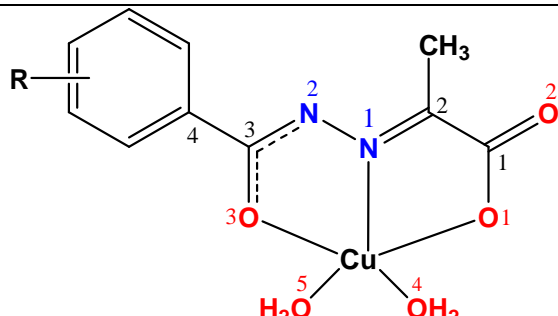
Table 3.5: Selected bond lengths (Å) of [Cu(II)(L9)(H₂O)₂] and [Cu(II)(L11)(H₂O)₂].H₂O

Bonds	[Cu(II)(L9)(H ₂ O) ₂]		[Cu(II)(L11)(H ₂ O) ₂].H ₂ O	
	Complex-1	Complex-2	Complex-1	Complex-2
C(1)-O(1)	1.291(3)	1.282(3)	1.297(3)	1.294(3)
C(1)-O(2)	1.226(3)	1.244(3)	1.2393(3)	1.248(3)
C(3)-O(3)	1.301(3)	1.295(3)	1.295(3)	1.302(3)
C(3)-N(2)	1.326(3)	1.328(3)	1.321(3)	1.332(3)
N(1)-N(2)	1.372(2)	1.371(2)	1.372(3)	1.375(3)
C(2)-N(1)	1.286(3)	1.289(3)	1.289(3)	1.290(3)
Cu-O(1)	1.9877(16)	1.9940(16)	2.0056(17)	2.0075(18)
Cu-O(3)	1.9873(16)	1.9939(16)	1.9941(18)	1.9945(17)
Cu-O(4)	1.958(2)	1.971(2)	2.001(2)	1.9379(18)
Cu-O(5)	2.218(2)	2.152(2)	2.147(2)	2.289(2)
Cu-N(1)	1.8988(19)	1.9065(19)	1.905(2)	1.902(3)

The bond lengths for crystallographically independent molecules are almost identical, except for the Cu-OH₂ distances. The equatorial bond distances involving the Cu(II) centre (Cu-O/N) are very similar; however the apical bond distances are significantly longer which is due to Jahn-Teller distortion, as expected for Cu(II) complexes.^{199,221} It is noteworthy that the C(3)-O(3) carbonyl bond distances for [Cu(II)(L9)(H₂O)₂] and [Cu(II)(L11)(H₂O)₂].H₂O range from 1.29-1.30 Å, whereas in the respective ligands the bond distances range from 1.20-1.23 Å. The expected lengthening of carbonyl bond distance in copper complexes indicates that the C(3)-O(3) bond changes from a double bond to a bond with more single bond character due to deprotonation at N(2). This clearly indicates that the ligand undergoes keto-enol tautomerisation in order to allow it to attain its dianionic form, making the overall

complex neutral. Selected bond angles, distortion angle and τ values are given in table 3.6.

Table 3.6: Selected bond angles ($^{\circ}$) and τ values for complexes 1 and 2 of $[\text{Cu}(\text{II})(\text{L9})(\text{H}_2\text{O})_2]$ and $[\text{Cu}(\text{II})(\text{L11})(\text{H}_2\text{O})_2]\cdot\text{H}_2\text{O}$



Bonds	$[\text{Cu}(\text{II})(\text{L9})(\text{H}_2\text{O})_2]$		$[\text{Cu}(\text{II})(\text{L11})(\text{H}_2\text{O})_2]\cdot\text{H}_2\text{O}$	
	Complex-1	Complex-2	Complex-1	Complex-2
O(1)-Cu-O(3)	161.11(7)	160.22(7)	160.38(7)	160.65(7)
N(1)-Cu-O(4)	156.67(9)	152.75(9)	147.52(9)	163.62(9)
O(4)-Cu-O(5)	93.73(9)	95.72(9)	96.26(10)	89.98(8)
N(2)-C(3)-O(3)	124.6(2)	124.1(2)	124.8(2)	124.4(2)
C(2)-C(1)-O(1)	114.82(19)	116.03(19)	115.7(2)	116.0(2)
N(2)-C(3)-C(4)	115.9(2)	116.4(2)	115.2(2)	116.1(2)
C(3)-N(2)-N(1)	107.91(18)	107.53(18)	108.12(19)	107.85(19)
N(1)-C(2)-C(1)	111.9(2)	111.5(2)	111.8(2)	111.4(2)
C(1)-C(2)-N(1)-N(2) (torsional angle)	177.69(19)	177.85(19)	179.3(2)	179.6(2)
τ	0.075	0.125	0.214	0.050

The dianionic nature of the ligand is also reflected in the carbonyl C(3)-O(3) and the carboxylate C(1)-O(1) bond lengths, as they have nearly similar bond distances in case of copper complexes. A similar effect was observed for the bond distance C(3)-N(2), where the bond length is shortened (1.32-1.33 Å) as compared to that of the free ligands (1.34-1.36 Å), indicating the delocalisation of π - electrons over the N(2)-C(3)-O(3) bonds. Additionally, the N(1)-N(2) bond lengths are also slightly shortened, whereas the imine bond C(2)-N(1) remains relatively unaffected. The τ value is calculated using the basal plane angles O1-Cu-O3 and N1-Cu-O4. Amongst the listed values, the ligand based bond angles are more or less similar for equivalent bonds of $[\text{Cu}(\text{II})(\text{L9})(\text{H}_2\text{O})_2]$ and $[\text{Cu}(\text{II})(\text{L11})(\text{H}_2\text{O})_2]$. The basal angles, N(1)-Cu-O(1) are different for the complexes, hence resulting in dissimilar τ values. Moreover, a

distortion of the square pyramidal geometry is indicated by the O4-Cu-O5 bond angle as for perfect square pyramidal geometry it should be 90° . The larger the τ value, the greater is the deviation from 90° .

The bond angles O1-C1-C2 and N2-C3-O3 suggest that the two 5-membered rings are not identical. It is interesting to note that in CuL9, the two crystallographically independent complexes lie nearly in the same plane as shown figure 3.21 a, whereas the two complexes in CuL11 lie in two different planes as shown in figure 3.21 b, with a distance of 4.875 Å between two Cu centres.

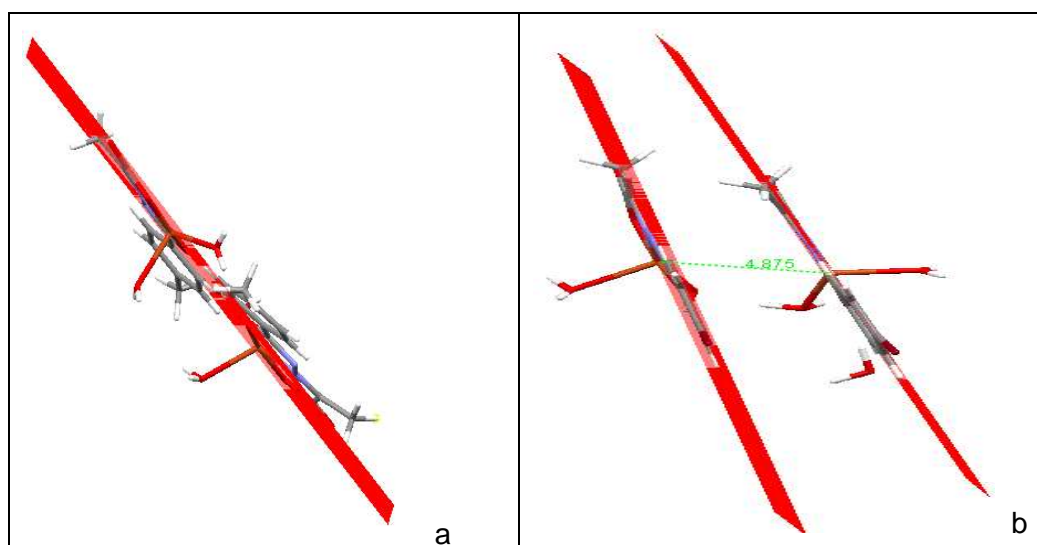


Figure 3.21: Planes passing through the copper complexes of two crystallographically independent molecules a) $[\text{Cu}(\text{II})(\text{L9})(\text{H}_2\text{O})_2]$, b) $[\text{Cu}(\text{II})(\text{L11})(\text{H}_2\text{O})_2] \cdot \text{H}_2\text{O}$

3.5.1.4 Comparing $[\text{Cu}(\text{II})(\text{L8})(\text{MeOH})_2]$, $[\text{Cu}(\text{II})(\text{L13})(\text{H}_2\text{O})(\text{MeOH})]$, $[\text{Cu}(\text{II})(\text{L17})(\text{H}_2\text{O})_2]$ and $[\text{Cu}(\text{II})(\text{L7})(\text{MeOH})_2]$

The Cu(II) complexes of other ligands, including L8^{2-} , L13^{2-} , L17^{2-} and L7^{2-} also crystallised with similar square pyramidal geometries, with the apical/equatorial positions occupied by H_2O and/or MeOH. The Cu(II) complex of L8^{2-} crystallises in the monoclinic space group $P2(1)/n$ with a molecular structure $[\text{Cu}(\text{II})(\text{L8})(\text{MeOH})_2]$, as indicated in the ORTEP plot (figure 3.22). The Cu(II) ion is coordinated in the plane by the tridentate ligand and a coordinated methanol molecule instead of water, as observed for $[\text{Cu}(\text{II})(\text{L9})(\text{H}_2\text{O})_2]$ and $[\text{Cu}(\text{II})(\text{L11})(\text{H}_2\text{O})_2]$. A weakly bound methanol completes the coordination sphere in the axial position, indicating appreciable Jahn-Teller distortion. The τ value of 0.05 indicates a slight distortion from the ideal square-pyramidal geometry.

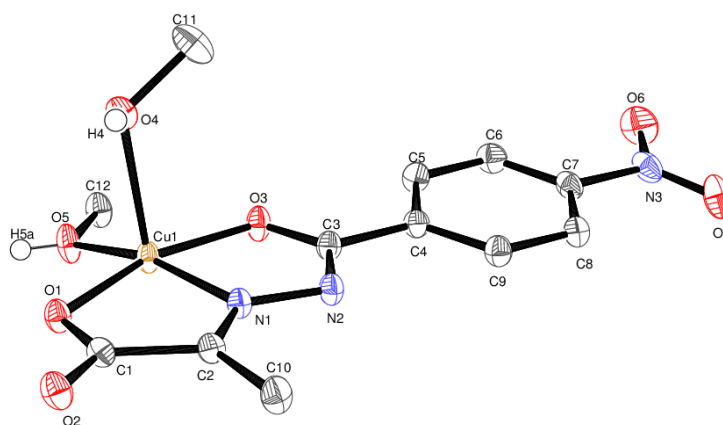


Figure 3.22: ORTEP plot (50% probability ellipsoids) of the molecular structure of $[\text{Cu}(\text{II})(\text{L8})(\text{MeOH})_2]$

The coordinated methanol molecules in $[\text{Cu}(\text{II})(\text{L8})(\text{MeOH})_2]$ are involved in intermolecular hydrogen bonding with adjacent symmetry-generated molecules, with the mercury plot of the crystal lattice showcasing hydrogen bonds shown in figure 3.23.

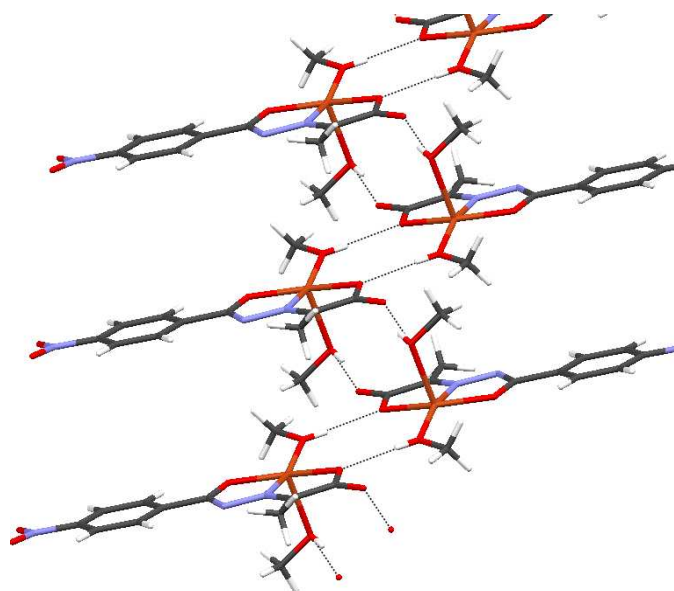


Figure 3.23: Crystal packing of $[\text{Cu}(\text{II})(\text{L8})(\text{MeOH})_2]$ showing intermolecular hydrogen bonds with the symmetry generated molecules. Colours of the atom: grey - C, blue - N, red - O, white - H, brown - Cu

The equatorial methanol molecule forms hydrogen bond with one of the symmetry generated carboxyl O(1) atom (O(5)-H---O(1)) with a bond distance of 2.7072(15) Å. The apical methanol is involved in hydrogen bonding with O(1) atom (O(4)-H---O(2)) of another symmetry generated molecule with a bond distance of 2.7085(15) Å.

The Cu(II) complex of L7²⁻ crystallises in the monoclinic space group P2₁/n with a molecular structure of [Cu(II)(L7)(MeOH)₂]. The ORTEP plot of the corresponding complex is shown figure 3.24. The copper complex shows similar characteristics to [Cu(II)(L8)(MeOH)₂].

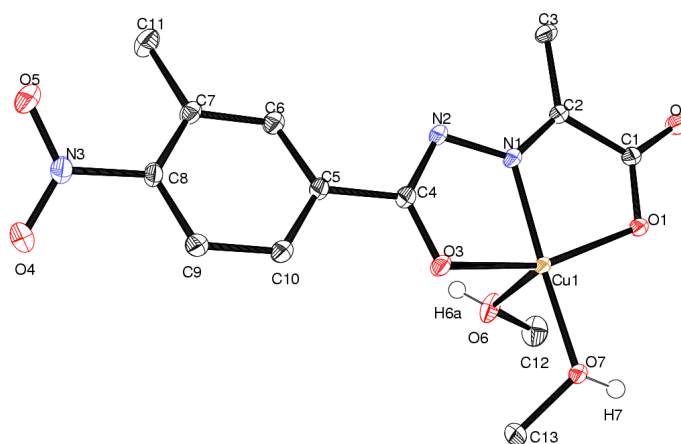


Figure 3.24: ORTEP plot (50% probability ellipsoids) of the molecular structure of [Cu(II)(L7)(MeOH)₂]

The Cu(II) complexes of L13²⁻ and L17²⁻ crystallise in the triclinic space group P-1 and the monoclinic space group P2₁/n with the molecular structures [Cu(II)(L13)(H₂O)(MeOH)] and [Cu(II)(L17)(H₂O)₂], respectively. The ORTEP plots of the corresponding Cu(II) complexes are shown in figures 3.25 and 3.26. The methoxy group in [Cu(II)(L13)(H₂O)(MeOH)] is disordered over two positions.

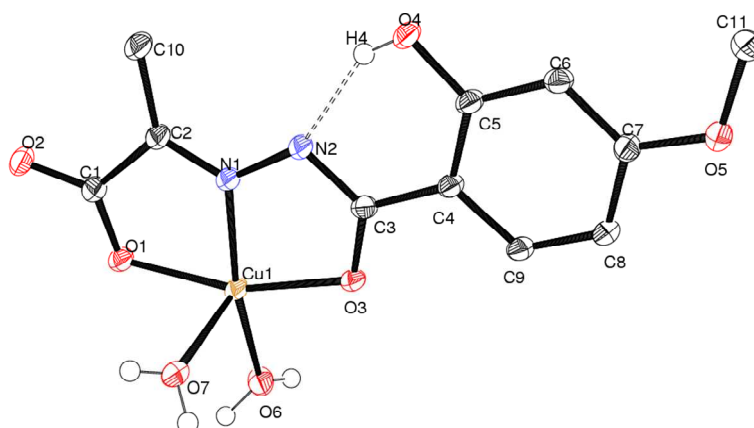


Figure 3.25: ORTEP plot (50% probability ellipsoids) of the molecular structure of [Cu(II)(L17)(H₂O)₂]

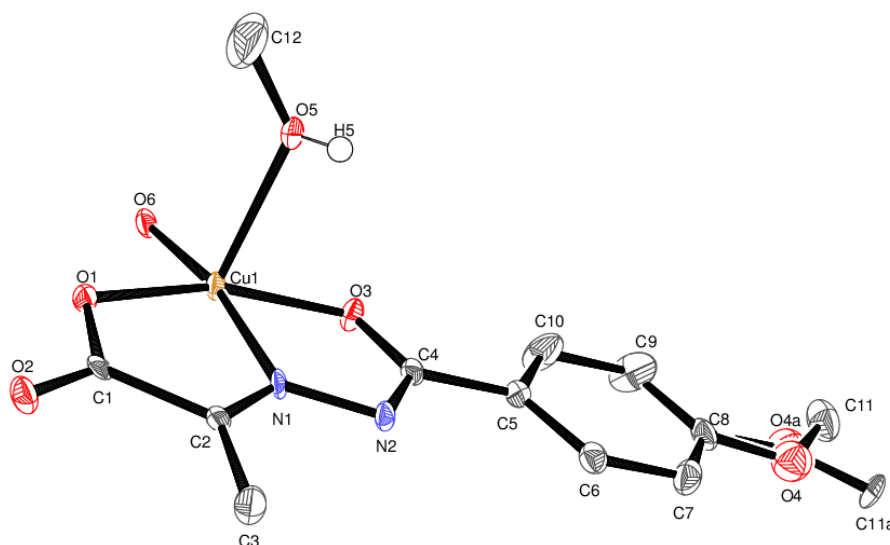


Figure 3.26: ORTEP plot (50% probability ellipsoids) of the molecular structure of [Cu(II)(L13)(H₂O)(MeOH)]

It is interesting to note that the methoxy group on the aromatic ring takes part in C-H--- π interactions and are displayed in figures 3.27 and 3.28 for [Cu(II)(L13)(H₂O)(MeOH)] and [Cu(II)(L17)(H₂O)₂], respectively. For both the methoxy containing complexes, the proton on OC(11)H₃ and the delocalised π electrons of the neighbouring aromatic ring give rise to C-H--- π interactions with distance ranging from 2.60-2.90 Å. The adjacent symmetry generated molecules stack almost coplanar to each other with an average distance of 3.67 Å and 3.91 Å for [Cu(II)(L13)(H₂O)(MeOH)] and [Cu(II)(L17)(H₂O)₂], consistent with C-H--- π interactions. The distance is measured

between the two oxygens (O(4)) of methoxy group for $[\text{Cu}(\text{II})(\text{L17})(\text{H}_2\text{O})_2]$, whereas for $[\text{Cu}(\text{II})(\text{L13})(\text{H}_2\text{O})_2]$ it is measured between oxygen (O(4)) of methoxy and C(3) of carbonyl carbon.

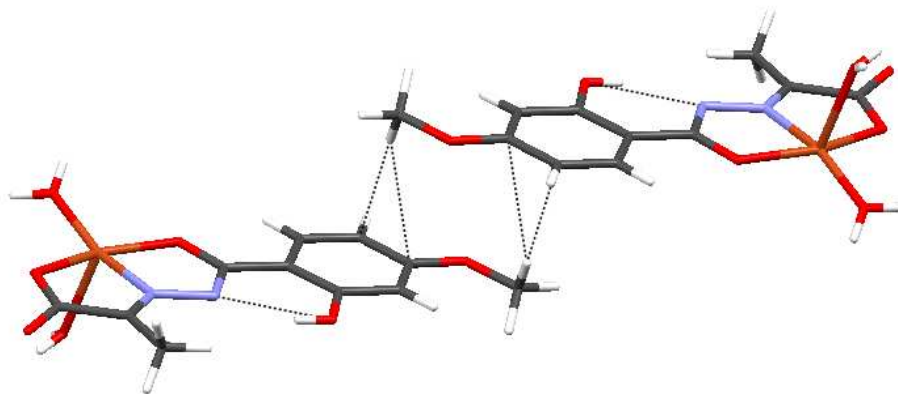


Figure 3.27: Crystal packing of $[\text{Cu}(\text{II})(\text{L17})(\text{H}_2\text{O})_2]$ showing C-H $\cdots\pi$ and intramolecular hydrogen bonding interactions (indicated with dotted lines). grey - C, blue - N, red - O, white - H, brown - Cu

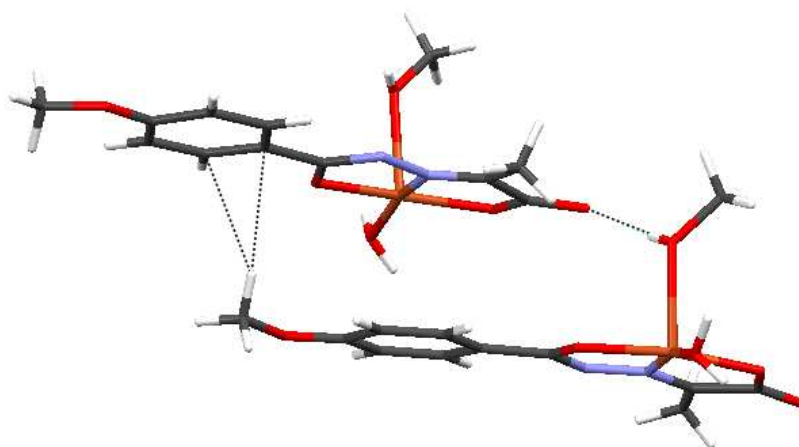


Figure 3.28: Crystal packing of $[\text{Cu}(\text{II})(\text{L13})(\text{H}_2\text{O})(\text{MeOH})]$ showing C-H $\cdots\pi$ and intramolecular hydrogen bonding interactions (indicated with dotted lines). grey - C, blue - N, red - O, white - H, brown - Cu

Furthermore, intermolecular hydrogen bonding is observed for the coordinated solvent molecules in both complexes. Due to the presence of the OH group in *ortho* position, $[\text{Cu}(\text{II})(\text{L17})(\text{H}_2\text{O})_2]$ exhibits intramolecular hydrogen bonding between N-H and the OH group present in *ortho*-position. The N-H \cdots O bond distance is 2.576(2) Å. Selected bond lengths and bond angles for the copper complexes $[\text{Cu}(\text{II})(\text{L8})(\text{MeOH})_2]$,

[Cu(II)(L13)(H₂O)(MeOH)], [Cu(II)(L17)(H₂O)₂] and [Cu(II)(L7)(MeOH)₂] are given in figure 3.7 and 3.8, respectively. The torsional angle including the imine bond, (C(1)-C(2)-N(1)-N(2)) as well as the τ value are provided in the same table.

The listed bond lengths of all four copper complexes of equivalent bonds are similar to the monomeric copper complexes, [Cu(L9)(H₂O)₂] and [Cu(L11)(H₂O)₂].H₂O. This implies that the electron-withdrawing or electron-donating group on the aromatic ring has little or no effect on the listed bond lengths. As expected the equatorial coordinate bonds (Cu-N(1)/O(1)/O(3)/O(4)) are similar, whereas Jahn – Teller distortion affects the apical bond distance (Cu-O(5)), making it longer than the equatorial bonds. A change of the coordinating solvent molecule from aqua to methanol does not significantly affect the bond distances. This shows that the Cu(II) centre plays an important role in controlling the immediate bond lengths surrounding it.

Table 3.7: Selected bond lengths (Å) for [Cu(II)(L8)(MeOH)₂], [Cu(II)(L13)(H₂O)(MeOH)], [Cu(II)(L17)(H₂O)₂] and [Cu(II)(L7)(MeOH)₂]

Bonds	R			
	[Cu(L8)(MeOH) ₂]	[Cu(L7)(H ₂ O)(MeOH)]	[Cu(L13)(H ₂ O)(MeOH)]	[Cu(L17)(H ₂ O) ₂]
C(1)-O(1)	1.2970(17)	1.3008(17)	1.300(4)	1.289(2)
C(1)-O(2)	1.2322(17)	1.2296(18)	1.230(4)	1.242(2)
C(3)-O(3)	1.2862(17)	1.2896(18)	1.277(4)	1.299(2)
C(3)-N(2)	1.3355(18)	1.3305(19)	1.343(4)	1.341(2)
N(1)-N(2)	1.3724(16)	1.3791(16)	1.381(3)	1.371(2)
C(2)-N(1)	1.2852(18)	1.2829(19)	1.278(4)	1.286(2)
Cu-O(1)	2.0033(10)	1.9988(12)	1.989(2)	2.0061(12)
Cu-O(3)	1.9688(11)	1.9725(11)	1.973(2)	1.9755(12)
Cu-O(4)	1.9285(11)	1.9506(11)	1.933(2)	1.9357(13)
Cu-O(5)	2.2824(11)	2.2138(14)	2.284(2)	2.2227(14)
Cu-N(1)	1.9128(12)	1.9130(13)	1.910(3)	1.9129(14)

Similarly, the bond angles of equivalent bonds are little affected by the R group on the aromatic ring. The τ values indicate a slight distortion from the perfect square pyramidal geometry. Although the differences in the values of the basal angle O(1)-Cu-O(3), are insignificant, the differences in the basal angle N(1)-Cu-O(4), contribute to the small differences in the τ value. The dissimilarity of the bond angles, comprising of two chelate rings, especially O(3)-Cu-N(1) and O(1)-Cu-N(1) signifies that the two 5-membered ring are not exactly the same. The distortion angle reveals that the ligand binds to the Cu(II) centre in a *E* confirmation with respect to the imine (C=N) bond, and are in agreement with the Cu(II) complexes of PVAHs described before.

Table 3.8: Selected bond angles ($^{\circ}$) for [Cu(II)(L8)(MeOH)₂], [Cu(II)(L13)(H₂O)(MeOH)], [Cu(II)(L17)(H₂O)₂] and [Cu(II)(L7)(MeOH)₂]

Bonds	R			
	[Cu(L8)(MeOH) ₂]	[Cu(L7)(H ₂ O)(MeOH)]	[Cu(L13)(H ₂ O)(MeOH)]	[Cu(L17)(H ₂ O) ₂]
O(1)-Cu-O(3)	161.64(4)	160.24(5)	161.10(9)	161.06(5)
N(1)-Cu-O(4)	164.51(5)	171.44(5)	166.59(11)	166.52(6)
O(4)-Cu-O(5)	96.62(5)	90.04(5)	98.63(10)	93.16(6)
O(3)-Cu-N(1)	80.06(5)	79.88(5)	79.58(10)	79.99(5)
O(1)-Cu-N(1)	81.87(5)	82.12(5)	82.12(9)	81.35(6)
N(2)-C(3)-O(3)	125.75(13)	125.69(13)	124.1(3)	122.78(15)
C(2)-C(1)-O(1)	116.51(12)	116.24(12)	116.0(3)	116.34(14)
C(3)-N(2)-N(1)	106.74(11)	106.71(12)	107.4(2)	109.02(14)
N(1)-C(2)-C(1)	111.65(12)	111.74(13)	111.6(3)	111.23(14)
C(1)-C(2)-N(1)-N(2) (torsional angle)	179.43(12)	177.71(12)	179.6(2)	179.36(14)
τ	0.05	0.18	0.09	0.09

3.5.2 The dimeric Cu(II) square pyramidal complex $[\text{Cu}(\text{II})_2(\text{HL9})_2\text{Cl}_2]$

Interestingly, the Cu(II) complex of ligand L9 also crystallises as a dimer with molecular structure $[\text{Cu}(\text{II})_2(\text{HL9})_2\text{Cl}_2]$ in monoclinic space group $P2(1)/n$. The ORTEP plot is shown in figure 3.28. The asymmetric unit contains one half of the dimeric molecule and the other half of the complex is generated by a centre of inversion. The ligand binds to the Cu centre in a tridentate manner as described for the monomeric $[\text{Cu}(\text{II})\text{L9}(\text{H}_2\text{O})_2]$ complex, whereas the other two coordination sites of the square pyramidal complex are occupied by bridging chloride ions. The τ value of 0.18 indicates distortion from the perfect square pyramidal geometry. However, the ligand coordinates in its monoanionic form, contrary to the dianionic coordination mode observed in the monomeric square pyramidal Cu(II) complexes. This is evident from the fact that N(2) remains protonated allowing the overall copper complex to remain neutral.

Moreover, the carbonyl C(3)-O(3) has more of a double bond character as the bond distance is 1.254(2) Å as compared to the $[\text{Cu}(\text{II})\text{L9}(\text{H}_2\text{O})_2]$ complex (1.301(3) Å), which suggests that O(3) is neutral when coordinated to the Cu centre. Due to Jahn-Teller distortion, the apical Cu-Cl bond distance is larger than the basal Cu-Cl distance. The intramolecular Cu-Cu bond distance is 3.332 Å, typical of chloride-bridged dimeric copper complexes, but reported values vary slightly depending on the ligand system.²²²⁻²²³

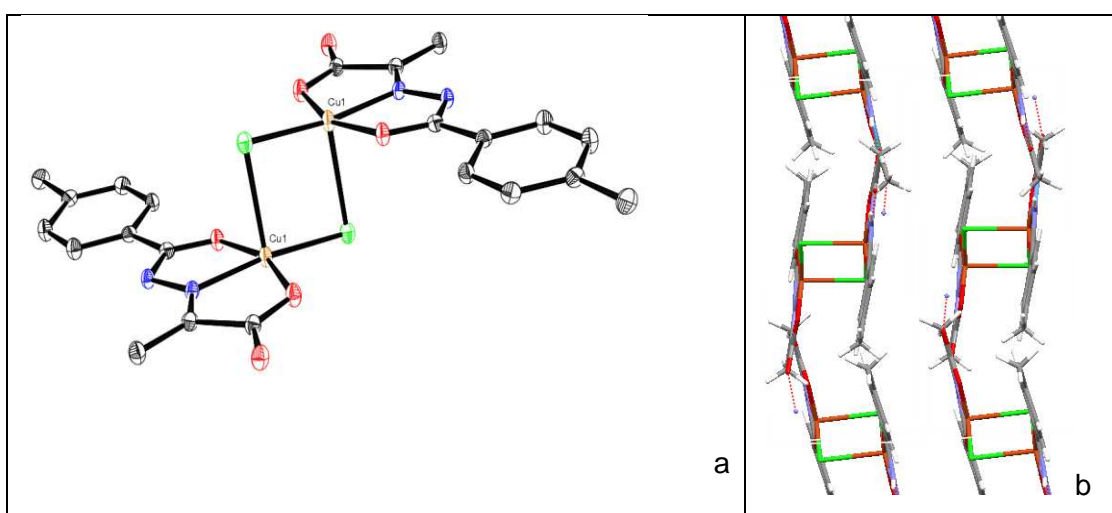
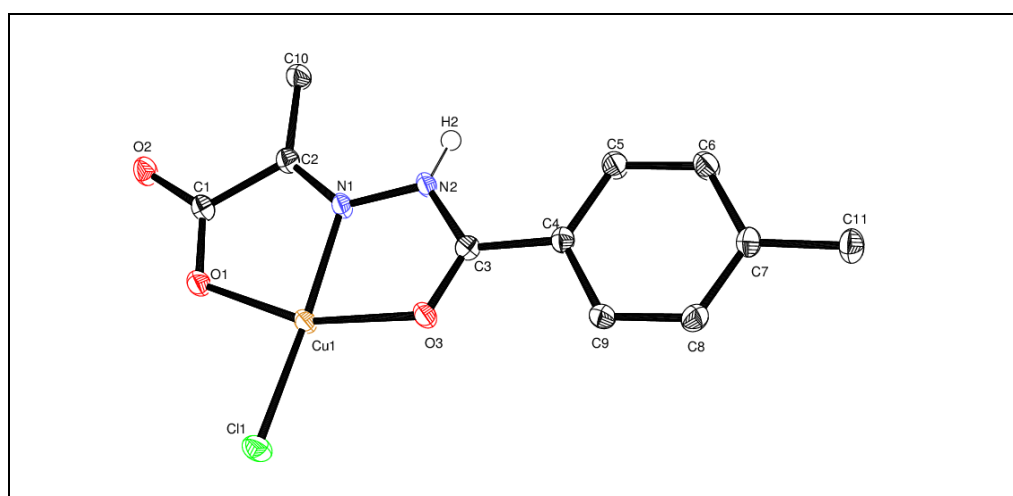


Figure 3.29: a) ORTEP plot and b) crystal packing diagram of $[\text{Cu}(\text{II})_2(\text{HL9})_2\text{Cl}_2]$

Furthermore, the crystal lattice of the complex displays a two dimensional array of a ladder-like zig-zag structure, as shown in figure 3.15 b, where the Cu_2Cl_2 core is

planar. In addition, Cu_2Cl_2 is almost perpendicular to the two basal 5-membered ring with a interplanar angle of 88.40° . Each unit of the complex forms an intermolecular hydrogen bond involving the proton on N2, and O(2) of the other symmetry-generated copper complex unit. The distance observed for N(2)-H---O(2) is 2.819(2) Å. Selected bond lengths and bond angles are given in Table 3.9 and are in agreement with the literature values.²²³⁻²²⁴ The τ value calculated using basal angles O(1)-Cu-O(3) and N(1)-Cu-Cl(1) is equal to 0.18 and indicates distortion of square pyramidal geometry, similarly observed for the monomeric Cu(II) square pyramidal complexes of PVAHs.

Table 3.9: Selected bond lengths (Å) and bond angles ($^\circ$) of $[\text{Cu}(\text{II})_2(\text{HL9})_2\text{Cl}_2]$



Bonds	Å	Bond angles	$^\circ$
C(1)-O(1)	1.274(2)	O(1)-Cu-O(3)	159.50(6)
C(1)-O(2)	1.239(2)	N(1)-Cu- Cl(1)	170.55(5)
C(3)-O(3)	1.254(2)	Cl(1)-Cu- Cl(1)#1	94.718(18)
C(3)-N(2)	1.368(2)	N(2)-C(3)-O(3)	119.53(17)
N(1)-N(2)	1.377(2)	C(2)-C(1)-O(1)	116.78(16)
C(2)-N(1)	1.281(2)	N(2)-C(3)-C(4)	121.31(16)
Cu(1)-O(1)	1.9562(14)	C(3)-N(2)-N(1)	111.96(15)
Cu(1)-O(3)	1.9967(13)	N(1)-C(2)-C(1)	110.17(16)
Cu(1)-Cl(1)	2.2198(5)	O(1)-C(1)-C(2)	116.78(16)
Cu(1)-Cl(1)#1	2.6737(6)	Cu(1)-Cl(1)-Cu(1) #1	85.282(18)
Cu(1)-N(1)	1.9545(16)	C(1)-C(2)-N(1)-N(2)	179.42(17)
N(2)-H	0.87(2)	τ	0.18

Symmetry transformations used to generate equivalent atoms: #1 -x+2,-y+1,-z+1

The apical bond distance, Cu(1)-Cl(1)#1 (2.6737(6) Å) is quite long as compared to other Cu(II) complexes of square pyramidal complexes of PVAH. The

bond length is too long to be considered as a true coordinate bond. Hence, the monomeric unit containing one Cu(II) centre of $[\text{Cu}_2(\text{HL9})_2\text{Cl}_2]$ (structure shown in table 3.9) can be best described as pseudo square pyramidal complex or can be alternatively designated as square planar complex, if the apical coordinate bond is not taken into consideration.

3.5.3 Cu(II) octahedral complex of PVAH

Interestingly, the Cu(II) complexes of L15^{2-} crystallise with octahedral geometry, having the molecular formulae $[\text{Cu}(\text{HL15})_2]$ and $\text{Na}[\text{Cu}(\text{HL15})(\text{L15})]$. The copper complexes crystallise in the triclinic space group P-1 with two crystallographically independent molecules present in the unit cell. As indicated in the ORTEP plot (figure 3.30), each ligand is coordinated as a tridentate ONO ligand around the Cu(II) centre, giving rise to octahedral geometry. The ligands coordinate meridionally because of the planarity of the conjugated hydrazone ligand system.²²⁵⁻²²⁶

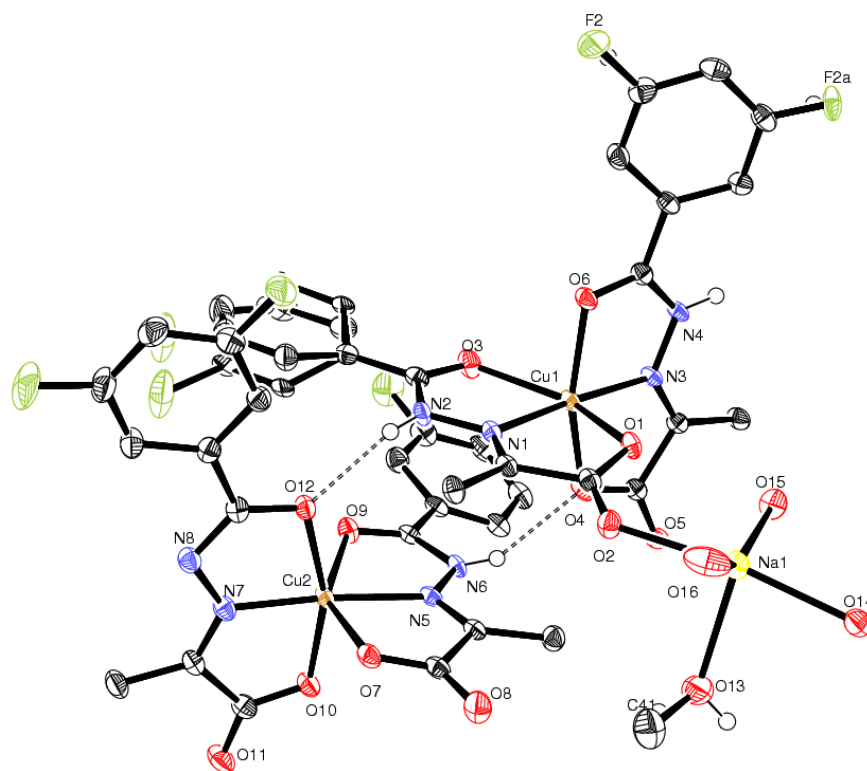


Figure 3.30: Ortep plot of the molecular structure $[\text{Cu}(\text{HL15})_2]\text{Na}[\text{Cu}(\text{HL15})(\text{L15})]$

The two crystallographically independent molecules differ due to their charge on the overall complex. One of the copper complexes is neutral, whereas the other

complex carries one negative charge overall, making it anionic. This is evident due to the fact that in one of the ligands the proton on N-H is lost upon coordination, making it dianionic, whereas the other ligands attain monoanionic nature by retaining the N-H proton. Hence, in order to balance the negative charge, a Na^+ cation is present in the crystal lattice.

The sodium counterion exhibits octahedral geometry, as observed for NaHL9 and NaHL11, although the coordination around the Na ion is slightly different for $[\text{Cu}(\text{HL15})_2] \text{Na}[\text{Cu}(\text{HL15})(\text{L15})]$ as can be seen in figure 3.31. In the dimeric complex, the two sodium cations are bridged by two water molecules, whereas the rest of the coordinating sites are occupied by two more water molecules, neutral methanol and O(2) of the neutral $[\text{Cu}(\text{HL15})_2]$ complex. The other sodium cation is associated with the symmetry-generated neutral complex in a similar fashion. While Na^+ is directly bonded to O(2), the coordinated water molecules on the Na^+ atom are involved in hydrogen bonding with the carboxylate O(1) atom. At the same time, intermolecular hydrogen bonding is also observed between N-H of one complex and carbonyl O(3) atom of other crystallographically independent molecule. The N(2)-H-----O(3) bond distance is 2.884(3) Å. One of the phenyl rings is disordered over two positions and also the F atom is disordered over two *meta*-positions.

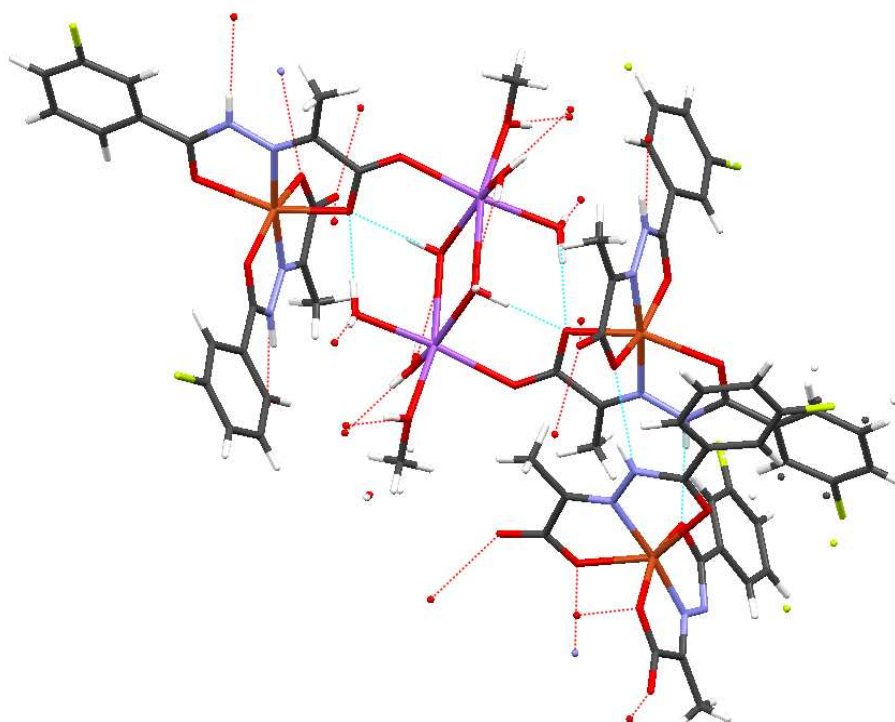


Figure 3.31: Mercury plot of $[\text{Cu}(\text{HL15})_2] \text{Na}[\text{Cu}(\text{HL15})(\text{L15})]$ showing the coordination around the sodium cation and intermolecular hydrogen bonding

The coordination plane around the Cu(II)-centre which includes Cu-C(1)-C(2)-O(1)-N(1)-N(2)-C(3)-O(3) is essentially planar. On the other hand, the deviation of the mean plane of the 5-membered ring and the aromatic ring is considerably larger. The deviations for the anionic complex are 8.93° and 20.77° for each ligand, whereas for the neutral complex the deviation is 11.73° and 27.68° Å. The loss of planarity of the ligand may be due to the steric repulsion caused by two ligands when coordinating to the copper centre, since in the square pyramidal complex the ligand remains almost planar. The distortion angle suggests *E* conformation for both ligands with respect to the imine bond and the values fall in the range 176.0 – 180.0° and are similar to the square pyramidal complexes. The bond angles of 173° consisting of the basal angle, N(1)-Cu-N(3) for both the complexes suggests a distortion from idealised octahedral geometry as perfect octahedral geometry requires this angle to be 180°. ²²⁷⁻²²⁸

In order to evaluate the differences in the geometric parameters of the two complexes, selected bond lengths and bond angles are given in table 3.10. Subsequently, these were then compared to a similar Cu(II) complex of 2-[2-(2-hydroxybenzoyl)hydrazone]propanoic acid synthesized by Feng Liu and group as shown in figure 3.32. ²²⁹

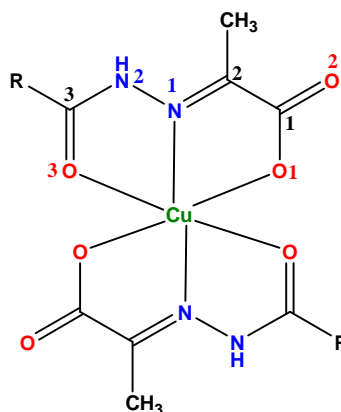


Figure 3.32: Numbering scheme for $[\text{Cu}(\text{HL15})_2]$ showing immediate bonds surrounding the Cu(II) centre, R= Ar-3-F, Feng Liu's copper complex R= Ar-2-OH²²⁹

Table 3.10: Selected bond lengths (Å) and bond angles (°) of neutral $[\text{Cu}(\text{HL15})_2]$ and anionic $\text{Na}[\text{Cu}(\text{HL15})(\text{L15})]$ in comparison with an example described in the literature²²⁹

Bonds	Complex 1 (neutral)		Complex 2 (anionic)		Lit ref ²²⁹	
	(HL ¹⁻)	(HL ²⁻)	(HL ¹⁻)	(L) ²⁻	(HL ¹⁻)	(HL ²⁻)
Cu-O(1)	2.1956(18)	2.0008(18)	2.2574 (18)	2.0059 (18)	2.047(2)	2.092(3)
Cu-O(3)	2.2820(19)	2.0277(18)	2.3696 (19)	2.0397 (18)	2.208(3)	2.281(3)
Cu-N(1)	2.013(2)	1.949(2)	2.015(2)	1.911(2)	1.942(3)	1.982(3)
C(3)-O(3)	1.232(3)	1.251(3)	1.227(3)	1.301(3)	1.246(4)	1.228(4)
C(1)-O(2)	1.225(3)	1.228(3)	1.225(3)	1.233(3)	1.279(4)	1.264(4)
C(3)-N(2)	1.372(3)	1.361(3)	1.371(3)	1.324(3)	1.352(4)	1.358 (14)
C(1)-O(1)	1.276(3)	1.284(3)	1.270(3)	1.290(3)	1.279(4)	1.264(4)
C(2)-N(1)	1.283(3)	1.278(3)	1.281(3)	1.281(3)	1.281(3)	1.282(4)
O(1)-Cu-N(1)	76.98(8)	80.65(8)	75.29(7)	81.83(8)	78.90 (11)	75.37 (10)
O(3)-Cu-N(1)	73.98(8)	79.17(8)	73.22(7)	78.87(8)	77.76 (11)	74.94 (10)
O(1)-Cu-O(3)	150.34(7)		147.99(6)		156.66(10)	
N(1) (L ¹⁻)-Cu-N(1) (L ²⁻)	173.68(9)		173.59(9)		175.97(12)	

The coordination characteristics of Feng Liu's copper complex are identical to the neutral complex of $[\text{Cu}(\text{HL15})_2\text{Cu}(\text{HL15})(\text{L15})]$.

The comparison of bond lengths is done in three ways, which are as follows

i. Comparison between the ligands on the same Cu(II) centre

The coordinate bonds especially Cu-O(1) and Cu-O(3) are significantly and Cu-N(2) moderately longer in one of the ligands, this may be accounted to the steric repulsion caused by two ligands in order to form octahedral environment around the metal centre. As a consequence, C(1)-O(1) and C(3)-O(3) show similar trend, although the differences are small. This may also be accounted to Jahn-Teller distortion of the axial ligands. Feng Liu's copper complex show similar behaviour, however the differences are not large. The reverse trend was noticed for the bond angles, O(1)-Cu-N(1) and O(3)-Cu-N(1), which signifies that ligand having greater coordinate bond lengths have shorter chelate bond angles comprising of the Cu(II) centre.

ii. Comparison between neutral and anionic complex

As a result of deprotonation of N(2) proton of one of the ligand, the C(3)-O(3) (1.301(3) bond distance is significantly greater than other ligand (1.227(3) Å), similarly observed for monomeric square pyramidal complex of pyruvate hydrazones. The bond distance has partial single bond character making it negatively charged, hence dianionic in nature.

iii. Comparison with the Feng Liu's Cu(II) complex.

Although most of the bond lengths and bond angles of equivalent bonds don't show significant differences, it is observed that the Cu-O(1), Cu-N(1) bond distances are slightly longer as compared to Feng Liu's complex. The complex also indicates that C(1)-O(2) has more single bond character when compared with the copper complexes of PVAHs.

3.6 Structural investigation of Cu(I) complexes of PVAHs

Cu(I) complexes of NaHL8 and NaHL9 were synthesized in order to investigate the coordination behaviour of PVAHs around the Cu(I) centre. As discussed in chapter-2, PPh_3 were introduced in order to stabilise the soft Cu(I) centre. As expected for Cu(I) complexes both the ligands form a tetrahedral environment around the copper centre.²³⁰

3.6.1 Structural aspects of $[\text{HL9}(\text{PPh}_3)_5]\text{PF}_6$ and $[\text{Cu}(\text{I})_2\text{HL8}(\text{PPh}_3)_5]\text{PF}_6$

Both the Cu(I) complexes crystallise as dimeric structures and the two crystal structures show a similar kind of environment around the Cu(I) centre. $[\text{Cu}(\text{I})_2\text{HL9}(\text{PPh}_3)_5]\text{PF}_6$ crystallises in a monoclinic space group $\text{P2}_1/\text{n}$, and the ORTEP plot is displayed in figure 3.33. Due to the rigidity of the PVAHs, HL8^- and HL9^- can only act as bidentate ligands, coordinating through O and N donor atoms to form a tetrahedral arrangement around the Cu(I) centre. The remaining two coordination sites are occupied by two PPh_3 ligands, similar to the structure observed for a related Cu(I) hydrazone complex synthesized by Krishnamoorthy and group¹⁷⁶. The O atom of the carboxylate group of the ligand binds to the other Cu(I) centre and the other three tetrahedral coordination sites are occupied by PPh_3 ligands. The overall positive charge of the complex is balanced by a PF_6^- anion.

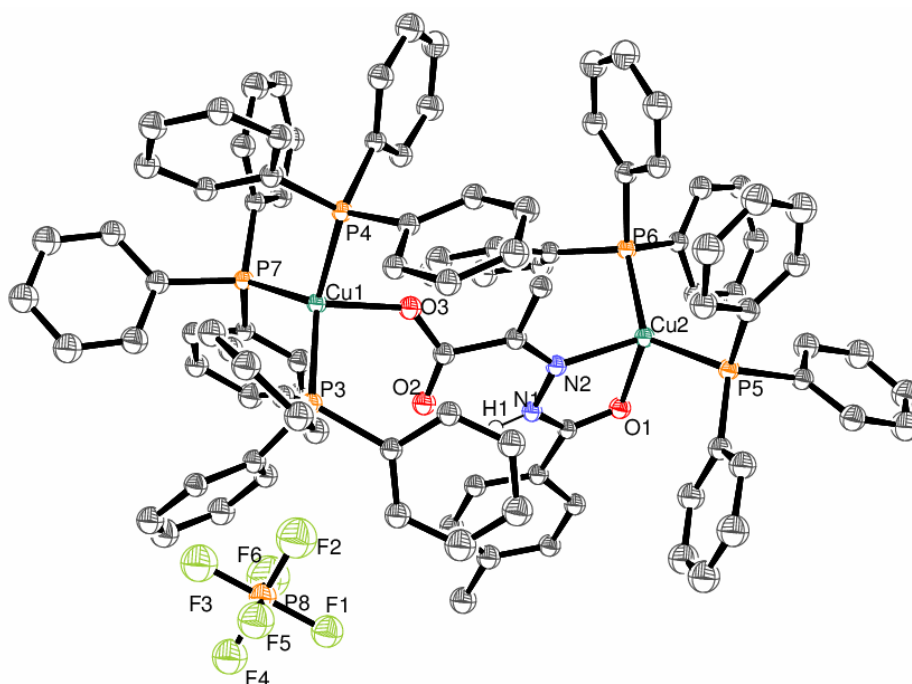


Figure 3.33: ORTEP plot (50% probability ellipsoids) of the molecular structure of $[\text{Cu}(\text{I})_2\text{HL9}(\text{PPh}_3)_5]\text{PF}_6$

As seen from the ORTEP plot, the hydrazide part of the pyruvate hydrazone binds to one of the Cu(I) centre, whereas the pyruvate moiety acts a bridge, connecting the other copper centre. Similar bridging by dicarboxylates between two Cu(I) centres has been investigated by Lang and group.¹⁷⁹ The complex $[\text{Cu}(\text{I})_2\text{HL8}(\text{PPh}_3)_5]\text{PF}_6$ crystallises in the monoclinic space group $\text{P}2_1/n$ with two crystallographically independent molecules in the same unit cell. The ORTEP plot of the corresponding complexes is shown in figure 3.34. It is important to note that the ligand prefers to remain in the *Z* confirmation, when coordinating to the Cu(I) centre which is revealed from the torsional angle $(\text{C}(1)-\text{C}(2)-\text{N}(1)-\text{N}(2))$. The torsional angles values are provided in table 3.11 and are similar to the sodiated PVAHs.

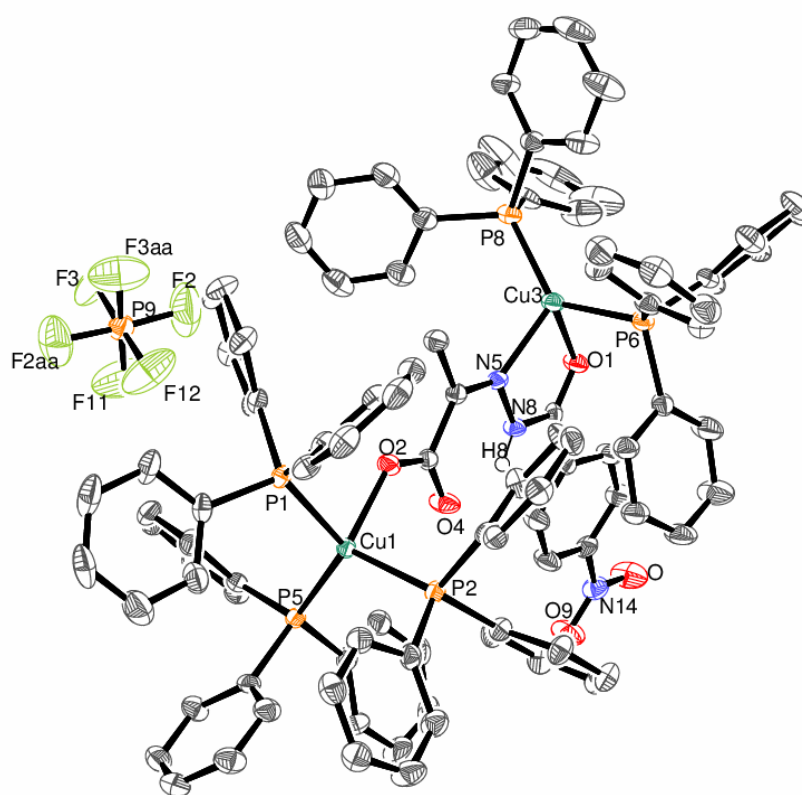


Figure 3.34: ORTEP plot (50% probability ellipsoids) of the molecular structure of $[\text{Cu}(\text{I})_2\text{HL8}(\text{PPh}_3)_5]\text{PF}_6$

3.6.3 Structural aspects of $[\text{Cu}(\text{I})_2\text{HL9}(\text{PPh}_3)_4]\text{PF}_6 \cdot 2\text{Et}_2\text{O} \cdot \text{H}_2\text{O}$

Interestingly, the Cu(I) complex of HL9⁻, which crystallised out of Et_2O has three coordinate geometry around the Cu(1) centre with one less PPh_3 group. It is surprising to notice that, changing the solvent system from polar MeOH to non-polar Et_2O can change the geometry around the copper centre. However, the coordination behaviour around the Cu(2) centre remains the same as can be seen from the ORTEP plot as

indicated in figure 3.35. The crystal structure crystallises in the triclinic space group P-1. Eventhough three-coordinate copper complexes are rare, a few examples of three-coordinate Cu(I) and Cu(II) complexes are known to exist in the literature.^{177,231-232} There is an increasing interest, towards making of low coordinate copper complexes, as they are known to exist in the biological systems.²³³⁻²³⁴ Moreover, the crystal structure of a linear, two- coordinate Cu(I) complex, is also reported in the literature²³⁵.

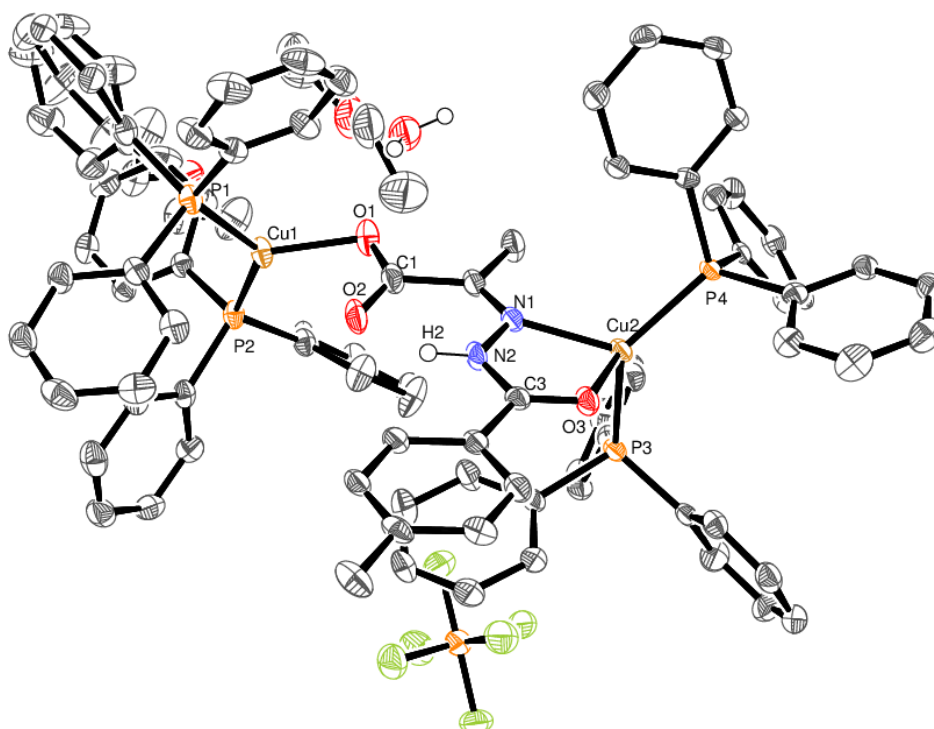


Figure 3.35: ORTEP plot (50% probability ellipsoids) of the molecular structure of $[\text{Cu}(\text{I})_2\text{HL9}(\text{PPh}_3)_4]\text{PF}_6 \cdot 2\text{Et}_2\text{O} \cdot \text{H}_2\text{O}$

The details of the bond lengths and angles of $[\text{Cu}(\text{I})_2\text{HL8}(\text{PPh}_3)_5]\text{PF}_6$, $[\text{Cu}(\text{I})_2\text{HL9}(\text{PPh}_3)_5]\text{PF}_6$ and $[\text{Cu}(\text{I})_2\text{HL9}(\text{PPh}_3)_4]\text{PF}_6 \cdot 2\text{Et}_2\text{O} \cdot \text{H}_2\text{O}$ are provided in tables 3.11 and 3.12, respectively and are consistent with the literature. The proton on the N atom of the hydrazide is not lost during coordination, which is also reflected in the bond length of the (C(3)-O(3) carbonyl group. In case of the Cu(I) complex, the carbonyl C(3)-O(3) bond length is more towards a double bond (1.23 - 1.24 Å), whereas in case of the monomeric square pyramidal Cu(II) complex, the same bond length is more towards a single bond (1.3 Å).²²⁹

3.6.3 Comparison of $[\text{Cu}(\text{I})_2\text{HL9}(\text{PPh}_3)_5]\text{PF}_6$, $[\text{Cu}(\text{I})_2\text{HL9}(\text{PPh}_3)_4]\text{PF}_6 \cdot 2\text{Et}_2\text{O} \cdot \text{H}_2\text{O}$ and $[\text{Cu}(\text{I})_2\text{HL8}(\text{PPh}_3)_5]\text{PF}_6$

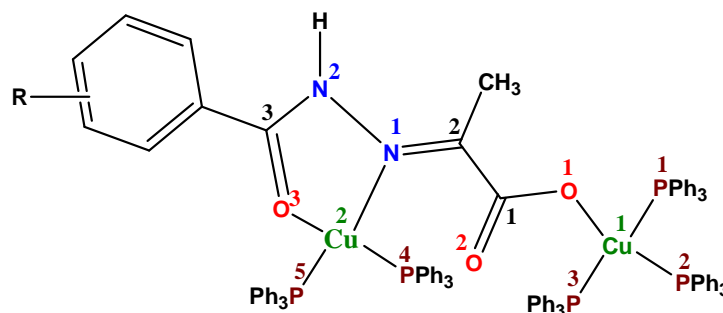


Figure 3.36: General structure of the Cu(I) complex showing the atom numbering scheme, R = 4-Me for $[\text{Cu}(\text{I})_2\text{HL9}(\text{PPh}_3)_5]\text{PF}_6$, R = 4NO₂ for $[\text{Cu}(\text{I})_2\text{HL8}(\text{PPh}_3)_5]\text{PF}_6$

Table 3.11: Selected bond lengths (Å) $[\text{Cu}(\text{I})_2\text{HL9}(\text{PPh}_3)_5]\text{PF}_6$, $[\text{Cu}(\text{I})_2\text{HL9}(\text{PPh}_3)_4]\text{PF}_6 \cdot 2\text{Et}_2\text{O} \cdot \text{H}_2\text{O}$, $[\text{Cu}(\text{I})_2\text{HL8}(\text{PPh}_3)_5]\text{PF}_6$

	$[\text{Cu}(\text{I})_2\text{HL9}(\text{PPh}_3)_5]\text{PF}_6$	$[\text{Cu}(\text{I})_2\text{HL9}(\text{PPh}_3)_4]\text{PF}_6 \cdot 2\text{Et}_2\text{O} \cdot \text{H}_2\text{O}$	$[\text{Cu}(\text{I})_2\text{HL8}(\text{PPh}_3)_5]\text{PF}_6$	
			Complex 1	Complex 2
C(1)-O(1)	1.256(4)	1.256(4)	1.252(4)	1.256(4)
C(1)-O(2)	1.250(4)	1.251(4)	1.257(4)	1.247(4)
C(3)-O(3)	1.238(4)	1.241(4)	1.238(5)	1.236(4)
C(3)-N(2)	1.339(4)	1.353(4)	1.341(5)	1.336(4)
N(1)-N(2)	1.385(3)	1.384(3)	1.377(4)	1.377(4)
C(2)-N(1)	1.293(4)	1.288(4)	1.295(5)	1.298(4)
N(2)-H(1)	0.83(4)	0.88(3)	0.87(4)	0.90(5)
Cu(2)-N(1)	2.052(3)	2.081(3)	2.092(3)	2.072(3)
Cu(2)-O(3)	2.175(2)	2.162(2)	2.142(3)	2.205(2)
Cu(1)-O(1)	2.024(2)	2.024(2)	2.131(2)	2.108(2)
Cu(1)-O(2)	3.530(2)	2.756(2)	3.424(2)	3.434(2)
Cu(2)-P(4)	2.2253(8)	2.2176(12)	2.2127(12)	2.2242(10)
Cu(2)-P(5)	2.2602(9)	2.2676(12)	2.2656(12)	2.2614(11)
Cu(1)-P(1)	2.2981(8)	2.2289(11)	2.3056(9)	2.3292(9)
Cu(1)-P(2)	2.3013(9)	2.2417(11)	2.3446(10)	2.3596(9)
Cu(1)-P(3)	2.3299(8)	-	2.3288(9)	2.3285(9)

The electron donating methyl group and the electron withdrawing nitro group fail to have any significant effect on the Cu(I) centre, similar to the observation made for the Cu(II) complexes. The small differences in bond lengths and bond angles may be due to packing effects in the crystal lattice. This is evident from the fact that, small differences are observed for the two crystallographically independent molecules of $[\text{Cu}(\text{I})_2\text{HL8}(\text{PPh}_3)_5]\text{PF}_6$ which crystallise in the same unit cell.

Within the Cu(I) complex, the Cu(1)-O(1) bond distance is slightly shorter than Cu(2)-O(3). Furthermore, the Cu-P bond distances on the Cu(2) centre are shorter than those coordinated to the Cu(1) centre except for $[\text{Cu}(\text{I})_2\text{HL9}(\text{PPh}_3)_4]\text{PF}_6 \cdot 2\text{Et}_2\text{O} \cdot \text{H}_2\text{O}$. This may be attributed to the steric repulsion caused due to three PPh_3 ligands on the Cu(1) centre, hence longer bond lengths. It is interesting to note that in case of the three-coordinate complex of $[\text{L9Cu}_2(\text{PPh}_3)_4]\text{PF}_6 \cdot 2\text{Et}_2\text{O} \cdot \text{H}_2\text{O}$ the Cu(1)-O(2) non bonding distance is significantly smaller than in the other Cu(I) complexes, which are provided in table 3.3. The bond distances taken from the mercury software indicate that there might be considerable interaction of O(2) with the Cu(I) centre. Therefore the Cu(I) centre in the corresponding complex can be described as pseudo tetrahedral complex as indicated figure 3.37.

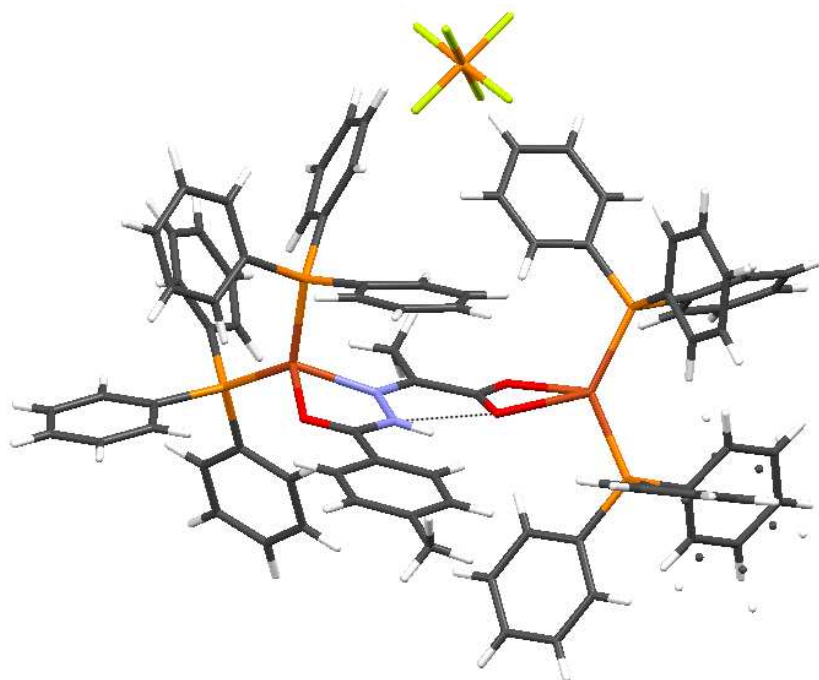


Figure 3.37: Mercury plot of $[\text{Cu}(\text{I})_2\text{HL9}(\text{PPh}_3)_5]\text{PF}_6$ illustrating the strongly asymmetric didentate carboxylate coordination to Cu(1) and intramolecular hydrogen bonding (indicated with dotted line). Colour of the atom: grey - C, white - H, red - O, blue - N, brown - Cu, yellow - P, green - F.

As the Cu(I) centre is coordinatively unsaturated, with one missing PPh₃ molecule with respect to other Cu(I) complexes, the other Cu-P coordinating bond distances are affected accordingly. This is reflected by the Cu(1)-P(2) and Cu(1)-P(2) bond distances, which have shorter bond lengths as compared to other Cu(I) complexes and also Cu(2)-P distances within the same molecule. Fujisawa and group observed a similar behaviour when they isolated a three-coordinate Cu(I) crystal structure bearing one PPh₃ along with other ligand containing pyrazole rings as shown in figure 3.38. In fact, the isolated Cu(I) complex exhibited an even shorter Cu-P bond distance of 2.1726 Å. This is due to the fact that it has only PPh₃ molecule, which results in less sterical hindrance and hence, a shorter bond length.

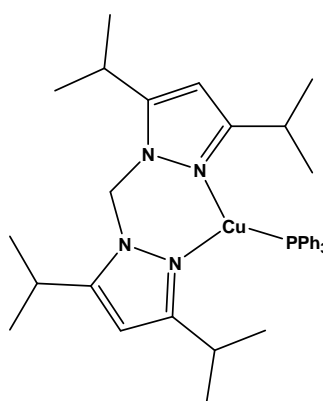


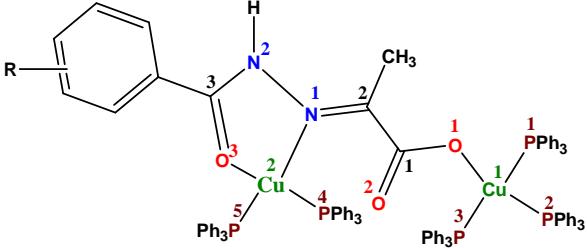
Figure 3.38 : Fujisawa three-coordinate Cu(I) complex¹⁷⁷

All the Cu(I) complexes of PVAHs described in this chapter participate in intramolecular hydrogen bonding which involve the N(2)-H and carboxylate O(2) atoms as can be seen from figure 3.37. The selected bond angles of all the three Cu(I) complexes are provided in table 3.12. The ligand-based angles of equivalent bonds remains unaffected, which signifies that the bond angles are not affected by electron withdrawing and donating groups or the Cu(I) coordination geometry. Although the crystal packing of the molecule might have little influence on values of ligand based bond angles, but it considerably affects the angles comprising of Cu(I) centre. Hence, two crystallographically independent molecules for [Cu(I)₂HL8(PPh₃)₅]PF₆ are observed, where the bond angles, especially N(1)-Cu(2)-P(5) show significant differences in complex 1 and 2, respectively, as can be seen from the values in table 3.12.

In addition, there is considerable deviation from regular tetrahedral angle 109°, which is reflected from the bond angles of O-Cu-P of both Cu(I) centres within the molecule²³⁶, hence the obtained Cu(I) complexes can be described as distorted

tetrahedral geometry. It can be noted that in the three-coordinate Cu(I) complex, $[\text{L9Cu}_2(\text{PPh}_3)_4]\text{PF}_6 \cdot 2\text{Et}_2\text{O} \cdot \text{H}_2\text{O}$, the Cu(1)-O(1)-C(1) bond angles is substantially smaller than other Cu(I) complexes. This can be explained on the basis that, the carboxylate O(2) donor atom is inclined towards Cu(1) atom in order to form pseudo tetrahedral geometry around the Cu(1) centre which makes the bond angle shorter.

Table 3.12: Selected bond angles ($^\circ$) for $[\text{Cu}(\text{I})_2\text{HL9}(\text{PPh}_3)_5]\text{PF}_6$, $[\text{Cu}(\text{I})_2\text{HL9}(\text{PPh}_3)_4]\text{PF}_6 \cdot 2\text{Et}_2\text{O} \cdot \text{H}_2\text{O}$ and $[\text{Cu}(\text{I})_2\text{HL8}(\text{PPh}_3)_5]\text{PF}_6$



	$[\text{Cu}(\text{I})_2\text{HL9}(\text{PPh}_3)_5]\text{PF}_6$	$[\text{Cu}(\text{I})_2\text{HL9}(\text{PPh}_3)_4]\text{PF}_6 \cdot 2\text{Et}_2\text{O} \cdot \text{H}_2\text{O}$	$[\text{Cu}(\text{I})_2\text{HL9}(\text{PPh}_3)_5]\text{PF}_6$	
			Complex 1	Complex 2
Cu(1)-O(1)-C(1)	133.7(2)	107.9(2)	129.4(2)	131.1(2)
O(1)-C(1)-O(2)	127.8(3)	125.1(3)	126.4(3)	126.3(3)
C(1)-C(2)-N(1)	124.3(3)	124.5(3)	124.4(4)	124.7(3)
C(2)-N(1)-N(2)	116.3(3)	118.4(3)	116.6(3)	117.1(3)
N(1)-N(2)-C(3)	118.3(3)	118.0(3)	118.2(3)	118.4(3)
N(2)-C(3)-O(3)	122.2(3)	121.6(3)	122.6(4)	122.5(3)
C(3)-O(3)-Cu(2)	110.39(19)	110.9(2)	109.8(3)	109.7(2)
O(3)-Cu(2)-N(1)	78.00(9)	77.61(9)	77.97(12)	76.94(10)
N(1)-Cu(2)-P(4)	104.65(7)	102.48(8)	100.41(10)	105.05(8)
N(1)-Cu(2)-P(5)	116.19(7)	121.88(8)	129.51(10)	119.38(8)
O3-Cu(2)-P(4)	109.98(6)	97.51(7)	100.14(10)	95.30(7)
O3-Cu(2)-P(5)	102.59(6)	117.63(7)	115.87(3)	112.97(7)
P(4)-Cu(2)-P(5)	131.65(3)	127.12(4)	122.11(5)	131.06(4)
O(1)-Cu(1)-P(1)	92.90(6)	118.68(8)	92.36(8)	87.77(7)
O(1)-Cu(1)-P(2)	100.77(7)	111.46(8)	104.80(7)	100.44(7)
O(1)-Cu(1)-P(3)	110.47(6)	-	113.83(7)	117.41(7)
C(1)-C(2)-N(1)-N(2) (torsional angle)	5.6(4)	2.3(5)	0.2(5)	1.6(5)

3.7 Structural diversity observed in copper complexes pyruvate hydrazones

As discussed in the introduction (section 3.1), copper complexes of hydrazones adopt a wide variety of structures. This is also observed in the crystal structures of Cu(II) and Cu(I) complexes of the PVAHs. However, Cu(II) complexes mostly adopt a mononuclear square pyramidal geometry in the solid state, but dinuclear square pyramidal complexes and complexes with octahedral geometry were also isolated. The reduction of Cu(II) to Cu(I), changes the coordination geometry to distorted tetrahedral around the Cu(I) centre, whereas three-coordinate Cu(I) complexes are also isolated.

In order to compare the different types of copper complexes obtained from ligand L9, selected bond length and bond angles of each representative geometry are tabulated in figure 3.13. The copper complexes include [Cu(II)(L9)(H₂O)₂] (monomeric square pyramidal), [Cu₂(HL9)₂Cl₂] (dimeric square pyramidal), [Cu(II)(HL15)₂] (octahedral) and [Cu(I)₂HL9(PPh₃)₅]PF₆ (tetrahedral). Although, all the copper complexes used for comparison are of same ligand except [Cu(II)(HL15)₂], as it is the only complex which crystallises out as an octahedral complex. Also, it is observed that the R-group does not have much influence on the bond lengths and bond angles in direct vicinity of the Cu centre, hence [Cu(II)(HL15)₂] can be used to compare the octahedral complex with the other copper geometries

As discussed in section 3.2, NaHL9 binds to two Na⁺ ions in a monodentate manner as shown 3.39 a and same ligand binds to Cu(II) in a tridentate fashion (3.39 b)

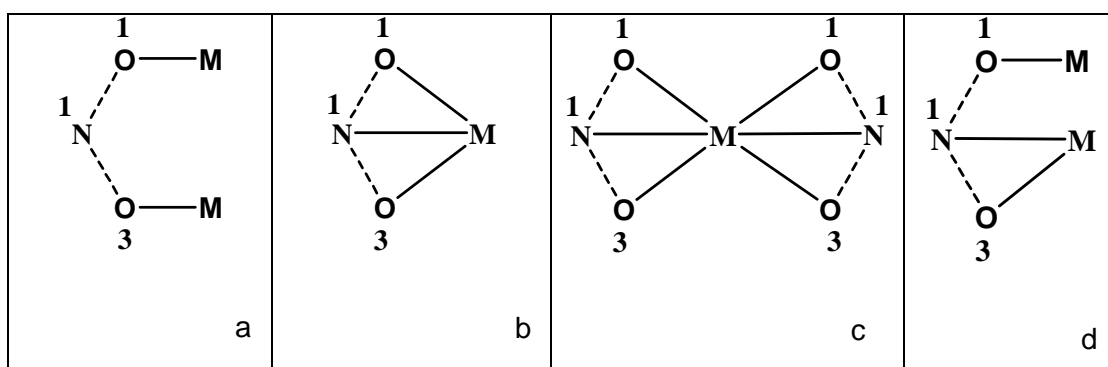


Figure 3.39: Schematic representation of different coordination modes of PVAH hydrazones

Furthermore, two ligands can bind to Cu(II) centre in a similar binding mode resulting in octahedral geometry (figure 3.39 c). However, in the Cu(I) complex the

binds to two different Cu(I) centres in a bidentate and monodentate manner, respectively (figure 3.39 d). Furthermore, the Cu(II) complex is stable with the O and N donor atoms, whereas the Cu(I) complex prefers soft P donors.

In square pyramidal complexes, the ligand can act as a dianionic donor, which involves deprotonation of N(2)-H in order to make the overall complex neutral. In the case of the dimeric square pyramidal copper complex, where the Cu(II) is coordinated to chloride ion, N(2)-H remains protonated which allows the ligand to remain in its monoanionic form. Similarly, the ligand remains in monoanionic form in the case of the neutral octahedral complex, [Cu(II)(HL15)₂]. In addition, the ligand behaves as a single negatively charged molecule when coordinated to Cu(I). This eventually affects the C(3)-O(3) bond length as indicated in table 3.13. In the ligand, dimeric, octahedral and tetrahedral complexes, this bond length ranges from 1.23 to 1.25 Å, which signifies more of a double bond character. Whereas in the case of the mononuclear square pyramidal complex, the bond length (1.295 (3)) indicates partial single bond character.

As indicated in table 3.13, the coordinate bond lengths around the Cu(I) centre (M-N, M-O) are significantly longer than those observed in the Cu(II) complexes. This may be attributed to the filled d shell of Cu(I) centre, resulting in weaker interactions than in d⁹ Cu(II) complex. As the electron density is contributed from donor atoms of both ligands, the coordinate bonds are not significantly longer in case of octahedral complex. C(1)-O(1) and C(1)-O(2) bond distances are similar in the Cu(I) complex as compared to the ligand and Cu(II) complexes, indicating the delocalisation of π - electrons over O(1)-C(1)-O(2) bond. Although, the metal centre does not have much appreciable contribution towards imine C(2)-N(1) bond distance.

The O(3)-Cu-N(1) bond angle which is part of one of the five-membered rings ranges from 78.0 – 81.6 °, indicating the rigidity of the ring. On the other hand, the X(1)-Cu-X(2) bond distances vary considerably and it defines the geometry of the copper complexes. The highest value observed is 159.64(7) for the octahedral complex, whereas the lowest observed is for the square pyramidal complex.

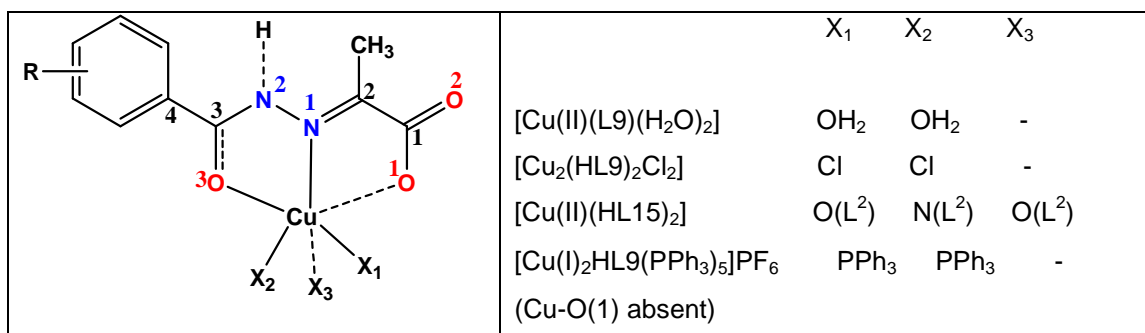


Figure 3.40: General structure showing numbering scheme for copper complex of PVAHs, dashed line indicates the presence or absence of bond depending on geometry

Table 3.13: Selected bond lengths (Å) and bond angles (°) of NaHL9, [Cu(II)(L9)(H₂O)₂], Cu(II)(HL9)₂Cl₂, Cu(II)(HL15)₂, [Cu(I)₂HL9(PPh₃)₅]PF₆

Bonds	NaHL9 (ligand)	Cu(II)L9(H ₂ O) ₂ (Monomeric Square pyramidal)	Cu(II)(HL9) ₂ Cl ₂ (Dimeric Pseudo-Square pyramidal)	Cu(II)(HL15) ₂ (Octahedral)		[Cu(I) ₂ HL9 (PPh ₃) ₅]PF ₆ (Tetrahedral)
				L9 ¹	L9 ²	
C(1)-O(1)	1.2743 (16)	1.282(3)	1.274(2)	1.276(3)	1.284(3)	1.256(4)
C(1)-O(2)	1.2380 (16)	1.244(3)	1.239(2)	1.225(3)	1.228(3)	1.250(4)
C(3)-O(3)	1.2330 (15)	1.295(3)	1.254(2)	1.232(3)	1.251(3)	1.238(4)
C(3)-N(2)	1.3522 (16)	1.328(3)	1.368(2)	1.372(3)	1.361(3)	1.339(4)
C(2)-N(1)	1.2897 (17)	1.289(3)	1.281(2)	1.283(3)	1.278(3)	1.293(4)
Cu-O(1)	-	1.9940(16)	1.9562(14)	2.1956(18)	-	2.024(2)
Cu-O(3)	-	1.9939(16)	1.9967(13)	2.2820(19)	-	2.175(2) (Cu(2))
Cu-X(1)	-	1.971(2)	2.2198(5)	-	2.0008(18)	2.2253(8)
Cu-X(2)	-	2.152(2)	2.6737(6)	-	2.0277(18)	2.2602(9)
Cu-N(1)		1.9065(19)	1.9545(16)	2.013(2)	1.949(2)	2.052(3)
O(3)-Cu- N(1)	-	81.66(7)	78.81(6)	73.98(8)	79.17(8)	78.00(9)
X(1)-Cu- X(2)	-	95.72(9)	94.718(18)	159.64(7)		131.65(3)
C(1)- C(2)- N(1)-N(2) (torsional angle)	2.06 (2)	177.69(19)	179.42(17)	176.6(2)	178.4(2)	5.6(4)

The torsional angle (C(1)-C(2)-N(1)-N(2)) for the Cu(II) complexes lie in the range 176.0 – 180.0°, revealing *E* conformation with respect to the imine (C=N) bond, irrespective of different geometries. In contrast, the Cu(I) complex [Cu(I)₂HL9(PPh₃)₅]PF₆ exhibits a torsional angle of 5.6(4) °, which is similar to the sodiated ligand NaHL9 (2.06(2) °) indicating *Z*-conformation.

3.8 Structural investigation of Zinc(II) complexes of PVAHs

The crystals of Zn(II) complexes of PVAHs suitable for X-ray crystallography were successfully isolated from the NMR solvent, DMSO-d₆. Unlike Cu(II) complexes of PVAHs, Zn(II) complexes failed to produce diffraction quality crystals from the reaction solvent MeOH, indicating the instability of the Zn(II) complex in the solution as compared to the Cu(II) complexes. This may be attributed to the acidic environment due to MeOH as compared to DMSO. Ligand binds to Zn(II) in 2:1 manner forming an octahedral complex, with the coordination around the zinc centre being similar to Cu(II) octahedral complex of HL15⁻.

3.8.1 Structural aspects of [Zn(II)(HL7)₂] · H₂O · DMSO, [Zn(II)(HL8)₂] and [Zn(II)(HL9)₂] · H₂O · CH₃OH

Zn(II) complexes of HL7⁻, HL8⁻ and HL9⁻ crystallise in the triclinic space group P-1. The ORTEP plots for [Zn(II)(HL7)₂] · H₂O · DMSO, [Zn(II)(HL8)₂] · H₂O and [Zn(II)(HL9)₂] · H₂O · CH₃OH are shown in figure 3.41a, 3.42 and 3.43, respectively. As indicated from the ORTEP plots of the corresponding Zn(II) complexes, N(2)-H remains protonated on both ligands. This allows the ligand to attain monoanionic form, hence forming an overall neutral Zn(II) complex. As expected, the two ligands are coordinated meridionally to the Zn(II)-centre.²²⁵⁻²²⁶ The crystal structures of the Zn(II) complexes of PVAHs mentioned in this chapter have meridional arrangement, unless otherwise mentioned. The structure of a representative example, [Zn(II)(HL7)₂] · H₂O · DMSO, is displayed in figure 3.41 b. Two perpendicular planes are pass through the chelate rings of the two ligands coordinated to the same Zn(II) centre. The interplanar angle of the two planes measures 81.45°.

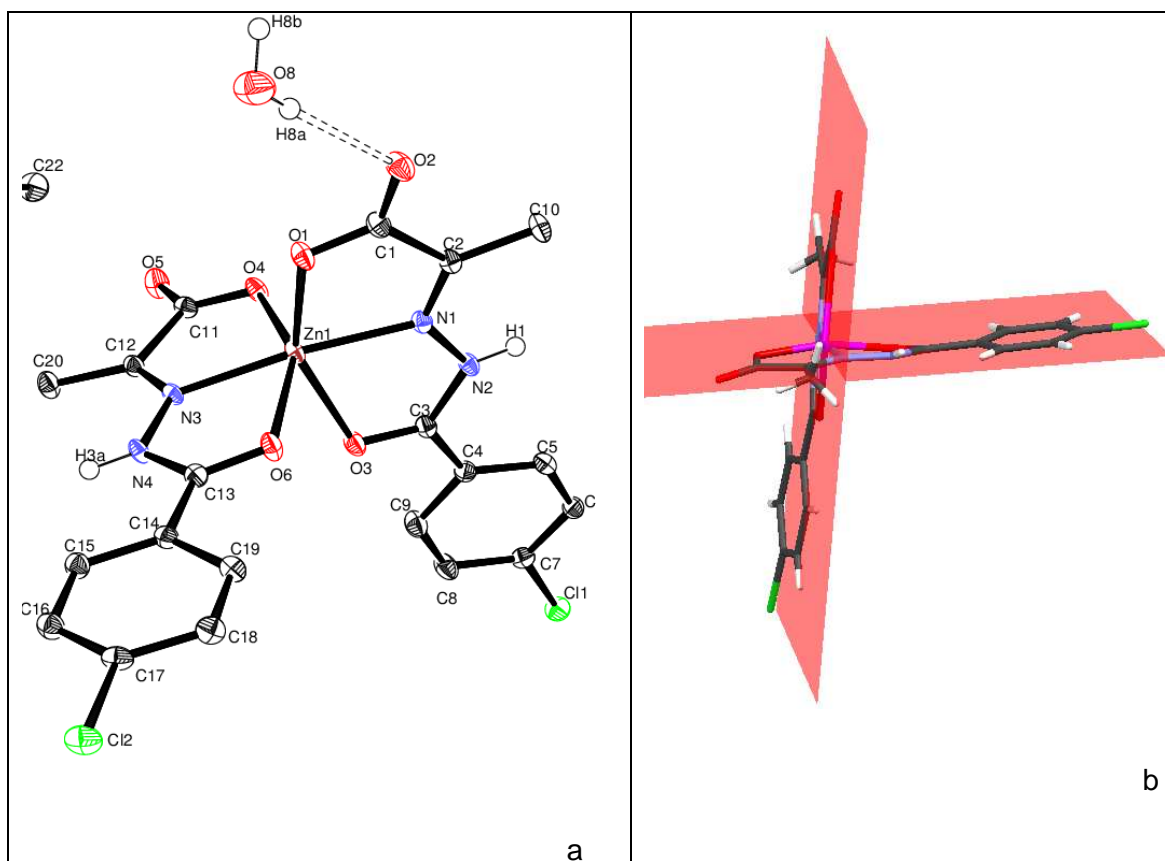


Figure 3.41: a) ORTEP plot (50% probability ellipsoids) of the molecular structure of *mer*-[Zn(II)(HL7)₂].H₂O.DMSO b) planes showing the meridional arrangement of the ligands around the Zn(II) centre

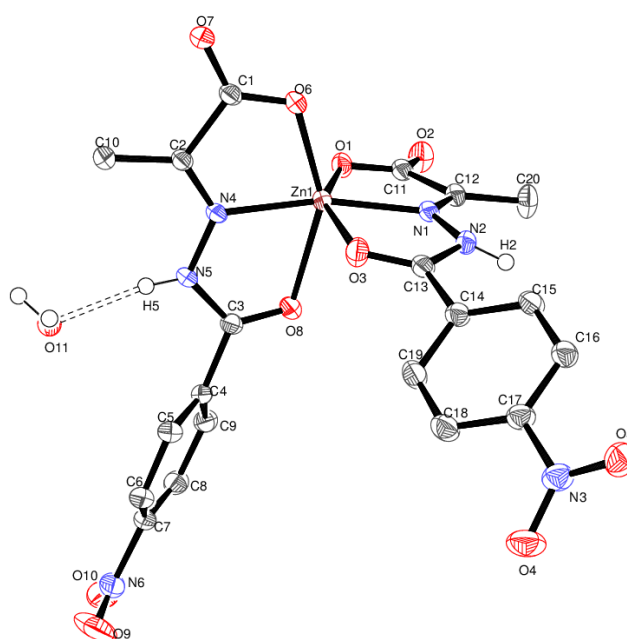


Figure 3.42: ORTEP plot (50% probability ellipsoids) of the molecular structure of *mer*-[Zn(II)(HL8)₂].H₂O

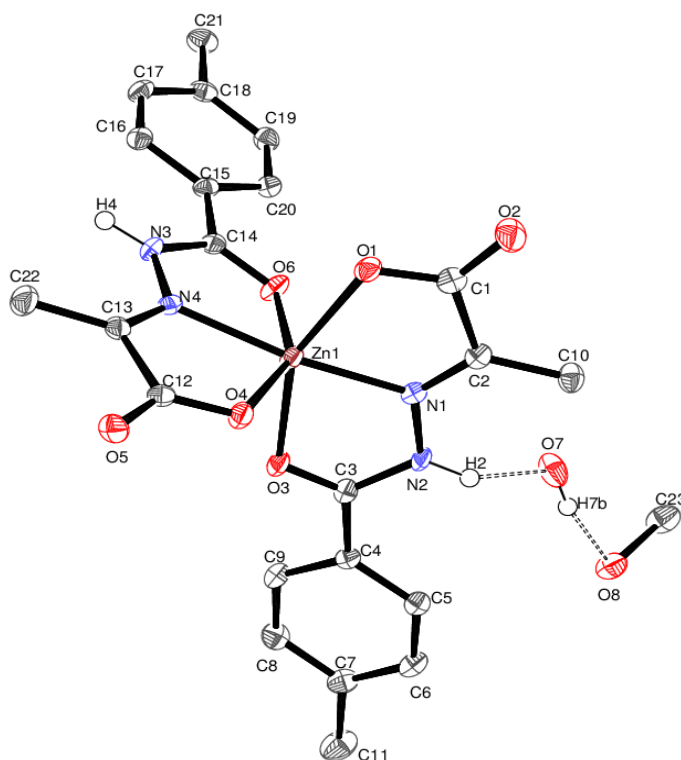


Figure 3.43: ORTEP plot (50% probability ellipsoids) of the molecular structure *mer*-[Zn(II)(HL9)₂].H₂O.CH₃OH

As indicated in the ORTEP plots, the zinc complexes crystallise with solvent molecules, such as H₂O, MeOH, and DMSO in the case of [Zn(II)(HL7)₂].H₂O.DMSO. Hydrogen bonding between the solvent molecules and the coordinated ligand atoms helps in stabilising the crystal lattice. In addition to the intermolecular hydrogen-bonding network, weak π interactions also occur in the crystal lattice with adjacent symmetry generated molecules. The Mercury plot of a representative example, [Zn(II)(HL7)₂].H₂O.DMSO is shown in figure 3.44. The π - π aromatic interactions, which are in the range of 3.31-3.5 Å allow the molecules to stack coplanar to each other. Similarly, weak electrostatic interactions between the electronegative chloride ion and electron deficient carbon atoms (C-Cl---C) C(1) (3.41 Å) and C(2) (3.37 Å) are also seen.

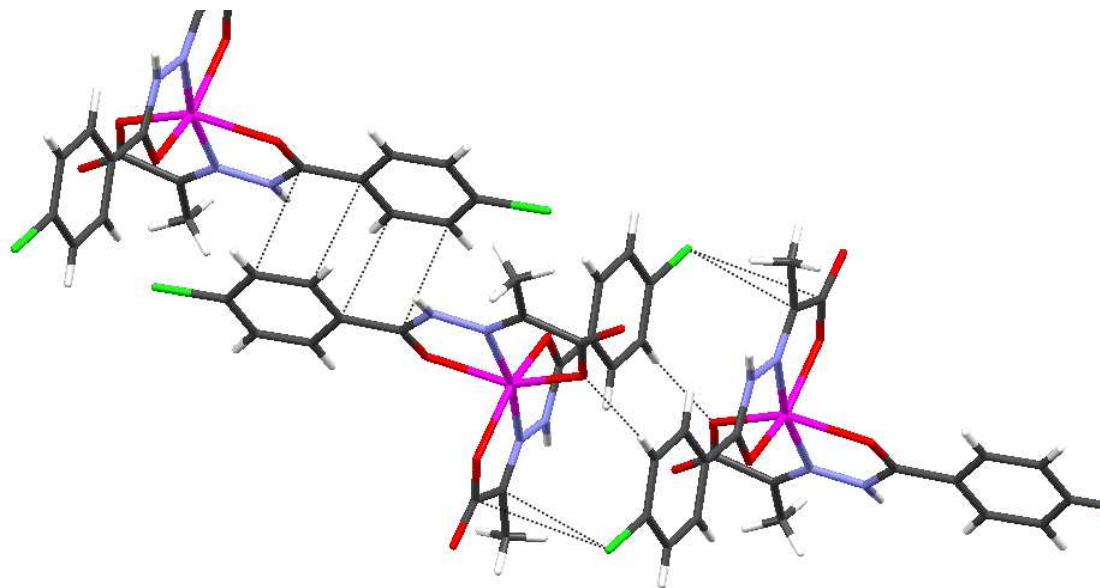


Figure 3.44: Mercury plot of *mer*- [Zn(II)(HL7)₂].H₂O.DMSO showing π interactions

3.8.2 Comparison of [Zn(II)(HL7)₂].H₂O.DMSO, [Zn(II)(HL8)₂].H₂O and [Zn(II)(HL9)₂].H₂O.CH₃OH

Selected bond lengths and bond angles of [Zn(II)(HL7)₂].H₂O.DMSO, [Zn(II)(HL8)₂].H₂O and [Zn(II)(HL9)₂].H₂O.CH₃OH are given in table 3.14. The bond lengths and bond angles are in agreement with the literature values.²³⁷ The tridentate ligand binds to the zinc centre resulting in a distorted octahedral geometry which is indicated by the equatorial bond angles. As indicated in the table, the equatorial angles for N1(HL¹)-Zn-N1(HL²) are not exactly 180° but lie in the range 168-170°, hence indicating distortion from perfect octahedral geometry.²³⁸ A general schematic representation of Zn(II) octahedral complex coordinating to the same ligands HL¹ and HL² along with the numbering scheme is shown in figure 3.45. In order to make the comparison easier, the numbering scheme may not be in accordance with the ORTEP plot numbering system.

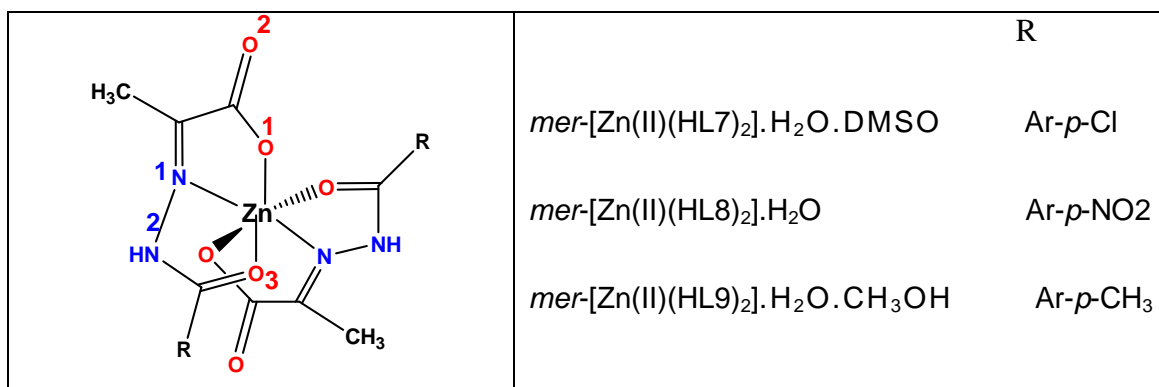


Figure 3.45: Numbering scheme for zinc complexes showing immediate bonds around the Zn(II) centre, *mer*-[Zn(II)(HL7)₂].H₂O.DMSO, *mer*-[Zn(II)(HL8)₂].H₂O, *mer*-[Zn(II)(HL9)₂].H₂O.CH₃OH

Table 3.14: Selected bond lengths (Å) and bond angles (°) of selected Zn(II) complexes of PVAHs

Bonds	<i>mer</i> -[Zn(II)(HL7) ₂].H ₂ O.DMSO		<i>mer</i> -[Zn(II)(HL8) ₂].H ₂ O		<i>mer</i> -[Zn(II)(HL9) ₂].H ₂ O.CH ₃ OH	
	(HL ¹) ⁻	(HL ²) ⁻	(HL ¹) ⁻	(HL ²) ⁻	(HL ¹) ⁻	(HL ²) ⁻
Zn-O(1)	2.1965 (14)	2.1588 (14)	2.0596 (12)	2.0502 (12)	2.091(2)	2.039(2)
Zn-O(3)	2.0238 (14)	2.1014 (14)	2.1919 (12)	2.2975 (12)	2.169(2)	2.138(2)
Zn-N(1)	2.0667(1 6)	2.0728 (16)	2.0635 (13)	2.0673 (13)	2.048(2)	2.079(3)
C(3)-O(3)	1.239(2)	1.227(2)	1.235(2)	1.232(2)	1.240(3)	1.242(3)
C(1)-O(2)	1.236(2)	1.238(2)	1.230(2)	1.238(2)	1.221(4)	1.249(4)
C(3)-N(2)	1.369(2)	1.371(3)	1.358(2)	1.359(2)	1.370(4)	1.372(4)
C(1)-O(1)	1.272(2)	1.280(2)	1.278(2)	1.269(2)	1.290(4)	1.264(3)
C(2)-N(1)	1.280(2)	1.279(2)	1.278(2)	1.282(2)	1.274(4)	1.273(4)
O(1)-Zn-N(1)	73.07(6)	74.04(6)	77.30(5)	77.68(5)	77.24(9)	77.60(8)
O(3)-Zn-N(1)	78.17(6)	76.59(6)	74.02(5)	72.56(5)	74.62(8)	73.70(9)
O(1)-Zn-O(3)	150.37 (5)	150.54 (5)	151.13(5)	150.05(5)	151.83 (8)	150.05()
C(1)-C(2)- N(1)-N(2) (torsional angle)	179.5(2)	179.8(2)	177.49 (13)	174.74 (13)	177.49	174.74
N(1) (L ¹)-Zn- N(1) (L ²)	168.87(6)		165.03(5)		169.75(9)	
O(1) (L ¹)-Zn- O(1) (L ²)	90.67(6)		95.75(5)		98.21(8)	
O(3)(L ¹)-Zn- O(3) (L ²)	92.40(6)		87.53(5)		91.38(8)	

The R group on the aromatic ring does not have a significant effect on bond distances and bond angles in direct vicinity of Zn(II) centre. The ligand based bond lengths are more or less similar for corresponding bonds of [Zn(II)(HL7)₂].H₂O.DMSO, [Zn(II)(HL8)₂].H₂O, [Zn(II)(HL9)₂].H₂O.CH₃OH. On comparison of the coordinate bond Zn-O(3) bond distances are appreciably longer than Zn-O(1) and Zn-N(1) bonds. The Zn-O and Zn-N bond distances are consistent with literature values. Although, some of the literature values slightly differ, depending on the surrounding ligand system.²³⁹⁻²⁴¹ While it was observed in Cu(II) octahedral complex that coordinate bonds (M-O/N) show significant difference between the two ligands binding to same Cu(II) centre, in the case of Zn(II) complexes the difference between the two ligands is quite small. Also, the equivalent bonds of the M-O/N distances in d¹⁰ Cu(I) and Zn(II) are slightly longer than in d⁹ Cu(II) complex. In [Zn(II)(HL7)₂].H₂O.DMSO, carboxylate O(2) atom of HL¹ forms intermolecular hydrogen bond with water. Whereas in [Zn(II)(HL8)₂].H₂O and [Zn(II)(HL9)₂].H₂O.CH₃OH the N-H proton (N(5), N(2)) hydrogen bonds with non coordinating water.

Each ligand bound to the Zn(II) centre loses its planarity in order to form stable zinc complexes, similar to observations made for octahedral complex of Cu(II) complex. The interplanar angle for each ligand in [Zn(II)(HL8)₂].H₂O is 5.07 and 10.29°, whereas for [Zn(II)(HL9)₂].H₂O.CH₃OH this deviations are 3.38 and 17.33°, respectively. The values are obtained by measuring the angles between two planes, passing through the aromatic ring, and the two pentacoordinate rings surrounding the metal centre. Furthermore, [Zn(II)(HL8)₂].H₂O exhibits the greatest mean plane of deviation with 40.34 and 56.12°, which is likely due to the bulkier NO₂ group. The torsional angle (C(1)-C(2)-N(1)-N(2)) indicates that both the ligands bind to the Zn(II) centre in *E* conformation, as observed for Cu(II) complexes and the values are not significantly different within the molecule.

3.8.3 Structural aspects of [Zn(II)(HL13)₂]

The crystal structure of Zn(II)(HL13)₂ was also obtained. The zinc complex crystallises in the tetragonal space group P4₃2₁2 with two crystallographically independent molecules in the unit cell. The ORTEP plot for corresponding molecule is given in figure 3.46. The molecules differ slightly in their bond lengths and bond angles, which may arise from the crystal packing effect. The mean plane of deviation of each ligand is 5.64 and 8.47° for complex 1 and is similar to complex 2 (5.07, 8.53°). The

bond lengths and bond angles listed in table 3.15 are similar to the other zinc complexes.

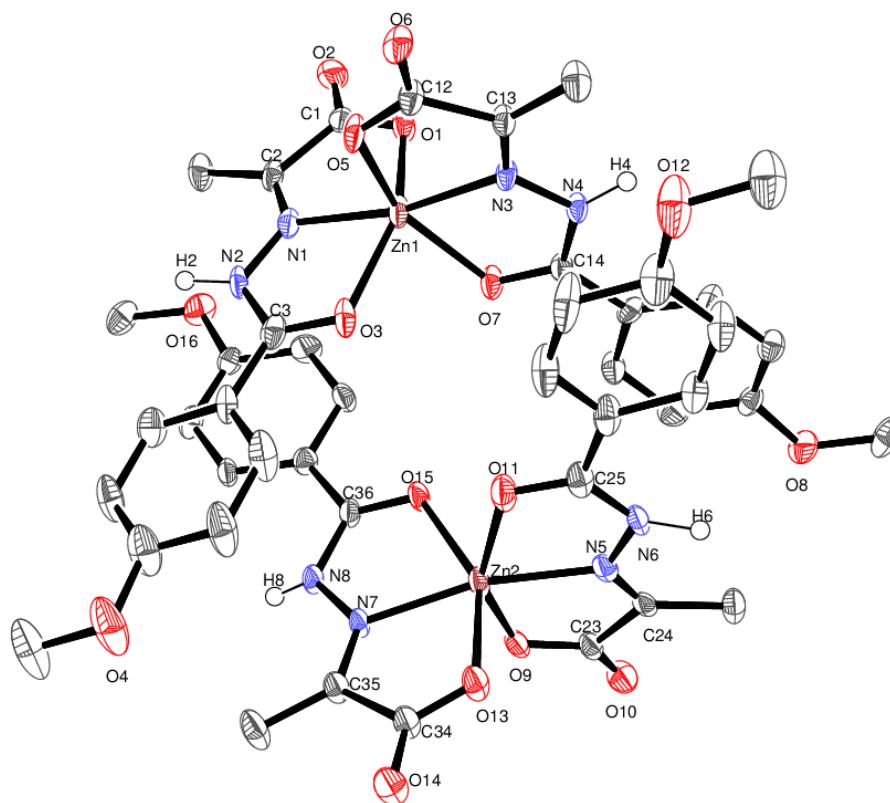


Figure 3.46: ORTEP plot (50% probability ellipsoids) of the molecular structure of *mer*-Zn(II)(HL13)₂

Table 3.15: Selected bond lengths (Å) and bond angles (°) of *mer*-Zn(II)(HL13)₂

Bonds	Complex-1		Complex-2	
	(HL ¹) ⁻	(HL ²) ⁻	(HL ¹) ⁻	(HL ²) ⁻
Zn-O(1)	2.101(3)	2.109(3)	2.111(3)	2.104(3)
Zn-O(3)	2.096(3)	2.117(3)	2.111(4)	2.102(3)
Zn-N(1)	2.080(4)	2.076(3)	2.081(4)	2.084(3)
O(1)-Zn-N(1)	76.23 (14)	75.99(12)	76.28(14)	75.94(12)
O(3)-Zn-N(1)	75.01(14)	74.57(12)	74.42(14)	74.87(12)
O(1)-Zn-O(3)	149.86(13)	149.09(12)	149.10(13)	149.47(12)
N(1) (L ¹)-Zn-N(1) (L ²)	168.81(14)		167.64(14)	
C(1)-C(2)-N(1)-N(2)	178.5(4)	176.9(4)	176.5(4)	178.4(4)

3.9 Summary of Chapter - 3

PVAHs and CAHs crystallise predominantly in the keto form. The PVA ligands are essentially planar, although the two phenyl rings in CA hydrazones lie in a different plane with the an angle ranging from 53.0 – 58.0°. Under the synthetic conditions chosen, ligands NaHL9 and NaHL11, HCA5, HCA2 coordinate in their monoprotonated form. In the sodium salts NaHL9 and NaHL11, the negative charge on the carboxylate group present in the pyruvate hydrazones is balanced by the Na⁺ counter ion. On the other hand, H₂L20 was crystallised in its di-protonated form. The sodium cation in NaHL9 and NaHL11 is surrounded by six ligands completing the octahedral geometry. Ligands HL9⁻ and HL11⁻ acts as monodentate ligand towards the Na ion and the rest of the octahedral coordination site is completed by water molecules. PVAHs show extensive intra and intermolecular hydrogen bonding, in contrast to cinnamaldehyde hydrazones. Hence, calculated CLogP values are greater for CAHs, whereas some of the PVAHs have even negative values. The greater CLogP values may lead to poor oral drug absorption but may prove to be advantageous in promoting permeation through the lipid bilayer of the mycobacterial cell wall.

The torsional angles suggest that the sodiated ligands adopt *Z* confirmation, whereas the non-sodiated PVAH crystallises in *E* conformation. All the isolated crystals of Cu(II) and Zn(II) complexes of PVAHs exhibit *E* confirmation, whereas Cu(I) complexes prefer to remain in *Z* confirmation in the solid state. Pyruvate binds to Cu(II) and Zn(II) in a tridentate fashion, forming two stable five membered rings around the metal centre. Cu(II) complexes of PVAHs mostly adopt monomeric square pyramidal geometry, although a dimeric complex of similar geometry is also observed for L9. In the case of monomeric complexes, one ligand is bound to the Cu(II) with ONO donor atoms, whereas solvent (water/methanol) molecules occupy the remaining coordination sites. In the dimeric copper complex, the two Cu(II) centres are bridged by two chloride ions. The apical bond distances are significantly longer than the equatorial bond distances, indicating an appreciable Jahn - Teller distortion. In the monomeric square pyramidal complexes, the ligand is dianionic giving rise to an overall neutral complex .

In the case of [Cu(II)(L9)(H₂O)₂] and [Cu(II)(L11)(H₂O)₂].H₂O, the complexes crystallise as two crystallographically independent molecules in one unit cell, which is reflected in their different τ values. The τ value indicates slight distortion from a perfect

square pyramidal geometry. The other copper complexes of L8⁻, L13⁻, L17⁻ and L7⁻ exhibit similar structural characteristics. Bond lengths and bond angles are comparable with literature values and the R group on the aromatic rings have little or no influence on the bond distances in the direct vicinity of metal centre. The ligand remains essentially planar when bound to Cu(II) centre.

In the dimeric complex, the ligand is coordinated in its monoanionic form with the positive charge of Cu(II) centre balanced by an additional chloride ion. Similarly, the ligand remains with a single positive charge in case of octahedral Cu(II) and Zn(II) complex. Two ligands bind to the metal centre making the overall complex neutral. The two ligands are organised in a meridionally around the metal centre due to the rigidity of the planar ligand. However, the copper complex of HL15 crystallises as two crystallographically independent molecules, one neutral and one anionic. In the latter, one of the ligands bound to the Cu(II) centre is dianionic, making the overall copper complex negatively charged which is balanced by a sodium counter ion. In the case of octahedral complexes, the coordinating ligand loses its planarity in order to reduce the steric repulsion caused by two ligands bound to the same metal centre. This is evident from the mean plane of deviation, which varies from 5.0 to 56.1°. It is also found that the deviation for one ligand is smaller than for the other ligand bound to the same metal centre. Greater values are obtained for the [Zn(II)(HL8)₂].H₂O, as it bears a bulkier NO₂ at *para*-position on the aromatic ring. The distorted octahedral geometry is indicated by the bond angles.

The PVAH ligand binds to one of the Cu(I) centre partially in a bidentate manner, thus allowing the Cu(I) complex to adopt a tetrahedral geometry. Whereas, the other part of the PVAH coordinates in a monodentate manner to the second Cu(I) centre. PPh₃ occupies the rest of the tetrahedral sites. The overall copper complex is positively charged, hence PF₆⁻ is also present in the crystal lattice in order to balance the charge. Soft P donors provided by PPh₃ stabilise the crystal structures of the Cu(I) complexes. The bond angles indicate distortion from perfect tetrahedral geometry. A three-coordinate Cu(I) complex is also isolated along with the dimeric complex of [Cu(I)₂HL9(PPh₃)₄]. 2Et₂O.H₂O.

Chapter-4
**Electrochemistry and EPR
studies**

4.0 Electrochemistry and Electron paramagnetic resonance studies

4.1 Introduction

Electrochemistry (Echem) is a useful technique, as it allows studying the redox processes of molecules. It has various applications, such as electrosynthesis²⁴²⁻²⁴³, evaluation of redox potential of metal complexes and enzymes containing redox active metal centres.²⁴⁴⁻²⁴⁶ Furthermore, in bioinorganic chemistry, the model complexes mimicking metalloenzymes have also been explored with the help of electrochemistry. This allows the study of electron / proton transfer processes associated with the metal centre, hence can be useful in elucidating mechanistic aspects of catalytic activities of certain enzymes.²⁴⁷ Moreover, the redox potentials of metal complexes can be tuned by employing appropriate ligand systems which can be useful in effective drug design.²⁴⁸

The electrochemistry of transition metal complexes has been extensively studied in the last two decades owing to their various redox states.²⁴⁹ Out of the various metal ions present in biological systems, copper, iron and molybdenum are preferred for redox processes.²⁵⁰ Copper is known to exist in oxidation states Cu(0), Cu(I), Cu(II) and Cu(III) depending on the conditions.²⁵¹⁻²⁵³ Since the redox potential for $\text{Cu}^{3+}/\text{Cu}^{2+}$ is normally very high, the Cu(III) oxidation state is generally not found in biological systems.²⁵¹ Applying an electric potential to copper complexes in solution allows the copper centre to be present in different oxidation states at certain electric potentials, ranging from 0 to 3. These can be monitored using different electrochemical techniques, but linear-sweep cyclic voltammetry (LSCV or CV) is most commonly used to study transition metal complexes.

As discussed in chapter - 3, the Cu-centre reorganises its coordination sphere while changing from one oxidation state to another. Whereas Cu(II) mainly prefers a 5-coordinate square pyramidal geometry, Cu(I) adopts a 4-coordinate tetrahedral geometry. This type of structural reorganisation is known to be hindered in copper-containing metalloproteins. In order to lower the activation energy during electron transfer processes, the coordination geometry in blue copper proteins is a compromise between Cu(I) and Cu(II) (entatic state), which can be considered as opposing Jahn-Teller distortion.²⁵⁴⁻²⁵⁵

Solomon *et al.* have performed extensive studies on the blue copper protein plastocyanin which displays such a compromised geometry, as explained in figure

4.1. As indicated in figure 4.1a, a normal Cu(II) complex exhibits strong σ -bonding and weak π -interactions as a lobe of the $d_{x^2-y^2}$ orbital is oriented along the metal-ligand bond which give rise to a high energy σ charge transfer transitions. However, in case of plastocyanin (fig 4.1b) the $d_{x^2-y^2}$ lobes are rotated by 45° which results in weak σ and strong π interactions. Thus, the unusual geometry prevents the protein to undergo drastic geometric change upon oxidation, hence allowing rapid electron transfer.

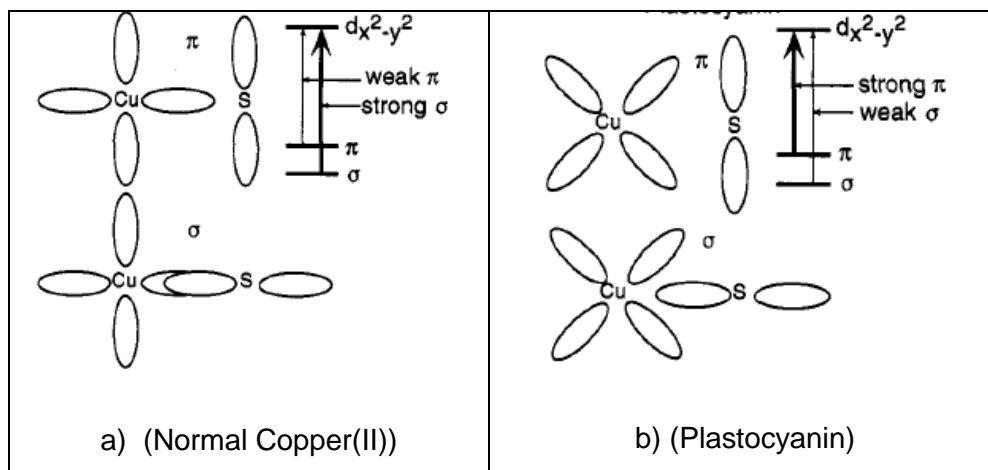


Figure 4.1: a) Normal Cu-S (cysteine) bonding interactions b) Cu-S (cysteine) bonding interaction in plastocyanin.²⁵⁵

Hence, most of the redox processes in biological systems are reversible, whereas in synthetic coordination chemistry, especially in copper complexes of Schiff bases, redox processes tend to exhibit either quasi-reversible or irreversible behaviour.²⁵⁶⁻²⁵⁷ This can be due to the major change of the geometry upon reduction of Cu(II) to Cu(I). As a result, the dissociation of partially or fully coordinated rigid molecules in order to attain the desired coordination geometry around the metal centre is often observed. However, McMaster and group, successfully synthesized Cu(I) and Cu(II) complexes of di-imidazole containing ligands (shown in figure 4.2) which are similar in structure.

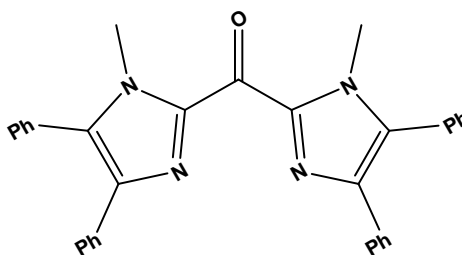


Figure 4.2: Bis(1-methyl-4,5-diphenylimidazol-2-yl) ketone²⁵⁸

Both complexes adopt a geometry that lies in between tetrahedral and square planar, as confirmed by X-ray crystallography. The redox behaviour of the Cu(II) complex is completely reversible which implies that there is no significant structural change at the copper centre upon reduction to Cu(I).²⁵⁸

As discussed earlier, electrochemical properties of metalloenzymes or their model complexes have been helpful in elucidating the mechanistic aspects of catalytic properties of the metal centres. Furthermore, Echem in combination with other techniques, such as electron paramagnetic (EPR) spectroscopy, NMR and X-ray crystallography can be useful in investigating the electronic and structural properties of metalloenzymes.^{246,259-260} Moreover, Echem and EPR can be employed to investigate the behaviour of metal complexes in solution containing paramagnetic centres. Nonetheless, EPR has been widely used by several researchers in the past to predict the potential geometries and nature of Cu(II) centres in solution.²⁶¹⁻²⁶²

For example, Solomon and group also explored the Cu(II)-containing blue copper protein plastocyanin with the help of EPR. Figure 4.3 indicates the EPR spectra of the protein (top) and normal copper (bottom). From the EPR studies, especially, the 2-fold reduction in A_{\parallel} values of plastocyanin indicates a distortion from tetrahedral geometry.²⁵⁵

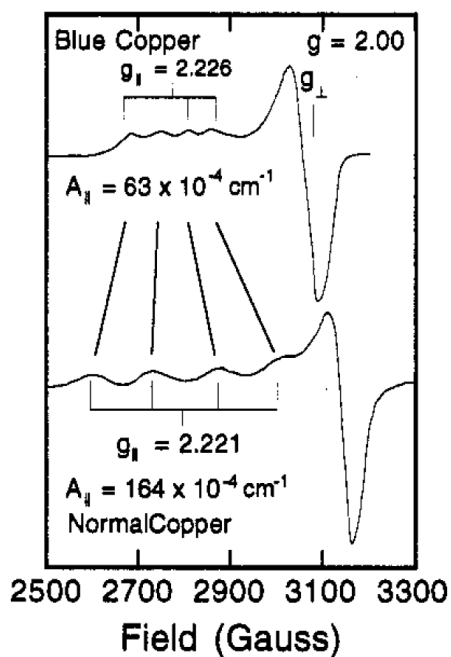


Figure 4.3: X-band EPR spectrum of plastocyanin (top) and D_{4h} CuCl_4^{2-} (bottom)²⁵⁵

In this chapter, CV is used to explore the redox behaviour of the Cu(II) and Cu(I) complexes of selected pyruvate hydrazones. The investigated copper complexes have different substituents on the aromatic ring, ranging from electron withdrawing NO_2 to electron donating CH_3 . This allowed the examination of the influence of different substituent on the redox properties of the copper complexes. Furthermore, to elucidate the behaviour of Cu(II) complexes of PVAHs in the electrochemical solvent (DMSO), selected copper complexes were also examined using EPR spectroscopy.

4.2 Redox properties of pyruvate hydrazones and their copper complexes

Cyclic voltammetry (CV), was employed to investigate the redox properties of the sodium salts of the ligands, NaHL3, NaHL8, NaHL9, NaHL12, the Cu(II) complexes [Cu(II)L1(H₂O)₂], [Cu(II)L3(H₂O)₂], [Cu(II)L8(H₂O)₂], [Cu(II)L9(H₂O)₂], [Cu(II)L10(H₂O)₂], [Cu(II)L12(H₂O)₂], [Cu(II)L21(H₂O)₂] and the Cu(I) complexes [Cu(I)₂HL8(PPh₃)₅] and [Cu(I)₂HL9(PPh₃)₅].

The CV studies were carried out at room temperature using a standard three electrode configuration, consisting of a platinum working electrode, platinum wire as auxiliary electrode and a Ag/AgCl reference electrode. The supporting electrolyte used was 0.1 M *tetra*-butyl ammonium hexafluorophosphate in DMSO. The solution was purged with N₂ gas prior to use. The details of the procedure can be found in the chapter-7. The concentrations of the ligands and complexes were approximately 1 mM and the cyclic voltammograms were scanned within the potential range of +1.0 to –1.0 V. DMSO decomposes beyond the potentials +1.0 and –1.0 V, hence only processes observed within these two limits were assigned in the present study.

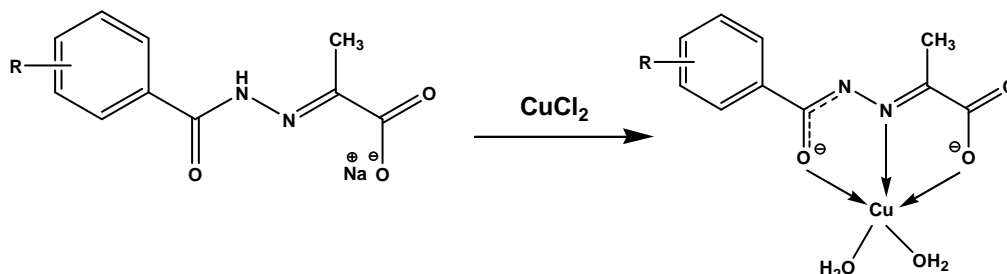
The redox potential ($E_{1/2}$) of the ferrocene/ferrocenium (Fe²⁺/Fe³⁺) couple in DMSO was observed at 0.45 ± 0.2 V versus standard calomel electrode (SCE), consistent with literature values within the error limits.²⁶³ In order to compare with literature values, potentials monitored with respect to the Ag/AgCl reference electrode were converted into SCE as per equation A.²⁴⁹

$$E_{vs\ SCE} = E_{vs\ Ag/AgCl} - 0.0450\ V \text{ -----equation A}^{249}$$

In case of the pyruvate hydrazone (PVAH) ligands and their Cu(II) complexes the potential is recorded from voltage E_1 at +1.0 V to voltage E_2 (-1.0) and then back to E_1 . This scan direction will subsequently be called forward scan. For Cu(I) complexes, a reverse scan was employed due to the different oxidation state.

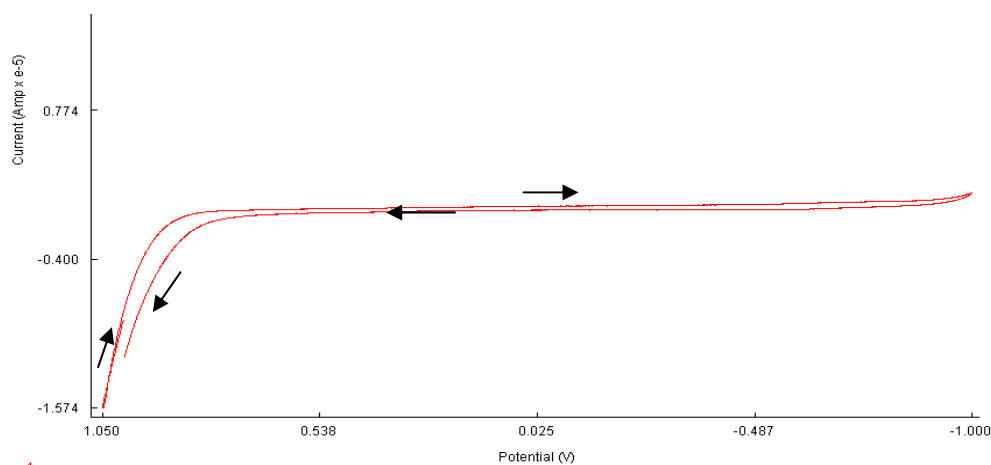
4.2.1 Electrochemical investigation of PVAHs

As discussed in chapter-2, Cu(II) complexes of PVAHs were synthesized using one equivalent of NaHLx and CuCl₂ as shown in Scheme 4.1



Scheme 4.1: Synthesis of Cu(II) complex of PVAHs

In order to examine the redox behaviour of starting material, before investigating the Cu(II) complexes, selected PVAH ligands and CuCl₂ were also studied using CV. A representative example, NaHL3, is shown in figure 4.4. The CV indicates that the ligand does not show any redox activity.



1

Figure 4.4: CV of NaHL3 in DMSO over the potential range from +1.0 to -1.0 in the forward sweep at the scan rate of 100 mV s⁻¹ (the arrow represents the direction of the potential sweep)

Other ligands, including NaHL9, NaHL12, NaHL15 exhibited similar characteristics and no redox peaks were observed. However, the ligand bearing an NO₂ substituent on the aromatic ring (NaHL8) shows redox activity in the region -0.06 to -0.1 V. This can be attributed to the redox activity of NO₂ and will be

discussed further in detail when comparing with its respective Cu(I) and Cu(II) complexes.

4.2.2 Electrochemical investigation of copper complexes

In order to understand the behaviour of the Cu(II) complexes in electrochemical DMSO and in particular to investigate potential ligand exchange reactions in this co-ordinating solvent, the CV of free Cu(II) was recorded. CuCl₂ was used as source of Cu(II) as it was used as the starting material in the synthesis of the Cu(II) complexes of PVAHs. If there is complete dissociation of the ligand, then it is likely that the copper complexes would exhibit similar behaviour to CuCl₂ in DMSO (Cu-DMSO complex). It can be observed from figure 4.5, that CuCl₂ in DMSO gives well defined symmetrical waves Epc (**A**) and Epa (**B**), which can be attributed to the Cu²⁺/ Cu¹⁺ redox couple. The potentials for Epc and Epa are 0.22 V and 0.53 V at 100 mV s⁻¹, respectively.

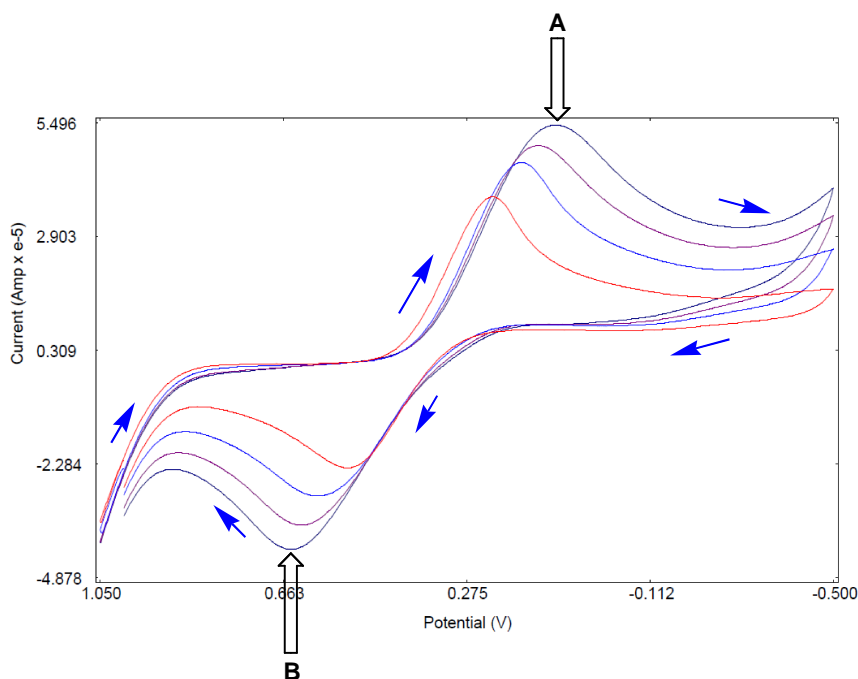


Figure 4.5: CV of scan rate dependence for CuCl₂ in DMSO over the potential range from +1.0 to -0.5 in the forward sweep at the scan rate of 100, 200, 300, 400 mV s⁻¹ (inner-outer) (blue arrows represents the direction of the potential varied)

Ukpong and coworkers, studied the electrode potential of CuCl₂ in different solvents against a Pt working electrode and SCE as reference electrode. The observed Epc and Epa values in DMSO at 0.25 mV s⁻¹ are 0.20 V and 0.40 V

respectively. Furthermore, it was also observed that the electrode potential shifts towards more positive potential while going from DMSO < DMF < Acetonitrile (AN). This is likely due to the fact that, DMSO stabilises the Cu(II) species in solution.²⁶⁴ Similar behaviour was observed for ferrocene in different solvents by Tsierkezos, although the shift is not as significant as observed for CuCl₂.²⁶⁵

4.2.2.1 Electrochemical investigation of Cu(II) complexes of PVAHs

[Cu(II)L9(H₂O)₂]

The CV of [Cu(II)L9(H₂O)₂] (figure 4.6) exhibits cathodic waves at 0.26 V (**A**) and -0.64 V (**B**), whereas anodic waves are observed at 0.18 V (**C**) and 0.56 V (**D**) at a scan rate of 10 mV s⁻¹. This potential was monitored in a forward scan ranging from +1.0 to -1.0 V. The cathodic waves (**A** and **B**) and the corresponding anodic waves (**C** and **D**) can be assigned to metal-based redox processes. The peak **A** may be assigned to the reduction of Cu²⁺ to Cu¹⁺ (equation 4.1), whereas the peak **D** may be attributed to the oxidation of Cu¹⁺ to Cu²⁺ (equation 4.2). Moreover, the cathodic peak **B** can be assigned to the formation of Cu⁰ (equation 4.3), where the metallic copper starts depositing on the electrode. And the anodic peak **C** might be due to the redissolution of Cu⁰ (equation 4.4)

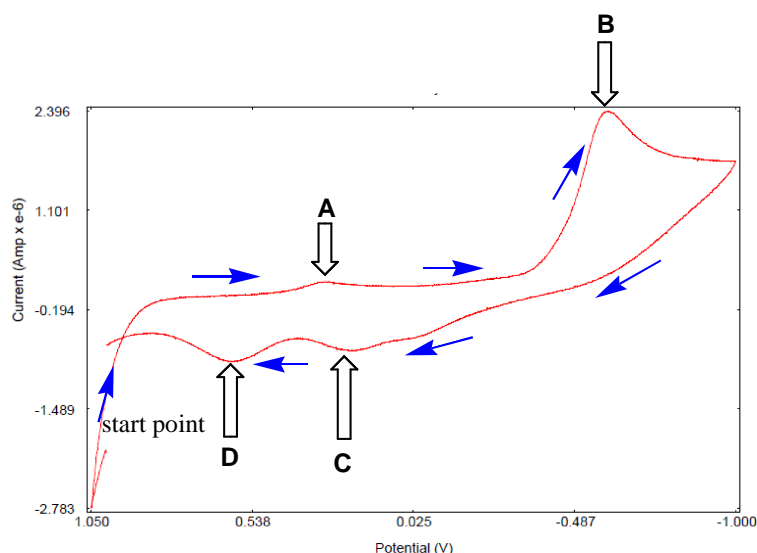


Figure 4.6: CV of [Cu(II)L9(H₂O)₂] in DMSO over the potential range from +1.0 to -1.0 in the forward sweep at the scan rate of 10 mV s⁻¹ (the arrow represents the direction of the potential sweep)



Going towards higher scan rates also leads to broadening and shifting of the peak **D** towards more positive potentials resulting in the merging of **C** and **D** peaks. The broadening of peaks can also be due to the presence of intermediates at higher scan rate. The intensity of peaks increases as scan rate increases, which can be observed from the scan rate dependence spectra as shown in figure 4.7. It is observed that the peak **D** increases in greater intensity as compared to peak **A** after repeated scanning. The greater intensities of anodic peaks might be due to the redissolution of elemental copper (Cu^0) (equation 4.4).

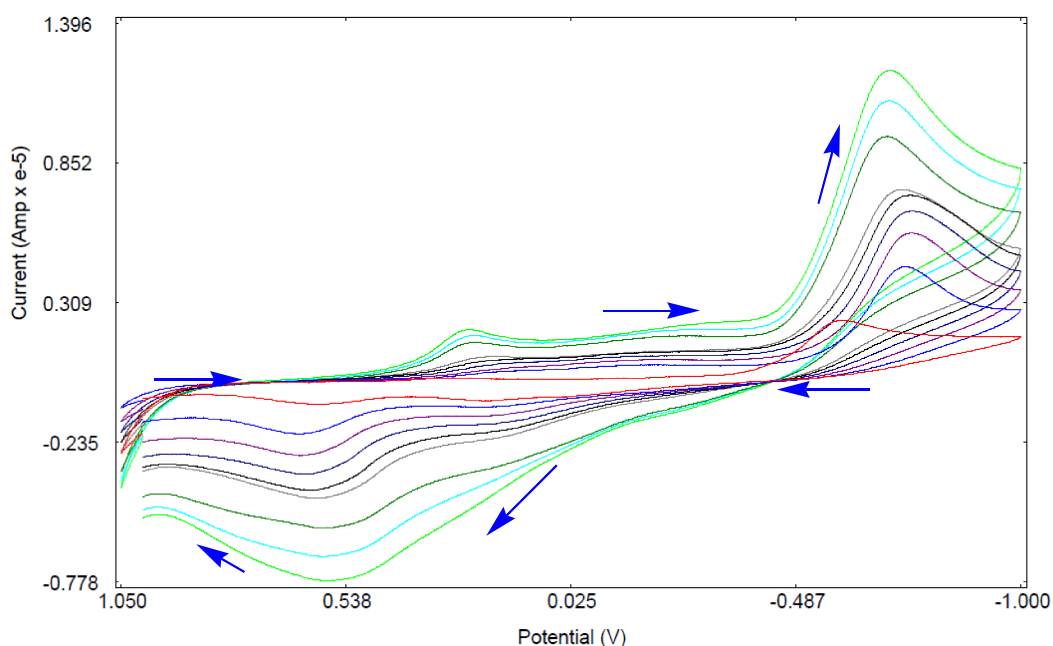


Figure 4.7: CV for $[\text{Cu}(\text{II})\text{L9}(\text{H}_2\text{O})_2]$ recorded at different scan rates in DMSO over the potential range from +1.0 to -0.5 V in the forward sweep at scan rates of 10 - 300 mV s^{-1} (blue arrows represent the direction of the potential sweep).

These assignments were made according to similar work reported by Darchen *et al* for $[\text{Cu}(\text{NH}_3)_4]^{2+}$. They observed a redox couple due to $\text{Cu}^{2+}/\text{Cu}^{1+}$, whereas the cathodic and anodic peak potential observed due to $\text{Cu}^{1+}/\text{Cu}^0$ occurs at a slower rate, due to the redissolution of copper electrodeposited which leads to the higher value of the peak current. $[\text{Cu}(\text{NH}_3)_4]^{2+}$ exhibits similar CV spectra to that of

[Cu(II)L9(H₂O)₂] and the electrode potential for the equivalent peaks were observed at -0.22 V (**A**), -0.84 V (**B**), -0.32 V (**C**), -0.15 V (**D**) in aqueous solution at a vitreous carbon electrode with respect to SCE.²⁶⁶ The difference in the potentials observed may be attributed to 1) different ligand system, 2) electrochemical solvent and the 3) working electrode.

When [Cu(II)L9(H₂O)₂] was scanned in the limited potential range between +1.0 and -0.5 V, peaks **B** and **C** disappeared, giving more well defined **A** and **D** peaks. The CV was recorded at different scan rates (from inner to outer) of 10, 30, 50, 70, 90, 100, 150, 200, 250, 300 mV s⁻¹ as indicated in figure 4.8. The peak separation (ΔE) of **A** and **D** peaks along with ferrocene redox peaks are provided in table 4.1.

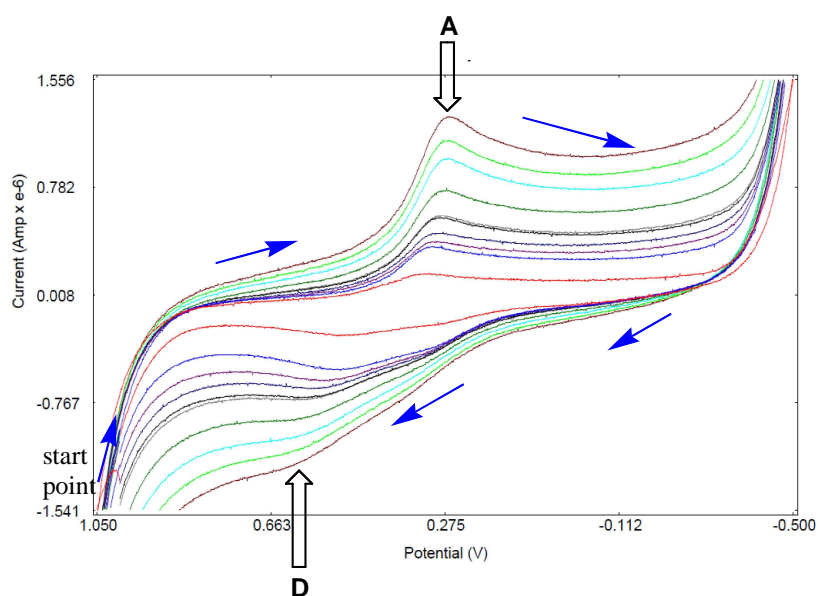


Figure 4.8: Scan rate dependence for [Cu(II)L9(H₂O)₂] in DMSO over the potential range from +1.0 to -0.5 V in the forward sweep at the scan rate of 10 – 300 (inner-outer) mV s⁻¹ (blue arrows represents the direction of the potential varied).

With the increase of the sweep rate the value of ΔE ($E_{\text{ox}} - E_{\text{red}}$) also increases, as evident from table 4.1, which is indicative of quasi-reversible behaviour. The ΔE observed for one electron reversible process for ferrocene at 10 mVs^{-1} is 0.08 V. While, 0.18 V for $[\text{Cu(II)L9(H}_2\text{O)}_2]$ at the same scan rate associates with slow electron transfer kinetics which indicates quasi-reversibility. For an ideal one electron reversible process (fast electron transfer) it is 0.06 V and independent of the scan rate.²⁶⁷

Table 4.1: ΔE values of $[\text{Cu(II)L9(H}_2\text{O)}_2]$ and ferrocene at different scan rate

v (mVs^{-1})	ΔE (V) $[\text{Cu(II)L9(H}_2\text{O)}_2]$	ΔE (V) ferrocene
10	0.18	0.08
30	0.20	0.08
50	0.24	0.08
70	0.26	0.09
90	0.27	0.09
100	0.27	0.09

[Cu(II)L8(H₂O)₂]

NaHL8 studied under similar conditions exhibited reversible peak potential, which is indicated in figure 4.9.

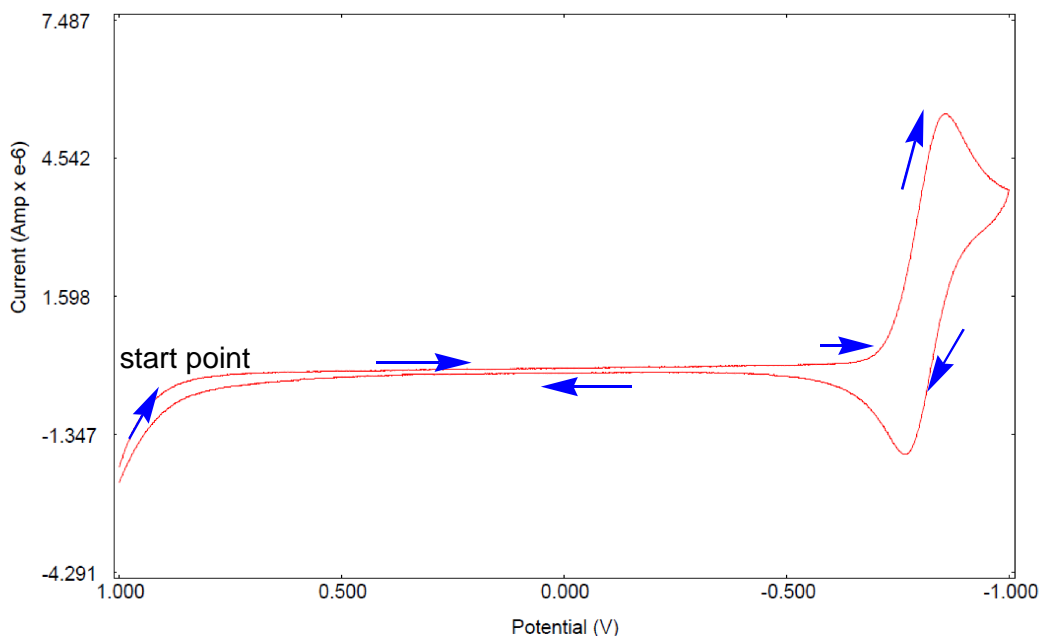
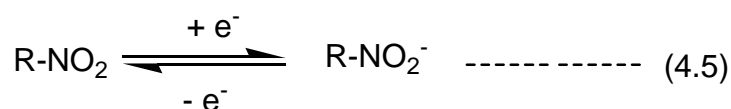


Figure 4.9: CV of NaHL8 in DMSO over the potential range from +1.0 to -1.0 in the forward sweep at the scan rate of 10 mV s⁻¹ (the arrows represents the direction of the potential sweep).

The CV wave corresponds to the redox process of NO₂ is given by equation 4.5.²⁶⁸ The cathodic peak at -0.86 V corresponds to the reduction of the NO₂ substituent to NO₂⁻, whereas the anodic peak at -0.76 V can be attributed to the re-oxidation of NO₂⁻ with a E_{1/2} value of -0.81 V. The peak separation (ΔE) is 0.089 V at 10 mV s⁻¹ and is independent of increased scan rates, which is indicative of reversibility.



The copper complex of NaHL8 displays a rather complicated CV as indicated in figure 4.10. The copper complex [Cu(II)L8(H₂O)₂] with R = NO₂ exhibits

cathodic peaks at +0.27 V (A), -0.56 V (B) and -0.84 V (C) at a scan rate of 10 mV s^{-1} . In addition, the anodic peaks are observed at -0.76 V (D), -0.16 V (E), +0.07 V (F), +0.06 V (G), +0.35 V (H). C and D can be attributed to the redox processes occurring due to NO_2 . Whereas, the rest of the peaks can be attributed to the metal based redox peaks and can be related to $\text{Cu}^{2+}/\text{Cu}^{1+}$ and $\text{Cu}^{1+}/\text{Cu}^0$ (equation 4.1-4.4, page-168) as assigned for $[\text{Cu}(\text{II})\text{L9}(\text{H}_2\text{O})_2]$.

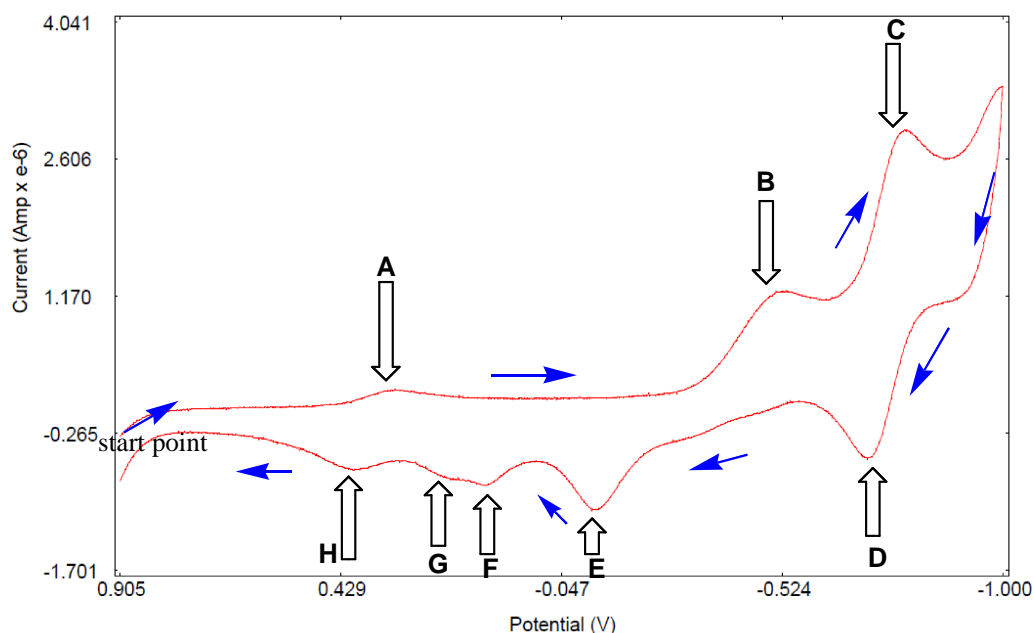


Figure 4.10: CV of $[\text{Cu}(\text{II})\text{L8}(\text{H}_2\text{O})_2]$ in DMSO over the potential range from +1.0 to -1.0 V in the forward sweep at the scan rate of 10 mV s^{-1} (the arrow represents the direction of the potential sweep)

The additional anodic and cathodic peaks observed for $[\text{Cu}(\text{II})\text{L8}(\text{H}_2\text{O})_2]$ might be due to the presence of more than one species of copper complex in the DMSO solution. This may be due to structural reorganisation of the coordination sphere taking place while going from one oxidation to different oxidation state.

$[\text{Cu}(\text{II})\text{L8}(\text{H}_2\text{O})_2]$ was also scanned for different scan rates, similar to that of $[\text{Cu}(\text{II})\text{L9}(\text{H}_2\text{O})_2]$. As observed for later complex, the former complex displays similar behaviour, where the peaks tend to broaden which result in merging of bands as indicated in figure 4.11. Interestingly, certain species exists only at lower scan rate, which results in complete disappearance of peak E at higher scan rates

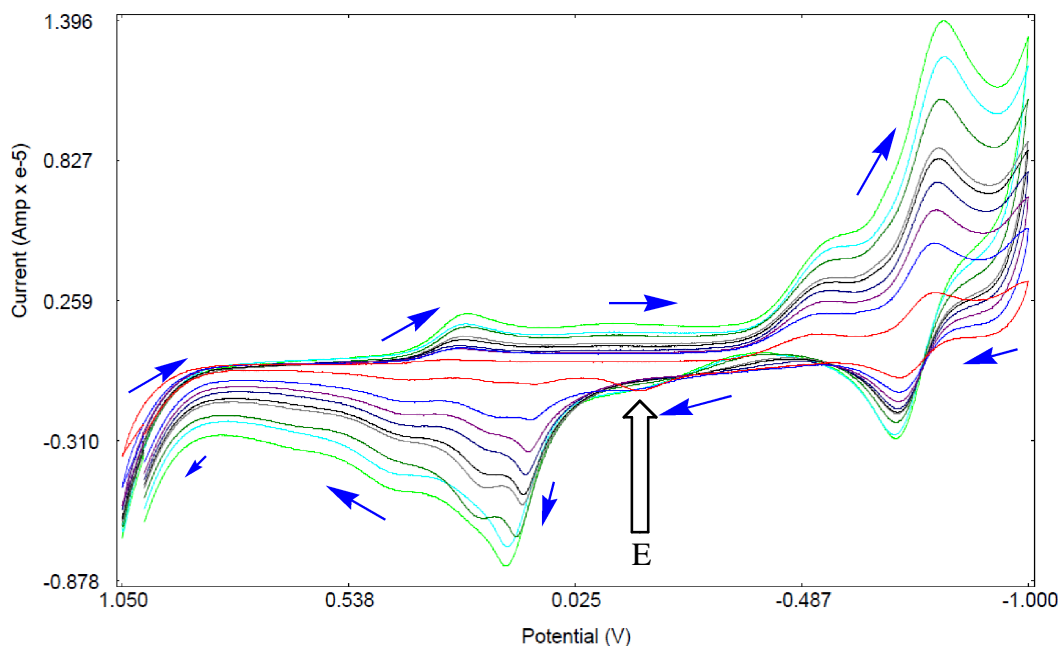


Figure 4.11: CV of scan rate dependence for $[\text{Cu(II)L9(H}_2\text{O)}_2]$ in DMSO over the potential range from +1.0 to -1.0 V in the forward sweep at the scan rate of 10- 300 (inner-outer) mV s^{-1} (the arrows represent the direction of the potential varied)

Moreover, when $[\text{Cu(II)L8(H}_2\text{O)}_2]$ was scanned in the limited range from +1.0 to -0.5 V better defined **A** and **H** peaks were observed as indicated in figure 4.12. These peaks may be assigned as shown in equations 4.1 and 4.4, similarly observed for $[\text{Cu(II)L9(H}_2\text{O)}_2]$



It can be noted that, when both the complexes are scanned in the potential range from +1.0 to -0.5 V, the cathodic and anodic peaks exhibit nearly symmetric peak heights as compared to the spectra ranging from +1.0 to -1.0 V. This can be due to fact that, as there is no process occurring due to $\text{Cu}^{1+}/\text{Cu}^0$ hence no Cu(0) deposition takes place which allows $\text{Cu}^{2+}/\text{Cu}^{1+}$ to take place at similar rate. However, the large ΔE (V) which rises with increase in the scan rate indicates quasi-reversible behaviour.

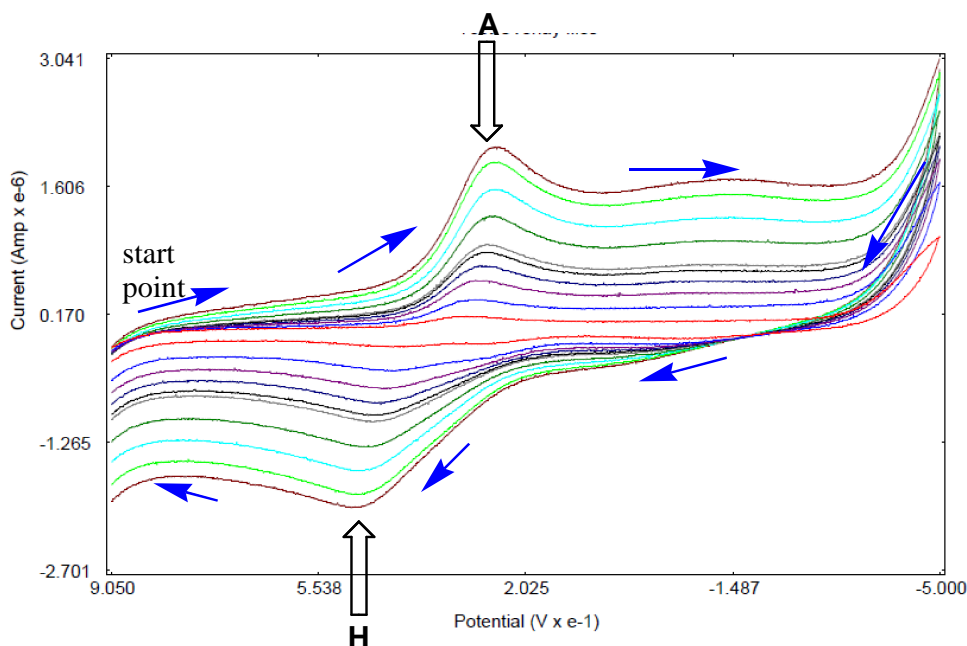


Figure 4.12: CV of scan rate dependence for $[\text{Cu}(\text{II})\text{L}8(\text{H}_2\text{O})_2]$ in DMSO over the potential range from +1.0 to -0.5 V in the forward sweep at the scan rate of 10 - 300 (inner-outer) mV s^{-1} (arrows represent the direction of the potential varied)

The quasi-reversible behaviour of copper complexes observed for $\text{Cu}^{2+}/\text{Cu}^{1+}$ is likely to be due to the change in the coordination environment of the Cu(I) centre. In case of PVAH copper complexes, Cu(II) adopts either square pyramidal or octahedral geometry whereas Cu(I) prefers tetrahedral geometry²⁶⁹. Upon reduction to Cu(I), the rigid ligand either partially dissociates to form a Cu(I) complex as shown in Figure 4.13 or fully dissociates to form a Cu(I)-DMSO complex.

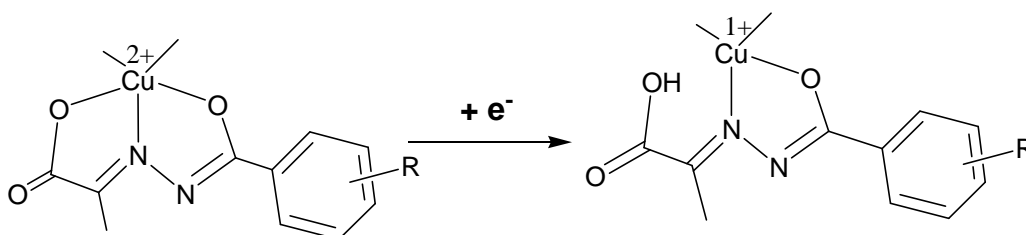


Figure 4.13: Structural reorganisation from Cu(II) \rightarrow Cu(I) complex of PVAHs.

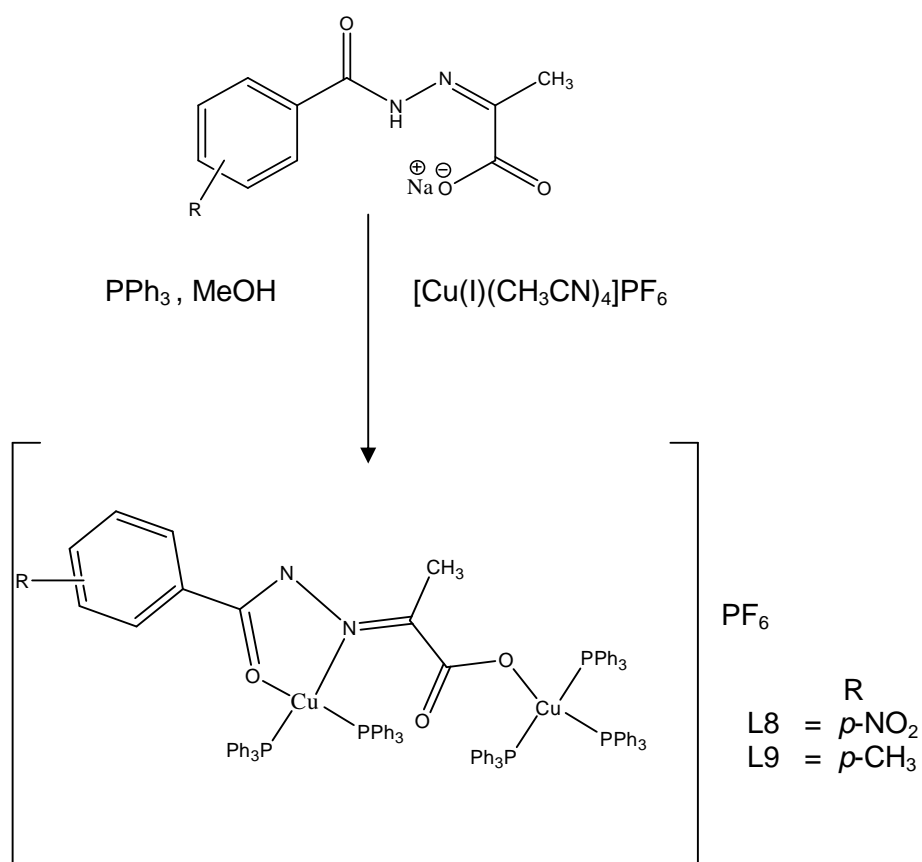
It has been confirmed by X-ray crystal crystallography, as described in chapter-3, that Cu(I) complexes of PVAHs adopt tetrahedral geometry and are more stable in presence of soft donor atoms like P, whereas Cu(II) complexes mainly adopt square pyramidal geometry and are stable with O,N donor atoms. The

structural reorganisation of the coordination sphere can account for the quasi-reversible behaviour of the investigated Cu(II) complexes of PVAHs.

In order to compare the electrochemical behaviour of Cu(I) complexes, $[\text{HL8Cu}_2(\text{I})(\text{PPh}_3)_5]\text{PF}_6$ and $[\text{HL9Cu}_2(\text{I})(\text{PPh}_3)_5]\text{PF}_6$ were also investigated under similar conditions.

4.2.2.2 Electrochemical investigation of Cu(I) complexes of PVAHs

Synthetic scheme for Cu(I) complexes of PVAHs which is discussed in detail in chapter-2 is shown in scheme 4.2.



Scheme 4.2: Synthesis of Cu(I) complex of PVAHs

Likewise, PVAHs ligands were investigated for their redox behaviour, PPh_3 is also examined using CV, as it is also part of the coordination sphere of Cu(I) complex. The cathodic and anodic peak potentials of PPh_3 are observed at -0.45 V and -0.37 V respectively as indicated in figure 4.14. The peaks can be assigned to the redox potential of the PPh_3 group as indicated in equation 4.6. The ΔE value is

88 mV at 50 mV s^{-1} but increases slightly with the rise in the scan rate which is indicative of quasi-reversibility.

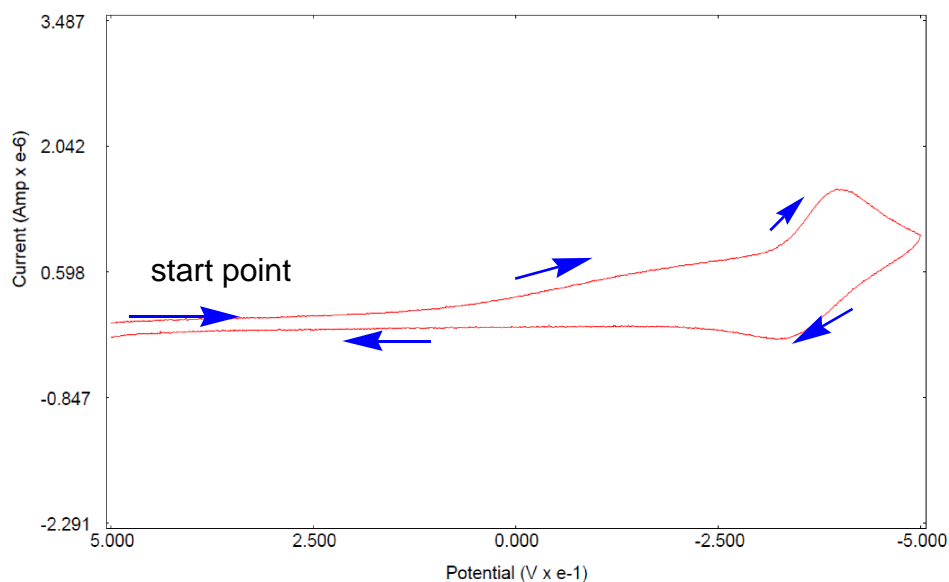
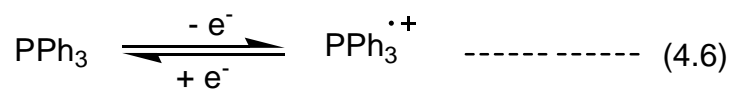


Figure 4.14: CV of PPh_3 in DMSO over the potential range from +0.5 to -0.5 V in the forward sweep at the scan rate of 30 mV s^{-1} (the arrows represents the direction of the potential sweep)

The CV for $[\text{Cu}(\text{I})_2\text{HL9}(\text{PPh}_3)_5]\text{PF}_6$ recorded at a scan rate of 10 mV s^{-1} is shown in figure 4.15. The reverse scan direction is followed for Cu(I) complexes, hence the start and end potential (E_1) is -1.0 V and the turning potential E_2 is +1.0 V. The CV of the copper complex $[\text{HL9Cu}_2(\text{I})(\text{PPh}_3)_5]\text{PF}_6$ exhibits two cathodic peaks at +0.24 V (**A**) and -0.67 V (**B**), whereas the anodic peak is observed at +0.52 V (**C**), when scanned in the range from -1.0 to +1.0 V.

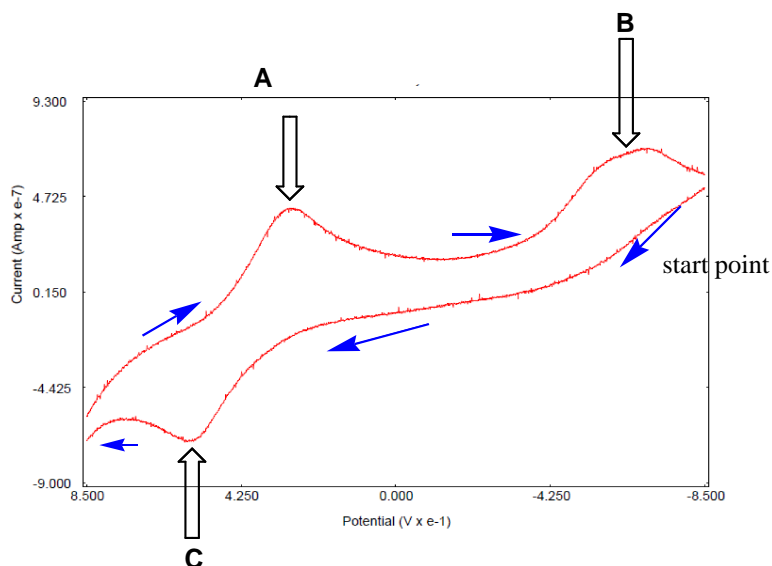
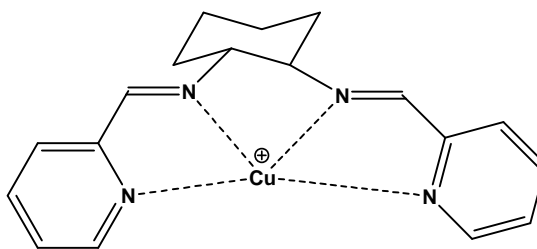


Figure 4.15: CV of $[\text{Cu}(\text{I})_2\text{HL9}(\text{PPh}_3)_5]\text{PF}_6$ in DMSO over the potential range from -1.0 to +1.0 V in the forward sweep at the scan rate of 10 mV s^{-1} (arrows represent the direction of the potential sweep)

Peaks **A** and **C** can be assigned to the metal centred redox process of the complex. The peak **A** may be assigned to the reduction of $\text{Cu}(\text{II})$ to $\text{Cu}(\text{I})$ (equation 4.1), whereas the peak **C** may be attributed to the oxidation $\text{Cu}(\text{I})$ to $\text{Cu}(\text{II})$ (equation 4.2). The irreversible cathodic peak **B** can be assigned to the formation of $\text{Cu}(0)$ (equation 4.3).



Similar results were obtained for the $\text{Cu}(\text{I})$ precursor complex, $[\text{Cu}(\text{I})(\text{CH}_3\text{CN})_4]\text{PF}_6$ and the $\text{Cu}(\text{I})$ complex synthesized by Ouali and group.²⁷⁰ The $\text{Cu}(\text{I})$ complex shown in figure 4.16 displayed a quasi-reversible behaviour for $\text{Cu}^{1+}/\text{Cu}^{2+}$ and the cathodic peak corresponding to the oxidation of $\text{Cu}^{1+} \rightarrow \text{Cu}^{2+}$ (**C**) was observed at 0.44 V, whereas the irreversible reduction process for $\text{Cu}^{1+} \rightarrow \text{Cu}^0$ occurs at -1.35 V (**B**). Furthermore, Ouali and group also observed that corresponding processes for the precursor complex, $[\text{Cu}(\text{I})(\text{CH}_3\text{CN})_4]\text{PF}_6$ was observed towards more positive potential, at +1.10 V (**C**) and -0.80 V (**B**), respectively, versus SCE in acetonitrile.²⁷⁰

Figure 4.16: Ouali's Cu(I) complex²⁷⁰

The intensity of the peaks of $[\text{HL9Cu}_2(\text{I})(\text{PPh}_3)_5]\text{PF}_6$ increases as the scan rate increases, which can be observed from the scan rate dependence plots, as shown in figure 4.17. Going towards higher scan rates leads to shifting of the peak **C** towards more positive potentials and also leads to the broadening of the peaks, similarly observed for Cu(II) complexes. This might also be due the presence of intermediate at higher scan rates resulting from the structural reorganisation taking place while going from $\text{Cu}^{1+} \rightarrow \text{Cu}^{2+}$.

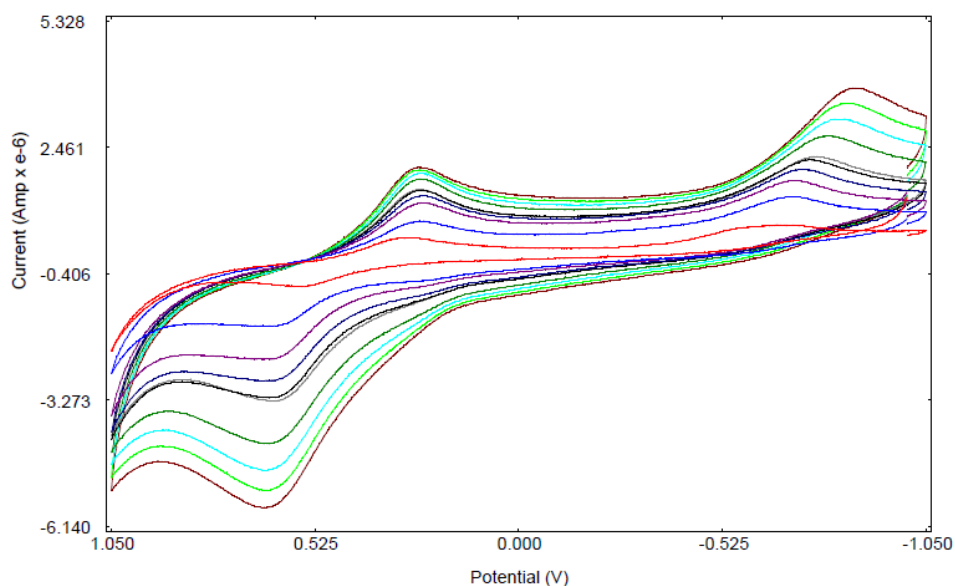


Figure 4.17: CV of scan rate dependence for $[\text{HL9Cu}_2(\text{I})(\text{PPh}_3)_5]\text{PF}_6$ in DMSO over the potential range from +1.0 to -1.0 in the forward sweep at the scan rate of 10-300 mV s^{-1} (arrow represents the direction of the potential varied)

Figure 4.18 shows a comparison between the CVs of the Cu(I) complex $[\text{HL9Cu}_2(\text{I})(\text{PPh}_3)_5]\text{PF}_6$ (blue spectrum, peaks with suffix a) and Cu(II) (red spectrum, peaks with suffix b) complex $[\text{Cu}(\text{II})\text{L9}(\text{H}_2\text{O})_2]$. As the ΔE in these complexes are quite high (0.22 V), the electron transfer processes in these complexes are quasi-reversible. Figure 4.18 also indicates that the metal based peaks corresponding to

Aa/Ab, Ba/Bb and **Ca/Cb**, of Cu(I) and Cu(II) complexes occur at nearly similar potentials. The peak potentials for $[\text{Cu(I)}_2\text{HL9(PPh}_3)_5]\text{PF}_6$ and $[\text{Cu(II)L9(H}_2\text{O)}_2]$ reported versus SCE are listed in table 4.2.

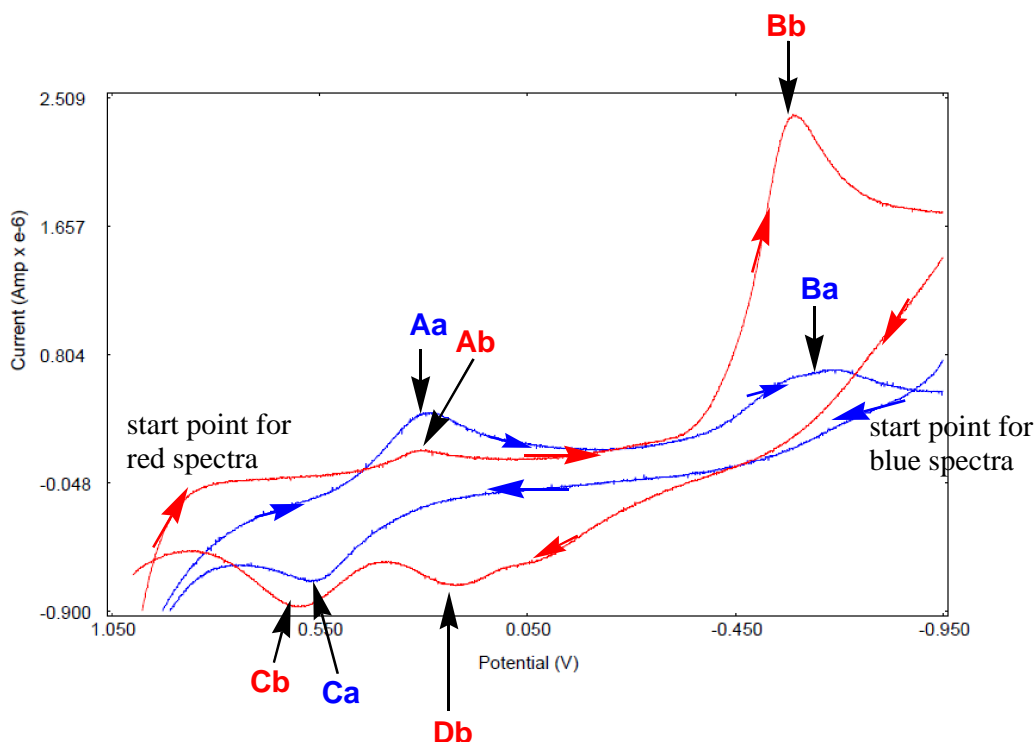


Figure 4.18: Comparison of the CVs of $[\text{Cu(II)L9(H}_2\text{O)}_2]$ (-) and $[\text{Cu(I)}_2\text{HL9(PPh}_3)_5]\text{PF}_6$ (-) in DMSO over the potential range from +1.0 V to -1.0 V at the scan rate of 10 mV s^{-1} (the arrows represent the direction of the potential varied)

Table 4.2: Electrode peak potentials $[\text{Cu(I)}_2\text{HL9(PPh}_3)_5]\text{PF}_6$ and $[\text{Cu(II)L9(H}_2\text{O)}_2]$ reported versus SCE, (^a measured versus Ag/AgCl)

	Peaks	$[\text{Cu(I)}_2\text{HL9(PPh}_3)_5]\text{PF}_6$ (V)	Peaks	$\text{Cu(II)L9(H}_2\text{O)}_2$ (V)
Cathodic peaks in mV	Aa	+0.24 (0.29 ^a)	Ab	+0.26 (0.31 ^a)
	Ba	-0.67 (-0.62 ^a)	Bb	-0.64 (-0.59 ^a)
Anodic peaks in mV	Ca	+0.52 (0.56 ^a)	Ca	+0.56 (0.61 ^a)
			Da	+0.18 (0.22 ^a)

Electrochemical studies were also performed on the Cu(I) and Cu(II) complexes of NaHL8 under similar conditions. The overlaid CV spectra of $[\text{HL8Cu}_2\text{(I)(PPh}_3)_5]\text{PF}_6$ (red spectrum with suffix a) and $[\text{Cu(II)L8(H}_2\text{O)}_2]$ (blue spectrum with suffix b) are shown in figure 4.19 and the peak potentials are listed in

table 4.3. The metal based peaks can be assigned to the oxidation and reduction of the Cu centre as described earlier. There are additional peaks as compared to the copper complexes of NaHL9. The peaks **Ca/Cb** and **Da/Db** in case of Cu(I)/Cu(II) complex can be assigned to the ligand based NO₂ redox peaks. Electrode peak potentials of [HL8Cu₂(I)(PPh₃)₅]PF₆ and Cu(II)L8(H₂O)₂ reported versus SCE are listed in table 4.3.

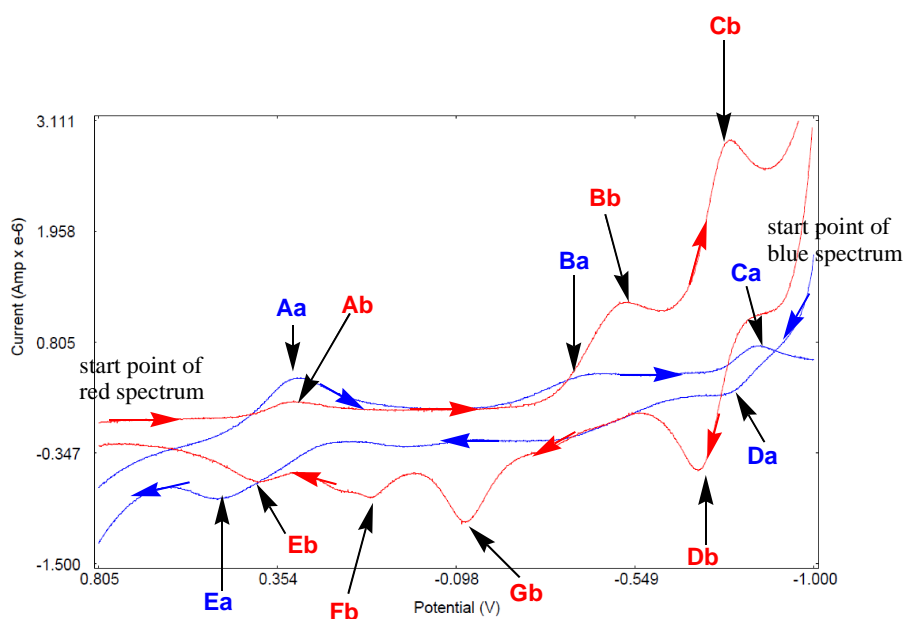


Figure 4.19: Overlaid CV of Cu(II)L8(H₂O)₂ (-) and [Cu(I)₂HL8(PPh₃)₅]PF₆ (-) in DMSO over the potential range from +1.0 V to -1.0 V at the scan rate of 10 mV s⁻¹ (blue/red arrow represents the direction of the potential varied)

Table 4.3: Electrode peak potentials [Cu(I)₂HL8(PPh₃)₅]PF₆ and Cu(II)L8(H₂O)₂ reported versus SCE, (^a measured versus Ag/AgCl)

	Peaks	[Cu(I) ₂ HL8(PPh ₃) ₅]PF ₆ PF ₆ (V)	Peaks	Cu(II)L8(H ₂ O) ₂ (V)
Cathodic peaks in mV	Aa	+0.26 (0.31 ^a)	Ab	+0.27 (0.32 ^a)
	Ba	-0.47 (-0.43 ^a)	Bb	-0.56 (-0.52 ^a)
	Ca	-0.91 (-0.86 ^a)	Cb	-0.84 (-0.79 ^a)
Anodic peaks in mV	Da	-0.83 (-0.79 ^a)	Db	-0.76 (-0.71 ^a)
	Ea	+0.45 (0.50 ^a)	Eb	+0.35 (0.40 ^a)
			Fb	+0.07 (0.18 ^a)
			Gb	-0.16 (-0.18 ^a)

When the voltammogram was scanned in the limited potential range between -1.0 and $+0.5$ V, it gave more well defined **Aa/Ca** and **Aa/Ea** peaks for $[\text{Cu}(\text{I})_2\text{HL9}(\text{PPh}_3)_5]\text{PF}_6$ and $[\text{Cu}(\text{I})_2\text{HL8}(\text{PPh}_3)_5]\text{PF}_6$, respectively, similarly observed for their respective Cu(II) complexes. As expected, with the increase in the scan rate, the value of ΔE also increases significantly, strongly suggesting quasi-reversibility. The values are given in table 4.4.

Table 4.4: ΔE values for $[\text{Cu}_2(\text{I})\text{HL9}(\text{PPh}_3)_5]\text{PF}_6$ and $[[\text{Cu}_2(\text{I})\text{HL8}(\text{PPh}_3)_5]\text{PF}_6$ reported versus SCE, (a measured versus Ag/AgCl)

	Scan rate v (mVs^{-1})	ΔE (V)	ΔE (V)
		$[\text{Cu}(\text{I})_2\text{HL9}(\text{PPh}_3)_5]\text{PF}_6$	$[\text{Cu}(\text{I})_2\text{HL8}(\text{PPh}_3)_5]\text{PF}_6$
1	10	0.224	0.220
2	30	0.275	0.292
3	50	0.279	0.308
4	70	0.309	0.330
5	90	0.317	0.335
6	100	0.334	0.335

The overlaid spectra of $[\text{Cu}(\text{I})_2\text{HL8}(\text{PPh}_3)_5]\text{PF}_6$ (red spectrum), $[\text{Cu}(\text{II})\text{L8}(\text{H}_2\text{O})_2]$ (blue spectrum) and NaHL8 (purple spectrum) in the region -0.2 V and -1.0 V are shown in figure 4.20. All the spectra were scanned in the forward sweep in order to compare the NO_2 reduction potential and the redox peak potentials for NO_2 -substituent are listed in table 4.5.

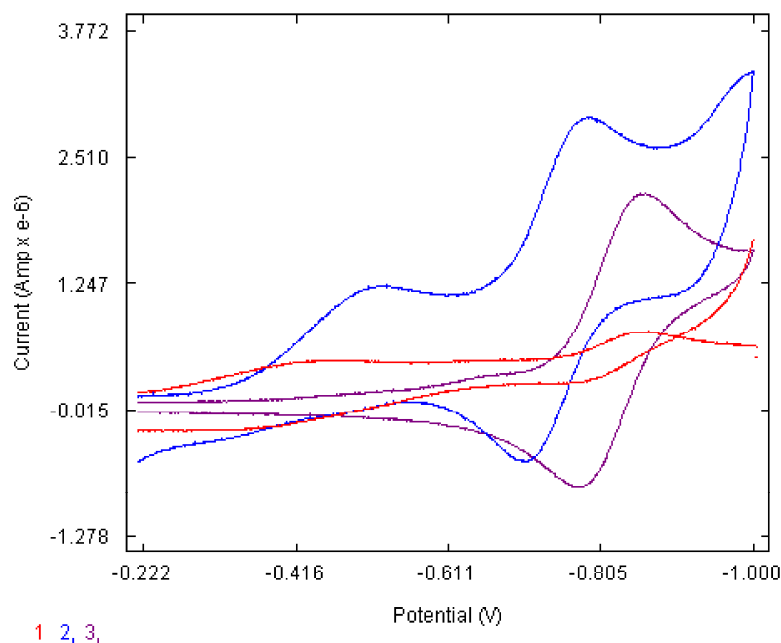


Figure 4.20: Overlaid CVs of $[\text{Cu}(\text{I})_2\text{HL8}(\text{PPh}_3)_5]\text{PF}_6$ (-), $[\text{Cu}(\text{II})\text{L8}(\text{H}_2\text{O})_2]$ (-) and NaHL8 (-) in DMSO over the potential range from -0.2 V to -1.0 V at the scan rate of 10 mV s^{-1} (arrow represents the direction of the potential varied)

Table 4.5: Redox peak potentials of NO_2 reported versus SCE, (^a measured versus Ag/AgCl)

	NO_2 in $[\text{Cu}(\text{I})_2\text{HL8}(\text{PPh}_3)_5]\text{PF}_6$ (V)	NO_2 in $\text{Cu}(\text{II})\text{L8}(\text{H}_2\text{O})_2$ (V)	NO_2 in NaHL8 (V)	Ferrocene (V)
E_c	- 0.91 (-0.86 ^a)	- 0.84 (-0.79 ^a)	- 0.91 (-0.86 ^a)	+ 0.47 (0.51 ^a)
E_a	- 0.83 (-0.79 ^a)	- 0.76 (-0.71 ^a)	- 0.82 (-0.77 ^a)	+ 0.39 (0.43 ^a)
ΔE	0.071	0.078	0.089	0.079
$E_{1/2}$	- 0.87 (-0.04 ^a)	- 0.80 (-0.75 ^a)	- 0.87 (-0.76 ^a)	+ 0.43 (0.47 ^a)

The ΔE value suggests that the aromatic NO_2 -substituent undergoes a one electron reduction process to give NO_2^- ²⁷¹. In $\text{Cu}(\text{I})$ complex, the $E_{1/2}$ for NO_2 is similar to that of NaHL8 . Whereas, in case of $\text{Cu}(\text{II})$ complex they are shifted towards positive potentials, implying that the NO_2 is more easily reduced in the $\text{Cu}(\text{II})$ complex than in the $\text{Cu}(\text{I})$ complex.

It is noteworthy, that the two $\text{Cu}(\text{I})$ centres in the dimeric copper complex appear to exhibit identical redox properties, as no distinguishable redox processes

could be observed. The higher ΔE value for Cu(I) complex of NaHL9 (0.22 V) and Cu(I) complex of NaHL8 (0.22 V) can be due to the quasi-reversible behaviour and/or presence of more than one Cu(I) centres. Furthermore, when compared with investigated Cu(II) and Cu(I) complexes, it is observed that the CVs of the Cu(I) complexes have fewer redox waves than the corresponding Cu(II) complexes. This may indicate that the Cu(I) complexes are less flexible in adopting intermediate geometries in the solution as compared to the Cu(II) complexes. This is perhaps likely due to bulkier PPh₃ groups surrounding Cu(I) centre, making it difficult to change geometry drastically during structural reorganisation of the copper centre. Hence, the metal based redox waves observed in Cu(I) complexes are more well defined as compared to the broad peaks of Cu(II) complexes.

Both the Cu(I) complexes of NaHL8 and NaHL9 show similar behaviour as can be seen from figure 4.21, when scanned in the limited potential range of +1.0 and 0.5 V. The voltammogram in red corresponds to free PPh₃ and the peaks can be assigned to the processes related to PPh₃ cation (equation 4.6).²⁷²⁻²⁷³ The cathodic and anodic peak potentials of PPh₃, observed at -0.45 V and -0.37 V, respectively, are absent when the phosphine is coordinated to the Cu(I) centre.

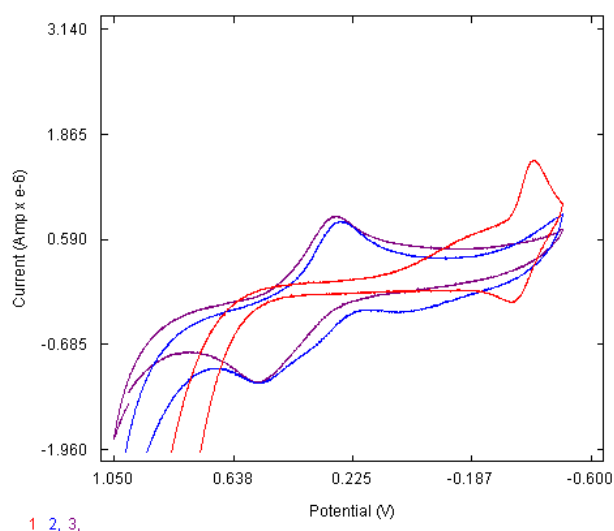


Figure 4.21: Overlaid CV of [Cu(I)₂HL8(PPh₃)₅]PF₆ (-), [Cu(I)₂HL9(PPh₃)₅]PF₆ (-) and TPP (-) in the DMSO over the potential range from +1.0 V to -0.6 V at the scan rate of 50 mV s⁻¹

4.2.2.3 Comparing electrode potentials of Cu(II) complexes of PVAHs

The Cu(II) complexes of the other ligands NaHL1, NaHL3, NaHL10, NaHL12, NaHL16, NaHL21 displayed electrochemical behaviour similar to [Cu(II)L8(H₂O)₂] and [Cu(II)L9(H₂O)₂].

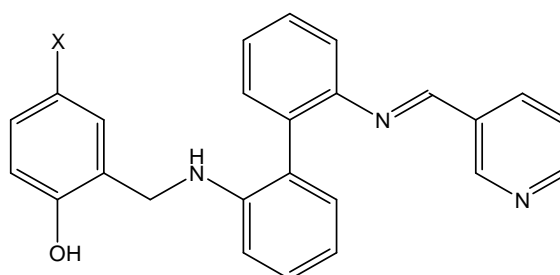
Anodic and cathodic peak potentials of selected Cu(II) complexes of PVAHs along with CuCl₂ are listed in table 4.6. The anodic peak potential and the cathodic potential for the pyruvate hydrazone copper complexes are observed in the range of 0.23 V-0.25 V and 0.41-0.52 V at a scan rate of 100 mV (table 4.6). However, in case of CuCl₂, the potentials are observed at 0.22 V and 0.53 V, respectively. The larger range for cathodic peak potentials (0.41-0.52 V) is due to the broadness of the peak associated with Cu²⁺ → Cu¹⁺. The anodic peak potential assigned to Cu¹⁺ → Cu²⁺ for CuCl₂ in DMSO falls below 0.20 V when compared with pyruvate hydrazone copper complex. Hence, it is quite evident that the ligand environment around the Cu(II) centres in free Cu ion (CuCl₂) and the Cu(II) complexes of PVAHs is not same.

Most of the studied copper complexes give similar E_{pa} values at a particular scan rate and these differ significantly from that of CuCl₂. Hence, the redox potentials of the Cu(II) complexes of investigated PVAHs are similarly affected by their surrounding ligand system and the different substituents on the aromatic ring of the PVAHs does not have significant influence on the electrode potentials. Similar observations were reported by Tas and group, where the E_{1/2} values of copper Schiff base complexes were independent of substituents on the aromatic ring, falling in the range 0.86 - 0.88 V vs SCE in DMSO.²⁷⁴

Table 4.6: E_{pa} and E_{pc} values for copper complexes at a scan rate of 100 mV s⁻¹ reported versus SCE

Molecular formula	R	E_{pa} (V)	E_{pc} (V)
Cu(II)Cl ₂ .2H ₂ O		0.18	0.49
[Cu(II)L1(H ₂ O) ₂]	H	0.23	0.39
[Cu(II)L3(H ₂ O) ₂]	<i>m</i> -OH	0.23	0.41
[Cu(II)L10(H ₂ O) ₂]	<i>m</i> -Br	0.23	0.41
[Cu(II)L12(H ₂ O) ₂]	<i>m</i> -OCH ₃	0.23	0.44
[Cu(II)L21(H ₂ O) ₂]	Heterocyclic N at 2,5	0.23	0.39
[Cu(II)L8(H ₂ O) ₂]	<i>p</i> -NO ₂	0.23	0.42
[Cu(II)L9(H ₂ O) ₂]	<i>p</i> -CH ₃	0.25	0.52

On the other hand, Chen and group found that the electron withdrawing nitro group and the electron donating methyl group significantly affects the copper centre electrode potentials. The electrochemical properties of square pyramidal Cu(II) Schiff base complexes containing 2-aminopyridine-2-aminobiphenyl (N₃O-mpy) ligand (figure 4.22) were investigated against in acetonitrile Ag/AgCl electrode. The $E_{1/2}$ values for the quasi-reversible peak potentials for the Cu²⁺/ Cu¹⁺ wave for complex-1 (with CH₃) 0.24 V, whereas for complex -2 (NO₂) it is 0.54 V against SCE.²⁷⁵ While, the $E_{1/2}$ values for Cu(II) complexes of PVAHs are 0.32 V (CH₃) and 0.38 (NO₂). The smaller change observed in case of Cu(II) complexes of PVAHs as compared to Cu(II) complexes of N₃O-mpy can be attributed to ligand system or electrochemical solvent used.



X= CH₃, NO₂

Figure 4.22: Structure of 2-aminopyridine-2-aminobiphenyl (N₃O-mpy)²⁷⁵

Due to the similarity of the Cu-centred redox processes in the complexes under investigation, further studies were required to ascertain the identity and confirm the stability of the complexes in DMSO solution. Hence, electron paramagnetic resonance (EPR) studies were carried out on selected Cu(II) complexes of PVAHs which will be discussed further in the following section.

4.3 Electron Paramagnetic Resonance (EPR) studies:

Cu(II) contains one unpaired electron in the 3d shell, with $S = \frac{1}{2}$, hence it is suitable for EPR spectroscopy. The spectra discussed below were recorded in frozen DMSO at 77K and were referenced against the standard diphenylpicrylhydrazyl (DPPH) radical at a concentration of 1 mM. The EPR data of frozen solutions of selected complexes, $[\text{Cu(II)L8(H}_2\text{O)}_2]$, $[\text{Cu(II)L13(H}_2\text{O)}_2]$, $[\text{Cu(II)L16(H}_2\text{O)}_2]$, $[\text{Cu(II)L14(H}_2\text{O)}_2]$ were compared with the spectra of CuCl_2 and CuSO_4 recorded under the same conditions.

4.3.1 EPR spectra of CuSO_4 and $[\text{Cu(II)L14(H}_2\text{O)}_2]$

$^{63,65}\text{Cu(II)}$, has nuclear spin quantum number (I) of $\frac{3}{2}$, hence it should give rise to 4 hyperfine splittings, as given by $2nI+1$.²⁷⁶ This is true for Cu(II) complexes when there are no interactions with the neighbouring atoms and is observed for CuSO_4 and CuCl_2 . The EPR spectrum of CuSO_4 is given in Figure 4.23. Whereas, in case of the studied Cu(II) complexes of PVAHs the spectra only show three lines. The EPR spectrum of $[\text{Cu(II)L14(H}_2\text{O)}_2]$ is shown as a representative example in figure 4.24. The spectrum indicates coordination of the Cu(II) centre to the donor atoms of PVAHs.

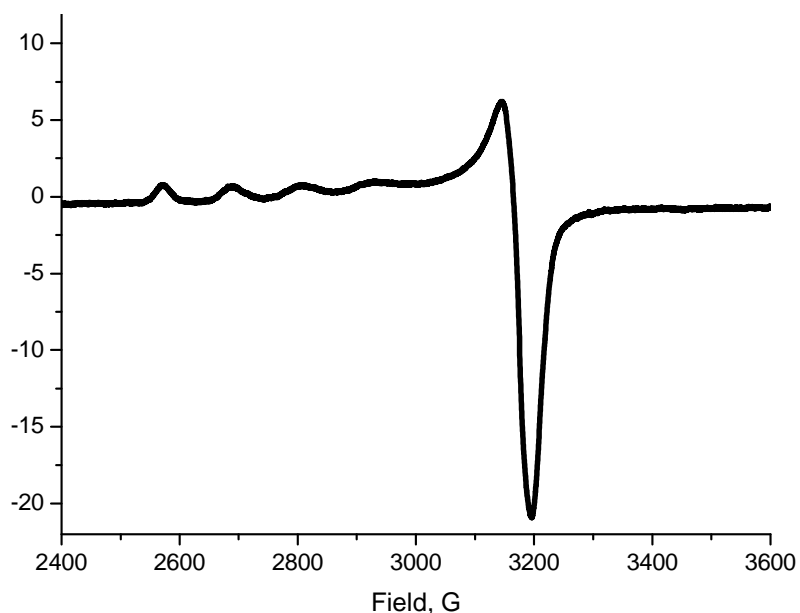


Figure 4.23: X-band EPR spectrum of a frozen solution of CuSO_4 in DMSO

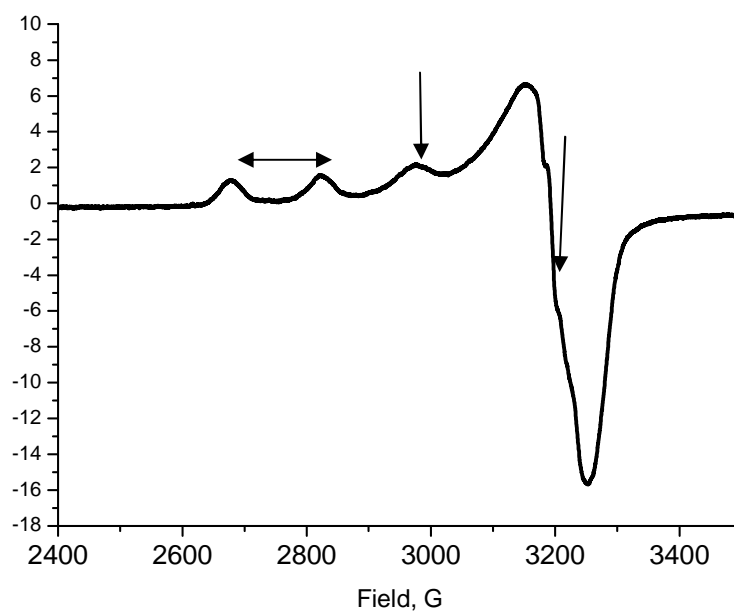


Figure 4.24: X-band EPR spectrum of a frozen solution of $[\text{Cu(II)L14(H}_2\text{O)}_2]$ in DMSO

4.3.2 Comparison of EPR spectra of investigated Cu(II) complexes of PVAHs

The overlaid spectra of Cu(II) complexes of ligands NaHL8, NaHL13, NaHL14 and NaHL16 are shown in figure 4.25. It is evident that electron donating or electron withdrawing substituents do not have a significant effect on the Cu(II) centre, resulting in similar EPR spectra. $[\text{Cu(II)L16(H}_2\text{O)}_2]$ gives a less intense spectrum as compared to other three complexes. This can be due to the precipitation of the complex in the polar aprotic DMSO solution as it possesses hydrophobic tertiary group on the aromatic ring.

The EPR parameters g_{\parallel} and g_{\perp} can be calculated using the equation, $g = hv / (\beta H)$, where h is the Planck constant, ν is the microwave frequency at which the EPR machine operates, H is the resonance magnetic field (G) and β is the Bohr magneton. A_{\parallel} is the distance between two parallel peaks as shown in figure 4.24, whereas A_{\perp} cannot be determined as the peaks were not very well resolved for perpendicular lines.

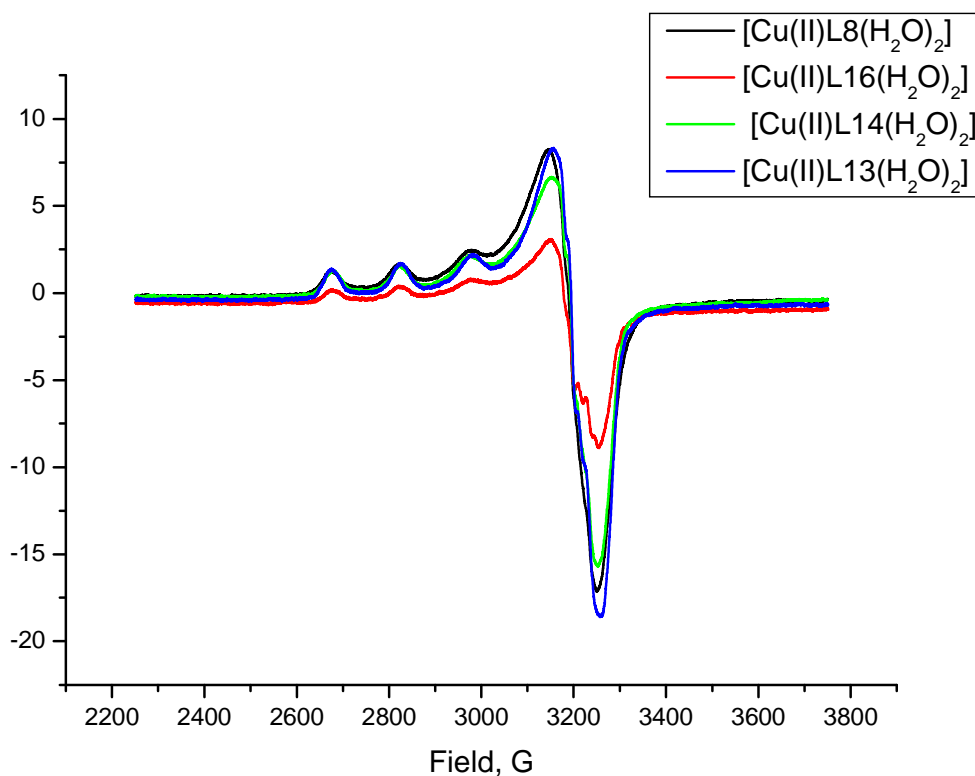


Figure 4.25: Overlaid X-band EPR spectra of $[\text{Cu}(\text{II})\text{L8}(\text{H}_2\text{O})_2]$, $[\text{Cu}(\text{II})\text{L13}(\text{H}_2\text{O})_2]$, $[\text{Cu}(\text{II})\text{L16}(\text{H}_2\text{O})_2]$, $[\text{Cu}(\text{II})\text{L14}(\text{H}_2\text{O})_2]$

The EPR parameters (A_{\parallel} , g_{\parallel} and g_{\perp} value) are listed in table 4.7. It can be seen that both CuSO_4 and CuCl_2 have a value of $g_{\parallel} \geq 2.3$, whereas for the complexes under study the value $g_{\parallel} < 2.3$. Kivelson and co-workers have reported that the compounds having $g_{\parallel} \geq 2.3$ are ionic in nature, while those with $g_{\parallel} < 2.3$ have covalent character²⁷⁷. In addition the EPR parameters for CuSO_4 and CuCl_2 are very similar, which might be due to formation of CuXDMSO ($X=\text{Cl}/\text{SO}_4$) solvated species in DMSO ²⁷⁸.

It is established that, the hydrazones hydrolyse under extreme acidic conditions, which may lead to decomplexation of the copper. This was also reflected in the EPR spectra of $[\text{CuL13}(\text{H}_2\text{O})_2]$ at acidic $\text{pH} < 1.5$. In acidic pH , the spectra started to shift towards free Cu (CuSO_4) as indicated in figure 4.26. Furthermore, the g and A values are similar to those of CuCl_2 and CuSO_4 , which indicates that the DMSO coordinates to the free $\text{Cu}(\text{II})$ ion once its released from the ligand. In order to throw more light on the stability of the copper complexes, detailed investigation of selected PVAHs and their copper complexes at different pH conditions is discussed in chapter-5.

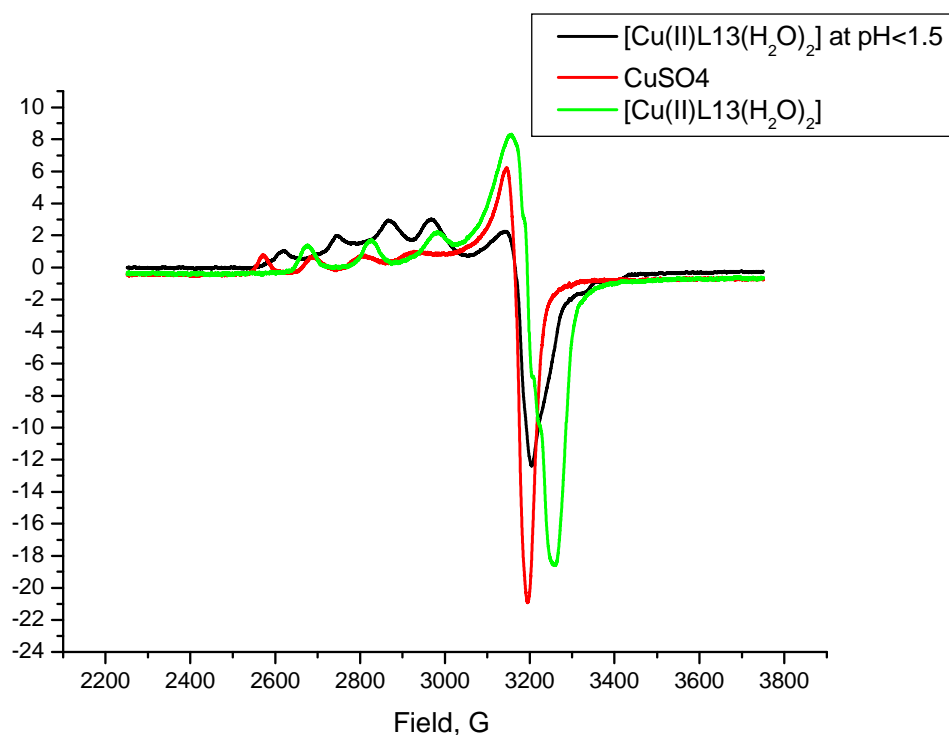


Figure 4.26: Overlaid X-band EPR spectra of CuSO_4 (red), $[\text{Cu}(\text{II})\text{L13}(\text{H}_2\text{O})_2]$ (green), and $[\text{Cu}(\text{II})\text{L13}(\text{H}_2\text{O})_2]$ at $\text{pH} < 1.5$ (black)

The EPR parameters of $\text{Cu}(\text{II})$ complexes listed in table 4.7 are in consistent with the reported literature values for $\text{Cu}(\text{II})$ Schiff base complexes.²⁷⁹⁻²⁸⁰ The expected g value for a free unpaired electron is 2.0023. Deviation of g value from 2.0023 in metal complexes indicates the coupling of metal orbital's containing unpaired electron with either filled or empty ligand orbitals involved in molecular orbitals.

Table 4.7: EPR data for selected for selected Cu(II) complexes of PVAHs

Complex	R	g_{\perp}	g_{\parallel}	$A_{\parallel} \times 10^{-4}$ cm^{-1}	$f(\alpha)$ cm
[CuL8(H ₂ O) ₂]	<i>p</i> -NO ₂	2.062	2.273	159	143
[CuL16(H ₂ O) ₂]	<i>p</i> - <i>tert</i> - butyl	2.077	2.293	161	142
[CuL14(H ₂ O) ₂]	<i>p</i> -CF ₃	2.068	2.275	159	143
[CuL13(H ₂ O) ₂]	<i>p</i> -OCH ₃	2.064	2.279	160	142
[CuL13(H ₂ O) ₂] at pH > 1.5	<i>p</i> -NO ₂	2.083	2.360	132	179
CuSO ₄	-	2.083	2.400	129	186
CuCl ₂	-	2.090	2.400	127	189

Furthermore, $g_{\parallel} > g_{\perp} > 2$ indicates a tetragonally elongated Cu(II) complex which is expected due to Jahn-Teller distortion along the z axis.²⁸¹ X-ray crystal structures of square pyramidal Cu(II) complexes discussed in chapter-3 gives a evidence in the solid state structure, where the apical coordinate bond distance is considerably longer than the basal Cu-O/N bond distances. In addition, g and A can also be useful in elucidating the degree of tetrahedral distortion of square planar complexes in solution. The degree of distortion is given by the equation 4.7.

$$f(\alpha) = (g_{\parallel} / A_{\parallel}) \dots \dots \dots (4.7)$$

For ideal square planar complexes the values lies in the range 110-120 cm, while 130-150 cm indicates slight to moderate distortion and 180-250 cm signifies large distortion. The values for Cu(II) complexes PVAHs is around 150, which indicates that, there is a moderate distortion from the planar complex due to rigidity of the tridentate hydrazone ligand. However, for copper salts (CuSO₄ and CuCl₂) it is $\sim 200 \text{ cm}^{-1}$ which implies that the copper salts show considerable distortion which may be accounted to the flexibility of monodentate ions (Cl⁻, SO₄²⁻, solvent).²⁸²

4.4 Summary of Chapter 4

The investigated PVAH ligands are redox inactive except for NaHL8, which exhibits reversible redox peaks corresponding to the $-\text{NO}_2$ substituent. The electrochemical studies indicate that there are copper centred redox processes corresponding to the conversion of Cu(II) to Cu(I) and vice-versa. Peaks corresponding to $\text{Cu}^{1+}/\text{Cu}^0$ have also been observed, where the investigated Cu(II) complexes are reduced to Cu(0), through the Cu(I) intermediate. The redissolution of Cu(0) deposited on the electrode surface leads to higher anodic peak current as compared to its corresponding cathodic peak current. The corresponding peaks are observed in both the Cu(I) and Cu(II) complexes, but they are more well defined in case of the Cu(I) complexes.

The ΔE value of Cu(I) and Cu(II) complexes corresponding to $\text{Cu}^{2+}/\text{Cu}^{1+}$ indicates quasi-reversible behaviour and also the additional multiple peaks observed may be accounted to the presence of more than one species present in solution. This is likely due to structural reorganisation taking place within the coordination sphere whilst changing from a Cu(II) square-pyramidal to a tetrahedral Cu(I) complex geometry. The E_{p_a} values of Cu(II) complexes indicate that the PVAH ligand affects the metal-based redox peaks, irrespective of substituent on the aromatic ring.

Similarly, the EPR parameters, A_{\parallel} , g_{\parallel} and g_{\perp} are similar for studied Cu(II) complexes of PVAHs, but distinct from 'free' Cu(II) ions (CuCl_2 , CuSO_4). Hence, it can be concluded from the EPR studies that the ligands remain bound to the Cu(II) centre, even though there is large excess of DMSO present in solution.

Chapter-5

Stability studies and Antitubercular studies

5.0 Stability studies and Antitubercular activity

5.1 Introduction

Pyruvate hydrazones (PVAHs) and their metal complexes have been extensively studied in the past for their coordination properties,^{227,229,283-285} however, little is known about their antitubercular activity. Recent computational studies have illustrated that pyruvate hydrazones may inhibit the active site of isocitrate lyase of *M. tuberculosis* (Mtb).⁸⁴ As discussed in chapter-1, several hydrazones derived from other aldehydes/ketones and their respective metal complexes have previously been investigated for their potential activity against Mtb.^{78,80-81,85-87}

The presence of O, N and S donor sites in these hydrazone ligands allows the chelation to essential metal ions thereby disrupting physiological processes relying on these essential metal ions in bacteria. For example sequestration of Fe(III) or Fe(II) can lead to iron starvation in bacteria.⁷⁹ Metal-containing antitubercular agents have been reported to possess excellent antimycobacterial activity, with some complexes even retaining activity against resistant strains.²⁸⁶ Since certain bacterial resistance mechanisms are modulated by intracellular oxidative stress,⁴¹ the redox activity of the metal centres of metallodrugs is significant.

This chapter describes the testing of pyruvate hydrazones (PVAHs) and their Cu(II) and Zn(II) complexes against Mtb. grown in Middlebrook 7H9 medium. All the antitubercular studies discussed in this chapter were done by Dr. Manjula Sritharan's research group at the Department of Animal Sciences, University of Hyderabad, India. Furthermore, the compounds exhibiting promising antitubercular activities in terms of low minimum inhibitory concentration (MIC) values were further screened under high iron (8 µg Fe(II)/mL) and low iron (0.02 µg Fe(II)/mL) conditions.

As discussed in chapter-2, the azomethine bond in hydrazones is more prone to hydrolysis under extreme acidic and basic conditions. In acidic conditions, the nitrogen of the azomethine bond becomes protonated, which makes the carbon more susceptible to the attack by a water molecule and in turn cleaves the C=N bond. In basic conditions, the electrophilic azomethine carbon can be attacked by a nucleophile (OH⁻) which makes it prone to hydrolysis. In order to gain insight into the stabilities of the compounds in aqueous solution, their UV-visible spectra were

recorded at a range of pH values. Moreover, the stability of the compounds was also examined in PBS (phosphate buffered saline) whilst maintaining the solution at 37 °C and at the biological pH of 7.4, which could possibly allow a comparison with physiological conditions in human plasma.²⁸⁷

5.2 Stability studies of PVAHs and CAHs and their metal complexes at different pH

A drug can be administered into the body using different routes, including oral, injection, epithelial and inhalation. The preferred method is usually oral administration of a drug, which involves passing the drug through the gastrointestinal tract (GIT) consisting of mouth, throat, stomach and intestines. The pH varies at different parts of the body, for example in the mouth the pH of saliva is slightly acidic to neutral (pH 6.5 to pH 7.5). In the lower stomach it is extremely acidic (pH 1.5), whereas in the intestines the pH ranges from pH 5 – 7. Oral bioavailability then refers to the fraction of the orally taken drug reaching the blood (pH 7.4). Bioavailability is the term used in drug pharmacokinetics, which implies the concentration of a drug reaching the blood supply after absorption, distribution, metabolism and excretion, collectively abbreviated as ADME.²⁸⁸ Hence, the stability of a compound at different pH plays an important role in drug discovery. An orally effective drug should be stable at the extremely low pH of the stomach; hence the stability of a compound under different pH conditions plays a vital role in deciding the mode of administration of a drug.

Hydrazones of biological relevance have been investigated before in order to determine their pK_a values and stability towards hydrolysis in basic and acidic conditions. UV-Vis studies conducted by Richardson *et al.* indicate that the rate of hydrolysis of pyridoxal isonicotinic hydrazone (PIH) and pyridoxal benzoyl hydrazone (PBH) occurs at a faster rate in extreme acidic and basic conditions, whereas it is very slow in neutral pH.²⁸⁹ Potentiometric titrations revealed that the pK_a of the amide proton of these hydrazones varies from 9.94 to 11.40, depending on the R group present in the respective hydrazone.²⁹⁰ These type of ligands can strongly bind to Cu(II), for example the formation constant (K_c) of the Cu(II)-salicylaldehyde acetylhydrazone complex is reported to be 16.2, as expected for a Cu(II) complex of a tridentate ligand.²⁹¹

PVAHs, CAHs and their metal complexes are designed for their antitubercular potential, hence it is essential to investigate the stability of these compounds. Therefore, the behaviour of selected compounds from the PVAH, CAH series, mainly those which exhibited potential antitubercular activity, were investigated at different pH. The change was monitored using UV-visible absorption spectroscopy. As discussed above, hydrazones hydrolyse at a faster rate at extremely low and high pH, hence two sets of titrations were performed. The compounds under investigation (0.05 mM for PVAHs and 0.02 for CAHs) were dissolved in water and were titrated with 0.01 M HCl (acid titration) and 0.01 M NaOH (base titration) and the spectral changes were recorded manually using a UV-vis spectrophotometer at regular intervals. Experimental details of the UV-vis studies can be found in chapter-7. However, for those compounds which exhibited limited solubility in water, a mixture of solvents (DMSO/MeOH: H₂O) were used.

5.2.1 Stability studies of NaHL20 and its Cu(II) and Zn(II) complexes

NaHL20 and its respective Cu(II) and Zn(II) complexes were investigated for their stability in water at pH values ranging from 1 to 12. Overlaid UV spectra of NaHL20 and its respective Cu(II) and Zn(II) complexes along with the starting material, pyrazinoic acid hydrazide, are depicted in figure 5.2, whereas the corresponding structures are provided in figure 5.1. The spectra were recorded in HEPES buffer at pH 7.4 with concentration of 0.05 mM.

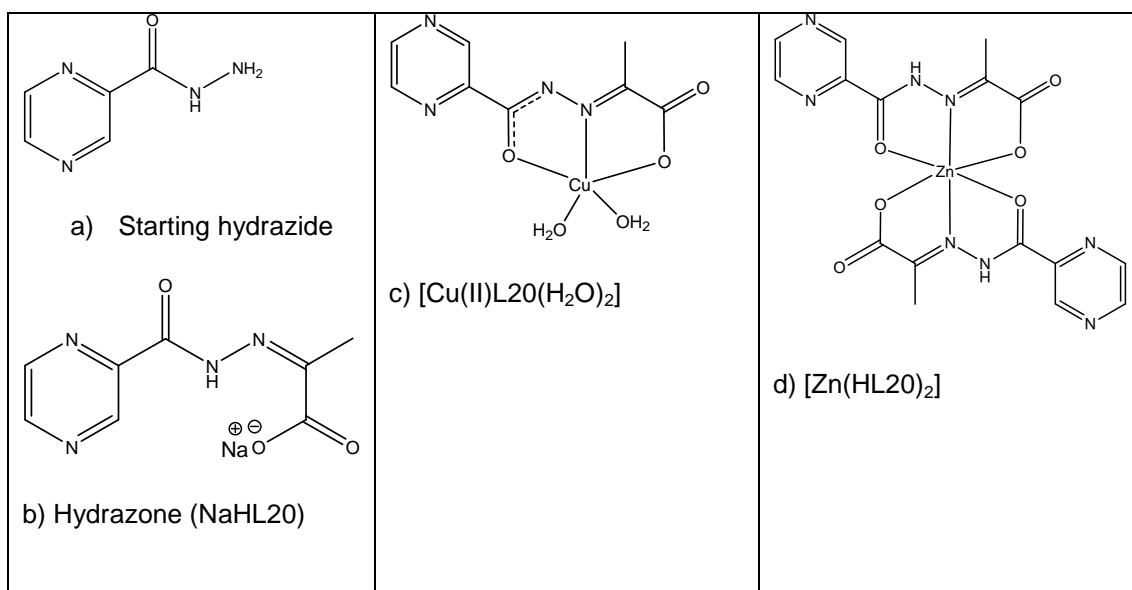


Figure 5.1: Structures of a) the starting hydrazide b) the hydrazone NaHL20 c) the Cu(II) complex and d) the Zn(II) complex of NaHL20

Both the hydrazone (NaHL20) and its starting hydrazide (pyrazinoic acid hydrazide) exhibit two distinct bands at 212 nm and 270 nm. The absorption maxima (λ_{max}) for the electronic transitions observed at 212 nm for NaHL20 ($\epsilon = 19.5 \times 10^3 \text{ dm}^3 \text{ mol}^{-1} \text{ cm}^{-1}$) and pyrazinoic acid hydrazide ($\epsilon = 11.2 \times 10^3 \text{ dm}^3 \text{ mol}^{-1} \text{ cm}^{-1}$) can be assigned to $\pi\text{-}\pi^*$ transitions. The higher absorption coefficient of NaHL20 may result from the greater π -conjugation of the hydrazone due to the additional azomethine bond (C=N) compared to the hydrazide. Furthermore, the band at 270 nm can be attributed to $\pi\text{-}\pi^*$ transitions of the C=O bond in the hydrazide ($\epsilon = 9.98 \times 10^3 \text{ dm}^3 \text{ mol}^{-1} \text{ cm}^{-1}$). The resultant broad band at 270 nm in NaHL20 can be assigned to overlapped C=N and C=O $\pi\text{-}\pi^*$ transitions ($\epsilon = 15.7 \times 10^3 \text{ dm}^3 \text{ mol}^{-1} \text{ cm}^{-1}$).

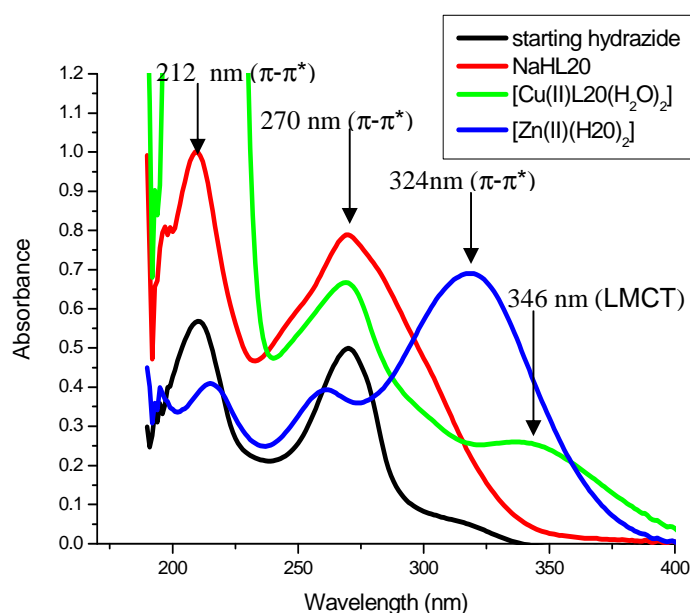


Figure 5.2: Electronic absorption spectra recorded for hydrazide (black spectrum), NaHL20 (red spectrum) and its Cu(II) (green spectrum) and Zn(II) complex (red spectrum) in HEPES buffer at pH 7.4 and a concentration of 0.05 mM

In the spectrum of the Zn(II) complex, [Zn(II)(HL20)₂] (blue spectrum, figure 5.2), two absorption bands attributed to $\pi\text{-}\pi^*$ transitions were observed at 268 nm ($\epsilon = 7.45 \times 10^3 \text{ dm}^3 \text{ mol}^{-1} \text{ cm}^{-1}$) and 324 nm ($\epsilon = 13.5 \times 10^3 \text{ dm}^3 \text{ mol}^{-1} \text{ cm}^{-1}$). Although, the $\pi\text{-}\pi^*$ transitions at 268 nm exhibits a slight blue shift as compared to NaHL20 (270 nm), the $\pi\text{-}\pi^*$ transitions show a small red shift and appear at 215 nm ($\epsilon = 13.5 \times 10^3 \text{ dm}^3 \text{ mol}^{-1} \text{ cm}^{-1}$).⁶ In the Cu(II) complex, [Cu(II)L20(H₂O)₂] (green spectrum,

figure 5.2), an additional moderately intense band is observed at 346 nm ($\epsilon = 5.01 \times 10^3 \text{ dm}^3 \text{ mol}^{-1} \text{ cm}^{-1}$), which might be due to ligand to metal charge transfer (LMCT) transitions and can be assigned to $\text{O} \rightarrow \text{Cu(II)}$, which is usually observed in copper Schiff base complexes.^{7, 8} Moreover, $\text{Cu(II)L20(H}_2\text{O)}_2$ exhibits similar $\pi\text{-}\pi^*$ transitions at 270 nm ($\epsilon = 13.3 \times 10^3 \text{ dm}^3 \text{ mol}^{-1} \text{ cm}^{-1}$) to that of NaHL20.

5.2.2.1 Stability studies of NaHL20 at different pH

NaHL20 (0.05 mM) dissolved in water, exhibits the absorption maximum (λ_{max}) at 270 nm ($\epsilon = 11.46 \times 10^3 \text{ dm}^3 \text{ mol}^{-1} \text{ cm}^{-1}$) as depicted in figure 5.3. The absorbance at 270 nm was monitored in order to investigate the stability of NaHL20 in solution as this electronic absorption band is associated with $\pi\text{-}\pi^*$ of azomethine bond as discussed above. A change of pH from 4.34 to 1.48 does not seem to have a significant effect on the position of the ligand absorption band, as seen in figure 5.3. As the absorption maximum of the $\pi\text{-}\pi^*$ transitions band for the parent hydrazide and its respective hydrazone are similar, it cannot be accurately determined from the band position when hydrolysis occurs. Additionally, the hydrolysis may also occur when dissolved in water, as water triggers the hydrolysis reaction.

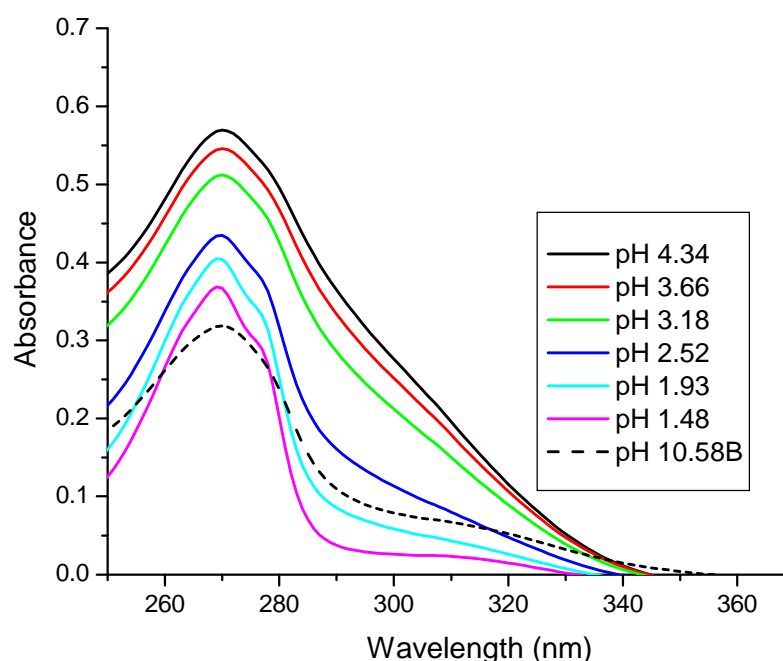


Figure 5.3: Electronic absorption spectra recorded for NaHL20 during acid titration using 0.01 M HCl in the pH range 1.4-4.4

However, as can be seen from figure 5.3, there is a decrease in the intensity of the band at 270 nm as the pH is lowered (pH 1.48, figure 5.3). In addition, the broad band tends to get narrower going towards extreme acidic conditions comparable to parent hydrazide. This indicates hydrolysis at low pH. The compound remains hydrolysed even after back titrating to extreme basic pH 10.58 (dashed spectrum 10.58B, figure 5.3) indicating an irreversible process. To gain more insight into hydrolysis of NaHL20, a plot of absorbance at 300 nm is illustrated in figure 5.4. The decrease in the absorbance values at 300 nm towards acidic pH values (pH 4.33 → pH 1.98) indicates hydrolysis of NaHL20 to the starting hydrazide.

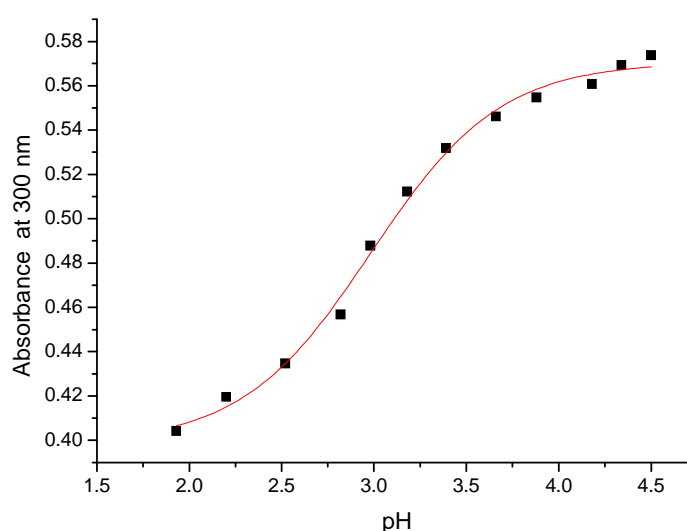


Figure 5.4: Titration curve obtained for NaHL20 at 300 nm during acid titration in the pH range 1.4-4.4

NaHL20 was also investigated under basic conditions. The spectra recorded with increasing pH (basic) are shown in figure 5.5, which indicates that there is not a significant change in the overall shape of the UV spectra up to a pH of approximately 10.

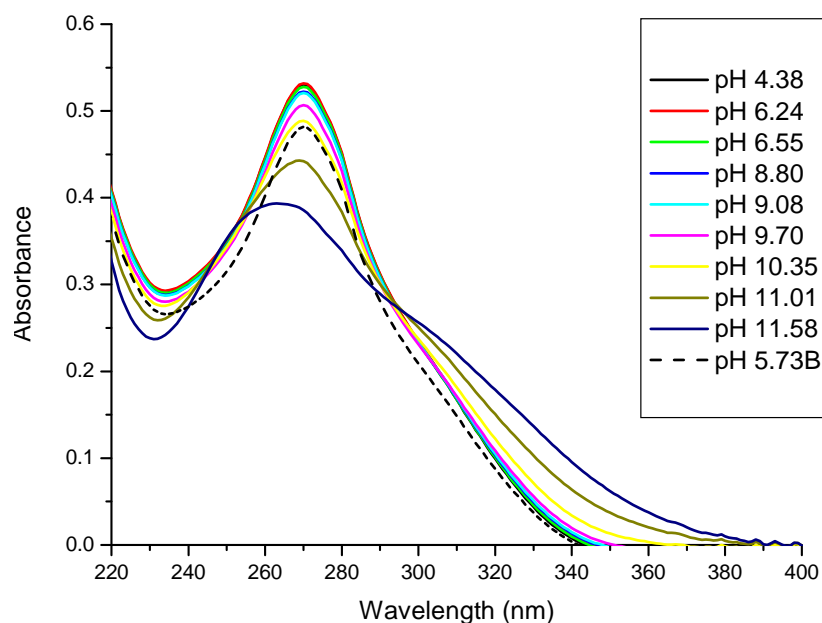


Figure 5.5: Electronic absorption spectra recorded for NaHL20 during base titration using 0.01 NaOH in the pH range 4.3-11.6

The absorbance at 310 nm tends to increase with increase in pH above pH 10, as indicated in figure 5.6. However, the original spectra is regained when the solution is back titrated to 5.73 (dashed spectrum 5.73B, figure 5.5). This indicates that the chemical process is reversible and may be associated with the deprotonation of the hydrazone. The pKa of the amide proton (N-H) is around 11 and is consistent with the literature.²⁹⁰

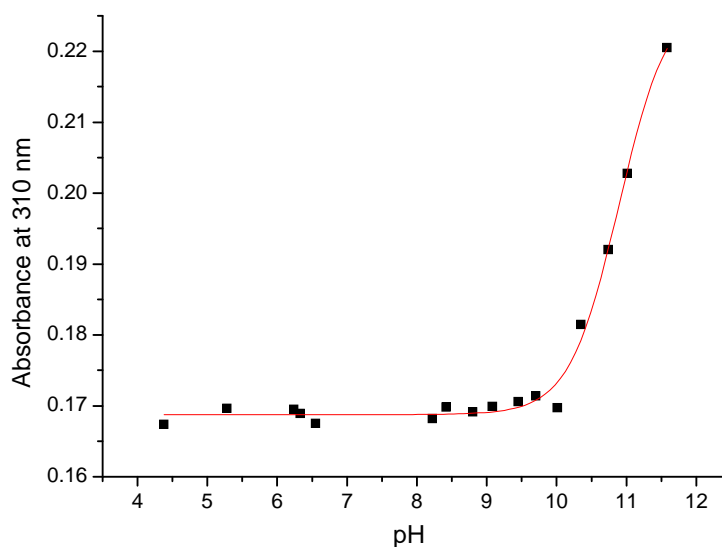
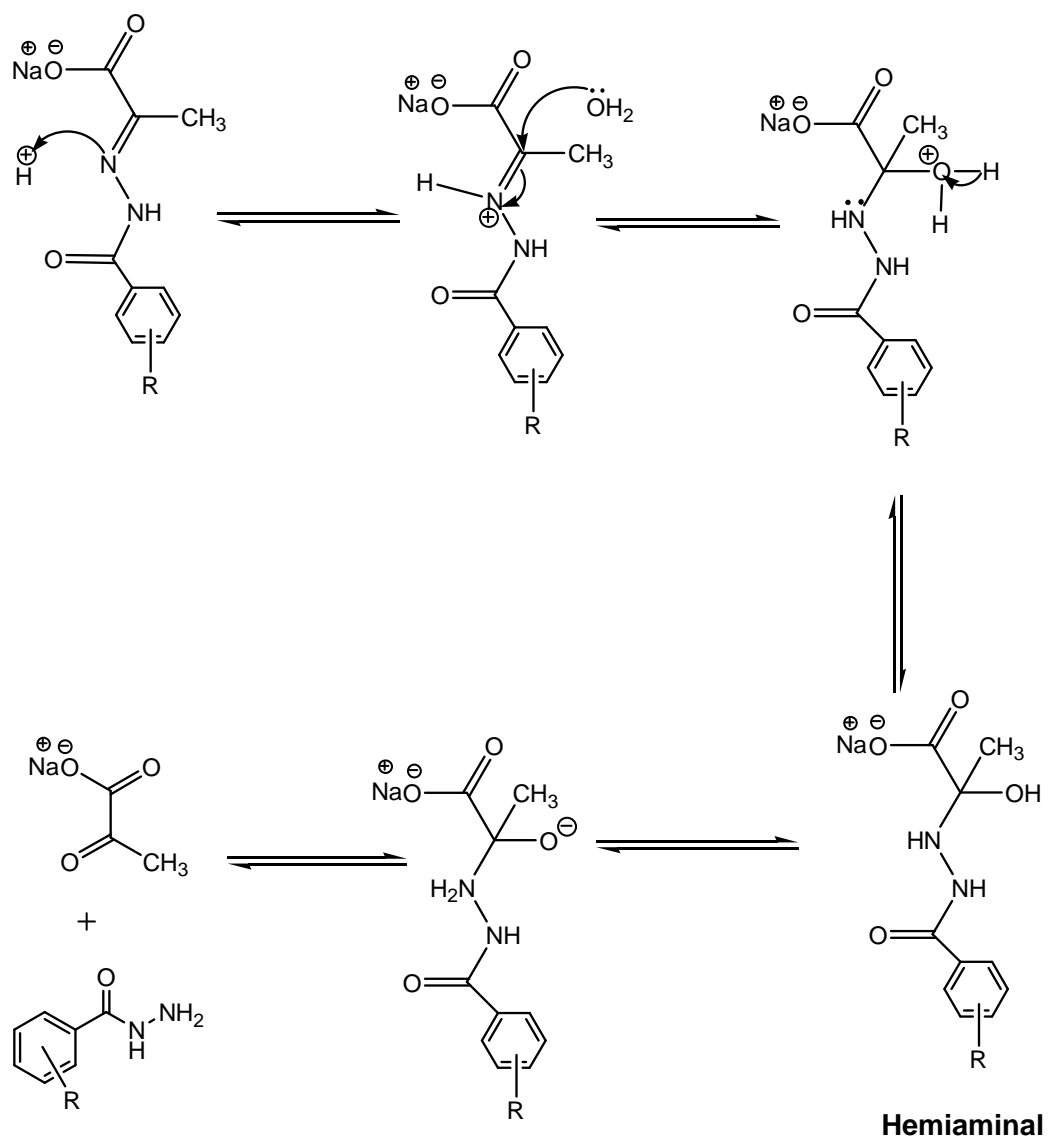


Figure 5.6: Titration curve obtained for NaHL20 at 310 nm during base titration using 0.01 NaOH in the pH range 4.3-11.6

It can be concluded that NaHL20 undergoes irreversible hydrolysis in aqueous solution below pH 4, whereas it remains stable under basic conditions. These observations confirm earlier reports on hydrolysis under acidic conditions.²⁸⁹ Moreover, hydrazones with N as heteroatom and also those with electron-withdrawing groups on the aromatic ring undergo hydrolysis at a faster rate than other hydrazones possessing electron donating group. This was illustrated by Buss and Ponka¹⁸⁰, where they studied the stability of acyl hydrazones in PBS buffer at pH 7.4 and 37 °C. Hydrazones possessing an isonicotinic ring (PIH) exhibit rate of hydrolysis at $8.2 \times 10^3 \text{ min}^{-1}$. While the hydrazone possessing benzoyl hydrazone ring (PBH) have a rate constant of $2.1 \times 10^3 \text{ min}^{-1}$. This is due to the electron withdrawing effect of the pyridine ring, which is expected to decrease electron density on the imine carbon atom through the highly conjugated system.

The hydrolysis occurs at C=N imine bond, as confirmed by Raines and his group.¹⁸² Raines *et al.* also observed that the rate of hydrolysis is very slow at pH 7. The mechanism of hydrolysis of PVAHs is given in scheme 5.1. The reaction is initiated by the addition of a proton to the azomethine nitrogen, followed by an attack of a water molecule on the electrophilic azomethine carbon. The reaction gives rise to the starting materials sodium pyruvate and hydrazide *via* the formation of a hemiaminal intermediate and can be classified as a reversible mechanism.

Scheme 5.1: Mechanism for hydrolysis of PVAHs¹⁸²

5.2.1.2 Stability of the $[\text{Cu(II)L20(H}_2\text{O)}_2]$ at different pH

The stability of the Cu(II) complex of NaHL20, $[\text{Cu(II)L20(H}_2\text{O)}_2]$, was also investigated at a range of different pH values. The band with absorption maximum (λ_{max}) at 346 nm at pH 5.80, decreases in intensity whilst titrating from pH 5.8 to pH 2.46, as shown in figure 5.7. This decrease might be due to the dissociation of the copper complex.

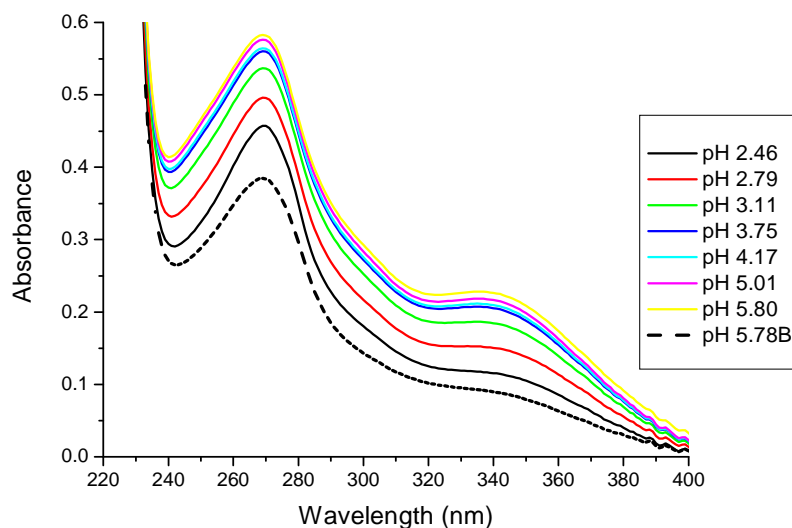


Figure 5.7: Electronic absorption spectra recorded for $[\text{Cu(II)L20(H}_2\text{O)}_2]$ during acid using 0.01 HCl titration in the pH range 5.7 –2.4

A back titration from pH 2.46 to pH 5.78 (dashed spectrum 5.78B, figure 5.7) was performed. The spectra taken at 5.78 resembles to that of obtained at pH 2.46 which confirms that the copper complex remains dissociated once acidified. This can be accounted to the hydrolysis of the ligands followed by decomplexation of copper complex. As the ligand hydrolysis is irreversible, as can be gathered from the NaHL20 pH studies, the dissociation of $[\text{Cu(II)L20(H}_2\text{O)}_2]$, which may be associated with the hydrolysis of the ligand can also be classified as an irreversible process.

Whilst titrating towards basic pH the overall shape of the UV spectra changes only little, as can be seen from figure 5.8. This indicates that the complex seems to be fairly stable even in extreme basic conditions.

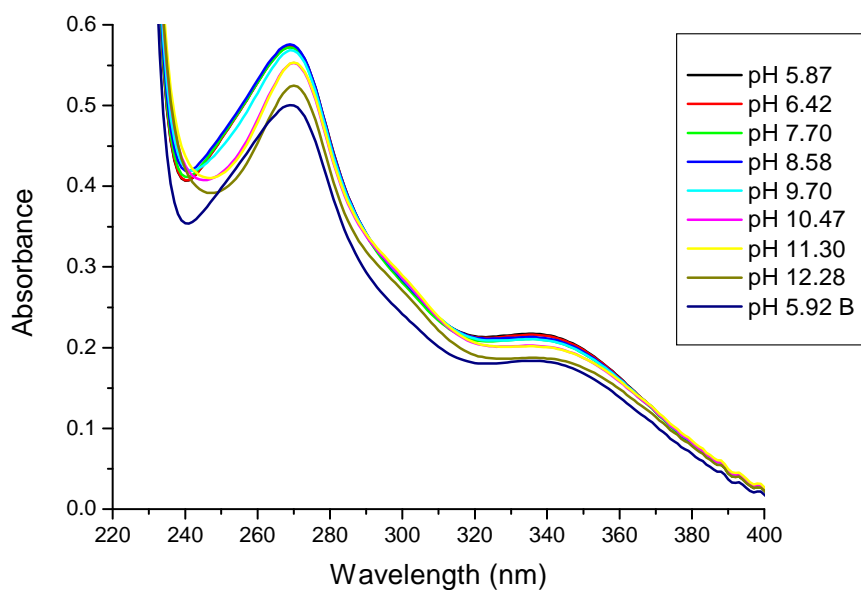


Figure 5.8: Electronic absorption spectra recorded for $[\text{Cu(II)L20(H}_2\text{O)}_2]$ during titration with using 0.01 M NaOH base in the pH range 5.9 –12.2

Hence, it can be concluded that $[\text{Cu(II)L20(H}_2\text{O)}_2]$ is unstable in acidic media, whereas it remains stable in basic conditions as indicated by the titration curve (figure 5.9) plotted for the absorbances in the pH range 2.4 – 12.3 at 346 nm.

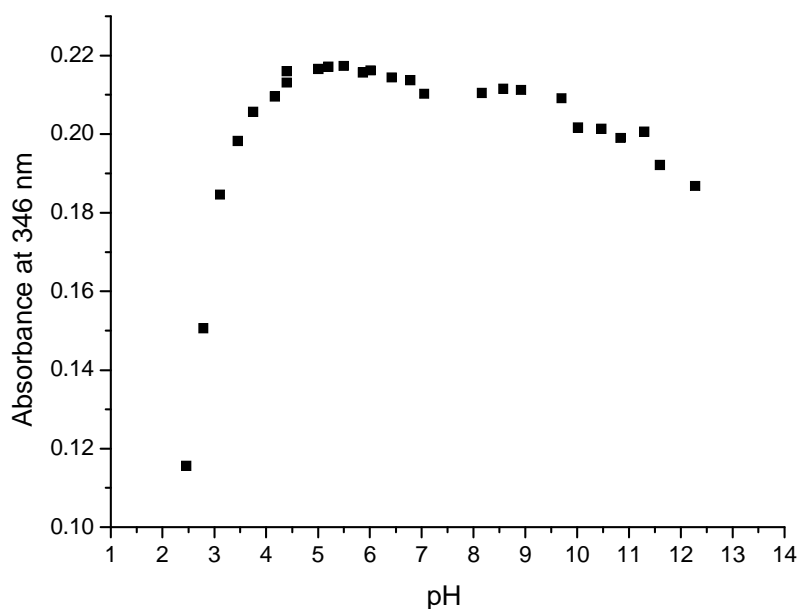


Figure 5.9: Titration curve obtained for $[\text{Cu(II)L20(H}_2\text{O)}_2]$ at 346 nm in the pH range 2.4-12.3

5.2.1.3 Stability studies of $[\text{Zn}(\text{HL20})_2]$ at different pH

A similar trend is observed for the Zn(II) complex of NaHL20. $[\text{Zn}(\text{II})(\text{HL20})_2]$ dissociates under acidic conditions, but is stable in basic conditions. As indicated in figure 5.10, the spectrum recorded at pH 1.14, closely resembles that of the starting hydrazide. This is consistent with the behaviour observed for $[\text{Cu}(\text{II})\text{L20}(\text{H}_2\text{O})_2]$ and can be accounted for the hydrolysis of NaHL20 followed by decomplexation of the zinc complex.

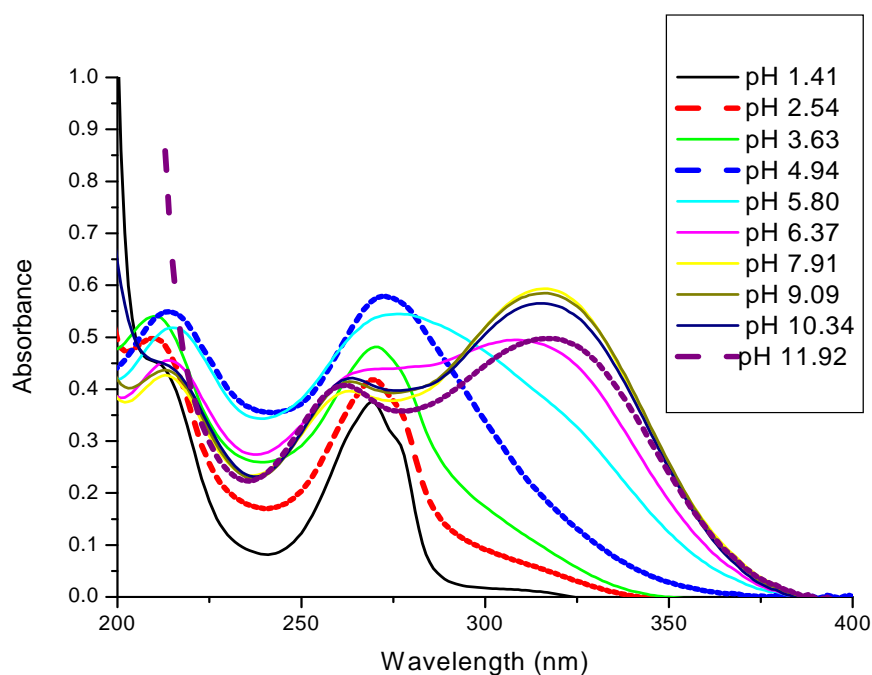


Figure 5.10: Electronic absorption spectra recorded for $[\text{Zn}(\text{II})(\text{HL20})_2]$ in the pH range 1.4-11.9

5.2.2 Stability studies of NaHL9

The stability of NaHL20 cannot be clearly determined from pH studies due to the similarity of the λ_{max} values of the ligand and the starting hydrazide. Therefore, in order to get more insight into the stability of PVAHs, acid and base titrations were performed with NaHL9 instead. The titrations were also performed in water at a concentration of 0.05 mM. The λ_{max} for the electronic absorption band of NaHL9 is observed at 269 nm as indicated in figure 5.11 ($\epsilon = 15.7 \times 10^3 \text{ dm}^3 \text{ mol}^{-1} \text{ cm}^{-1}$) and may be attributed to overlapping C=N and C=O, π - π^* transitions. The band decreases in intensity with the emergence of a new band at 243 nm upon titration from pH 5.7 to 3.5. The spectrum recorded at pH 3.5 closely resembles the spectrum of the starting hydrazide, which suggests the hydrolysis of NaHL9 to the starting hydrazide. This was confirmed by performing a back titration to pH 5.6, (dashed spectrum 5.60R, figure 5.11) which resulted in the same band remaining, proving the instability of the ligand under acidic conditions.

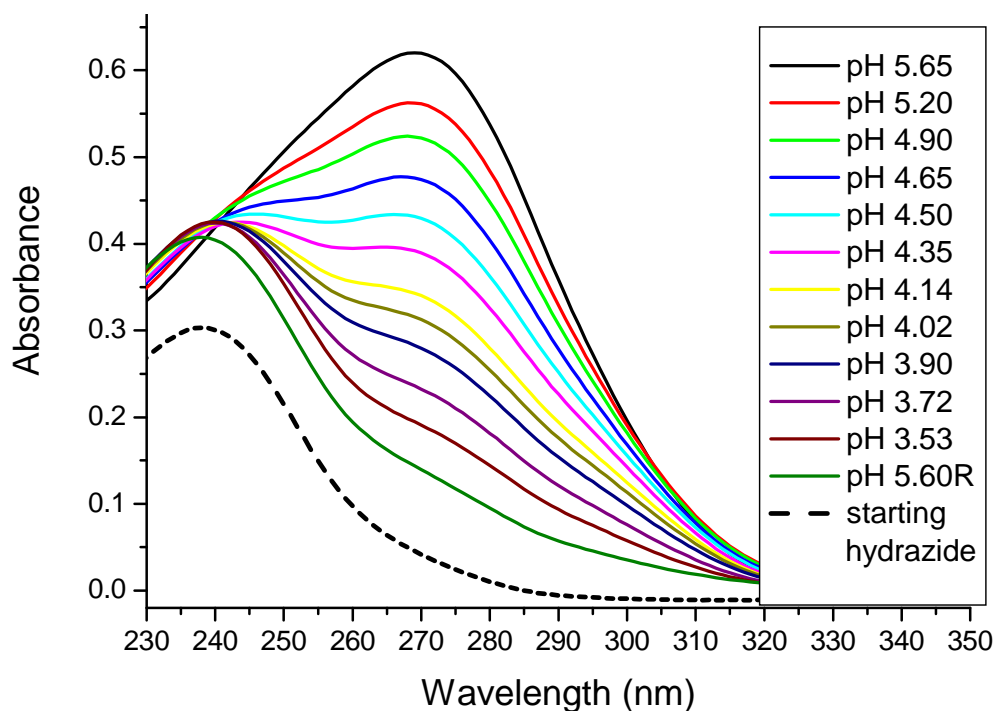


Figure 5.11: Electronic absorption spectra recorded for NaHL9 during acid titration using 0.01 M HCl in the pH range 3.5-5.6

In order to investigate the stability of NaHL9 in basic conditions, titrations were performed under similar conditions as use for the acid titrations. The same stock solution was used for basic titration which was used for the acid titration. The spectrum obtained at pH 5.80, figure 5.12, shows two bands at 269 nm and 243 nm, respectively. As discussed earlier, the band at 243 nm is characteristic for the starting hydrazide. This may be due to slow hydrolysis of NaHL9, since the base titrations were performed 2 hours after the acid titrations. From the figure 5.12, it can be noticed that the λ_{\max} at 270 nm does not shift significantly even going up to pH 11.6 indicating stability of the compound in basic conditions. Although, for the ligand NaHL9 hydrolysis occurs at a faster rate in acidic conditions, it remains fairly stable in basic pH. However, there is a slight decrease in the intensity of the bands with an increase in the intensity at 310 nm with an increase in pH, which may be associated with the pK_a of the ligand. As can be seen from the figure 5.12, the isosbestic point for this change is observed at 290 nm. The titration curve obtained for NaHL9 at 270 nm in the pH range 3.5 – 12.0 is shown in figure 5.13.

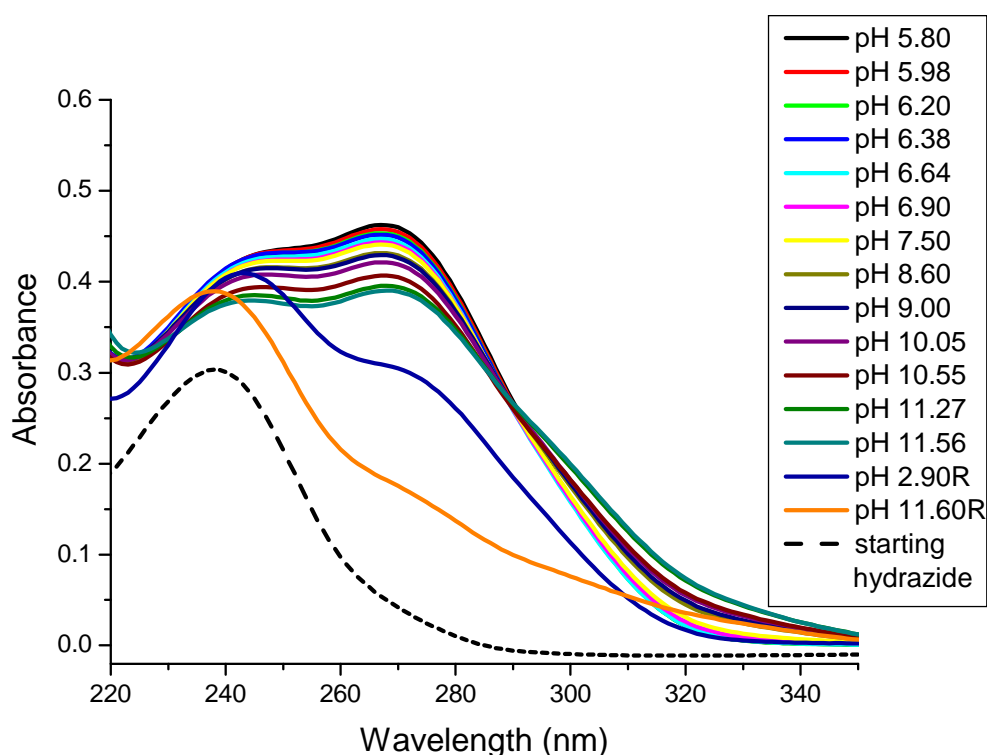


Figure 5.12: Electronic absorption spectra recorded for NaHL9 during base titration using 0.01 M NaOH in the pH range 5.8-11.6

A similar observation is discussed above for NaHL20. Back titrating to pH 2.90 (spectrum 2.90R, figure 5.12) results in the decrease of band at 310 nm and leads to hydrolysis of the ligand as the band at 264 nm, corresponding to the starting hydrazide, becomes more prominent. It can be concluded that NaHL9 undergoes hydrolysis in acidic conditions, which is confirmed by back titrating to pH 11.60 (spectrum 11.60R, figure 5.12), as it remains hydrolysed at pH below 4.

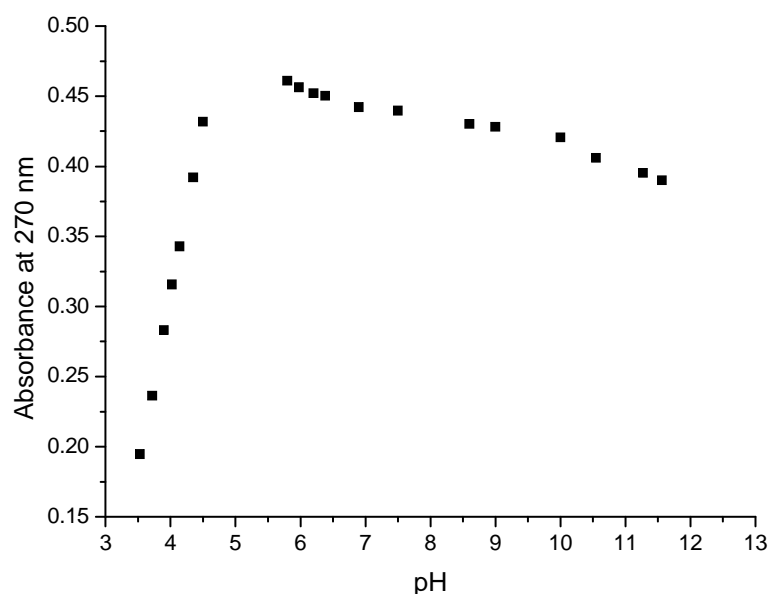


Figure 5.13: Titration curve obtained for NaHL9 at 270 nm in the pH range 3.5-11.6

Hence, from the pH studies described above it can be concluded that PVAH ligands and their Cu(II) and Zn(II) complexes are fairly stable in basic conditions, but undergo hydrolysis under acidic conditions.

5.3 Stability studies of CAHs at different pH

5.3.1 Stability of HCA1

Due to the limited solubility of CAHs in aqueous solution, a 0.02 mM solution of HCA1 in a mixture of methanol: water (4:1) was titrated between pH 1.8 - 11.2. However, using a mixture of solvents does not provide a pH value that is directly comparable with a pH value measured in aqueous solution, but the results of the study in the mixed solvent system can provide a rough estimate of the stability of the compounds. The UV-vis spectra from these titrations are shown in figure 5.14. The λ_{\max} is observed at 323 nm and can be attributed to overlapping π - π and π - π^* transitions of the C=O and C=N bonds²⁹². The starting reactants of HCA1, cinnamaldehyde and hydrazide gave a λ_{\max} values at 287 and 264 nm, respectively.

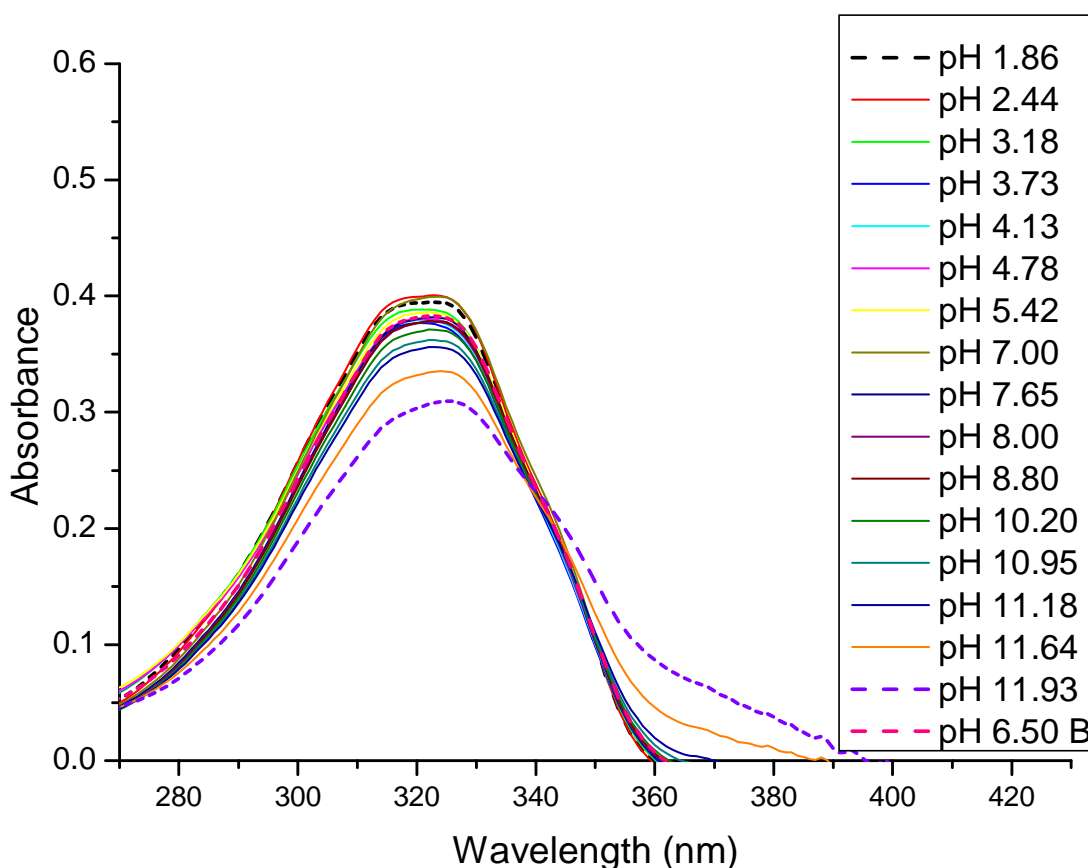


Figure 5.14: Electronic absorption spectra recorded for HCA1 in the pH range of 1-

12

With increasing pH, there is a decrease in the intensity of the maximum absorption band observed at 323 nm. Above pH 11, there is a significant decrease of the band at 323 nm with an additional band appearing at 360 nm, which goes

back to the original spectra when back titrated to pH 6.50 (spectrum 6.50B, figure 5.14). The plot of absorbances at 360 nm with varying pH (1.5 – 12.0) is indicated in figure 5.15. This reversible process can be associated with the deprotonation of the amide proton (N-H) of HCA1, similarly discussed previously for PVAHs. Unlike PVAHs, no permanent new bands corresponding to the starting material appear with the change in pH, indicating that HCA1 is stable under acidic and basic conditions.

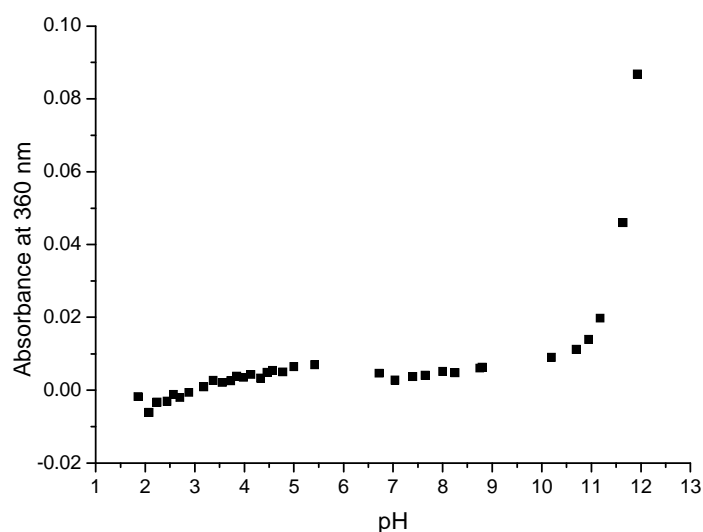


Figure 5.15: Titration curve obtained for HCA1 at 360 nm in the pH range 1.5-12.0

The reason why HCA1 appears to be more stable in acidic conditions than the investigated PVAHs, may be due to the increased conjugation present in HCA1. This extra conjugation reduces the electrophilicity on the azomethine carbon, hence making it less favourable for the attack of water which in turn prevents hydrolysis. Kali and Raines illustrated that hydrazones exhibit greater hydrolytic stability than imines due to their ability to delocalise electron density through multiple resonance forms.¹⁸²

5.3.2 Stability studies of HCA5

Similarly, HCA5 was found to be stable in both acidic and basic conditions. In order to investigate the longer-term stability of HCA5 at pH 1.78, the UV-visible spectrum was recorded after 5 hours. There is a significant reduction in the intensity at the λ_{\max} of 329 nm ($\epsilon = 20.87 \times 10^3 \text{ dm}^3 \text{ mol}^{-1} \text{ cm}^{-1}$) as indicated in figure 5.16. With a further increase in time, there is progressive reduction in intensity of the corresponding band and a new broad band appear at 289 nm ($\epsilon = 14.40 \times 10^3 \text{ dm}^3 \text{ mol}^{-1} \text{ cm}^{-1}$) (spectrum pH 1.78, 48 hours, figure 5.16). The new band is very similar to that of cinnamaldehyde (287 nm). This indicates that HCA5 is prone to hydrolysis under acidic conditions at pH 1.78 over the time monitored and converts back to the starting materials used in its synthesis, cinnamaldehyde and hydrazide. Cinnamaldehyde was shown to have a higher molar absorption coefficient than the starting hydrazide. Hence, the λ_{\max} of the hydrazide is likely to be masked by that of cinnamaldehyde.

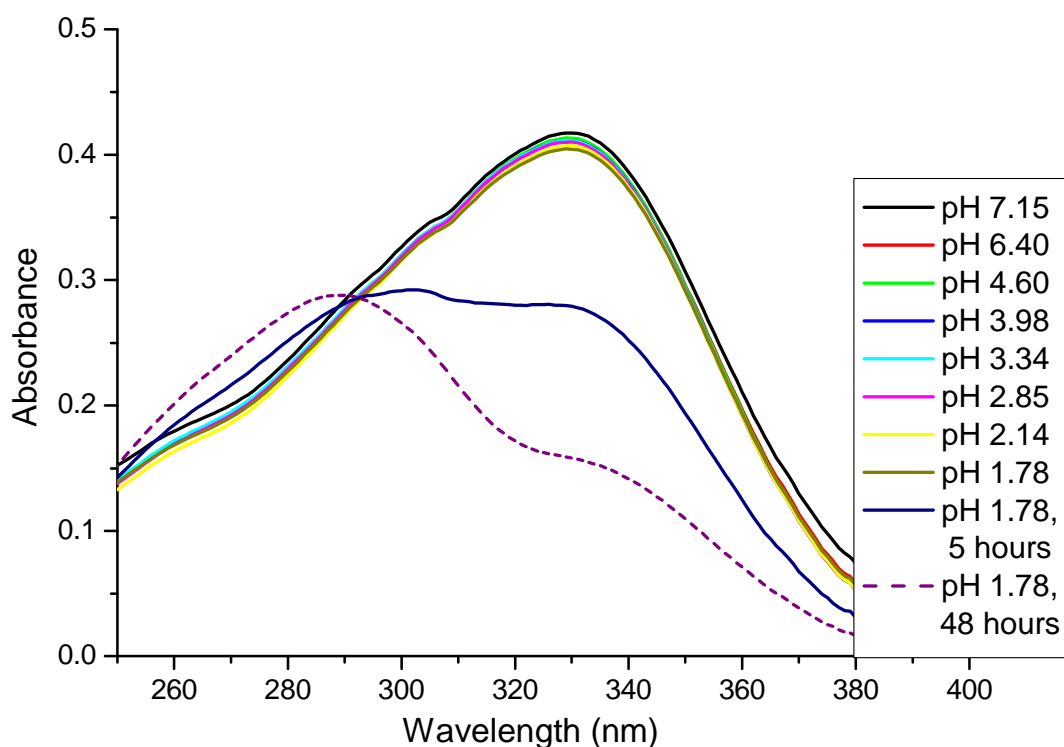
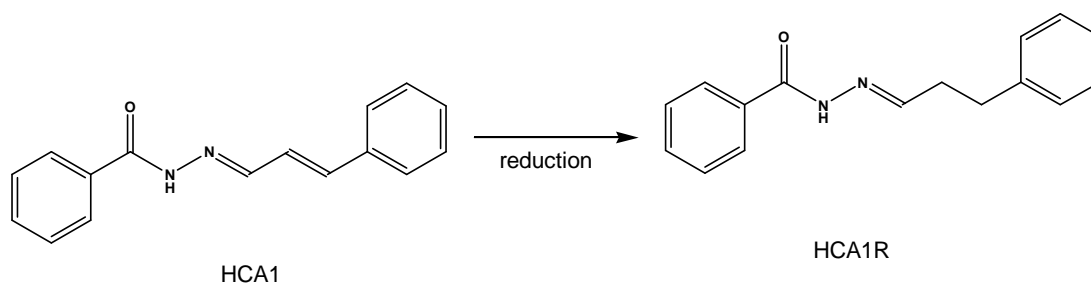


Figure 5.16: Electronic absorption spectra recorded for HCA5 during acid titration using 0.01 M HCl in the pH range of 7.1-1.7

The hydrolysis of HCA5 in acidic pH over time led to the further investigation of the behaviour of an acidic solution of HCA1 over time. The UV-visible spectrum of a solution HCA1 at a pH of 1.5 was recorded at regular intervals for a period of 48 hours. However, there was no significant change in the spectra over this time period. This indicates that HCA1 is even more hydrolytically stable than HCA5 under acidic conditions. The instability of HCA5 can be due to the electron withdrawing effect of the NO₂ substituent on the aromatic ring. This makes the azomethine carbon more electrophilic and susceptible to attack by H₂O. HCA1 does not possess an EWG on the aromatic ring and is thus more stable. This is in line with the observation made by Buss and Ponka in that the hydrazones possessing EWGs accelerates the rate of hydrolysis when compared to those having EDGs.¹⁸⁰

The reduced form of HCA1 (HCA1R) indicated in scheme 5.2, in which the olefin bond was reduced as discussed in chapter-3, was also tested for its stability at acidic pH under similar conditions. A solution of HCA1R was titrated to pH 1.5 with using 0.01 M HCl and its UV-visible spectrum was monitored over time. Although HCA1 was stable over a period of 48 hours, its reduced form HCA1R had hydrolysed after 4 hours. The instability of HCA1R may be due to loss of conjugation within the molecule resulting in restricted delocalisation of electrons across the reduced species.



Scheme 5.2: Reduction of HCA1 at olefin bond resulting in HCA1R

The base titrations of HCA5 indicate that there is an additional band at 390 nm, the intensity of which increases whilst the intensity at 330 nm decreases, as indicated in figure 5.17. Moreover, back titration to pH 7.14 (spectrum 7.14 B, figure 5.17) leads to complete disappearance of the band at 390 nm and the band at 330 nm ($\epsilon = 17.42 \times 10^3 \text{ dm}^3 \text{ mol}^{-1} \text{ cm}^{-1}$) is restored, similar to the observations made for HCA1. The titration curve obtained for HCA5 at 390 nm is depicted in figure 5.18.

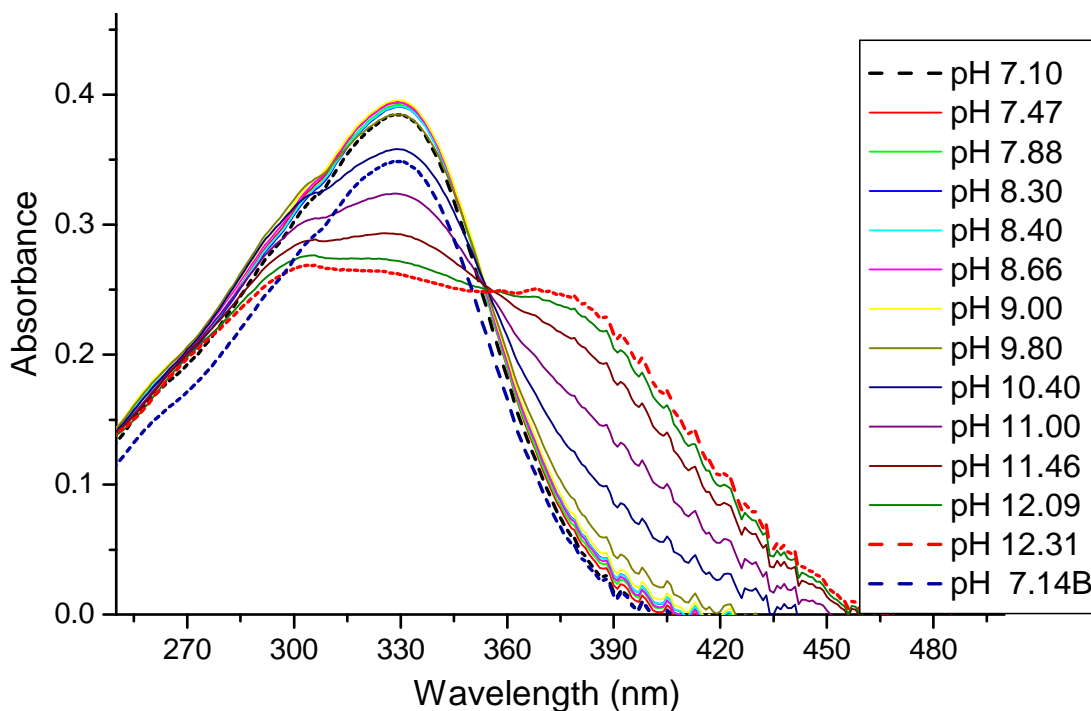


Figure 5.17: Electronic absorption spectra recorded for HCA5 during base titration using 0.01 M NaOH in the pH range of 7.1-12.31

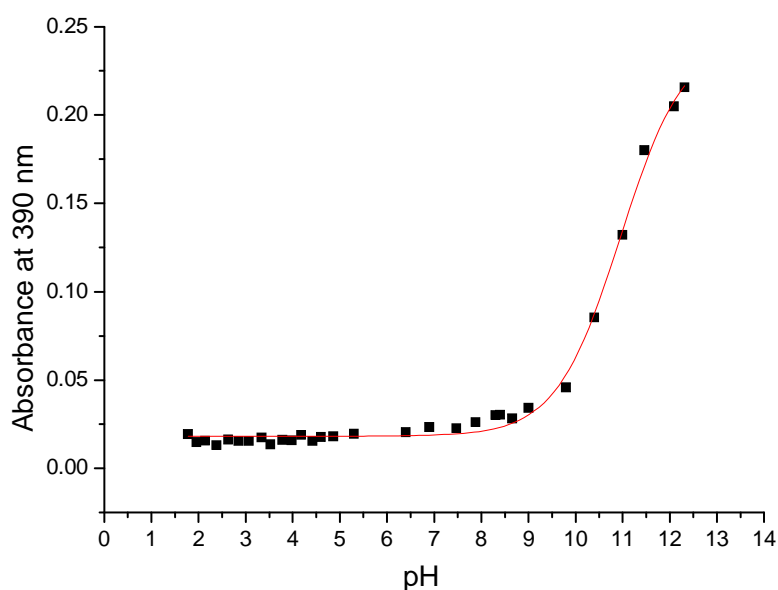


Figure 5.18: Titration curve obtained for HCA5 at 310 nm in the pH range 2.1 – 12.3

As discussed previously for HCA1, this reversible process can be attributed to the deprotonation of amide proton of HCA5 with a rough estimation of a pK_a of 11 as expected for acyl hydrazones.²⁹⁰ It can also be noted that deprotonation of the amide proton in HCA1 starts above pH 11, whereas for HCA5 it begins around 10.

This can be attributed to the strong electron withdrawing nature of the nitro substituent in HCA5 as compared to the phenyl ring of HCA1. The nitro group withdraws electron density making the amide proton more susceptible to deprotonation by stabilising the resulting negative charge.

5.3.3 Stability of Cu(II) complexes of CAHs

The Cu(II) complexes of CAHs also showed poor water solubility, hence their stability was investigated in a 4:1 (DMSO:H₂O) mixture. Initially, a solution containing 0.02 mM of [Cu(CA1)₂] was titrated towards acidic pH, from pH 7.95 to pH 2.40. The UV-visible spectra as displayed in figure 5.19 show a broad absorption band between 300 – 410 nm with a λ_{max} at 365 nm and another prominent absorption at 382 nm. These absorptions can either be attributed to the ligand-based π - π^* transitions, which undergo a red shift upon complexation as compared to the free ligand HCA1 (330 nm) or can be assigned to a LMCT band of the Cu(II) complex.

As soon as acid is added to the solution, the two absorption bands at 365 nm and 382 nm decrease in intensity, whilst a new band at 330 nm emerges. With further lowering of the pH, the band at 330 nm increases in intensity, whilst there is a decrease in absorbance for the bands at 382 nm and 365 nm. This process can be associated with the dissociation of [Cu(CA1)₂]. Below pH 4 the absorption bands assigned to the copper complex have nearly disappeared, indicating that both ligands have been released from the Cu(II) centre. A back titration was performed to basic pH 10.24 (spectrum pH 10.24 back, figure 5.19) during which the bands at 382 nm ($\epsilon = 15.3 \times 10^3 \text{ dm}^3 \text{ mol}^{-1} \text{ cm}^{-1}$) and 365 nm ($\epsilon = 16.0 \times 10^3 \text{ dm}^3 \text{ mol}^{-1} \text{ cm}^{-1}$) reappeared. On the other hand, the absorbance at 330 nm decreased in intensity suggesting re-formation of the [Cu(CA1)₂].

In contrast, the Cu(II) complex is stable in solution under basic conditions (figure 5.20) as no change in the overall shape of the UV-visible spectra is evident, similarly observed for Cu(II) complex of PVAH ([Cu(II)L20(H₂O)₂]). The plot of absorbances at 382 nm with varying pH (2.4 – 11.8) for ([Cu(II)L20(H₂O)₂]) is indicated in the figure 5.21.

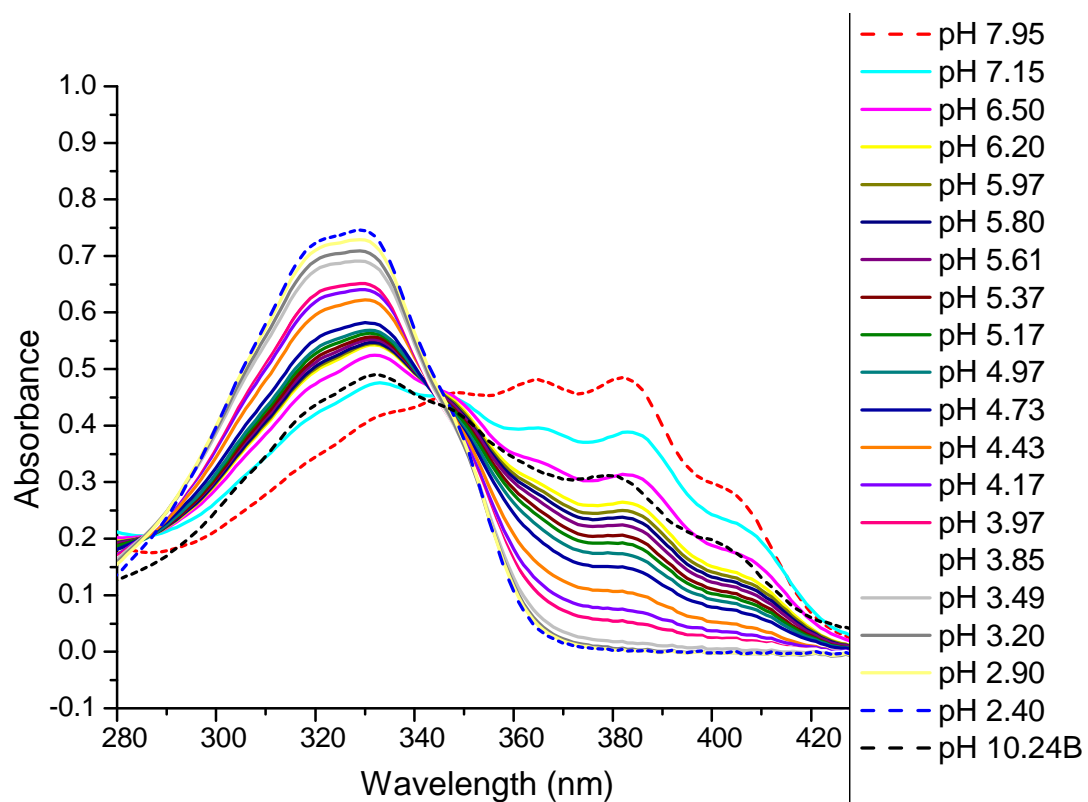


Figure 5.19: Electronic absorption spectra recorded for $[\text{Cu}(\text{CA1})_2]$ during acid titration using 0.01 M HCl in the pH range of 7.9-2.4

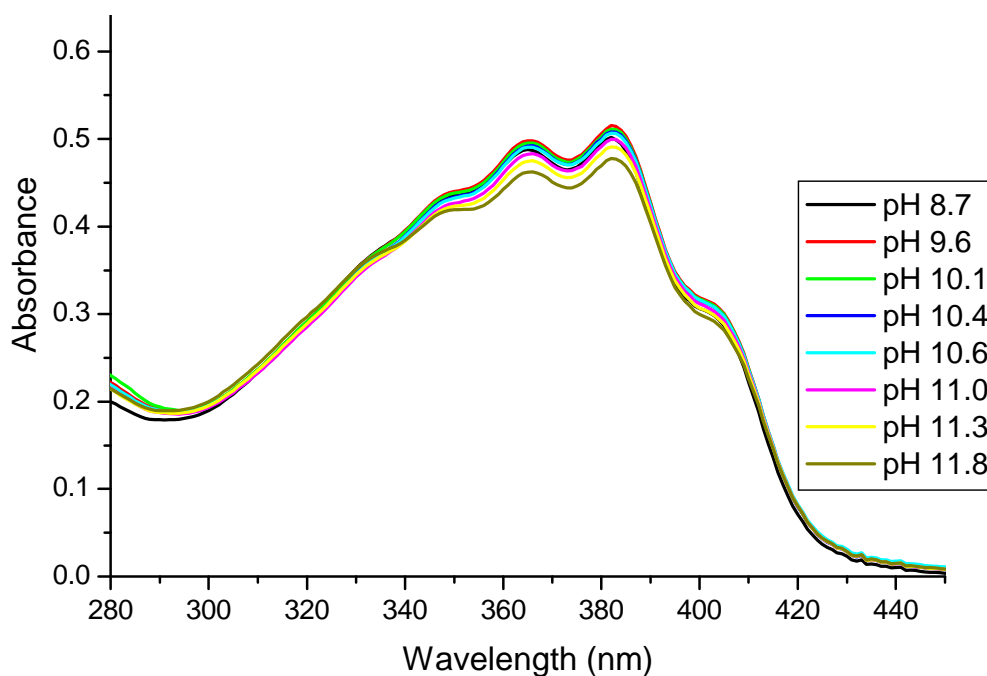


Figure 5.20: Electronic absorption spectra recorded for $[\text{Cu}(\text{CA1})_2]$ during base titration using 0.01 M NaOH in the pH range of 8.7-14.0

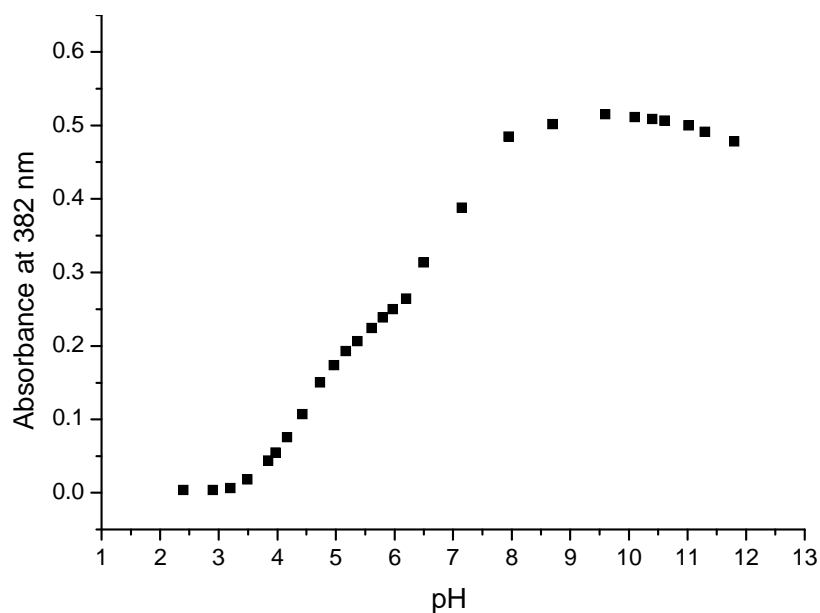
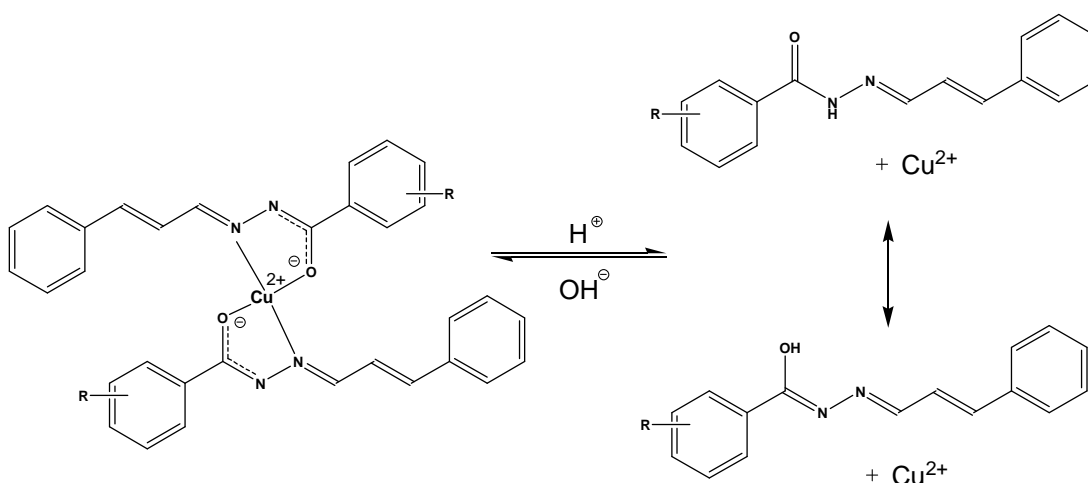


Figure 5.21: Titration curve obtained for $[\text{Cu}(\text{CA1})_2]$ at 382 nm in the pH range 2.4 – 11.8

The re-formation of the $[\text{Cu}(\text{CA1})_2]$ complex at basic pH indicates that the complex formation is a reversible process, unlike the behaviour observed for the Cu(II) complexes of PVAHs. This can be accounted for the hydrolysis of the PVAH ligands in acidic solution, whereas CAHs tends to remain stable under acidic conditions. The mechanism of decomplexation for the copper complex is thought to proceed either via protonation of the amide nitrogen or anionic O atom, hence making the ligand neutral which is turn dissociates from the Cu(II) centre as indicated in scheme 5.3. The Cu-O bond cannot be maintained and the ligand dissociates from the copper complex.



Scheme 5.3: Decomplexation of CAH from a Cu(II) complex

Hence, the pH studies of the CAHs investigated and the $[\text{Cu}(\text{CA1})_2]$ complex suggest that the ligand is fairly stable in both acidic and basic conditions for a reasonable period of time. CAHs possessing EWG start to undergo hydrolysis at acidic pH values below 1.78 during prolonged period of time. The ligand dissociates from the Cu(II) centre in acidic conditions, however, reformation of the copper complex takes place when titrated back to basic pH 10.28 and the ligand remains coordinated even in extreme basic conditions (pH 11.8).

5.4 Stability studies in PBS buffer

5.4.1 Stability studies of PVAHs in PBS buffer

In order to gain further insight into the rates of the hydrolysis of PVAHs and their corresponding metal complexes, a selection of compounds was investigated in PBS (phosphate buffer saline) buffer over a period of time. PBS is isotonic with human plasma and buffer to pH 7.4, hence mimicking the physiological conditions of human plasma. These properties make PBS a suitable medium for preliminary stability studies of a drug and PBS has been used before to explore the stability of related hydrazones.¹⁸⁰ Dulbecco's PBS buffer, purchased from Sigma, was used to study the hydrolysis of PVAHs and their metal complexes (0.05 mM) at 37 °C and pH 7.4. Stock solutions were made in DMSO and then diluted with PBS buffer maintaining a final ratio of 9:1 PBS: DMSO for investigated PVAH compounds. However, for compounds of the CAH series, the ratio had to be 5:5 due to their limited solubility in PBS buffer. The final 10 ml of solution was incubated in a sample tube immersed in a water bath, which was maintained at 37 °C. The sample tube was closed to limit the evaporation of solvent and to provide accurate results. Spectral changes of the solution were recorded manually at regular intervals using a UV-vis spectrophotometer, as discussed in the following section. Experimental details can be found in chapter-7.

The absorbance at λ_{max} for NaHL11 (*p*-Br) was monitored at 270 nm ($\epsilon = 18.2 \times 10^3 \text{ dm}^3 \text{ mol}^{-1} \text{ cm}^{-1}$), as illustrated in figure 5.22. The associated band may be attributed to overlapping C=N and C=O π - π^* transitions.²⁹² When ligand NaHL11, was incubated with PBS buffer at 37 °C over a period of 6 days, a new band at 240 nm emerged with a simultaneous decrease in the intensity of the band at 270 nm. The plot of decay of NaHL9 is indicated in figure 5.23 and the $t_{1/2}$ is 38 hours. The

band at 240 nm is due to $\pi \rightarrow \pi^*$ transitions of the aromatic ring of the starting hydrazide (dashed spectrum, figure 5.22).

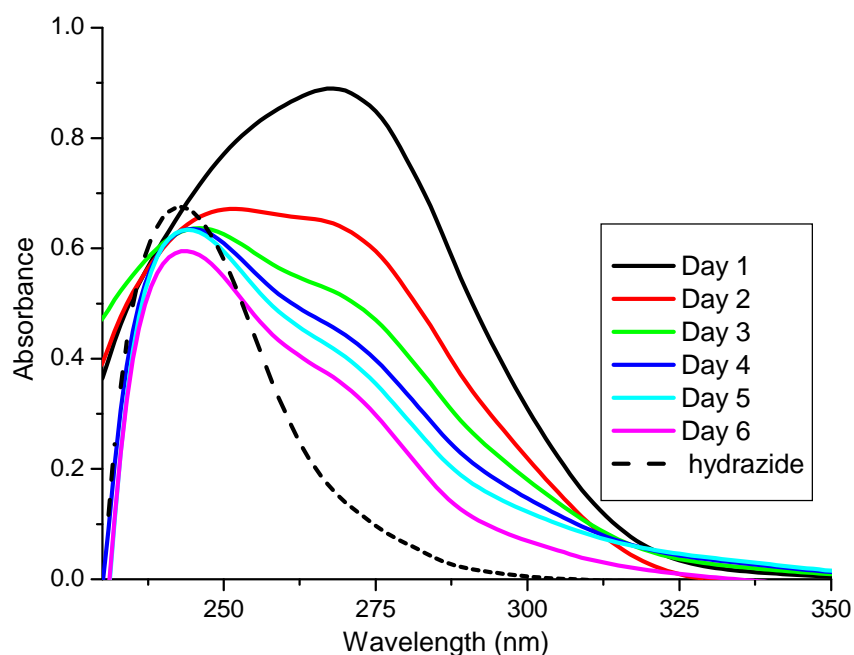


Figure 5.22: Electronic absorption spectra recorded for NaHL11 in PBS buffer – Day 1-6

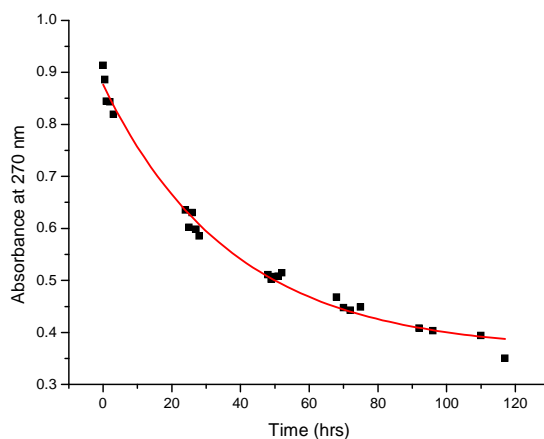


Figure 5.23: Exponential decay obtained for NaHL11 at 270 nm over the period of 6 days in terms of hours with a $t_{1/2}$ of 38 hours

NaHL14 ($p\text{-CF}_3$) and NaHL16 ($p\text{-(CH}_3)_3$) were studied under similar conditions and showed comparable results to that of NaHL11 ($p\text{-Br}$). The plot illustrated in figure 5.24 indicates gradual hydrolysis of NaHL14, which is evident by

a decrease in the intensity of the band at 270 nm. In addition, this absorption band broadens with time while the final spectrum being almost comparable to the spectrum of the parent hydrazide shown as dotted line. The plot of decay of NaHL14 is indicated in figure 5.25 and the $t_{1/2}$ is 54 hours, while for NaHL16 $t_{1/2}$ is 57 hours.

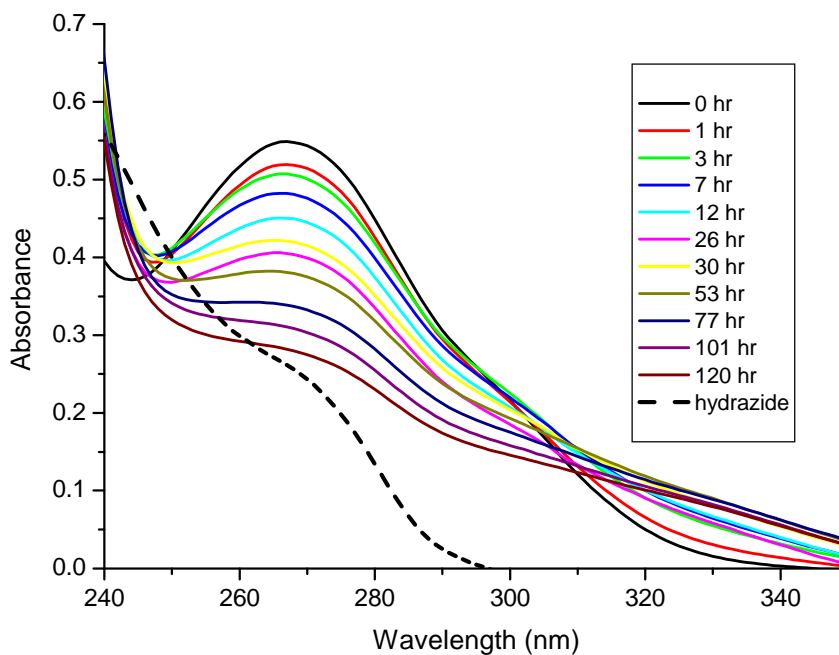


Figure 5.24: Electronic absorption spectra recorded for NaHL14 in PBS buffer (0 – 120 hrs)

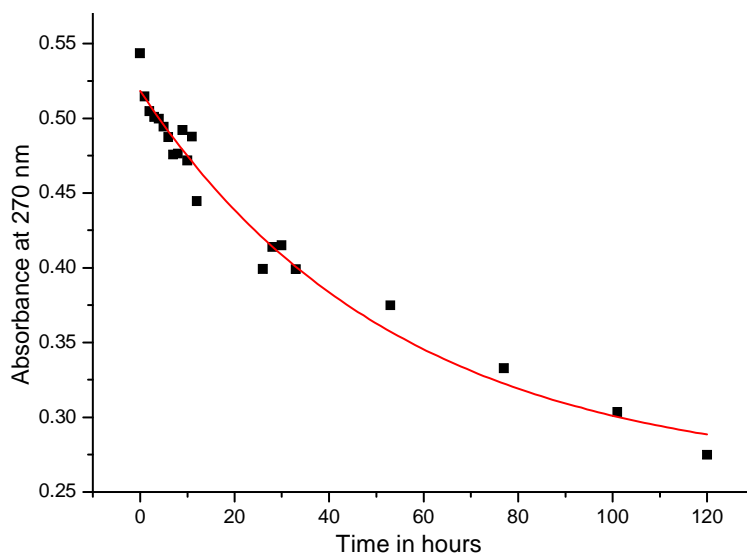


Figure 5.25: Exponential decay obtained for NaHL14 at 270 nm over the period of 6 days in terms of hours with a $t_{1/2}$ of 54 hours

Along with the decrease in the intensity of the band at 270 nm there is a small increase in the absorbance at around 330 nm. This may be due to formation of additional chemical species in solution, which can be attributed to either degradation or oxidation processes associated with hydrolysis of NaHL14. NaHL16 studied under similar conditions exhibit similar behaviour and the UV spectra of PBS studies can be found in Appendix 23.

5.4.2 Stability studies of Cu(II) complexes of PVAHs in PBS buffer

Although the investigated PVAHs hydrolyse over longer periods of time, the copper complexes appear to be stable in PBS buffer. The absorption maxima (λ_{max}) of $[\text{Cu(II)L11(H}_2\text{O)}_2]$ (figure 5.26) are observed at 277 nm ($\epsilon = 19.0 \times 10^3 \text{ dm}^3 \text{ mol}^{-1} \text{ cm}^{-1}$) and 320 nm ($\epsilon = 11.6 \times 10^3 \text{ dm}^3 \text{ mol}^{-1} \text{ cm}^{-1}$) and can be assigned to $\pi \rightarrow \pi^*$ transitions of the aromatic ring and overlapping of C=N and C=O $\pi\text{-}\pi^*$ transitions, respectively.²⁹²

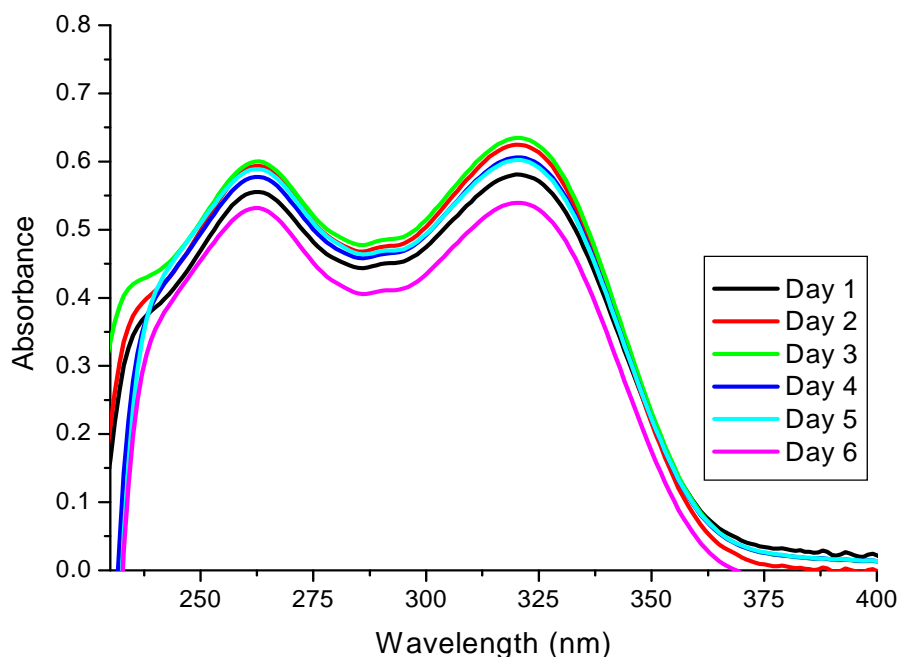


Figure 5.26: Electronic absorption spectra recorded for $[\text{Cu(II)L20(H}_2\text{O)}_2]$ in PBS buffer - Day 1-6

As evident from figure 5.26, there is no shift in the maximum of the band over 6 days. However, there is a slight decrease in the intensity of the band which can be accounted for the slow precipitation of the Cu(II) complex from PBS buffer due to the limited solubility of the complex in water. This leads to the conclusion that

copper coordination helps to stabilise the ligand. Hence, the copper complex can act as a potential drug candidate as the copper coordination may help to facilitate entry of the active drug into the bacterial cell without it being hydrolysed.

The Cu(II) complexes of NaHL14 and NaHL16 exhibit similar behaviour to that of $[\text{Cu(II)L11(H}_2\text{O)}_2]$ as they remain stable over a period of 49 hours. As indicated in the plot for $[\text{Cu(II)L14(H}_2\text{O)}_2]$ (figure 5.27) there is only little change in the overall shape of the UV-vis spectra over time. It can be noticed there is also a slight decrease in the intensity of the band at 320 nm which can be due to precipitation of the compounds with time.

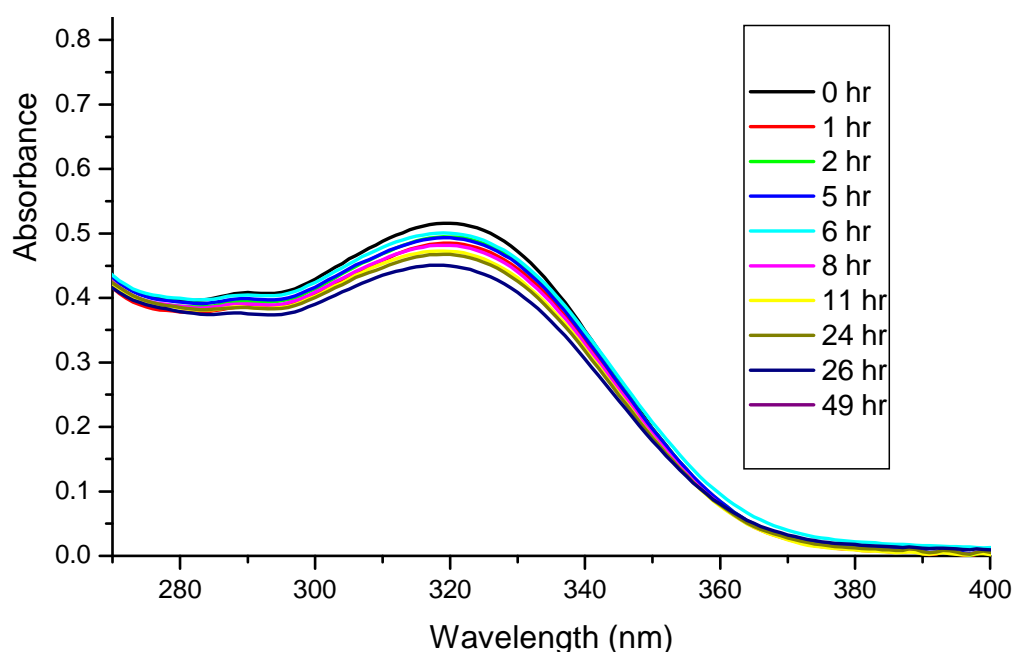


Figure 5.27: Electronic absorption spectra recorded for $[\text{Cu(II)L14(H}_2\text{O)}_2]$ in PBS buffer (0-49 hours)

$[\text{Cu(II)L14(H}_2\text{O)}_2]$ studied under similar conditions exhibits similar behaviour and the UV spectra of the PBS studies can be found in Appendix 23.

5.4.3 Stability studies of $[\text{Zn}(\text{HL11})_2]$ in PBS buffer

In contrast to the Cu(II) complexes of PVAHs, the Zn(II) complex of NaHL11 is unstable in PBS buffer over time. $[\text{Zn}(\text{HL11})_2]$ displayed similar behaviour to that of the PVAHs with the complex hydrolysing to the starting hydrazide (figure 5.28). The intensity of the band assigned to the π - π^* transition of L11 in the zinc complex, observed at 312 nm ($\epsilon = 16.9 \times 10^3 \text{ dm}^3 \text{ mol}^{-1} \text{ cm}^{-1}$), decreases and gives rise to a new band corresponding to the starting hydrazide. The exponential decay of $[\text{Zn}(\text{HL11})_2]$ is depicted in figure 5.29 with a $t_{1/2}$ of 32 hours.

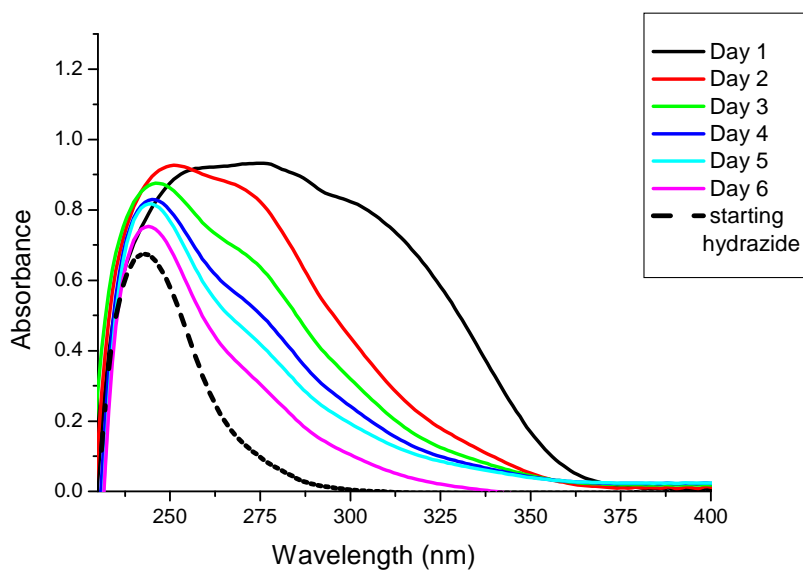


Figure 5.28: Electronic absorption spectra recorded for $[\text{Zn}(\text{HL11})_2]$ in PBS buffer - Day 1-6

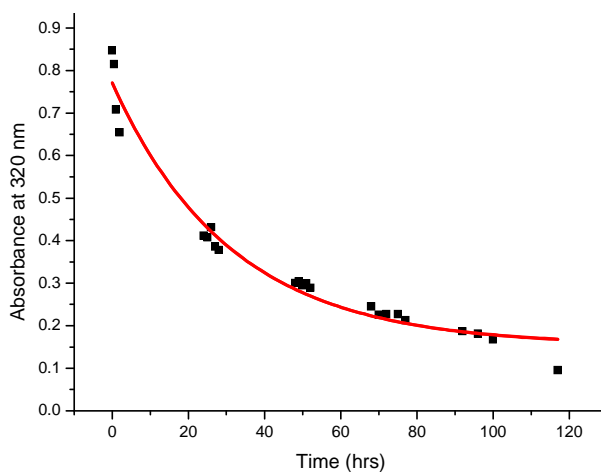


Figure 5.29: Exponential decay of the absorption of $[\text{Zn}(\text{HL11})_2]$ at 270 nm over the period of 6 days(117 hours) with a $t_{1/2}$ of 32 hours

The instability of $[\text{Zn}(\text{HL11})_2]$ can be attributed to the lability of the Zn(II) complex in the solution. This indicates that the Zn(II) ion is not coordinated strongly to PVAH ligand unlike Cu(II). Hence, when the zinc complex is dissolved in PBS decomplexation occurs followed by hydrolysis of the NaHL11 giving rise starting hydrazide.

5.4.4 Stability studies of the di-hydrazide analogue $\text{NaH}_3\text{D1}$

As discussed in chapter-2, the di-hydrazide analogue of PVAH, $\text{NaH}_3\text{D1}$, is expected to be more hydrolytically stable than PVAHs owing to its C-N single bond. To gain insight into the stability of $\text{NaH}_3\text{D1}$, its behaviour was investigated in PBS buffer. The absorption coefficient at the λ_{max} of $\text{NaH}_3\text{D1}$ was determined at 275 nm ($\epsilon = 21.5 \times 10^3 \text{ dm}^3 \text{ mol}^{-1} \text{ cm}^{-1}$) as shown figure 5.30. The associated band may be attributed to overlapping C=N and C=O, $\pi\text{-}\pi^*$ transitions.²⁹² The intensity of the band decreases over a period of 98 hours. However, the decrease in the intensity is not as significant as observed for NaHL11, NaHL14 and NaHL16. Moreover, there is very little or no shift in the λ_{max} value for the band observed at 275 nm. The slight decrease in the intensity can be attributed to the precipitation of the compound in the aqueous media and/or may be due to slow hydrolysis of the $\text{NaH}_3\text{D1}$.

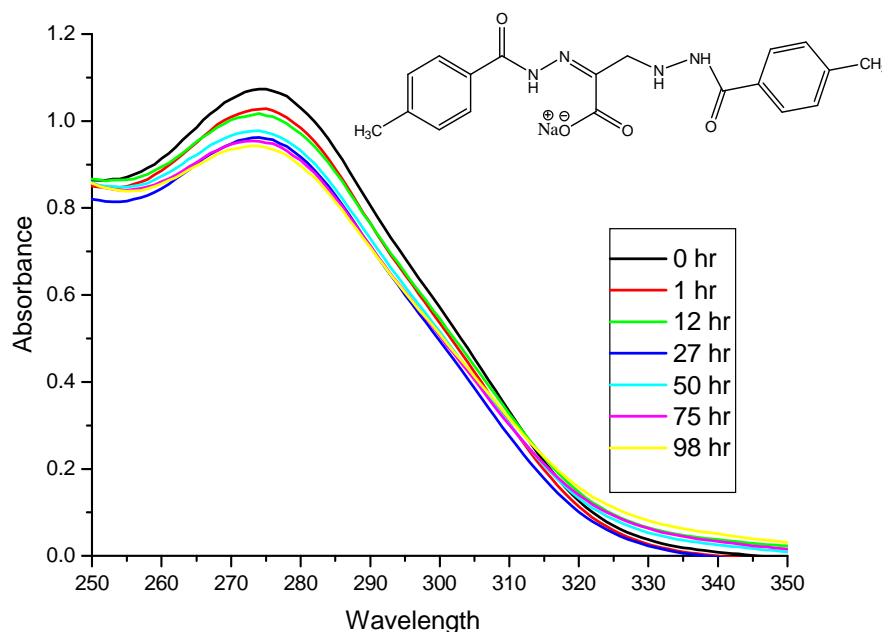


Figure 5.30: Electronic absorption spectra recorded for $\text{NaH}_3\text{D1}$ in PBS buffer (0 - 98 hr)

Hence, it can be concluded that the dianologue $\text{NaH}_3\text{D1}$ is fairly stable over the investigated time period. This suggests that PVAH analogues with C-N single bonds are more stable than those with C=N double bonds. The stability could also be due to an additional aromatic ring. This is indicated from the pH studies, as CAHs which are highly conjugated appear to be more stable than PVAHs. The stability of a compound over a long period of time can prove to be useful, since it may aid in a higher cellular uptake of the drug in bacteria.

5.4.5 Stability studies of CAHs in PBS buffer

Due to the poor solubility of CAHs and their copper complexes in PBS a mixture of PBS and DMSO (1:1 v/v) was used to investigate the stability of HCA1 and its respective Cu(II) complex $[\text{Cu}(\text{CA1})_2]$ (figure 5.31). The UV-visible spectra of the corresponding solutions were monitored over a period of 50 hours. For HCA1, there is no change observed in the overall shape of the UV spectra over the time period of 50 hours indicating its stability in PBS.

The initial UV-visible spectrum of $[\text{Cu}(\text{CA1})_2]$ in PBS recorded at 0 hours, as shown in figure 5.31, shows an absorption band at around 350 – 450 nm suggesting the presence of the copper complex. An intense band observed at 329 nm corresponds to the free ligand, HCA1. As can be seen from figure 5.31, the band observed in the region 350 – 450 nm disappears after one hour, and a prominent band at 329 nm develops. These spectral changes indicate that the complex rapidly dissociates to give free ligand and solvated Cu(II). The uncoordinated ligand HCA1 remains stable for the period of 50 hours as there is no further shift observed in the λ_{max} .

The poor stability of the copper complexes in PBS buffer is likely to be associated with the additional DMSO used in the PBS study in order to make the copper complexes soluble in solution. DMSO is known to be a more coordinating solvent than water²⁹³ and it can replace weakly coordinated ligands in complexes²⁹⁴. Therefore, the complex could have been more stable in 100% PBS buffer solution. However, the solubility issues could not be solved as the copper complexes of CAHs were only soluble in DMSO and DMF. However, it is reported in the literature that complexes are less stable in DMF than DMSO²⁶⁴, hence replacing DMSO solvent with DMF may not have proven to be useful.

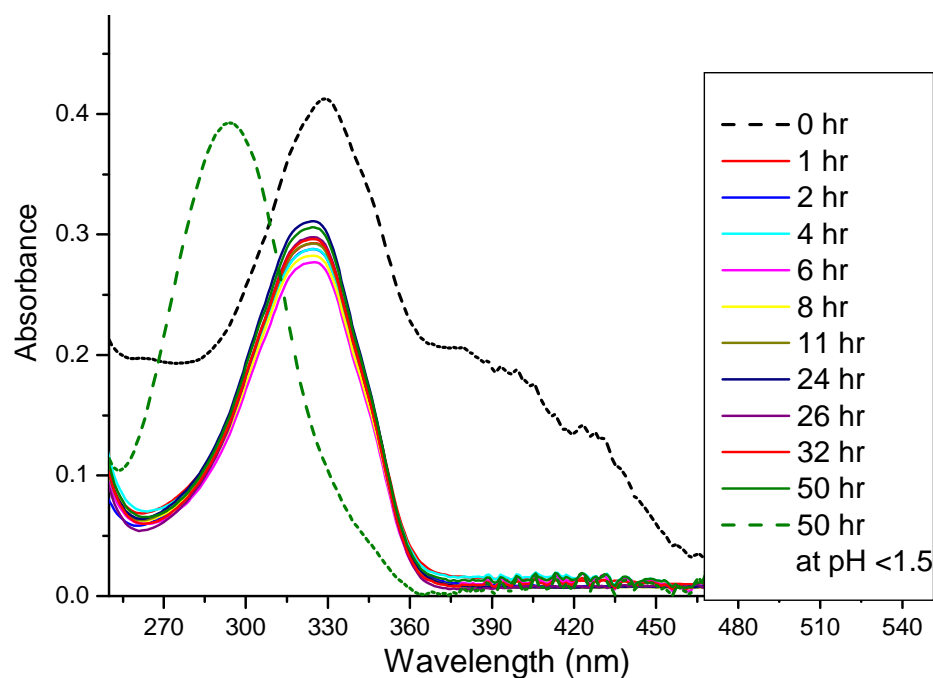


Figure 5.31: Electronic absorption spectra recorded for HCA1 in PBS buffer solution over a period of 50 hours then acidified to pH 1.5 with HCl

Furthermore, the band at 329 nm shifts to 290 nm with lowering to pH 1 and appears at similar wavelength after 1 hour. The band at 290 nm closely resembles that of the starting material cinnamaldehyde (289 nm) suggesting the hydrolysis of HCA1 at pH 1. However, this contradicts results obtained in the pH studies of HCA1, where the ligand appears to be stable at pH 1.5. This suggests that PBS buffer accelerates the hydrolysis of the hydrazone at acidic pH.

Buss and Ponka, showed that similar hydrazones dissociate at a slower rate in PBS buffer.¹⁸⁰ However, when these compounds were further investigated by Kovaříková and group for their stability in animal plasma, they found that these compounds undergo rapid degradation in the plasma as compared to PBS solution¹⁸¹.

Hence, PBS studies of CAH indicate that the ligand HCA1 appears to be stable in the buffer over the monitored time of 50 hours. However, copper complex, $[\text{Cu}(\text{HCA1})_2]$ rapidly dissociates within an hour.

From the combined stability studies it can be concluded that the investigated ligands and metal complexes remain stable under basic pH conditions, however, they undergo fast dissociation in acidic pH. This may be considered as a drawback for

the oral administration of the compounds as the pH of stomach is below 2, hence it is likely the the drugs hydrolyse.

5.5 Comparing CLogP values of PVAHs and CAHs

It is well known that the CLogP plays an important role in drug design.²¹⁶ As previously discussed in chapter-3, the theoretical CLogP values for PVAHs and CAHs lie between -1.03 to 2.74 and 2.58 to 5.18 respectively, depending on the substituent on the aromatic ring. It is obvious that the greater CLogP values for CAHs are due an additional aromatic ring as compared to PVAHs. Moreover, the lower CLogP values for PVAHs signify greater number of hydrogen-bonding interactions than the CAHs which is evident from the obtained X-ray crystal structures. The CLogP value for di-hydrazide analogue (NaH₃D1) is 1.35, whereas its equivalent monoanalogue (NaHL9) is 1.34. As NaHL₃D1 has two aromatic rings as compared to NaHL9 it should give higher CLogP values but gives similar values as indicated in table 5.1. The reduced CLogP value is more likely due to the presence of a greater number of hydrogen bond donor/acceptor atoms on NaH₃L1. This is confirmed by comparing with the equivalent ligand (*p*-CH₃ substituted hydrazone) of CAH series HCA9, which has a CLogP of 3.98. Hence, the greater CLogP of HCA9 can be accounted to a greater number or aromatic rings and a decrease in the number of hydrogen bond donor/ acceptor atoms over NaHL9 and NaH₃D1.

Table 5.1: Selected compounds with their structure and CLogP values

Compound	Structure	CLogP
NaH ₃ D1 (Di-hydrazide analogue of a PVAH)		1.35
NaHL9 (Monoanalogue of a PVAH)		1.34
HCA9 (CAH)		3.98

As the lipophilicity of a drug increases with the increase in the ClogP values, CAHs can prove to be more useful in antitubercular drug design than PVAH ligands. This is because an increased lipophilicity would facilitate the passage of the

molecule through the lipid bilayer of the waxy mycobacterial cell wall.^{189,218} However, the hydrophobic nature of a drug can pose a serious issue of solubility in aqueous media, which may result in reduced uptake of a drug in the body resulting in low bioavailability of active pharmacophore.

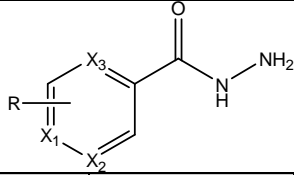
5.6 Antitubercular activity

5.6.1 Antitubercular activity of PVAHs and their metal complexes

As mentioned earlier, the antitubercular studies which will be discussed in this chapter, were done by our collaborators. All the synthesized PVAHs and their respective Cu(II) and Zn(II) complexes compounds were screened initially for antitubercular activity against *Mycobacterium tuberculosis* H37Rv at a concentration of 256 µg /mL. The tested compounds that exhibited an inhibitory effect were further examined to determine their minimum inhibitory concentrations (MIC). Although, PVAHs and their parent hydrazides exhibit inhibitory action, their MIC values were significantly higher than that of isoniazid, which is a well known antitubercular drug. However, when PVAHs were complexed to Cu(II), the activity increases tremendously.

Cu(II) complexes exhibiting similar MIC value to that of isoniazid were screened along with their parent hydrazones and hydrazides under both high iron (8 µg Fe(II)/mL) and low iron (0.02 µg Fe(II)/mL) conditions. MIC values of hydrazides and their respective PVAHs and Cu(II) complexes in different conditions are provided in tables 5.2, 5.3 and 5.4, respectively. The experimental details of the antitubercular assay are provided in chapter-7.

Table 5.2: MIC values of selected hydrazides along with INH under different conditions

					
Compound	R	MIC value in 7H9 conditions (µg/mL)	MIC value in high iron conditions (µg/mL)	MIC value in low iron conditions (µg/mL)	Fold difference between high and low iron MIC values
INH	X ₁ = N	0.25	0.125	32	256
H9	<i>p</i> -CH ₃	256	32	256	8
H8	<i>p</i> -NO ₂	128	16	256	16
H16	<i>p</i> -(CH ₃) ₃	128	32	>256	<8
H7	<i>p</i> -NO ₂ , <i>m</i> -Me	128	32	>256	<8
H14	<i>p</i> -CF ₃	64	32	256	8
H15	<i>m</i> -F	128	64	256	4
H3	<i>m</i> -OH	128	32	>256	<8
H20	X ₂ , X ₃ = N	64	32	256	8

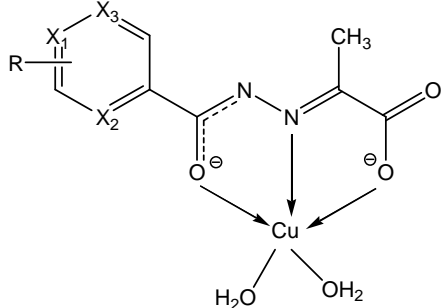
Isoniazid (INH) is a widely used antitubercular drug, whilst other hydrazides have proven to be less efficient than INH itself. However, hydrazones derived from INH and related hydrazides have been known to have improved activities if compared with their parent hydrazides.^{78,81} In addition, coordinating hydrazones to metal ions, such as Cu(II) and Co(II) has been reported to enhance their activity significantly.⁸⁷ Metal complexation of such conjugates has been found to enhance their antibacterial properties due to enhanced lipophilicities facilitating passage through the lipophilic mycobacterial cell wall. The enhanced lipophilicities can be accounted to the binding of the anionic donor atoms to the copper centre, which is evident from the single crystal X-ray structures of Cu(II) complexes of PVAHs discussed in chapter-4. This renders the overall complex neutral. In addition, some metal complexes found in the literature are also found to inhibit resistant strains of bacteria.^{85-86,286}

Table 5.3: MIC values of selected PVAHs under different conditions

Monoanalogue PVAHs (NaHLX)		Dianalogue PVAH (NaH ₃ D1)			
compound	R	MIC value in 7H9 conditions (µg/mL)	MIC value in high iron conditions (µg/mL)	MIC value in low iron conditions (µg/mL)	Fold difference between high and low iron MIC values
NaHL9	<i>p</i> -CH ₃	32	16	256	16
NaHL8	<i>p</i> -NO ₂	32	8	256	32
NaHL16	<i>p</i> -(CH ₃) ₃	32	16	256	16
NaHL7	<i>p</i> -NO ₂ , <i>m</i> -Me	64	8	128	16
NaHL14	<i>p</i> -CF ₃	16	16	256	16
NaHL15	<i>m</i> -F	32	16	256	16
NaHL3	<i>m</i> -OH	32	32	256	8
NaHL20	X ₂ , X ₃ =N	64	8	256	32
NaH ₃ D1	<i>p</i> -Me	32	16	256	16

As previously discussed in the stability studies sections, the Cu(II) ion does not only provide stability towards hydrolysis, it also makes the overall molecule neutral which may facilitate the cellular uptake of their components. Poor activity of PVAHs may not necessarily indicate a lower intracellular potency but can be due to reduced cellular uptake. This can be attributed to many factors such as a) hydrophilicity b) unstability towards hydrolysis c) anionic nature at physiological pH. However, the synthesised di-hydrazide analogue, NaH₃D1, proven to be nearly stable at physiological conditions as evident from PBS studies was proven to be inefficient and the MIC value is similar to the monoanalogue NaHL9. Thus, the restricted uptake of the monoanalogue and dianalogue PVAHs is likely to be due to the anionic nature of the PVAHs.

Table 5.4: MIC values of selected Cu(II) complexes of PVAHs obtained under the indicated conditions



Compound	R	MIC value in 7H9 conditions (µg/mL)	MIC value in high iron conditions (µg/mL)	MIC value in low iron conditions (µg/mL)	Fold difference between high and low iron MIC values
[Cu(II)L9 (H ₂ O) ₂]	<i>p</i> -CH ₃	8	<0.5	128	>256
[Cu(II)L8 (H ₂ O) ₂]	<i>p</i> -NO ₂	1	2	256	128
[Cu(II)L16 (H ₂ O) ₂]	<i>p</i> -(CH ₃) ₃	16	1	64	64
[Cu(II)L7 (H ₂ O) ₂]	<i>p</i> -NO ₂ , <i>m</i> -Me	4	<0.5	128	>256
[Cu(II)L14 (H ₂ O) ₂]	<i>p</i> -CF ₃	8	<0.5	128	>256
[Cu(II)L15 (H ₂ O) ₂]	<i>m</i> -F	8	0.5	64	128
[Cu(II)L3 (H ₂ O) ₂]	<i>m</i> -OH	8	1	32	32
[Cu(II)L20 (H ₂ O) ₂]	X ₂ , X ₃ = N	16	<0.5	256	>512

The stable Cu(II) complexes of PVAHs may be able to passively diffuse through the cell membrane owing to their neutral form. Our hypothesis supports the sequestering of the copper ions from the copper complex by mycobacterial metallothionein²⁹⁵, which in turn releases the hydrazone. Subsequent hydrolysis of the released hydrazone yields the hydrazide and pyruvate moiety. The inhibitory action may be attributed to the combination of the activity of released hydrazide and redox active Cu(II) ions. It can be seen from the MIC values that isoniazid and PVAHs and their copper complexes were less potent in limiting iron conditions. However, their potency increases with high iron levels, suggesting similar mode of inhibitory action towards mycobacteria to that of isoniazid. A schematic representation of our proposed mechanism of action is shown in figure 5.32.

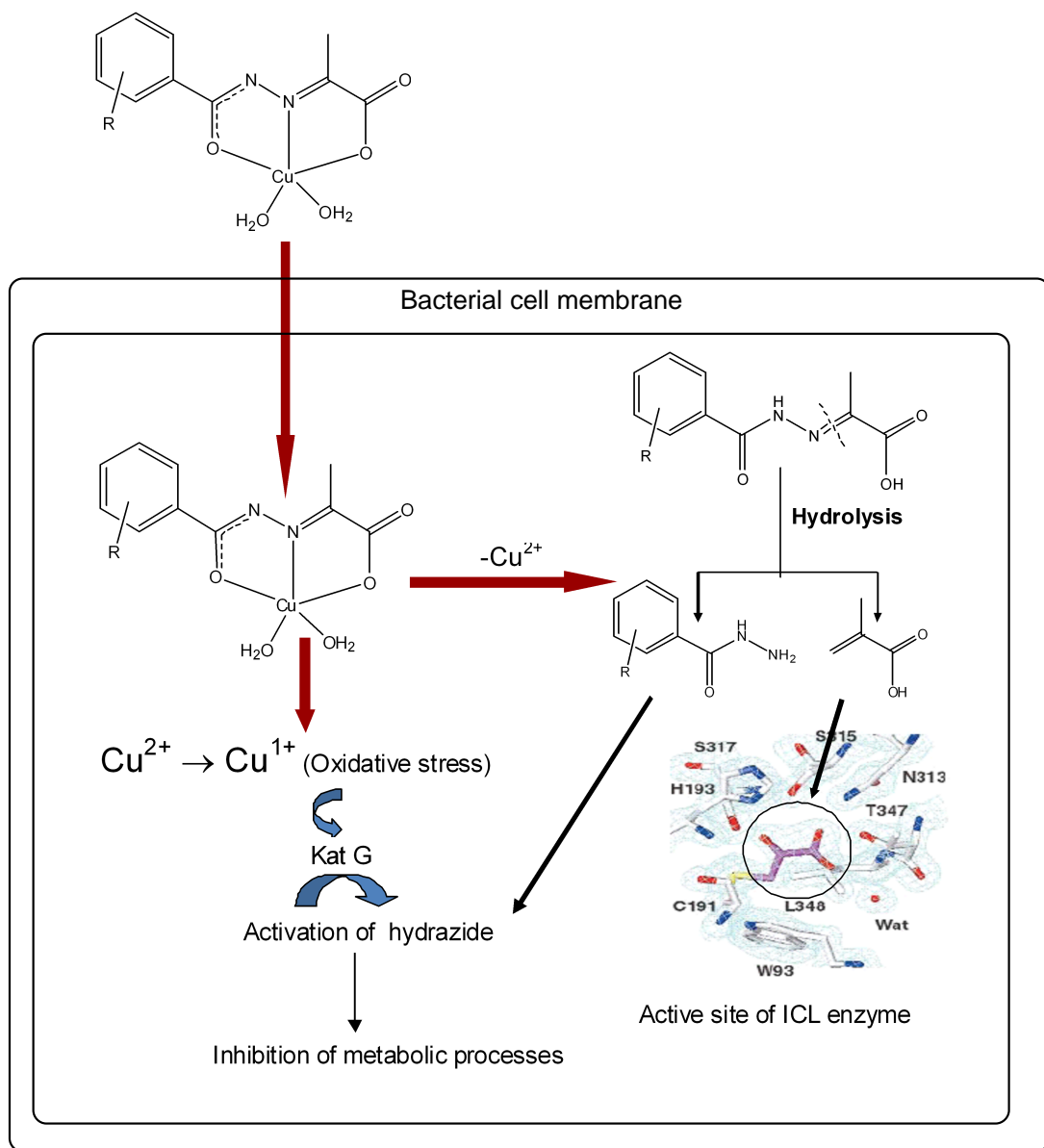


Figure 5.32. Suggested mechanism of action of Cu(II) complexes of PVAHs (active site of ICL enzyme⁵³)

Linking the hydrazinic chain (R-NH-NH_2) of hydrazides with either aldehydes or ketones, such as pyruvate moiety, could possibly block the acetylation of these hydrazinic drugs. The serum concentration of the hydrazide has been shown to be affected by *N*-acetyltransferase (NAT)-mediated acetylation of the amine centre, leading to either reduced or no antitubercular activity. Thus, the blocking of hydrazide acetylation would lead to an increase or the maintenance of their inhibitory activity against mycobacteria. NAT enzymes are not only present in humans but also known to exist in *Mycobacterium smegmatis* and *Mycobacterium tuberculosis*. It has been reported that the different forms of NAT enzymes have

been able to acetylate various substrates including INH and sulfonamide based antibacterial drugs under *in vitro* conditions. NAT enzymes can be classified into fast and slow acetylators and variable effective therapeutic doses of INH could possibly depend on different enzyme profiles.^{18,42}

One of the drawbacks of INH is that it causes vitamin B₆ deficiency. This is due to the fact that the amine group of INH forms Schiff base conjugate with the carbonyl group of vitamin B₆.²⁹⁶ Conjugating the amine group of hydrazide with appropriate aldehyde/ketone could possibly overcome the issue of vitamin B₆ deficiency.

In addition, the pyruvate moiety provides an extra anionic donor oxygen atom which balances the positive charge of the bound Cu(II) centre making the overall complex neutral. Pyruvate analogs such as nitropropionate and bromopyruvate have shown to inhibit the active site of isocitrate lyase (ICL).^{48,53} The ICL enzyme is known to play a vital role in the persistence of mycobacteria, hence it is considered as an attractive target for discovering new antitubercular drugs especially for persistent strains.

Recent computational studies done by Padhye and group illustrated that pyruvate hydrazones can potentially bind and inhibit the active site of ICL.⁸⁴ Moreover, the hydrazide/ hydrazone (NaHL20) derived from pyrazinoic acid is of particular interest, since this hydrolysis product of another well known antitubercular drug pyrazinamide is able to target persisting Mtb. Very recent studies in the literature illustrate that it is found to inhibit *trans*-translation, a vital process found to occur in stress survival and recovery from nutrient starvation.⁵⁸

As already discussed in chapter-1, isoniazid acts on mycolic acid biosynthesis⁸. The compound is believed to be a pro-drug, requiring activation by Mtb catalase-peroxidase (KatG)²⁹⁷ to generate a range of reactive oxygen species (ROS) and reactive organic radicals, which then damage multiple regions in the tubercle bacillus. INH can be activated *in vitro* by KatG with Mn²⁺ whereupon it loses its -NH-NH₂ side chain to form an isonicotinic acyl radical as indicated in figure 5.33 (step a).¹⁵ This active pharmacophore then reacts with NAD to form an INH-NAD adduct as shown in figure 5.33 (step b). This adduct formed within the active site of InhA enzyme in turn inhibits the InhA enzyme^{16-17,298}.

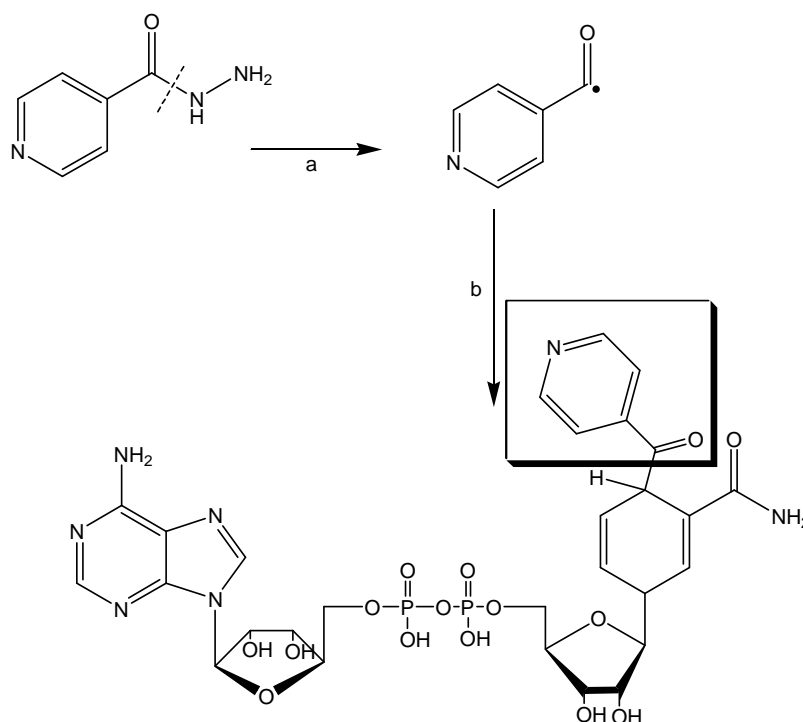


Figure 5.33: a) Formation of active pharmacophore, isonicotinic acyl radical (top right) from isonicotinic acid hydrazide (INH) (top left) b) formation of INH-NAD adduct¹⁵

In addition, the redox activity of metal ions is significant since bacterial resistance is known to be modulated by intracellular oxidative stress.⁴¹ It is known that an excess of free Cu(II) or Fe(II), causes oxidative stress, which in turn initiates the transcription of the catalyse-peroxidase (KatG) gene. Consequently, more KatG, which activates the hydrazide is produced, eventually leading to destruction of the bacterial cell.²⁹⁹ Resistance to isoniazid can occur in strains with impaired KatG proteins and lack of redox activity is associated with resistance to INH.⁴⁰ KatG appears to utilize superoxide anions to activate INH, as the INH turnover by the purified enzyme is completely abolished in the presence of a catalytic quantity of superoxide dismutase (SOD).⁴¹

Hence, Cu(II) complexes of pyruvate hydrazone can serve multiple purposes in antitubercular drug design which are as follows:

- 1) Eradicating the actively growing bacteria, this is proven from the present antitubercular studies and has been recently published by us.³⁰⁰
- 2) Mycobacteria which are resistant to present antibacterial drugs may be targeted with the Cu(II) complex of PVAHs since metal complexes, especially copper complexes, are known to inhibit the bacterial resistant strains.^{85,286}
- 3) Inhibition of persistent bacteria, which could possibly be achieved by pyruvate moiety, if it is capable of blocking the active site of ICL similar to other pyruvate analogs.^{48-50,53,301} In addition, hydrazone analogues derived from the pyrazinamide-containing pharmacophore may prove to be useful in inhibiting *trans*-translation process which are required to maintain the persistent state of bacteria.⁵⁸

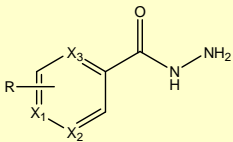
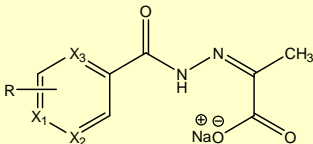
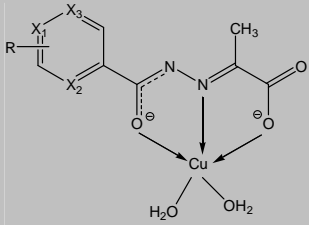
The failure of Zn(II) complexes of PVAHs to exhibit low MIC values can be attributed to the labile nature of the zinc complexes, which may eventually form Zn(II)-OH₂ species in aqueous solution. This is evident from the PBS study of the investigated Zn(II) complex, where [Zn(II)(HL20)₂] dissociates and releases its ligand, which then undergoes hydrolysis back to its parent hydrazide. Even though the overall Zn(II) complex is neutral, as evident from the single crystal X-ray structure, it fails to cross the bacterial cell membrane due to dissociation of PVAHs from the Zn(II) centre. The reason for the lower uptake of Zn(II) complexes can also be due to their limited solubility in aqueous media.

The other possible reason for high MIC values of Zn(II) complexes of PVAHs may be due to the redox inactive nature of the Zn(II) ion. If this is true then it supports the theory that oxidative stress is essential for the inhibitory activity of hydrazide type molecules. This is also reflected in the present antitubercular studies on PVAHs, where it is proven that the inhibitory action is greatly improved under high Fe conditions.

It should also be considered that the MIC values obtained are given in µg/mL, whereas the compounds have different molecular weights. Therefore, in order for a direct comparison of hydrazides with their respective hydrazones and

Cu(II) complexes the MIC values obtained in $\mu\text{g/mL}$ under high iron concentration were converted into picomolar concentrations ($\text{pM} = 10^{-12} \text{ M}$). The values are provided in Table 5.5 and the graphical representation of these MICs values are shown in figure 5.34. The number given on the X-axis corresponds to the number of the compound provided in Table 5.5.

Table 5.5: MIC values of selected hydrazides, PVAHs and their respective Cu(II) complexes in pM concentration under high iron conditions

No	Compound/R	Hydrazides	Hydrazones	Cu(II) complex
		(pM)	(pM)	(pM)
				
	INH	0.9	-	-
1	<i>p</i> -Me	213	66	<1.5
2	<i>p</i> -NO ₂	88	29	5.7
3	<i>p</i> - (CH ₃) ₃	167	56	2.8
4	<i>p</i> -NO ₂ , <i>m</i> -Me	164	27	<1.4
5	<i>p</i> -CF ₃	157	54	<1.3
6	<i>m</i> -F	415	65	1.5
7	<i>m</i> -OH	210	130	3.1
8	X ₂ , X ₃ = N	232	34	<1.6
	NaH ₃ D1	213	43	-

As can be gathered from Table 5.5, the MIC values of the Cu(II) complexes of PVAHs determined under high Fe conditions have comparable values to that of the frontline antitubercular drug INH (0.9 pM) ranging from <1.5 - 5.7 pM. While, the MIC values of hydrazides and hydrazones obtained under similar conditions falls in the range 88-415 pM and 27-130 pM respectively. Even though there is no improvement in terms of MIC values of the Cu(II) complexes with respect to INH, the copper complexes may be useful in targeting the bacterial strains which are proving resistant to INH.³⁰² Although, the MIC value in $\mu\text{g/mL}$ for the di-hydrazide

analogue (NaH₃D1) and its equivalent monoanalogue PVAH (NaHL9) is 16 µg/mL, but in pM concentration it is 43 and 66 pM, respectively. The slightly lower MIC value of NaH₃D1 is likely due to its increased cellular uptake, which may perhaps be due to its stability towards hydrolysis as evident from the PBS studies.

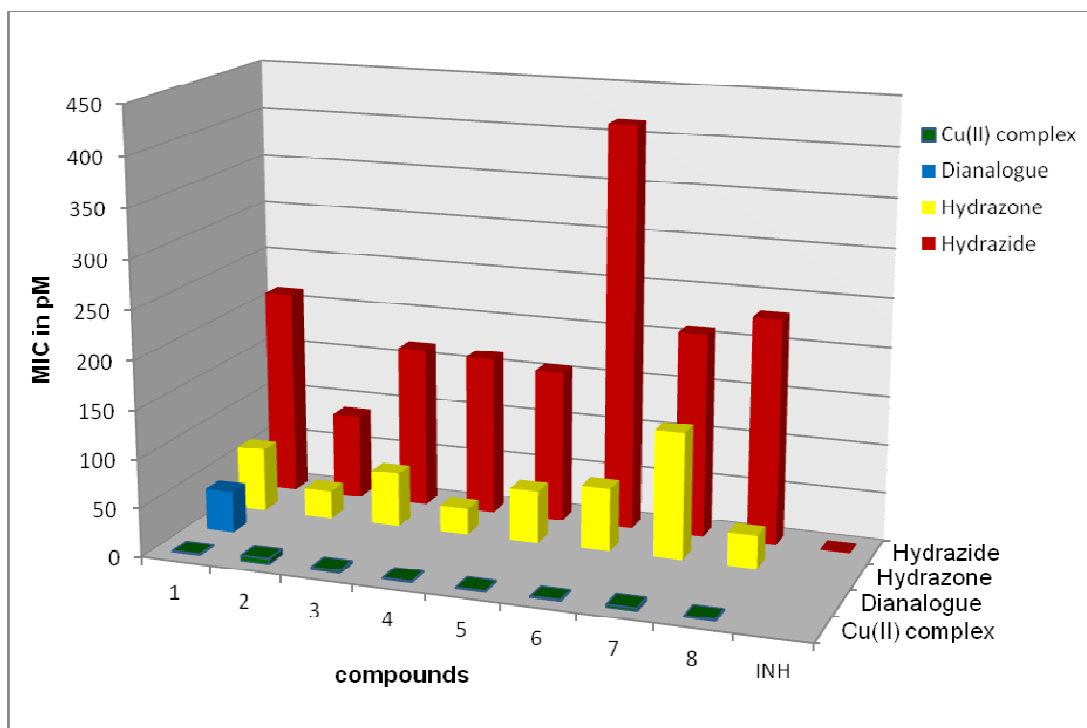


Figure 5.34: Graphical representation of MICs of listed compounds in table 5.5 in pM concentration

Surprisingly, another front-line antitubercular drug, pyrazinamide (prodrug for pyrazinoic acid (PZA)) is known to possess a MIC value as high as 200 µg/mL under certain conditions.³⁰³ In spite of its high MIC value, it is used in the treatment of tuberculosis and is one of the most widely used drugs in modern chemotherapy in addition to isoniazid, rifampicin and ethambutol. Interestingly, pyrazinoic acid hydrazide, a congener of pyrazinamide, exhibits a MIC value of 232 pM, whereas its hydrazone and Cu(II) complex have a MIC of 34 and <1.6 pM as listed in Table 5.5. Hence, active Cu(II) complexes of PVAHs may prove useful as potential prodrugs and may provide an excellent alternative to current drugs to which resistance is emerging.

5.6.2 Structure activity relationship (SAR) of active compounds (Cu(II) complexes) of the PVAHs series

- 1) Cu(II) complexes of PVAHs bearing electron donating groups such as *p*-CH₃ ([Cu(II)L9(H₂O)₂] and *p*-(CH₃)₃ ([Cu(II)L16(H₂O)₂]), exhibit promising antitubercular activity which can be attributed to the enhanced liposolubility due to the hydrophobic R groups on aromatic ring.⁷⁸
- 2) Those bearing fluoro [Cu(II)L15(H₂O)₂] (*m*-F) and trifluoro [Cu(II)L14(H₂O)₂] (*p*-CF₃) groups also exhibit low MIC values. Vigorita and coworker have extensively studied fluoro containing hydrazones and found that it enhances the antitubercular activities.⁸⁰
- 3) Complexes bearing electron withdrawing groups, such as nitro [Cu(II)L7(H₂O)₂] (*m*-CH₃, *p*-NO₂) and [Cu(II)L8(H₂O)₂] (*p*-NO₂) are potent against mycobacteria. Density functional theory (DFT) calculations done by Tawari *et.al.* on a series of antitubercular compounds illustrated that the negative potential resulting from the NO₂ group makes them more active than other compounds which do not possess a nitro substituent.³⁰⁴
- 4) [Cu(II)L20(H₂O)₂] containing two heterocyclic nitrogen atoms within the aromatic ring, which represents a pyrazinamide analogue of PVAH, possesses excellent activity. In contrast, the copper complexes of PVAHs bearing one heterocyclic nitrogen atom including the INH analogues of PVAH ([Cu(II)L18(H₂O)₂] and [Cu(II)L19(H₂O)₂]) failed to show any activity due to their insoluble nature, hence little or no cellular uptake is observed for these compounds.
- 5) [Cu(II)L3(H₂O)₂] bearing a OH group in *meta* position proved to be active, however [Cu(II)L2(H₂O)₂] and [Cu(II)L4(H₂O)₂] bearing OH groups in *ortho* and *para* position, respectively were inactive.
- 6) Copper complexes bearing OCH₃ groups, [Cu(II)L12(H₂O)₂] (*m*-OCH₃), [Cu(II)L13(H₂O)₂] (*p*-OCH₃), [Cu(II)L17(H₂O)₂] (*o*-OH, *p*-OCH₃) Br group, [Cu(II)L10(H₂O)₂] (*m*-Br), [Cu(II)L11(H₂O)₂] (*p*-Br) and Cl group, [Cu(II)L6(H₂O)₂] exhibited very high MIC values.

Hence, from the SAR analysis it can be concluded that the Cu(II) complexes containing a pyrazine ring in addition to methyl, *tert*-butyl, fluoro and nitro substituents on the aromatic ring proved to be active. In contrast, the copper complexes containing Br, Cl, OCH₃ substituents exhibited very high MIC values.

5.6.3 Antitubercular studies involving the CAH series

Due to low solubility of the CAH ligands and their corresponding Cu(II) complexes in aqueous solution, the compounds precipitated from the buffer solution that was used for the antitubercular testing. Hence, the activity studies could not be performed on the CAH series using the technique employed for the PVAHs series. However, this does not rule out the possibility that CAHs may exhibit *in vivo* inhibitory activity. In order to overcome this problem, testing could also be done using the disc diffusion method. In this assay, a compound is dissolved in an appropriate solvent (in which they are soluble) and the disc impregnated with the inhibitor solution is placed on the agar (media used to grow bacteria) plate with the bacterial culture. The zone of inhibition observed directly relates to the antibacterial activity of the tested compound.³⁰⁵ This would limit the requirement of an aqueous solution and allow hydrophobic molecules like CAHs to be put in direct contact with the bacterial cells, hence would increase their cellular uptake. Once the *in vitro* studies of compounds prove to be successful, the lead compound/s can be further modified to improve its bioavailability. The solubility issues may potentially be solved by encapsulating the hydrophobic drug in a cyclodextrin, which has been successfully achieved in related studies.³⁰⁵ Due to time constraints, however, the CAHs could not yet be tested using such methods, but these can serve as a future goal.

Hence, overall conclusions from the antitubercular studies that can be drawn are that the Cu(II) complexes of PVAHs are highly potent if compared with the hydrazone ligands and Zn(II) complexes. The low activity of PVAHs can be attributed to their anionic nature, whereas the neutrality of the Cu(II) complex of certain PVAHs facilitates the crossing of the bacterial cell membrane thereby inhibiting bacterial growth. The lower activity of neutral Zn(II) complexes may be related to the redox inactive nature of Zn(II) and/or their low uptake into bacterial cells due to their decreased stability and limited solubility in aqueous media. Similar solubility issues were encountered with the CAH series, as these compounds precipitated out in the buffer solution used. Hence, other methods like disc diffusion assays might be more suitable for such hydrophobic molecules.

Therefore, for a drug to be orally active there should be a balance between its hydrophilic and lipophilic character. Thus, Cu(II) complexation of PVAHs may represent an promising strategy in antitubercular drug design, because the ligand

part (PVAH) is water soluble and the Cu(II) ion renders it less polar and neutral by binding to its anionic donor atoms. This in turn facilitates the passive diffusion of the copper complex through the lipophilic cell membrane. In addition, the redox nature of Cu(II) centre may aid the antitubercular activity of metal complexes.

5.7 Summary of Chapter- 5

The pH-dependent stability studies of selected PVAHs indicate the hydrolysis of this type of ligands under acidic conditions, whereas the ligands are reasonably stable at basic pH. Similarly, the Cu(II) and Zn(II) complexes of NaHL20 are stable in basic pH. However $[\text{Cu(II)L20(H}_2\text{O)}_2]$ undergo irreversible dissociation in acidic pH below 2 which can be attributed to the simultaneous dissociation and hydrolysis of the coordinated PVAH. Whereas $[\text{Zn(II)(HL11)}_2]$ undergoes ligand dissociation below pH 5 followed by hydrolysis of the ligand below pH 2.

On the other hand, HCA1 and HCA5 from the CAH series remain almost stable under both basic and acidic conditions over a certain period of time. HCA5, which possesses an electron withdrawing group, undergoes hydrolysis as indicated from the spectrum recorded after 5 hours, no change was observed for HCA1. In addition, the corresponding Cu(II) complex $[\text{Cu(CA1)}_2]$ undergoes dissociation in acidic pH, however it re-forms and remains stable at basic pH.

Stability studies in PBS buffer at pH 7.4 studies indicate that NaHL11, NaHL14 and NaHL16 undergo slow hydrolysis with a $t_{1/2}$ ranging from 36 – 57 hours. Similarly, $[\text{Zn(HL11)}_2]$ proved to be unstable in PBS solution with a $t_{1/2}$ 32 hours. However, their respective Cu(II) complexes are stable over a monitored period of up to 6 days. Hence, the coordination of Cu(II) to PVAHs, helps to stabilise the ligands by preventing them from undergoing hydrolysis. Although, HCA1 appears to be stable in PBS buffer over the monitored period of time, its respective Cu(II) complex rapidly dissociates in the buffer solution. This indicates that the bidentate mode of binding of CAH is not as strong as the tridentate mode of binding of the PVAH ligands.

The di-hydrazide analogue of PVAH (NaH₃D1) proves to be fairly stable in PBS solution, which can attributed to the C-N single bond character of the molecule. This suggests that the reduction of azomethine bond can provide hydrolytic stability to a hydrazone ligand.

The antitubercular activity tests revealed that hydrazone formation increases the inhibitory activity of the corresponding hydrazides by almost 3-7 fold when tested under high iron conditions. In addition, coordinating the hydrazones to Cu(II), increases the activity further to up to 270 fold in certain complexes. The activities of some of the Cu(II) complexes of PVAHs are similar to that of the present

antitubercular drug isoniazid and may potentially prove useful in resistant bacterial strains. In addition, the redox active nature of Cu(II) may add to the activity of the compounds and, the coordination of Cu(II) to di-anionic PVAHs provided stability and lipophilicity to the resulting copper complexes. This cannot be achieved in Zn(II) complexes of PVAHs, which fail to show any promising activity.

The clogP values indicate greater lipophilicity of CAHs over PVAHs, which can prove to be useful as it can facilitate the higher uptake of hydrophobic molecules across the lipophilic cell membrane of bacteria. Unfortunately, CAHs could not be tested for their antimycobacterial activity using the assay used for PVAH series due to their limited solubility in aqueous buffer solution.

Hence, Cu(II) complexes of PVAHs can be considered as potential prodrug candidates for the treatment of TB and a further investigation of these complexes on MDR strains of mycobacteria would be very informative.

Chapter-6
Conclusions and Future Work

6.0 Conclusions and Future work

6.1 Overall Conclusions

A series of sodium pyruvate-based hydrazones (PVAHs); NaHL1-NaHL20, with a selection of aromatic substituents, ranging from electron withdrawing to electron donating groups, were synthesised and characterised by ^1H NMR spectroscopy, ^{13}C NMR spectroscopy, high resolution ESI mass spectrometry, infrared spectroscopy, elemental analysis and melting point analysis. Variable temperature ^1H NMR studies indicate that PVAHs exist as a mixture of *E* and *Z* isomers in solution, with the *Z* form predominating owing to the strong hydrogen bond formed between amide N-H and carboxylate oxygen atom. This assignment was further confirmed by the torsional angle obtained from the single crystal X-ray structure data of NaHL9 and NaHL11, which confirm that the sodium salts of the ligands adopt the *Z* conformation. In contrast, NaHL20, which was crystallised in its protonated form ($\text{H}_2\text{L20}$) adopts the *E* conformation in the solid state.

Furthermore, the Cu(II) and Zn(II) complexes of the PVAHs were synthesised and characterised by using the above mentioned techniques, as appropriate. Single crystal X-ray diffraction data indicates that the Cu(II) complexes mainly exhibit square pyramidal geometry, whereas Zn(II) coordinates two ligands to obtain octahedral geometry. The two ligands are coordinated meridionally due to the rigidity of the two ligands. The PVAH ligands bind to both Cu(II) and Zn(II) centres in a tridentate manner through the ONO donor system, forming two stable five membered chelate rings around the metal centre. In order to bind to the metal centre in a tridentate fashion the ligand has to change to *E* conformation, as was confirmed by the torsional angle determined for selected Cu(II) and Zn(II) complexes by X-ray crystallography.

In the square pyramidal Cu(II) complexes the PVAH ligand binds in a dianionic manner (L^{2-}), whereas in the octahedral Zn(II) complexes two PVAH ligands bind to Zn(II) centre in a monoanionic fashion (HL^-), giving rise to overall neutral metal complexes in both cases. The remaining two coordination sites of the square pyramidal complexes are occupied by chloride or neutral solvent molecules such as water and methanol. The τ value of obtained for the square pyramidal Cu(II) complexes of PVAHs, indicates a slight distortion from perfect square pyramidal geometry. The apical bond distances are significantly longer than the equatorial bond distances, indicating an appreciable Jahn - Teller distortion, as expected for Cu(II) complexes due to the d^9 electron count. The aromatic substituents have little or no influence on the

bond lengths and bond angles in the direct vicinity of metal centre. The ligands remain essentially planar when bound to Cu(II) in the square pyramidal complexes, however the ligands lose their planarity when bound in an octahedral geometry in order to reduce the steric repulsion between the two ligands bound to the same metal centre.

Infrared studies indicate that electron withdrawing groups on the aromatic ring shift the stretching frequencies of carbonyl functional groups towards higher frequencies, whereas electron donating groups have the opposite effect. A similar effect is observed in NMR spectroscopy, where the resonances assigned to the amide proton and azomethine carbon of PVAHs possessing electron withdrawing groups exhibit downfield shifts in comparison to those containing non-substituted and/or electron withdrawing groups. As a general trend, metal complex formation leads to the shifting and consequently merging of stretching frequencies assigned to the carbonyl, carboxylate and azomethine groups.

The investigated PVAH ligands are redox inactive except for NaHL8, which exhibits reversible redox behaviour due to the $-\text{NO}_2$ substituent. The cyclic voltammetric studies indicate that the Cu(II) is reduced to Cu(I) when a negative potential starting from -1000 mV with respect to Ag/AgCl is applied. The redox peak associated with the $\text{Cu}^{2+}/\text{Cu}^{1+}$ couple is classified as a quasi-reversible process, as the ΔE value increases with an increase in scan rate and $\Delta E \gg 59$ mV. The quasi-reversible behaviour is likely to be due to structural reorganisation taking place within the coordination sphere, whilst changing from a square-pyramidal Cu(II) to a tetrahedral Cu(I) coordination geometry. In order to obtain evidence in support of this theory, the Cu(I) complexes of NaHL8 and NaHL9 were synthesised. The crystal structure of both Cu(I) complexes indicate that PVAH ligands bind partially to the Cu(I) centre in a bidentate manner, thus allowing the Cu(I) complex to adopt a tetrahedral geometry. The other two coordination sites are occupied by the soft phosphorus donor atoms of PPh_3 ligands which were introduced during the synthesis of the Cu(I) complex in order to stabilise the soft Cu(I) centre. The ^1H NMR spectra of the Cu(I) complexes confirm their diamagnetic nature, whereas broad phosphorus signals in ^{31}P NMR spectra at room temperature indicate ligand-exchange processes in solution.

In the cyclic voltammograms, redox waves corresponding to the reduction of Cu^{1+} to Cu^0 have also been observed, indicating that the investigated Cu(II) complexes are reduced to Cu(0), through a Cu(I) intermediate. The redissolution of the Cu(0) deposited on the electrode surface leads to a higher anodic peak current as compared

to its corresponding cathodic peak current. The peak potential values obtained for the Cu(II) complexes indicate that the type of PVAH ligand affects the metal-based redox potential, when compared with Cu(II) for example in CuCl₂, irrespective of the substituent on the aromatic ring.

In order to investigate the stability of the Cu(II) complexes in the electrochemical solvent, DMSO, EPR spectra were recorded for selected complexes and these were compared with the spectra of 'free' Cu(II) ions (CuCl₂, CuSO₄). The EPR parameters, A_{\parallel} , g_{\parallel} and g_{\perp} were found to be similar for the studied Cu(II) complexes of PVAHs, but distinct from 'free' Cu(II) ions (CuCl₂, CuSO₄). Hence, it can be concluded from the EPR studies that the ligands remain bound to the Cu(II) centre, even though there is large excess of DMSO present in solution.

In addition, a series of cinnamaldehyde hydrazones; HCA1-HCA2 and their respective Cu(II) complexes was synthesised and characterised. ESI-MS and elemental analysis data indicate a 1:2, Cu(II):L ratio with a possible bidentate mode of binding allowing for a square planar geometry. The reduction of the azomethine bond of HCA1 was unsuccessful, as the olefinic bond was reduced instead, as indicated by ESI-MS and NMR spectroscopic analysis. The X-ray crystal structures of PVAHs reveal extensive intra and intermolecular hydrogen bonding, in contrast to CAHs. This may be accounted for by the higher number of hydrogen bond donor and acceptor atoms in PVAHs. Accordingly, higher CLogP values are obtained for CAHs. These higher CLogP values may lead to poor oral drug absorption but may prove to be advantageous in promoting permeation through the lipid bilayer of the mycobacterial cell wall.

Positive ion ESI-MS of the Cu(II) complexes of PVAHs and CAHs indicated the presence of two positive charges, either due to Na⁺ and H⁺ or two protons. This can be rationalised by the reduction of Cu(II) to Cu(I) during the ionisation process.

The pH-dependent stability studies of selected PVAHs and their respective Cu(II) and Zn(II) complexes indicate that these are unstable under acidic conditions, but reasonably stable at basic pH. The instability of the compounds is due to the hydrolysis of the azomethine bond under acidic conditions. On the other hand, HCA1 and HCA5 from the CAH series remain reasonably stable under both basic and acidic conditions over a certain period of time. HCA5, which possesses an electron withdrawing substituent, undergoes hydrolysis, as indicated from the spectrum recorded after 5 hours, no change was observed for HCA1. In addition, the corresponding Cu(II)

complex $[\text{Cu}(\text{CA1})_2]$ undergoes dissociation in acidic pH, however it re-forms and remains stable at basic pH.

Stability studies in PBS buffer at pH 7.4 indicate that NaHL11, NaHL14 and NaHL16 undergo slow hydrolysis with a $t_{1/2}$ ranging from 36 – 57 hours. Similarly, $[\text{Zn}(\text{HL11})_2]$ proved to be unstable in PBS buffer with a $t_{1/2}$ of 32 hours. In contrast, the corresponding Cu(II) complexes are stable over a period of up to 6 days. Hence, the coordination of Cu(II) to PVAHs, helps to stabilise the ligands by preventing them from undergoing hydrolysis. Although HCA1 appears to be stable in PBS buffer over the monitored period of time, its Cu(II) complex rapidly dissociates in the buffer solution. This indicates that the bidentate mode of binding of CAHs is not as strong as the tridentate mode of binding of the PVAH ligands.

The reaction of 4-methyl benzoyl hydrazide and 3-bromopyruvate leads to the formation the di-hydrazide analogue (NaH₃D1) *via* dehalogenation. The identity of the product was confirmed using ESI MS and NMR spectroscopy. NaH₃D1 is fairly stable in PBS buffer, which can be attributed to the C-N single bond and/or the two aromatic rings of the molecule.

Antitubercular activity tests revealed that the hydrazone formation increases the inhibitory activity of the corresponding hydrazides by almost 3-7-fold when tested under high iron conditions. In addition, coordinating the hydrazones to Cu(II) increases the activity further to up to 270-fold in certain complexes. The activity of some of the Cu(II) complexes of PVAHs are similar to that of the present antitubercular drug isoniazid and may potentially prove useful in resistant bacterial strains. The Cu(II) complexes of PVAHs possessing nitro, fluoro, methyl and *tert*-butyl groups are active, whereas those with methoxy, bromo and chloro substituents were inactive. In addition, the redox active nature of Cu(II) may add to the activity of the compounds and the coordination of Cu(II) to di-anionic PVAHs provided stability and lipophilicity to the resulting copper complexes. This cannot be achieved in Zn(II) complexes of PVAHs, and these hence fail to show any promising activity.

The clogP values indicate greater lipophilicity of CAHs than PVAHs, which can be useful as it can facilitate the uptake of hydrophobic molecules across the lipophilic cell membrane of mycobacteria. Unfortunately, CAHs could not be tested for their antimycobacterial activity using the assay used for PVAH series due to their limited solubility in aqueous buffer.

In summary, the aim of this project to synthesise a series of metal-based antitubercular compounds has been achieved. The Cu(II) complexes of PVAHs which exhibited potential activity against Mtb can be considered as potential prodrugs for TB.

6.2 Future Work

This project can be taken to various directions which are as follows:

- The reduction of the azomethine bond could not be achieved using sodium borohydride and catalytic hydrogenation. Hence strong reducing agents, such as LiAlH₄ could be tried. If this proves to be successful, then the complexation of the reduced hydrazones could also be tried. The reduced hydrazones and their respective metal complexes can be further investigated for their stability in various pH conditions and their half-life can be determined using PBS buffer. In addition, antitubercular activity testing can also be carried out.
- It is evident from the antitubercular studies that adding Fe(II) salts improves the activity of the compounds drastically. Hence, the synthesis of Fe(II) complexes of PVAHs can also serve as a good strategy to improve the MIC values of hydrazones and antitubercular studies could help to achieve a comparative study with Cu(II) complexes of PVAHs.
- According to literature studies metal complexes have proven to combat bacterial resistance.⁸⁷ Therefore, Cu(II) complexes of PVAHs which exhibited promising MIC values against INH susceptible bacteria can be tested for their potential against INH resistant strains.
- As compounds containing the pyruvate moiety have been shown to inhibit the ICL enzyme⁵³, PVAHs can be explored for ICL inhibition. This could be achieved by either co-crystallising PVAHs with the ICL enzyme so as to study the binding mode of the ligand with the active of the enzyme. Earlier computational studies have shown that PVAHs can bind in the active site of ICL⁸⁴, hence to prove this concept co-crystallising PVAH/s with ICL can be tried. ICL enzyme inhibitory assays as reported earlier for hydrazones⁸³ can also be tried in order to study the behavior of direct inhibition of the enzyme by PVAHs and their metal complexes.
- Due to low solubility of the CAH ligands and their corresponding Cu(II) complexes in aqueous solution, the compounds precipitated from the buffer solution that was used for the antitubercular testing. In order to overcome this problem, testing could also be done using the disc diffusion method.³⁰⁶ This

would limit the requirement of an aqueous solution and allow hydrophobic molecules like CAHs to be put in direct contact with the bacterial cells, hence would increase their cellular uptake.

- ClogP values of PVAH and CAH ligands were calculated using OSIRIS software programme²¹⁷, however this software does not allow calculating the values of metal complexes. Instead, the logP could be obtained using the octanol/water partition coefficient method. The logP obtained for the ligands can be used as a comparative study with clogP values calculated using computational methods.

Chapter-7
Experimental

7.0 Experimental

7.1 Materials

Chemicals were purchased from the following suppliers: Pyruvic acid (Fluka), all commercial hydrazides, cinnamaldehyde and metal salts (Sigma-Aldrich), TLC plates F₂₅₄ (Merck), solvents, NaOH pellets, conc. HCl (Fisher scientific), Dulbecco's PBS buffer (Sigma).

7.2 Instrumentation

¹H and ¹³C NMR spectra were recorded on a JEOL ECS, ECX 400 (¹H NMR 400 MHz, ¹³C 100.6 MHz). Chemical shifts (δ) are given in terms of parts per million (ppm) referenced to the residual solvent *d*₆-DMSO: ¹H NMR 2.50 ppm, ¹³C NMR 39.52 ppm, *d*₄-MeOD: ¹H NMR 3.30 ppm, ¹³C NMR 49.50 ppm, D₂O: ¹H NMR 4.90 ppm. All carbon-13 experiments were confirmed using carbon-DEPT experiments. VT experiments were recorded on a Bruker 500 MHz instrument (¹H NMR 500 MHz) and carried out by Heather Fish. The spectra were processed using Bruker's Topspin software. TLC was carried out on a Merck silica gel 60 F₂₅₄ aluminium backed plates using a chloroform:methanol solvent system and visualised under a UV lamp (chromato-vue Model CC-10) and/or stained with iodine. Infrared spectra were recorded on an Avatar 370 FT-IR Thermo Nicolet instrument (400 – 4000 cm⁻¹) using KBr discs. The data was processed using OMNIC software. The KBr purchased from Sigma-Aldrich was used as obtained. Electro spray ionisation mass spectrometry (ESI-MS) spectra were recorded on a Bruker microTOF electrospray mass spectrometer by Dr. T. Dransfield and Dr. K. Heaton. Elemental (CHN) analysis was performed by Dr. P. Helliwell and Dr. G. McAllister on an Exeter analytical CE-440 elemental analyser. Melting points were measured on a Stuart Scientific SMP3 apparatus. Electron paramagnetic resonance (EPR) was performed on JEOL JESRE-1 X-band machine in Dr. Victor Chechik's laboratory by Kazim Naqvi.

7.3 X-ray Crystallography

Single crystal X-ray diffraction data was collected and processed with the help of Dr. A. Whitwood, Dr. R. Thatcher and Dr. S. Hart.

7.3.1 Bruker SMART Apex

Diffraction data for **NaHL9.2H₂O**, **NaHL112H₂O**, **[Cu(L7)(H₂O)(MeOH)]**, **[Cu(L8)(MeOH)₂]**, **[Cu(L9)(H₂O)₂]**, **[Cu(L11)(H₂O)₂].H₂O**, **[Cu(L17)(H₂O)₂]**, **[Cu(HL9)₂Cl₂]**, **[Cu(HL15)₂Cu(HL15)(L15)]** and **[Zn(HL8)₂].H₂O** were collected on a Bruker Smart Apex diffractometer with Mo-K_α radiation ($\lambda = 0.71073 \text{ \AA}$) using a SMART CCD camera. Absorption corrections were applied by SADABS (v2.10).³⁰⁷ Structures were solved by either direct or Patterson methods using SHELXS-97 and refined by full-matrix least squares using SHELXL-97.³⁰⁸ All non-hydrogen atoms were refined anisotropically. Hydrogen atoms were placed using a riding model and included in the refinement at calculated positions. Acidic protons were placed using difference map method.

7.3.2 Oxford Diffraction SuperNova

Diffraction data for **H₂L20.H₂O**, **[Cu(L13)(H₂O)(MeOH)]**, **[Zn(II)(HL7)₂].H₂O.DMSO**, **[Zn(HL9)₂].H₂O.CH₃OH**, **[Zn(HL13)₂]**, **[Cu(I)₂HL8(PPh₃)₅]PF₆**, **[Cu(I)₂HL9(PPh₃)₅]PF₆**, **[Cu(I)₂HL9(PPh₃)₄]PF₆.2Et₂O.H₂O**, **HCA2** and **HCA5** were collected on an Oxford Diffraction SuperNova diffractometer with Mo-K_α radiation ($\lambda = 0.71073 \text{ \AA}$) using a EOS CCD camera. The crystals were cooled with an Oxford Instruments Cryojet. Face-indexed absorption corrections were applied using SCALE3 ABSPACK scaling. OLEX2³⁰⁹ was used for overall structure solution, refinement and preparation of computer graphics and publication data. Within OLEX2, the algorithms used for structure solution were either direct or Patterson methods using SHELXS-97 and refinement by full-matrix least-squares used SHELXL-97 within OLEX2. All non-hydrogen atoms were refined anisotropically. Hydrogen atoms were placed using a riding model and included in the refinement at calculated positions. Acidic hydrogen atoms were placed using difference map method.

7.4 Stability Studies using UV/vis Spectroscopy

7.4.1 pH titrations

7.4.1.1 Preparation of solution

Accurate weight measurements were conducted on a Mettler AE 240 five figure balance. The stock solution for pH titrations of PVAH series including NaHL9, NaHL20, [Cu(L20)(H₂O)₂], [Zn(HL20)₂] each with a concentration of 1mM was prepared in deionised water. 5 mL of 1mM respective stock solution accurately measured using Eppendorf pipette were made up to a final concentration of 0.05 mM using deionised water with 100 mL volumetric flask. The stock solution for pH titrations of CAH series including HCA1, HCA5 and [Cu(CA1)₂] each with a concentration of 1mM was prepared in methanol. 2 mL of a 1mM respective stock solution accurately measured using Eppendorf pipette were made up to a final concentration of 0.02 mM using methanol:deionised water(4:1) with 100 mL volumetric flask. pH were adjusted using 0.001 M HCl and 0.001 M NaOH for acid and base titrations respectively. 0.001 M NaOH was made by dissolving NaOH pellets in deionised water and 0.001 M HCl was made using conc. HCl (12 M) in deionised water. pH values were determined using a WTW Profilab pH 597 pH meter with a Mettler Toledo Inlab 422 electrode.

7.4.1.2 UV/vis measurements

Acid and base titrations were performed individually in two sets of experiments. The UV/vis spectra were recorded on a HP 8453 Agilent Diode Array spectrophotometer using a 5Q quartz UV cell with path length 10 mm. Dropwise addition of either 0.001 M HCl or 0.001 M NaOH was added to the respective stock solution (approx 40 mL) at regular intervals. Once the pH was stabilised, the solution was transferred into the UV cell and the UV/vis spectra were recorded in the 1.0 – 13.0 pH range at room temperature. These spectra were recorded manually at an interval ranging from 0.2-1.0 pH units. The UV/vis spectra were recorded in the range 200-1100 nm.

7.4.2 PBS stability studies**7.4.2.1 Preparation of solution**

The stock solution for PBS stability studies of PVAH series including NaHL11, NaHL14, NaHL16, NaH₃D1, [Cu(L11)(H₂O)₂], [Cu(L14)(H₂O)₂], [Cu(L16)(H₂O)], [Zn(HL11)₂] each with a concentration of 1mM was prepared in spectroscopic grade DMSO. 0.05 mL of 1mM respective stock solution accurately measured using Eppendorf pipette were made up to a final concentration of 0.05 mM using PBS buffer:DMSO (9:1) with 10 mL volumetric flask. Dulbecco's PBS buffer purchased from Sigma was used as obtained. For CAHs series, the compounds including HCA1 and [Cu(CA1)₂] the final concentration of 0.02 mM with a ratio of 1:1; PBS buffer:DMSO was used.

7.4.1.2 UV/vis measurements

10 mL of final stock solution was incubated at 37 °C in a closed container (carousel tube). The temperature was maintained using a water bath with the carousel tube immersed in it. Solution was transferred to the UV cells at regular intervals (at indicated hours in the study) and the UV/vis spectra were recorded ranging from 200-1100 nm.

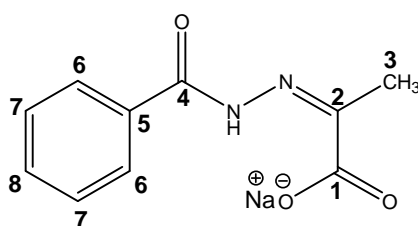
7.5 Electrochemistry

Cyclic voltammetric experiments were performed on an Epsilon, bioanalytical system instrument (BASi). The studies were carried out at room temperature using a standard three electrode configuration, consisting of a platinum working electrode, 1.6 mm (MF-2013), platinum wire as auxiliary electrode, 7.5 cm (MW-1032) and Ag/AgCl reference electrode (MF-2013) with supporting electrolyte 0.1 M *tetra*-butyl ammonium hexafluorophosphate (TBAHFP) in DMSO. The Ag/AgCl reference electrode was stored in 3M NaCl solution. The solution was purged with N₂ gas prior to use and maintained under a layer of N₂ throughout the experiment. The platinum working electrode was polished with alumina on textmet pads, washed with deionised water and DMSO which was further dried before using. The concentration of the ligand and the complexes was approximately 2 mM and the cyclic voltammogram was scanned in DMSO. After use of the electrodes were washed with DMSO, water and conc. HNO₃. Electrochemical grade, TBAHFP (99% CHN) was purchased from Fluka and used as obtained, whereas spectrophotometric grade DMSO (99.9%) was purchased from Sigma and dried over molecular sieves (3 Å) before use. Ferrocene (98 %) was purchased from Sigma-Aldrich and recrystallised using ethanol and then sublimed under vacuum using Schlenk lines. The sublimed ferrocene was used as an internal standard.

7.6 General synthetic procedure and characterisation detail of PVAHs (NaHL1-NaHL20)

The respective hydrazide (1.82 mmol) and sodium pyruvate (1.82 mmol) were dissolved in 25 ml of a water-methanol mixture (methanol-water; 7:3). The solution was heated under reflux for 2 hours. The product was precipitated with Et₂O, isolated and recrystallised from ethanol. The purified product was dried in *vacuo*

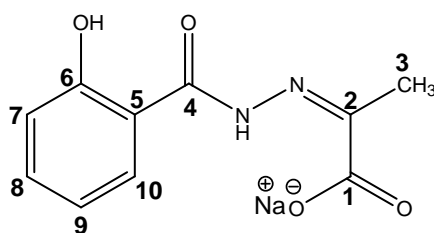
NaHL1



Sodium 2-[(benzoyl)-hydrazono]-propionate

NaHL1 was synthesised using sodium pyruvate 0.20 g (1.82 mmol) and benzoyl hydrazide 0.25 g (1.82 mmol) to give NaHL1, 0.34 g (1.49 mmol, 82%); **Melting point:** 110-112 °C; **ESI-MS:** positive ion $m/z = 229.0586$, 100%, HR ESI-MS: For C₁₀H₁₀N₂O₃Na ([M+H]⁺), observed mass 229.0586, calculated mass 229.0584, difference -0.3 mDa; **δ ¹H NMR** (400 MHz, *d*₆-DMSO): Major isomer: 2.01 (s, 3H, H-3), 7.45-7.90 (m, 5H, H-6-8), 16.17 (bs, 1H, H-N), Minor isomer: 2.15 (s, H-3); **δ ¹³C NMR** (100.6 MHz, *d*₆-DMSO): Major isomer: 166.3 (4°), 162.0 (4°), 150.7 (4°), 133.7 (4°), 131.7 (CH), 128.8 (CH), 126.9 (CH), 21.2 (CH₃), Minor isomer: 132.2 (CH), 128.4 (CH), 128.2 (CH), 13.9 (CH₃); **Significant IR bands :** (KBr disc, cm⁻¹): (ν C=O, ν_{asym} COO, ν C=N) 1645*br*.

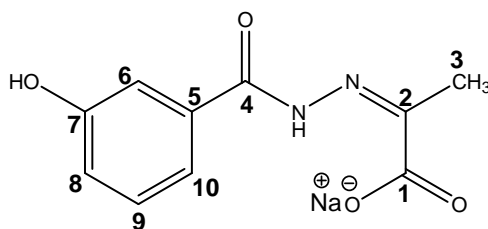
NaHL2



Sodium 2-[(2-hydroxy-benzoyl)-hydrazono]-propionate

NaHL2 was synthesized using sodium pyruvate 0.20 g (1.82 mmol) and 3-hydroxy benzoyl hydrazide 0.28 g (1.82 mmol) to give NaHL2, 0.40 g (1.63 mmol, 89%); **Melting point**: >350 °C; **ESI-MS**: positive $m/z = 245.0541$, 100%, HR ESI-MS: For $C_{10}H_{10}N_2O_4Na$ ($[M+H]^+$), observed mass 245.0541, calculated mass 245.0533, difference -0.8 mDa; δ **1H NMR** (400 MHz, d_6 -DMSO): Major isomer: 2.05 (s, 3H, H-3), 6.89 (apparent t, 1H, $J_{H-H} = 7.4$ Hz, H-8 or H-9), 7.14 (d, 1H, $J_{H-H} = 8.4$ Hz, H-7 or H-10), 7.39 (apparent t, 1H, $J_{H-H} = 7.4$ Hz, 1.4 Hz, H-7 or H-10), 7.68 (d, 1H, $J_{H-H} = 8.4$ Hz, 1.2 Hz, H-7 or H-10), 13.04 (1H, br, H-O) 16.02 (1H, br, H-N), Minor isomer: 2.09 (s, H-3), 6.83 (apparent t, $J_{H-H} = 7.4$ Hz, H-8 or H-9), 7.01 (d, $J_{H-H} = 8.4$ Hz, H-7 or H-10), 7.33 (apparent t, $J_{H-H} = 7.4$ Hz, H-8 or H-9), 7.95 (d, $J_{H-H} = 8.4$ Hz, H-7 or H-10); δ **^{13}C NMR** (100 MHz, d_6 -DMSO): Major isomer: 165.9 (4°), 164.6 (4°), 160.2 (4°), 151.5 (4°), 133.7 (CH), 130.5 (CH), 117.8 (CH), 118.7 (CH), 115.5 (C-4), 21.3 (CH₃), Minor isomer: 167.2 (4°), 133.6 (CH), 130.5 (CH), 117.9 (CH), 117.3 (CH), 48.6 (CH₃), 12.9 (CH₃); **Significant IR bands** : (KBr disc, cm^{-1}): (ν OH) 3499br, (ν C=O) 1661s, (ν_{asym} COO, ν C=N) 1606s.

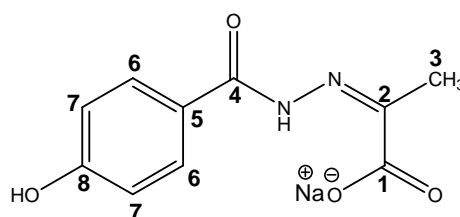
NaHL3



Sodium 2-[(3-hydroxy-benzoyl)-hydrazone]-propionate

NaHL3 was synthesised using sodium pyruvate 0.20 g (1.82 mmol) and 3-hydroxy-benzoyl hydrazide 0.27 g (1.82 mmol) to give NaHL3, 0.39 g (1.59 mmol, 87%); **Melting point:** 278-281 °C; **ESI-MS:** positive $m/z = 245.0533$, 100%; HR ESI-MS: For $C_{10}H_{10}N_2O_4Na$ ($[M+H]^+$), observed mass 245.0533, calculated mass 245.0533, difference 0.0 mDa; δ **¹H NMR** (400 MHz, d_6 -DMSO): Major isomer: 2.01 (s, 3H, H-3), 6.97 (dd, 1H, $J_{H-H} = 7.8$ Hz, 2.08 Hz, H-8 or H-10), 7.78 (m 3H, H-6, H-9, H-8 or H-10), 10.20 (bs, 1H, H-O), 15.92 (bs, 1H, H-N), Minor isomer: 2.16 (s, H-3), 7.02 (d, $J_{H-H} = 7.8$ Hz, H-8 or H-10); δ **¹³C NMR** (100.6 MHz, d_6 -DMSO): Major isomer: 166.4 (4°), 162.3 (4°), 157.9 (4°), 150.5 (4°), 135.1 (4°), 129.8 (CH), 118.9 (CH), 117.3 (CH), 114.1 (CH), 21.2 (CH₃), Minor isomer: 129.6 (CH), 118.7 (CH), 115.0 (CH), 13.9 (CH₃); **Anal. Calcd.** for $C_{10}H_9N_2O_4Na_1 \times 1.6 H_2O$: C, 44.00; H, 4.50; N, 10.26. Found: C, 44.16; H, 4.43; N, 10.10; **Significant IR bands** : (KBr disc, cm^{-1}): (ν OH) 3426 br , (ν C=O) 1663 s , (ν_{asym} COO) 1633 s , (ν C=N) 1612 s .

NaHL4

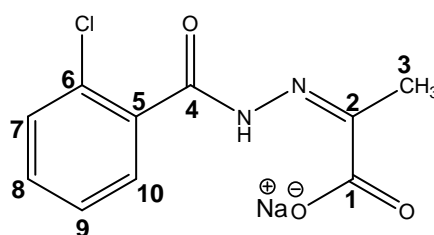


Sodium 2-[(4-hydroxy-benzoyl)-hydrazone]-propionate

NaHL4 was synthesised using sodium pyruvate 0.20 g (1.82 mmol) and 3-hydroxy-benzoyl hydrazide 0.28 g (1.82 mmol) to give NaHL4, 0.37 g (1.51 mmol, 83%); **Melting point:** 310-312 °C; **ESI-MS:** positive $m/z = 245.05$, 100%, HR ESI-MS: For $C_{10}H_9N_2O_4Na$ ($[M+H]^+$), observed mass 245.0533, calculated mass

245.0533, difference -0.0 mDa; δ $^1\text{H NMR}$ (400 MHz, d_6 -DMSO): Major isomer: 2.01 (s, 3H, H-3), 6.88 (d, 2H, $J_{\text{H-H}} = 8.4$ Hz, H-6 or H-7), 7.68 (d, 2H, $J_{\text{H-H}} = 8.4$ Hz, H-6 or H-7), 10.82 (bs, 1H, O-H), 15.75 (bs, 1H, N-H), Minor: 2.16 (s, H-3), 7.84 (d, $J_{\text{H-H}} = 8.4$ Hz, H-6 or H-7); δ $^{13}\text{C NMR}$ (100.6 MHz, d_6 -DMSO): Major isomer: 166.5 (4°), 162.0 (4°), 149.5 (4°), 135.1 (4°), 128.9 (CH), 123.8 (4°), 115.4 (CH), 21.0 (CH_3), Minor: 130.4 (CH), 115.1 (CH), 12.9 (CH_3); **Significant IR bands** : (KBr disc, cm^{-1}): (ν OH) 3452 br , (ν C=O) 1684 m , (ν C=O) 1659 s , (ν_{asym} COO) 1630 s , (ν C=N) 1610 s .

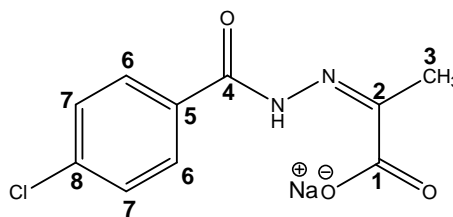
NaHL5



Sodium 2-[(2-chloro-benzoyl)-hydrazono]-propionate

NaHL5 was synthesized using sodium pyruvate 0.20 g (1.82 mmol) and 3-hydroxy benzoyl hydrazide 0.25 g (1.82 mmol) to give NaHL5, 0.40 g (1.52 mmol, 83%); **Melting point**: 105-108 $^\circ\text{C}$; **ESI-MS**: positive $m/z = 263.02$, 100%, HR ESI-MS: For $\text{C}_{10}\text{H}_9\text{N}_3\text{O}_3\text{Cl}_1\text{Na}$ ($[\text{M}+\text{H}]^+$), observed mass 263.0202, calculated mass 263.0194, difference -0.8 mDa; δ $^1\text{H NMR}$ (400 MHz, d_6 -DMSO): Major isomer: 2.04 (s, 3H, H-3), 7.31-7.57 (m, 4H, H-7-10), 15.48 (bs, 1H, H-N), Minor: 1.96, 1.72 (s, H-3), 11.33 (bs, H-N), 15.10 (bs, H-N); δ $^{13}\text{C NMR}$ (100.6 MHz, d_6 -DMSO): 135.6-165.6 (4°), (126.7-131.6 (CH), 21.1, 14.0 (CH_3); **Anal. Calcd** for $\text{C}_{10}\text{H}_8\text{N}_2\text{O}_3\text{Cl}_1\text{Na}_1 \times 0.95 \text{CH}_3\text{OH} \times 0.05 \text{moles H}_2\text{O}$: C, 44.74; H, 4.08; N, 9.53. Found: C, 44.77; H, 3.85; N, 9.31; **Significant IR bands**: (KBr disc, cm^{-1}): (ν C=O) 1660 s , (ν C=N) 1610 s .

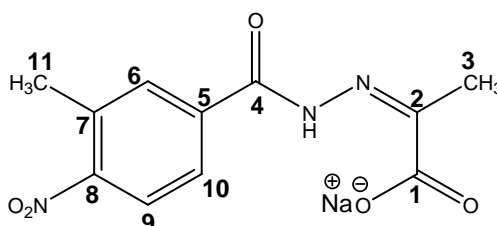
NaHL6



Sodium 2-[(4-chloro-benzoyl)-hydrazono]-propionate

NaHL6 was synthesised using sodium pyruvate 0.2 g (1.82 mmol) and 4-chloro-benzoyl hydrazide 0.31 g (1.82 mmol) to give NaHL6, 0.43 g (1.64 mmol, 90%); **Melting point:** 279-281 °C; **ESI-MS:** positive $m/z = 263.0202$, 100%; HR ESI-MS: For $C_{10}H_9N_2O_3Cl_1Na$ ($[M+H]^+$), observed mass 263.0202, calculated mass 263.0194, difference -0.8 mDa; δ **1H NMR** (400 MHz, d_6 -DMSO): Major isomer: 2.01 (s, 3H, H-3), 7.58 (d, 2H, $J_{H-H} = 8.8$ Hz, H-6 or H-7), 7.81 (d, 2H, $J_{H-H} = 8.8$ Hz, H-6 or H-7), 16.48 (bs, 1H, H-N), Minor: 2.15 (s, H-3), 7.98, 7.85 (d, $J_{H-H} = 8.8$ Hz, H-6 or H-7); δ **^{13}C NMR** (100.6 MHz, d_6 -DMSO): Major isomer: 166.3 (4°), 160.9 (4°), 151.1 (4°), 136.5 (4°), 132.5 (4°), 128.8 (CH), 128.4 (CH), 21.2 (CH₃), Minor isomer: 130.2 (CH), 128.4 (CH); **Significant IR bands** : (KBr disc, cm^{-1}): (ν C=O) 1684s, (ν_{asym} COO) 1649s, (ν C=N) 1612s.

NaHL7

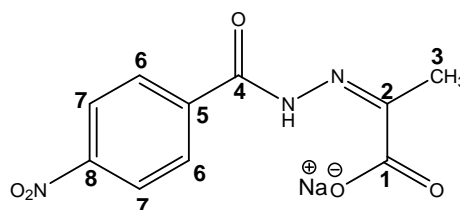


Sodium 2-[(3-methyl-4-nitro-benzoyl)-hydrazono]-propionate

NaHL7 was synthesised using sodium pyruvate 0.20 g (1.82 mmol) and 3-methyl-4-nitro-benzoyl hydrazide 0.35 g (1.82 mmol) to give NaHL7, 0.43 g (1.5 mmol, 82%); **Melting point:** 243-245 °C; **ESI-MS:** positive $m/z = 288.06$, 100%, HR ESI-MS: For $C_{11}H_{11}N_3O_5Na$ ($[M+H]^+$), observed mass 288.0581, calculated mass 288.0596, difference 1.5 mDa; δ **1H NMR** (400 MHz, d_6 -DMSO): 2.01 (s, 3H, H-3), 2.56 (s, 3H, H-11), 7.78 (dd, 1H, $J_{H-H} = 8.3$ Hz, 1.1 Hz, H-9 or H-10), 7.87 (s, 1H, H-

6), 8.09 (d, 1H, $J_{H-H} = 8.5$ Hz, H-9 or H-10), 16.60 (bs, 1H H-N); δ ^{13}C NMR (100.6 MHz, d_6 -DMSO): 165.9 (4°), 160.1 (4°), 151.7(4°), 150.5 (4°), 137.9 (4°), 133.2 (4°), 131.4 (CH), 125.5 (CH), 124.9 (CH), 21.1 (CH₃), 19.4 (CH₃); **Anal. Calcd.** for $\text{C}_{11}\text{H}_{10}\text{N}_3\text{O}_5\text{Na}_1 \times 0.25 \text{ CH}_3\text{OH} \times 1.8 \text{ H}_2\text{O}$: C, 40.95; H, 4.13; N, 12.45. Found: C, 41.24; H, 4.49; N, 12.82; **Significant IR bands:** (KBr disc, cm^{-1}): (ν C=O) 1662s, (ν_{asym} COO) 1627s, (ν_{asym} (N=O)₂) 1522s, (ν_{sym} (N=O)₂) 1356s.

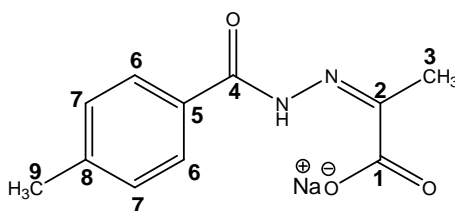
NaHL8



Sodium 2-[(4-nitro-benzoyl)-hydrazone]-propionate

NaHL8 was synthesised using sodium pyruvate 0.20 g (1.82 mmol) and 4-nitro-benzoyl hydrazide 0.33 g (1.82 mmol) to give NaHL8, 0.47 g (1.72 mmol, 95%); **Melting point:** 204-205 °C; **ESI-MS:** positive $m/z = 274.0429$, 100%, HR ESI-MS: For $\text{C}_{10}\text{H}_9\text{N}_3\text{O}_5\text{Na}$ ($[\text{M}+\text{H}]^+$), observed mass 274.0429, calculated mass 274.0434, difference 0.5 mDa; δ ^1H NMR (400 MHz, d_6 -DMSO): Major isomer: 2.01 (s, 3H, H-3), 8.03 (d, 2H, $J_{H-H} = 8.8$ Hz, H-6 or H-7), 8.34 (d, 2H, $J_{H-H} = 8.8$ Hz, H-6 or H-7), 16.70 (bs, 1H, H-N), Minor isomer: 2.17 (s, H-3), 7.88, 8.15 (d, H-6 or H-7); δ ^{13}C NMR (100.6 MHz, d_6 -DMSO): 166.1 (4°), 160.2 (4°), 151.9 (4°), 149.2 (4°), 139.6 (4°), 128.4 (CH), 124.0, (CH), 21.2 (CH₃); **Anal. Calcd.** for $\text{C}_{10}\text{H}_8\text{N}_3\text{O}_5\text{Na}_1 \times 2.2 \text{ H}_2\text{O}$: C, 38.40; H, 4.00; N, 13.28. Found: C, 38.69; H, 3.87; N, 13.43; **Significant IR bands :** (KBr disc, cm^{-1}): (ν C=O) 1665s, (ν_{asym} COO) 1633s, (ν C=N) 1600s, (ν_{asym} (N=O)₂) 1521s, (ν_{sym} (N=O)₂) 1352s.

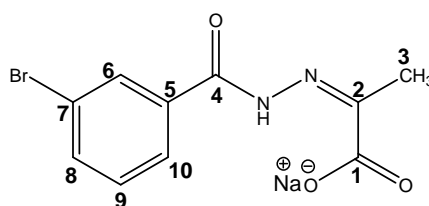
NaHL9



Sodium 2-[(4-methyl-benzoyl)-hydrazono]-propionate

NaHL9 was synthesised using sodium pyruvate 0.20 g (1.82 mmol) and 4-methyl benzoyl hydrazide 0.27 g (1.82 mmol) to give NaHL9, 0.38 g (1.57 mmol, 86%); **Melting point:** 242-244 °C; **ESI-MS:** positive $m/z = 243.07$, 100%, HR ESI-MS: For $C_{11}H_{12}N_2O_3Na$ ($[M+H]^+$), observed mass: 243.0738, calculated mass: 243.0740, difference: 0.2 mDa; δ **1H NMR** (400 MHz, d_6 -DMSO): Major isomer: 1.98 (s, 3H, H-3), 2.36 (s, 3H, H-9), 7.31 (d, 2H, $J_{H-H} = 8.0$ Hz, H-6 or H-7), 7.71 (d, 2H, $J_{H-H} = 8.0$ Hz, H-6 or H-7), 16.20 (bs, 1H, H-N), Minor isomer: 2.14 (s, H-3), 7.34, 7.84 (d, $J_{H-H} = 8.1$ Hz, H-6 or H-7); δ **^{13}C NMR** (100.6 MHz, d_6 -DMSO): Major isomer: 166.3 (4°), 161.9 (4°), 150.5 (4°), 141.7 (4°), 130.9 (4°), 129.3 (CH), 127.0 (CH), 21.24 (CH₃), 21.0 (CH₃), Minor isomer: 128.9 (CH), 128.3 (CH), 21.1 (CH₃), 13.9 (CH₃); **Anal. Calcd** for $C_{11}H_{12}N_2O_3Na \times 2.2 H_2O$: C, 46.88; H, 5.51; N, 9.94. Found: C, 46.92; H, 5.41; N, 9.75; **Significant IR bands** : (KBr disc, cm^{-1}): (ν C=O) 1649s, (ν_{asym} COO) 1631s, (ν C=N) 1610s.

NaHL10

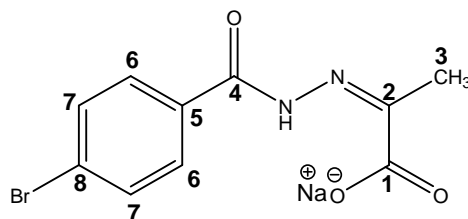


Sodium 2-[(4-bromo-benzoyl)-hydrazono]-propionate

NaHL10 was synthesised using sodium pyruvate 0.20 g (1.82 mmol) and 4-bromo-benzoyl hydrazide 0.39 g (1.82 mmol) to give NaHL10, 0.48 g (1.56 mmol, 86%); **Melting point:** 276 - 278 °C; **ESI-MS:** positive $m/z = 306.97$, 100%, HR ESI-MS: For $C_{10}H_9N_3O_3Br_1Na$ ($[M+H]^+$), observed mass 306.9685, calculated mass 306.9689, difference 0.4 mDa; δ **1H NMR** (400 MHz, d_6 -DMSO): Major isomer: 2.01 (s, 3H, H-3), 7.48 (apparent t, 1H, $J_{H-H} = 7.88$ Hz, H-9), 7.78 (m 2H, H-6, H-8 or H-

10), 7.92 (s, 1H, H-6), 16.46 (bs, 1H, H-N), Minor isomer: 2.16 (s, H-3), 8.09 (bs, 1H, H-N); δ ^{13}C NMR (100.6 MHz, d_6 -DMSO): 166.1 (4°), 160.3 (4°), 151.3 (4°), 134.4 (CH), 131.0 (CH), 129.7 (CH), 129.3 (4°), 125.7 (CH), 122.1 (4°), 21.1 (CH₃); **Significant IR bands** : (KBr disc, cm^{-1}): (ν C=O) 1666s, 1649s, (ν_{asym} COO) 1627s, (ν C=N) 1606s.

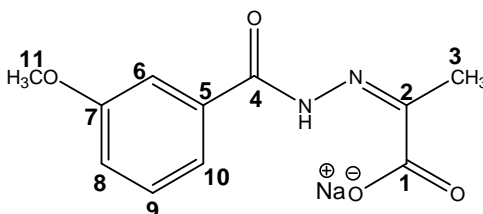
NaHL11



Sodium 2-[(3-bromo-benzoyl)-hydrazone]-propionate

NaHL11 was synthesised using sodium pyruvate 0.20 g (1.82 mmol) and 4-bromo-benzoyl hydrazide 0.39 g (1.82 mmol) to give NaHL11, 0.54 g (1.75 mmol, 96%); **Melting point**: 279-281 °C; **ESI-MS**: positive m/z = 306.9678, 100%, HR ESI-MS: For $\text{C}_{10}\text{H}_9\text{N}_2\text{O}_3\text{Na}$ ($[\text{M}+\text{H}]^+$), observed mass 306.9678, calculated mass 306.9689, difference 1.1 mDa; δ ^1H NMR (400 MHz, d_6 -DMSO): Major isomer: 2.01 (s, 3H, CH₃), 7.73 (apparent d, 4H, $J_{\text{H-H}} = 1.6$ Hz, H-6 and H-7), 16.36 (bs, 1H, H-N); δ ^{13}C NMR (100.6 MHz, d_6 -DMSO): 166.2 (4°), 161.0 (4°), 151.1 (4°), 131.8 (CH), 132.9 (4°), 129.0 (CH), 125.4 (4°), 21.2 (CH₃); **Significant IR bands** : (KBr disc, cm^{-1}): (ν C=O) 1687s, (ν_{asym} COO) 1648s, (ν C=N) 1627s.

NaHL12

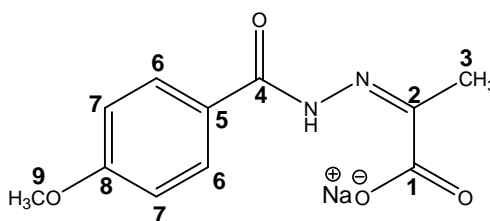


Sodium; 2-[(3-methoxy-benzoyl)-hydrazone]-propionate

NaHL12 was synthesised using sodium pyruvate 0.20 g (1.82 mmol) and 3-methoxy-benzoyl hydrazide 0.30 g (1.82 mmol) to give NaHL12, 0.38 g (1.47 mmol, 81%); **Melting point**: 268-270 °C; **ESI-MS**: positive m/z = 259.07, 100%, HR ESI-

MS: For $C_{11}H_{12}N_2O_4Na$ ($[M+H]^+$), observed mass 259.0692, calculated mass 259.0689, difference -0.3 mDa; δ 1H NMR (400 MHz, d_6 -DMSO): Major isomer: 2.00 (s, 3H, H-3), 3.80 (s, 3H, H-11), 7.13 (d, 1H, J_{H-H} = 8.0 Hz, H-8 or H-10), 7.42 (m, 3H, H-6 and/or H-8-10), 16.22 (bs, 1H, H-N), Minor isomer: 2.14 (s, H-3), 3.80 (s, H-11), 11.05 (bs, 1H, NH); δ ^{13}C NMR (100.6 MHz, d_6 -DMSO): Minor isomer: 166.3 (4°), 161.7 (4°), 159.4 (4°), 150.7 (4°), 135.1 (4°), 129.9 (CH), 118.8 (CH), 117.3 (CH), 112.4 (CH), 55.2 (CH_3), 21.2 (CH_3), Minor isomer; 164.7 (4°), 162.6 (4°), 159.1 (4°), 149.0 (4°), 129.5 (CH), 120.4 (CH), 117.8 (CH), 113.6 (CH), 55.3 (CH_3), 12.7 (CH_3); **Significant IR bands** : (KBr disc, cm^{-1}): (ν C=O) 1644s, (ν_{asym} COO) 1628s, (ν C=N) 1601s.

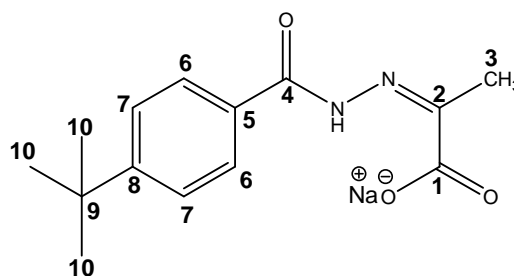
NaHL13



Sodium 2-[(4-methoxy-benzoyl)-hydrazono]-propionate

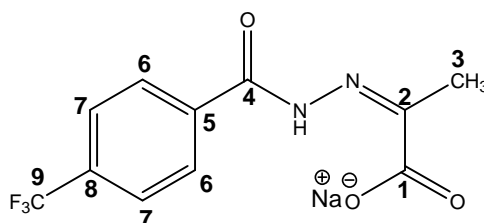
NaHL13 was synthesised using sodium pyruvate 0.2 g (1.82 mmol) and 4-bromo-benzoyl hydrazide 0.30 g (1.82 mmol) to give NaHL13, 0.39 g (1.51 mmol, 83%); **Melting point**: 240 - 242 $^\circ C$; **ESI-MS**: positive m/z = 259.0697, 100%, HR ESI-MS: For $C_{11}H_{12}N_2O_4Na$ ($[M+H]^+$), observed mass 259.0697, calculated mass 259.0689, difference -0.7 mDa; δ 1H NMR (400 MHz, d_6 -DMSO): Major isomer: 1.99 (s, 3H, H-3), 3.79 (s, 3H, H-9), 7.03 (d, 2H, J_{H-H} = 8.8 Hz, H6 or H-7), 7.77 (d, 2H, J_{H-H} = 8.8 Hz, H6 or H-7), 16.09 (bs, 1H, H-N), Minor isomer: 2.13 (s, H-3), 3.78 (s, H-9), 6.98, 7.85 (d, J_{H-H} = 7.2 Hz, 8.8 Hz, H-6 or H-7), 10.89 (bs, 1H, H-N); δ ^{13}C NMR (100.6 MHz, d_6 -DMSO): Major isomer: 166.3 (4°), 161.5 (4°), 161.9(4°), 150.1 (4°), 141.7 (4°), 128.8 (CH), 114.0 (CH), 21.2 (CH_3), 55.4 (CH_3), Minor isomer: 162.4 (4°), 130.3 (CH), 113.5 (CH), 55.4 (CH_3), 13.8 (CH_3); **Significant IR bands** (KBr disc, cm^{-1}): (ν C=O) 1642s, (ν_{asym} COO) 1625s, (ν C=N) 1607s.

NaHL14

Sodium 2-[(4-*tert*-butyl-benzoyl)-hydrazono]-propionate

NaHL16 was synthesised using sodium pyruvate 0.2 g (1.82 mmol) and 4-*tert*-butyl-benzoyl hydrazide 0.35 g (1.82 mmol) to give NaHL16, 0.46 g (1.75 mmol, 96 %); **Melting point:** 260-262 °C; **ESI-MS:** positive $m/z = 263.14$, 100%, HR ESI-MS: For $C_{14}H_{19}N_2O_3$ ($[M-Na+2H]^+$), observed mass 263.1391, calculated mass 263.1390, difference -0.1 mDa; δ **1H NMR** (400 MHz, d_6 -DMSO): Major isomer: 1.29 (s, 9H, H-10), 1.99 (s, 3H, H-3), 7.74 (d, 2H, $J_{H-H} = 8.0$ Hz, H-6 or H-7), 7.51 (d, 2H, $J_{H-H} = 8.0$ Hz, H-6 or H-7), 16.17 (bs, 1H, H-N) Minor isomer: 7.84 (d, $J_{H-H} = 8.0$ Hz, Ar-H), 2.15 (s, **8**); δ **^{13}C NMR** (100.6 MHz, d_6 -DMSO): Major isomer: 166.1 (4°), 161.7 (4°), 154.4 (4°), 150.4 (4°), 131.1 (4°), 126.7 (CH), 125.4 (CH), 34.6 (4°), 30.9 ((CH_3)₃), 21.2 (CH₃), Minor isomer: 128.0 (CH), 125.1 (CH), 34.7 (4°), 30.8 ((CH_3)₃), 13.8 (CH₃); **Anal. Calcd** for $C_{14}H_{17}N_2O_3Na \times 1.75 H_2O$: C, 53.24; H, 6.54; N, 8.87. Found C, 53.45; H, 6.41; N, 8.64; **Significant IR bands** (KBr disc, cm^{-1}): (ν C=O) 1651s, (ν_{asym} COO) 1635s, ν (C=N) 1609s.

NaHL15

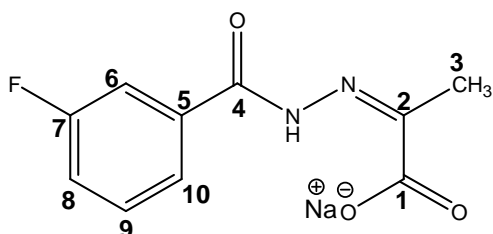


Sodium; 2-[(4-trifluoro-benzoyl)-hydrazono]-propionate

NaHL15 was synthesised using sodium pyruvate 0.20 g (1.82 mmol) and 4-trifluoromethyl benzoyl hydrazide 0.37 g (1.82 mmol) to give NaHL15, 0.48 g (1.62 mmol, 89%); **Melting point:** 126-128 °C; **ESI-MS:** positive $m/z = 297.04$, 100%, HR ESI-MS: For $C_{11}H_9N_2O_3F_3Na$ ($[M+H]^+$), observed mass 297.0465, calculated mass

297.0457, difference -0.7 mDa; δ $^1\text{H NMR}$ (400 MHz, d_6 -DMSO): 2.01 (s, 3H, H-3), 7.89 (d, 2H, $J_{\text{H-H}} = 8.3$ Hz, H-6 or H-7), 7.99 (d 2H, $J_{\text{H-H}} = 8.3$ Hz, H-6 or H-7) 16.60 (bs, 1H, H-N) ; δ $^{13}\text{C NMR}$ (100.6 MHz, d_6 -DMSO): 165.9 (4°), 151.6 (4°), 160.5 (4°), 137.8 (CH), 127.8 (CH) 131.3 (4°), 123.8 (C-9, 1J , $J_{\text{C-F}} = 271$), 21.1 (CH_3); **Anal. Calcd.** for $\text{C}_{11}\text{H}_7\text{N}_2\text{O}_3\text{F}_3\text{Na}_2 \times 1.4 \text{ CH}_3\text{OH} \times 1.7 \text{ H}_2\text{O}$: C, 37.83; H, 4.10; N, 7.12. Found: C, 37.46; H, 3.73; N, 6.74; **Significant IR bands** (KBr disc, cm^{-1}): (ν C=O) 1653s, (ν_{asym} COO, ν C=N) 1632s.

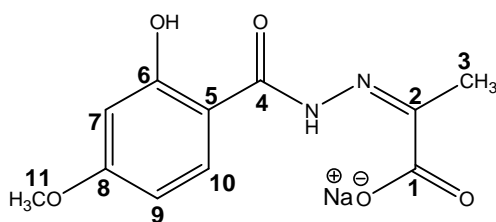
NaHL16



Sodium 2-[(3-fluoro-benzoyl)-hydrazono]-propionate

NaHL16 was synthesised using sodium pyruvate 0.20 g (1.82 mmol) and 3-fluoro-benzoyl hydrazide 0.27 g (1.82 mmol) to give NaHL16, 0.36 g (1.46 mmol, 80%); **Melting point**: 255-256 $^\circ\text{C}$; **ESI-MS**: positive $m/z = 247.05$, 100%, HR ESI-MS: For $\text{C}_{10}\text{H}_9\text{N}_2\text{O}_3\text{Na}$ ($[\text{M}+\text{H}]^+$), observed mass 247.0496, calculated mass 247.0489, difference -0.7 mDa; δ $^1\text{H NMR}$ (400 MHz, d_6 -DMSO): Major isomer: 1.99 (s, 3H, H-3), 7.40-7.80 (m, 4H, H-6, H-8-10), 16.42 (bs, 1H, H-N), Minor isomer: 2.15 (s, H-3), 11.15 (bs, 1H, H-N); δ $^{13}\text{C NMR}$ (100.6 MHz, d_6 -DMSO): Major isomer: 166.2 (4°), 162.0 (1J , $J_{\text{C-F}} = 247$, C-7), 160.6 (4J , $J_{\text{C-F}} = 3$, C-4), 151.2 (4°), 136.0 (3J , $J_{\text{C-F}} = 7$, C-9), 122.0 (4J , $J_{\text{C-F}} = 3$, C-10), 131.0 (3J , $J_{\text{C-F}} = 7$, C-9), 118.0 (2J , $J_{\text{C-F}} = 22$, C-6 or C-8), 113.0 (2J , $J_{\text{C-F}} = 22$, C-6 or C-8), 21.1 (CH_3); **Anal. Calcd.** for $\text{C}_{10}\text{H}_8\text{N}_2\text{O}_3\text{FNa}_1 \times 0.15 \text{ 7H}_3\text{OH} \times 1.1 \text{ H}_2\text{O}$: C, 45.02; H, 4.02; N, 10.34. Found: C, 45.03; H, 3.92; N, 10.30; **Significant IR bands** : (KBr disc, cm^{-1}): (ν C=O, ν_{asym} COO, ν C=N) 1635br.

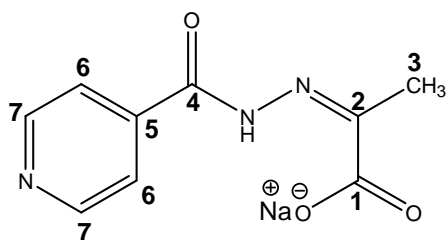
NaHL17



Sodium 2-[(2-hydroxy-4-methoxy-benzoyl)-hydrazono]-propionate

NaHL17 was synthesised using sodium pyruvate 0.20 g (1.82 mmol) and 2-hydroxy-4-methoxy-benzoyl hydrazide 0.33 g (1.82 mmol) to give NaHL17, 0.46 g (1.68 mmol, 92%); **Melting point:** 258-260 °C, **ESI-MS:** negative $m/z = 251.07$, 100%, HR ESI-MS: For $C_{11}H_{11}N_2O_5$ ($[M-Na]^-$), observed mass 251.0665, calculated mass 251.0673, difference 0.9 mDa; δ 1H NMR (400 MHz, d_6 -DMSO): Major isomer: 2.03 (s, 3H, H-3), 6.38 (d, 1H, $J_{H-H} = 6.8$ Hz, H-9 or H-10), 6.54 (s, 1H, H-7), 7.86 (d, 1H, $J_{H-H} = 8.0$ Hz, H-9 or H-10), 15.81 (bs, 1H, H-N), Minor isomer: 2.05 (s, 3H, H-3), 6.48 (d, 1H, $J_{H-H} = 8.8$ Hz, H-9, H-10), 6.68 (s, 1H, H-7), 7.57 (d, 1H, $J_{H-H} = 8.8$ Hz, H-9 or H-10), 13.39 (bs, 1H, NH); δ ^{13}C NMR (100.6 MHz, d_6 -DMSO): Major isomer: 166.1 (4°), 164.7 (4°), 163.7 (4°), 150.6 (4°), 128.8 (4°), 128.8 (CH), 101.5 (CH), 106.5 (CH), 55.5 (CH₃), 21.2 (CH₃), Minor isomer: 167.6 (4°), 164.8 (4°), 162.6 (4°), 148.7 (4°), 132.0 (CH), 128.8 (4°), 101.6 (CH), 105.1 (CH), 55.1 (CH₃), 48.6 (CH₃), 18.6 (CH₃), 12.7 (CH₃); **Significant IR bands** : (KBr disc, cm^{-1}): (ν C=O) 1652s, (ν_{asym} COO, ν C=N) 1610s.

NaHL18

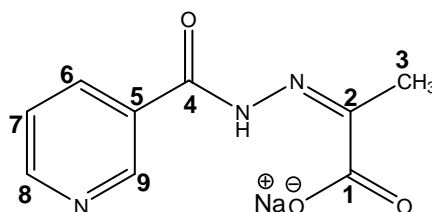


Sodium 2-[(pyridine-4-carbonyl)-hydrazono]-propionate

NaHL18 was synthesised using sodium pyruvate 0.20 g (1.82 mmol) and pyridine-4-carbonyl-benzoyl hydrazide 0.25 g (1.82 mmol) to give NaHL18, 0.37 g (1.62 mmol, 89%), **Melting point:** 281-282 °C; **ESI-MS:** positive $m/z = 208.07$, 100%, HR ESI-MS: For $C_9H_{10}N_3O_3Na$ ($[M-Na+2H]^+$), observed mass 208.0719,

calculated mass 208.0717, difference -0.2 mDa; δ $^1\text{H NMR}$ (400 MHz, d_6 -DMSO): 2.03 (s, 3H, H-3), 8.75 (dd, 2H, $J_{\text{H-H}} = 4.4$ Hz, 1.6 Hz, H-6 or H-7), 7.70 (dd 2H, $J_{\text{H-H}} = 4.4$ Hz, 1.6 Hz, H-6 or H-7), 16.46 (bs, 1H, H-N); δ $^{13}\text{C NMR}$ (100.6 MHz, d_6 -DMSO): 166.3 (4°), 160.5 (4°), 152.0 (4°), 150.7 (CH), 132.5 (4°), 121.0 (CH), 21.2 (CH₃); **Significant IR bands** : (KBr disc, cm^{-1}): (ν C=O, ν_{asym} COO, ν C=N) 1644br.

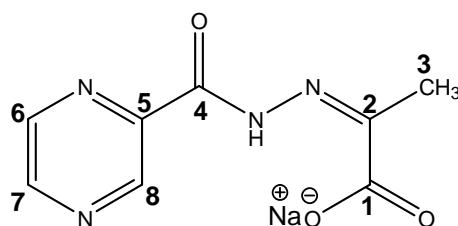
NaHL19



Sodium 2-[(pyridine-3-carbonyl)-hydrazono]-propionate

NaHL19 was synthesised using sodium pyruvate 0.20 g (1.82 mmol) and pyridine-3-carbonyl-benzoyl hydrazide 0.25 g (1.82 mmol) to give NaHL19, 0.34 g (1.49 mmol, 82%); **Melting point**: 265-267 $^\circ\text{C}$; **ESI-MS**: positive $m/z = 208.0717$, 100%, HR ESI-MS: For $\text{C}_9\text{H}_{10}\text{N}_3\text{O}_3\text{Na}$ ($[\text{M}-\text{Na}+2\text{H}]^+$), observed mass 208.0717, calculated mass 208.0717, difference -0.0 mDa; δ $^1\text{H NMR}$ (400 MHz, d_6 -DMSO): 2.02 (s, 3H, H-3), 8.97 (d, 1H, $J_{\text{H-H}} = 1.8$ Hz, H-9), 8.74 (dd, 1H, $J_{\text{H-H}} = 1.6$ Hz, 4.8 Hz, H-6 or H-8), 8.14 8.74 (d,d 1H, $J_{\text{H-H}} = 1.9$ Hz, 8.0 Hz, H-7), 7.55 (q, 1H, $J_{\text{H-H}} = 4.8$ Hz, H-7), 16.46 (bs, 1H, H-N); δ $^{13}\text{C NMR}$ (100.6 MHz, d_6 -DMSO): 166.3 (4°), 160.5 (4°), 152.4 (CH), 151.4 (4°), 148.0 (CH), 134.8 (CH), 129.4 (4°), 124.0 (CH), 21.2 (CH₃); **Significant IR bands**: (KBr disc, cm^{-1}): (ν C=O, ν_{asym} COO, ν C=N) 1640br.

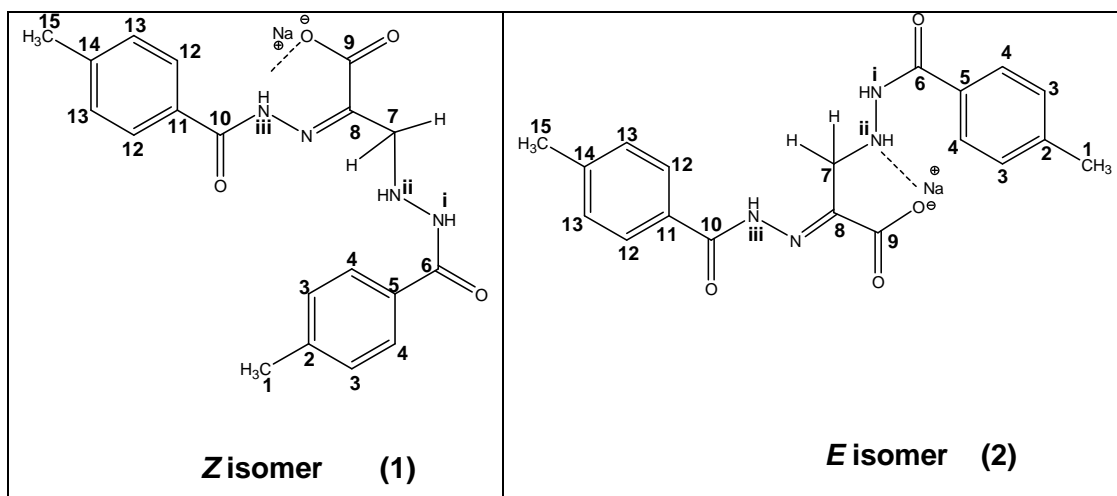
NaHL20



Sodium 2-[(pyrazine-2-carbonyl)-hydrazono]-propionate

NaHL20 was synthesised using sodium pyruvate 0.20 g (1.82 mmol) and pyrazinoyl hydrazide 0.27 g (1.82 mmol) to give NaHL20 0.36 g (1.46 mmol, 80%); **Melting point:** decomp. > 200 °C; ESI-MS: positive $m/z = 209.07$, 100%, HR ESI-MS: For $C_8H_9N_4O_3$ ($[M-Na+2H]^+$), observed mass 209.0670, calculated mass 209.0669, difference -0.1 mDa; δ **1H NMR** (400 MHz, d_6 -DMSO): 2.02 (s, 3H, H-3), 8.72 (dd, 1H, $J_{H-H} = 2.5$ Hz, 1.5 Hz, H-7), 8.85 (d, 1H, $J_{H-H} = 2.5$ Hz, H-6), 9.21 (d, 1H, $J_{H-H} = 1.4$ Hz, H-8); δ **^{13}C NMR** (100.6 MHz, d_6 -DMSO): 165.7 (4°), 159.1 (4°), 152.0 (4°), 147.6 (CH), 143.9 (CH), 143.6 (4°), 21.4 (CH₃); **Anal. Calcd.** for $C_8H_7N_4O_3Na_1 \times 0.15 CH_3OH \times 1.75 H_2O$: C, 36.73; H, 4.20; N, 21.02. Found: C, 36.55; H, 3.90; N, 20.76; **Significant IR bands:** (KBr disc, cm^{-1}): (ν C=O) 1670s, (ν_{asym} COO, ν C=N) 1625br.

7.7 Synthetic procedure and characterisation detail of the dihydrazide analogue; NaH₃D1



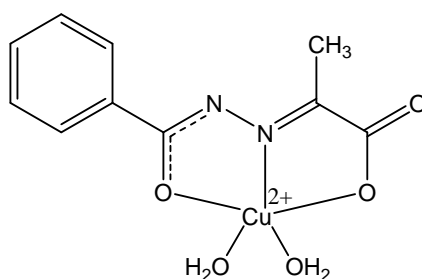
Sodium 3-[N'-(4-methyl-benzoyl)-hydrazino]-2-[(4-methyl-benzoyl)-hydrazono]-propionate

NaH₃D1 was synthesized by dissolving 3-bromopyruvate (0.2 g, 1.10 mmol) and 4-methyl benzoic acid hydrazide (0.32 mg, 2.05 mmol) in methanol with an equimolar amount of NaHCO₃ (95 mg, 1.13 mmol). The reaction mixture was heated under reflux for 2 hours. A white precipitate was obtained, which was washed with an excess of methanol and water, filtered and dried under *vacuum* to give NaH₃D1, 0.24 g (0.06 mmol, 55%); **Melting point:** 248-250 °C; ESI-MS: negative *m/z* = 367.1428, 100%, HR ESI-MS: For C₁₉H₁₉N₄O₄ ([([M-H-Na]⁻), observed mass 367.1428, calculated mass 367.1412, difference -1.6 mDa; **¹H NMR** (400 MHz, *d*₆-DMSO): **Z isomer:** 2.36, (bs, 6H, H-1 and H-15), 3.69 (d, 2H, CH₂, H-7), 5.70 (apparent q, 1H, N(ii)-H), 7.22-7.76 (m, 8H, H-3-4 & H-12-13), 10.11 (d, 1H, N(i)-H), 16.38, (s, 1H, N(iii)-H); **E isomer :** 2.33/2.30 (s, H-1 and H-15), 3.88 (s, CH₂, H-7), 7.22-7.76 (m, H-3-4 & H-12-13) 9.83 (bs, N(iii)H), 16.38 (s, 1H, N(i/ii)-H); **¹³C NMR** (100.6 MHz, *d*₆-DMSO): **Z and E isomers:** 166.59(4°), 166.25(4°), 165.96(4°), 165.34(4°), 163.53(4°), 162.80(4°), 149.47(4°), 148.73(4°), 142.89(4°), 142.44(4°), 142.03(4°), 141.55(4°), 131.15(4°), 130.93(4°), 130.75(4°), 130.35(4°), 129.91(CH), 129.81(CH), 129.30(CH), 129.28(CH), 127.84(CH), 127.53(CH), 127.49(CH), 127.45(CH), 60.45(CH₂), 54.68(CH₂), 20.94(CH₃), 20.91(CH₃), 20.85(CH₃), 20.84(CH₃); **Anal. Calcd.** for C₁₉H₁₉N₄O₄Na x 1.6 H₂O: C, 54.44; H, 5.34; N, 13.37. Found C, 54.01; H, 4.86; N, 13.11; **Significant IR bands :** (KBr disc, cm⁻¹): (ν C=O) 1639s, (ν_{asym} COO, ν C=N) 1620br.

7.8 General synthetic procedure and characterisation detail of Cu(II) complexes of PVAHs [Cu(L1)(H₂O)₂]- [Cu(L20)(H₂O)₂]

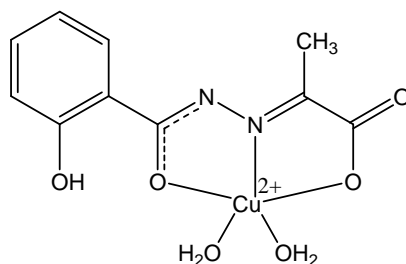
To a methanolic solution of the respective pyruvate-based aroylhydrazone (0.58 mmol) was added CuCl₂ x 2 H₂O (0.58 mmol). The mixture was stirred for 2 hours. The resultant clear green solution was allowed to evaporate slowly giving green coloured crystalline powders which were isolated, washed with water and then re-dissolved in methanol. The resultant solution was allowed to evaporate slowly at room temperature, giving rise to green coloured crystals, which were isolated and dried in vacuo.

[Cu(L1)(H₂O)₂]

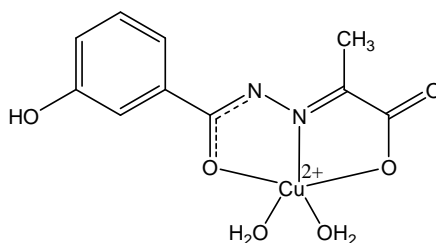


[(Bis-hydroxy)(2-[(benzoyl)-hydrazone]-propionate)]copper(II)

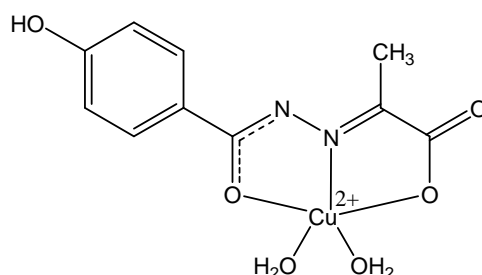
[Cu(L1)(H₂O)₂] was synthesised using NaHL1, 0.13 g (0.58 mmol) and CuCl₂.2H₂O, 0.10 g (0.58 mmol), to give [Cu(L1)(H₂O)₂], 0.067 g (0.22 mmol, 37 %); **Melting point:** 245-247 °C; **ESI-MS:** positive ion m/z = 309.01, 20 %, ESI-MS: For ⁶³Cu₁(I)C₁₀H₁₁N₂O₄Na₁ ([M-H₂O+H+Na]⁺), observed mass: 309.01, calculated mass: 308.99; **Anal. Calcd.** for Cu₁C₁₀H₁₂N₂O₅ x 0.45 H₂O: C, 38.51; H, 4.17; N, 8.98. Found C, 38.35; H, 4.00; N, 8.83; **Significant IR bands** (KBr disc, cm⁻¹): (ν C=O, ν_{asym} COO, ν C=N) 1629br.

[Cu(L2)(H₂O)₂]**[(Bis-hydroxy)(2-[(2-hydroxy-benzoyl)-hydrazono]-propionate)]copper(II)**

[Cu(L2)(H₂O)₂] was synthesised using NaHL2, 0.14 g (0.58 mmol) and CuCl₂·2H₂O 0.1 g (0.58 mmol), to give [Cu(L2)(H₂O)₂] 0.065 g (0.20 mmol, 35%); **Melting point:** > 350 °C; **ESI-MS:** positive ion m/z = 309.01, 20%, ESI-MS: For ⁶³Cu₁(I)C₁₀H₁₁N₂O₄Na₁ [M-H₂O+H+Na]⁺, observed mass: 309.01, calculated mass: 308.99; **Significant IR bands** (KBr disc, cm⁻¹): (ν C=O, ν_{asym} COO, ν C=N) 1618br.

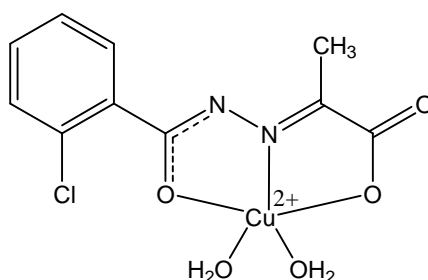
[Cu(L3)(H₂O)₂]**[(Bis-hydroxy)(2-[(3-hydroxy-benzoyl)-hydrazono]-propionate)]copper(II)**

[Cu(L3)(H₂O)₂] was synthesised using NaHL3, 0.14 g (0.58 mmol) and CuCl₂·2H₂O 0.1 g (0.58 mmol), to give [Cu(L3)(H₂O)₂] 0.064 g (0.20 mmol, 34 %); **Melting point:** 265-268 °C; **ESI-MS:** positive ion m/z = 325.01, 67 %, ESI-MS: For ⁶³Cu₁(I)C₁₀H₁₁N₂O₅Na₁ [M-H₂O+H+Na]⁺, observed mass: 325.01, calculated mass: 324.99; **Anal. Calcd.** for Cu₁C₁₀H₁₂N₂O₆: C, 37.56; H, 3.78; N, 8.76. Found: C, 37.53; H, 3.85; N, 8.23; **Significant IR bands** (KBr disc, cm⁻¹): (ν C=O, ν_{asym} COO, ν C=N) 1645br.

[Cu(L4)(H₂O)₂]

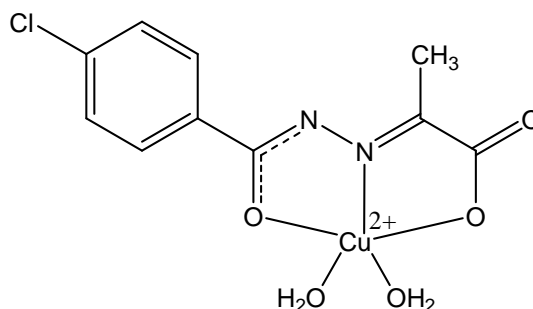
[(Bis-hydroxy)(2-[(4-hydroxy-benzoyl)-hydrazono]-propionate)]copper(II)

[Cu(L4)(H₂O)₂] was synthesised using NaHL4, 0.14 g (0.58 mmol) and CuCl₂·2H₂O 0.1 g (0.58 mmol), to give [Cu(L4)(H₂O)₂] 0.061 g (0.20 mmol, 34 %); **Melting point:** 310-312 °C; **ESI-MS:** positive ion m/z = 325.01, 15 %, ESI-MS: For ⁶³Cu₁(I)C₁₀H₁₁N₂O₅Na₁ ([M-H₂O+H+Na]⁺), observed mass: 325.01, calculated mass: 324.99; **Significant IR bands** (KBr disc, cm⁻¹): (ν C=O, ν_{asym} COO, ν C=N) 1642br.

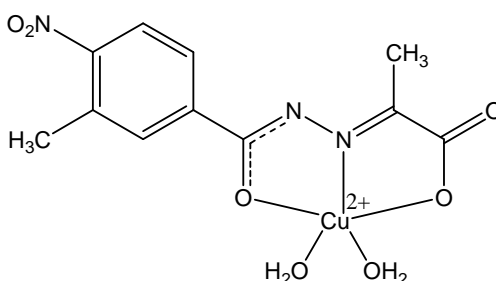
[Cu(L5)(H₂O)₂]

[(Bis-hydroxy)(2-[(2-chloro-benzoyl)-hydrazono]-propionate)]copper(II)

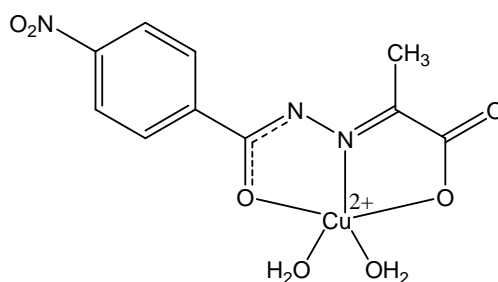
[Cu(L5)(H₂O)₂] was synthesized using NaHL5, 0.15 g (0.58 mmol) and CuCl₂·2H₂O, 0.10 g (0.58 mmol), to give (0.32 mg, 2.05 mmol) [Cu(L5)(H₂O)₂], 0.06 g (0.18 mmol, 31 %); **Melting point:** decomposes above 200 °C; **ESI-MS:** positive ion m/z = 360.32, 100 %, ESI-MS: For ⁶³Cu₁C₁₀H₁₁N₂O₅Cl₁Na₁ ([M+Na]⁺), observed mass: 360.32, calculated mass: 359.95; **Significant IR bands** (KBr disc, cm⁻¹): (ν C=O, ν_{asym} COO, ν C=N) 1630br.

[Cu(L6)(H₂O)₂]**[(Bis-hydroxy)(2-[(4-chloro-benzoyl)-hydrazono]-propionate)]copper(II)**

[Cu(L6)(H₂O)₂] was synthesised using NaHL6, 0.15 g (0.58 mmol) and CuCl₂·2H₂O, 0.10 g (0.58 mmol), to give [Cu(L6)(H₂O)₂], 0.10 g (0.30 mmol, 52%); **Melting point:** 249-251 °C; **ESI-MS:** positive ion m/z = 325.01, 80 %, ESI-MS: For ⁶³Cu₁(I)C₁₀H₁₁N₂O₅Na₁ ([M-H₂O+H+Na]⁺), observed mass: 342.98, calculated mass: 324.95; **Anal. Calcd.** for Cu₁C₁₀H₁₁N₂O₅Cl (0.5 CH₃OH, 0.15 x H₂O): C, 35.33; H, 3.76; N, 7.85. Found C, 34.95; H, 3.33; N, 7.43; **Significant IR bands** (KBr disc, cm⁻¹): (ν C=O, ν_{asym} COO, ν C=N) 1633br.

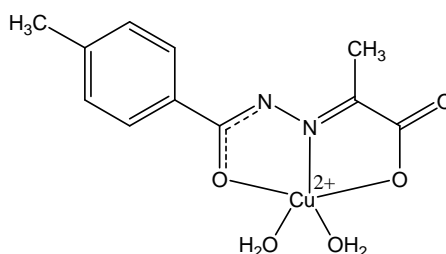
[Cu(L7)(H₂O)₂]**[(Bis-hydroxy)(2-[(3-methyl-4-nitro-benzoyl)-hydrazono]-propionate)]copper(II)**

[Cu(L7)(H₂O)₂] was synthesized using NaHL7, 0.17 g (0.58 mmol) and CuCl₂·2H₂O, 0.10 g (0.58 mmol), to give [Cu(L7)(H₂O)₂], 0.12 g (0.31 mmol, 54%); **Melting point:** 210-212 °C; **ESI-MS:** positive ion m/z = 368.02, 19 %, ESI-MS: For ⁶³Cu(I)C₁₁H₁₂N₃O₆Na₁ ([M-H₂O+H+Na]⁺), observed mass: 368.02, calculated mass: 368.00; **Anal. Calcd.** for Cu₁C₁₁H₁₃N₃O₇ x 0.1 H₂O: C, 36.06; H, 3.69; N, 11.47. Found: C, 36.06; H, 3.55; N, 11.35; **Significant IR bands:** (KBr disc, cm⁻¹): (ν C=O, ν_{asym} COO, ν C=N) 1642 br, (ν_{asym} (N=O)₂) 1524s, (ν_{sym} (N=O)₂) 1360s.

[Cu(L8)(H₂O)₂]

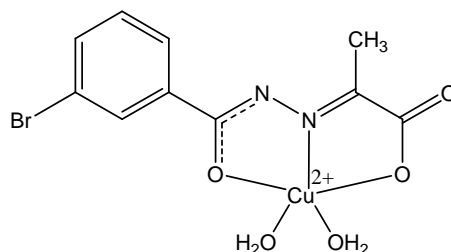
[(Bis-hydroxy)(2-[(4-nitro-benzoyl)-hydrazono]-propionate)]copper(II)

[Cu(L8)(H₂O)₂] was synthesised using NaHL8, 0.16 g (0.58 mmol) and CuCl₂·2H₂O, 0.10 g (0.58 mmol), to give [Cu(L8)(H₂O)₂], 0.08 g (0.24 mmol, 41 %); **Melting point:** 250-252 °C; **ESI-MS:** positive ion m/z = 372.01, 100 %, ESI-MS: For ⁶³Cu(I)₁C₁₀H₁₂N₃O₇Na₁ ([M+H+Na]⁺), observed mass: 372.01, calculated mass: 371.99; **Anal. Calcd.** for Cu₁C₁₀H₁₁N₃O₇ x 1.15 H₂O: C, 32.51; H, 3.63; N, 11.37. Found: C, 32.67; H, 3.31; N, 11.05; **Significant IR bands** (KBr disc, cm⁻¹): (ν C=O, ν_{asym} COO, ν C=N) 1639br, (ν_{asym} (N=O)₂) 1527s, (ν_{sym} (N=O)₂) 1347s.

[Cu(L9)(H₂O)₂]

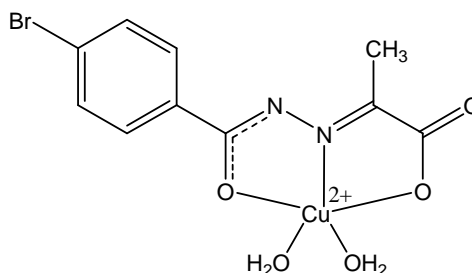
[(Bis-hydroxy)(2-[(4-methyl-benzoyl)-hydrazono]-propionate)]copper(II)

[Cu(L9)(H₂O)₂] was synthesised using NaHL9, 0.14 g (0.58 mmol) and CuCl₂·2H₂O, 0.10 g (0.58 mmol), to give [Cu(L9)(H₂O)₂] 0.13 g (0.38 mmol, 65 %); **Melting point:** 223-225 °C; **ESI-MS:** positive ion m/z = 341.04, 100 %, ESI-MS: For ⁶³Cu(I)₁C₁₁H₁₄N₂O₅ ([M+H+Na]⁺), observed mass: 341.04, calculated mass: 341.02; **Anal. Calcd.** for Cu₁C₁₁H₁₄N₂O₅ x 0.3 H₂O: C, 40.88; H, 4.55; N, 8.67. Found C, 40.54; H, 4.23; N, 8.48; **Significant IR bands:** (KBr disc, cm⁻¹): (ν C=O) 1653s, (ν_{asym} COO) 1637s, (ν C=N) 1609br.

[Cu(L10)(H₂O)₂]

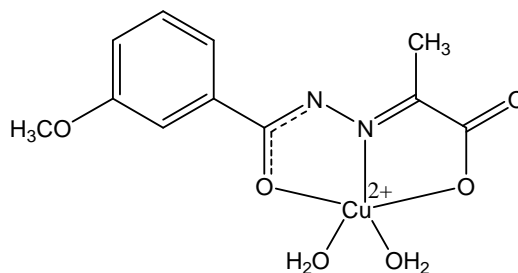
[(Bis-hydroxy)(2-[(3-bromo-benzoyl)-hydrazono]-propionate)]copper(II)

[Cu(L10)(H₂O)₂] was synthesised using NaHL10, 0.18 g (0.58 mmol) and CuCl₂·2H₂O, 0.10 g (0.58 mmol), to give [Cu(L10)(H₂O)₂], 0.092 g (0.24 mmol, 42 %); **Melting point:** 247-249 °C; **ESI-MS:** positive ion *m/z* = 327.01, 100 %, ESI-MS: For ⁶³Cu(I)₁C₁₀H₁₀N₂O₄Br₁Na₁ ([M-H₂O+H+Na]⁺), observed mass: 388.93, calculated mass: 388.63; **Significant IR bands:** (KBr disc, cm⁻¹): (ν C=O, ν_{asym} COO, ν C=N) 1643*br*

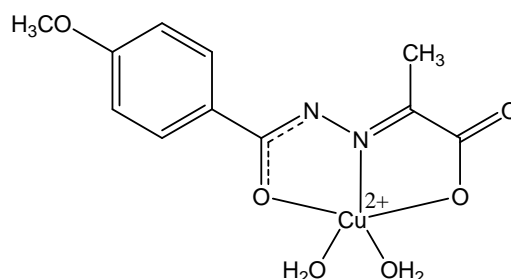
[Cu(L11)(H₂O)₂]

[(Bis-hydroxy)(2-[(4-bromo-benzoyl)-hydrazono]-propionate)]copper(II)

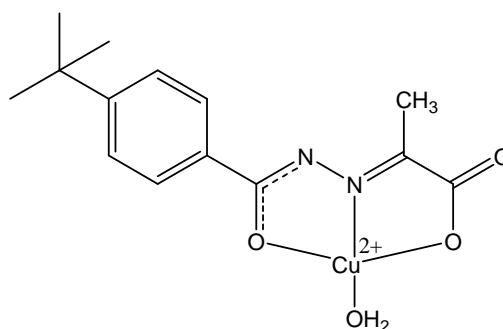
[Cu(L11)(H₂O)₂] was synthesised using NaHL11, 0.18 g (0.58 mmol) and CuCl₂·2H₂O, 0.10 g (0.58 mmol), to give [Cu(L11)(H₂O)₂], 0.12 g (0.31 mmol, 54%); **Melting point:** 239-241 °C; **ESI-MS:** positive ion *m/z* = 388.93, 100 %, ESI-MS: For ⁶³Cu(I)₁C₁₀H₁₀N₂O₄Br₁Na₁ ([M-H₂O+H+Na]⁺), observed mass: 388.93, calculated mass: 388.63; **Anal. Calcd.** for Cu₁C₁₁H₁₃N₂O₅Br: C, 33.31; H, 3.30; N, 7.06. Found C, 33.41; H, 2.84; N, 7.11; **Significant IR bands:** (KBr disc, cm⁻¹): (ν C=O, ν_{asym} COO, ν C=N) 1635*br*.

[Cu(L12)(H₂O)₂]**[(Bis-hydroxy)(2-[(3-methoxy-benzoyl)-hydrazono]-propionate)]copper(II)**

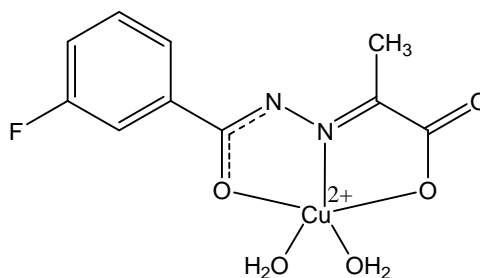
[Cu(L12)(H₂O)₂] was synthesised using NaHL12, 0.15 g (0.58 mmol) and CuCl₂·2H₂O, 0.10 g (0.58 mmol), to give [Cu(L12)(H₂O)₂], 0.088 g (0.23 mmol, 39%); **Melting point:** 229-231 °C; **ESI-MS:** positive ion m/z = 339.03, 15 %, ESI-MS: For ⁶³Cu₁(I)C₁₁H₁₄N₂O₆ ([M-H₂O+H+Na]⁺), observed mass: 339.03, calculated mass: 339.00; **Significant IR bands:** (KBr disc, cm⁻¹): (ν C=O, ν_{asym} COO) 1642br, (ν C=N) 1609s.

[Cu(L13)(H₂O)₂]**[(Bis-hydroxy)(2-[(3-methoxy-benzoyl)-hydrazono]-propionate)]copper(II)**

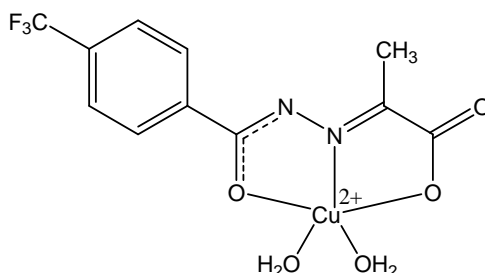
[Cu(L13)(H₂O)₂] was synthesized using NaHL13, 0.15 g (0.58 mmol) and CuCl₂·2H₂O, 0.10 g (0.58 mmol), to give [Cu(L13)(H₂O)₂], 0.11 g (0.30 mmol, 51%); **Melting point:** 229-231 °C; **ESI-MS:** positive ion m/z = 339.03, 15 %, ESI-MS: For ⁶³Cu₁(I)C₁₁H₁₄N₂O₆ ([M-H₂O+H+Na]⁺), observed mass: 339.03, calculated mass: 339.00; **Anal. Calcd** for Cu₁C₁₁H₁₄N₂O₆: C, 39.58; H, 4.23; N, 8.39 C, Found 39.70; H, 4.01; N, 8.24; **Significant IR bands:** (KBr disc, cm⁻¹): (ν C=O, ν_{asym} COO) 1639br, (ν C=N) 1603s.

[Cu(L14)(H₂O)₂]**[(2-[(4-*tert*-butyl-benzoyl)-hydrazono]-propionate)(hydroxy)]copper(II)**

[Cu(L14)(H₂O)] was synthesized using NaHL14, 0.16 g (0.58 mmol) and CuCl₂·2H₂O 0.1 g (0.58 mmol), to give [Cu(L14)(H₂O)] 0.1 g (0.27 mmol, 47 %); **Melting point:** 244-247 °C; **ESI-MS:** positive ion *m/z* = 365.08, 100 %, ESI-MS: For ⁶³Cu(I)₁C₁₄H₁₉N₂O₄Na₁ ([M-H+Na]⁺), observed mass: 365.08, calculated mass: 365.05; **Anal. Calcd.** for Cu₁C₁₄H₁₈N₂O₄ x 0.25 CH₃OH: C, 48.92; H, 5.47; N, 8.01. Found: C, 49.09; H, 5.38; N, 7.87; **Significant IR bands** (KBr disc, cm⁻¹): (ν C=O) 1645s (ν_{asym} COO) 1628s, (ν C=N) 1602s.

[Cu(L15)(H₂O)₂]**[(Bis-hydroxy)(2-[(3-flouro-benzoyl)-hydrazono]-propionate)]copper(II)**

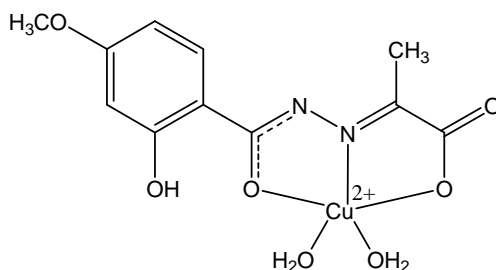
[Cu(L15)(H₂O)₂] was synthesized using NaHL15, 0.14 g (0.58 mmol) and CuCl₂·2H₂O, 0.10 g (0.58 mmol), to give [Cu(L15)(H₂O)₂], 0.06 g (0.19 mmol, 32 %); **Melting point:** 232-235 °C; **ESI-MS:** positive ion *m/z* = 327.01, 4 %, ESI-MS: For ⁶³Cu(I)₁C₁₀H₁₀N₂O₄F₁Na₁ ([M-H₂O+H+Na]⁺), observed mass: 327.01, calculated mass: 326.98; **Anal. Calcd.** for Cu₁C₁₀H₁₁N₂O₅F₁ x 0.27 H₂O: C, 45.02; H, 3.56; N, 8.57. Found: C, 45.03; H, 3.29; N, 8.25; **Significant IR bands** (KBr disc, cm⁻¹): (ν C=O, ν_{asym} COO, ν C=N) 1630br.

[Cu(L16)(H₂O)₂]

[(Bis-hydroxy)(2-[(4-trifluoromethyl -benzoyl)-hydrazone]-propionate)]copper(II)

[Cu(L16)(H₂O)₂] was synthesized using NaHL16, 0.17 g (0.58 mmol) and CuCl₂·2H₂O 0.1 g (0.58 mmol), to give [Cu(L16)(H₂O)₂], 0.08 g (0.21 mmol, 36 %);

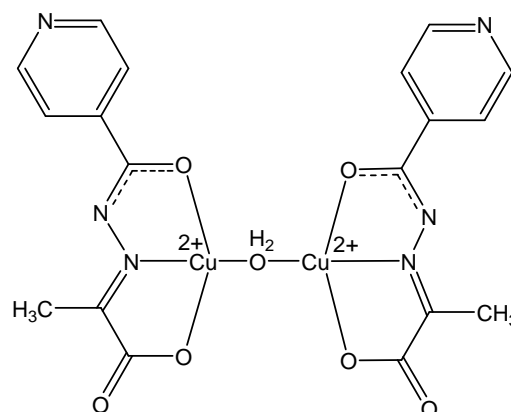
Melting point: 214-217°C; **ESI-MS:** positive ion m/z = 394.99, 100 %, ESI-MS: For ⁶³Cu(I)₁C₁₁H₁₂N₂O₅F₃Na₁ ([M+H+Na]⁺), observed mass: 394.99, calculated mass: 395.01; **Anal. Calcd.** for Cu₁C₁₁H₁₁N₂O₅F₃ x 0.27 H₂O: C, 34.28; H, 3.27; N, 7.27. Found: C, 34.28; H, 3.07; N, 6.77; **Significant IR bands (KBr disc, cm⁻¹):** (ν C=O, ν_{asym} COO, ν C=N) 1633br.

[Cu(L17)(H₂O)₂]

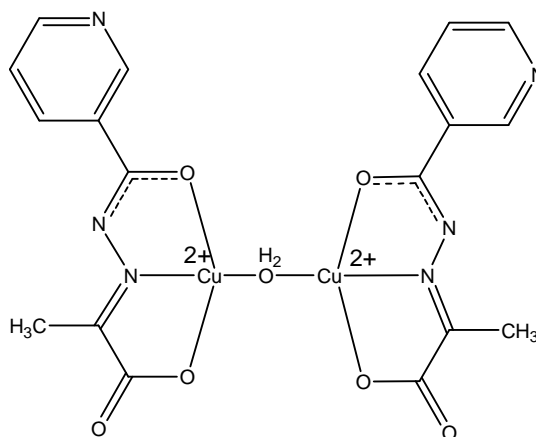
[(Bis-hydroxy)(2-[(2-hydroxy-4-methoxy-benzoyl)-hydrazone]-propionate)]copper(II)

[Cu(L17)(H₂O)₂] was synthesized using NaHL17, 0.16 g (0.58 mmol) and CuCl₂·2H₂O, 0.10 g (0.58 mmol), to give [Cu(L17)(H₂O)₂], 0.07 g (0.19 mmol, 34 %);

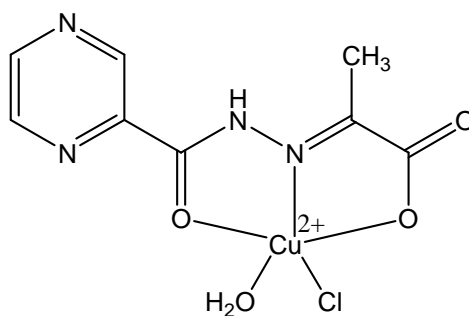
Melting point: 244-246 ° C; **ESI-MS:** positive ion m/z = 353.07, 60 %, ESI-MS: For ⁶³CuC₁₁H₁₂N₂O₆Na₁ ([M-H₂O+Na]⁺), observed mass: 353.07, calculated mass: 353.98; **Significant IR bands:** (KBr disc, cm⁻¹): (ν C=O) 1676s, (ν_{asym} COO) 1614s, (ν C=N) 1600s.

[Cu(L18)(H₂O)Cu(L18)]**[2-[(pyridine-4-carbonyl)-hydrazone]-propionate] μ -hydroxy copper(II)**

[Cu(L18)(H₂O)Cu(L18)] synthesized using NaHL18, 0.13 g (0.58 mmol) and CuCl₂·2H₂O, 0.10 g (0.58 mmol), to give [Cu(L18)(H₂O)Cu(L18)], 0.10 g (0.36 mmol, 62 %); **Melting point:** decomposes above 300 °C; **Anal. Calcd.** for Cu₂C₁₈H₁₆N₆O₇ x 0.2 CH₃OH, 0.1 H₂O: C, 38.78; H, 3.04; N, 14.91. Found C, 38.71; H, 2.77; N, 14.63; **Significant IR bands:** (KBr disc, cm⁻¹): (ν C=O) 1670s, (ν_{asym} COO) 1640s, (ν C=N) 1619s.

[Cu(L19)(H₂O)Cu(L19)]**[2-[(pyridine-3-carbonyl)-hydrazone]-propionate]copper(II)**

[Cu(L19)(H₂O)Cu(L19)] was synthesized using NaHL19, 0.13 g (0.58 mmol) and CuCl₂·2H₂O, 0.10 g (0.58 mmol), to give [Cu(L19)(H₂O)Cu(L19)], 0.11 g (0.39 mmol, 68 %); **Melting point:** decomposes above 300 °C; **Significant IR bands:** (KBr disc, cm⁻¹): (ν C=O) 1661s, (ν_{asym} COO, ν C=N) 1614br.

[Cu(L20)(H₂O)(Cl)]**[2-[(pyrazine-2-carbonyl)-hydrazono]-propionate]copper(II)**

[Cu(L20)(H₂O)(Cl)] synthesized using NaHL20, 0.13 g (0.58 mmol) and CuCl₂·2H₂O, 0.10 g (0.58 mmol), to give [Cu(HL20)(H₂O)(Cl)], 0.11 g (0.34 mmol, 58 %). **Melting point:** 137-139 °C; **ESI-MS:** positive ion $m/z = 311.02$, 100 %, ESI-MS: For ⁶³Cu(I)₁C₈H₉N₄O₄Na₁ ([M-Cl+Na]⁺), observed mass: 311.02, calculated mass: 310.99; **Anal. Calcd.** for Cu₁C₈H₉N₄O₄Cl x 1.0 H₂O x 0.1 CH₃OH: C, 28.00; H, 3.17; N, 16.03. Found C, 27.81; H, 2.88; N, 15.78; **Significant IR bands:** (KBr disc, cm⁻¹): (ν C=O) 1645s, (ν_{asym} COO, ν C=N) 1614br.

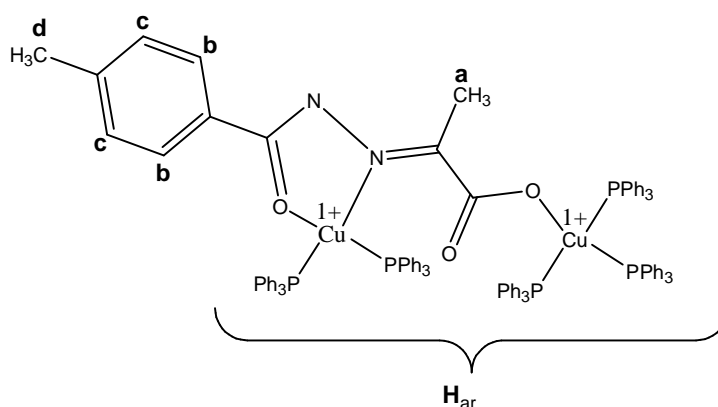
7.9 Synthesis and characterisation detail of the Cu(I) complexes of HL8⁻ and HL9⁻

Synthesis of [Cu(I)(CH₃CN)₄]PF₆⁻

To a stirred suspension of Cu₂O (1g, 7 mmol) in acetonitrile (20 ml) was added 60 % HPF₆ (2.5 ml) in 0.5 ml portions. The heat released helps to dissolve the white solid formed. The hot solution was stirred for 3 minutes. The solution was then cooled to room temperature and left in the freezer for 3 hours. The resulting precipitate was isolated by filtration and dried in *vacuo* to afford the title compound as a white solid (2.6 g, 50 %). The solid was stored under N₂.¹⁷³

δ ¹H NMR (400 MHz, CDCl₃): δ 2.19 (s)

Synthesis of [Cu(I)₂HL9(PPH₃)₅]PF₆⁻



[Cu(I)(CH₃CN)₄]PF₆⁻ (0.6 g, 1.65 mmol) was dissolved in anhydrous and degassed THF (15 mL) and added to a methanolic solution (15 mL) of ligand L9 (0.20 g, 0.82 mmol) under an atmosphere of N₂ to yield a yellow-brown solution. After stirring the reaction mixture for 10 minutes at room temperature, triphenylphosphine (1.08 g, 4.13 mmol), dissolved in dry and degassed THF (10 mL), was added to the reaction mixture. The resultant pale yellow solution was concentrated in *vacuo* to a volume of 5 mL, to which Et₂O was added. The resulting precipitate obtained after addition of Et₂O was filtered and dried under *vacuo* to yield the title compound as pale yellow solid. The solid was recrystallised from hot MeOH to yield a colourless crystalline powder. Crystals suitable for single crystal X-ray diffraction were obtained from MeOH and Et₂O.

Yield: 90 mg (0.69 mmol, 84%); **Melting point:** 163-165 °C;

ESI-MS: The dinuclear copper complex gave the following ESI-MS peaks corresponding to the two different Cu(I) centres

Positive ion, m/z reported for ^{63}Cu :

587.1111 (60 %) – $[\text{Cu}(\text{PPh}_3)_2]^+$

807.1956 (60 %) – $[\text{L9Cu}_2(\text{PPh}_3)_2]^+$

849.2031 (100 %) – $[\text{Cu}(\text{PPh}_3)_3]^+$

1) $[\text{L9Cu}_2(\text{PPh}_3)_2]^+$

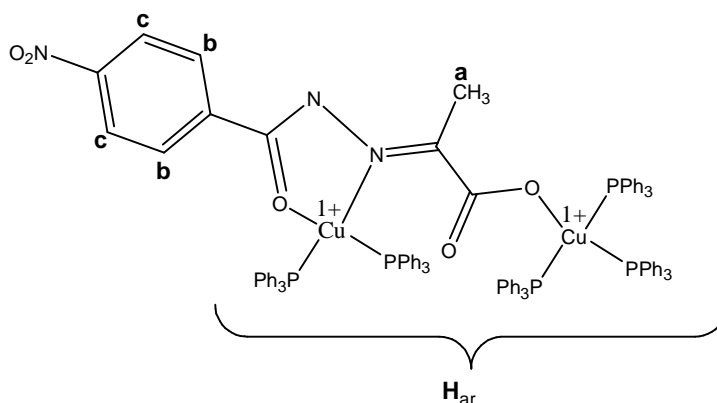
HR ESI-MS for $\text{C}_{47}\text{H}_{42}\text{CuN}_2\text{O}_3\text{P}_2$ $[\text{M}^+]$, observed mass 807.1956, calculated mass 807.3380, difference -1.4 mDa

2) $[\text{Cu}(\text{PPh}_3)_3]^+$

HR ESI-MS for $\text{C}_{54}\text{H}_{45}\text{CuP}_3$ $[\text{M}^+]$, observed mass 849.2043, calculated mass 849.2025, difference -1.8 mDa

δ ^1H NMR (400 MHz, d_4 - MeOH): 1.84 (s, 3H, H-a), 2.41 (s, 3H, H-d), 7.33 (d, 2H, $J_{\text{H-H}} = 8.1$ Hz, H-b or H-c), 7.69 (d, 2H, $J_{\text{H-H}} = 8.1$ Hz, H-b or H-c), 7.40 (m, 15 H, H_{ar} (PPh₃)), 7.23 (m, 60 H, H_{ar} (PPh₃)); **Anal. Calcd.** for $\text{Cu}_2\text{C}_{101}\text{H}_{86}\text{N}_2\text{O}_3\text{P}_6\text{F}_6$ (3.75 x CH_3OH): C, 65.43; H, 4.29; N, 1.46. Found C, 65.08; H, 4.94; N, 1.54; **Significant IR bands:** (KBr disc, cm^{-1}): (ν_{asym} COO, ν C=O, ν C=N) 1622 *br*.

Synthesis of $[\text{Cu}(\text{I})_2\text{HL8}(\text{PPh}_3)_5]\text{PF}_6$



$[\text{Cu}(\text{I})(\text{CH}_3\text{CN})_4]\text{PF}_6$ (0.3 g, 0.8 mmol) was dissolved in anhydrous and degassed methanol (15 ml) and added to a methanolic solution (15 ml) of ligand L8 (0.22g, 0.4 mmol) under an atmosphere of N_2 to yield a yellow-brown solution. After stirring the reaction mixture for 10 minutes at room temperature, triphenylphosphine (0.42g, 2.0 mmol) dissolved in dry and degassed MeOH was added to the reaction mixture. The resultant green solution was concentrated in vacuo to yield a light green precipitate. The reaction mixture was filtered and the filtrate was left to stand

at room temperature for 24 hours. Bright yellow single crystals suitable for X-ray diffraction were obtained from the filtrate. The solution was filtered and the solid obtained was dried in *vacuo* to yield the title compound as yellow crystalline solid.

Yield: 0.33 g (45 %, 0.18 mmol); **Melting point:** 210-212 °C;

ESI-MS: The dinuclear complex yielded the following ESI-MS peaks corresponding to the two different Cu(I) centres

Positive ion, m/z reported for ^{63}Cu

587.1120 (100 %) – $[\text{Cu}(\text{PPh}_3)_2]^+$

838.1663 (10 %) – $[\text{L}8\text{Cu}_2(\text{PPh}_3)_2]^+$

849.2043 (40 %) – $[\text{Cu}(\text{PPh}_3)_3]^+$

1) $\text{L}8\text{Cu}_2(\text{PPh}_3)_2$

HR ESI-MS for $\text{C}_{46}\text{H}_{39}\text{CuN}_3\text{O}_5\text{P}_2$ $[\text{M}^+]$, observed mass 838.1663, calculated mass 838.1655, difference -0.7 mDa

2) $\text{Cu}(\text{PPh}_3)_3$

HR ESI-MS for $\text{C}_{54}\text{H}_{45}\text{CuP}_3$ $[\text{M}^+]$, observed mass 849.2043, calculated mass 849.2025, difference -1.8 mDa

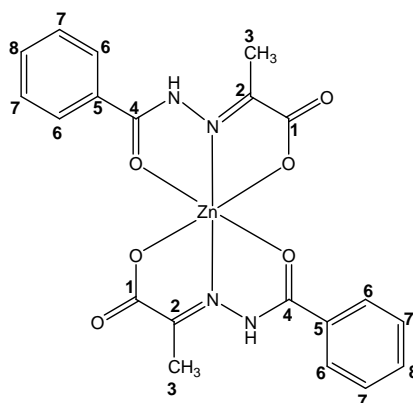
δ ^1H NMR (400 MHz, d_4 - MeOH): 1.94 (s, 3H, H-a), 7.98 (d, 2H, $J_{\text{H-H}} = 8.8$ Hz, H-a or H-b), 8.35 (d, 2H, $J_{\text{H-H}} = 8.8$ Hz, H-a or H-b), 7.27-7.44 (m, 75H, H_{ar} (PPh_3))

Significant IR bands: (KBr disc, cm^{-1}): (ν_{asym} COO, ν C=O) 1632 *br*, (ν C=N) 1597 *s*, (ν_{asym} (N=O) $_2$) 1527 *s*, (ν_{sym} (N=O) $_2$) 1346 *s*.

7.10 General synthetic procedure and characterisation detail of Zn(II) complexes of PVAHs [Zn(HL1)₂] - [Zn(HL20)₂]

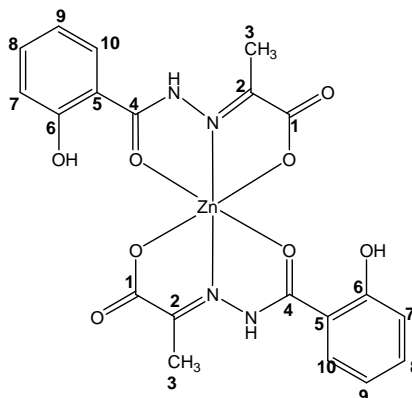
To a methanolic solution of the respective pyruvate-based aroylhydrazone (0.35 mmol) was added ZnSO₄·7H₂O (0.17 mmol). The mixture was stirred for 2 hours. The resultant white precipitate, which was isolated was washed with water and dried in *vacuo*.

[Zn(HL1)₂]



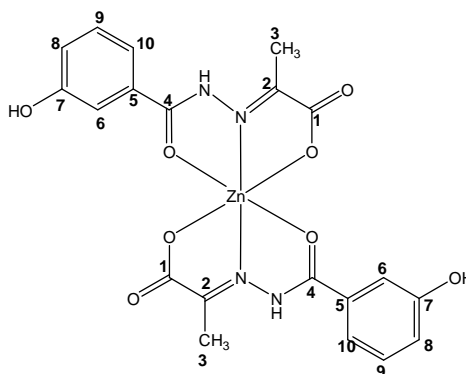
Bis[2-[(benzoyl)-hydrazone]-propionate] zinc(II)

[Zn(HL1)₂] was synthesised using ZnSO₄·7H₂O 0.05 g (0.17 mmol) and NaHL1 0.080 g (0.35 mmol) to give 0.040 g [Zn(HL1)₂], (0.068 mmol, 40 %); Melting point: 266-268 °C; **ESI-MS**: positive ion $m/z = 475.0564$, 10 %, HR ESI-MS: For ⁶⁴ZnC₂₀H₁₉N₄O₆ [(M+H)⁺], observed mass: 475.0564, calculated mass: 475.0591, difference mDa: 2.7 mDa; **δ ¹H NMR** (400 MHz, *d*₆-DMSO): 2.36 (s, 6H, H-3), 7.54 (m, 4H, H-6 or H-7), 7.65 (m, 2H, H-8), 7.97 (s, 4H, H-6 or H-7); **Anal. Calcd.** for Zn₁C₂₀H₁₈N₄O₆ x 2.25 H₂O: 46.53; H, 4.39; N, 10.85. Found: C, 46.17; H, 4.02; N, 10.55; **Significant IR bands**: (KBr disc, cm⁻¹): (ν C=O, ν_{asym} COO, ν C=N) 1631 *br*.

Zn(HL2)₂

Bis[2-[(2-hydroxy-benzoyl)-hydrazono]-propionate] zinc(II)

[Zn(HL2)₂] was synthesised using ZnSO₄·7H₂O 0.05 g (0.17 mmol) and NaHL2 0.09 g (0.35 mmol) to give 0.050 g [Zn(HL2)₂] (0.10 mmol, 58%); Melting point: >350 °C; **ESI-MS**: positive ion *m/z* = 507.0491, 46 %, HR ESI-MS: For ⁶⁴ZnC₂₀H₁₈N₄O₈ [(M+H)⁺], observed mass: 507.0491, calculated mass: 507.0489, difference: -0.4 mDa; **δ ¹H NMR** (400 MHz, *d*₆-DMSO): 2.18 (s, 3H, H-3), 6.93 (m, 2H, Ar-H), 7.39 (d,t, 2H, *J*_{H-H} = 7.8 Hz, 1.6 Hz Ar-H), 7.87 (d, 1H, *J*_{H-H} = 7.5 Hz, Ar-H); **Anal. Calcd.** for Zn₁C₂₂H₂₃N₄O₆ × 0.45 H₂O: 46.57; H, 3.69; N, 10.86. Found: C, 46.49; H, 3.57; N, 10.74; **Significant IR bands**: (KBr disc, cm⁻¹): (ν OH) 3406*br*, (ν C=O) 1650*s*, (ν_{asym} COO, ν C=N) 1614*br*.

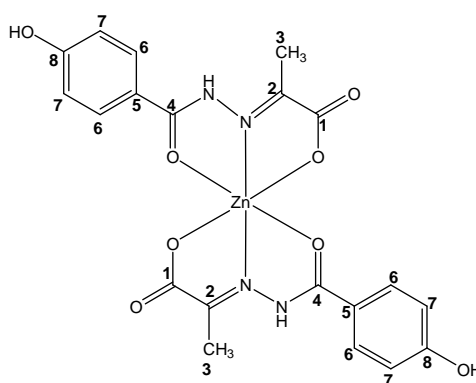
[Zn(HL3)₂]

Bis[2-[(3-hydroxy-benzoyl)-hydrazono]-propionate] zinc(II)

[Zn(HL3)₂] was synthesised using ZnSO₄·7H₂O 0.05 g (0.17 mmol) and NaHL3 0.086 g (0.35 mmol) to give 0.035 g [Zn(HL3)₂], (0.07 mmol, 40%); **Melting**

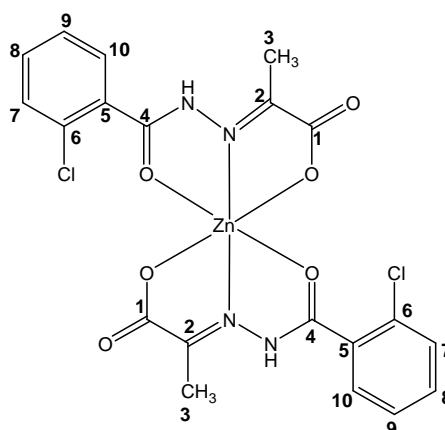
point: 312-314 °C; **ESI-MS:** positive ion $m/z = 507.0501$, 40 % HR ESI-MS: For $^{64}\text{ZnC}_{20}\text{H}_{19}\text{N}_4\text{O}_8$ $[(\text{M}+\text{H})^+]$, observed mass: 507.0501, calculated mass: 507.0489, difference: -1.3 mDa; δ $^1\text{H NMR}$ (400 MHz, d_6 -DMSO): 2.37 (s, 6H, H-3), 7.05 (d, 2H, $J_{\text{H-H}} = 7.4$ Hz, H-8 or H-10), 7.34 (m, 4H, H-9 and/or H-8,10), 7.41 (s, 2H, $J_{\text{H-H}} = 7.8$ Hz, H-6), 9.93 (bs, 2H, H-O), 12.72 (bs, 2H, H-N); **Anal. Calcd.** for $\text{Zn}_1\text{C}_{20}\text{H}_{19}\text{N}_4\text{O}_6 \times 2.1 \text{ H}_2\text{O}$: 44.03; H, 4.10; N, 10.27. Found: C, 43.54; H, 3.52; N, 10.04; **Significant IR bands:** (KBr disc, cm^{-1}): (ν OH) 3341br, (ν C=O) 1640s, (ν_{asym} COO, ν C=N) 1618br

[Zn(HL4)]

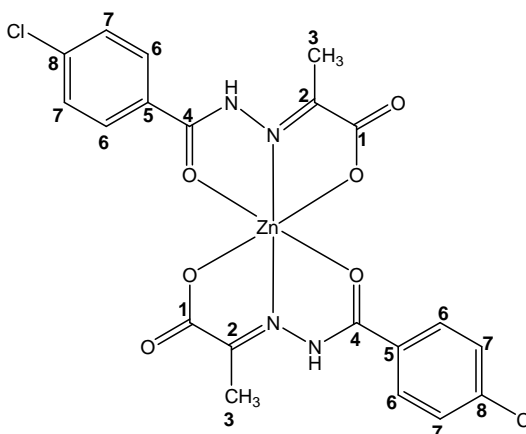


Bis[2-[(4-hydroxy-benzoyl)-hydrazono]-propionate] zinc(II)

[Zn(HL4)] was synthesised using $\text{ZnSO}_4 \cdot 7\text{H}_2\text{O}$ 0.05 g (0.17 mmol) and NaHL4 0.09 g (0.35 mmol) to give [Zn(HL4)]₂, (0.01 mmol, 58%); **Melting point:** 322-324 °C; **ESI-MS:** positive ion $m/z = 507.0499$, 50 %, HR ESI-MS: For $^{64}\text{ZnC}_{20}\text{H}_{19}\text{N}_4\text{O}_8$ $[(\text{M}+\text{H})^+]$, observed mass: 507.0499, calculated mass: 507.0489, difference: -1.0 mDa; δ $^1\text{H NMR}$ (400 MHz, d_6 -DMSO): 2.20 (s, 6H, H-3), 7.49 (d, 4H, $J_{\text{H-H}} = 8.3$ Hz H-6 or H-7), 8.10 (d, 4H, $J_{\text{H-H}} = 8.3$ Hz, H-6 or H-7).

[Zn(HL5)₂]**Bis[2-[(2-chloro-benzoyl)-hydrazone]-propionate]zinc(II)**

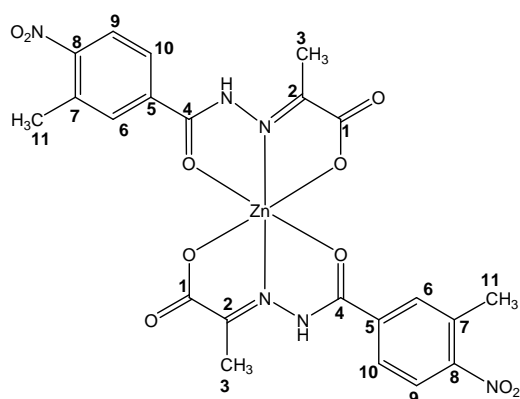
[Zn(HL5)₂] was synthesised using ZnSO₄·7H₂O 0.05 g (0.17 mmol) and NaHL5 0.09 g (0.35 mmol) to give [Zn(HL5)₂], (0.01 mmol, 58%); **Melting point:** 261-263 °C; **ESI-MS:** positive ion m/z = 542.9828, 5%, HR ESI-MS: For ⁶⁴ZnC₂₀H₁₇N₄O₆Cl₂ [(M+H)⁺], observed mass: 542.9828, calculated mass: 541.9811, difference: -1.7 mDa, difference: -1.0 mDa; **δ ¹H NMR** (400 MHz, d₆-DMSO): 2.18 (s, 6H, H-3), 6.47 (m, 4H, H-8,9), 7.80 (d, 4H, J_{H-H} = 8.8 Hz, H-7,10); **Significant IR bands:** (KBr disc, cm⁻¹): (ν C=O, ν_{asym} COO) 1625s, (ν C=N) 1609s.

[Zn(HL6)₂]**Bis[2-[(4-chloro-benzoyl)-hydrazone]-propionate]zinc(II)**

[Zn(HL6)₂] was synthesised using ZnSO₄·7H₂O 0.05 g (0.17 mmol) and NaHL6 0.09 g (0.35 mmol) to give [Zn(HL6)₂], 0.060 g (0.11 mmol, 65 %); **Melting point:** 249-251°C; **ESI-MS:** positive ion m/z = 542.9811, 20 % HR ESI-MS: For

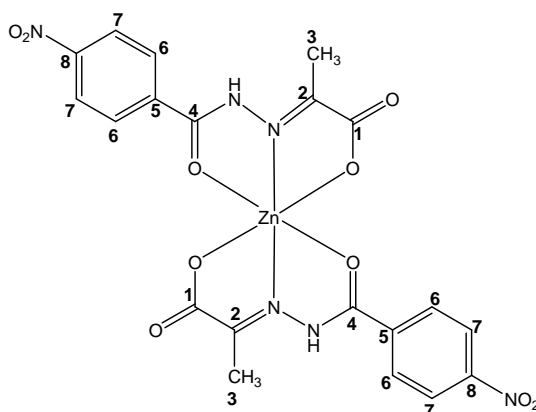
$^{64}\text{ZnC}_{20}\text{H}_{17}\text{N}_4\text{O}_6\text{Cl}_2$ [(M+H)⁺], observed mass: 542.9826, calculated mass: 541.9811, difference: -1.5 mDa; δ ¹H NMR (400 MHz, *d*₆-DMSO): 2.18 (s, 6H, H-3), 7.55 (d, 4H, Ar-H, *J*_{H-H} = 8.5 Hz H-6 or H-7), 8.04 (d, 4H, *J*_{H-H} = 8.5 Hz, H-6 or H-7); **Anal. Calcd** for $\text{Zn}_1\text{C}_{20}\text{H}_{16}\text{N}_4\text{O}_6\text{Cl}_2 \times 2.50 \text{H}_2\text{O}$: 40.74; H, 2.96; N, 10.29. Found: C, 40.52; H, 3.35; N, 9.38. **Significant IR bands**: (KBr disc, cm⁻¹): (ν C=O) 1650s, (ν_{asym} COO, ν C=N) 1614br

Zn(HL7)₂

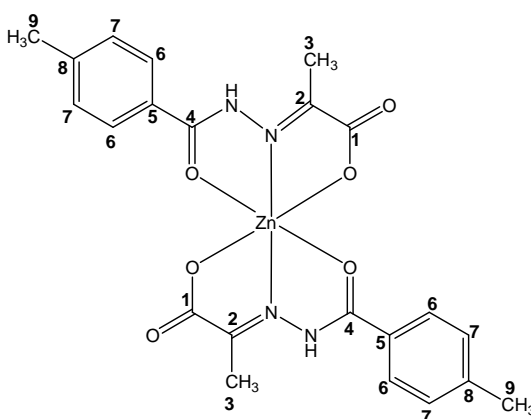


Bis[2-[(3-methyl-4-nitro-benzoyl)-hydrazono]-propionate]zinc(II)

[Zn(HL7)₂] was synthesised using $\text{ZnSO}_4 \cdot 7\text{H}_2\text{O}$ 0.05 g (0.17 mmol) and NaHL7 0.10 g (0.35 mmol) to give [Zn(HL7)₂], 0.051 g (0.085 mmol, 50 %); **Melting point**: 287-289 °C; **ESI-MS**: positive ion *m/z* = 593.0596, 10 %, HR ESI-MS: For $^{64}\text{ZnC}_{22}\text{H}_{21}\text{N}_6\text{O}_{10}$ [(M+H)⁺], observed mass: 593.0596, calculated mass: 593.0605, difference: 0.9 mDa; δ ¹H NMR (400 MHz, *d*₆-DMSO): 2.27 (s, 6H, H-3), 2.55 (s, 6H, H-11), 8.04 (bs, 6H, H-6,9,10); **Anal. Calcd.** for $\text{Zn}_1\text{C}_{22}\text{H}_{20}\text{N}_6\text{O}_{10} \times 1.6 \text{H}_2\text{O}$: 42.44; H, 3.76; N, 13.50. Found: C, 42.08; H, 3.36; N, 13.16; **Significant IR bands** (KBr disc, cm⁻¹): (ν C=O, ν_{asym} COO, ν C=N) 1631br, (ν_{asym} (N=O)₂) 1526s, (ν_{sym} (N=O)₂) 1358s.

[Zn(HL8)₂]

[Zn(HL8)₂] was synthesised using ZnSO₄·7H₂O 0.05 g (0.17 mmol) and NaHL8 0.10 g (0.35 mmol) to give [Zn(HL8)₂], 0.054 g (0.095 mmol, 56 %); **Melting point:** 282-284 °C; **ESI-MS:** positive ion m/z = 565.00, 5 %, ESI-MS: For ⁶⁴ZnC₂₀H₁₇N₆O₁₀ [(M+H)⁺], observed mass: 565.00, calculated mass: 565.00; **Anal. Calcd** for Zn₁C₂₀H₁₆N₆O₁₀ x 0.75 CH₃OH, 0.2 H₂O: 42.00; H, 3.30; N, 14.16. Found: C, 42.80; H, 3.02; N, 13.91; **Significant IR bands:** (KBr disc, cm⁻¹): (ν C=O) 1638s, (ν_{asym} COO, ν C=N) 1621br, (ν_{asym} (N=O)₂) 1530s, (ν_{sym} (N=O)₂) 1338br..

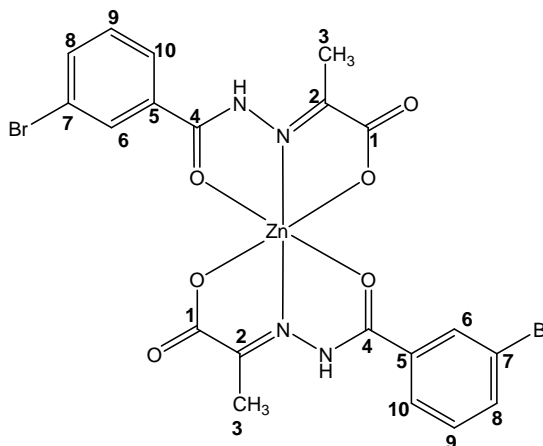
[Zn(HL9)₂]

Bis[2-[(4-methyl-benzoyl)-hydrazono]-propionate]zinc(II)

[Zn(HL9)₂] was synthesised using ZnSO₄·7H₂O 0.050 g (0.17 mmol) and NaHL9 0.85 g (0.35 mmol) to give 0.046 g [Zn(HL9)₂], 0.046 g (0.09 mmol, 54%); **Melting point:** 244-246 °C; **ESI-MS:** positive ion m/z = 503.0911, 30 %, HR ESI-MS: For ⁶⁴ZnC₂₂H₂₃N₄O₆ [(M+H)⁺], observed mass: 503.0911, calculated mass:

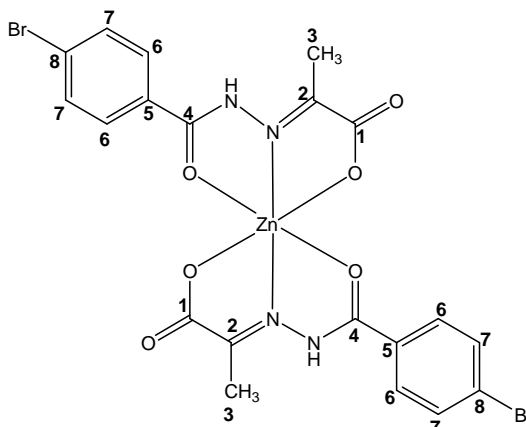
503.0904, difference: -1.6 mDa; δ $^1\text{H NMR}$ (400 MHz, d_6 -DMSO): 2.39 (s, 12H, H-3,9), 7.35 (d, 4H, $J_{\text{H-H}} = 7.9$ Hz, H-6 or H-7), 7.90 (d, 4H, $J_{\text{H-H}} = 7.9$ Hz, H-6 or H-7), 12.69 (bs, 1H, H-N); **Anal. Calcd** for $\text{Zn}_1\text{C}_{22}\text{H}_{22}\text{N}_4\text{O}_6 \times 2.25 \text{H}_2\text{O}$: 48.54; H, 4.91; N, 10.29. Found: C, 48.49; H, 4.79; N, 10.21; **Significant IR bands**: (KBr disc, cm^{-1}): (ν C=O) 1649s, (ν_{asym} COO) 1623s, (ν C=N) 1618s.

[Zn(HL10)₂]

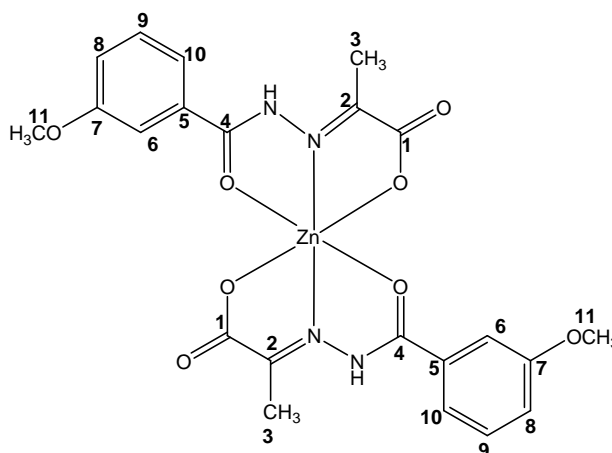


Bis[2-[(3-bromo-benzoyl)-hydrazono]-propionate] zinc(II)

[Zn(HL10)₂] was synthesised using $\text{ZnSO}_4 \cdot 7\text{H}_2\text{O}$ 0.05 g (0.17 mmol) and NaHL10 0.11 g (0.35 mmol) to give [Zn(HL10)₂], 0.09 g (0.14 mmol, 84%); **Melting point**: 262-263 °C; **ESI-MS**: positive ion $m/z =$, HR ESI-MS: For $^{64}\text{ZnC}_{20}\text{H}_{17}\text{N}_4\text{O}_6\text{Br}_2$ [(M+H)⁺], observed mass:, calculated mass: 630.8801, difference: 0.3 mDa; δ $^1\text{H NMR}$ (400 MHz, d_6 -DMSO): 2.29 (s, 6H, H-3), 7.76 (d, 2H, $J_{\text{H-H}} = 7.6$ Hz, H-8 or H-10), 7.44 (t, 2H, $J_{\text{H-H}} = 7.9$ Hz, H-9), 8.17 (s, 2H, H-6), 8.00 (d, 2H, $J_{\text{H-H}} = 7.2$ Hz, H-8 or H-10); **Anal. Calcd** for $\text{Zn}_1\text{C}_{20}\text{H}_{16}\text{N}_6\text{O}_6\text{Br}_2 \times 1.15 \text{H}_2\text{O}$: 36.72; H, 2.82; N, 8.56. Found: C, 36.92; H, 2.65; N, 8.35.

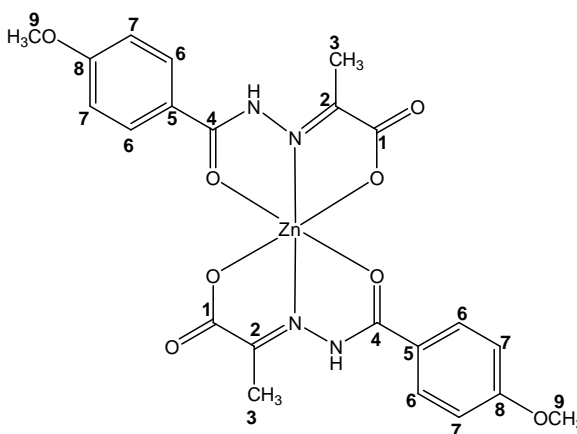
[Zn(HL11)₂]**Bis[2-[(4-bromo-benzoyl)-hydrazone]-propionate] zinc(II)**

[Zn(HL11)₂] was synthesised using ZnSO₄·7H₂O 0.05 g (0.17 mmol) and sodium; 2-[(4-bromo-benzoyl)-hydrazone]-propionate 0.11 g (0.35 mmol) to give [Zn(HL11)₂], 0.087 g (0.136 mmol, 81 %) **Melting point:** 260-262 °C; **ESI-MS:** positive ion *m/z* = 630.8799, 6 %, HR ESI-MS: For ⁶⁴ZnC₂₀H₁₇N₄O₆Br₂ [(M+H)⁺], observed mass: 630.8799, calculated mass: 630.8801, difference: -1.6 mDa; **¹H NMR** (400 MHz, *d*₆-DMSO): 2.30 (s, 6H, CH₃), 7.70 (d, 4H, *J*_{H-H} = 7.8 Hz Ar-H), 7.95 (d, 4H, *J*_{H-H} = 7.8 Hz Ar-H); **Anal. Calcd.** for Zn₁C₂₀H₁₆N₆O₆Br₂ × 2.15 H₂O: C, 35.73; H, 3.04; N, 8.33. Found: C, 35.98; H, 2.79; N, 8.08; **Significant IR bands:** (KBr disc, cm⁻¹): (ν C=O, ν_{asym} COO, ν C=N 1627 *br*).

[Zn(HL12)₂]

Bis [2-[(3-methoxy-benzoyl)-hydrazone]-propionate] zinc(II)

[Zn(HL12)₂] was synthesised using ZnSO₄·7H₂O 0.05 g (0.17 mmol) and NaHL12 0.09 g (0.35 mmol) to give [Zn(HL12)₂], (0.01 mmol, 58%); **Melting point:** 269-271 °C; **ESI-MS:** positive ion m/z = 535.0810, 60 %, HR ESI-MS: For ⁶⁴ZnC₂₂H₂₃N₄O₆ [(M+H)⁺], observed mass: 535.0810, calculated mass: 535.0802, difference: -1.6 mDa; **δ ¹H NMR** (400 MHz, d₆-DMSO): 2.34 (s, 6H, H-3), 3.81 (s, 6H, H-11), 7.19 (d, 2H, J_{H-H} = 7.0 Hz, H-8 or H-10), 7.43 (t, 2H, J_{H-H} = 8.0 Hz, H-9), 7.51 (s, 2H, H-6), 7.59 (d, 2H, J_{H-H} = 7.0 Hz, H-8 or H-10)

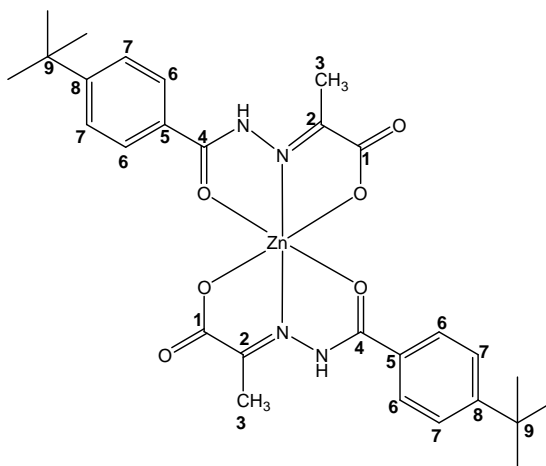
[Zn(HL13)₂]

Bis[2-[(4-methoxy-benzoyl)-hydrazone]-propionate] zinc(II)

[Zn(HL13)₂] was synthesised using ZnSO₄·7H₂O 0.05 g (0.17 mmol) and NaHL13 0.09 g (0.35 mmol) to give [Zn(HL13)₂], 0.055 g (0.10 mmol, 60 %);

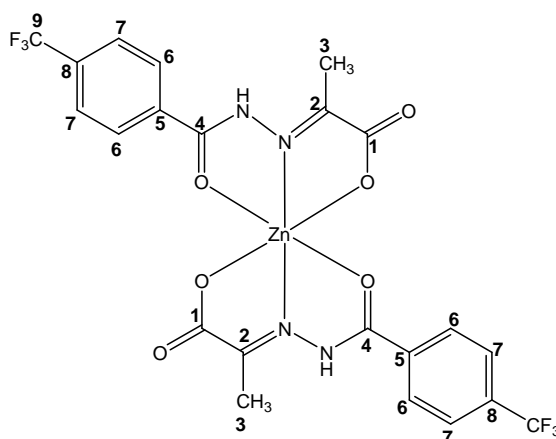
Melting point: 287-289 °C; **ESI-MS:** positive ion $m/z = 535.0805$, 85 %, HR ESI-MS: For $^{64}\text{ZnC}_{22}\text{H}_{23}\text{N}_4\text{O}_6$ $[(M+H)^+]$, observed mass: 535.0805, calculated mass: 535.0802, difference: 0.3 mDa; δ $^1\text{H NMR}$ (400 MHz, d_6 -DMSO): 2.22 (s, 6H, H-3), 3.81 (s, 6H, H-9), 7.00 (d, 4H, $J_{\text{H-H}} = 8.4$ Hz, H-6 or H-7), 8.05 (d, 4H, $J_{\text{H-H}} = 8.4$ Hz, H-6 or H-7); **Anal. Calcd.** for $\text{Zn}_1\text{C}_{22}\text{H}_{22}\text{N}_4\text{O}_8 \times 1.7 \text{ H}_2\text{O}$: 46.65; H, 4.52; N, 9.89. Found: C, 46.11; H, 3.92; N, 9.51; **Significant IR bands:** (KBr disc, cm^{-1}): (ν C=O, ν_{asym} COO) 1628s, (ν C=N) 1606s.

[Zn(HL14)₂]

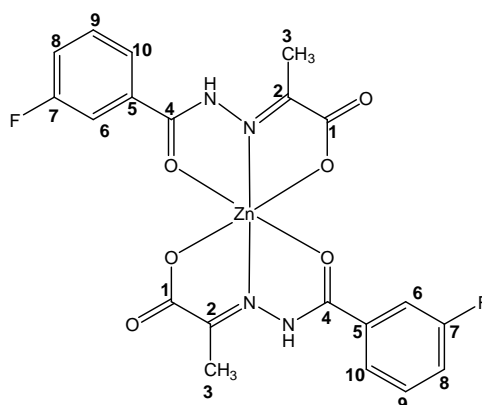


Bis[2-[(4-*tert*-butyl-benzoyl)-hydrazone]-propionate] zinc(II)

[Zn(HL14)₂] was synthesised using $\text{ZnSO}_4 \cdot 7\text{H}_2\text{O}$ 0.05 g (0.17 mmol) and NaHL14 0.10 g (0.35 mmol) to give [Zn(HL14)₂], (0.01 mmol, 58%); **Melting point:** 257-259 °C; **ESI-MS:** positive ion $m/z = 587.1857$, 10 %, HR ESI-MS: For $^{64}\text{ZnC}_{28}\text{H}_{35}\text{N}_4\text{O}_6$ $[(M+H)^+]$, observed mass: 587.1857, calculated mass: 587.1843, difference: -2.5 mDa; δ $^1\text{H NMR}$ (400 MHz, d_6 -DMSO): 2.27 (s, 6H, H-3), 1.29 (s, 18H, H-10), 7.45 (d, 4H, $J_{\text{H-H}} = 8.0$ Hz, H-6 or H-7), 7.97 (bs, 4H, H-6 or H-7); **Significant IR bands** (KBr disc, cm^{-1}): (ν C=O, ν_{asym} COO, ν C=N) 1624br.

[Zn(HL15)₂]Bis[2-[(4-*tri*-fluoro-methyl)-benzoyl-hydrazono]-propionate] zinc(II)

[Zn(HL15)₂] was synthesised using ZnSO₄·7H₂O 0.05 g (0.17 mmol) and NaHL15 0.10 g (0.35 mmol) to give [Zn(HL15)₂] 0.070 g (0.11 mmol, 67%); **Melting point:** 262-264 °C; **δ ¹H NMR** (400 MHz, *d*₆-DMSO): 2.26 (s, 6H, H-3), 7.86 (d, 2H, *J*_{H-H}= 6.9 Hz, H-6 or H-7), 8.20 (apparent bs, 4H, H-6 or H-7); **Anal. Calcd.** for Zn₁C₂₂H₁₆N₄O₆F₆ x 1.1 H₂O x 0.45 CH₃OH: C, 41.74; H, 3.12; N, 8.67. Found: C, 41.45; H, 2.75; N, 8.30, **Significant IR bands:** (KBr disc, cm⁻¹): (ν C=O, ν_{asym} COO, ν C=N) 1617 *br*.

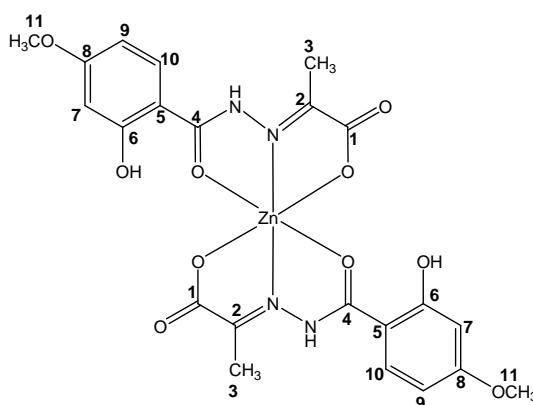
[Zn(HL16)₂]

Bis[2-[(3-fluoro-benzoyl)-hydrazono]-propionate] zinc(II)

[Zn(HL16)₂] was synthesised using ZnSO₄·7H₂O 0.05 g (0.17 mmol) and NaHL16 0.09 g (0.35 mmol) to give [Zn(HL16)₂], 0.047 g (0.09 mmol, 54%); **Melting point:** 249-251 °C; **ESI-MS:** positive ion *m/z* = 511.0399, 100 %, HR ESI-MS: For

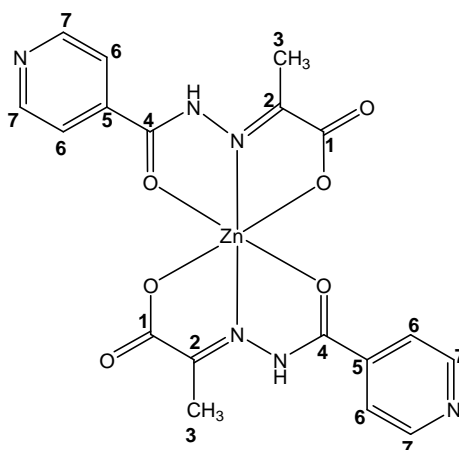
$^{64}\text{ZnC}_{20}\text{H}_{17}\text{N}_4\text{O}_6\text{F}_2$ [(M+H)⁺], observed mass: 511.0399, calculated mass: 511.0402, difference: 0.7 mDa; δ ¹H NMR (400 MHz, *d*₆-DMSO): 2.28 (s, 6H, CH₃), 7.45 (m, 2H, H_{ar}), 7.55 (d, 2H, J_{H-H} = 6.3 Hz, H_{ar}), 7.79 (m, 4H, H_{ar}), 12.74 (bs, 2H, NH); δ **Anal. Calcd.** for Zn₁C₂₀H₁₆N₄O₆F₂ x 1.55 H₂O: 44.51; H, 3.57; N, 10.38. Found: C, 44.35; H, 3.30; N, 10.12; **Significant IR bands** (KBr disc, cm⁻¹): (ν C=O, ν_{asym} COO, ν C=N) 1634 *br*.

[Zn(HL17)₂]



Bis[2-[(2-hydroxy-4-methoxy-benzoyl)-hydrazone]-propionate] zinc(II)

[Zn(HL17)₂] was synthesised using ZnSO₄·7H₂O 0.05 g (0.17 mmol) and NaHL17 0.09 g (0.35 mmol) to give [Zn(HL17)₂], 0.047 g (0.09 mmol, 52%); **Melting point:** 249-251 °C; **ESI-MS:** positive ion m/z = 511.0399, 30 %, HR ESI-MS: For $^{64}\text{ZnC}_{20}\text{H}_{17}\text{N}_4\text{O}_6\text{F}_2$ [(M+H)⁺], observed mass: 511.0399, calculated mass: 511.0402, difference: 0.7 mDa; δ ¹H NMR (400 MHz, *d*₆-DMSO): 2.16 (s, 6H, H-3), 3.76 (s, 6H, H-11), 6.47 (m, 4H, H-7, H-9 or H-10), 7.80 (d, 2H, J_{H-H} = 8.7 Hz, H-9 or H-10); **Significant IR bands:** (KBr disc, cm⁻¹): (ν OH) 3432 *br*, (ν C=O, ν_{asym} COO, ν C=N) 1606 *br*.

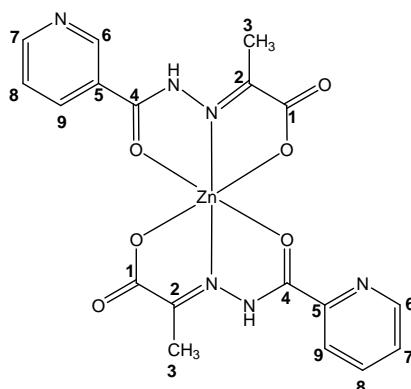
[Zn(HL18)₂]

Bis[2-[(pyridine-4-carbonyl)-hydrazone]-propionate] zinc(II)

[Zn(HL18)₂] was synthesised using ZnSO₄·7H₂O 0.05 g (0.17 mmol) and NaHL18 0.09 g (0.35 mmol) to give [Zn(HL18)₂], 0.065 g (0.14 mmol, 82%);

Melting point: decomposes above 300 °C; **Anal. Calcd.** for Zn₁C₁₈H₁₆N₆O₆ × 4.4 H₂O: 38.81; H, 4.49; N, 15.09. Found: C, 39.14; H, 4.12; N, 14.76.

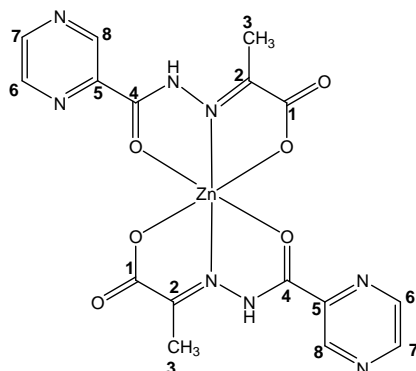
Significant IR bands: (KBr disc, cm⁻¹): (ν C=O, ν_{asym} COO, ν C=N) 1652 *br*.

[Zn(HL19)₂]

Bis[2-[(pyridine-4-carbonyl)-hydrazone]-propionate] zinc(II)

[Zn(HL19)₂] was synthesised using ZnSO₄·7H₂O 0.05 g (0.17 mmol) and NaHL19 0.09 g (0.35 mmol) to give [Zn(HL19)₂], 0.047 g (0.09 mmol, 55%);

Melting point: decomposes above 300 °C; **Significant IR bands:** (KBr Disc, cm⁻¹): (ν C=O) 1661 *s*, (ν_{asym} COO) 1634 *s*, (ν C=N) 1610 *s*.

[Zn(HL20)₂]

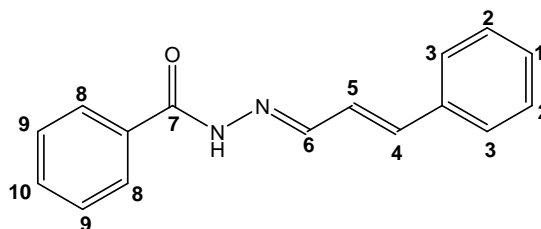
Bis[2-[(pyrazine-2-carbonyl)-hydrazono]-propionate] zinc(II)

[Zn(HL20)₂] was synthesised using ZnSO₄·7H₂O 0.05 g (0.17 mmol) and NaHL16 0.09 g (0.35 mmol) to give [Zn(HL20)₂], 0.057 g (0.12 mmol, 72%); **Melting point:** decomposes above 200 °C; **δ ¹H NMR** (400 MHz, D₂O): 2.03 (s, 6H, H-3), 8.60 (dd, 2H, J_{H-H} = 3.0 Hz, 1.2 Hz, H-6 or H-7), 9.14 (d, 2H, J_{H-H} = 2.8 Hz, H-6 or H-7), 9.67 (s, 2H, H-8); **Significant IR bands:** (KBr disc, cm⁻¹): (ν C=O, ν_{asym} COO, ν C=N) 1616 *br*.

7.10 General synthetic procedure and characterisation detail of CAHs (HCA1-HCA14)

Cinnamaldehyde (1.5 mmol) was added dropwise to an ethanolic solution of the respective hydrazide (1.25 mmol). The mixture was then refluxed for 5 hours and the precipitate that formed after slow cooling of the solution was isolated by filtration. The volume of the filtrate was reduced to approximately a quarter of the initial volume. The solid formed was isolated by filtration and the two solids were combined and dried under *vacuo*.

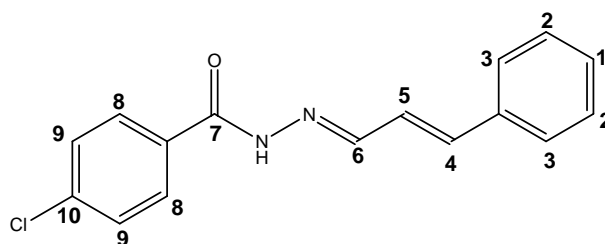
HCA1



Benzoic acid (3-phenyl-allylidene)-hydrazide

HCA1 was synthesised using cinnamaldehyde 0.24 g (1.85 mmol) and benzoyl hydrazide 0.18 g (1.32 mmol) to give HCA1, 0.23 g (0.92 mmol, 73%); **Melting point:** 193-194 °C; **ESI-MS:** positive ion $m/z = 251.1181$, 100%, HR ESI: For $C_{16}H_{15}N_2O_2$ ($[M+H]^+$), observed mass 251.1181, calculated mass 251.1179, difference 0.2 mDa; δ **1H NMR** (400 MHz, d_6 -DMSO): 11.75 (bs, 1H, H-N), 8.23 (dd, 1H, $J_{H-H} = 6.8$ Hz, 1.2 Hz, H-6), 7.89 (d, 2H, $J_{H-H} = 7.6$ Hz, H_{ar}), 7.31-7.90 (m, 8H, H_{ar}), 7.06 – 7.08 (m, 2H, H-4,5); δ **^{13}C NMR** (100.6 MHz, d_6 -DMSO): δ 163.0 (4°), 149.7 (CH), 139.0 (CH), 135.9 (4°), 133.4 (4°), 131.7 (CH), 128.8 (CH), 128.4 (CH), 127.6 (CH), 127.1 (CH), 125.6 (CH); **Significant IR bands** (KBr disc, cm^{-1}): (ν NH) 3268m, (ν C=O) 1646s, (ν C=N) 1624s.

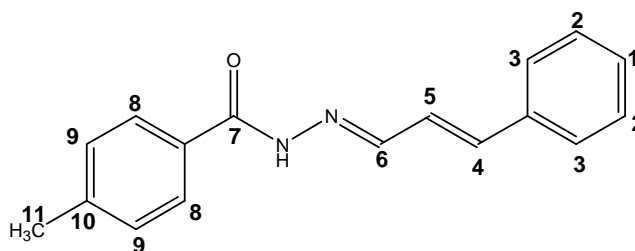
HCA2



4-Chloro-benzoic acid (3-phenyl-allylidene)-hydrazide

HCA2 was synthesised using cinnamaldehyde 0.2 g (1.50 mmol) and 4-chloro-benzoyl hydrazide 0.21 g (1.25 mmol) to give HCA2, 0.28 g (0.98 mmol, 78%); **Melting point:** 223-224 °C; **ESI-MS:** positive ion $m/z = 285.0786$, 100%, HR ESI-MS: For $C_{16}H_{14}N_2OCl$ ($[M+H]^+$), observed mass 285.0786, calculated mass 285.0789, difference 0.3 mDa; δ **1H NMR** (400 MHz, d_6 -DMSO): 11.80 (bs, 1H, H-N), 8.23 (t, 1H, $^3J_{H-H} = 4.0$ Hz, H-6), 7.93 (d, 2H, $J_{H-H} = 8.4$ Hz, H_{ar}), 7.31-7.64 (m, 7H, H_{ar}) 7.06 – 7.08 (m, 2H, H-4,5); δ **^{13}C NMR** (100.6 MHz, d_6 -DMSO): δ 161.8 (4°), 150.0 (CH), 139.1 (CH), 136.4 (4°), 135.8 (4°), 132.0 (4°), 129.4 (CH), 128.7 (CH), 128.4 (CH), 127.0 (CH), 125.5 (CH); **Anal. Calcd** for $C_{16}H_{13}N_2OCl$: C, 67.49; H, 4.60; N, 9.84. Found C, 67.44; H, 4.61; N, 9.74; **Significant IR bands** (KBr disc, cm^{-1}): (ν NH) 3268m, (ν C=O) 1660s, (ν C=N) 1625s.

HCA3

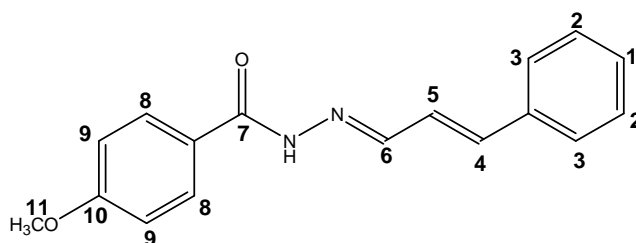


4-Methyl-benzoic acid (3-phenyl-allylidene)-hydrazide

HCA3 was synthesised using cinnamaldehyde 0.2 g (1.50 mmol) and 4-methyl-benzoyl hydrazide 0.19 g (1.25 mmol) to give HCA3, 0.27 g (1.00 mmol, 80%); **Melting point:** 125-127 °C; **ESI-MS:** positive ion $m/z = 265.1345$ 100%, HR ESI-MS: For $C_{17}H_{17}N_2O$ ($[M+H]^+$), observed mass 265.1345, calculated mass 265.1335, difference 1.0 mDa; δ **1H NMR** (400 MHz, d_6 -DMSO): δ 11.67 (bs, 1H, H-N), 8.24 (d, 1H, $^3J_{H-H} = 7.4$ Hz, H-6), 7.81 (d, 2H, $J_{H-H} = 8.1$ Hz, H_{ar}), 7.31 (m, 7H,

H_{ar}) 7.10 – 7.01 (m, 2H, H-4,5), 2.38 (s, 3H, H-11); δ ¹³C NMR (100.6 MHz, *d*₆-DMSO): δ 162.8 (4°), 149.3 (CH), 141.6 (4°), 138.6 (CH), 135.8 (4°), 130.4 (4°), 128.9 (CH), 128.7 (CH), 127.5 (CH), 126.9 (CH), 125.6 (CH), 21.5 (CH₃); **Anal. Calcd** for C₁₇H₁₆N₂O: C, 77.24; H, 6.10; N, 10.60. Found C, 77.07; H, 6.10; N, 10.70; **Significant IR bands** (KBr disc, cm⁻¹): ν (NH) 3200*m*, (ν C=O) 1637*s*, (ν C=N) 1525*s*.

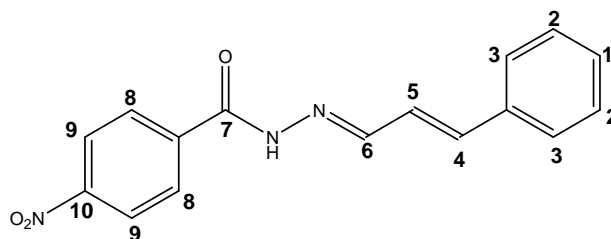
HCA4



4-Methoxy-benzoic acid (3-phenyl-allylidene)-hydrazide

HCA4 was synthesised using cinnamaldehyde 0.20 g (1.5 mmol) and 4-methoxy-benzoyl hydrazide 0.21 g (1.25 mmol) to give HCA4, 0.25 g (0.89 mmol, 71%); **Melting point:** 217-219 °C; **ESI-MS:** positive ion *m/z* = 281.1290, 100%; **HR ESI-MS:** For C₁₇H₁₇N₂O₂ ([M+H]⁺), observed mass 281.1290, calculated mass 281.1285, difference 0.6 mDa; δ ¹H NMR (400 MHz, *d*₆-DMSO): δ 11.62 (bs, 1H, H-N), 8.23 (d, 1H, ³J_{H-H} = 7.3 Hz, H-6), 7.90 (d, 2H, J_{H-H} = 8.4 Hz, H_{ar}), 7.62 (d, 2H, J_{H-H} = 7.4 Hz, H_{ar}), 7.04-7.40 (m, 7H, H_{ar}, H-4,5) 3.83 (s, 3H, H-11); δ ¹³C NMR (100.6 MHz, *d*₆-DMSO): δ 162.4 (4°), 162.0 (4°), 149.1 (CH), 138.6 (CH), 136.0 (4°), 129.5 (CH), 128.8 (CH), 127.0 (CH), 125.8 (CH), 125.4 (4°), 113.7 (CH), 55.4 (CH₃); **Significant IR bands** (KBr disc, cm⁻¹): (ν NH) 3195*m*, (ν C=O) 1634*s*, (ν C=N) 1622*s*.

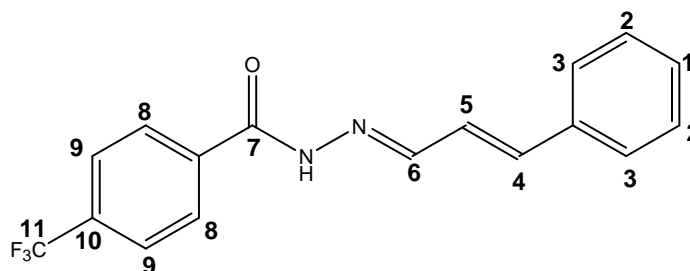
HCA5



4-Nitro-benzoic acid (3-phenyl-allylidene)-hydrazide

HCA5 was synthesised using cinnamaldehyde 0.20 g (1.5 mmol) and 4-nitro-benzoyl hydrazide 0.23 g (1.25 mmol) to give HCA5, 0.31 g (1.06 mmol, 85%); **Melting point:** 243-245 °C; **ESI-MS:** positive ion $m/z = 296.1023$, 100%; **HR ESI-MS:** For $C_{16}H_{14}N_3O_3$ ($[M+H]^+$), observed mass 296.1023, calculated mass 296.1030, difference 0.6 mDa; **δ 1H NMR** (400 MHz, d_6 -DMSO): δ 12.01 (bs, 1H, H-N), 8.37 (d, 2H, $^3J_{H-H} = 8.8$ Hz, H-8 or H-9), 8.25 (dd, 1H, $J_{H-H} = 6.2$ Hz, 2.5 Hz, H-6), 8.14 (d, 2H, $J_{H-H} = 8.8$ Hz, H-8 or H-9), 7.64 (d, 2H, $J_{H-H} = 7.2$ Hz, H-2 or H-3), 7.32-7.42 (m, 3H, H-1, H-2 or H-3) 7.09 – 7.10 (2H, m, H-4,5); **δ ^{13}C NMR** (100.6 MHz, d_6 -DMSO): δ 161.3 (4°), 150.9 (CH), 149.2 (4°), 139.8 (4°), 139.1 (CH), 135.8 (4°), 129.2 (CH), 129.0 (CH), 128.8 (CH), 127.2 (CH), 125.4 (CH), 123.6 (CH); **Anal. Calcd** for $C_{16}H_{13}N_3O_3$: C, 65.08; H, 4.43; N, 14.23. Found C, 64.70; H, 4.50; N, 13.96; **Significant IR bands** (KBr disc, cm^{-1}): (ν NH) 3276m, (ν C=O) 1657s, (ν C=N) 1625s, (ν_{asym} (N=O) $_2$) 1518s, (ν_{sym} (N=O) $_2$) 1347s.

HCA6

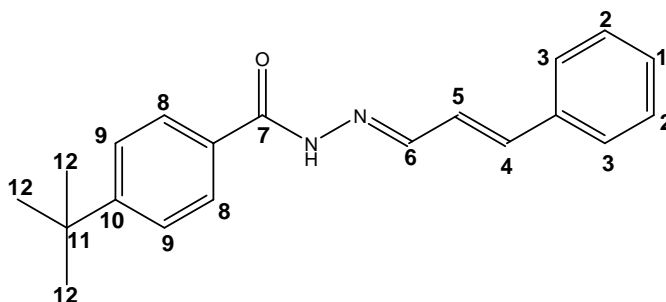


4-Trifluoromethyl-benzoic acid (3-phenyl-allylidene)-hydrazide

HCA6 was synthesised using cinnamaldehyde 0.23 g (1.76 mmol) and 4-trifluoromethyl-benzoyl hydrazide 0.35 g (1.26 mmol) to give HCA6, 0.33 g (1.04 mmol, 83%); **Melting point:** 206-208 °C; **ESI-MS:** positive ion $m/z = 319.1057$

100%, HR **ESI-MS**: For $C_{17}H_{14}N_2OF_3$ ($[M+H]^+$), observed mass 319.1057, calculated mass 319.1053, difference 0.4 mDa; δ **1H NMR** (400 MHz, d_6 -DMSO): δ 11.94 (bs, 1H, NH), 8.25 (t, 1H, $^3J_{H-H} = 4.4$ Hz, H-6), 8.10 (d, 2H, $^3J_{H-H} = 8.1$ Hz, H-9 or H-8), 7.91 (d, 2H, $^3J_{H-H} = 8.2$ Hz, H-9 or H-8), 7.64 (d, 2H, $^3J_{H-H} = 7.3$ Hz, H-2 or H-3), 7.31-7.42 (m, 3H, H-1, H-2 or H-3), 7.08 – 7.09 (m, 2H, m, H-4,5); δ **^{13}C NMR** (100.6 MHz, d_6 -DMSO): δ 161.9 (4°), 150.6 (CH), 139.6 (CH), 137.3 (4°), 135.8 (4°), 131.6 (4°), 128.9 (CH), 128.8 (CH), 128.6 (CH), 127.2 (CH), 125.5 (CH); **Anal. Calcd** for $C_{17}H_{13}N_2OF_3$: C, 64.15; H, 4.12; N, 8.80. Found C, 64.01; H, 4.10; N, 8.69; **Significant IR bands** (KBr disc, cm^{-1}): (ν NH) 3257m, (ν C=O) 1659s, (ν C=N) 1624s.

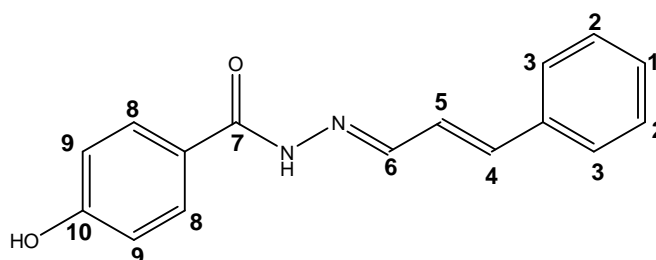
HCA7



4-*tert*-Butyl-benzoic acid (3-phenyl-allylidene)-hydrazide

HCA7 was synthesised using cinnamaldehyde 0.21 (1.6 mmol) and 4-*tert*-butyl benzoyl hydrazide 0.19 g (1.14 mmol) to give HCA7, 0.28 g (0.91 mmol, 80%); **Melting point**: 240-242 $^\circ C$; **ESI-MS**: positive ion $m/z = 307.1801$ 100%; HR **ESI-MS**: For $C_{20}H_{23}N_2O$ ($[M+H]^+$), observed mass 307.1081, calculated mass 307.1085, difference 0.8 mDa; δ **1H NMR** (400 MHz, d_6 -DMSO): δ 11.68 (bs, 1H, H-N), 8.23 (d, 1H, $J_{H-H} = 7.2$ Hz, H-6), 7.83 (d, 2H, $J_{H-H} = 8.3$ Hz, H-8 or H-9), 7.63 (d, 2H, $J_{H-H} = 7.4$ Hz, H-2 or H-3), 7.53 (d, 2H, $J_{H-H} = 8.3$ Hz, H-8 or H-9), 7.30-7.42 (m, 3H, H-1, H-2 or H-3), 7.05-7.07 (m, 2H, H-4, 5), 1.31 (s, 9H, H-12); δ **^{13}C NMR** (100.6 MHz, d_6 -DMSO): δ 163.0 (4°), 154.6 (4°), 149.5 (CH), 138.9 (CH), 135.9 (4°), 130.6 (4°), 128.8 (CH), 127.5 (CH), 127.1 (CH), 125.7 (CH), 125.2 (CH), 34.7 (4°), 30.9 ((CH₃)₃); **Significant IR bands** (KBr disc, cm^{-1}): (ν NH) 3204m, (ν C=O) 1635s, (ν C=N) 1624s.

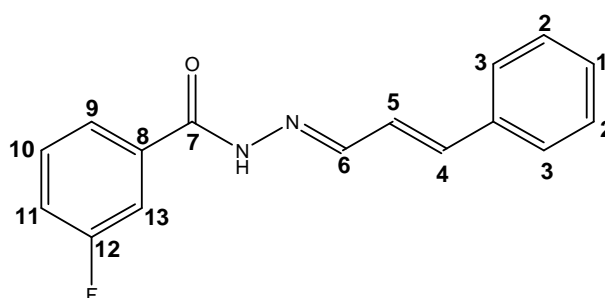
HCA8



4-Hydroxy-benzoic acid (3-phenyl-allylidene)-hydrazide

HCA8 was synthesised using cinnamaldehyde 0.21 g (1.5 mmol) and 4-hydroxy-benzoyl hydrazide 0.22 g (1.25 mmol) to give HCA8, 0.23 g (1.23 mmol, 70%); **Melting point:** 232-234 °C; **ESI-MS:** positive ion $m/z = 267.1124$, 100%, **HR ESI-MS:** For $C_{16}H_{15}N_2O_2$ ($[M+H]^+$), observed mass 267.1124, calculated mass 267.1128, difference 0.4 mDa; δ **1H NMR** (400 MHz, d_6 -DMSO): δ 11.53 (bs, 1H, H-N), 10.15 (bs, 1H, H-O), 8.21 (d, 1H, $J_{H-H} = 7.4$ Hz, 9), 7.78 (2H, d, $J_{H-H} = 8.7$ Hz, H- 8 or H-9), 7.62 (2H, d, $J_{H-H} = 7.4$ Hz, H-2 or H-3), 7.30-7.41 (m, 3H, H-1, H-2 or H-3), 6.98-7.09 (m, 2H, H-4,5), 6.85 (d, 2H, $J_{H-H} = 8.7$ Hz, H-8 or H-9); δ **^{13}C NMR** (100.6 MHz, d_6 -DMSO): δ 160.7 (4°), 148.7 (CH), 138.4 (CH), 136.0 (4°), 129.7 (CH), 128.8 (CH), 128.7 (CH), 127.0 (CH), 125.8 (CH), 123.8 (4°), 115.0 (CH); **Significant IR bands** (KBr disc, cm^{-1}): (ν NH) 3270 m , (ν C=O, C=N) 1621 s .

HCA9

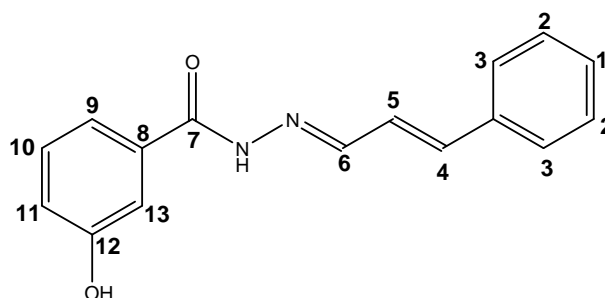


3-Fluoro-benzoic acid (3-phenyl-allylidene)-hydrazide

HCA9 was synthesized using cinnamaldehyde 0.2 g (1.53 mmol) and 3-fluoro-benzoyl hydrazide 0.19 g (1.26 mmol) to give HCA9, 0.27 g (1.00 mmol, 80%); **Melting point:** 207– 209 °C; **ESI-MS:** positive ion $m/z = 269.1084$, 100%; **HR ESI-MS:** For $C_{16}H_{14}N_2OF$ ($[M+H]^+$), observed mass 269.1092, calculated mass 269.1085, difference 0.8 mDa; δ **1H NMR** (400 MHz, d_6 -DMSO): 11.80 (1H, bs, H-

N), 7.31 – 7.77 (m, 9H, H_{ar}) 7.07 - 7.08 (2H, m, H-4, 5); δ ^{13}C NMR (100.6 MHz, d_6 -DMSO): 161.9 (d, $^1j_{\text{C-F}} = 243.4$ Hz, C-13), 161.7 (4°), 150.3 (CH), 139.4 (CH), 135.9 (4°), 135.8 (d, $^3j_{\text{C-F}} = 6.9$ Hz, C-8), 130.7 (d, $^3j_{\text{C-F}} = 5.5$ Hz, C-10), 128.9 (CH), 128.8 (CH), 127.2 (CH), 125.4 (CH), 123.8 (d, $^4j_{\text{C-F}} = 3.1$ Hz, C-9), 118.6 (d, $^2j_{\text{C-F}} = 20.7$ Hz, C-14), 114.4 (d, $^2j_{\text{C-F}} = 22.9$ Hz, C-13); **Anal. Calcd.** for $\text{C}_{16}\text{H}_{13}\text{N}_2\text{O}_2$: C, 71.63; H, 4.89; N, 10.44. Found C, 71.63; H, 4.91; N, 10.48; **Significant IR bands** (KBr disc, cm^{-1}): (ν NH) 3234m, (ν C=O) 1650s, (ν C=N) 1627s.

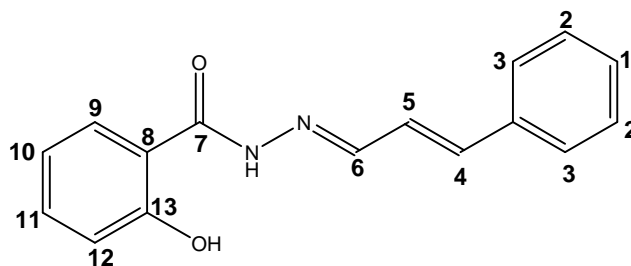
HCA10



3-Hydroxy-benzoic acid (3-phenyl-allylidene)-hydrazide

HCA10 was synthesised using cinnamaldehyde 0.24 g (1.84 mmol) and 3-hydroxy-benzoyl hydrazide 0.20 g (1.31 mmol) to give HCA10, 0.28 g (1.05 mmol, 80%); **Melting point:** 255 - 257 $^\circ\text{C}$; **ESI-MS:** positive ion $m/z = 267.1121$, 100%, HR **ESI-MS:** For $\text{C}_{16}\text{H}_{15}\text{N}_2\text{O}_2$ ($[\text{M}+\text{H}]^+$), observed mass 267.1121, calculated mass 267.1128, difference 0.7 mDa; δ ^1H NMR (400 MHz, d_6 -DMSO): δ 11.67 (bs, 1H, H-N), 9.77 (bs, 1H, H-O), 8.22 (d, 1H, $J_{\text{H-H}} = 7.4$ Hz, H-6), 7.63 (d, 2H, $J_{\text{H-H}} = 7.3$ Hz, H_{ar}), 7.26 – 7.42 (m, 6H, H_{ar}), 7.04 – 7.06 (2H, m, H-4, 5), 6.96 (1H, m, H_{ar}); δ ^{13}C NMR (100.6 MHz, d_6 -DMSO): δ 163.0 (4°), 157.4 (4°), 149.6 (CH), 138.9 (CH), 135.9 (4°), 134.8 (4°), 129.5 (CH), 128.8 (CH), 127.1 (CH), 125.7 (CH), 118.7 (CH), 118.1 (CH), 114.5 (CH); **Significant IR bands** (KBr disc, cm^{-1}): (ν NH) 3240m, (ν C=O) 1638s, (ν C=N) 1624s.

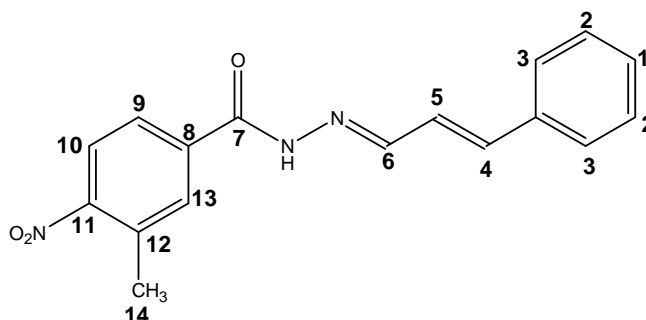
HCA11



2-Hydroxy-benzoic acid (3-phenyl-allylidene)-hydrazide

HCA11 was synthesised using cinnamaldehyde 0.24 g (1.84 mmol) and 2-hydroxy-benzoyl hydrazide 0.20 g (1.31 mmol) to give HCA11, 0.30 g (1.13 mmol, 87%); **Melting point:** 259 - 261 °C; **ESI-MS:** positive ion $m/z = 267.1122$, 100%, **HR ESI-MS:** For $C_{16}H_{15}N_2O_2$ ($[M+H]^+$), observed mass 267.1122, calculated mass 267.1128, difference 0.6 mDa; **δ 1H NMR** (400 MHz, d_6 -DMSO): δ 11.78 (bs, 1H, H-N), 8.24 (1H, dd, $J_{H-H} = 5.0$ Hz, 3.6 Hz, H-6), 7.87 (1H, dd, $^3J_{H-H} = 7.7$, 1.3 Hz, H_{ar}), 7.63 (2H, d, $^3J_{H-H} = 7.4$ Hz, H_{ar}), 7.32 - 7.45 (m, 4H, m, H_{ar}), 7.08 - 7.09 (2H, m, H-4, 5), 6.92 - 6.98 (2H, m, H_{ar}); **δ ^{13}C NMR** (100.6 MHz, d_6 -DMSO): δ 164.7 (4°), 159.2 (4°), 150.7 (CH), 139.7 (CH), 135.8 (4°), 133.8 (CH), 129.0 (CH), 128.9 (CH), 128.5 (CH), 127.2 (CH), 125.4 (CH), 118.9 (CH), 117.3 (CH), 115.8 (4°); **Significant IR bands** (KBr disc, cm^{-1}): (ν OH) 3457 *br*, (ν NH) 3258 *m*, (ν C=O) 1649 *s*, (ν C=N) 1626 *s*.

HCA12

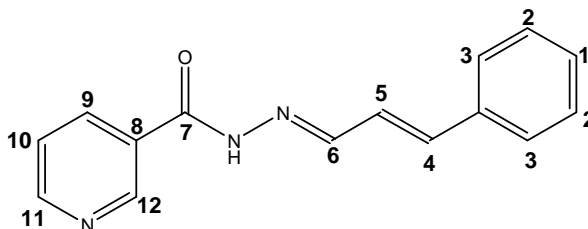


3-Methyl-4-nitro-benzoic acid (3-phenyl-allylidene)-hydrazide

HCA12 was synthesised using cinnamaldehyde 0.19 g (1.43 mmol) and 3-methyl-4-nitro-benzoyl hydrazide 0.20 g (1.03 mmol) to give HCA12, 0.26 g (0.83 mmol, 81%); **Melting point:** 184-186 °C; **ESI-MS:** positive ion $m/z = 310.1184$

100%, HR ESI-MS: For $C_{17}H_{16}N_3O_3$ ($[M+H]^+$), observed mass 310.1184, calculated mass 310.1186, difference 0.2 mDa; δ 1H NMR (400 MHz, d_6 -DMSO): δ 11.93 (bs, 1H, H-N), 8.24 (dd, 1H, $J_{H-H} = 5.0, 3.8$ Hz, H-6), 8.10 (d, 1H, $J_{H-H} = 8.4$ Hz, H-9 or H-10), 8.00 (s, 1H, H-13), 7.92 (1H, dd, $J_{H-H} = 8.4, 1.5$ Hz, H-9 or H-10), 7.64 (2H, d, $J_{H-H} = 7.3$ Hz, H-2 or H-3), 7.32-7.41 (m, 3H, H-1, H-2 or H-3), 7.08 – 7.10 (2H, m, H-4, 5), 2.58 (3H, s, H-14); δ ^{13}C NMR (100.6 MHz, d_6 -DMSO): δ 161.4 (4°), 150.6 (CH), 150.5 (4°), 139.7 (C7), 137.3 (4°), 135.8 (4°), 132.8 (4°), 132.0 (CH), 129.0 (CH), 128.8 (CH), 127.2 (CH), 126.4 (CH), 125.4 (CH), 124.5 (CH), 19.3 (CH₃); **Anal. Calcd** for $C_{17}H_{15}N_3O_3$: C, 66.01; H, 4.89; N, 13.58. Found C, 65.88; H, 4.90; N, 13.50; **Significant IR bands** (KBr disc, cm^{-1}): (ν NH) 3234m, (ν C=O) 1655s, (ν C=N) 1625s, (ν_{asym} (N=O)₂) 1518s, (ν_{sym} (N=O)₂) 1348s.

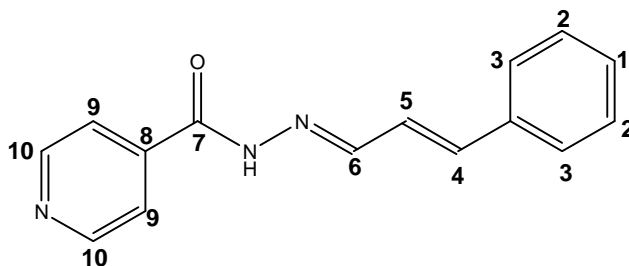
HCA13



Nicotinic acid (3-phenyl-allylidene)-hydrazide

HCA13 was synthesised using cinnamaldehyde 0.24 g (1.83 mmol) and nicotinic acid hydrazide 0.18 g (1.31 mmol) to give HCA13, 0.24 g (0.96 mmol, 73%), **Melting point**: 176-177 °C; **ESI-MS**: positive ion $m/z = 252.1128$, 100%, HR **ESI-MS**: For $C_{15}H_{14}N_3O$ ($[M+H]^+$), observed mass 252.1128, calculated mass 252.1131, difference 0.3 mDa; δ 1H NMR (400 MHz, d_6 -DMSO): δ 11.91 (bs, 1H, H-N), 9.05 (d, 1H, $J_{H-H} = 1.7$ Hz, H-12), 8.76 (dd, 1H, $J_{H-H} = 4.8$ Hz, 1.5 Hz, H-6), 8.21-8.25 (m, 2H, H_{ar}), 7.64 (d, 2H, $J_{H-H} = 7.3$ Hz, H_{ar}), 7.57 (dd, 1H, $J_{H-H} = 7.7$ Hz, 4.8 Hz, H_{ar}), 7.32-7.42 (m, 3H, H_{ar}), 7.08-7.10 (2H, m, H-4, 5); δ ^{13}C NMR (100.6 MHz, d_6 -DMSO): δ 161.5 (4°), 152.3 (CH), 150.4 (CH), 148.6 (CH), 139.6 (CH), 135.8 (4°), 135.5 (CH), 129.2 (4°), 129.0 (CH), 128.9 (CH), 127.2 (CH), 125.5 (CH), 123.6 (CH); **Significant IR bands** (KBr disc, cm^{-1}): (ν NH) 3242m, (ν C=O) 1646s, (ν C=N) 1625s.

HCA14



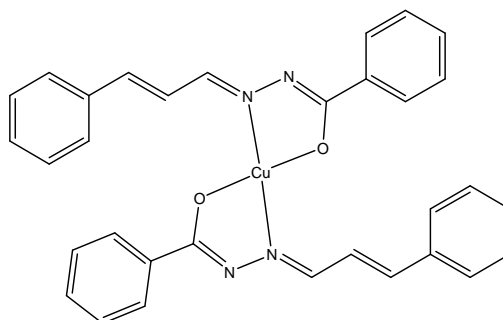
Isonicotinic acid (3-phenyl-allylidene)-hydrazide

HCA14 was synthesised using cinnamaldehyde 0.24 g (1.84 mmol) and isonicotinic acid hydrazide 0.18 g (1.31 mmol) to give HCA14, 0.23 g (0.90 mmol, 69%); **Melting point:** 201-203 °C; **ESI-MS:** positive ion $m/z = 252.1134$, 100%, HR ESI-MS: For $C_{15}H_{14}N_3O$ ($[M+H]^+$), observed mass 252.1134, calculated mass 252.1131, difference 0.2 mDa; δ **1H NMR** (400 MHz, d_6 -DMSO): 11.96 (bs, 1H, H-N), 8.78 (d, 2H, $J_{H-H} = 6.2$ Hz, H-9 or H-10), 8.24 (1H, dd, $J_{H-H} = 1.6$ Hz, 4.4 Hz, H-6), 7.81 (d, 2H, $J_{H-H} = 6.2$ Hz, H-9 or H-10), 7.64 (2H, d, $J_{H-H} = 7.2$ Hz, H-2 or H-3), 7.40 (2H, t, $^3J_{H-H} = 7.2$ Hz H-2, 4), 7.32 - 7.42 (m, 3H, H-1, H-2 or H-3), 7.09 - 7.10 (2H, m, H-4, 5); δ **^{13}C NMR** (100 MHz, d_6 -DMSO): 161.5 (4°), 151.0 (CH), 150.3 (CH), 140.5 (4°), 139.9 (CH), 135.8 (4°), 129.0 (CH), 128.9 (CH), 127.2 (CH), 125.4 (CH), 121.5 (CH); **Significant IR bands** (KBr disc, cm^{-1}): (ν NH) 3244m, (ν C=O) 1650s, (ν C=N) 1626s.

7.11 General synthetic procedure and characterisation detail copper(II) complexes of CAHs ([Cu(II)(CA1)₂]- [Cu(II)(CA1)₂])

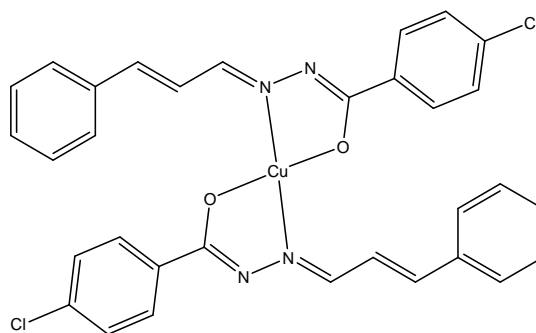
Copper(II) acetate (0.30 mmol) was added to a methanolic solution of the respective cinnamaldehyde hydrazone. The mixture was refluxed for 2 hours and the green precipitate formed was isolated and dried under *vacuo*.

[Cu(II)(CA1)₂]



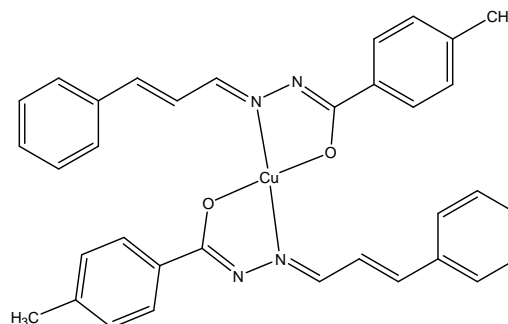
Bis[benzoic acid (3-phenyl-allylidene)-hydrazone]copper(II)

[Cu(II)(CA1)₂] was synthesised using copper acetate 0.06 g (0.31 mmol) and HCA1 0.10 g (0.38 mmol) to give [Cu(II)(CA1)₂], (1.23 mmol, 85%); **Melting point:** 343-345 °C; **ESI-MS:** positive ion $m/z = 563.1513$, 65%, HR ESI-MS: For ⁶³Cu(I)C₃₂H₂₈N₄O₂ ([M+2H]⁺), observed mass 563.1513, calculated mass 563.1503, difference 1.1 mDa; **Anal. Calcd.** for C₃₂H₂₆N₄O₂Cu: C, 68.13; H, 4.98; N, 9.93. Found C, 68.03; H, 4.65; N, 9.95; **Significant IR bands** (KBr disc, cm⁻¹): (ν C=O) 1612s, (ν C=N) 1589s.

[Cu(II)(CA2)₂]

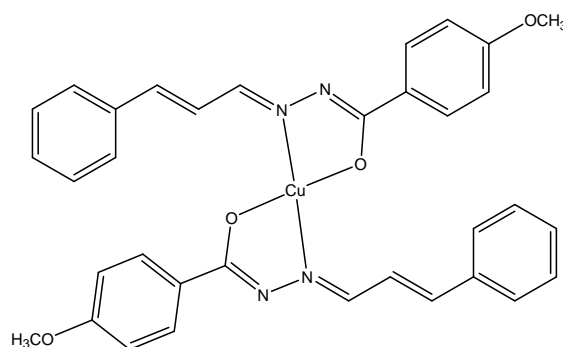
Bis[4-chloro-benzoic acid (3-phenyl-allylidene)-hydrazide]copper(II)

[Cu(II)(CA2)₂] was synthesised using copper(II) acetate 0.06 g (0.31 mmol) and HCA2 0.10 g (0.38 mmol) to give [Cu(II)(CA2)₂], 0.10 g (0.32 mmol, 84%); **Melting point:** 263-264 °C; **ESI-MS:** negative ion m/z = 628.0560, HR ESI-MS: For ⁶³Cu(I)C₃₂H₂₄N₄O₂Cl₂ ([M]⁻), observed mass 628.0560, calculated mass 629.0572, difference 1.0 mDa; **Anal. Calcd** for C₃₂H₂₆N₄O₂Cl₂Cu₁x 0.25 CH₃OH x 0.55 H₂O: C, 59.51; H, 4.35; N, 8.61. Found C, 59.45; H, 4.46; N, 8.73; **Significant IR Bands** (KBr disc, cm⁻¹): (ν C=O) 1616s, (ν C=N) 1593s.

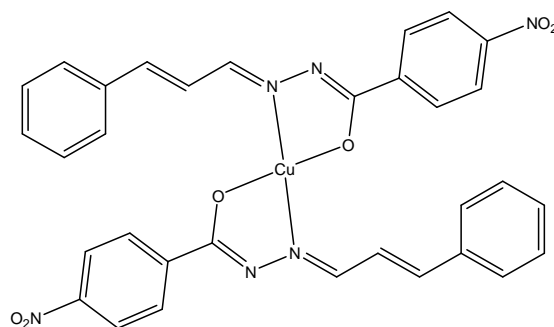
[Cu(II)(CA3)₂]

Bis[4-methyl-benzoic acid (3-phenyl-allylidene)-hydrazide]copper(II)

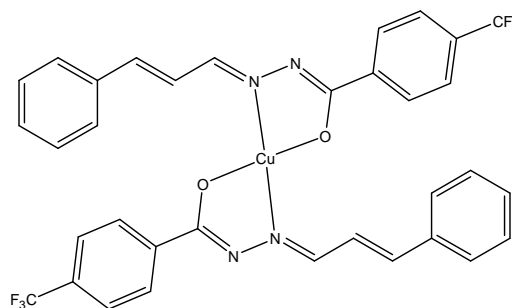
[Cu(II)(CA3)₂] was synthesised using copper(II) acetate 0.06 g (0.31 mmol) and HCA3 0.10 g (0.38 mmol) to give [Cu(II)(CA3)₂], (0.32 mmol, 84%); **Melting point:** 257-259 °C; **ESI-MS:** positive ion m/z = 591.1808, 40% HR ESI-MS: For ⁶³Cu(I)C₃₄H₃₂N₄O₂ ([M+2H]⁺), observed mass 591.1808, calculated mass 591.1816, difference 0.8 mDa; **Anal. Calcd** for C₃₄H₃₀N₄O₂Cu₁x 0.3 H₂O: C, 68.57; H, 5.18; N, 9.41. Found C, 68.57; H, 5.11; N, 9.33; **Significant IR bands:** (KBr disc, cm⁻¹): (ν C=O) 1611s, (ν C=N) 1587s.

[Cu(II)(CA4)₂]**Bis[4-methoxy-benzoic acid (3-phenyl-allylidene)-hydrazide]copper(II)**

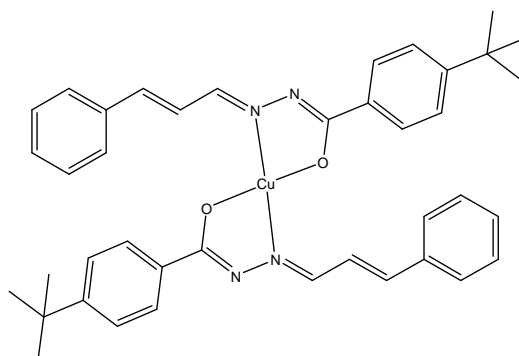
[Cu(II)(CA4)₂] was synthesised using copper(II) acetate (0.3 mmol) and HCA4 0.35 g (1.25 mmol) to give [Cu(II)(CA4)₂], 0.23 g (1.23 mmol, 70%); **Melting point:** 255-257 °C; **ESI-MS:** positive ion $m/z = 623.1715$, 100%; HR ESI-MS: For ⁶³Cu(I)C₃₄H₃₂N₄O₄ ([M+2H]⁺), observed mass 623.1715, calculated mass 623.1719, difference 0.5 mDa; **Significant IR bands:** (KBr disc, cm⁻¹): (ν C=O) 1610s, (ν C=N) 1590s.

[Cu(II)(CA5)₂]**Bis[4-nitro-benzoic acid (3-phenyl-allylidene)-hydrazide]copper(II)**

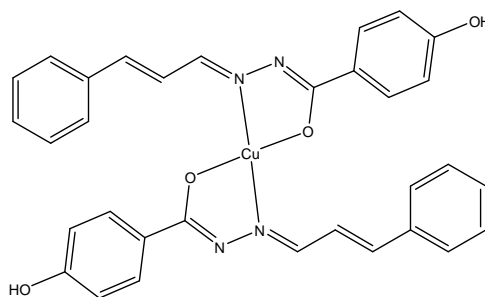
[Cu(II)(CA5)₂] was synthesised using copper(II) acetate 0.06 g (0.31 mmol) and HCA5 0.11 g (0.37 mmol) to give [Cu(II)(CA5)₂], 0.09 g (0.28 mmol, 76%); **Melting point:** 275 - 277 °C; **ESI-MS:** negative ion $m/z = 651.108$, 100%; HR ESI-MS: For ⁶³Cu(I)C₃₂H₂₄N₆O₆ ([M]⁻), observed mass 651.1081, calculated mass 651.1059, difference 2.2 mD; **Anal. Calcd.** for C₃₂H₂₄N₆O₆Cu x 1.5 H₂O: C, 56.59; H, 4.01; N, 12.37. Found C, 56.12; H, 3.62; N, 12.85; **Significant IR bands:** (KBr disc, cm⁻¹): (ν C=O) 1607s, ν (C=N) 1582s, (ν_{asym} (N=O)₂) 1534s, (ν_{sym} (N=O)₂) 1348br.

[Cu(II)(CA6)₂]**Bis[4-trifluoromethyl-benzoic acid (3-phenyl-allylidene)-hydrazide]copper(II)**

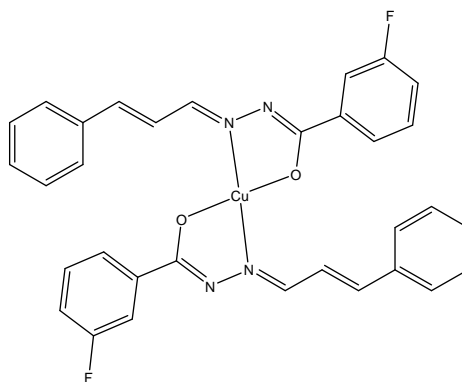
[Cu(II)(CA6)₂] was synthesised using copper(II) acetate 0.045 g (0.25 mmol) and HCA6 0.10 g (0.31 mmol) to give [Cu(II)(CA6)₂], 0.095 g (0.27 mmol, 87%); **Melting point:** 258-260 °C; **ESI-MS:** positive ion m/z = 699.1241, 10%, HR ESI-MS: For ⁶³Cu(I)C₃₄H₂₆N₄O₂F₆ ([M+2H]⁺), observed mass 699.1241, calculated mass 699.1250, difference 0.9 mDa; **Anal. Calcd** for C₃₄H₂₄N₄O₂F₆Cu₁ x 0.4 H₂O: C, 57.90; H, 3.54; N, 7.94. Found C, 57.81; H, 3.46; N, 8.02; **Significant IR bands** (KBr disc, cm⁻¹): (ν C=O) 1610s, (ν C=N) 1590s. [Cu(II)(CA7)₂]

**Bis[4-*tert*-butyl-benzoic acid (3-phenyl-allylidene)-hydrazide]copper(II)**

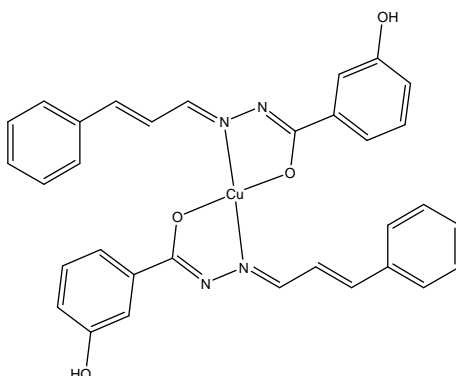
[Cu(II)(CA7)₂] was synthesised using copper(II) acetate 0.05 g (0.27 mmol) and HCA7 0.10 g (0.32 mmol) to give [Cu(II)(CA7)₂], 0.09 g (0.26 mmol, 81%); **Melting point:** 254-256 °C; **ESI-MS:** positive ion m/z = 675.2753, 7%, HR ESI-MS: For ⁶³Cu(I)C₄₀H₄₄N₄O₂ ([M+2H]⁺), observed mass 675.2753, calculated mass 675.2755, difference 0.2 mDa; **Anal. Calcd.** for C₄₀H₄₂N₄O₂Cu₁: C, 71.24; H, 6.28; N, 8.31. Found C, 71.03; H, 6.28; N, 8.24; **Significant IR bands** (KBr disc, cm⁻¹): (ν C=O) 1612s, (ν C=N) 1584s.

[Cu(II)(CA8)₂]**Bis[4-hydroxy-benzoic acid (3-phenyl-allylidene)-hydrazide]copper(II)**

[Cu(II)(CA8)₂] was synthesised using copper(II) acetate 0.057 g (0.31 mmol) and HCA8 0.10 g (0.37 mmol) to give [Cu(II)(CA8)₂], 0.077 g (0.26 mmol, 70%); **Melting point:** 256 - 258 °C; **ESI-MS:** positive ion m/z = 595.1401, 53%, HR ESI-MS: For ⁶³Cu(I)C₃₂H₂₈N₄O₄ ([M+2H]⁺), observed mass 595.1408, calculated mass 595.1401, difference 0.7 mDa; **Significant IR bands** (KBr disc, cm⁻¹): (ν C=O) 1610s, (ν C=N) 1595s.

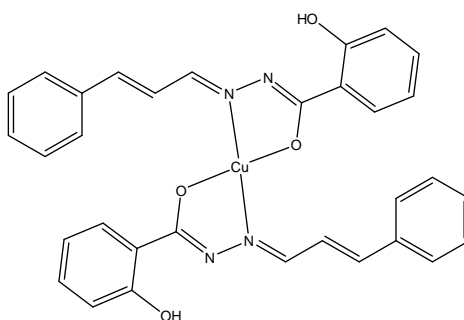
[Cu(II)(CA9)₂]**Bis[3-fluoro-benzoic acid (3-phenyl-allylidene)-hydrazide]copper(II)**

[Cu(II)(CA9)₂] was synthesised using copper(II) acetate 0.04 g (0.23 mmol) and HCA9 0.075 g (0.28 mmol) to give [Cu(II)(CA9)₂], 0.07 g (0.23 mmol, 84%); **Melting point:** 248-250 °C; **ESI-MS:** positive ion m/z = 599.1333, 30%, HR ESI-MS: For ⁶³Cu(I)C₃₂H₂₈N₄O₂ ([M+2H]⁺), observed mass 599.1333, calculated mass 599.1314, difference 1.9 mDa; **Significant IR bands** (KBr disc, cm⁻¹): (ν C=O) 1609s, (ν C=N) 1583s.

[Cu(II)(CA10)₂]

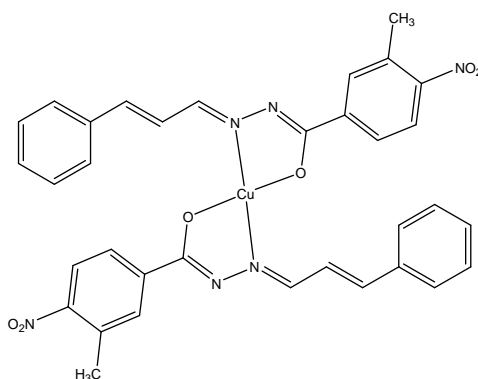
Bis[3-hydroxy-benzoic acid (3-phenyl-allylidene)-hydrazide]copper(II)

[Cu(II)(CA10)₂] was synthesised using copper(II) acetate 0.057 g (0.31 mmol) and HCA10 0.10 g (0.37 mmol) to give [Cu(II)(CA10)₂], 0.066 g (0.22 mmol, 60%); **Melting point:** 254-256 °C; **ESI-MS:** positive ion m/z = 595.1399, 100%, HR ESI-MS: For ⁶³Cu(I)C₃₂H₂₈N₄O₄ ([M+2H]⁺), observed mass 595.1399, calculated mass 595.1401, difference 0.2 mDa; **Anal. Calcd** for C₃₂H₂₆N₄O₄Cu₁ x 0.25 CH₃OH x 0.4 H₂O: C, 63.76; H, 4.58; N, 9.22. Found C, 63.74; H, 4.48; N, 9.12; **Significant IR bands** (KBr disc, cm⁻¹): (ν C=O) 1613s, (ν C=N) 1578s.

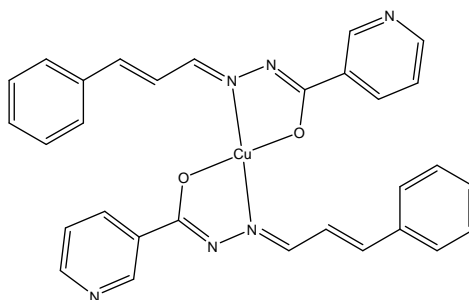
[Cu(II)(CA11)₂]

Bis[2-hydroxy-benzoic acid (3-phenyl-allylidene)-hydrazide]copper(II)

[Cu(II)(CA11)₂] was synthesised using copper(II) acetate 0.057 g (0.31 mmol) and HCA11 0.11 g (0.37 mmol) to give [Cu(II)(CA11)₂], 0.08 g (0.27 mmol, 73 %); **Melting point:** 279-281 °C; **ESI:** negative ion m/z = 593.1272, 100 % HR **ESI-MS:** For ⁶³Cu(I)C₃₂H₂₆N₄O₄ ([M]⁻), observed mass 593.1272, calculated mass 593.1256, difference 1.7 mDa; **Significant IR bands** (KBr disc, cm⁻¹): (ν C=O) 1617s, (ν C=N) 1593s.

[Cu(II)(CA12)₂]**Bis[3-methyl-4-nitro-benzoic acid (3-phenyl-allylidene)-hydrazide]copper(II)**

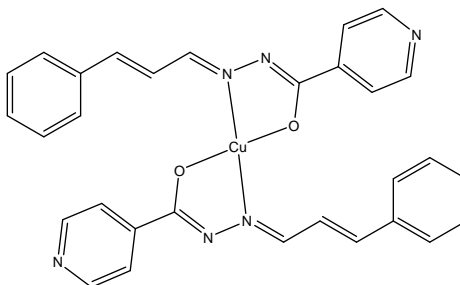
[Cu(II)(CA12)₂] was synthesised using copper(II) acetate 0.057 g (0.31 mmol) and HCA12 0.11 g (0.37 mmol) to give [Cu(II)(CA12)₂], 0.10 g (0.30 mmol, 82%); **Melting point:** 273-275°C; **ESI-MS:** negative ion m/z = 679.1402, 100%, HR ESI-MS: For ⁶³Cu(I)C₃₄H₂₈N₆O₆ ([M]⁻), observed mass 679.1402, calculated mass 679.1372, difference 3.0 mDa; **Anal. Calcd** for C₃₄H₂₈N₆O₆Cu₁ x 0.15 CH₃OH x 0.25 H₂O: C, 59.49; H, 4.25; N, 12.19. Found C, 59.48; H, 4.15; N, 12.35; Significant **IR bands** (KBr disc, cm⁻¹): (ν C=O) 1608s, (ν C=N) 1580s, (ν asym (N=O)₂) 1536br, (ν sym (N=O)₂) 1343br.

[Cu(II)(CA13)₂]**Bis[nicotinic acid (3-phenyl-allylidene)-hydrazide]copper(II)**

[Cu(II)(CA13)₂] was synthesised using copper(II) acetate 0.04 g (0.24 mmol) and HCA13 0.10 g (0.40 mmol) to give [Cu(II)(CA13)₂], 0.09 g (0.32 mmol, 79%); **Melting point:** 252-254 °C; **ESI-MS:** negative ion m/z = 563.1401, 81%, HR ESI-MS: For ⁶³Cu(I)C₃₀H₂₄N₆O₂ ([M]⁻), observed mass 563.1401, calculated mass 563.1413, difference 1.1 mDa; **Anal. Calcd.** for C₃₀H₂₄N₆O₂Cu x 0.6 CH₃OH: C,

63.01; H, 4.63; N, 14.41. Found C, 62.82; H, 4.56; N, 14.34; **Significant IR bands** (KBr disc, cm^{-1}): (ν C=O) 1621s, (ν C=N) 1592s.

[Cu(II)(CA14)₂]



Bis[isonicotinic acid (3-phenyl-allylidene)-hydrazide]copper(II)

[Cu(II)(CA14)₂] was synthesised using copper(II) acetate 0.04 g (0.24 mmol) and HCA14 0.10 g (0.40 mmol) to give [Cu(II)(CA14)₂], 0.09 g (0.31 mmol, 78 %); **Melting point:** 248-250 °C; **ESI-MS:** positive ion $m/z = 565.1399$, 37% HR ESI-MS: For $^{63}\text{CuC}_{30}\text{H}_{24}\text{N}_6\text{O}_2$ ($[\text{M}+\text{H}]^+$), observed mass 565.1399, calculated mass 565.1413, difference 1.3 mDa; **Significant IR bands** (KBr disc, cm^{-1}): (ν C=O) 1621s, (ν C=N) 1582s.

7.12. Single crystal X-ray data (Crystal data and structure refinement);

All other crystallographic data can be found in appendices 3-22

NaHL9.2H₂O

Empirical formula	C ₁₁ H ₁₅ N ₂ Na O ₅	
Formula weight	278.24	
Temperature	110(2) K	
Wavelength	0.71073 Å	
Crystal system	Rhombohedral	
Space group	R-3	
Unit cell dimensions	a = 30.7555(9) Å	α = 90°
	b = 30.7555(9) Å	β = 90°
	c = 7.3013(4) Å	γ = 120°
Volume	5981.0(4) Å ³	
Z	18	
Density (calculated)	1.390 Mg/m ³	
Absorption coefficient	0.136 mm ⁻¹	
F(000)	2628	
Theta range for data collection	1.32 to 28.30°	
Index ranges	-40 ≤ h ≤ 40, -40 ≤ k ≤ 40, -9 ≤ l ≤ 9	
Reflections collected	20886	
Independent reflections	3303 [R(int) = 0.0331]	
Completeness to theta = 28.30°	99.9 %	
Absorption correction	Semi-empirical from equivalents	
Max. and min. transmission	0.987 and 0.836	
Refinement method	Full-matrix least-squares on F ²	
Data / restraints / parameters	3303 / 0 / 194	
Goodness-of-fit on F ²	1.091	
Final R indices [I > 2σ(I)]	R1 = 0.0386, wR2 = 0.1026	
R indices (all data)	R1 = 0.0513, wR2 = 0.1192	
Largest diff. peak and hole	0.470 and -0.282 e.Å ⁻³	

NaHL11.2H₂O

Empirical formula	C ₁₀ H ₉ BrN ₂ NaO ₃
Formula weight	308.09
Temperature/K	566(2)
Crystal system	trigonal
Space group	R-3
a/Å	30.9014(4)
b/Å	30.9014(4)
c/Å	7.2710(2)
α/°	90.00
β/°	90.00
γ/°	120.00
Volume/Å ³	6012.9(2)
Z	23
ρ _{calc} /mg/mm ³	1.957
m/mm ⁻¹	5.777
F(000)	3519
2θ range for data collection	9.92 to 141.74°
Index ranges	-35 ≤ h ≤ 37, -32 ≤ k ≤ 37, -8 ≤ l ≤ 8
Reflections collected	10998
Independent reflections	2420[R(int) = 0.0305]
Data/restraints/parameters	2420/0/195
Goodness-of-fit on F ²	1.053
Final R indexes [I >= 2σ (I)]	R ₁ = 0.0243, wR ₂ = 0.0592
Final R indexes [all data]	R ₁ = 0.0307, wR ₂ = 0.0625
Largest diff. peak/hole / e Å ⁻³	0.313/-0.361

NaHL20.H₂O

Empirical formula	C ₁₀ H ₉ BrN ₂ NaO ₃
Formula weight	308.09
Temperature/K	566(2)
Crystal system	trigonal
Space group	R-3
a/Å	30.9014(4)
b/Å	30.9014(4)
c/Å	7.2710(2)
α/°	90.00
β/°	90.00
γ/°	120.00
Volume/Å ³	6012.9(2)
Z	23
ρ _{calc} /mg/mm ³	1.957
m/mm ⁻¹	5.777
F(000)	3519
2θ range for data collection	9.92 to 141.74°
Index ranges	-35 ≤ h ≤ 37, -32 ≤ k ≤ 37, -8 ≤ l ≤ 8
Reflections collected	10998
Independent reflections	2420[R(int) = 0.0305]
Data/restraints/parameters	2420/0/195
Goodness-of-fit on F ²	1.053
Final R indexes [I ≥ 2σ (I)]	R ₁ = 0.0243, wR ₂ = 0.0592
Final R indexes [all data]	R ₁ = 0.0307, wR ₂ = 0.0625
Largest diff. peak/hole / e Å ⁻³	0.313/-0.361

[Cu(L7)(H₂O)(MeOH)]

Empirical formula	C ₁₃ H ₁₇ CuN ₃ O ₇
Formula weight	390.84
Temperature □/□K	110.0
Crystal system	monoclinic
Space group	P2 ₁ /n
a/Å, b/Å, c/Å	10.159(3), 14.1559(7), 11.895(2)
α/°, β/°, γ/°	90.00, 114.11(3), 90.00
Volume □/□Å ³	1561.3(5)
Z	4
ρ _{calc} /mg mm ⁻³	1.663
μ/mm ⁻¹	1.441
F(000)	804
Crystal size □/□mm ³	0.1963 × 0.0833 × 0.042
2θ range for data collection	5.76 to 64.22°
Index ranges	-15 ≤ h ≤ 15, -21 ≤ k ≤ 20, -16 ≤ l ≤ 17
Reflections collected	13154
Independent reflections	4881 [R(int) = 0.0235]
Data/restraints/parameters	4881/0/229
Goodness-of-fit on F ²	1.058
Final R indexes [I > 2σ (I)]	R ₁ = 0.0300, wR ₂ = 0.0682
Final R indexes [all data]	R ₁ = 0.0377, wR ₂ = 0.0723
Largest diff. peak/hole/e Å ⁻³	0.466/-0.397

[Cu(L8)(MeOH)₂]

Empirical formula	C ₁₂ H ₁₅ Cu N ₃ O ₇
Formula weight	376.81
Temperature	110(2) K
Wavelength	0.71073 Å
Crystal system	Monoclinic
Space group	P2(1)/n
Unit cell dimensions	a = 7.8471(4) Å α = 90° b = 17.0584(8) Å β = 93.9220(10)° c = 11.0122(5) Å γ = 90°
Volume	1470.63(12) Å ³
Z	4
Density (calculated)	1.702 Mg/m ³
Absorption coefficient	1.527 mm ⁻¹
F(000)	772
Theta range for data collection	2.20 to 28.30°
Index ranges	-10 ≤ h ≤ 10, -22 ≤ k ≤ 22, -14 ≤ l ≤ 14
Reflections collected	15054
Independent reflections	3660 [R(int) = 0.0178]
Completeness to theta = 28.30°	99.9 %
Absorption correction	Semi-empirical from equivalents
Max. and min. transmission	0.941 and 0.823
Refinement method	Full-matrix least-squares on F ²
Data / restraints / parameters	3660 / 0 / 219
Goodness-of-fit on F ²	1.072
Final R indices [I > 2σ(I)]	R1 = 0.0255, wR2 = 0.0695
R indices (all data)	R1 = 0.0276, wR2 = 0.0709
Largest diff. peak and hole	0.454 and -0.338 e.Å ⁻³

[Cu(L9)(H₂O)₂]

Empirical formula	C ₁₁ H ₁₄ Cu N ₂ O ₅
Formula weight	317.78
Temperature	110(2) K
Wavelength	0.71073 Å
Crystal system	Triclinic
Space group	P-1
Unit cell dimensions	a = 7.3879(9) Å α = 93.602(2)° b = 11.4695(13) Å β = 102.437(2)° c = 15.3898(18) Å γ = 103.124(2)°
Volume	1231.6(3) Å ³
Z	4
Density (calculated)	1.714 Mg/m ³
Absorption coefficient	1.792 mm ⁻¹
F(000)	652
Theta range for data collection	1.84 to 28.33°
Index ranges	-9 ≤ h ≤ 9, -15 ≤ k ≤ 15, -20 ≤ l ≤ 19
Reflections collected	10913
Independent reflections	5970 [R(int) = 0.0181]
Completeness to theta = 28.33°	97.2 %
Absorption correction	Semi-empirical from equivalents
Max. and min. transmission	0.882 and 0.619
Refinement method	Full-matrix least-squares on F ²
Data / restraints / parameters	5970 / 2 / 371
Goodness-of-fit on F ²	1.047
Final R indices [I > 2σ(I)]	R1 = 0.0379, wR2 = 0.0982
R indices (all data)	R1 = 0.0471, wR2 = 0.1048
Largest diff. peak and hole	0.982 and -0.728 e.Å ⁻³

[Cu(HL9)₂Cl₂]

Empirical formula	C ₂₂ H ₂₂ Cl ₂ Cu ₂ N ₄ O ₆	
Formula weight	636.42	
Temperature	110(2) K	
Wavelength	0.71073 Å	
Crystal system	Monoclinic	
Space group	P2(1)/n	
Unit cell dimensions	a = 8.3637(8) Å	α = 90°
	b = 15.0338(15) Å	β = 94.701(2)°
	c = 9.4535(9) Å	γ = 90°
Volume	1184.7(2) Å ³	
Z	2	
Density (calculated)	1.784 Mg/m ³	
Absorption coefficient	2.069 mm ⁻¹	
F(000)	644	
Theta range for data collection	2.55 to 28.27°	
Index ranges	-11 ≤ h ≤ 11, -20 ≤ k ≤ 20, -12 ≤ l ≤ 12	
Reflections collected	12070	
Independent reflections	2927 [R(int) = 0.0257]	
Completeness to theta = 28.27°	99.7 %	
Absorption correction	Semi-empirical from equivalents	
Max. and min. transmission	0.940 and 0.857	
Refinement method	Full-matrix least-squares on F ²	
Data / restraints / parameters	2927 / 0 / 168	
Goodness-of-fit on F ²	1.058	
Final R indices [I > 2σ(I)]	R1 = 0.0277, wR2 = 0.0697	
R indices (all data)	R1 = 0.0352, wR2 = 0.0732	
Largest diff. peak and hole	0.482 and -0.239 e.Å ⁻³	

[Cu(L11)(H₂O)₂].H₂O

Empirical formula	C ₂₀ H ₂₄ Br ₂ Cu ₂ N ₄ O ₁₁	
Formula weight	783.33	
Temperature	110(2) K	
Wavelength	0.71073 Å	
Crystal system	Triclinic	
Space group	P-1	
Unit cell dimensions	a = 7.3908(6) Å	α = 82.329(2)°
	b = 11.0776(8) Å	β = 84.287(2)°
	c = 16.9653(13) Å	γ = 75.676(2)°
Volume	1330.56(18) Å ³	
Z	2	
Density (calculated)	1.955 Mg/m ³	
Absorption coefficient	4.666 mm ⁻¹	
F(000)	776	
Theta range for data collection	1.91 to 28.28°	
Index ranges	-9 ≤ h ≤ 9, -14 ≤ k ≤ 14, -22 ≤ l ≤ 22	
Reflections collected	13852	
Independent reflections	6557 [R(int) = 0.0212]	
Completeness to theta = 28.28°	99.2 %	
Absorption correction	Semi-empirical from equivalents	
Max. and min. transmission	0.756 and 0.565	
Refinement method	Full-matrix least-squares on F ²	
Data / restraints / parameters	6557 / 3 / 388	
Goodness-of-fit on F ²	1.069	
Final R indices [I > 2σ(I)]	R1 = 0.0304, wR2 = 0.0765	
R indices (all data)	R1 = 0.0383, wR2 = 0.0803	
Largest diff. peak and hole	1.193 and -0.774 e.Å ⁻³	

[Cu(L13)(H₂O)(MeOH)]

Empirical formula	C ₁₂ H ₁₆ CuN ₂ O ₆
Formula weight	347.81
Temperature/K	110.0
Crystal system	Monoclinic
Space group	P2 ₁ /n
a/Å, b/Å, c/Å	10.2445(5), 13.1835(5), 10.7163(5)
α/°, β/°, γ/°	90.00, 108.444(5), 90.00
Volume/Å ³	1372.97(11)
Z	4
ρ _{calc} /mg mm ⁻³	1.683
μ/mm ⁻¹	1.620
F(000)	716
Theta range for data collection	3.33 to 25.05°
Index ranges	-12 ≤ h ≤ 12, -15 ≤ k ≤ 15, -12 ≤ l ≤ 12
Reflections collected	13705
Independent reflections	2436[R(int) = 0.1120]
Data/restraints/parameters	2436/59/212
Goodness-of-fit on F ²	1.064
Final R indexes [<i>I</i> >2σ (<i>I</i>)]	R ₁ = 0.0387, wR ₂ = 0.0816
Final R indexes [all data]	R ₁ = 0.0482, wR ₂ = 0.0879
Largest diff. peak/hole/e Å ⁻³	0.411/-0.375

[Cu(HL15)₂Cu(HL15)(L15)].Na.3H₂O.CH₃OH

Empirical formula	C _{40.81} H ₄₁ Cu ₂ F ₄ N ₈ Na O _{16.19}	
Formula weight	1128.67	
Temperature	110(2) K	
Wavelength	0.71073 Å	
Crystal system	Triclinic	
Space group	P-1	
Unit cell dimensions	a = 9.9798(8) Å	α = 74.730(2)°
	b = 11.8246(10) Å	β = 81.705(2)°
	c = 20.4296(17) Å	γ = 82.246(2)°
Volume	2289.5(3) Å ³	
Z	2	
Density (calculated)	1.636 Mg/m ³	
Absorption coefficient	1.036 mm ⁻¹	
F(000)	1152.8	
Theta range for data collection	1.79 to 28.34°	
Index ranges	-13 ≤ h ≤ 13, -15 ≤ k ≤ 15, -27 ≤ l ≤ 26	
Reflections collected	24057	
Independent reflections	11321 [R(int) = 0.0382]	
Completeness to theta = 28.34°	99.0 %	
Absorption correction	Semi-empirical from equivalents	
Max. and min. transmission	0.920 and 0.796	
Refinement method	Full-matrix least-squares on F ²	
Data / restraints / parameters	11321 / 13 / 751	
Goodness-of-fit on F ²	1.019	
Final R indices [I > 2σ(I)]	R1 = 0.0454, wR2 = 0.0974	
R indices (all data)	R1 = 0.0726, wR2 = 0.1099	
Largest diff. peak and hole	0.623 and -0.377 e.Å ⁻³	

[Cu(L17)₂(H₂O)₂]

Empirical formula	C ₁₁ H ₁₆ Cu N ₂ O ₈	
Formula weight	367.80	
Temperature	110(2) K	
Wavelength	0.71073 Å	
Crystal system	Triclinic	
Space group	P-1	
Unit cell dimensions	a = 7.2658(7) Å	α = 81.01(2)°
	b = 7.3165(7) Å	β = 87.867(2)°
	c = 13.8816(13) Å	γ = 73.718(2)°
Volume	699.64(12) Å ³	
Z	2	
Density (calculated)	1.746 Mg/m ³	
Absorption coefficient	1.605 mm ⁻¹	
F(000)	378	
Theta range for data collection	2.92 to 28.29°	
Index ranges	-9 ≤ h ≤ 9, -9 ≤ k ≤ 9, -18 ≤ l ≤ 18	
Reflections collected	7147	
Independent reflections	3444 [R(int) = 0.0152]	
Completeness to theta = 28.29°	98.9 %	
Absorption correction	Semi-empirical from equivalents	
Max. and min. transmission	0.968 and 0.648	
Refinement method	Full-matrix least-squares on F ²	
Data / restraints / parameters	3444 / 0 / 229	
Goodness-of-fit on F ²	1.089	
Final R indices [I > 2σ(I)]	R1 = 0.0280, wR2 = 0.0729	
R indices (all data)	R1 = 0.0321, wR2 = 0.0755	
Largest diff. peak and hole	0.530 and -0.480 e.Å ⁻³	

[Cu(I)₂HL8(PPh₃)₅]PF₆

Empirical formula	C ₄₀₁ H ₃₃₆ Cu ₈ F ₂₄ N ₁₂ O ₂₁ P ₂₄
Formula weight	7366.42
Temperature/K	110.0
Crystal system	monoclinic
Space group	P2 ₁ /a
a/Å	25.9574(5)
b/Å	18.2375(3)
c/Å	37.8159(6)
α/°	90.00
β/°	100.0501(18)
γ/°	90.00
Volume/Å ³	17627.3(5)
Z	2
ρ _{calc} /mg/mm ³	1.388
m/mm ⁻¹	0.661
F(000)	7604.0
2θ range for data collection	5.7 to 57.84°
Index ranges	-35 ≤ h ≤ 24, -22 ≤ k ≤ 23, -49 ≤ l ≤ 44
Reflections collected	71520
Independent reflections	38784[R(int) = 0.0311]
Data/restraints/parameters	38784/114/2763
Goodness-of-fit on F ²	1.067
Final R indexes [I ≥ 2σ(I)]	R ₁ = 0.0614, wR ₂ = 0.1269
Final R indexes [all data]	R ₁ = 0.0874, wR ₂ = 0.1401
Largest diff. peak/hole / e Å ⁻³	1.03/-1.15

[Cu(I)₂HL9(PPh₃)₅]PF₆

Empirical formula	C ₁₀₄ H ₉₈ Cu ₂ F ₆ N ₂ O ₆ P ₆
Formula weight	1898.74
Temperature/K	110.00(10)
Crystal system	monoclinic
Space group	P2 ₁ /n
a/Å	12.7572(3)
b/Å	45.481(3)
c/Å	16.3277(4)
α/°	90.00
β/°	99.241(2)
γ/°	90.00
Volume/Å ³	9350.6(7)
Z	4
ρ _{calc} /mg/mm ³	1.349
m/mm ⁻¹	0.625
F(000)	3944.0
2θ range for data collection	5.82 to 58.28°
Index ranges	-11 ≤ h ≤ 16, -58 ≤ k ≤ 50, -21 ≤ l ≤ 21
Reflections collected	36824
Independent reflections	21014[R(int) = 0.0307]
Data/restraints/parameters	21014/26/1150
Goodness-of-fit on F ²	1.134
Final R indexes [I ≥ 2σ (I)]	R ₁ = 0.0614, wR ₂ = 0.1129
Final R indexes [all data]	R ₁ = 0.0770, wR ₂ = 0.1207
Largest diff. peak/hole / e Å ⁻³	0.91/-0.81

[Cu(I)₂HL9(PPh₃)₄]PF₆·2Et₂O·2H₂O

Empirical formula	C ₈₉ H _{86.36892} Cu ₂ F ₆ N ₂ O _{4.68446} P ₅
Formula weight	1654.85
Temperature/K	110
Crystal system	triclinic
Space group	P-1
a/Å	12.937(3)
b/Å	13.150(4)
c/Å	24.582(3)
α/°	90.543(15)
β/°	95.990(14)
γ/°	100.77(2)
Volume/Å ³	4084.2(17)
Z	2
ρ _{calc} /mg/mm ³	1.346
m/mm ⁻¹	0.685
F(000)	1718.0
2θ range for data collection	5.66 to 55.98°
Index ranges	-17 ≤ h ≤ 11, -16 ≤ k ≤ 15, -29 ≤ l ≤ 30
Reflections collected	25830
Independent reflections	16093[R(int) = 0.0315]
Data/restraints/parameters	16093/19/1032
Goodness-of-fit on F ²	1.060
Final R indexes [I ≥ 2σ (I)]	R ₁ = 0.0499, wR ₂ = 0.1137
Final R indexes [all data]	R ₁ = 0.0716, wR ₂ = 0.1260
Largest diff. peak/hole / e Å ⁻³	0.62/-0.62

[Zn(HL7)₂].H₂O.DMSO

Empirical formula	C ₂₃ H ₂₈ N ₄ O ₈ Zn
Formula weight	553.86
Temperature/K	110.4
Crystal system	triclinic
Space group	P-1
a/Å, b/Å, c/Å	9.5115(6), 10.4966(6), 13.7572(9)
α/°, β/°, γ/°	70.049(6), 79.268(5), 74.847(5)
Volume/Å ³	1239.03(13)
Z	2
ρ _{calc} /mg mm ⁻³	1.485
μ/mm ⁻¹	1.046
F(000)	576
Theta range for data collection	3.0009 to 49.9474°
Index ranges	-5 ≤ h ≤ 11, -10 ≤ k ≤ 12, -15 ≤ l ≤ 16
Reflections collected	6342
Independent reflections	4340[R(int) = 0.0211]
Data/restraints/parameters	4340/0/339
Goodness-of-fit on F ²	1.057
Final R indexes [I > 2σ (I)]	R ₁ = 0.0398, wR ₂ = 0.0881
Final R indexes [all data]	R ₁ = 0.0484, wR ₂ = 0.0937
Largest diff. peak/hole/e Å ⁻³	1.202/-0.375

[Zn(HL8)₂].H₂O

Empirical formula	C ₂₁ H ₂₂ N ₆ O ₁₂ Zn
Formula weight	615.82
Temperature	110(2) K
Wavelength	0.71073 Å
Crystal system	Triclinic
Space group	P-1
Unit cell dimensions	a = 9.1998(8) Å α = 98.2510(10)° b = 12.1658(10) Å β = 110.4530(10)° c = 12.4475(10) Å γ = 93.257(2)°
Volume	1283.20(18) Å ³
Z	2
Density (calculated)	1.594 Mg/m ³
Absorption coefficient	1.032 mm ⁻¹
F(000)	632
Theta range for data collection	1.70 to 28.33°
Index ranges	-12 ≤ h ≤ 12, -16 ≤ k ≤ 16, -16 ≤ l ≤ 16
Reflections collected	17406
Independent reflections	6364 [R(int) = 0.0178]
Completeness to theta = 28.33°	99.4 %
Absorption correction	Semi-empirical from equivalents
Max. and min. transmission	0.765 and 0.627
Refinement method	Full-matrix least-squares on F ²
Data / restraints / parameters	6364 / 0 / 383
Goodness-of-fit on F ²	1.046
Final R indices [I > 2σ(I)]	R1 = 0.0335, wR2 = 0.0888
R indices (all data)	R1 = 0.0365, wR2 = 0.0905
Largest diff. peak and hole	0.971 and -0.579 e.Å ⁻³

[Zn(HL9)₂].H₂O.CH₃OH

Empirical formula	C ₂₂ H ₂₄ Cl ₂ N ₄ O ₈ SZn
Formula weight	640.78
Temperature/K	110K
Crystal system	Triclinic
Space group	P-1
a/Å, b/Å, c/Å	8.5985(7), 10.5440(7), 15.5551(10)
α/°, β/°, γ/°	104.251(6), 95.218(6), 109.582(7)
Volume/Å ³	1264.36(15)
Z	2
ρ _{calc} /mg mm ⁻³	1.683
μ/mm ⁻¹	1.322
F(000)	656
Theta range for data collection	2.95 to 30.08°
Index ranges	-12 ≤ h ≤ 12, -11 ≤ k ≤ 14, -21 ≤ l ≤ 14
Reflections collected	11277
Independent reflections	7335[R(int) = 0.0270]
Data/restraints/parameters	7335/0/363
Goodness-of-fit on F ²	1.040
Final R indexes [I > 2σ (I)]	R ₁ = 0.0371, wR ₂ = 0.0847
Final R indexes [all data]	R ₁ = 0.0467, wR ₂ = 0.0913
Largest diff. peak/hole/e Å ⁻³	0.642/-0.655

[Zn(HL13)₂]

Empirical formula	C ₂₂ H _{24.5} N ₄ O _{9.25} Zn
Formula weight	1116.66
Temperature/K	110.0
Crystal system	tetragonal
Space group	P4 ₃ 2 ₁ 2
a/Å, b/Å, c/Å	21.1918(3), 21.1918(3), 21.6652(4)
α/°, β/°, γ/°	90.00, 90.00, 90.00
Volume/Å ³	9729.7(3)
Z	8
ρ _{calc} /mg mm ⁻³	1.525
μ/mm ⁻¹	1.070
F(000)	4616
2θ range for data collection	5.76 to 55.86°
Index ranges	-25 ≤ h ≤ 24, -26 ≤ k ≤ 13, -28 ≤ l ≤ 25
Reflections collected	32001
Independent reflections	10157[R(int) = 0.0233]
Data/restraints/parameters	10157/15/722
Goodness-of-fit on F ²	1.025
Final R indexes [I > 2σ (I)]	R ₁ = 0.0482, wR ₂ = 0.1155
Final R indexes [all data]	R ₁ = 0.0726, wR ₂ = 0.1329
Largest diff. peak/hole □/□ e Å ⁻³	0.788/-1.624

HCA2

Empirical formula	$C_{16}H_{13}N_2OCl$
Formula weight	284.73
Temperature/K	110.0
Crystal system	triclinic
Space group	P-1
$a/\text{\AA}$, $b/\text{\AA}$, $c/\text{\AA}$	5.2471(3), 8.3279(6), 15.3824(7)
$\alpha/^\circ$, $\beta/^\circ$, $\gamma/^\circ$	92.175(5), 91.516(4), 91.150(5)
Volume/ \AA^3	671.31(7)
Z	2
$\rho_{\text{calc}}/\text{mg mm}^{-3}$	1.409
μ/mm^{-1}	0.281
F(000)	296
Theta range for data collection	3.5322 to 59.9346°
Index ranges	$-7 \leq h \leq 7$, $-11 \leq k \leq 11$, $-20 \leq l \leq 21$
Reflections collected	5933
Independent reflections	3842[R(int) = 0.0224]
Data/restraints/parameters	3842/0/185
Goodness-of-fit on F^2	1.044
Final R indexes [$I > 2\sigma(I)$]	$R_1 = 0.0442$, $wR_2 = 0.1010$
Final R indexes [all data]	$R_1 = 0.0577$, $wR_2 = 0.1100$
Largest diff. peak/hole/ $e \text{\AA}^{-3}$	0.493/-0.284

HCA5

Empirical formula	$C_{16}H_{13}N_3O_3$
Formula weight	295.29
Temperature/K	110.0
Crystal system	monoclinic
Space group	$P2_1/c$
$a/\text{\AA}$, $b/\text{\AA}$, $c/\text{\AA}$	16.429(4), 5.3321(8), 17.054(3)
$\alpha/^\circ$, $\beta/^\circ$, $\gamma/^\circ$	90.00, 114.74(2), 90.00
Volume/ \AA^3	1356.8(5)
Z	4
$\rho_{\text{calc}}/\text{mg mm}^{-3}$	1.446
μ/mm^{-1}	0.103
F(000)	616
Theta range for data collection	2.8858 to 51.9984°
Index ranges	$-19 \leq h \leq 20$, $-6 \leq k \leq 4$, $-19 \leq l \leq 21$
Reflections collected	5760
Independent reflections	2686[R(int) = 0.0226]
Data/restraints/parameters	2686/0/203
Goodness-of-fit on F^2	0.985
Final R indexes [$I > 2\sigma(I)$]	$R_1 = 0.0428$, $wR_2 = 0.0939$
Final R indexes [all data]	$R_1 = 0.0608$, $wR_2 = 0.1039$
Largest diff. peak/hole/ $e \text{\AA}^{-3}$	0.204/-0.276

7.13 Screening of the compounds for anti-mycobacterial activity

The compounds were screened in the Department of Animal Sciences, School of Life Sciences, University of Hyderabad by Dr. Manjula Sritharan's research group

Mycobacterial strain and growth conditions:

Mycobacterium tuberculosis ATCC 27294 was grown in Middlebrook 7H9 broth medium (pH 7.0, Difco, Detroit, Mich., USA) containing 10% (v/v) albumin-dextrose-catalase (ADC; Difco) enrichment and 0.2% glycerol and maintained with shaking at 150 rpm at 37 °C.

Iron-regulated growth was performed in Proskauer and Beck medium (pH 6.8) with iron added at 0.02 µg Fe/mL (low iron) and 8 µg Fe/mL (high iron), respectively. Ferrous sulphate was used as the iron source. The iron-regulated cultures were harvested in the mid-log phase after 10 days of growth. The iron status of the organisms was confirmed by assaying the siderophores mycobactin and carboxymycobactin using established protocols.³¹⁰ Care was taken to ensure that the cells were harvested before the onset of iron limitation in high iron organisms. The cells were washed and re-suspended in the respective medium to get a cell density equivalent to McFarland 1 (3×10^8 cfu/mL) and further adjusted to get an OD_{600nm} of 0.15 (Biophotometer, Eppendorf, USA). This cell suspension was used for the screening of the compounds.

Preparation of the compounds for screening:

Stock solutions of the compounds were prepared in HPLC grade dimethyl sulfoxide (Sigma Chemical Co., St. Louis, Mo., USA) at a concentration of 10 mg/mL. These were filter-sterilized (0.22 µm filters, Sartorius) and stored at -80°C.

Screening of the compounds:

The compounds were first screened in the MB/BacT™ 240 Mycobacteria Detection System (BioMerieux / Organon Teknika, France) followed by the determination of the MIC values by Microplate Alamar Blue assay (MABA). Finally, the MIC values were confirmed in the MB/BacT™ 240 system by growth at MIC and sub-MIC concentrations of the compounds.

Compounds were screened for anti-mycobacterial activity in the MB/BacT™240 Mycobacteria Detection System (BioMerieux / Organon Teknika, France). The detection system employs standard bottles of 10 ml of culture media to which 0.5 mL of the mycobacterial cell suspension (prepared as detailed above) was added. The system also included the 'proportion control' that was inoculated with 0.5 mL of the cell suspension diluted 1:100. The system was standardised for the screening by adding INH at 0.1- 0.5 µg/mL final concentration. All the compounds were added at 256 µg/mL and checked for their effectiveness on *M. tuberculosis*.

This was carried out essentially as described earlier.³¹⁰ Briefly, it included testing of the compounds in 96 clear bottomed, sterile, microtitre plates (Corning, New York, USA). The outer perimeter wells were filled with 200 µL of sterile, distilled water to prevent evaporation from the experimental wells during incubation. 100 µL of 7H9 medium was added to all wells except those of column 2. 100 µL of the compound(s) to be tested was added to column 2. This represented the highest concentration of the compound(s). 100 µL of the compound(s) was added to column 3 followed by serial dilutions of the compounds from columns 3 – 10. Column 11 served as the control with no added drug. 100 µL of the cell suspension (1:50 dilution of the cell suspension prepared above) was added to all wells and the plate was incubated at 37 °C for 5 days. 50 µL of Alamar Blue [Invitrogen Corporation, Carlsbad, Ca., USA; prepared as a 1:1 (v/v) mixture with 10% Tween-80 (Sigma)] was added to the first control well and observed after 12 h. If the colour changed from blue to pink, Alamar Blue was added to all the wells and visual grading of the colour change was made 6 h after the dye addition. The MIC of the specific compound was taken as the lowest concentration in which there was no change of the blue colour of Alamar Blue indicating lack of any viable bacilli.

Once the MIC value was established by MABA, the MICs of the compounds were confirmed by adding them at MIC and sub-MIC concentrations in the MB/BacT™240 system.

Influence of iron levels on the anti-bacterial activity

The organisms were grown in high and low iron conditions as described above. The cells were harvested and re-suspended in the respective medium and tested by MABA, essentially as described above except that the 7H9 medium was replaced by high and low iron Proskauer and Beck medium.

Abbreviations:

4°	quaternary carbon (NMR)
σ	Hammett parameter
β	Bohr magneton (EPR)
δ	chemical shift
ϵ	molar absorption coefficient
λ_{\max}	wavelength of maximum absorption
τ	tau
°C	degrees Celcius
μ	micro
ν	microwave frequency
ν_{asym}	asymmetric stretching (IR)
ν_{sym}	symmetric stretching (IR)
Å	Angstroms (10^{-10} m)
Arg	Argenine
Asn	Arsenin
<i>br</i>	broad (NMR)
<i>bs</i>	broad singlet (NMR)
CAH/s	cinnamaldehyde hydrazone/s
clogP	calculated log P (lipohilicity)
cm^{-1}	wavenumber (IR)
CoA	coenzyme A
COSY	Correlation Spectroscopy
CV	Cyclic voltamometry
Cys	Cysteine
d_x	deuterated (NMR)
<i>d</i>	doublet (NMR)
<i>dd</i>	(double doublet)
DEPT	Distortion Enhancement by Polarisation Transfer
DFT	Density Functional Theory
DMF	Dimethyl formamide
DMSO	Dimethyl sulfoxide
DNA	Deoxyribonucleic acid
DPPH	Diphenylpicrylhydrazyl
EC99	Lowest concentrations, effecting 99% reductions in colony forming units

Et ₂ O	Diethyl ether
ESI-MS	Electronic spray ionisation-Mass Spectrometry
EPR	Electron Paramagnetic Resonance
FTIR	Fourier Transform Infrared spectroscopy
Glu	Glutamic acid
GSP	Glyoxylate shunt pathway
H	magnetic feild (EPR)
h	Planck's constant
hr	hour/s
H _{ar}	aromatic proton/s
His	Histidine
HPLC	High Pressure Liquid Chormatography
HRMS	High Resolution Mass Spectrometry
Hz	Hertz
INA	isonicotinic acid
INH	Isoniazid/ Isonicotinic acid hydrazide
ICL	Isocitrate lyase enzyme
INH	Isoniazid/ Isonicotinic acid hydrazide
IR	Infrared
J	coupling constant
KatG	Catalase-peroxidase
L	ligand
M	Metal
m	multiplet (NMR)
<i>m</i>	medium (IR)
MABA	Microplate Alamar Blue assay
MB/BacT™	Mycobacteria Detection System
MeOH	Methanol
mDa	milli Dalton
MDR	Multiple drug resistance
MIC	Minimum inhibitory concentration
mM	millimolar
Mtb	<i>Mycobacterium tuberculosis</i>
m/z	mass/charge
MHz	megahertz
min	minutes
mol	moles

nm	nanometer
NMR	Nuclear magnetic resonance
NaBH ₄	sodium borohydride
NADH	Nicotinamide Adenine Dinucleotide
LMCT	Ligand to metal charger transfer
PBS	Phosphate Buffered Saline
ppm	parts per million
PVAH/s	pyruvate hydrazone/s
q	quartet (NMR)
s	singlet (s)
s	sharp (IR)
SAR	Structure Activity Relationship
SOD	superoxide dismutase
Ser	Serine
Subsp	subspecies
t	triplet (NMR)
t _{1/2}	half-life
TB	Tuberculosis
THF	Tetrahedronfuran
TLC	Thin-Layer Chromatography
Thr	Threonine
TBAHFP	<i>tetra</i> -butyl ammonium hexafluorophosphate
UV-Vis	Ultraviolet-visible spectroscopy
VT	variable temperature (NMR)
W.H.O	World health organisation
XRD	X-ray Diffraction

References:

- (1) www.diamond.ac.uk/Home/Media/LatestNews/15February2008.html.
- (2) Barrera, L. *Tuberculosis 2007, From Basic Science to Patient Care* 2007, 93.
- (3) Golden, M. P. *Am. Fam. Physician* 2005, 72, 1761.
- (4) Qian, L.; Montellano, P. R. O. d. *Chemical Research Toxicology* 2006, 19, 443.
- (5) Ducati, R. G.; Ruffino-Netto, A.; Luiz Augusto Basso; Santos, D. S. *Mem Inst Oswaldo Cruz, Rio de Janeiro* 2006, 101, 697.
- (6) Jarliera, V.; Nikaido, H. *FEMS Microbiol. Lett.* 1994, 123, 11.
- (7) Zhang, Y. *Annu. Rev. Pharmacol. Toxicol.* 2005, 45, 529.
- (8) F.G.Winder; P.B.Collins *Journal of General Microbiology* 1970, 63, 41.
- (9) Zimhony, O.; Cox, J. S.; Welch, J. T.; Vilchèze, C.; Jacobs, W. R. *Nat. Med.* 2000, 6, 1043.
- (10) Hanouille, X.; Wieruszeski, J.-M.; Rousselot-Pailley, P.; Landrieu, I.; Baulard, A. R.; Lippens, G. *Biochem. Biophys. Res. Commun.* 2005, 331, 452.
- (11) Nishida, C. R.; Montellano, P. R. O. d. *Chemico-Biological Interactions* 2010.
- (12) Takayama, K.; Wang, C.; Besra, G. S. *Clin. Microbiol. Rev.* 2005, 18, 81.
- (13) Carballeira, N. M.; Cruz, H.; Kwong, C. D.; Wan, B.; Franzblau, S. *Lipids* 2004, 39, 675.
- (14) Freese, E.; W.Sheu, C.; Galliers, E. *Nature* 1973, 2, 321.
- (15) Scior, T.; Garcés-Eisele, S. J. *Curr. Med. Chem.* 2006, 13, 2205.
- (16) Rozwarski, D. A.; Grant, G. A.; Barton, D. H. R.; Jacobs, W. R.; Sacchettini, J. C. *Science* 1998, 279, 98.
- (17) Ghiladi, R. A.; Medzihdradszky, K. F.; M.Rusnak, F.; Montellano, P. R. O. d. *J. Am. Chem. Soc.* 2005, 127, 13428.
- (18) Ellard, G. A.; Gammon, P. T. *Journal of Pharmacokinetics and Pharmacodynamics* 1976, 4, 83.
- (19) I.R.Boone; Magee, M.; Turney, D. F. *J. Biol. Chem.* 1955, 781.
- (20) Zhang, Y.; Scorpio, A.; Nikaido, H.; Sun, Z. *J. Bacteriol.* 1999, 181, 2044.
- (21) Raynaud, C.; Lanéelle, M.-A.; Senaratne, R. H.; Draper, P.; Lanéelle, G.; Daffé, M. *Microbiology* 1999, 145, 1359.

- (22) Bamaga, M.; Wright, D. J. M.; Zhang, H. *Int. J. Antimicrob. Agents* 2002, 20, 275.
- (23) Dong, X.; Bhamidi, S.; Scherman, M.; Xin, Y.; McNeil, M. R. *Appl. Environ. Microbiol.* 2006, 72, 2601.
- (24) Feng, Z.; Barletta, R. I. G. *Antimicrob. Agents Chemother.* 2003, 47, 283.
- (25) Dalhoff, A.; Janjic, N.; Echols, R. *Biochem. Pharmacol.* 2006, *Bioorganic and Medicinal Chemistry letters*, 1085.
- (26) Häusler, H.; Kawakami, R. P.; Mlaker, E.; Severn, W. B.; Stütza, A. E. *Biorg. Med. Chem.* 2001, 11, 1679.
- (27) Kim, I. H.; Combrink, K. D.; Ma, Z.; Chapo, K.; Yan, D.; Paul Renick; Morris, T. W.; Pulse, M.; Simeckad, J. W.; Ding, C. Z. *Bioorg Med Chem Lett* 2007, 17, 1181.
- (28) Trampuz, A.; Murphy, C. K.; Rothstein, D. M.; Widmer, A. F.; Landmann, R.; Zimmerl, W. *Antimicrob. Agents Chemother.* 2007, 51, 2540.
- (29) Brufani, M.; Cerrini, S.; Fedeli, W.; Vaciago, A. *J. Mol. Biol.* 1974, 87, 409.
- (30) Levine, C.; Hiasa, H.; Mariani, K. J. *Biochim. Biophys. Acta* 1998, 1400, 29.
- (31) Browne, F. A.; Clark, C.; Bozdogan, B. I.; Dewasse, B. E.; Jacobs, M. R.; Appelbaum, P. C. *Int. J. Antimicrob. Agents* 2002, 20, 93.
- (32) Rivers, E. C.; L.Mancera, R. *Drug Discov. Today* 2008, 13, 1090.
- (33) Smith, C. V.; Sharma, V.; Sacchetti, J. C. *Tuberculosis* 2004, 84, 45.
- (34) Yee, D.; Valiquette, C.; Pelletier, M.; Parisien, I.; Rocher, I.; Menzies, D. *Am. J. Respir. Crit. Care Med.* 2003, 167, 1472.
- (35) WHO
http://www.who.int/tb/challenges/xdr/xdr_mdr_factsheet_2007_en.pdf 2008.
- (36) Rastogi, N.; Goh, K. S. *Antimicrob. Agents Chemother.* 1990, 34, 2061.
- (37) Broussy, S.; Bernardes-Génisson, V.; Quémard, A. k.; Meunier, B.; Bernadou, J. *J. Org. Chem.* 2005, 70, 10502.
- (38) Broussy, S.; Bernardes-Genisson, V.; Gornitzka, H.; Bernadou, J.; Meunier, B. *Org. Biomol. Chem.* 2005, 3, 666.
- (39) Delaine, T.; Bernardes-Génisson, V.; Quémard, A.; Constant, P.; Meunier, B.; Bernadou, J. *Eur.J.Med.Chem.*, 45, 4554.

- (40) Somoskovi, A.; Parsons, L. M.; Salfinger, M. *Respir. Res* 2001, 2, 164.
- (41) Wengenack, N. L.; Hoard, H. M.; Rusnak, F. *J. Am. Chem. Soc.* 1999, 121, 9748.
- (42) Payton, M.; Auty, R.; Delgoda, R.; Everett, M.; Sim, E. *J. Bacteriol.* 1999, 181, 1343.
- (43) Bentrup, K. H.; Miczak, A.; Swenson, D. L.; Russell, D. G. *J. Bacteriol.* 1999, 181, 7161.
- (44) McKinney, J. D.; Bentrup, K. H. n. z.; oz-ElôÃas, E. J. M.; Miczak, A.; Chen, B.; Chan, W.-T.; Swenson, D.; Sacchettini, J. C.; William R. Jacobs, J.; Russell, D. G. *Nature* 2000, 17, 735.
- (45) LaPorte, D. C.; Thorsness, P. E.; DanieEl . Koshland, J. *J. Biol. Chem.* 1985, 260, 10563.
- (46) Russell, D. G. *Nat. Rev. Mol. Cell Biol.* 2001, 2, 1.
- (47) Vanni, P.; Giachetti, E.; Pinzauti, G.; A.Mcfadden, B. *Comp. Biochem. Physiol.* 1990, 95B, 431.
- (48) Schloss, J. V.; Cleland, W. W. *Biochemistry (Mosc).* 1982, 21, 4420.
- (49) Ko, Y. H.; McFadden, B. A. *Arch. Biochem. Biophys.* 1990, 278, 373.
- (50) Ko, Y.-H.; Vanni, P.; McFadden, B. *Arch. Biochem. Biophys.* 1989, 274, 155.
- (51) B.A.McFadden; S.Purohit *Journal of Bacteriology* 1977, 131, 136.
- (52) Mackintosh, C.; Nimmo, H. G. *Biochem. J.* 1988, 250, 25.
- (53) Sharma, V.; Sharma, S.; Bentrup, K. H. z.; McKinney, J. D.; Russell, D. G.; Jr., W. R. J.; Sacchettini, J. C. *Nat. Struct. Biol.* 2000, 7, 663.
- (54) Kumar, R.; Bhakuni, V. *Proteins* 2008, 72, 892.
- (55) Lee, D.; Shin, J.; Yoon, K.-M.; Kim, T.-I.; Lee, S.-H.; Lee, H.-S.; Oh, K.-B. *Bioorg Med Chem Lett* 2008, 18, 5377.
- (56) Lee, H.-S.; Yoon, K.-M.; Han, Y.-R.; Lee, K. J.; Chung, S.-C.; Kim, T.-I.; Lee, S.-H.; Shin, J.; Oh, K.-B. *Bioorg Med Chem Lett* 2009, 19, 1051.
- (57) Oh, K.-B.; Jeon, H. B.; Han, Y.-R.; Lee, Y.-J.; Park, J.; Lee, S.-H.; Yang, D.; Kwon, M.; Shin, J.; Lee, H.-S. *Bioorg Med Chem Lett* 2010, *article in press*.
- (58) Shi, W.; Zhang, X.; Jiang, X.; Yuan, H.; Lee, J. S.; Barry, C. E.; Wang, H.; Zhang, W.; Zhang, Y. *Science* 2011, 333, 1630.
- (59) Bedia, K.-K.; Oruç Elçin, U. S.; Fatma, K.; Nathaly, S.; Sevima, R.; Dimoglo, A. *Eur.J.Med.Chem.* 2006, 41, 1253.
- (60) Ranford, J. D.; Vittal, J. J.; Wang, Y. M. *Inorg. Chem.* 1998, 37, 1226.

- (61) Kaushik, D.; Khan, S. A.; Chawla, G.; Kumar, S. *Eur.J.Med.Chem.* 2010, *45*, 3943.
- (62) Mohameda, M. M. A. Y. A.; El-Bayouki, K. A. M.; Basyouni, W. M.; Abbas, S. Y. *Eur.J.Med.Chem.* 2010, *45*, 3365.
- (63) Todeschinia, A. R.; Miranda, A. L. E. d.; Silva, K. C. M. d.; Parrini, S. C.; Barreiro, E. J. *Eur.J.Med.Chem.* 1998, *33*, 189.
- (64) Cuadro, A. M.; Valenciano, J. s.; Vaquero, J. J.; Alvarez-Builla, J.; Sunkel, C.; Casa-Juana, M. F. d.; Ortega, M. P. *Bioorg Med Chem Lett* 1998, *6*, 173.
- (65) Zhang, Y.; Zhang, L.; Liu, L.; Guo, J.; Wu, D.; Xu, G.; Wang, X.; Jia, D. *Inorg. Chim. Acta* 2010, *363*, 289.
- (66) Terzioglu, N.; Gu'rsoy, A. *Eur.J.Med.Chem.* 2003, *38*, 781.
- (67) Abdel-Aal, M. T.; El-Sayed, W. A.; El-Ashry, E.-S. H. *Arch. Pharm. (Weinheim)*. 2006, *339*, 656.
- (68) Tian, B.; He, M.; Tang, S.; Hewlett, I.; Tan, Z.; Li, J.; Jin, Y.; Yang, M. *Bioorg Med Chem Lett* 2009, *19*, 2162.
- (69) Patricia Melnyk; Leroux, V.; Sergheraert, C.; Grellier, P. *Bioorg Med Chem Lett* 2006, *16*, 31.
- (70) Leigh, M.; Castillo, C. E.; Raines, D. J.; Duhme-Klair, A. K. *ChemMedChem*, *6*, 612.
- (71) Oellerich, M.; Haeckel, R. *Horm. Metab. Res.* 1980, *12*, 182.
- (72) Mohapatra, R. K.; Mishra, U. K.; Mishra, S. K.; Mahapatra, A.; Dash, D. C. *J. Korean Chem. Soc.* 2011, *55*, 926.
- (73) Fraga, A. G. M.; Rodrigues, C. R.; de Miranda, A. L. P.; Barreiro, E. J.; Fraga, C. A. M. *Eur. J. Pharm. Sci.* 2000, *11*, 285.
- (74) Silva, A. G.; Zapata-Sudo, G.; Kummerle, A. E.; Fraga, C. A. M.; Barreiro, E. J.; Sudo, R. T. *Bioorg Med Chem Lett* 2005, *13*, 3431.
- (75) Rollas, S.; Küçüküzgel, Ş. G. *Molecules* 2007, *12*, 1910.
- (76) Suvarapu, L. N.; Seo, Y. K.; Baek, S. O.; Ammireddy, V. R. *E-Journal of Chemistry* 2012, *9*, 1288.
- (77) Belskaya, N. P.; Dehaen, W.; Bakulev, V. *Arkivoc* 2010, *i*, 275.
- (78) Pavan, F. R.; Maia, P. I. d. S.; Leite, S. R. A.; Deflon, V. M.; Batista, A. A.; Sato, D. N.; Franzblau, S. G.; Leite, C. Q. F. *Eur.J.Med.Chem.* 2010, *45*, 1898.
- (79) Rodriguez, G. M. *Trends Microbiol.* 2006, *14*, 320.
- (80) Maccari, R.; Ottana, R.; Vigorita, M. G. *Bioorg Med Chem Lett* 2005, *15*, 2509.

- (81) Maccari, R.; Ottana, R.; Monforte, F.; Vigorita, M. G. *Antimicrob. Agents Chemother.* 2002, 46, 294.
- (82) Vavříková, E.; Polanc, S.; Kočevár, M.; Horváti, K.; Bősze, S.; Stolaříková, J.; Vávrová, K.; Vinšová, J. *Eur.J.Med.Chem.* 2011, 46, 4937.
- (83) Sriram, D.; Yogeewari, P.; Senthilkumar, P.; Dewakar, S.; Rohit, N.; Debjani, B.; Pritesh, B.; B, V.; Pavan, V. V. S.; Thimmappa, H. M. *Med. Chem.* 2009, 5, 1.
- (84) Shingnapurkar, D.; Dandawate, P.; Anson, C. E.; Powell, A. K.; Afrasiabi, Z.; Sinn, E.; Pandit, S.; Venkateswara Swamy, K.; Franzblau, S.; Padhye, S. *Bioorg Med Chem Lett* 2012, 22, 3172.
- (85) Sandbhor, U.; Padhye, S.; Billington, D.; Rathbone, D.; Franzblau, S.; Anson, C. E.; Powell, A. K. *J. Inorg. Biochem.* 2002, 90, 127.
- (86) Maia, P. I. d. S.; Pavan, F. R.; Leite, C. Q. F.; Lemos, S. S.; Sousa, G. F. d.; Batista, A. A.; Nascimento, O. R.; Ellena, J.; Castellano, E. E.; Niquet, E.; Deflon, V. M. *Polyhedron* 2009, 28, 398.
- (87) Maccari, R.; Ottana, R.; Bottari, B.; Rotondo, E.; Vigorita, M. G. *Bioorg Med Chem Lett* 2004, 14, 5731.
- (88) Filho, A. C. M.; Hoffmann, M. E.; Meneghini, R. *Biochem. J.* 1984, 218, 273.
- (89) Jang, S.; Imlay, J. A. *J. Biol. Chem.* 2007, 282, 929.
- (90) Macomber, L.; Imlay, J. A. *Proc. Natl. Acad. Sci. U. S. A.* 2009, 106, 8344.
- (91) Macomber, L.; Rensing, C.; Imlay, J. A. *J. Bacteriol.* 2007, 189, 1616.
- (92) Sousa, E.; Basso, L.; Santos, D.; Diógenes, I.; Longhinotti, E.; de França Lopes, L.; de Sousa Moreira, Í. *J. Biol. Inorg. Chem.* 2012, 17, 275.
- (93) Oliveira, J. S.; Sousa, E. H. S.; Basso, L. A.; Palaci, M.; Dietze, R.; Santos, D. S.; Moreira, I. S. *Chem. Commun.* 2004, 312.
- (94) Basso, L. A.; Schneider, C. Z.; Santos, A. J. A. B. d.; Jr, A. A. d. S.; Campos, M. M.; Soutoa, A. A.; Santos, D. S. *Journal of Brazilian Chemical Society* 2010, 21, 1384.
- (95) Bodiguel, J.; Nagy, J. M.; Brown, K. A.; Jamart-Grégoire, B. *J. Am. Chem. Soc.* 2001, 123, 3832.
- (96) Culotta, V. *J. Biol. Inorg. Chem.* 2010, 15, 1.
- (97) Pym, A. S.; Domenech, P.; Honoré, N.; Song, J.; Deretic, V.; Cole, S. T. *Mol. Microbiol.* 2001, 40, 879.
- (98) Lucarelli, D.; Vasil, M.; Meyer-Klaucke, W.; Pohl, E. *International Journal of Molecular Sciences* 2008, 9, 1548.

- (99) Zhang, L.; Zheng, Y.; Xi, Z.; Luo, Z.; Xu, X.; Wang, C.; Liu, Y. *Mol. Biosyst.* 2009, 5, 644.
- (100) Zhang, L.; Xiao, N.; Pan, Y.; Zheng, Y.; Pan, Z.; Luo, Z.; Xu, X.; Liu, Y. *Chemistry – A European Journal* 2010, 16, 4297.
- (101) Zhang, L.; Zheng, Y.; Callahan, B.; Belfort, M.; Liu, Y. *J. Biol. Chem.* 2011, 286, 1277.
- (102) Patole, J.; Sandbhor, U.; Padhye, S.; Deobagkar, D. N.; Anson, C. E.; Powell, A. *Bioorg Med Chem Lett* 2003, 2003, 51.
- (103) Saha, D. K.; Padhye, S.; Anson, C. E.; Powell, A. K. *Inorg. Chem. Commun.* 2002, 5, 1022.
- (104) Saha, D. K.; Sandbhor, U.; Shirisha, K.; Padhye, S.; Deobagkar, D.; Anson, C. E.; Powell, A. K. *Bioorg Med Chem Lett* 2004, 14, 3027.
- (105) Hunoor, R. S.; Patil, B. R.; Badiger, D. S.; Vadavi, R. S.; Gudasi, K. B.; Chandrashekar, V. M.; Muchchandi, I. S. *Spectrochim. Acta, Pt. A: Mol. Spectrosc.* 2010, 77, 838.
- (106) Bottari, B.; Maccari, R.; Monforte, F.; Ottana, R.; Rotondo, E.; Vigorita, M. G. *Bioorg Med Chem Lett* 2001, 2001, 301.
- (107) Maiti, A.; Ghosh, S. *J. Inorg. Biochem.* 1989, 36, 131.
- (108) Budhani, P.; Iqbal, S. A.; Bhattacharya, S. M. M.; Mitu, L. *Journal of Saudi Chemical Society* 2010, 14, 281.
- (109) Bottari, B.; Maccari, R.; Monforte, F.; Ottana, R.; Rotondo, E.; Vigorita, M. G. *Bioorg Med Chem Lett* 2000, 10, 657.
- (110) Oliveira, J. S.; Sousa, E. H. S.; Basso, L. A.; Palaci, M.; Dietze, R.; Santos, D. S.; Moreira, Í. S. *Chem. Commun.* 2004, 2004, 312.
- (111) Cavicchioli, M.; Leite, C. Q. F.; Sato, D. N.; Massabni, A. C. *Archiv der Pharmazie - Chemistry in Life Sciences* 2007, 340, 538.
- (112) Cuin, A.; Massabni, A. C.; Leite, C. Q. F.; Sato, D. N.; Neves, A.; Szpoganicz, B.; Silva, M. S.; Bortoluzzi, A. I. J. *J. Inorg. Biochem.* 2007, 101, 291.
- (113) Pavan, F. R.; Poelhsitz, G. V.; Nascimento, F. B. d.; d, S. R. A. L.; Batista, A. A.; Deflon, V. M.; f, D. N. S.; Franzblau, S. G.; Leite, C. Q. F. *Eur. J. Med. Chem.* 2010, 2010, 598.
- (114) Nascimento, F. B. d.; Poelhsitz, G. V.; Pavan, F. R.; Sato, D. N.; Leite, C. Q. F.; Selistre-de-Araújo, H. S.; Javier Ellena, E. E. C.; Deflon, V. M.; Batista, A. A. *J. Inorg. Biochem.* 2008, 2008, 1783.
- (115) Vieira, L. M. M.; Almeida, M. V. d.; Lourenço, M. C. S.; Bezerra, F. A. F. M.; Fontes, A. P. S. *Eur. J. Med. Chem.* 2009, 44, 4107.

- (116) Anwar, M. U.; Elliott, A. S.; Thompson, L. K.; Dawe, L. N. *Dalton Trans.* 2011, 40, 4623.
- (117) Louloudi, M.; Nastopoulos, V.; Gourbatsis, S.; Perlepes, S. P.; Hadjiliadis, N. *Inorg. Chem. Commun.* 1999, 2, 479.
- (118) Bu, X.-H.; Du, M.; Zhang, L.; Song, X.-B.; Zhang, R.-H.; Clifford, T. *Inorg. Chim. Acta* 2000, 308, 143.
- (119) Tarafder, M. T. H.; Jin, K. T.; Crouse, K. A.; Ali, A. M.; Yamin, B. M.; Fun, H. K. *Polyhedron* 2002, 21, 2547.
- (120) Mukherjee, P.; Drew, M. G. B.; Tangoulis, V.; Estrader, M.; Diaz, C.; Ghosh, A. *Polyhedron* 2009, 28, 2989.
- (121) Shanbhag, V. M.; Martell, A. E. *Inorg. Chem.* 1990, 29, 1023.
- (122) Casella, L.; Gullotti, M. *J. Am. Chem. Soc.* 1981, 103, 6338.
- (123) P. Anderson, O.; la Cour, A.; Findeisen, M.; Hennig, L.; Simonsen, O.; F. Taylor, L.; Toftlund, H. *J. Chem. Soc., Dalton Trans.* 1997, 111.
- (124) Yang, P.-P.; Song, X.-Y.; Liu, R.-N.; Li, L.-C.; Liao, D.-Z. *Dalton Trans.* 2010, 39, 6285.
- (125) Mahalingam, V.; Chitrapriya, N.; Fronczek, F. R.; Natarajan, K. *Polyhedron* 2008, 27, 1917.
- (126) Liu, W.-Y.; Li, H.-Y.; Zhao, B.-X.; Shin, D.-S.; Lian, S.; Miao, J.-Y. *Carbohydr. Res.* 2009, 344, 1270.
- (127) Eswaran, S.; Adhikari, A. V.; Chowdhury, I. H.; Pal, N. K.; Thomas, K. D. *Eur.J.Med.Chem.* 2010, 45, 3374.
- (128) Bottari, B.; Maccari, R.; Monforte, F.; Ottanà, R.; Rotondo, E.; Vigorita, M. G. *Bioorg Med Chem Lett* 2000, 10, 657.
- (129) Carmo, A. M. L.; Silva, F. M. C.; Machado, P. A.; Fontes, A. P. S.; Pavan, F. R.; Leite, C. Q. F.; Leite, S. R. d. A.; Coimbra, E. S.; Da Silva, A. D. *Biomed. Pharmacother.* 2011, 65, 204.
- (130) Hoonur, R. S.; Patil, B. R.; Badiger, D. S.; Vadavi, R. S.; Gudasi, K. B.; Dandawate, P. R.; Ghaisas, M. M.; Padhye, S. B.; Nethaji, M. *Eur.J.Med.Chem.* 2010, 45, 2277.
- (131) Gökçe, M.; Utku, S.; Küpeli, E. *Eur.J.Med.Chem.* 2009, 44, 3760.
- (132) Smalley Jr, T. L.; Peat, A. J.; Boucheron, J. A.; Dickerson, S.; Garrido, D.; Preugschat, F.; Schweiker, S. L.; Thomson, S. A.; Wang, T. Y. *Bioorg Med Chem Lett* 2006, 16, 2091.
- (133) Vančo, J.; Marek, J.; Trávníček, Z.; Račanská, E.; Muselík, J.; Švajlenová, O. g. *J. Inorg. Biochem.* 2008, 102, 595.

- (134) Filipović, N.; Borrmann, H.; Todorović, T.; Borna, M.; Spasojević, V.; Sladić, D.; Novaković, I.; Andjelković, K. *Inorg. Chim. Acta* 2009, 362, 1996.
- (135) Despaigne, A. A. R.; Silva, J. G. d.; Carmo, A. C. M. d.; Sives, F.; Piro, O. E.; Castellano, E. E.; Beraldo, H. *Polyhedron* 2009, 28, 3797.
- (136) López-Torres, E.; Zani, F.; Mendiola, M. A. *J. Inorg. Biochem.* 2011, 105, 600.
- (137) Stadler, A.-M.; Harrowfield, J. *Inorg. Chim. Acta* 2009, 362, 4298.
- (138) Emara, A. A. A.; El-Sayed, B. A.; Ahmed, E.-S. A. E. *Spectrochim. Acta, Pt. A: Mol. Spectrosc.* 2008, 69, 757.
- (139) Deng, X.; Mani, N. S. *J. Org. Chem.* 2008, 73, 2412.
- (140) Parsons, A. F. *Keynotes in Organic chemistry* 1st ed.; Blackwell Publishing, 2003.
- (141) Bernhardt, P. V.; Martinez, M.; Rodriguez, C.; Vazquez, M. *Dalton Trans.* 2012, 41, 2122.
- (142) Aminabhavi, T. M.; Biradar, N. S.; Patil, C. S. *Inorg. Chim. Acta* 1983, 78, 107.
- (143) Palamarciuc, O. V.; Bourosh, P. N.; Revenco, M. D.; Lipkowski, J.; Simonov, Y. A.; Clérac, R. *Inorg. Chim. Acta* 2010, 363, 2561.
- (144) Monfared, H. H.; Vahedpour, M.; Yeganeh, M. M.; Ghorbanloo, M.; Mayer, P.; Janiak, C. *Dalton Trans.* 2011, 40, 1286.
- (145) Sathyadevi, P.; Krishnamoorthy, P.; Jayanthi, E.; Butorac, R. R.; Cowley, A. H.; Dharmaraj, N. *Inorg. Chim. Acta* 2012, 384, 83.
- (146) Ghosh, T.; Bhattacharya, S.; Das, A.; Mukherjee, G.; Drew, M. G. B. *Inorg. Chim. Acta* 2005, 358, 989.
- (147) Salman M, S. *Arabian Journal of Chemistry* 2010.
- (148) West, D. X.; Swearingen, J. K.; Valdés-Martínez, J.; Hernández-Ortega, S.; El-Sawaf, A. K.; van Meurs, F.; Castiñeiras, A.; Garcia, I.; Bermejo, E. *Polyhedron* 1999, 18, 2919.
- (149) Taylor, M. K.; Trotter, K. D.; Reglinski, J.; Berlouis, L. E. A.; Kennedy, A. R.; Spickett, C. M.; Sowden, R. J. *Inorg. Chim. Acta* 2008, 361, 2851.
- (150) Silva, Y. K. C. d.; Augusto, C. V.; Barbosa, M. L. d. C.; Melo, G. M. d. A.; Queiroz, A. C. d.; Dias, T. d. L. M. F.; Júnior, W. B.; Barreiro, E. J.; Lima, L. M.; Alexandre-Moreira, M. S. *Biorg. Med. Chem.* 2010, 18, 5007.
- (151) Kelly, T. L.; Milway, V. A.; Grove, H.; Niel, V.; Abedin, T. S. M.; Thompson, L. K.; Zhao, L.; Harvey, R. G.; Miller, D. O.; Leech, M.; Goeta, A. E.; Howard, J. A. K. *Polyhedron* 2005, 24, 807.

- (152) Turta, C. I.; Chapurina, L. F.; Donica, I. G.; Voronkova, V.; Healey, E. R.; Kravtsov, V. C. *Inorg. Chim. Acta* 2008, 361, 309.
- (153) Feng Liu, W.-T. W.; Zhang, W.-P.; Chen, F.-Y.; He, S.-Y. *Acta Crystallogr. Sect. E: Struct. Rep. Online* 2007, E63, m2450.
- (154) Frański, R. *J. Mass Spectrom.* 2004, 39, 272.
- (155) Gianelli, L.; Amendola, V.; Fabbrizzi, L.; Pallavicini, P.; Mellerio, G. *G. Rapid Commun. Mass Spectrom.* 2001, 15, 2347.
- (156) Enyedy, E. A.; Primik, M. F.; Kowol, C. R.; Arion, V. B.; Kiss, T.; Keppler, B. K. *Dalton Trans.* 2011, 40, 5895.
- (157) Palla, G.; Predieri, G.; Domiano, P.; Vignali, C.; Turner, W. *Tetrahedron* 1986, 42, 3649.
- (158) Landge, S. M.; Tkatchouk, E.; Benítez, D.; Lanfranchi, D. A.; Elhabiri, M.; Goddard, W. A.; Aprahamian, I. *J. Am. Chem. Soc.* 2011, 133, 9812.
- (159) Mezzina, E.; Spinelli, D.; Lamartina, L.; Buscemi, S.; Frenna, V.; Macaluso, G. *Eur. J. Org. Chem.* 2001, 2002, 203.
- (160) Hammett, L. P. *J. Am. Chem. Soc.* 1937, 59, 96.
- (161) Barba, V.; Va'zquez, J. n.; Lo'pez, F.; Santillan, R.; Farfa'n, N. *J. Organomet. Chem.* 2005, 690, 2351.
- (162) Neuvonen, H.; Neuvonen, K.; Koch, A.; Kleinpeter, E.; Pasanen, P. *J. Org. Chem.* 2002, 67, 6995.
- (163) Neuvonen, K.; lo", F. F.; Neuvonen, H.; Koch, A.; Kleinpeter, E.; Pihlaja, K. *J. Org. Chem.* 2003, 68, 2151.
- (164) Neuvonen, K.; Fülöp, F.; Neuvonen, H.; Pihlaja, K. *J. Org. Chem.* 1994, 59, 5895.
- (165) Neuvonen, K.; Fülöp, F.; Neuvonen, H.; Simeonov, M.; Pihlaja, K. *J. Phys. Org. Chem.* 1997, 10, 55.
- (166) Bell, C. F.; Mortimore, G. R.; Reed, G. L. *Org. Magn. Resonance* 1976, 8, 45.
- (167) Oomens, J.; Steill, J. D. *J. Phys. Chem. A* 2008, 112, 3281.
- (168) Alexandrou, N. E.; Vasilikiotis, G. S. *Spectrochim. Acta, Pt. A: Mol. Spectrosc.* 1967, 23, 677.
- (169) Perjéssy, A.; Hrnčiar, P.; Frimm, R.; Fišera, L. *Tetrahedron* 1972, 28, 3781.
- (170) West, D. X.; Salberg, M. M.; Bain, G. A.; Liberta, A. E. *Transition Met. Chem.* 1997, 22, 180.
- (171) Bernhardt, P. V.; Chin, P.; Sharpe, P. C.; Richardson, D. R. *Dalton Trans.* 2007, 36, 3232.

- (172) Zafiropoulos, T. F.; Plakatouras, J. C.; Perlepes, S. P. *Polyhedron* 1991, 10, 2405.
- (173) Kubas, G. J.; Monzyk, B.; Crumbliss, A. L. *Inorg. Syn.* 1979, 19, 90.
- (174) Sivasankar, C.; Sadhukhan, N.; Bera, J. K.; Samuelson, A. G. *New J. Chem.* 2007, 31, 385.
- (175) Saravanabharathi, D.; Nethaji, M.; Samuelson, A. G. *Polyhedron* 2002, 21, 2793.
- (176) Krishnamoorthy, P.; Sathyadevi, P.; Senthilkumar, K.; Muthiah, P. T.; Ramesh, R.; Dharmaraj, N. *Inorg. Chem. Commun.* 2011, 14, 1318.
- (177) Fujisawa, K.; Noguchi, Y.; Miyashita, Y.; Okamoto, K.-i.; Lehnert, N. *Inorg. Chem.* 2007, 46, 10607.
- (178) Nilsson, K. B.; Persson, I. *Dalton Trans.* 2004, 33, 1312.
- (179) Jakob, A.; Ruffer, T.; Ecorchard, P.; Walfort, B.; Körbitz, K.; Frühauf, S.; Schulz, S. E.; Gessner, T.; Lang, H. *Z. Anorg. Allg. Chem.* 2010, 636, 1931.
- (180) Buss, J. L.; Ponka, P. *Biochim. Biophys. Acta* 2003, 1619, 177.
- (181) Kovařík, P.; Mrkvíčková, Z.; Klimeš, J. r. i. *Journal of Pharmaceutical and Biomedical Analysis* 2008, 47, 360.
- (182) Kalia, J.; Raines, R. T. *Angew. Chem. Int. Ed.* 2008, 47, 7523.
- (183) Klayman, D. L.; Scovill, J. P.; Bartosevich, J. F.; Bruce, J. J. *Med. Chem.* 1983, 26, 35
- (184) Scarpellini, M.; Neves, A.; Hörner, R.; Bortoluzzi, A. J.; Szpoganics, B.; Zucco, C.; Silva, R. A. N.; Drago, V.; Mangrich, A. S.; Ortiz, W. A.; Passos, W. A. C.; Oliveira, M. C. B. d.; Terenzi, H. *Inorg. Chem.* 2003, 42, 8353.
- (185) Liu, S.; Yang, Y.; Zhen, X.; Li, J.; He, H.; Feng, J.; Whiting, A. *Org. Biomol. Chem.* 2012, 10, 663.
- (186) Periasamy, M.; Thirumalaikumar, M. *J. Organomet. Chem.* 2000, 609, 137.
- (187) Wong, S. Y. Y.; Grant, I. R.; Friedman, M.; Elliott, C. T.; Situ, C. *Appl. Environ. Microbiol.* 2008, 74, 5986.
- (188) Carvalho, S. A.; Silva, E. F. d.; Souza, M. V. N. d.; Lourenc, M. C. S.; Vicente, F. R. *Bioorg Med Chem Lett* 2008, 18, 538.
- (189) Yoya, G. K.; Belval, F. B.; Constant, P.; Duran, H.; Daffé, M.; Baltas, M. *Bioorg Med Chem Lett* 2009, 19, 341.
- (190) Bairwa, R.; Kakwani, M.; Tawari, N. R.; Lalchandani, J.; Ray, M. K.; Rajan, M. G. R.; Degani, M. S. *Bioorg Med Chem Lett* 2010, 20, 1623.
- (191) Domadia, P.; Swarup, S.; Bhunia, A.; Sivaraman, J.; Dasgupta, D. *Biochem. Pharmacol.* 2007, 74, 831.

- (192) Dong, X.; Li, Y.; Li, Z.; Cui, Y.; Zhu, H. *J. Inorg. Biochem.* 2012, 108, 22.
- (193) Ming-Ming, W.; A-Gui, X.; Hui, W.; Hao, C.; Zhi-Dong, L.; Yang, Q. *Chinese Journal of Inorganic Chemistry* 2009, 25, 942.
- (194) Sousa, A.; Bermejo, M. R.; Fondo, M.; Garcia-Deibe, A.; Sousa-Pedrares, A.; Piro, O. *New J. Chem.* 2001, 25.
- (195) Shit, S.; Chakraborty, J.; Samanta, B.; Slawin, A.; Gramlich, V.; Mitra, S. *Struct. Chem.* 2009, 20, 633.
- (196) Banerjee, S.; Ray, A.; Sen, S.; Mitra, S.; Hughes, D. L.; Butcher, R. J.; Batten, S. R.; Turner, D. R. *Inorg. Chim. Acta* 2008, 361, 2692.
- (197) Sousa-Pedrares, A.; Camiña, N.; Romero, J.; Durán, M. L.; García-Vázquez, J. A.; Sousa, A. *Polyhedron* 2008, 27, 3391.
- (198) Singh, V. P.; Singh, P.; Singh, A. K. *Inorg. Chim. Acta* 2011, 379, 56.
- (199) Bacci, M. *Chem. Phys.* 1986, 104, 191.
- (200) Zhang, L.; Liu, L.; Jia, D.; Xu, G.; Yu, K. *Inorg. Chem. Commun.* 2004, 7, 1306.
- (201) Despaigne, A. A. R.; Silva, J. G. D.; Carmo, A. C. M. d.; Piro, O. E.; Castellano, E. E.; Beraldo, H. *Inorg. Chim. Acta* 2009, 362, 2117.
- (202) Parrilha, G. L.; Vieira, R. P.; Rebolledo, A. P.; Mendes, I. C.; Lima, L. M.; Barreiro, E. J.; Piro, O. E.; Castellano, E. E.; Beraldo, H. *Polyhedron* 2011, 30, 1891.
- (203) Rigamonti, L.; Cinti, A.; Forni, A.; Pasini, A.; Piovesana, O. *Eur. J. Inorg. Chem.* 2008, 23, 3633.
- (204) Nakajima, K.; Yokoyama, K.; Kano, T.; Kojima, M. *Inorg. Chim. Acta* 1998, 282, 209.
- (205)
- (206) Ketcham, K. A.; Swearingen, J. K.; Castiñeiras, A.; Garcia, I.; Bermejo, E.; West, D. X. *Polyhedron* 2001, 20, 3265.
- (207) Hansen, D. F.; Led, J. J. *Proc. Natl. Acad. Sci. U. S. A.* 2006, 103, 1738.
- (208) Solomon, E. I.; Hare, J. W.; Gray, H. B. *Proc. Natl. Acad. Sci. U. S. A.* 1976, 73, 1389.
- (209) Konecny, R.; Li, J.; Fisher, C. L.; Dillet, V.; Bashford, D.; Noodleman, L. *Inorg. Chem.* 1999, 38, 940.
- (210) Suni, V.; Kurup, M. R. P.; Nethaji, M. *Polyhedron* 2007, 26, 3097.
- (211) Prochniak, G.; Videnova-Adrabska, V.; Daszkiewicz, M.; Pietraszko, A. *J. Mol. Struct.* 2008, 891, 178.

- (212) Wong, H. W.; Lo, K. M.; Ng, S. W. *Acta Crystallogr. Sect. E: Struct. Rep. Online* 2009, *E65*, o419.
- (213) Wong, H. W.; Lo, K. M.; Ng, S. W. *Acta Crystallogr. Sect. E: Struct. Rep. Online* 2009, *E65*, o816.
- (214) Song, Y.; Bac, B. H.; Lee, Y.-B.; Kim, M. H.; Kang, I. M. *CrystEngComm* 2011, *13*.
- (215) Naskar, S.; Naskar, S.; Mondal, S.; Majhi, P. K.; Drew, M. G. B.; Chattopadhyay, S. K. *Inorg. Chim. Acta*, *371*, 100.
- (216) Lipinski, C. A.; Lombardo, F.; Dominy, B. W.; Feeney, P. J. *Adv. Drug Del. Rev.* 2001, *46*, 3.
- (217) <http://www.chemexper.com/tools/propertyExplorer/main.html>.
- (218) Hearn, M. J.; Cynamon, M. H.; Chen, M. F.; Coppins, R.; Davis, J.; Joo-On Kang, H.; Noble, A.; Tu-Sekine, B.; Terrot, M. S.; Trombino, D.; Thai, M.; Webster, E. R.; Wilson, R. *Eur.J.Med.Chem.* 2009, *44*, 4169.
- (219) Metcalfe, C.; Macdonald, I. K.; Murphy, E. J.; Brown, K. A.; Raven, E. L.; Moody, P. C. E. *J. Biol. Chem.* 2007, *283*, 6193.
- (220) Addison, A.; T.Rao *J. Chem. Soc., Dalton Trans.* 1984, *1*, 1349.
- (221) Wood, J. S.; Keijzers, C. P.; De Boer, E.; Buttafava, A. *Inorg. Chem.* 1980, *19*, 2213.
- (222) Lee, H. W.; Sengottuvelan, N.; Seo, H.-J.; Choi, J. S.; Kang, S. K.; Kim, Y.-I. *Bull. Korean Chem. Soc.* 2008, *29*, 1711.
- (223) Li, R.; Zhao, P.; Tang, G.; Tang, X. *Acta Crystallogr. Sect. C: Cryst. Struct. Commun.* 2008, *64*, m339.
- (224) Dayan, O.; Dinçer, M.; Çetinkaya, B.; Özdemir, N. *Acta Crystallogr. Sect. C: Cryst. Struct. Commun.* 2006, *62*, m315.
- (225) Richardson, D. R.; Bernhardt, P. V. *J. Biol. Inorg. Chem.* 1999, *4*, 266.
- (226) Chen, F.; Jin, Z.; Li, H.; He, S. *J. Coord. Chem.* 2011, *64*, 3146.
- (227) Wu, W. P.; Zeng, F. C.; Wu, Y. *Acta Crystallogr. Sect. E: Struct. Rep. Online* 2007, *E63*, m2664.
- (228) Bikas, R.; Hosseini Monfared, H.; Lis, T.; Siczek, M. *Inorg. Chem. Commun.* 2012, *15*, 151.
- (229) Liu, F.; Zhang, W.; Zeng, F.; He, S. *Acta Crystallogr. Sect. E: Struct. Rep. Online* 2007, *E63*, m2450.
- (230) Housecroft, C. E.; Sharpe, A. *Inorganic Chemistry*; 1 ed.; Pearson Education Limited, 2001.
- (231) Holland, P. L.; Tolman, W. B. *J. Am. Chem. Soc.* 1999, *1999*, 7270.

- (232) Munakata, M.; Maekawa, M.; Kitagawa, S.; Matsuyama, S.; Masudat, H. *Inorg. Chem.* 1989, 28, 4300.
- (233) Ducros, V.; Brzozowski, A. M.; Wilson, K. S.; Brown, S. H.; Ostergaard, P.; Schneider, P.; Yaver, D. S.; Pedersen, A. H.; Davies, G. J. *Nat. Struct. Mol. Biol.* 1998, 5, 310.
- (234) Zaitseva, I.; Zaitsev, V.; Card, G.; Moshkov, K.; Bax, B.; Ralph, A.; Lindley, P. *J. Biol. Inorg. Chem.* 1996, 1, 15.
- (235) Sorrell, T. N.; Jameson, D. L. *J. Am. Chem. Soc.* 1983, 105, 6013.
- (236) Manbeck, G. F.; Brennessel, W. W.; Eisenberg, R. *Inorg. Chem.* 2011, 50, 3431.
- (237) Tandon, S. S.; Chander, S.; Thompson, L. K.; Bridson, J. N.; McKeec, V. *Inorg. Chim. Acta* 1994, 219, 55.
- (238) Wu, W.; Zeng, F.; Wu, Y. *Acta Crystallogr. Sect. E: Struct. Rep. Online* 2007, E63, m2664.
- (239) Nilsson, K. B.; Eriksson, L.; Kessler, V. G.; Persson, I. *J. Mol. Liq.* 2007, 131–132, 113.
- (240) Wałęsa-Chorab, M.; Gorczyński, A.; Kubicki, M.; Hnatejko, Z.; Patroniak, V. *Polyhedron* 2012, 31, 51.
- (241) Liu, X.; Xie, Y.; Liu, Q.; Du, C.; Zhu, Y.; Xu, X. *J. Mol. Struct.* 2003, 654, 235.
- (242) Fotouhi, L.; Dehghanpour, S.; Heravi, M. M.; Ardakani, M. D. *Molecules* 2007, 12, 1410.
- (243) Olijnyka, V. V.; Filinchukb, Y. E.; Lenkivs'kac, T. P. *Z. Anorg. Allg. Chem.* 2008, 634, 1587.
- (244) Domenech, A.; Garcia-Espana, E.; Navarro, P.; Miranda, C. *Dalton Trans.* 2006, 35, 4926.
- (245) Sweigert, P.; Xu, Z.; Hong, Y.; Swavey, S. *Dalton Trans.* 2012, 41.
- (246) Azab, H. A.; Banci, L.; Borsari, M.; Luchinat, C.; Sola, M.; Viezzoli, M. S. *Inorg. Chem.* 1992, 31, 4649.
- (247) Durfee, W. S.; Pierpont, C. G. *Inorg. Chem.* 1993, 32, 493.
- (248) Reisner, E.; Arion, V. B.; Guedes da Silva, M. F. t. C.; Lichtenecker, R.; Eichinger, A.; Keppler, B. K.; Kukushkin, V. Y.; Pombeiro, A. J. L. *Inorg. Chem.* 2004, 43, 7083.
- (249) Astruc, D. *Electron Transfer and Radical Processes in Transition-Metal Chemistry*; VCH Publishers 1995.

- (250) Taylor, M. K.; Stevenson, D. E.; Berlouis, L. E. A.; Kennedy, A. R.; Reglinski, J. *J. Inorg. Biochem.* 2006, 100, 250.
- (251) Kaim, W.; Rall, J. *Angew. Chem. Int. Ed.* 2003, 35, 43.
- (252) Compton, R. G.; Sanders, G. H. W. *Electrode Potentials, Oxford Chemistry Primer 41*
Oxford University Press: Oxford, 1996.
- (253) Lamour, E.; Routier, S.; Bernier, J.-L.; Catteau, J.-P.; Bailly, C.; Vezin, H. *J. Am. Chem. Soc.* 1999, 121, 1862.
- (254) Shepard, W. E. B.; Anderson, B. F.; Lewandoski, D. A.; Norris, G. E.; Baker, E. N. *J. Am. Chem. Soc.* 1990, 112, 7817.
- (255) Solomon, E. I.; LaCroix, L. B.; Randall, D. W. *Pure Appl. Chem.* 1998, 70, 799.
- (256) Losada, J.; del Peso, I.; Beyer, L. *Inorg. Chim. Acta* 2001, 321, 107.
- (257) Kilic, A.; Tas, E.; Deveci, B.; Yilmaz, I. *Polyhedron* 2007, 26, 4009.
- (258) McMaster, J.; Beddoes, R. L.; Collison, D.; Eardley, D. R.; Helliwell, M.; Garne, C. D. *Chemistry – A European Journal* 1996, 2, 685.
- (259) Hagen, W. R. *Dalton Trans.* 2006, 35, 4415.
- (260) Hüttermann, J.; Kappl, R. In *Electron Paramagnetic Resonance*; Gilbert, B. C., McLauchlan, K. A., Davies, M. J., Eds.; The Royal Society of Chemistry: 2000; Vol. 17, p 246.
- (261) Chandra, S.; Sharma, A. K. *Spectrochim. Acta, Pt. A: Mol. Spectrosc.* 2009, 72, 851.
- (262) de la Fuente, M.; Cozar, O.; David, L.; Navarro, R.; Hernanz, A.; Bratu, J. *Spectrochim. Acta, Pt. A: Mol. Spectrosc.* 1997, 53, 637.
- (263) Connelly, N. G.; Geiger, W. E. *Chem. Rev.* 1996, 96, 877.
- (264) Ukpong, E. J.; Akpanudo, N. W.; Prasad, J. *African Journal of Pure and Applied Chemistry* 2010, 4, 38.
- (265) Tsierkezos, N. G. *J. Solution Chem.* 2007, 36, 289.
- (266) Darchen, A.; Drissi-Daoudi, R. *J. Appl. Electrochem.* 1997, 27, 448.
- (267) Cameron, P. J.; Peter, L. M.; Zakeeruddin, S. M.; Grätzel, M. *Coord. Chem. Rev.* 2004, 248, 1447.
- (268) Stefanelli, M.; Mandoj, F.; Mastroianni, M.; Nardis, S.; Mohite, P.; Fronczek, F. R.; Smith, K. M.; Kadish, K. M.; Xiao, X.; Ou, Z.; Chen, P.; Paolesse, R. *Inorg. Chem.* 2011, 50, 8281.
- (269) Sarkar, S.; Patra, A.; Drew, M. G. B.; Zangrando, E.; Chattopadhyay, P. *Polyhedron* 2009, 28, 1.
- (270) Ouali, A.; Taillefer, M. *Organometallics* 2007, 26, 65.

- (271) Vijay, M.; Sahay, B.; Gupta, M.; Sharma, I. K.; Verma, P. S. *Asian J. Exp. Sci.* 2007, 21, 377.
- (272) Tsierkezos, N. G.; Ritter, U. *Anal. Lett.* 2011, 44, 1416.
- (273) Caram, J. A.; Vasini, E. J. *Electrochim. Acta* 1994, 39, 2395.
- (274) Tas, E.; Onal, I. H.; Yilmaz, I.; Kilic, A.; Durgun, M. *J. Mol. Struct.* 2009, 927, 69.
- (275) Chen, J.; Russo, R.; Chao, W.; Margerum, L. D.; Malachowski, M. R.; White, R.; Thawley, Z.; Thayer, A.; Rheingold, A. L.; Zakharov, L. N. *Dalton Trans.* 2007, 36, 2571.
- (276) Ottaviani, M. F.; Montalti, F.; Turro, N. J.; Tomalia, D. A. *J. Phys. Chem. B* 1997, 101, 158.
- (277) Neiman, D. K. A. R. *J. Chem. Phys.* 1961, 35, 149.
- (278) Ukpong, E. J.; Akpanudo, N. W.; Prasad, J. *African Journal of Pure and Applied Chemistry* 2010, 4, 38
- (279) Rigamonti, L.; Forni, A.; Pievo, R.; Reedijk, J.; Pasini, A. *Dalton Trans.* 2011, 40, 3381.
- (280) Creaven, B. S.; Czegledi, E.; Devereux, M.; Enyedy, E. A.; Foltyn-Arfa Kia, A.; Karcz, D.; Kellett, A.; McClean, S.; Nagy, N. V.; Noble, A.; Rockenbauer, A.; Szabo-Planka, T.; Walsh, M. *Dalton Trans.* 2010, 39, 10854.
- (281) Syamal, A.; R.L.Dutta *Elements of Magnetochemistry*, Second ed.; Affiliated East-West Press (Pvt.) Ltd., 2010.
- (282) Chikate, R. C.; Belapure, A. R.; Padhye, S. B.; West, D. X. *Polyhedron* 2005, 24, 890.
- (283) Yang, Z.; Yang, R. *Polyhedron* 1996, 15, 3771.
- (284) Saha, C. R. *J. Inorg. Nucl. Chem.* 1979, 42, 159.
- (285) Yin, H. D.; Chen, S. W. *Inorg. Chim. Acta* 2006, 359, 3330.
- (286) Kanwar, S.; Lumba, K.; Gupta, S.; Katoch, V.; Singh, P.; Mishra, A.; Kalia, S. *Biotechnol. Lett.* 2008, 30, 677.
- (287) Zhu, L.; Verma, R.; Roccatano, D.; Ni, Y.; Sun, Z.-H.; Schwaneberg, U. *ChemBioChem* 2010, 11, 2294.
- (288) Patrick, G. L. *An Introduction to Medicinal Chemistry*, 3rd edition ed.; Oxford University Press, 2005.
- (289) Richardson, D.; Vitolo, L. W.; Bakers, E.; Webb, J. *BioMetals* 1989, 2, 69.
- (290) Doungee, P.; Sarel, S.; Wongvisetsirikul, N.; Avramovici-Grisaru, S. *J. Chem. Soc., Perkin Trans. 2* 1995, 319.
- (291) Ranford, J. D.; Vittal, J. J.; Wang, Y. M. *Inorg. Chem.* 1998, 37, 1226.

- (292) Angelusiu, M. V.; Barbuceanu, S.-F.; Draghici, C.; Almajian, G. L. *Eur.J.Med.Chem.* 2010, *45*, 2055.
- (293) Kosak, A.; Janauer, G. E. *Z. Anorg. Allg. Chem.* 1974, *407*, 119.
- (294) Lawson, K.; Gross, J.; Crawford, P. W. *Helv. Chim. Acta* 2004, *87*, 120.
- (295) Wolschendorf, F.; Ackart, D.; Shrestha, T. B.; Hascall-Dove, L.; Nolan, S.; Lamichhane, G.; Wang, Y.; Bossmann, S. H.; Basaraba, R. J.; Niederweis, M. *Proc. Natl. Acad. Sci. U. S. A.* 2011, *108*, 1621.
- (296) Boone, I. U.; Magee, M.; Turney, D. F. *J. Biol. Chem.* 1956, *221*, 781.
- (297) Zhang, Y.; Heym, B.; Allen, B.; Young, D.; Cole, S. *Nature* 1992, *358*, 591.
- (298) Wilming, M.; Johnsson, K. *Angew. Chem. Int. Ed.* 1999, *38*, 2588.
- (299) Chouchane, S.; Lippai, I.; Magliozzo, R. S. *Biochemistry (Mosc.)* 2000, *39*, 9975.
- (300) Jamadar, A.; Duhme-Klair, A.-K.; Vemuri, K.; Sritharan, M.; Dandawate, P.; Padhye, S. *Dalton Trans.* 2012, *41*, 9192.
- (301) McFadden, B. A.; Purohit, S. *J. Bacteriol.* 1977, *131*, 136.
- (302) Kim, Y. H.; G.Y.Suh; M.P.Chung; Kim, H.; O.J.Kwon; S.Y.Lim; S.Y.Lim; Koh, W. J. *BioMed Central Infectious Diseases* 2008, *8*, 1.
- (303) Salfinger, M.; Heifets, L. B. *Antimicrob. Agents Chemother.* 1988, *32*, 1002.
- (304) Tawari, N. R.; Degani, M. S. *J. Comput. Chem.* 2010, *31*, 739.
- (305) Kata, M.; Selmeczi, B. *J. Incl. Phenom. Macro* 1987, *5*, 39.
- (306) Md-Saleh, S. R.; Chilvers, E. C.; Kerr, K. G.; Milner, S. J.; Snelling, A. M.; Weber, J. P.; Thomas, G. H.; Duhme-Klair, A.-K.; Routledge, A. *Bioorg Med Chem Lett* 2009, *19*, 1496.
- (307) Sheldrick, G. M.; Bruker AXS Inc.: Madison, Wisconsin, USA, 2007.
- (308) Sheldrick, G. M. University of Göttingen, Germany, 1997.
- (309) Dolomanov, O. V.; Bourhis, L. J.; Gildea, R. J.; Howard, J. A. K.; Puschmann, H. *J. Appl. Electrochem.* 2009, *42*.
- (310) Sritharan, M.; Yeruva, V. C.; Sivasailappan, S. C.; Duggirala, S. *World J. Microbiol. Biotechnol.* 2006, *22*, 1357.

